Appendix 1:

Meltable copolymeric elastomers based on polydimethylsiloxane with multiplets of pendant liquid-crystalline groups as physical crosslinker: A self-healing structural material with a potential for smart applications

Sabina Horodecka[1,2], Adam Strachota[1]*, Beata Mossety-Leszczak[3], Miroslav Šlouf[1], Alexander Zhigunov[1], Michaela Vyroubalová[1], Dana Kaňková[1], Miloš Netopilík[1]

[1] *Institute of Macromolecular Chemistry, Czech Academy of Sciences, Heyrovskeho nam. 2, CZ-162 06 Praha, Czech Republic*

[2] *Faculty of Science, Charles University, Albertov 6, CZ-128 00 Praha 2, Czech Republic*

[3] *Faculty of Chemistry, Rzeszow University of Technology, al. Powstancow Warszawy 6, PL-35-959 Rzeszow, Poland*

Abstract:

Elastomers with strong physical crosslinks were prepared, based on alternating polydimethylsiloxane (PDMS) spacer segments and pendant quartets of mesogenic building blocks (LC) of azobenzene type. They are structurally related to the well-studied polymers with pendant-chain LC units (light-sensitive actuators), but are generally highly different: The LC units make up only a small volume fraction in our materials and they do not generate elastic energy upon irradiation, but they act as physical crosslinkers with thermotropic properties. Our elastomers lack permanent chemical crosslinks – their structure is fully linear (with some dangling units). The aggregation of the relatively rare and spatially separated LC quartets (of small mesogen units) nevertheless proved to be an efficient crosslinking mechanism: The most attractive product displays a rubber plateau extending over 100°C, melts near 70°C and is soluble in organic solvents. The LC nano-aggregates were also found to be responsible for a continuous temperature region of phase transitions, e.g. two gel points observed by rheology. The physical crosslinks are reversibly disconnected by large mechanical strain at room temperature, but they undergo self-healing, also after sample disruption. The elastomers might be of interest for the development of passive smart materials (e.g. meltable rubbers for 3D-printing, or thermo-reversible visco-elastic mechanical coupling). Our study focuses on the comparison of physical properties and structure-property relationships in two systems, with long and with short PDMS spacer segments.

*Corresponding author
Tel.: (+420) 296 809 451
e-mail address: strachota@imc.cas.cz

1. Introduction

Polysiloxane copolymers with liquid crystalline (mesogenic) building blocks are compounds which can offer fascinating material properties, due to the combination of the highly flexible and hydrophobic polysiloxane with the phase behavior of the mesogenic (LC) units [1, 2]. These materials attract deserved research interest since Finkelmann's pioneering works in the 1980s [3–7]. Since then, most of the studies were dedicated to liquid-crystalline siloxane polymers (LCPs) with mesogens as side chains, whereas main-chain copolymers were studied much less frequently (see e.g. [8–11]). In 1991, Finkelmann prepared mono-domain-oriented nematic LCPs (with side-chain mesogens) via a two-step-crosslinking process [12]. A structural variation of the 'side-chain polysiloxane LCPs' are copolymers with side-on bonded pendant mesogens, i.e. via a linker in the central part of the rod-like LC, which leads to a different ordering behaviour [13]. Long pendant LC chains consisting of multiple mesogen units have also been attached to functionalized polydimethylsiloxane (PDMS), namely via ATRP grafting polymerization [14]. All **the above-discussed polysiloxane LCPs are very rich in the LC component** (typically one LC per siloxane repeat unit), which makes up a dominant volume fraction, and the behaviour of the usually more or less fixed (via chemical crosslinking) mesogens is responsible for practically all the material properties. In contrast to that, **in the presented work, the mesogen makes up a relatively small volume fraction** of the copolymer. The elastic product properties originate from the PDMS component, while melting, solidification, sensitivity to strain damage, as well as self-healing are controlled by the phase behaviour of the mesogen.

Polysiloxane LCPs are most frequently **synthesized** via hydrosilylation (as is the case in this work), namely by grafting vinyl-functional mesogens onto hydrido-functional (Si-H) PDMS. Alternative routes include the use of alkynyl-functional mesogens in the hydrosilylation reaction [15], leading to a more rigid link between PDMS and the mesogen, the thiol-ene addition using vinyl-functionalized PDMS and mesogenic thiol [13, 29, 32], or the azide-yne cycloaddition (Huisgen 'click reaction') [28, 16].

From the **application** point of view, the **polysiloxane LCPs** have been investigated as electro-optic- [17], as light-emitting- [18], gas-separation- (membrane-) [19, 20] and chromatography materials [21], as well as actuators (see e.g. [11, 22–24]). The latter, often referred-to as 'liquid-crystalline elastomers' (LCEs), gained by far the most research attention, especially in recent years. The mechanisms of stimulus response include UV-triggered *cis/trans* isomerization of azobenzene mesogens (e.g. [13, 25–28]), or the nematic → isotropic transition of polyaromatic mesogens (*T*-triggering), e.g. [11, 29, 30, 32]). Other remarkable polysiloxane LCEs include electrostrictive [31], multiple-stimuli-responsive [32], or stimulus-converting systems [30], as well as actuators with programmable shape-memory [25]. In contrast to that, **in this work, the polysiloxane LCPs** were studied **as potential structural smart materials**.

The **aggregation and micro-phase-separation** of the pendant mesogenic (LC) units in the copolymers, which are studied in this work, results in an organic-organic nanocomposite morphology. This morphology plays a key role in the copolymers' material properties,

especially in physical crosslinking and in thermo-mechanical transitions. In **their previous work**, the authors studied in detail the effects of **aggregation behaviour in epoxy-POSS nanocomposites**. A general advantage of such nano-composites in comparison to conventional ones consists in the small size of the reinforcing phase, which allows for the use of the same processing techniques like for filler-free matrices (or thermoset precursors), while optical transparency often can be preserved [33,34]. Additionally, the finely dispersed nanofillers can provide specific chemical [35,36], optical [37,38], electrical [39,40], magnetic [41,42], or gas barrier [43-45] properties to the hybrid material. Last but not least, a marked mechanical reinforcement can be achieved with small amounts of nanofillers, due to their high specific surface [46-50]. In the mentioned studies of the epoxy-POSS hybrids which contained covalently bonded POSS nano-building blocks of molecular type [51–54], the authors demonstrated the key importance of POSS−POSS aggregation. This effect could lead to true nanocomposite morphology (with relatively large inorganic POSS nano-domains) and to very strong mechanical reinforcement, as well as to thermal stabilization. The mutual interactions of organic substituents which covered the POSS surface were found to control the aggregation: The substituents with the strongest crystallization tendency were the most efficient for achieving nano-aggregation and reinforcement. Similar results concerning aggregation were observed also for the heavier homologue of POSS, the stannoxane dodecamer cages (Sn-POSS), which additionally introduced the chemical reactivity of the filler phase (matrix-repair reactions) under oxidizing conditions [55-62].

The experience with the physical crosslinking via aggregation of crystallizing inorganic molecular nano-building blocks, as well as the previous study of liquid-crystalline copolymer networks [42], inspired the authors to the present work, in which the crystallization of mesogenic building blocks is used to reversibly crosslink an elastomer.

The aim of this work was the synthesis of side-chain-type LCP elastomers with reversible physical crosslinks, which could be disconnected by heat or by a suitable solvent. The polymers were based on linear polydimethylsiloxane chains (PDMS) grafted with quartets of mesogens, in which the mesogen-free PDMS segments act as elastic spacers between the grafts. Nano-crystallization of the attached mesogen, further enhanced by PDMS/mesogen incompatibility, was expected to serve as the physical cross-linker, similarly like POSS aggregation in previous works. It was planned to obtain products which combine the mechanical properties of covalently crosslinked elastomers with the processability (fusibility, solubility) of linear polymers. This would open the potential application of such non-covalent networks in the field of 3D-printing, or as viscoelastic coupling materials. A more fundamental aim of this work was to elucidate the structure-property relationship in the PDMS-LC elastomers, namely the efficiency as physical crosslinker of the relatively small mesogen units, as well as the influence of the thermotropic properties of the pendant LC groups on the whole copolymer.

2. Experimental section

2.1. Materials

2.1.1. Commercial chemicals

The dimethylsiloxane-methylhydrosiloxane(25–35%) copolymer "HMS 301" (Mn = 1 900–2 100 g/mol) and the dimethylsiloxane-methylhydrosiloxane(4–8%) copolymer "HMS 064" (Mn = ca. 60 000–65 000 g/mol; for both structures see *Scheme 3* were purchased from Gelest. Chlorofom (solvent) was purchased from Sigma-Aldrich, while a 2% solution of the Karstedt's catalyst (see *Scheme 4*) was purchased from Merck. All the commercial products were used as received. Prior to use, however, the equivalent molecular masses per SiH group of HMS 301 and HMS 064 were more precisely determined by ^{1}H-NMR (see *SI-Fig. 5*, *SI-Table 3* and accompanying text). The so-obtained equivalent molecular masses (per SiH function: HMS 301: 248.700 g/mol, HMS 064: 1320.558 g/mol) were then used for calculations of reactants' amounts in syntheses.

2.1.2. Azo-type mesogen "BAFKU"

The azo-type mesogen BAFKU (see *Scheme 1*, MW = 420.587 g/mol) was synthesized in three stages by the authors according to a previous work [38].
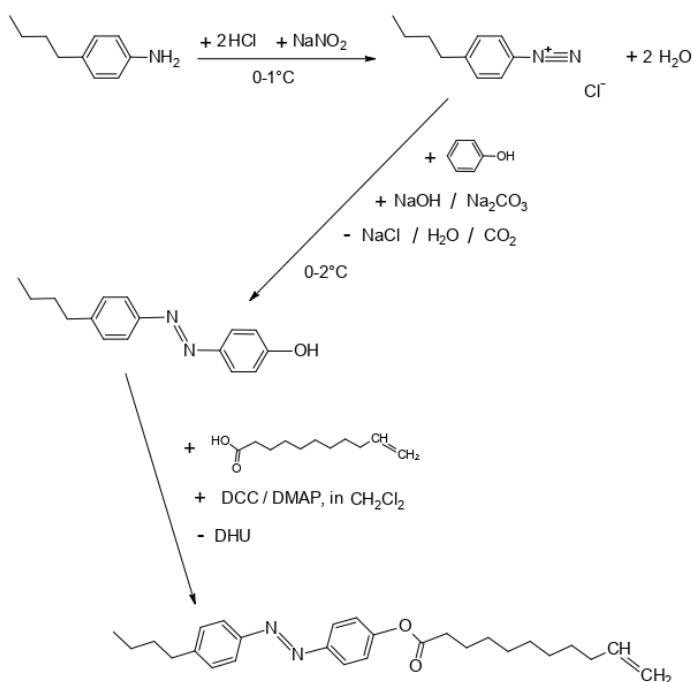
Scheme 1: *Synthesis of the liquid-crystalline mesogen BAFKU [38].*

Table 1: *Amounts of the components used in the synthesis of the copolymers based on PDMS grafted with BAFKU.*

component / Sample name	BAFKU				HMS 301				HMS 064				Chloroform		Karstedt's catalyst	
	[g]	[mmol]	wt%	Vol%	[g]	[mmol]	wt%	Vol%	[g]	[mmol]	wt%	Vol%	[g]	[mL]	[g]	[mmol]
BAFKU$_8$–HMS301	0.492	1.17	61.90	60.26	0.291	1.17	38.10	39.74	-	-	-	-	2.978	2	0.0087	0.0228
BAFKU$_{41}$–HMS064	0.492	1.17	24.14	22.72	-	-	-	-	1.545	1.17	75.86	77.28	2.978	2	0.0087	0.0228

2.1.3. Preparation of the LC-grafted copolymers BAFKU$_8$–HMS301 and BAFKU$_{41}$–HMS064

0.291 g of HMS 301 (1.17 mmol of SiH groups) or 1.545 g of HMS 064 (1.17 mmol of SiH groups) and 0.492 g of the BAFKU mesogen (1.17 mmol) were placed in a small vessel equipped with a magnetic stirring bar. 2 mL of chloroform were added, and after flushing the reactants with argon, they were dissolved by brief stirring at 60°C. Subsequently, Karstedt's catalyst (8.7 mg of a 2 wt% solution ≡ 0.0228 mmol Pt) was added and the solution was stirred at 60°C for 5 min. Thereafter, the reaction mixture was cooled down to room temperature and the solvent was removed under reduced pressure. The BAFKU$_8$–HMS 301 product was free of side-products, but the BAFKU$_{41}$–HMS 064 copolymer contained a crosslinked fraction, which prevented its melting or full dissolution. Hence, raw BAFKU$_{41}$–HMS064 obtained after solvent removal was further purified by dissolving it in tetrahydrofuran, filtering through a syringe filled with 1 cm of cotton wool, after which the solvent was evaporated again. Finally, both copolymers were further dried under vacuum (10 mbar) for 30 min at 90°C (molten state). Thereafter, they were cooled to room temperature and stored.

Yield: BAFKU$_8$–HMS 301: 0.783 g (1.17 mmol) ≡ 100% of theory.

BAFKU$_{41}$–HMS 064: 1.082g (0.622 mmol) ≡ 53.1% of theory.

Characterization by ^{1}H-NMR (CDCl3), δ (ppm):

(BAFKU)$_8$-HMS 301: 7.95 (16H, d, arom.),7.84 (16H, d, arom.), 7.30 (16H, d, arom.), 7.21 (16H, d, arom.), 2.55 (16H, m, CH2), 1.7 (48H, m, CH2), 1.28 (144H, m, CH2), 0.96 (24H, m, CH3), 0.07 (144H, m, CH3)

(BAFKU)$_{45}$-HMS 064: 8.15 (90H, d, arom.), 7.85 (90H, d, arom.), 7.4 (90H, d, arom.), 7.32 (90H, d, arom.), 2.73 (90H, m, CH2), 2.65 (135H, m, CH2), 2.08 (270H, m, CH3), 1.25 (810H, m, CH3), 0.1 (3963H, m, CH3)

5

for comparison:

neat BAFKU: 7.90 (2H, d, arom.), 7.82 (2H, d, arom.), 7.31 (2H, d, arom.), 7.22 (2H, d, arom.), 5.79 (1H, m, CH), 4.94 (2H, m, CH2), 2.59 (2H, m, CH2), 2.56 (2H, m, CH2), 2.03 (2H, m, CH2), 1.65 (2H, m, CH2),1.60 (2H, m, CH2), 1.31 (12H, m, CH2), 0.92 (3H, m, CH3)

neat HMS 301: 4.68 (8H, Si-H), 0.1 (42H, m, CH3),0.07 (120H, m, CH3)

neat HMS 064: 4.72 (45H, Si-H), 0.01 (153H, m, CH3),0.07 (4590H, m, CH3)

<u>**Check of quantitative conversion**</u>:

<u>**FTIR:**</u> Complete disappearance of the peak of the Si–H bond stretching at about 2120 cm^{-1} (see ***SI-Fig. 1 – 3***).

<u>**NMR:**</u> Complete disappearance of the peaks near 4.68 ppm (Si-H) and of the multiplets near 5.79 and 4.94 ppm (vinyl groups of BAFKU) see ***SI-Fig. 1*** and ***6***.

2.2. Characterization of the LC-grafted copolymers

2.2.1. Chemical microstructure

^{1}H-NMR: The chemical structure of the synthesized grafted copolymers was verified using ^{1}H-NMR spectroscopy. The same method was also used for verifying the purity of the mesogen "BAFKU" and for determining the equivalent molecular masses per SiH of the pendant-hydrido-functional polydimethylsiloxanes HMS 301 and HMS 064. The spectra were recorded on a Bruker (Karlsruhe, Germany) Avance DPX 300 spectrometer at 300 MHz. CDCl$_3$-d$_1$ was used as solvent for all experiments. Tetramethylsilane (TMS; $\delta = 0$ ppm) was employed as internal standard.

FT-IR: Completion of hydrosilylation reactions between SiH-functional polydimethyl-siloxanes and the monovinyl-functional mesogen was verified by means of FT-IR spectroscopy. The spectra were recorded in the attenuated total reflection (ATR) mode using a Nicolet 8700 spectrometer (from Thermo Scientific, Madison, WI, USA). The ATR spectra were recorded using a Golden Gate^{TM} heatable Diamond ATR Top-Plate (MKII single reflection ATR system, from Specac, Orprington, UK).

Molecular masses (GPC): The molecular masses of the prepared copolymers and of their precursors were determined by gel permeation chromatography (GPC). For this purpose, we used the Deltachrom pump with computer-controlled piston movement (from Watrex Ltd., Prague, Czech Republic), the autosampler Spark MIDAS (from DataApex Ltd., Prague, Czech Republic), the column "PLgel 5 μm MIXED-D" (5 μm particles; from Polymer Laboratories, now Agilent Technologies, Shropshire, UK), which – according to the manufacturer – separates in the molecular mass range of approximately $10^2 \leq M \leq 4-5 \times 10^5$. The UV/VIS DeltaChrom UVD 200 detector (Watrex Ltd.) with the flow-cell volume of 8 μl, operating at wavelength

λ = 264 nm, the light-scattering photometer DAWN Heleos II measuring at 18 angles of observation, as well as the Optilab T-rEX differential refractometer (both Wyatt Technology Corp., Santa Barbara, CA, USA), were used as detectors in the order of flow. The data were collected into the Astra 6.1 (Wyatt Technology Corp.) and Clarity (DataApex Ltd.) softwares, which communicated with the detectors using a U-PAD2 USB acquisition device.

The mobile phase was tetrahydrofuran (from Fisher Scientific, UK) at 25°C (controlled ambient temperature), used as received. The concentration of measured solutions was 5 mg/mL. Polystyrene standards obtained from Polymer Standards Services (Mainz, Germany) were used for calibration.

2.2.2. Thermal, thermo-mechanical and rheological properties

DMTA and **Rheology**: The advanced multi-functional rheometer ARES-G2 (from TA Instruments, New Castle, DE, USA – part of Waters, Milford, MA, USA) was used for characterizing both the thermo-mechanical and the rheological properties of the prepared copolymers.

The **thermo-mechanical characterization** (including glassy state, glass transition, rubbery region and melting) was carried out using small parallel plate geometry (exchangeable stainless-steel plates, diameter: 6.1 mm). An oscillatory shear deformation at the constant frequency of 1 Hz and at a small strain amplitude (0.001 to 4%, adjusted by auto-strain) was applied. In a first scan, the samples were cooled down from the molten state at 80°C to -130°C, at the rate of 3°C/min. Subsequently, in the second scan, the samples were heated with the same rate back to 80°C. For both scans, the temperature dependences of the storage- and of the loss shear modulus were recorded, as well as of the loss factor (G', G" and tan(δ), respectively).

The **gelation behaviour near the melting point** (rheology) was additionally studied using the multi-frequency temperature sweep test: the temperature range was: 80°C → 20°C (first scan - cooling), followed by 20°C → 80°C (second scan - heating). The simultaneously applied frequencies were 1 Hz (strain amplitude: 1%), 2 Hz (1%), 4 Hz (0.8%), 8 Hz (0.6%), 16 Hz (0.4%), 32 Hz (0.3%) and 64 Hz (0.1%).

In order to evaluate the **rate with which the physical network is formed** after abrupt cooling of molten copolymer to different temperatures, **time sweep tests** with the oscillatory frequency of 1 Hz and the strain amplitude of 1% have been performed. The samples were rapidly cooled from 80°C to the final temperature of 0, 15, 40, 50, 55, 60 and 70°C. The oscillatory time sweep test was running and recording G', G" and tan(δ), as well as the actual temperature, from the beginning of the cooling. In this way, eventual rapid crosslinking during the cooling also could be observed (in addition to slower crosslinking which occurred after the sample temperature stabilized on its final value).

The **possibility to disconnect the reversible physical networks by mechanical strain** was investigated using the **strain sweep test**: at 1 Hz oscillatory frequency, the strain was gradually increased from 0.1 to 1000% and G', G" as well as tan(δ) were recorded. Such experiments were carried out at 0, 10, 20, 30 40, 50, 60, 70, 80 and 90°C.

Eventual **sample stiffening at moderately high oscillatory deformation frequencies** was studied by means of the **frequency sweep test**, where the deformation frequency was gradually

increased from 0.001 to 100 Hz. The data were recorded in five logarithmic series of points – 'decades', with constant deformation amplitude in each decade, namely 50% (at 0.001 Hz), 20, 10, 5 and 1% (at 100 Hz). Such frequency sweep tests were carried out at several different sample temperatures, namely at 0, 20, 30, 50, 60, and 80°C.

DSC: The **nature of the transitions** observed in the copolymers in the DMTA tests was further investigated by differential scanning calorimetry. The standard experiments (with temperatures going down to -90°C) were performed on a DSC1 instrument from Mettler Toledo (Columbus, OH, USA) under nitrogen atmosphere. The heating and cooling rate was always 10°C/min. The samples were first cooled down to -90°C, after which they were subjected to the first heating scan from -90 to +80°C (with final temperature corresponding to the isotropic state of the polymer melt), followed by the first cooling scan (+80 → -90°C) and the second heating scan. **Low-temperature experiments** in the range from -140 up to -80°C (designed to observe the freezing of pendant methyl groups' mobility in PDMS) were carried out under nitrogen atmosphere, using a "8500" calorimeter from PerkinElmer (Waltham, MA, USA) cooled with liquid nitrogen. The heating and cooling rate was always 10°C/min. The samples were first cooled down to -140°C, after which the first heating scan (up to -80°C) was performed, followed by a cooling scan (-80 → -140°C) and the second heating scan.

2.2.3. Phase transitions and ordering of LC domains

Polarized light microscopy (PLM) [63,64]: In order to visualize phase transitions in the studied copolymers, polarized light microscopy was employed. PLM micrographs were recorded with a microscope Nikon Eclipse 80i (Nikon; Japan) equipped with a digital camera ProgRes CT3 (Jenoptik; Germany) and THMS 600 heating stage (Linkam Scientific Instruments Ltd.; UK).

Thin specimens for PLM (thickness <10 μm) were prepared by compression moulding on a heating bar (temperature of the bar 120 °C, compression between two glasses, load 5 kg for 10 min). The best PLM micrographs were obtained for the thinnest polymer films after slight shear deformation, which was induced by manual shift of the two glasses used for compression moulding.

All PLM experiments started at room temperature. The samples were then gradually heated with the rate of 1 °C/min up to a final temperature, where the melt was fully isotropic. After a short pause at the maximum temperature (5 min), the sample was cooled down to room temperature using the same rate.

The intensity of illumination was kept constant and PLM micrographs were recorded during the whole process. The intensity of polarized light was evaluated from the image analysis of the individual micrographs as the mean intensity of all pixels within given micrograph (using the software NIS Elements 4.0 from Laboratory Imaging, Czech Republic; morphological descriptor *MeanIntensity*). As the final output, the normalized *MeanIntensity* as a function of temperature was plotted. It has been demonstrated in our previous studies **[63,64]** that the

polarized light intensity recorded in this way is proportional to the amount of crystalline/anisotropic structures in the investigated specimen.

Small- and wide-angle X-ray scattering (SAXS and WAXS) were employed in order to characterize the crystalline structure of neat BAFKU and of the BAFKU$_{41}$–HMS064 copolymer at different temperatures, as well as to estimate the size of BAFKU domains in the copolymer.

The XRD experiments (SAXS and WAXS) were performed using a pinhole camera (Molecular Metrology System, 'MolMet', Rigaku, Japan, modified by SAXSLAB/Xenocs) attached to a micro-focused X-ray beam generator (Rigaku MicroMax 003) operating at 50 kV and 0.6 mA (30 W). The camera was equipped with a vacuum version of the Pilatus 300K detector. The experimental setup covered the momentum transfer (q) range of $0.05 - 1.5$ Å^{-1}, where q, the scattering vector, is defined as: $q = (4\pi/\lambda) \sin\theta$, where λ (in the given case 1.54 Å) is the wavelength and 2θ is the scattering angle. Calibration of primary beam position and of the sample-to-detector distances was performed using AgBehenate powder. Exposure time for recording one XRD pattern was 1 hour. In order to obtain accurate positions of reflection (interference) peaks, these were fitted by Gaussian peak function.

The tested materials were placed into thin glass capillaries of 2 mm internal width and of 0.01 mm wall thickness, which were sealed after sample filling. The capillaries with the specimens were subsequently placed into a heated holder and were measured at the initial room temperature (20°C), at 85°C (molten) and then at decreasing temperatures of 55°C, 35°C and 20°C (return to room temperature). Except the initial measurement at room temperature, all the following patterns were recorded after the specimens dwelt 10 min at the selected temperature.

2.2.4. Tensile tests (self-healing evaluation)

The tensile properties of the prepared elastomer BAFKU$_{41}$–HMS064 were measured using the same ARES-G2 from TA Instruments which was used for DMTA and rheology tests (maximum allowed tensile force: 20 N), using the method "Axial". The experiments were performed at room temperature, with a cross-head speed of 0.25 mm/s. Rectangular specimens of total specimen length of 20 mm, (length between jaws: 3 mm), width of 5 mm and thickness of 2 mm were used. The copolymer specimens were obtained via melting of the necessary material amounts at 80°C in Teflon moulds.

3. Results and discussion

3.1. Synthesis

Strongly **physically crosslinked meltable rubbers** were synthesized in this work, the **general structure** of which is depicted in the (simplified) *Scheme 2*. Such elastomers offer an application promise as passive smart materials.
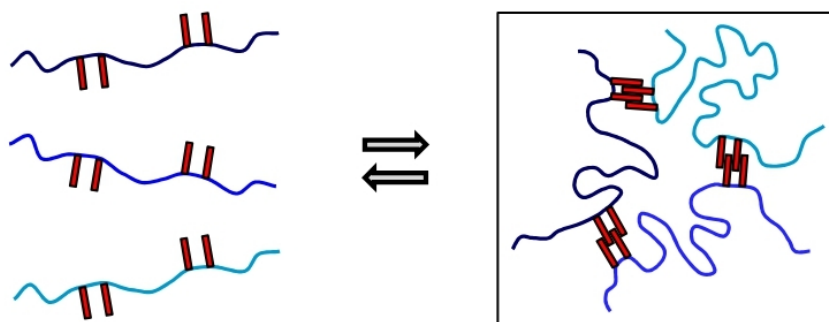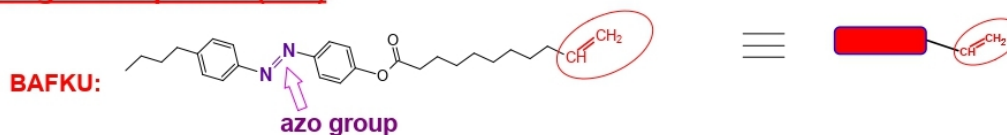

Scheme 2: *Symbolic representation of PDMS grafted with BAFKU and of its physical crosslinking via aggregation of the pendant mesogen (BAFKU) units.*

PDMS components:
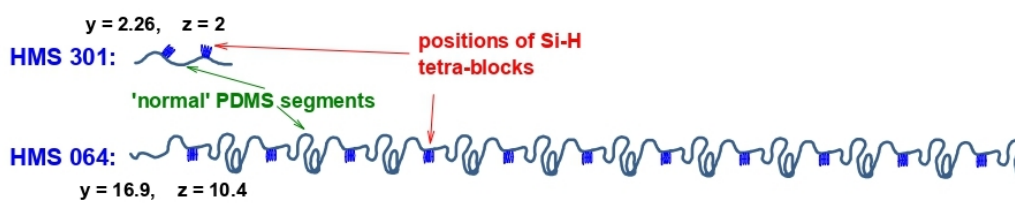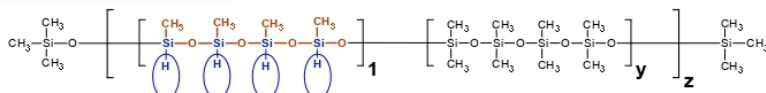
Mesogen component (Azo):

Scheme 3: *Components employed to synthesize the studied copolymers: (top): general structure of the tested PDMS precursors with pendant Si-H functions, as well as the representation of typical molecules of the 'hydrido-polysiloxanes' HMS 301 and HMS 064; (bottom): the mono-vinyl-functional mesogen BAFKU, which was grafted onto the PDMS precursors.*

10

The prepared copolymers are based on hydrido-functional polydimethylsiloxane (PDMS) chains (see **Scheme 3 top**) tethered with pendant liquid-crystalline (LC) building blocks named "BAFKU" (**Scheme 3 bottom**). The pendant BAFKU units occur in separated quartets (see **Scheme 4** and **5**; the above **Scheme 2** is simplified and shows just doublets in their place). The BAFKU quartets originate in the use of cyclic tetramers (named "D4") as starting compounds in the synthesis of the commercial hydrido-functional PDMS precursors (see Supplementary Information: **SI-Scheme 1**), thus leading to scattered quartets of grafting-able SiH functions in the PDMS precursors.
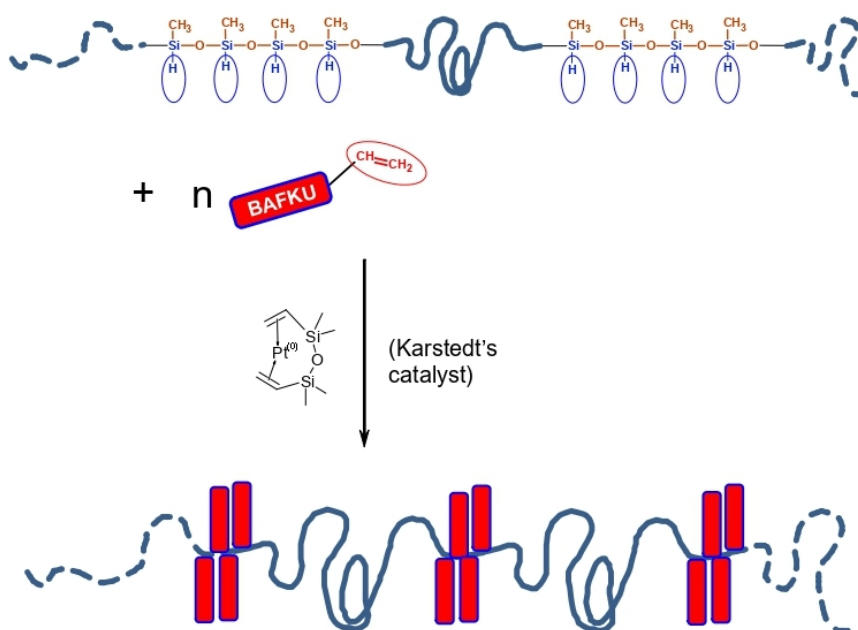
Scheme 4: *Synthesis of BAFKU–PDMS copolymers via hydrosilylation catalysed by the Karstedt catalyst (the formula of the full structure of the products is in **SI-Scheme 2**).*

The **constituent materials** (see **Scheme 3**) of the studied elastomers were **chosen** in order to supply highly flexible polymer chains with a low glass transition temperature (PDMS), as well as building blocks with a strong crystallization tendency (polyaromatic BAFKU mesogen). An important feature was the immiscibility (in absence of solvent) of both components, which favoured the aggregation (nano-phase-separation, see **Scheme 2**) of the pendant mesogen units, and thus the physical crosslinking of the copolymer molecules at the graft sites. The occurrence of the pendant LC units in quartets also was highly favourable for the stability of their nano-aggregates. The BAFKU mesogen was expected to play a similar role in the studied copolymers, like the inorganic POSS nano-building blocks played in the elastomeric epoxy/POSS nanocomposites mentioned in the Introduction **[51–54]**, with the important difference that BAFKU is fully organic. As mesogen, BAFKU also offers the possibility of orientation, if present at sufficient volume fractions. Additionally, UV-light-induced *cis/trans*

isomerization of the azobenzene derivative BAFKU could be of interest for employing the studied polymers as smart materials.

The **copolymers were synthesized via hydrosilylation reactions** (*Scheme 4*), in which two different commercial pendant-Si-H-functional PDMS precursor polymers were grafted with mono-vinyl-functional BAFKU mesogens. The synthesis was considered to be practically a 'click reaction'. One PDMS precursor was "HMS 301" (average molecule: M_n = 1 950 g/mol, 27.6-mer, 8 Si-H functions in 2 quartet blocks, average distance between SiH quartets: 9 repeat units; see structure in *Scheme 3*). The other tested PDMS precursor was the much longer "HMS 064", with large distances between the SiH quartets (average molecule: M_n = 55 000 g/mol, 749-mer, 41.6 Si-H functions in 10.4 quartet blocks, distance between SiH quartets: 67.8 repeat units; see structure in *Scheme 3*). The syntheses were carried out in chloroform (at SiH group concentration of 0.52 or 0.33 mol/L, with HMS301 or HMS064, respectively) at room temperature and catalysed by the Karstedt catalyst (SiH : Pt ratio was 52 : 1). In order to determine highly precise equivalent molecular masses per single SiH functional group, the precursor polymers HMS301 and HMS064 were analysed by ^{1}H-NMR prior to the syntheses (see Supplementary Information: *SI-Fig. 5* and accompanying text which follows after it).
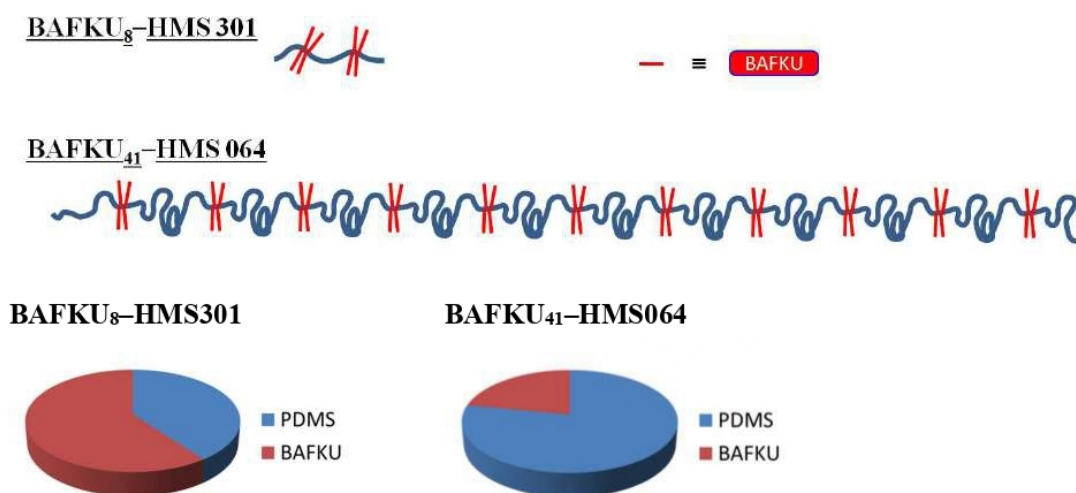
Scheme 5: (top): *Semi-realistic representation of the prepared grafted copolymers BAFKU$_8$–HMS301 and BAFKU$_{41}$–HMS064, highlighting elastic chain length between the BAFKU grafts and the size of the pendant BAFKU groups; (bottom): diagrams of volume fractions (calculated by using* **Equation (1)**) *of the BAFKU mesogen units in the copolymers.*

General properties: The grafting of the colourless liquid PDMS polymers (viscosity: HMS301: 30 mPa*s, HMS064: 7 300 mPa*s) with the azobenzene derivative BAFKU (orange solid) profoundly changed their appearance, as well as their mechanical properties: Both grafted products are orange solids (BAFKU colour), either brittle and waxy (BAFKU$_8$–HMS301), or

rubbery and transparent (BAFKU$_{41}$–HMS064). Already the appearance of the copolymers hence indicates physical crosslinking via LC–LC aggregation, which is of considerable strength (nano-crystallization, as shown in **Scheme 2**). In the elastomer BAFKU$_{41}$–HMS064, the nano-crystallites are sufficiently small in order not to disturb the transparency, while solid BAFKU$_8$–HMS301 is opaque (its melt is transparent). Both copolymers reversibly melt near 60°C, in the temperature range where also neat BAFKU melts (65.7°C) – if tested as pure compound. Both copolymers also can be dissolved in common organic solvents like tetrahydrofuran, chloroform or toluene. The structures of the average molecules of the products are illustrated in **Scheme 5**. In the same Scheme, the volume fractions of the aggregation-able mesogen BAFKU are additionally shown (see also **Table 1**). They were calculated using **Equation (1)** under consideration of the densities ($\rho_{(BAFKU)} = 1.05\ g/cm^3$, $\rho_{(HMS\ 301)} = 0.98\ g/cm^3$ and $\rho_{(HMS\ 064)} = 0.97\ g/cm^3$) and of the stoichiometric synthesis amounts (see **Table 1**) of the individual components.

$$\textit{volume percent } (\textbf{Vol}\%) = \frac{m(component)/\rho(component)}{\Sigma(\frac{m(i)}{\rho(i)})} * \textbf{100\%} \qquad (1)$$

The efficiency of the **grafting of PDMS via hydrosilylation** was of great importance: The reaction observationally went smoothly for the reactant pair HMS301/BAFKU, while it was more difficult with HMS064/BAFKU. In the latter case, side reactions (probably radical reactions of Si-H) were observed, which led to crosslinked by-products (see also literature mentions in **[13,14]**). The synthesis of the copolymer HMS064/BAFKU was optimized, as described in the Experimental Part, so that a practically quantitative conversion was achieved, in combination with acceptably low (47%) material losses due to the undesired crosslinking. The **completeness of conversion** in the hydrosilylation reactions was **verified by** means of **FTIR** (see **SI-Fig. 1a** in the Supplementary Information File) **and ¹H-NMR** (**SI-Fig. 1b**). Quantitative conversion would lead to the disappearance of the very characteristic signals of the Si–H bond in both spectra (FTIR and NMR), and of vinyl-signals in ¹H-NMR. The NMR method is more accurate, especially in case of the lower-functional copolymer HMS064/BAFKU. The recorded NMR spectra (see **SI-Fig. 6**) indicate quantitative conversion in case of HMS301/BAFKU and a nearly quantitative one in case of HMS064/BAFKU, 6.3% of un-reacted SiH groups, as well as ca. 3.3% of un-reacted vinyl groups. A more detailed discussion of the spectra is included in the SI File, preceding **SI-Fig. 1**.

The **molecular masses** of the prepared grafted copolymers, and especially their distributions, were evaluated by means of size exclusion chromatography (**SEC, "GPC"**), using tetrahydrofuran as eluent (sample concentration: 5 mg/mL) and polystyrene standard calibration (valid for the range of 100–500 000 g/mol), with simultaneous UV/Vis-refraction-index- (at λ = 254 nm) and evaporative-light-scattering- (ELSD) detection. The results are shown in **SI-Fig. 7** and **SI-Table 4** in the Supplementary Information File, where also a detailed discussion is included. It can be observed, that the **GPC analysis provides some valuable information** about the obtained PDMS-LC copolymers, **but that it is not well-suited to analyse** their molecular masses **with high precision**, due to their complex structure and

properties (possible BAFKU aggregation in solution). In both the studied products, the content of non-bonded BAFKU is grossly over-estimated by GPC (if compared to ^{1}H-NMR), because of the high sensitivity of both detectors to BAFKU (see details in the discussion in the SI File). Hence, the ^{1}H-NMR spectroscopy remained the most accurate method to evaluate the completeness of the grafting reaction of BAFKU onto the PDMS precursors.

3.2. Thermo-mechanical properties

The reversible physical crosslinking in the prepared copolymers BAFKU$_8$–HMS301 and BAFKU$_{41}$–HMS064, and especially its effect on the thermo-mechanical properties, was studied by means of dynamic-mechanical thermal analysis (DMTA). The results are illustrated in *Figure 1* and *Figure 2*.

In *Figure 1*, the course of the temperature-dependent storage modulus in a heating- and cooling run can be compared for both the copolymers. The *Figure 2* shows the assignment of the DMTA transitions for BAFKU$_{41}$–HMS064 (main graph), as well as the overlay of temperature-dependent storage modulus (G'), loss modulus (G'') and loss factor ($tan\ \delta$) in the inlay image.
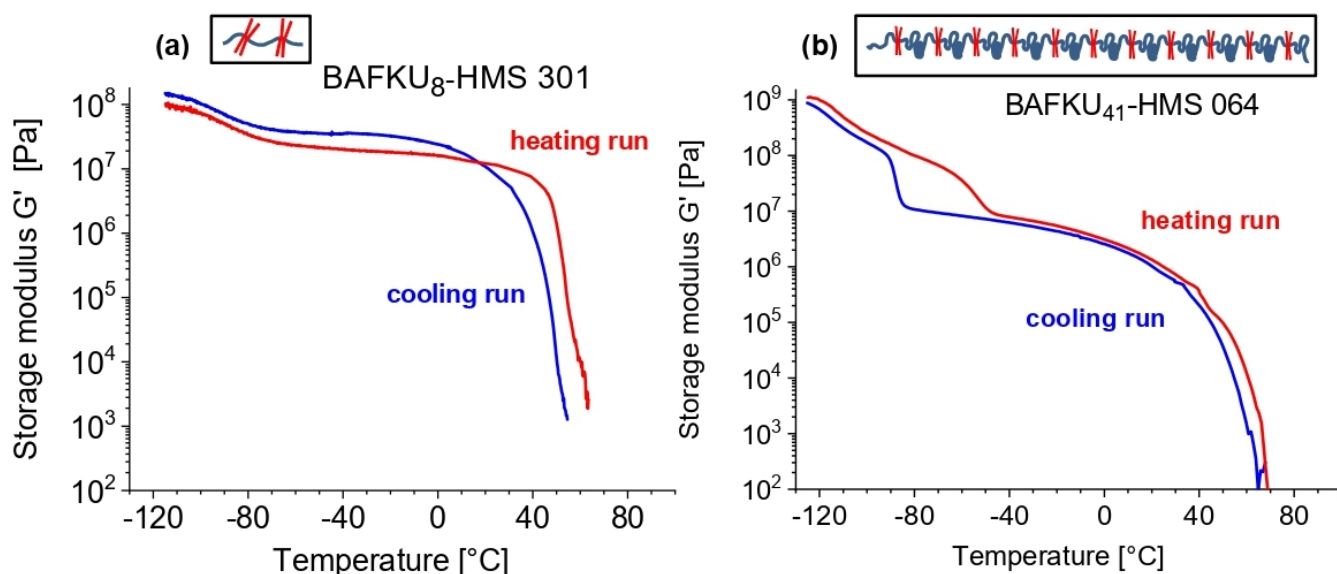
Figure 1: DMTA profiles (temperature-dependent storage modulus G' only) of the copolymers (a) BAFKU$_8$–HMS 301 and (b) BAFKU$_{41}$–HMS 064 recorded in heating and cooling regime.

In *Figure 1*, it can be observed, that the **elastomeric copolymer BAFKU$_{41}$–HMS064**, which contains long PDMS spacer segments (68 repeat units) between the BAFKU quartets (see structure in *Scheme 5*), displays a fairly broad rubbery region which extends from ca. -60 to +40°C, where the storage modulus exceeds 1 MPa (*Figure 1b*). The efficiency of physical crosslinking via BAFKU aggregation (see *Scheme 2*) likely is enhanced by the high number of BAFKU graft positions, namely in average 10.4 per macromolecule (see *Scheme 5* and

structure parameters in **SI-Table 3**). The occurrence of mesogens in quartets further favours their efficient aggregation. Hence, even a small crystallizing pendant group like BAFKU achieves a considerable crosslinking effect.
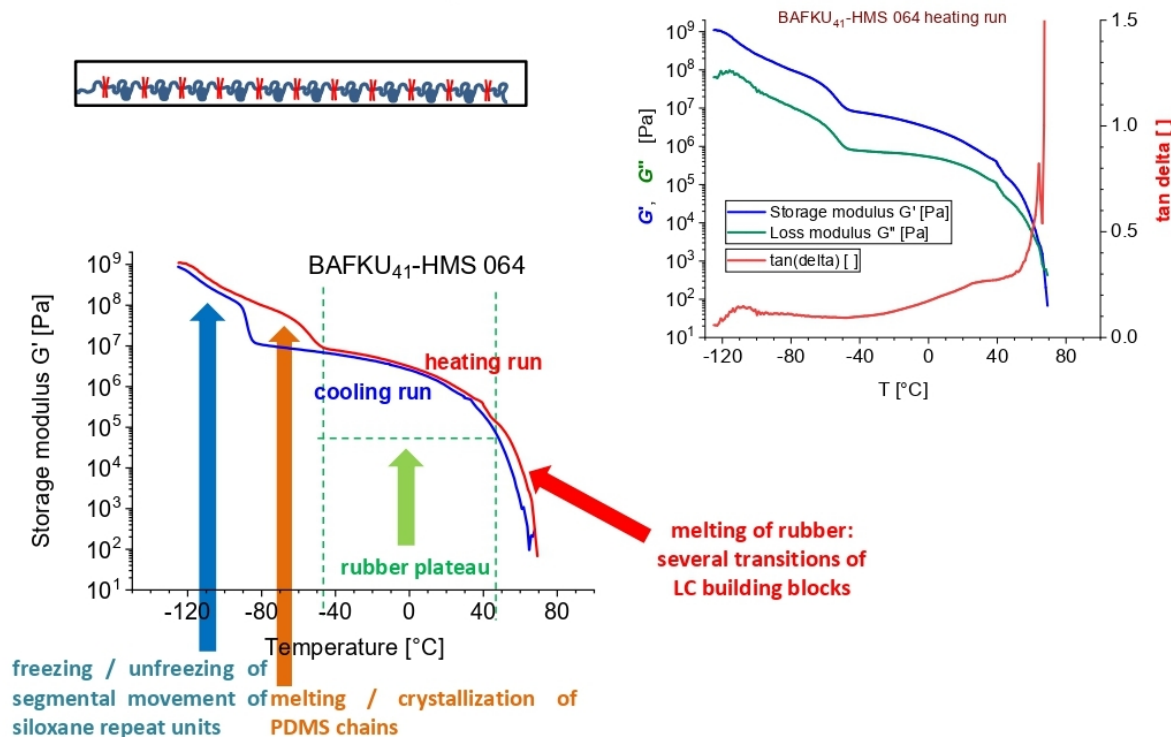
Figure 2: *(main image): Assignment of the transitions observed by DMTA in the copolymer BAFKU$_{41}$–HMS 064; (inlay top right): full DMTA profile of BAFKU$_{41}$–HMS 064 showing the temperature-dependence of the storage modulus G', of the loss modulus G'' and of tan δ.*

Figure 2 (main graph) shows the **assignment of thermo-mechanical transitions** in this copolymer: Near -110°C there is a small step in *G'* (highlighted with blue arrow), which can be assigned to the start of segmental mobility of the pendant methyl groups of PDMS. It is practically the true glass transition of PDMS, in spite of the small step. Next, at -85°C (cooling scan) or at -55°C (heating scan), there is a major step in *G'*, which seemingly appears to be the main glass transition associated with the PDMS chains of the copolymer. However, in view of the observed undercooling of this transition by 30°C ('hysteresis'), as well as of the DSC results discussed further below, these steps in *G'* can be clearly assigned to crystallization/melting of PDMS. The melting and cold crystallization of PDMS has been already discussed in literature, especially in case of linear products with longer chains, see e.g. **[65]**. The PDMS freezing/melting step is followed by a relatively extended rubbery region with gradually decreasing *G'* in the range of $10^7 – 10^5$ Pa, which in turn is succeeded by a relatively steep 'final melting region' (50 – 70°C). This latter feature can be assigned to the loosening of the previously stiff aggregates (nano-crystallites) of BAFKU units, which are responsible for physical crosslinking in the copolymer. The decreasing course of the modulus *G'* in the rubbery

15

region suggests that the physical crosslinks likely could be reversible under mechanical deformation, even at the temperatures of the rubbery region.

An interesting feature, which can be observed in the *Figure 2* (inlay: *G'*, *G''*, *tan δ* = f(*T*)) is the very similar shape and the **proximity of the *G'* and *G''* curves**. As a consequence, *tan δ* displays only one small peak (*tan δ* = 0.15) near -110°C, followed by a nearly invisible flat shoulder in the PDMS melting region and by subsequent relatively high *tan δ* values. In the **rubbery region**, where some mesogenic transitions in the BAFKU aggregates could be suspected, the value of ***tan δ* gradually rises up to 0.25**. Hence, relatively high plastic losses are typical for the copolymer BAFKU$_{41}$–HMS064 in the whole rubbery region. In 'ideal' rubbery materials, *tan δ* can be as low as 0.001. A shoulder (*tan δ* = 0.25) is observed at 40°C (heating run) – possibly a transition in the BAFKU aggregates. Between 50 and 70°C, in the final melting region, *tan δ* increases very steeply from 0.27 to 6.5, which is the most marked *tan δ* change in the whole DMTA profile of BAFKU$_{41}$–HMS064. At the chosen test frequency of 1 Hz, *G''* becomes larger than *G'* at 67°C (simple definition of solid–liquid transition). The gelation/melting near 70°C, the viscoelasticity, as well as the reversibility of the crosslinking in the rubbery region of BAFKU$_{41}$–HMS064 were studied in more detail in rheological experiments described further below.

The **copolymer with the shorter elastic polysiloxane segments, BAFKU$_8$–HMS301,** contains in average 9 repeat units, statistically mixed from octamer and dodecamer segments, between the BAFKU grafts, and it contains in average only 2 grafting regions (see structure in *Scheme 5*). This copolymer displays much simpler thermo-mechanical characteristics than its elastomeric counterpart: It behaves like a brittle 'vitrimer', which near 70°C transforms directly from glass to melt, with no glass → rubber transition. Similarly like in case of BAFKU$_{41}$–HMS064, there can be observed a small step in *G'* in the range -100 to -90°C, assigned to activation/freezing of the wagging movement of pendant methyl groups on PDMS. The only other observable DMTA transition is the melting near +70°C. No crystallization of PDMS chains is observed due to their relatively short length (see also DSC results further below). The properties of the material appear to be dominated by the LC component (BAFKU), whose volume fraction is very high (60%). This product might be of interest as a model compound or as an 'LC oligomer'.

3.3. Phase transitions in the copolymers

3.3.1. DSC: thermal transition behaviour

The nature, and especially the involved values of specific heat of the thermal transitions in the prepared copolymers were investigated in detail by means of differential scanning calorimetry (DSC). The results are summarized in *Figure 3* and *4* (comparison of neat BAFKU mesogen

with the copolymer BAFKU$_8$–HMS301, and the DSC trace of BAFKU$_{41}$–HMS064, respectively).
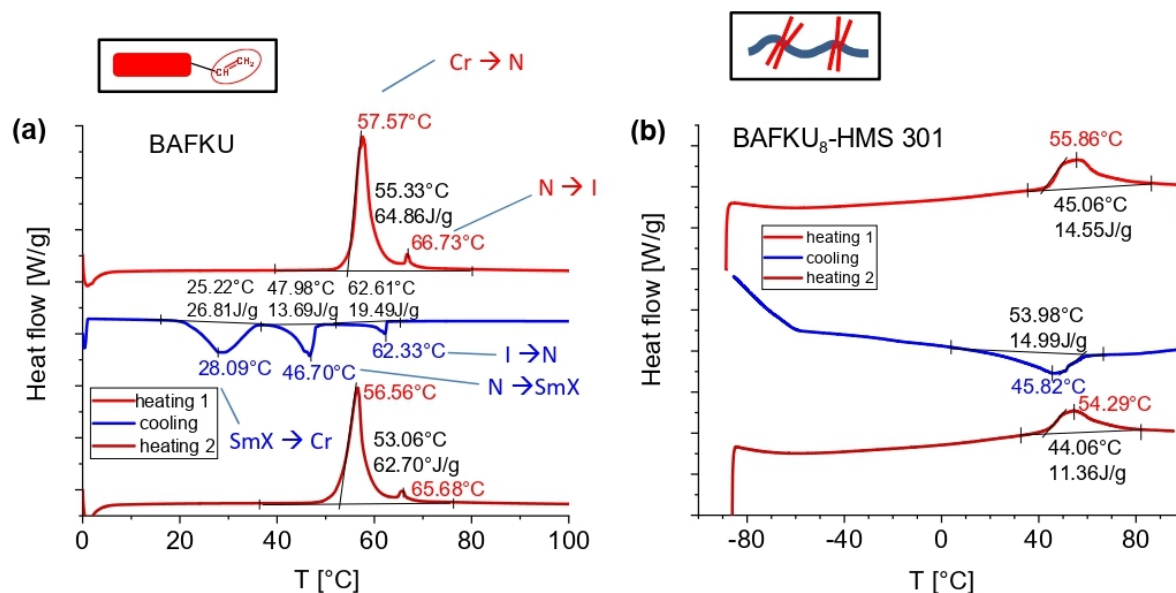

Figure 3: DSC traces of (a) neat BAFKU mesogen; (b) of the copolymer BAFKU$_8$–HMS 301.

In case of the **neat mesogen** (see *Figure 3a*), different behaviour can be observed upon heating and cooling. **BAFKU** generally displays very similar transitions like its epoxy derivative 'BAFKUU' (with oxidized double bond on the longer hydrocarbon chain), which was described in a previous work of the authors **[38]**. Upon heating, only two sharp transitions can be observed in BAFKU, which can be assigned (in analogy to BAFKUU) as crystalline → nematic (57.6°C) and nematic → isotropic (66.7°C). Upon cooling, three distinct transitions occur: isotropic → nematic at 62.3°C, nematic → smectic at 46.7°C, and smectic → crystalline at 28.1°C. The described transitions hence extend over the range from 50 to 70°C while heating, and from 65 to 20°C while cooling (wider range, shifted to lower temperatures).

The **copolymers BAFKU$_8$–HMS301** (*Figure 3b*) and **BAFKU$_{41}$–HMS064** (*Figure 4 b*) display similarly positioned and extended (but somewhat narrower) transition regions like neat BAFKU (*Figure 3a*), but the individual mesogenic transitions are not separated at all in both copolymers: they are joined into broad single transition regions. This behaviour seems to be a consequence of the relatively large volume fractions of BAFKU units in both products (60 and 20 Vol.%, respectively) and of the proximity of the BAFKU units at the grafting sites on one hand, as well as of the higher disorder and of eventual strain in BAFKU aggregates (nano-crystallites), on the other. From the *Figure 3b* it can be seen, that in case of BAFKU$_8$–HMS301, the region of the thermotropic transitions extends from 43 to 70°C upon heating, and from 60 to 20°C upon cooling. In case of the elastomeric BAFKU$_{41}$–HMS064, the analogous regions are 40 to 80°C and 70 to 30°C. The difference in the 'width' of the range of thermotropic

transitions in heating- and cooling regime is much smaller in BAFKU$_8$–HMS301, than in neat BAFKU, and this difference in transition range width practically disappears in BAFKU$_{41}$–HMS064. In the cooling scan of BAFKU$_8$–HMS301 and in both scans of BAFKU$_{41}$–HMS064, the width of the region of mesogen transitions is very similar to the transition region in neat BAFKU in the cooling scan, where three transitions occur between four phases (I→N→Sm→Cr). In case of BAFKU$_8$–HMS301, and even more so in case of BAFKU$_{41}$–HMS064, the upper-limit-temperature of the thermotropic transitions is higher than the temperature of the nematic→ isotropic (final) transition in neat BAFKU. This effect can be attributed to a reduced mobility of the polymer-bonded mesogen units.
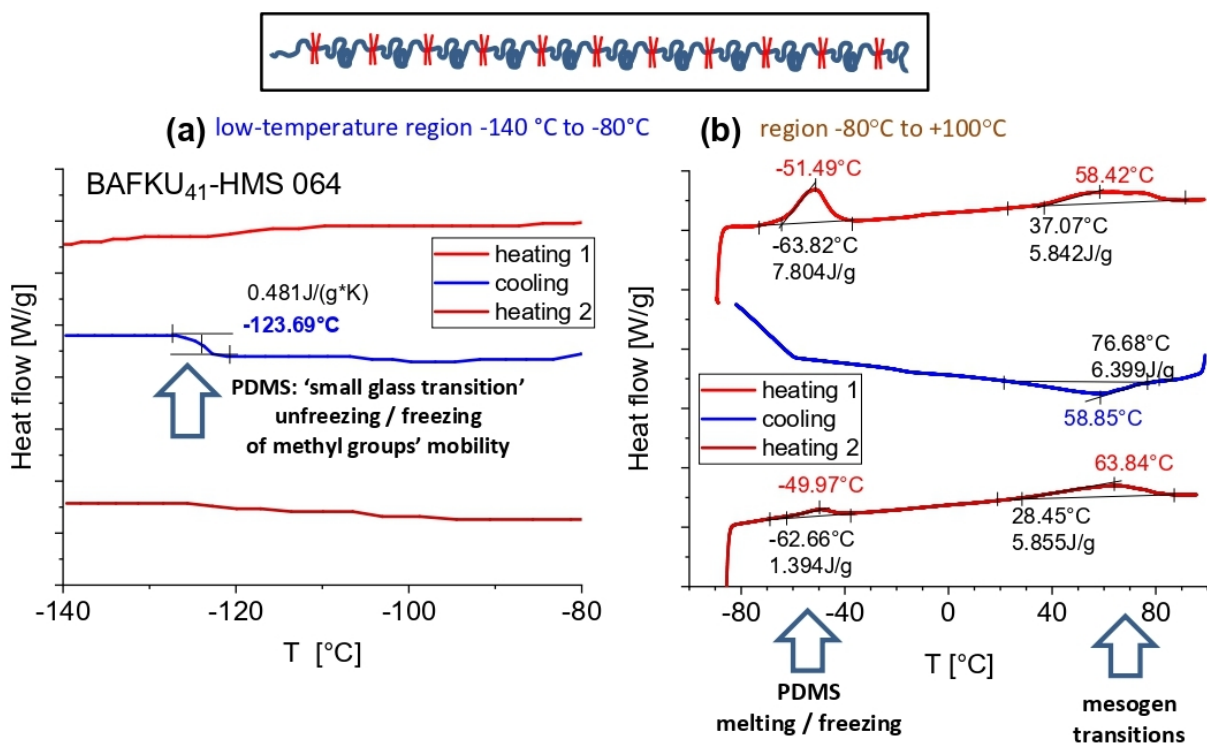
Figure 4: DSC traces of the copolymer BAFKU$_{41}$–HMS064: (a): in the low-temperature region (-140°C to -80°C); (b): in the region from -80°C to +100°C.

Rheological investigations of BAFKU$_{41}$–HMS064, which will be discussed further below (see *Figure 12* and *Figure 13*), suggest that there are **two well-detectable transitions** ('partial gelations') **in the temperature range** of the transitions **observed by DSC**, during both cooling and heating. In case of the rheology experiment done while cooling, the 'second gelation' in the rubbery state is less pronounced than in the heating run (where it is very distinct). The 'second gelation' observed by rheology appears to be induced by an LC transition of BAFKU. The 'first gelation' occurs upon sample solidification, which corresponds to the I→N transition of the BAFKU units. In case of the heating run (rheology), some anomaly (a small step in modulus), yet not a clear third partial gelation, can be recognized near 23°C, in the range of the Cr→Sm transition in BAFKU. It can be hence concluded, that the **domains of aggregated**

BAFKU in the copolymers undergo similar thermotropic transitions like the neat mesogen, although in a less ordered way.

The DSC traces in *Figure 4b* ('normal range') and *Figure 4a* (low-temperature range) also elucidate the vitrification/cold crystallization/melting behaviour of PDMS chains in BAFKU$_{41}$–HMS064: In the cooling runs in both graphs, the PDMS vitrification near -80°C and a definitive one near -123°C can be seen, while in the heating run a PDMS melting (not glass transition) peak is observed (its size depends on exact previous history). The vitrification/cold crystallization/melting behaviour of PDMS in BAFKU$_{41}$–HMS064 is discussed in detail in the SI File, preceding *SI-Fig. 14*.

If the DSC and the further-above DMTA results are considered, it can be concluded, that the copolymer BAFKU$_{41}$–HMS064 combines the complex thermal behaviour of both its constituents, although the ordering of the mesogen units is less perfect in BAFKU$_{41}$–HMS064 than in neat BAFKU. In case of the vitrimeric (BAFKU)$_8$-HMS 301, the copolymer is dominated by the properties of the mesogen (although the ordering of the latter is also disturbed), so that the thermal properties of the small PDMS component are practically not visible in DSC.

3.3.2. X-ray scattering analysis of the phase transitions

In order to deeper elucidate the phase transition behaviour of the copolymer BAFKU$_{41}$–HMS064, which displays the most promising material properties, **temperature-dependent X-ray diffractograms** (SAXS and WAXS) of this product were taken and compared with diffractograms of the pure mesogen BAFKU. The first diffractogram of each series was taken at room temperature (20°C), the next one at 85°C in the fully molten state after a 10 min dwell at this temperature. Subsequent diffractograms were recorded at decreasing temperatures positioned past transition points observed by DSC (cooling) for neat BAFKU, namely at 55, 35 and 20°C (the DSC transitions were at 62, 47 and 28°C, see *Figure 3a* further above). The results of the X-ray experiments are summarized in *Figure 5 – 8* and in *Table 2* and *3* (see also *SI-Fig. 15*, *16*, *SI-Table 5–7* and accompanying comments in the SI File).

In case of **neat BAFKU** (*Figure 5*, as well as *SI-Fig. 15*), the X-ray **diffractogram displays little change between all the test temperatures** (except if it is molten): The BAFKU peaks slightly change their position with temperature (see WAXS: *Figure 5* and *SI-Fig. 15a*): Some minor reflections (see *SI-Fig. 15* and *SI-Table 5*) move to slightly higher angles (and hence to higher q values) with decreasing temperature, which corresponds to a moderate shrinking of the characteristic distances in the crystal or LC structure, in response to sample cooling. No marked changes in the XRD pattern are observed at the temperatures past (below) the respective DSC (cooling run) transitions. After returning to 20°C, the WAXS peaks reach only ¼ of the

original intensity, which means that a considerable part of the sample stays amorphous, possibly due to undesired polymerization of BAFKU via vinyl groups, to which this mesogen has a tendency at elevated temperatures. A **major change** occurs when the isotropic **molten state** is reached (at 85°C), where all peaks disappear, thus confirming a completely disordered **isotropic liquid.** Two amorphous-halo-type features are observed for the melt in the double logarithmic scale in *SI-Fig. 15*, which is typical for an isotropic liquid with rod-like molecules. One of the halos is centred around 4.5° (0.32 Å^{-1} / 2 nm) and appears to originate in the combined reflections caused by both the BAFKU length and width. The other is centred on 18.9° (1.34 Å^{-1} / 0.47 nm), which corresponds to the typical organic inter-molecular distance.
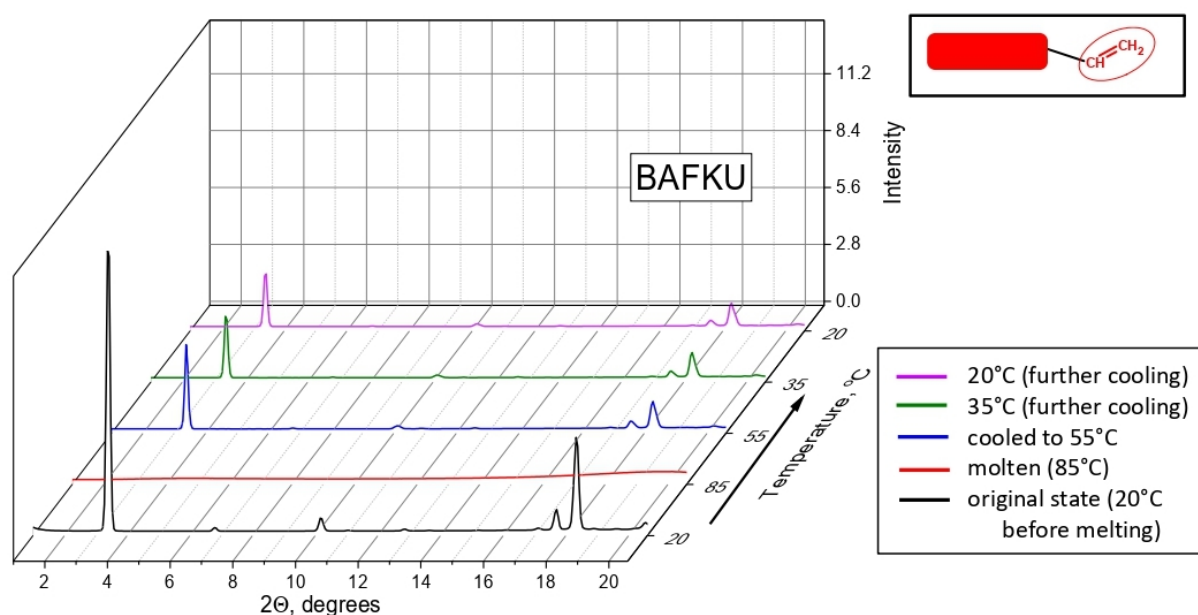
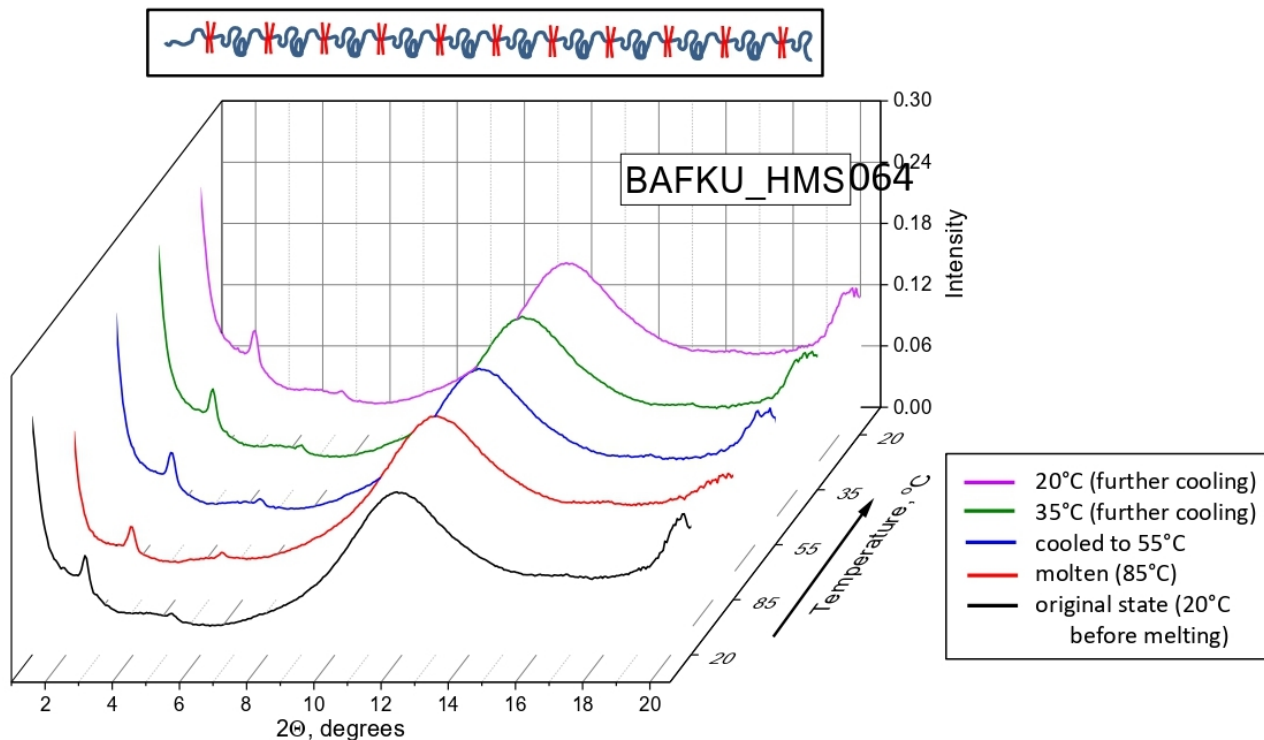***Figure 5:*** *X-ray scattering patterns of neat BAFKU at room temperature (20°C), then at 85°C (molten), and after subsequent cooling to 55°C, to 35°C and to 20°C (back at room temperature).*

Table 2*: X-ray diffraction results: Interference maxima and the corresponding characteristic distances in neat BAFKU (an extended list including weak reflections is in **SI-Table 5**).*

BAFKU			
2Θ [°]	*q* [Å^{-1}]	*d* [nm]	comment
3.40	0.242	2.60	<u>very intense</u>, somewhat diminishes irreversibly
6.80	0.484	1.30	medium/weak, diminishes irreversibly (second order of 3.40°)
10.18	0.724	0.87	<u>medium</u>, diminishes irreversibly
17.70	1.255	0.50	<u>medium</u>, slightly shifts and somewhat diminishes
18.36	1.301	0.48	<u>intense</u>, somewhat diminishes

The **characteristic interference peaks of neat BAFKU** (as observed in *Figure 5*) are listed in the above *Table 2*. An extended list including weak reflections is in *SI-Table 5* and diffractograms in double logarithmic scale, where more peaks are visible, are shown in *SI-Fig. 15a*. Some of the peaks in *Figure 5* can be easily assigned to the dimensions of the mesogen molecule: The peak at 3.40° (scattering vector $q = 0.242$ Å^{-1}, corresponding to the distance $d = 2.60$ nm) can be correlated with the length of the rod-like mesogen, while the peak at 6.80° (0.484 Å^{-1}) appears to be a second-order reflection on the same distance. The peak at 10.18° (0.72 Å^{-1} / 0.87 nm) can be assigned to the width of benzene rings, and hence of the whole mesogen (similarly like in [38]). Finally, both the peaks near 18–20° (1.4 Å^{-1} / 0.45 nm) can be assigned to standard Van der Waals distances between organic molecules, e.g. in different directions in the crystal. The BAFKU peaks are all sharp (also in *SI-Fig. 15a*), thus indicating a highly ordered state in neat BAFKU at all temperatures (except in the isotropic melt at 85°C).

The **size L of the primary BAFKU crystallites** can be obtained via analysis of the full width at half maxima (FWHM) values of the reflection peaks in the WAXS region (see *Figure 5*), using the Scherrer equation:

$$L = \frac{K\lambda}{\beta \cdot \cos\Theta}$$

where K is the shape factor (set equal to 0.9), β is FWHM, and Θ is the Bragg angle (2Θ is the angle at which the ray is deflected).

The initial value of L in neat BAFKU (before melting) was found to be ca. 67 nm, while after melting and cooling (no peaks in melt), similar but somewhat larger values, near 78 nm were observed.

The larger-scale **aggregation behaviour of neat BAFKU** could be to some extent evaluated from eventual features in the **SAXS region** of the recorded XRD patterns. In *Figure 5*, one such feature very barely is visible in case of the pattern recorded at 20°C prior to sample heating (black line), at 0.7 – 1.4° ($q = 0.05 – 0.10$ Å^{-1}). In the double logarithmic scale in *SI-Fig. 15a* (in the SI file), a distinct linear increase in scattering intensity can be observed in this range. It can be assigned to the **presence of larger secondary aggregates of smaller primary BAFKU crystallites**, which formed during rapid solvent evaporation after BAFKU synthesis. The size of the secondary aggregates cannot be accurately estimated due to the too narrow experimental range of the SAXS region. The initial SAXS feature does not re-appear after melting and subsequent cooling of neat BAFKU (see *SI-Fig. 15a*), which suggests that the newly formed secondary aggregates are much larger after melting/cooling.

The X-ray **diffractogram of the copolymer BAFKU₄₁–HMS064** (see *Figure 6* and *SI-Fig. 15b* in the SI file) **displays little temperature-dependence**: Even in the molten state, the pattern is very similar like at room temperature.

Figure 6: X-ray scattering patterns of the copolymer BAFKU₄₁–HMS064 at room temperature (20°C), then at 85°C (molten), and after subsequent cooling to 55°C, to 35°C and to 20°C (back at room temperature).

Table 3: X-ray diffraction results: Interference maxima and the corresponding characteristic distances in the copolymer BAFKU₄₁–HMS064 (an extended list including weak reflections is in *SI-Table 6*).

copolymer BAFKU₄₁–HMS064			
2Θ [°]	**q** [Å⁻¹]	**d** [nm]	**comment**
2.57	0.183	3.43	medium/weak, somewhat broad, fully reversibly shifts to 2.68° ≡ 0.191Å⁻¹ (3.29nm), perhaps related to BAFKU peak at 3.40° (0.24Å⁻¹ / 2.60 nm)
5.14	0.366	1.72	weak, partly reversibly shifts to 5.42° ≡ 0.386 Å⁻¹ (1.63 nm), returns only to 5.28° ≡ 0.376 Å⁻¹ (1.67 nm), secondary reflection of 2.57°
11.86	0.843	0.75	intense and very broad, irreversibly slightly diminishes: it is an amorphous halo observed in neat PDMS (besides the main one above 20°)
20.34	1.440	0.44	medium, broadened, reversibly diminishes, perhaps related to the BAFKU peaks at 20.5 and 21.1° ≡ 1.45 and 1.49 Å⁻¹

The **characteristic reflections of BAFKU₄₁–HMS064** are listed in *Table 3*. An extended list including weak reflections is in *SI-Table 6*, followed by some additional comments. In analogy to neat BAFKU, **some peaks can be correlated with mesogen dimensions**: The reflection at $2.57°$ (0.183 Å^{-1} / 3.43 nm) can be assigned to the length occupied by the pendant mesogen units. In the copolymer, this length is larger than in case of neat BAFKU, which indicates a different and looser packing of BAFKU units in its nano-aggregates, which act as physical crosslinks in the copolymer. A relatively sharp peak is observed at $5.14°$ (0.366 Å^{-1}), which is assigned as second-order reflection of the $2.57°$ peak, in analogy to a similar situation with neat BAFKU. Moreover, both the peaks at 2.57 and $5.14°$ display analogous shifts upon heating. The very broad and intense peak at $11.9°$ (0.84 Å^{-1}, / 0.75 nm) is assigned to the **amorphous-halo-type reflection caused by PDMS** (see e.g. [66]). Another amorphous halo of PDMS should extend from 17 to $33°$ ([66]) and is only partly visible in *Figure 6*. Finally, a relatively sharp small peak near $20°$ (1.4 Å^{-1} / 0.45 nm) can be observed, which grows on the slope of the high-angle amorphous halo of PDMS: it can be assigned to intermolecular Van der Waals distances of the pendant BAFKU units, similarly like in neat BAFKU.
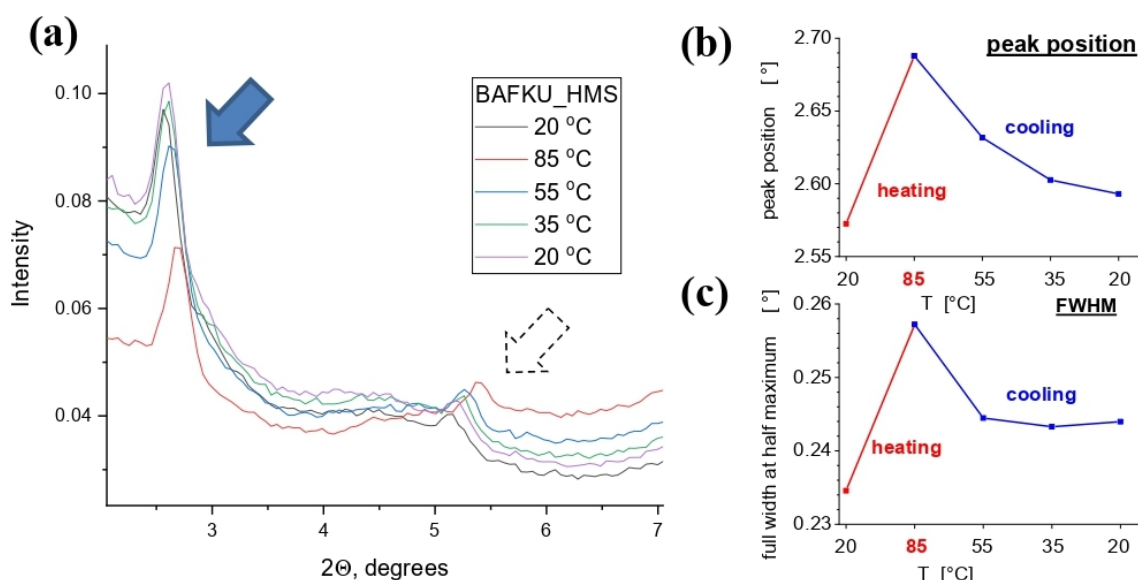
Figure 7: *(a) Temperature-dependent shift of the peak near 2.57° (highlighted with full arrow) in the copolymer BAFKU₄₁–HMS064; the second-order reflection related to this peak at 5.14° (highlighted with dotted arrow) also shows an analogous position shift; the different temperature trends of the underlying curve below both peaks generate different trends in apparent intensity of the reflections at 2.57° and 5.14°; (b) position of the '2.57° peak' in dependence of temperature; (c) T-dependent full-width at half maximum of this peak.*

An interesting feature in the XRD patterns of the **copolymer BAFKU₄₁–HMS064** is the **temperature-dependence of the position of the peak at 2.57°**, which corresponds to the mesogen length (see *Figure 7* and *SI-Table 7*). In contrast to the trends in neat BAFKU, the characteristic distance, which generates the $2.57°$ peak in the copolymer, moderately increases

with decreasing temperature, by up to 4.4%. This means that the BAFKU units are more closely packed in the longitudinal direction at elevated temperatures, and less so at lower ones.

The **size L of the primary nano-aggregates of BAFKU units in the copolymer BAFKU$_{41}$–HMS064** was obtained via analysis of the temperature-dependent full width at half maximum (FWHM) values of the characteristic peak at 2.57° (in **Figure 7**), using the **Scherrer equation** (cited further above: discussion of L in neat BAFKU). The **size of primary crystallites (nano-aggregates)** in the copolymer was found to shrink from initial 37.5 nm (at 20 °C) to 34.2 nm (at 85 °C in melt) and then to grow again upon subsequent cooling, up to 36.2 nm at 55 °C. After that, the crystallites did not markedly grow any more upon further cooling down to 20 °C. This trend generally suggests, that the crystallites are denser-packed at higher temperatures.

The **larger-scale aggregation behaviour of the pendant mesogen units in the copolymer BAFKU$_{41}$–HMS064** was evaluated from features in the **SAXS region** of the XRD pattern. **Figure 8** shows a zoom of this region in the double logarithmic scale, which is preferable for SAXS evaluation. A distinct growth of scattering intensity is observed at all temperatures in the region $q = 0.01 – 0.10$ Å^{-1} ($0.14 – 1.40°$). A temperature-dependent flat maximum is observed in this region, which at 20°C (prior to any heating) has the position of 0.035 Å^{-1} (0.49°). This maximum partly reversibly moves with temperature: It practically disappears at 85°C (molten state), then it re-appears at 0.028 Å^{-1} (0.39°) at 55°C and moves upwards to 0.0314 Å^{-1} (0.44°) at 35°C, and up to 0.0335Å^{-1} (0.47°) at 20°C, after being cooled down to room temperature.
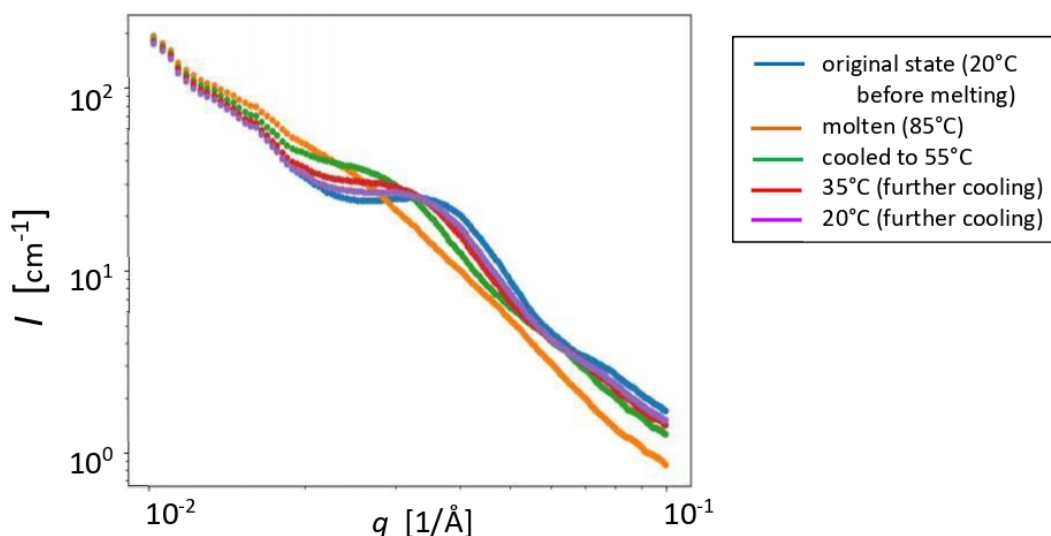
Figure 8: *SAXS region of the X-ray diffractogram of the copolymer BAFKU$_{41}$–HMS064, depicted as scattering intensity (logarithmic) in dependence of the scattering vector q (in Å^{-1}, also logarithmic scale); the whole diffractogram of the copolymer in this format is shown in* **SI-Fig. 15b**.

The true size of the domains which generate the SAXS pattern cannot be precisely determined, due to the too narrow experimental range of the SAXS region. Nevertheless, the domains can

be estimated to be larger than the primary aggregates (sized ca. 37 nm, see above) whose width was calculated using the Scherrer equation. The domains also are expected to be smaller than 1 μm, as no anisotropy is observed by polarized light microscopy if the copolymer sample is not previously shear-oriented. Hence, the true size of BAFKU domains in the copolymer can be estimated to be in the order of 100 nm. The above-mentioned temperature-dependent SAXS maximum can be tentatively assigned (Bragg law) to a characteristic intra-domain distance, which is equal to 17.9 nm in the initial state at 20°C (prior to heating). In the molten state (85°C), it cannot be observed. After cooling the melt down to 55°C, it reaches 22.4 nm. Continued cooling leads to shrinkage: $d = 20.0$ nm at 35°C and 18.8 nm after reaching 20°C again. This distance hence does not fully revert to its original value, but stays somewhat expanded after the experiment. In view of the temperature-dependent size of primary crystallite-like mesogen aggregates in the BAFKU$_{41}$–HMS064 copolymer (34–38 nm), which is discussed below, the characteristic **distance which generates the *T*-dependent SAXS maximum** in ***Figure 8*** might be **assigned to less ordered regions in secondary BAFKU-rich aggregates**, which separate the stronger and more ordered primary aggregates. The less ordered regions also (in view of the chemical structure in ***Scheme 2*** and ***5***) could contain some PDMS chains. They expand rather than shrink upon heating (simple behaviour).

To sum up, the XRD experiments indicate that **BAFKU nano-aggregates in the copolymer BAFKU$_{41}$–HMS064 display a reduced overall degree of ordering** in comparison with neat BAFKU. The **characteristic distances** marked by the interference peaks **are different in BAFKU and in the copolymer**, thus **indicating different molecular packing**. Additionally, the ordering in the copolymer **does not markedly change even after crossing the melting point** (in contrast to neat BAFKU): The nano-aggregates just become liquid, and do not act as mechanically efficient physical crosslinks anymore: Upon excessive deformation, they eventually dynamically disconnect and coalesce again like droplets, but they persist (see ***Scheme 7*** further below), due to the immiscibility of PDMS and BAFKU. The bonding of quartets of BAFKU units at closely neighbouring positions on the PDMS chains ('grafting sites', see also ***Scheme 6*** further below), as well as the relatively small size of the now liquid primary nano-aggregates, both likely support the predominantly parallel alignment of the mesogens even in the molten state of the copolymer (as observed by XRD), instead of full isotropization, like in case of molten neat BAFKU.

3.3.3. PLM observation of anisotropy and mesophases

The phase transition behaviour, as well as the crystallization of the promising copolymer BAFKU$_{41}$–HMS064 was additionally evaluated by means of polarized light microscopy (PLM). The results are summarized in ***Figure 9–11***. If the copolymer is simply molten and cooled down back to room temperature between microscopy glasses, no anisotropy can be observed by PLM (black field, not shown). However, if **orientation is induced by mechanical shear**, extended sub-millimetre-sized highly anisotropic areas appear after melt cooling (see

25

Figure 9). These regions cannot be lamellae of aggregated BAFKU, in view of its small volume fraction in the copolymer, and also in view of the copolymer architecture (shown in *Scheme 5*), which does not easily allow for the growth of very large BAFKU domains, even after shearing. Hence, the observed areas can be assigned to regions in the copolymer, in which small BAFKU nano-domains have some prevalent orientation.
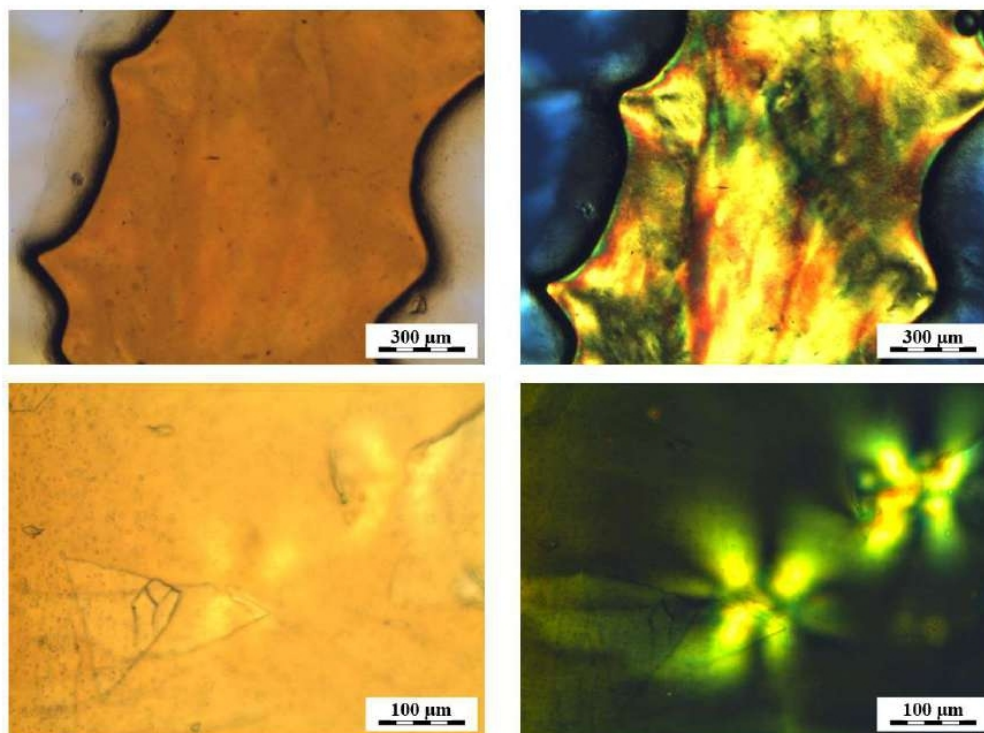
Figure 9: Textures observed in BAFKU$_{41}$–HMS064 by polarized light microscopy (PLM) after melting, shearing, cooling down to room temperature and subsequent renewed heating between room temperature and 50°C.

In order to quantitatively evaluate the temperature-induced **disconnection or fluctuation of the higher-order BAFKU aggregates**, which were observed further above by XRD, a series of PLM images was taken in the 'white-light mode' (see Experimental Part and [63,64]) at temperatures gradually increasing up to 80°C. An overview is shown in *Figure 10*. (Only some images are depicted in this Figure, in order to highlight changes; the whole collection of images which were recorded at numerous temperatures is shown in *SI-Fig. 17*). Visually, it can be observed that a significant decrease in anisotropy (seen as intensity of the white domains) occurs between 40 and 50°C, and even a stronger one between 50 and 55°C. At 60°C, the residual anisotropy is very small, while at 80°C, the sample is seemingly isotropic. The anisotropy does not recover, if cooling after the heating run is done without mechanical shear. The decrease of overall orientation via BAFKU domains' disconnection or fluctuation is investigated more thoroughly in *Figure 11*: This Figure plots the average intensity of white light (taken from a bright part of one of the domains in *Figure 10* / *SI-Fig. 17*) against the temperature: A continuous decrease of intensity is observed, which becomes relatively steep

and nearly linear between 45 and 58°C. A constant minimum value is reached at 63°C. The residual intensity, which is recorded for the dark images of the melt, likely stems from polarization generated by small (perhaps primary) BAFKU aggregates, which were demonstrated to persist in melt (see above-discussed XRD experiments).
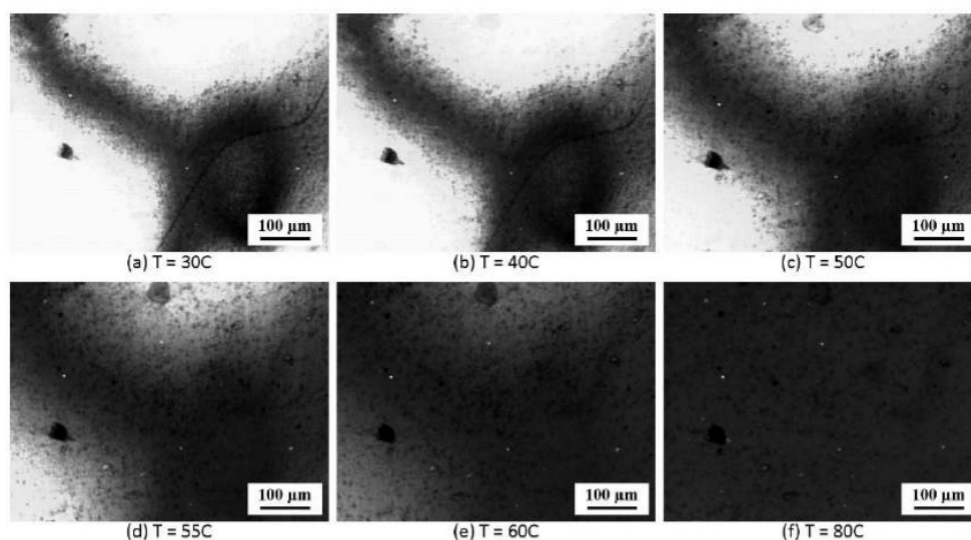
Figure 10: *Temperature-dependent changes in the images of a selected group of anisotropic domains in the copolymer BAFKU$_{41}$–HMS064, observed by PLM in the 'black and white mode' (all colours are reproduced as white light), during a heating scan (from 30 to 80°C) of a previously shear-oriented sample (oriented in melt).*

If the temperature-dependent light intensity from the PLC experiment is overlaid with the plot of the decreasing storage modulus of a copolymer sample (*G'*, logarithmic scale) heated over the same temperature range (see ***Figure 11 a***), it can be seen that the curves show a similar shape. However, the *G'* curve sharply turns down at somewhat more elevated temperatures (by ca. 10°C). A comparison with the DSC trace shows (***Figure 11 a*** vs. ***c***), that the loss of (larger-scale) optical anisotropy is completed at the temperature of the maximum heat absorption of the copolymer in the DSC curve. Here, the larger secondary BAFKU aggregates (observed by XRD) likely start to disconnect and coalesce again, and lose their predominant orientation direction. Smaller primary aggregates no more visible in PLM still absorb heat above 64°C, in order to be molten to liquid-like nano-domains, which still are anisotropic, but which are oriented in random directions. Finally, a comparison of the 'quantified anisotropy' with the DSC (heating) trace of neat BAFKU indicates (***Figure 11 a*** vs. ***b***), that the sharp decrease in anisotropy occurs in the region of the first (and dominant) peak in the heating scan (56.6°C: crystalline → nematic), and that the anisotropy disappears close to the position of the second (small and final) peak of the DSC heating run (66.7°C: nematic → isotropic).

An interesting aspect are the colourful textures observed in the shear-oriented copolymer BAFKU$_{41}$–HMS064 in *Figure 9* (further above): These textures do not change over the tested temperature range and are neither typical for well-ordered crystals (the latter were not expected in view of the above DSC results), nor for smectic or nematic phases. Hence, the **PLC experiments** also **confirm, that the BAFKU aggregates** in the BAFKU$_{41}$–HMS064 copolymer **are imperfectly ordered**, **especially on the larger scale**, or that (to some extent) multiple arrangements might occur simultaneously in the aggregates. The results further show, that the **decay of the anisotropy with increasing temperature** realistically correlates with thermotropic changes in the BAFKU nano-aggregates, which are too small to be directly observed PLM.
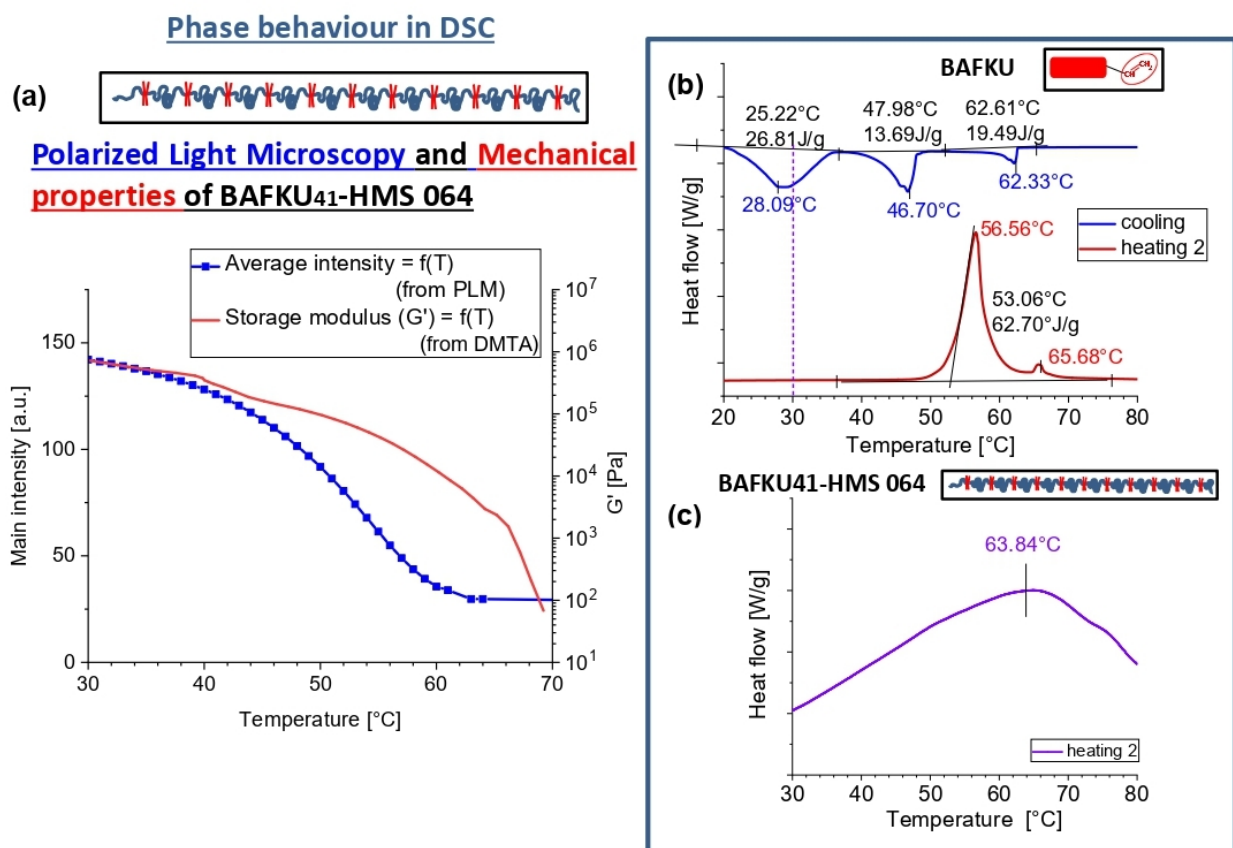
Figure 11: *(a): Temperature-dependence (from 30 to 80°C) of the average polarized light intensity ('black and white mode') calculated from the images of a group of selected anisotropic domains in BAFKU$_{41}$–HMS064, some of which were shown in **Figure 10**; decrease of the storage modulus G' as observed by DMTA in the same temperature range; (b): peaks in the DSC trace of the neat BAFKU mesogen in the same temperature range; (c): DSC trace of BAFKU$_{41}$–HMS064 in the same temperature range.*

3.3.4. Structure in the aggregates of pendant BAFKU units

In view of the combined data about the BAFKU$_{41}$–HMS064 copolymer, which were obtained by thermo-mechanical analysis (DMTA), DSC, X-ray and by polarization microscopy (PLM), it can be concluded, that the BAFKU domains in the copolymer are imperfectly ordered at any temperature (X-ray, DSC). Also, the packing of BAFKU in nano-aggregates in the copolymer (i.e. the characteristic distances) was found to be different from the one observed for neat BAFKU in its crystals and mesophases (X-ray).
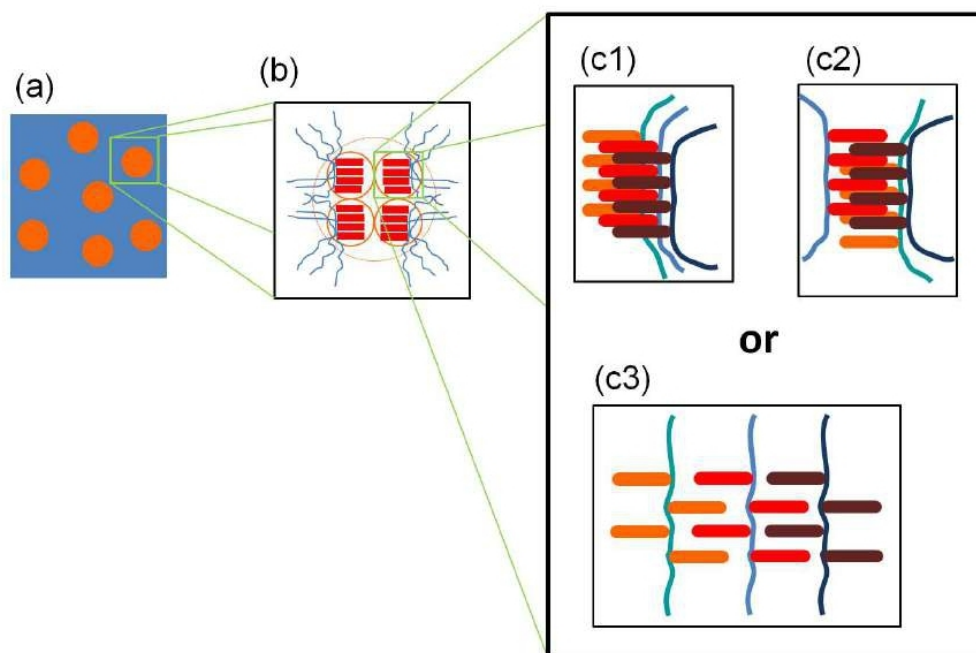
Scheme 6: *Symbolic representation of: (a) the nano-structured morphology of the elastomeric copolymer BAFKU$_{41}$–HMS064 with BAFKU domains in orange colour; (b) of the BAFKU domains composed of smaller primary aggregates; (c1–c3) of the primary aggregates of BAFKU units attached to PDMS chains.*

The **BAFKU domains**, which act as physical crosslinks in the BAFKU$_{41}$–HMS064 copolymer, undergo a **broad range of thermotropic transitions**. The latter are visible in DMTA as gradual weakening of the crosslinking strength in the rubbery plateau (modulus decrease), and in DSC, they generate a very broad and relatively flat endotherm peak ('region of thermal transitions'). This region of thermal transitions of the BAFKU domains in the copolymer roughly corresponds in its position and extent with the entire range of the thermal transitions in the neat BAFKU mesogen (three transitions, range width: 45°C, if also the metastable smectic phase is considered). Additionally, PLM data visualize a similarly wide range of thermal transformations in the BAFKU domains in the copolymer, which lead to a gradual loss of predominant orientation in them. Finally, also the further-below-discussed results of

29

rheological experiments (especially the multi-frequency gelation tests) support the occurrence of multiple thermal transitions in the domains, one from liquid state to solid (rubber), and one or two in the solid state.

The following **structure** hence can be **postulated for the BAFKU domains in the BAFKU$_{41}$– HMS064 copolymer** (see *Scheme 6*): Small nanometre-sized primary aggregates of BAFKU, which possess a somewhat different packing than neat BAFKU, are arranged to larger and less strong secondary BAFKU aggregates sized tens of nanometres (X-ray). The regularity of the primary aggregates is not very high (see X-ray peaks), due to local mechanical strains or steric effects, but at different temperatures, structures are formed, which are more or less related to the crystalline, to the smectic and to the nematic phase of neat BAFKU.
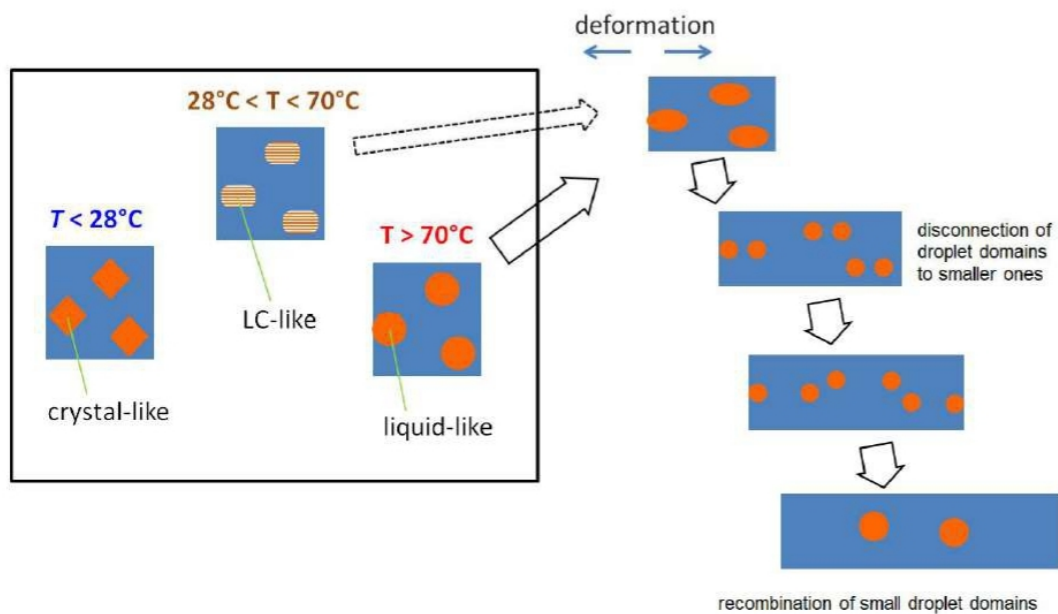
Scheme 7: *BAFKU nano-domains in BAFKU$_{41}$–HMS064, their transition from crystalline to liquid-crystalline (LC) and liquid state, under domain preservation; mechanical disconnection to smaller domains and recombination (coalescence) to bigger ones upon large shear deformation in the liquid or LC state.*

Upon heating, the **aggregates undergo transitions** at temperatures similar to the ones observed in neat BAFKU, but due to the mentioned irregularities and strains, the individual transitions are not sharp, but occur and overlap in a broader range of temperatures. Possibly, some of the different nanocrystallite alignments co-exist in a broader temperature range ('mixed composition'), which would explain, why the observed PLM textures are not typical for any single thermotropic phase.

Upon **crossing the melting point**, the BAFKU domains in the copolymer are molten and can split or coalesce (see *Scheme 7*), but the primary and secondary aggregates persist (WAXS, SAXS), albeit in a liquid-like state. The reason for the domains' persistence is the

incompatibility (and hence phase-separation-tendency) of PDMS and BAFKU, which was desired in order to support physical crosslinking. A certain degree of alignment always is present in the primary aggregates (X-ray), due to spatial constraint, small nano-aggregate size, and due to the fixation of rod-like mesogens close to each other (in quartets) on the PDMS backbone.

Upon **cooling the copolymer melt**, the primary and secondary BAFKU aggregates become more ordered, and solidify again to different packing structures, which succeed each other, or sometimes form simultaneously. The BAFKU domains then undergo thermal transformations in an equally wide T range like in course of the heating scan. This is a difference in comparison to neat BAFKU, where the range of thermal transformations is narrower in case of heating (2 transitions), while in case of cooling it is wider (3 transitions).

The less attractive (and hence less investigated) **vitrimeric BAFKU$_8$–HMS301** copolymer can be **expected** to display an **analogous behaviour**, in view of its DSC characteristics, which are very similar to the characteristics of BAFKU$_{41}$–HMS064.

3.4. Rheological properties

The reversible physical crosslinking in the copolymer BAFKU$_{41}$–HMS064 was investigated in detail by means of **rheology** in several test types: **Multi-frequency temperature scans** (both heating and cooling) were carried out in order to characterize in a detailed way the process of gelation / crosslink disconnection upon cooling / heating. The **kinetics of physical crosslinking** upon abrupt cooling of copolymer melt from 80°C to different final temperatures was evaluated in single-frequency time sweep tests, while the possibility of physical **crosslink disconnection by mechanical strain** was studied in **strain sweep tests**. Finally, **frequency stiffening** was characterized in **frequency sweep tests**.

3.4.1. Reversible gelation near the melting point

Results of the **rheological multi-frequency temperature scans**, which studied the **thermo-reversible gelation** of BAFKU$_{41}$–HMS064, as well as further transitions in the rubbery state, are shown in *Figure 12* and *13*. The graph sets are generally similar to analogous graphs obtained in case of chemical crosslinking (gelation), e.g. of simple epoxies ('chemorheology'). The latter are recorded as time sweeps at constant temperature, with time instead of the temperature as x-axis. The sets of graphs obtained for BAFKU$_{41}$–HMS064 somewhat differ for cooling vs. heating scans, see *Figure 12a* vs. *Figure 13a*.
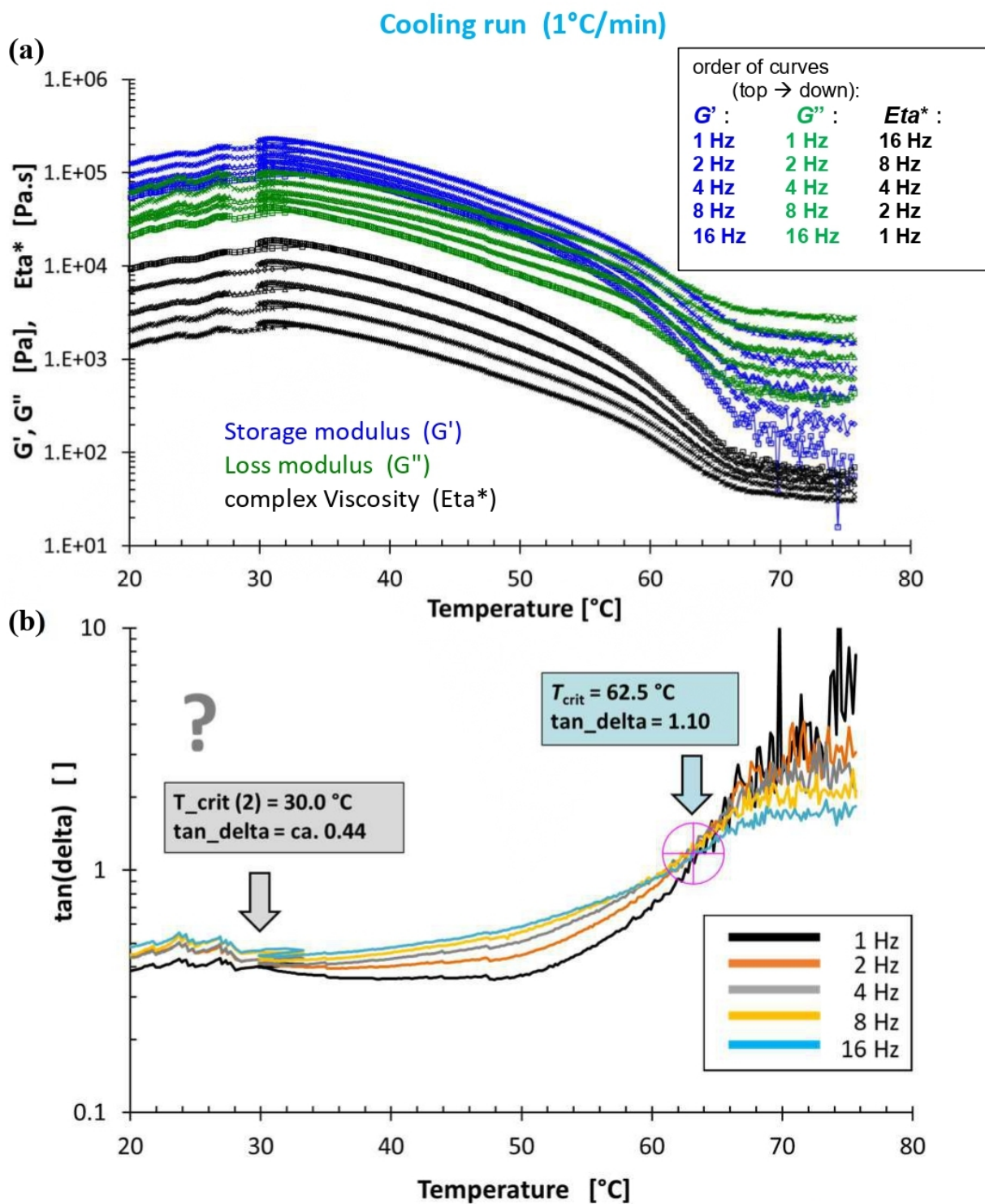
Figure 12: *Multi-frequency temperature ramp tests carried out from molten to rubbery state of BAFKU$_{41}$–HMS064: (a) temperature dependence of the storage shear moduli G', of the loss moduli G'', of the complex viscosity Eta* and of tan δ recorded at the simultaneously applied frequencies of 1, 2, 4, 8 and 16 Hz; (b): cooling scan with detail of the sets of the tan δ curves with marked crossover points.*
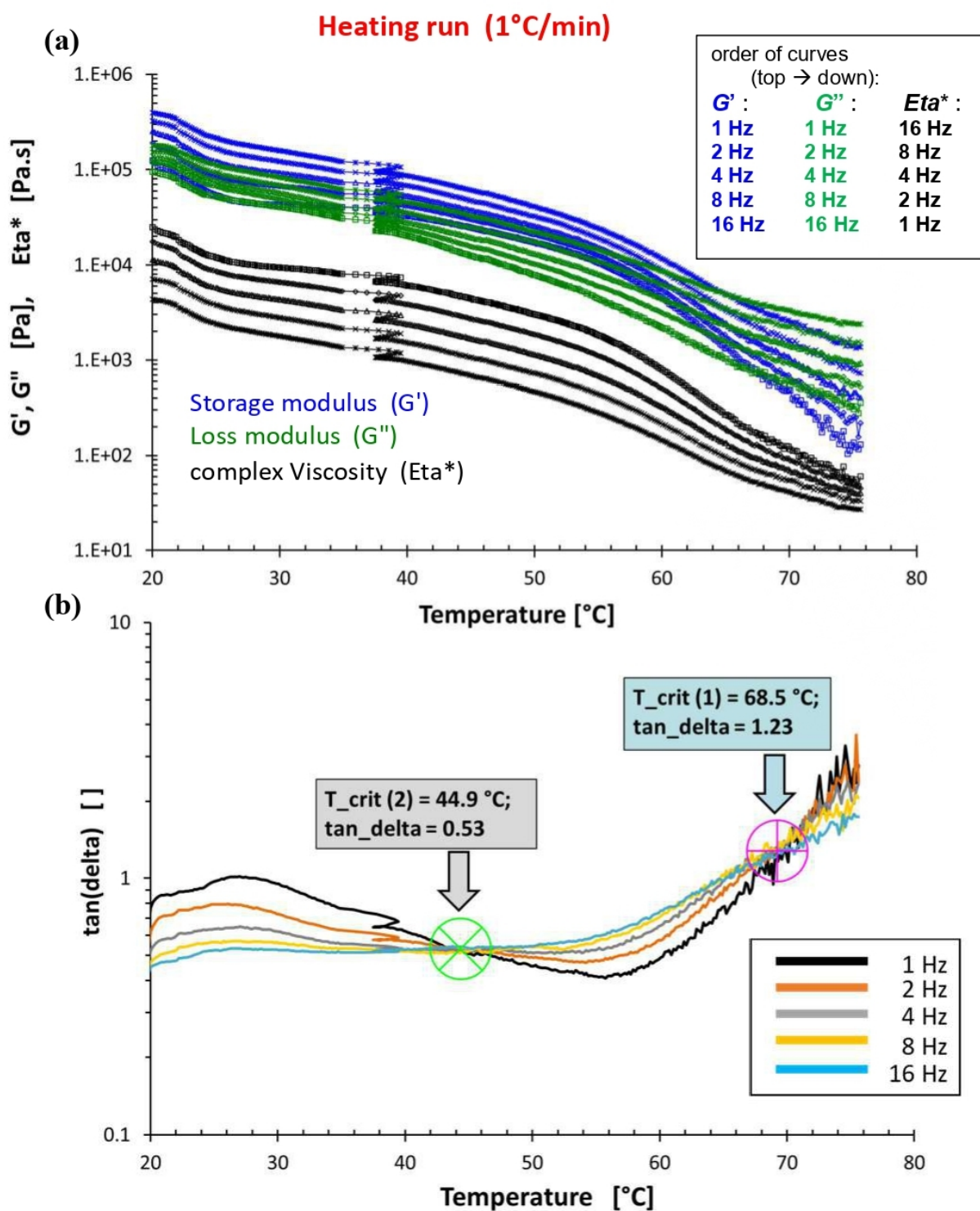
Figure 13: *Multi-frequency temperature ramp tests carried out from rubbery to molten state of BAFKU$_{41}$–HMS064: (a) temperature dependence of the storage shear moduli G', of the loss moduli G", of the complex viscosity Eta* and of tan δ recorded at the simultaneously applied frequencies of 1, 2, 4, 8 and 16 Hz; (b): heating scan with detail of the sets of the tan δ curves with marked crossover points.*

According to the Chambon-Winter theory [67], the **point of gelation can be identified as** the point of *tan δ crossover* in multi-frequency experiments (*tan δ* independent of frequency). In the rheology experiments illustrated in *Figure 12* and *13*, the rate of cooling and heating, respectively, was relatively slow, 1°C/min, in order for the gelation/melting to occur similarly slowly like in the above-mentioned chemorheology tests (e.g. as carried out by the authors in [53]): Thus, for scanning the narrower region near the gel point, from 75 down to 60°C, ca. 15 min were needed. In *Figure 12b* (*tan δ* curves at different frequencies, cooling run) it can be seen, that the BAFKU$_{41}$–HMS064 melt gelates to rubber at 62.5°C. In the heating run (see *tan δ* curves in *Figure 13b*), the rubbery BAFKU$_{41}$–HMS064 melts at 68.5°C, in a reverse process of the mentioned gelation. Both transition temperatures are close to the isotropic melting point of neat (non-bonded) BAFKU (DSC: 62.33/66.73°C, while cooling or heating at 10°C/min, respectively).

An interesting feature is the **second *tan δ* cross-over**, which upon heating very clearly is observed at 44.9°C, and which occurs already in the rubbery region of the sample (see *Figure 13b*). This **'second gelation'** most probably is caused by a liquid-crystalline phase transition. No crossover close to 44 or 40°C is appears during the cooling scan (*Figure 12b*), but a near cross-over is observed in more distant neighbourhood, namely at 30.0°C (see *Figure 12b*): Here the *tan δ* curves (cooling run) approach each other but do not cross, before moving away again on further cooling. This specific point is immediately followed by a region of dynamic-mechanical instability (observed during the cooling scan only), down to 17°C (test end, see *Figure 12a,b*). This instability is possibly related to the properties of various imperfectly ordered solidifying BAFKU domains, which might undergo transitions induced by mechanical deformation (compare with DSC: the final crystallization of neat BAFKU occurs at 28.09°C and generates a relatively broad peak in *Figure 3a*). The near-crossover and the adjacent 'instability region' might be a combination of an undercooled LC transition (which would be expected between 40 and 30°C) with the starting final crystallization of BAFKU domains. In case of the heating scan (*Figure 13*), a **third interesting feature** can be observed in the broader region of the three thermotropic transitions of BAFKU: When the sample is heated above 23–24°C, there is a small stepwise decrease in the moduli *G'*, *G"* and also in the dynamic viscosity, but no *tan δ* crossover or near-crossover (only a slight narrowing of the set of curves is observed).

To sum-up, the rheology results in *Figure 12* and *13* additionally support the further-above-postulated **irregular multi-phase nature of the BAFKU aggregates** in the BAFKU$_{41}$–HMS064 copolymer, which display several transitions and possibly also several co-existing phases.

3.4.2. Rate of physical gelation upon abrupt cooling of the melt

Figure 14 illustrates the **kinetics of the gelation of the melt of BAFKU$_{41}$–HMS064 upon abruptly cooling** from 80°C down to the temperatures of 15, 55 and 70°C. 'Melt cooling results' for additional final temperatures are shown in *SI-Fig. 18*. The gelation process occurs

via LC-ordering, or even via full (3D) crystallization of nanodomains of BAFKU. These latter were shown to persist as 'nano-droplets' also in the liquid state of the copolymer, as discussed in the section dedicated to XRD analysis. It can be observed in ***Figure 14***, that the physical crosslinking can proceed fairly quickly: 2–3 min are needed for perfect gelation (modulus *G'* reaches its equilibrium value), if cooling down from 80°C to 15°C. But the time needed for initial cooling (ca. 50 s) also is included in this equilibration time, as the sample could not be cooled instantly. (The 'immediate cooling' regime used in the experiments led to very short, but somewhat different cooling times, which decreased if the temperature jump was smaller). It further can be observed in ***Figure 14***, that nearly the entire modulus change occurs in the 50 s after reaching the final temperature (15°C), not during the fast cooling itself. If the melt is cooled down only to 55°C (close to the second DSC transition of neat BAFKU), the modulus reaches an equilibrium value in ca. 3.5 min, from which the 3 min after the completion of rapid cooling are the 'true time of gelation'. If cooling down to 60°C (***SI-Fig. 18***), the modulus stabilizes in 5 min, from which 4.6 min are 'true gelation time'.
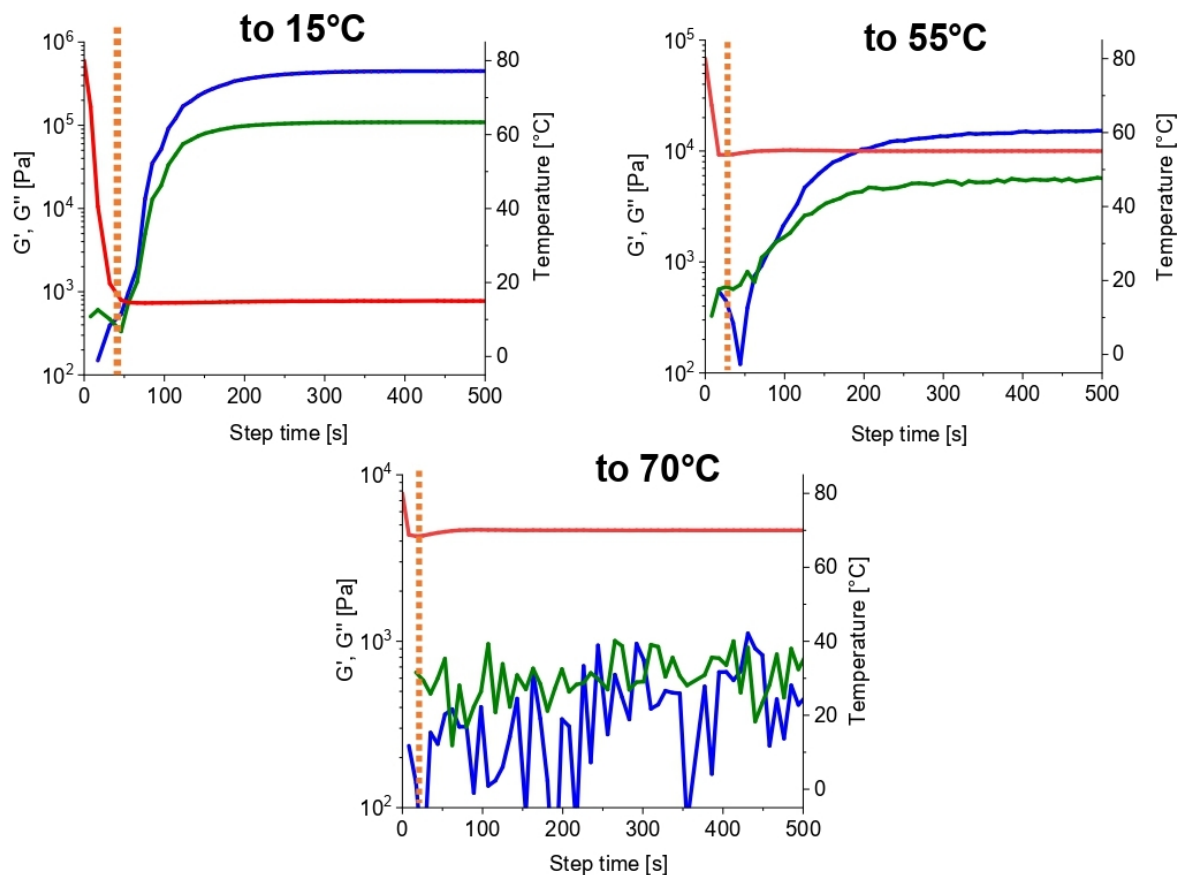
Figure 14: *Kinetics of the change in storage (G') and loss (G") modulus (kinetics of physical gelation) upon cooling molten BAFKU$_{41}$–HMS064 from 80°C to different temperatures: 15, 55 and 70°C; the course of the temperature of the plates (between which the sample was loaded) is also depicted; the dotted line depicts the approximate end of the sample cooling.*

Finally, if the sample is cooled down only to 70°C (at the edge of the melt range), there is only a minimum modulus change, which extends over ca. 10 min, while the loss modulus (G'') is slightly higher or equal to the storage modulus (G'). The increase of the time of gelation after melt cooling as consequence of rising final temperature well illustrates the **thermo-reversibility and the dynamic nature of the physical crosslinking via BAFKU aggregation**: The greater prominence of the reverse process (crosslink disconnection) at higher temperatures leads to slower gelation.

3.4.3. Disconnection of the physical network by high mechanical strain

The **possibility of mechanical disconnection of the physical network** in the elastomer BAFKU$_{41}$–HMS064 was evaluated in **strain sweep tests**, the results of which are summarized in *Figure 15*.
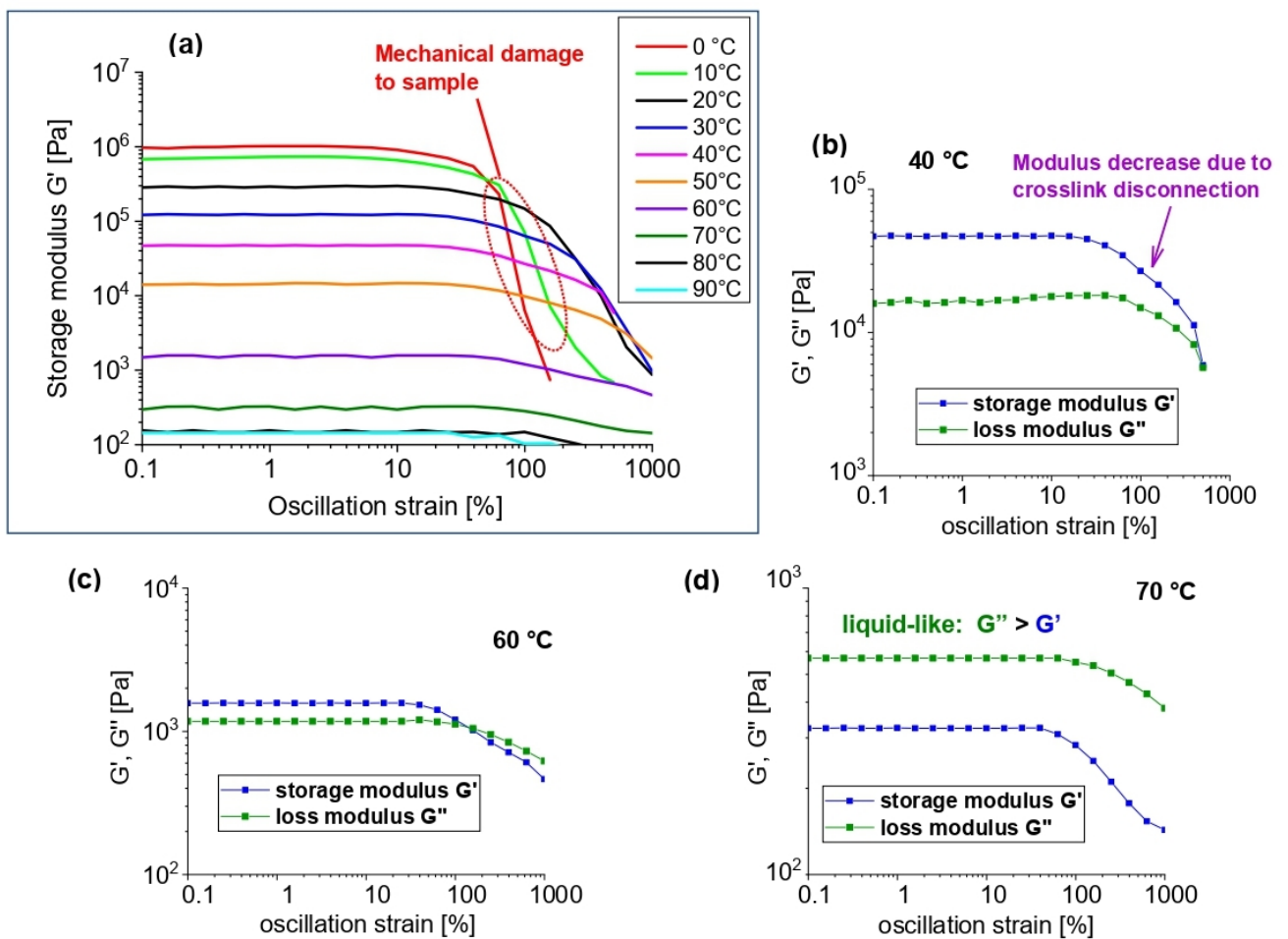
Figure 15: *Disconnection of the physical crosslinks in BAFKU$_{41}$–HMS064 by mechanical strain: (a): overview of strain-dependent storage modulus G' at different temperatures (at 0 to 30°C, specimen failure – 'roll-out' is observed at the highest strains); (b), (c), (d): strain-dependence of storage (G') and loss (G'') modulus of BAFKU$_{41}$–HMS064 at the temperatures of 40, 60 and 70°C, respectively.*

At the lowest temperatures deep in the rubbery region (especially at 0°C and 10°C) the network can be **mechanically disconnected only to a small extent**, if the applied oscillatory stress reaches amplitudes in the range of 7–40% (see ***Figure 15a***). At higher deformations, the sample fails: it rolls out of the parallel plate fixture employed in the experiment (visual observation), which manifests itself as a steep modulus decrease in ***Figure 15a*** (see highlight). This mechanical failure is clearly observed at 0 and 10°C, while at 20 and 30°C, the failure is less dramatical and shifted to higher deformations, as the sample becomes more plastic.

At 40°C and above, sample **failure** practically **does not occur**, while the **onset of the modulus decrease shifts to higher deformation** values. Additionally, the initial equilibrium moduli steadily decrease. Mechanical **disconnection** of crosslinking is observed **even in the** semi-molten (60°C) and **molten state** (clearly visible at 70°C): A 3- and 2-fold modulus decrease can be noted, respectively (with onset of disconnection at 40 and 50%, respectively). At 80 and 90°C (molten state), the storage moduli are very low (ca. 200 Pa) and the effects of high deformations on them are close to noise level. The shift of the onset of modulus decrease to higher strain values with rising experiment temperature is an interesting effect: It can be assigned to an increasing prominence of the **temperature-induced regeneration of physical crosslinks** (self-healing, see also further below), as a consequence of a higher mobility of BAFKU segments. Without this effect, the increased experiment temperature should lead to easier mechanical disconnection of crosslinks at low deformations.

3.4.4. High-frequency stiffening and self-healing effects

Frequency sweep experiments (see ***Figure 16*** and ***SI-Fig. 20***) indicate the **stiffening of the elastomer BAFKU$_{41}$–HMS064 at high frequencies**, which is an expected effect in polymers with flexible chains in general: Both G' and G'' rise with f, but G' dominates, although at low frequencies G' and G'' come closer to each other. Except for the steps observed in the curves in ***Figure 16*** and ***SI-Fig. 20***, frequency-dependent G' and G'' curves of typical polymer melts or of rubbery materials are similar like the ones observed for the copolymer BAFKU$_{41}$–HMS064 (especially the ones at 30°C). In all such cases, the increase of G' with frequency is given by increasingly more difficult rapid disentanglement of long and flexible elastic chains, so that increasing numbers of entanglements start to act as crosslinks (on the timescale of the given test frequency). On the other hand, the increase of G'' with frequency is caused by the higher energy of collisions of the moving molecular segments at higher frequencies (faster movement), but in typical melts and elastomers, G'' always rises less steeply than G' in frequency sweep tests.

In case of **BAFKU$_{41}$–HMS064** tested at temperatures up to 60°C (gradual melting is in progress at this latter temperature), G' always prevails over G'', even at the smallest tested frequency of 1 mHz. At 80°C (liquid region), both moduli run parallel over the whole frequency range, and G'' is slightly higher than G' (stronger liquid-like-character). The **frequency-stiffening effect** was found to be the most marked (on relative scale) at 80°C in the molten state (viscoelastic liquid), where both moduli rise over several orders of magnitude, but they still remain fairly

low. BAFKU–BAFKU Van der Waals interactions in liquid nano-aggregates most likely contribute to the observed trends of *G'* and *G"* in melt at 80°C, namely the increase of *G'* via labile physical crosslinks and entanglements constructed with their help, and the increase in *G"* via increased friction caused by disconnection and re-assembly of (liquid but phase-separated) BAFKU nano-droplets. The same Van der Waals interactions also are responsible for 'holding together' the crystals of neat BAFKU.
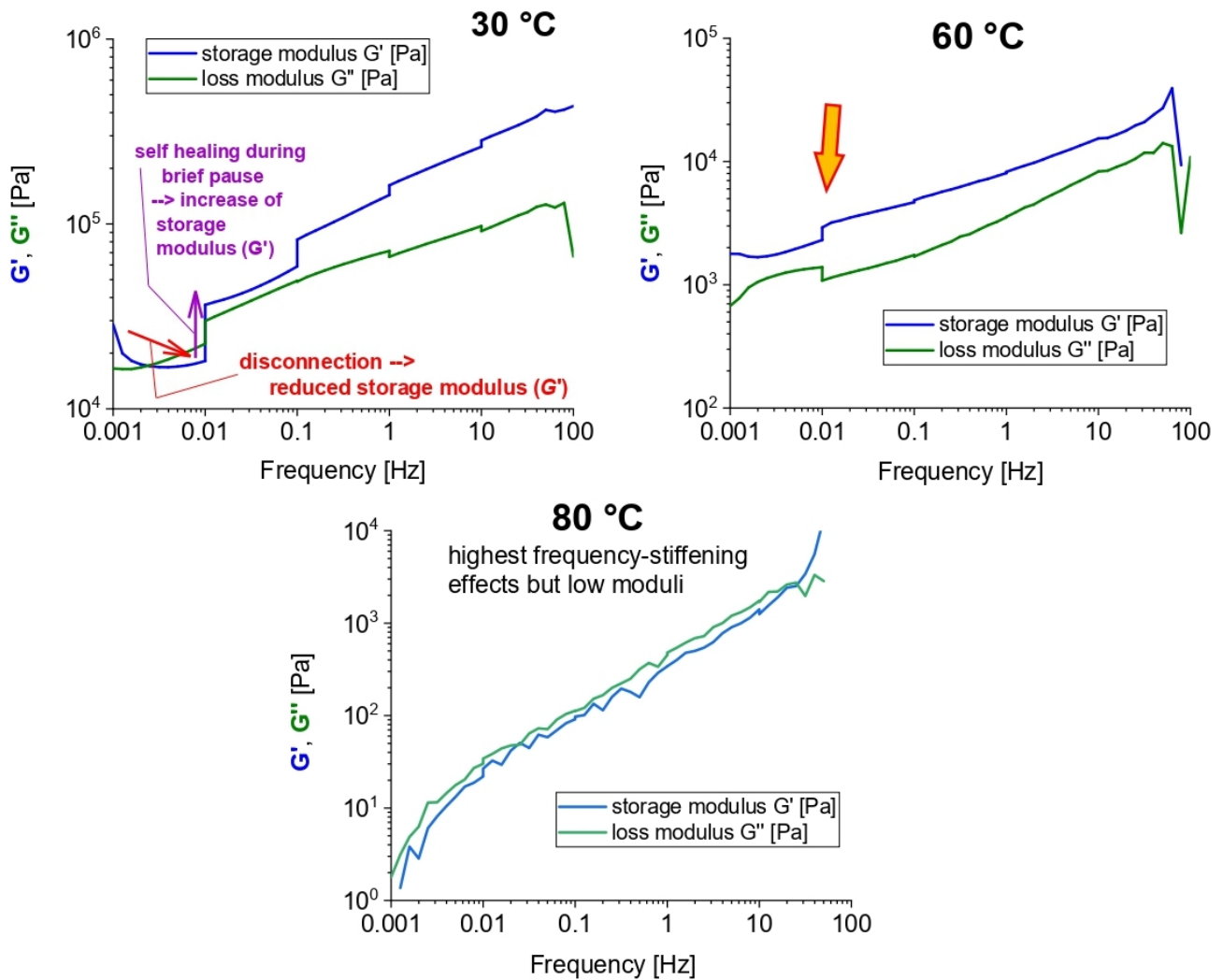
Figure 16: *Frequency-stiffening of BAFKU₄₁–HMS064 observed in frequency sweep tests (1 mHz to 100 Hz) conducted at 30, 60, and 80°C; the strain amplitude was different in each frequency decade, ranging from 50% at 1 mHz to 1% at 100 Hz; the effect of strain-induced damage to the network, as well as of its recovery between the frequency decades is clearly visible, especially in case of G' curves at lower temperatures.*

The frequency sweep tests in ***Figure 16*** supply also an additional interesting result, namely an indication of **self-healing ability** in the tested BAFKU₄₁–HMS064 elastomer, which manifests itself as steps in many of the experimental curves (see ***Figure 16*** and ***SI-Fig. 20***). A general

possibility of self-healing was expected in case of the copolymer BAFKU$_{41}$–HMS064, because of the physical and hence reversible nature of its crosslinks. The origin of the observed steps is that for technical reasons, the rheometer made brief (in the range of seconds) delays between frequency decades. In case of simultaneously occurring strain damage (partial disconnection of BAFKU nano-aggregates during measurement) and rapid self-healing (re-aggregation of BAFKU during delay), the experiment delays would lead to step-wise (vertical) increase in G'. The indeed observed 'step-effect' thus indicates the ability of rapid self-healing of BAFKU$_{41}$–HMS064, at least in case of strain damage (without sample disruption). A detailed discussion of the 'step effects' in G' and G'' is included in the Supplementary Information file (discussion of *SI-Fig. 20*). Inspired by these results, standard self-healing tests with disrupted samples were also conducted, and are discussed below.

3.5. Self-healing properties

An interesting property of the copolymer **BAFKU$_{41}$–HMS 064** is its self-healing ability. Two successful preliminary tests were carried out, which prove this ability at healing temperatures of 22 and 45°C. The results indicate, that **self-healing of fully disrupted samples** is relatively slow, if they are not brought close to melting, in contrast to the above-discussed healing of strain damage. On the other hand, disrupted samples grow together even at relatively low temperatures (in the rubbery temperature region).

Figure 17: *The copolymer BAFKU$_{41}$–HMS 064 after preparation as bulk material (small vial), as re-melted material in the shape of platelets (see inlay; another re-melted sample is visible in the large image while still being in the mould), as solution in chloroform (large vial: dissolved piece of re-melted material).*

Figure 17 shows several samples of the copolymer BAFKU$_{41}$–HMS 064: one just after synthesis and solvent removal in a small vial (during final drying, the open vial was put into a flask which was heated, and vacuum was applied until pressure constancy), or re-melted (80°C) rectangular platelets sized 20 x 5 x 2 mm (shown in Figure inlay), as well as a re-melted piece after its full dissolution in chloroform (large vial with yellow-orange solution). Both the re-

melting and the dissolution of the rubbery copolymer clearly demonstrate the reversible character of its crosslinks.

The **rectangular platelet samples** of BAFKU$_{41}$–HMS 064 were **subjected to tensile tests**. These tests were carried out after re-melting in the mould, as well as after destruction and subsequent self-healing. One self-healed sample, which failed in its central region during a tensile test, was 're-assembled' and pressed together for 48 h by a force of ca. 100 g at room temperature (22°C in the laboratory) (see *Figure 18 top*). The sample was not sticky, and its pieces fell immediately apart, if they were pressed together only for seconds or minutes. The **temperature of the attempted room-temperature-healing**, 22°C, was **below the region of thermotropic transitions** in the copolymer (but still in the rubbery range). The second sample for self-healing was obtained by cutting an intact platelet into two pieces. The latter were subsequently pressed together by a force of ca. 100 g at 45°C for 48 h (see *Figure 18 bottom*). In case of this **second sample**, the **healing temperature** already was **in the range of the thermotropic transitions** (DSC) of the copolymer, **but** still well **below** the range of gradual **melting**.
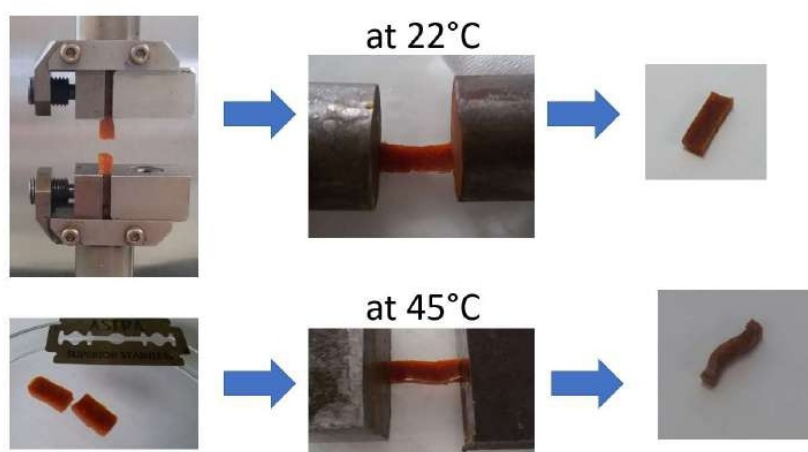
Figure 18: *Disrupted samples of BAFKU$_{41}$–HMS 064 prior to self-healing, during this process and after its conclusion; healing temperatures: 22°C (top) and 45°C (bottom). The sample healed at 22°C was initially disrupted during a tensile experiment, while the one healed at 45°C was initially cleanly cut to two pieces.*

In *Figure 18* (healed specimens) and *Figure 19* (tensile tests), it can be seen that **self-healing took place at both the tested temperatures**, albeit it was not complete after 48 h in both cases. During the tensile tests, both the healed samples failed at the self-healing joint, and both reached only partly the initial extensibility: 1/6 of it in case of self-healing at room temperature, and 1/3 of it after healing at 45°C. The moduli (slopes of the tensile curves in *Figure 19*), however, can be considered as fully restored. In case of the sample healed at 45°C, some creep occurred during the healing (see healed specimen in *Figure 18 bottom, right*), so that the shape of the specimen changed to a bent one (but no melting occurred). Such a shape always leads to a moderately reduced apparent modulus (initial slope of the tensile curve), because stretching the

bent sample to the straight shape makes possible an elongation, which is opposed by a smaller force than outright linear extension of a straight specimen. Upon re-melting, however, the tensile properties of all samples are 're-set' to original.
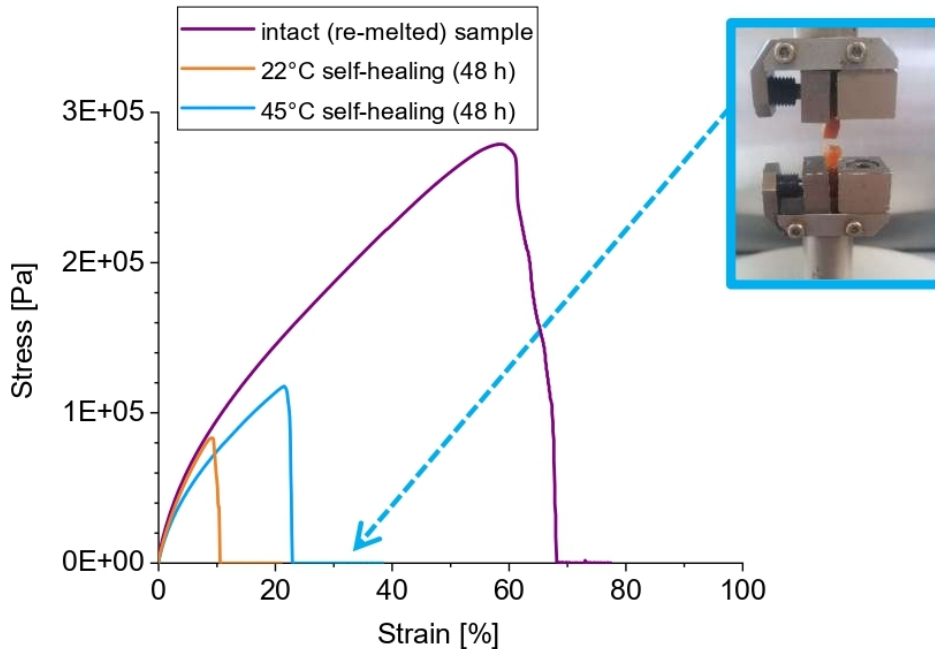
Figure 19: *Tensile curves measured for an intact, previously re-melted sample of BAFKU$_{41}$– HMS 064 (violet line),   for a disrupted and subsequently self-healed (22°C, 48h) sample (orange line),   as well as for a cut and subsequently self-healed (45°C, 48h) sample (turquoise line); the inlay shows the failure of the sample healed at 45°C at the smooth cutting plane.*

To sum up, the above results prove the presence of the self-healing effect in the rubbery copolymer BAFKU$_{41}$–HMS 064 in the solid rubbery state, but they also indicate, that a careful optimization of the healing temperature (key parameter), healing time, as well as of contact pressure (to prevent permanent deformation at higher temperatures) is needed to achieve 100% restoration of tensile properties by solid-state self-healing (these properties are otherwise easily restored by re-melting). A detailed investigation of the temperature-dependent self-healing, creep- and strain-damage-recovery behaviour is planned in a new work by the authors.

Conclusions

- Strongly physically cross-linked rubbers were successfully prepared, based on alternating polydimethylsiloxane (PDMS) spacer segments and pendant quartets of mesogenic building blocks (LC) of azobenzene type called "BAFKU".

- These materials are structurally related to the well-studied polymers with pendant-chain LC units (light sensitive actuators), but are generally highly different: The LC units make up only a small volume fraction and do not generate elastic energy upon irradiation, but they act as physical crosslinkers. The studied materials also display a fully linear structure, albeit with some dangling units.

- The physical crosslinking via aggregation of the spatially separated quartets of relatively small pendant BAFKU mesogens was found to be fairly efficient, as well as reversible by heat, by organic solvents, and by high mechanical strain.

- The most attractive product displays a rubber plateau extending over 100°C, melts near 70°C and is soluble in organic solvents.

- The pendant mesogen units were found to form imperfectly ordered nano-aggregates of several types, which are responsible for a continuous temperature region of phase transitions, extending from +30 to +70°C, which is also the range of the three discrete transitions in neat (non-bonded) BAFKU mesogen. The thermotropic behaviour of the physical crosslinks strongly influences all material properties.

- Very interesting was the observation by rheology of a second thermally induced gel point deep in the rubbery state (with the first gel point being the melting/solidification of the copolymer), obviously connected with thermotropic transitions in the physical crosslinks.

- The rheology investigations further proved a fast formation of physical network upon abrupt melt cooling (in one to several minutes).

- Samples (in rubbery state) damaged by excessive mechanical strain were shown to undergo rapid self-healing (multi-second scale) near room temperature, via BAFKU re-aggregation.

- Self-healing of disrupted samples at T far below the melting range was also proven.

- The prepared reversible elastomers might be of interest for advanced applications like soft material for 3D printing, as a temperature-switchable elastic / liquid-viscoelastic coupling material, due to reversible physical gelation, relatively low melt viscosity (30 000 mPa*s) and good adhesion to metal surfaces (as observed in rheology tests), or in elastomeric damping materials (*tan δ* has the high value of ca. 0.2 in the whole rubbery region).

- The synthesis path to the studied copolymers offers an easy possibility to optimize them for specific applications via modification of the pendant mesogen units.

- A copolymer with short PDMS spacer units, BAFKU$_8$–HMS 301, was also synthesized in this work. This relatively mesogen-rich material displays vitrimeric behaviour, and might be of interest as a model compound, e.g. for mesogen orientation experiments, or as a 'BAFKU oligomer'.

Acknowledgement

Data availability

The raw/processed data required to reproduce these findings cannot be shared at this time due to technical or time limitations.

x

x

References

_____

[1] J. C. Dubois, P. LeBarny, M. Mauzac, C. Noel, D. Demus, J. W. Goodby, G. W. Gray, H.W. Spiess, V. Vill. Handbook of liquid crystals, published by Verlag Chemie (now Wiley-VCH), Weinheim (DE), (1998), Print ISBN: 9783527295029, Online ISBN: 9783527619276, DOI: https://doi.org/10.1002/9783527619276.

[2] C. S. Hsu, The application of side-chain liquid-crystalline polymers. *Progress in Polymer Science* 22 (1997) 829–871. DOI: https://doi.org/10.1016/S0079-6700(97)00008-7.

[3] H. Finkelmann, G. Rehage, Investigations on liquid crystalline polysiloxanes, 1. Synthesis and characterization of linear polymers. *Macromolecular Rapid Communications* 1 (1980) 31–34. DOI: https://doi.org/10.1002/marc.1980.030010107.

[4] H. Finkelmann, G. Rehage, Investigations on liquid crystalline polysiloxanes, 2. Optical properties of cholesteric phases and influence of the flexible spacer on the mobility of the mesogenic groups. *Macromolecular Rapid Communications* 1 (1980) 733–740. DOI: https://doi.org/10.1002/marc.1980.030011206.

[5] H. Finkelmann, H. J. Kock, G. Rehage, Investigations on liquid crystalline polysiloxanes 3. Liquid crystalline elastomers — a new type of liquid crystalline material. *Macromolecular Rapid Communications* 2 (1981) 317–322. DOI: https://doi.org/10.1002/marc.1981.030020413.

[6] H. Finkelmann, G. Rehage, Investigations on liquid crystalline polysiloxanes, 4. Cholesteric homopolymers—synthesis and optical characterization. *Macromolecular Rapid Communications* 3 (1982) 859–864. DOI: https://doi.org/10.1002/marc.1982.030031203.

[7] H. Finkelmann, H. J. Kock, W. Gleim, G. Rehage, Investigations on liquid crystalline polysiloxanes 5. Orientation of LC-elastomers by mechanical forces. *Macromolecular Rapid Communications* 5 (1984) 287–293. DOI: https://doi.org/10.1002/marc.1984.030050508.

[8] C. Aguilera, J. Bartulin, B. Hisgen, H. Ringsdorf, Liquid crystalline main chain polymers with highly flexible siloxane spacers. *Die Makromolekulare Chemie / Macromolecular Chemistry (since 1994: Macromolecular Chemistry and Physics)* 184 (1983) 253–262. DOI: https://doi.org/10.1002/macp.1983.021840202.

[9] B. Donnio, H. Wermter, H. Finkelmann, A Simple and Versatile Synthetic Route for the Preparation of Main-Chain, Liquid-Crystalline Elastomers, *Macromolecules* 33 (2000) 7724–7729. DOI: https://doi.org/10.1021/ma0002850.

[10] H. P. Patil, J. Liao, R. C. Hedden, Smectic Ordering in Main-Chain Siloxane Polymers and Elastomers Containing p-Phenylene Terephthalate Mesogens, *Macromolecules* **2007**, *40*, 6206–6216. DOI: https://doi.org/10.1021/ma0706374.

[11] K. A. Burke, I. A. Rousseau, P. T. Mather, Reversible actuation in main-chain liquid crystalline elastomers with varying crosslink densities. *Polymer* 55 (2014) 5897–5907. DOI: http://dx.doi.org/10.1016/j.polymer.2014.06.088

[12] J. Küpfer, H. Finkelmann, Nematic liquid single crystal elastomers. *Macromolecular Rapid Communications* 12 (1991) 717–726. DOI: https://doi.org/10.1002/marc.1991.030121211.

[13] M. Wang, L. X. Guo, B. P. Lin, X. Q. Zhang, Y. Sun, H. Yang, Photo-responsive polysiloxane-based azobenzene liquid crystalline polymers prepared by thiol-ene click chemistry. *Liquid Crystals* 43 (2016) 1626–1635. DOI: https://doi.org/10.1080/02678292.2016.1191686.

[14] G. F. Wang, Y. Xiong, H. D. Tang, Synthesis and characterization of a graft side-chain liquid crystalline polysiloxane. *Journal of Organometallic Chemistry* 775 (2015) 50–54. DOI: https://doi.org/10.1016/j.jorganchem.2014.10.026.

[15] W. Zhao, B. P. Lin, X. Q. Zhang, Y. Sun, H. Yang, Polysiloxane Side-chain Liquid Crystalline Polymers Prepared by Alkyne Hydrosilylation. *Chinese Journal of Polymer Science* 33 (2015) 1431–1441. DOI: https://doi.org/10.1007/s10118-015-1697-9.

[16] S. Pandey, S. P. Mishra, B. Kolli, T. Kanai, A. B. Samui, Hyperbranched Photo Responsive and Liquid Crystalline Azo-Siloxane Polymers Synthesized by Click Chemistry. *Journal of Polymer Science, Part A: Polymer Chemistry* 50 (2012) 2659–2668. DOI: https://doi.org/10.1002/pola.26042.

[17] I. G. Shenouda, L. C. Chien, New ferroelectric liquid-crystalline polysiloxanes containing cyanohydrin chiral mesogens: L-norleucine series. *Macromolecules* 26 (1993) 5020– 5023. DOI: https://doi.org/10.1021/ma00071a006.

[18] Q. L. Zhou, J. T. Zhang, Z. J. Ren, S. K. Yan, P. Xie, R. B. Zhang, A Stable and High-Efficiency Blue-Light Emitting Terphenyl-Bridged Ladder Polysiloxane. *Macromolecular*

Rapid Communications 29 (2008) 1259–1263. DOI: https://doi.org/10.1002/marc.200800188.

[19] H. Kawakami, Y. Mori, H. Abe, S. Nagaoka, Gas transport properties of liquid crystalline polysiloxane with laterally attached side chain. *Journal of Membrane Science* 133 (1997) 245–253. DOI: https://doi.org/10.1016/S0376-7388(97)00086-0.

[20] H. X. Rao, Z. Y. Zhang, Preparation, Characterization, and Permeation Property of a Liquid Crystal/PDMS Membrane Material. *Journal of Applied Polymer Science* 123 (2012) 191–199. DOI: https://doi.org/10.1002/app.34450

[21] T. Ganicz, W. A. Stanczyk, J. Chmielecka, J. Kowalski, Liquid crystalline polycarbosilanes and poly(di-n-butylsiloxane) as stationary phases in gas chromatography. *Polymer International* 58 (2009) 248–254. DOI: https://doi.org/10.1002/pi.2527.

[22] M. Warner, E. Terentjev, Liquid crystal elastomers, published by Oxford University Press, Oxford (UK) (2003), ISBN: 9780198527671.

[23] T. Ikeda, J. Mamiya, Y. Yu, Photomechanics of Liquid-Crystalline Elastomers and Other Polymers. *Angewandte Chemie International Edition* 46 (2007) 506–528. DOI: https://doi.org/10.1002/anie.200602372.

[24] C. Ohm, M. Brehmer, R. Zentel, Liquid Crystalline Elastomers as Actuators and Sensors. *Advanced Materials* 22 (2010) 3366–3387. DOI: https://doi.org/10.1002/adma.200904059.

[25] T. Ube, K. Kawasaki, T. Ikeda, Photomobile Liquid-Crystalline Elastomers with Rearrangeable Networks. *Advanced Materials* 28 (2016) 8212–8217. DOI: https://doi.org/10.1002/adma.201602745.

[26] X. L. Pang, B. Xu, X. Qing, J. Wei, Y. L. Yu, Photo-Induced Bending Behavior of Post-Crosslinked Liquid Crystalline Polymer/Polyurethane Blend Films. *Macromolecular Rapid Communications* 39 (2018) #1700237   DOI: https://doi.org/10.1002/marc.201700237.

[27] A. B. Samui, S. Pandey, S. P. Mishra, Main chain photoresponsive liquid crystalline polymer synthesized through hydrosilylation. *RSC Advances* 5 (2015) 68351–68355. DOI: https://doi.org/10.1039/c5ra14818a.

[28] S. Pandey, B. Kolli, S. P. Mishra, A. B. Samui, Siloxane polymers containing azo moieties synthesized by click chemistry for photo responsive and liquid crystalline applications. *Journal of Polymer Science, Part A: Polymer Chemistry* 50 (2012) 1205–1215. DOI: https://doi.org/10.1002/pola.25885.

[29] M. O. Saed, R. H. Volpe, N. A. Traugutt, R. Visvanathan, N. A. Clark, C. M. Yakacki, High strain actuation liquid crystal elastomers via modulation of mesophase structure. *Soft Matter* 13 (2017) 7537–7547. DOI: https://doi.org/10.1039/c7sm01380a.

[30] J. J. Xu, S. Chen, W.L. Yang, B. Qin, X. X. Wang, Y. C. Wang, M. S. Cao, Y. C. Gao, C. S. Li, Y. M. Dong, Photo actuation of liquid crystalline elastomer nanocomposites incorporated with gold nanoparticles based on surface plasmon resonance. *Soft Matter* 15 (2019) 6116–6126. DOI: https://doi.org/10.1039/c9sm00984a.

[31] W. Lehmann, H. Skupin, C. Tolksdorf, E. Gebhard, R. Zentel, P. Kruger, M. Losche, F. Kremer, Giant lateral electrostriction in ferroelectric liquid-crystalline elastomers. *Nature* 410 (2001) 447–450. DOI: https://doi.org/10.1038/35068522.

[32] M. Wang, S. M. Sayed, L. X. Guo, B. P. Lin, X. Q. Zhang, Y. Sun, H. Yang, Multi-Stimuli Responsive Carbon Nanotube Incorporated Polysiloxane Azobenzene Liquid Crystalline Elastomer Composites. *Macromolecules* 49 (2016) 663–671. DOI: https://doi.org/10.1021/acs.macromol.5b02388.

[33] A. Durmus, N. Ercan, G. Soyubol, H. Deligoz, A. Kasgoz, Nonisothermal crystallization kinetics of poly(ethylene terephthalate)/clay nanocomposites prepared by melt processing. *Polymer Composites* 31 (2010) 1056–1066. DOI: https://doi.org/10.1002/pc.20892.

[34] H. R. Hakimelahi, L. Hu, B. B. Rupp, M. R. Coleman, Synthesis and characterization of transparent alumina reinforced polycarbonate nanocomposite. *Polymer* 51 (2010) 2494–2502. DOI: https://doi.org/10.1016/j.polymer.2010.04.023.

[35] W. Zhou, Y. Yu, H. Chen, F. J. DiSalvo, H. D. Abruna, Yolk–Shell Structure of Polyaniline-Coated Sulfur for Lithium–Sulfur Batteries. *Journal of the American Chemical Society* 135 (2013) 16736–16743. DOI: https://doi.org/10.1021/ja409508q.

[36] S. Matteucci, E. Van Wagner, B. D. Freeman, S. Swinnea, T. Sakaguchi, T. Masuda, Desilylation of Substituted Polyacetylenes by Nanoparticles. *Macromolecules* 40 (2007) 3337–3347. DOI: https://doi.org/10.1021/ma062421s.

[37] Y. Q. Rao, S. Chen, Molecular Composites Comprising TiO2 and Their Optical Properties. *Macromolecules* 41 (2008) 4838–4844. DOI: https://doi.org/10.1021/ma800371v.

[38] A. Miniewicz, J. Girones, P. Karpinski, B. Mossety-Leszczak, H. Galina, M. Dutkiewicz, Photochromic and nonlinear optical properties of azo-functionalized POSS nanoparticles dispersed in nematic liquid crystals. *Journal of Materials Chemistry C* 2 (2014) 432–440. DOI: https://doi.org/10.1039/C3TC31791A.

[39] H. Kim, A. A. Abdala, C. W. Macosko, Graphene/Polymer Nanocomposites, *Macromolecules* 43 (2010) 6515–6530. DOI: https://doi.org/10.1021/ma100572e.

[40] K. Depa, A. Strachota, M. Šlouf, J. Brus, V. Cimrová, Synthesis of conductive doubly filled poly(N-isopropylacrylamide)-polyaniline-SiO2 hydrogels. *Sensors and Actuators B-Chemical* 244 (2017) 616–634. DOI: https://doi.org/10.1016/j.snb.2016.12.121.

[41] A. S. Robbes, J. Jestin, F. Meneau, F. Dalmas, O. Sandre, J. Perez, F. Boue, F. Cousin, Homogeneous Dispersion of Magnetic Nanoparticles Aggregates in a PS Nanocomposite:

Highly Reproducible Hierarchical Structure Tuned by the Nanoparticles' Size. *Macromolecules* 43 (2010) 5785–5796. DOI: https://doi.org/10.1021/ma100713h.

[42] B. Mossety-Leszczak, B. Strachota, A. Strachota, M. Steinhart, M. Šlouf, The orientation-enhancing effect of diphenyl aluminium phosphate nanorods in a liquid-crystalline epoxy matrix ordered by magnetic field. *European Polymer Journal* 72 (2015) 238–255. DOI: https://doi.org/10.1016/j.eurpolymj.2015.09.018.

[43] P. K. Maji, N. K. Das, A. K. Bhowmick, Preparation and properties of polyurethane nanocomposites of novel architecture as advanced barrier materials. *Polymer* 51 (2010) 1100–1110. DOI: https://doi.org/10.1016/j.polymer.2009.12.040.

[44] M. Spirkova, J. Brus, L. Brozova, A. Strachota, J. Baldrian, M. Urbanova, J. Kotek, B. Strachotova, M. Slouf, A view from inside onto the surface of self-assembled nanocomposite coatings. *Progress in Organic Coatings* 61 (2008) 145–155. DOI: https://doi.org/10.1016/j.porgcoat.2007.07.032

[45] N. Yan, G. Buonocore, M. Lavorgna, S. Kaciulis, S. K. Balijepalli, Y. H. Zhan, H. S. Xia, L. Ambrosio, The role of reduced graphene oxide on chemical, mechanical and barrier properties of natural rubber composites. *Composites Science and Technology* 102 (2014) 74–81. DOI: https://doi.org/10.1016/j.compscitech.2014.07.021.

[46] H. W. Milliman, H. Ishida, D. A. Schiraldi, Structure Property Relationships and the Role of Processing in the Reinforcement of Nylon 6-POSS Blends. *Macromolecules* 45 (2012) 4650–4657. DOI: https://doi.org/10.1021/ma3002214.

[47] J. C. Yu, B. Tonpheng, G. Grobner, O. Andersson, A MWCNT/Polyisoprene Composite Reinforced by an Effective Load Transfer Reflected in the Extent of Polymer Coating. *Macromolecules* 45 (2012) 2841–2849. DOI: https://doi.org/10.1021/ma202604d.

[48] M. Lutecki, B. Strachotová, M. Uchman, J. Brus, J. Pleštil, M. Šlouf, A. Strachota, L. Matějka, Thermosensitive PNIPA-based organic-inorganic hydrogels. *Polymer Journal* 38 (2006) 527–541. DOI: https://doi.org/10.1295/polymj.PJ2005112

[49] G. Huerta-Angeles, K. Hishchak, A. Strachota, B. Strachota, M. Šlouf, L. Matějka, Super-porous nanocomposite PNIPAm hydrogels reinforced with titania nanoparticles, displaying a very fast temperature response as well as pH-sensitivity. *European Polymer Journal* 59 (2014) 341–352. DOI: https://doi.org/10.1016/j.eurpolymj.2014.07.033

[50] K. Depa, A. Strachota, M. Šlouf, J. Brus, Poly(N-isopropylacrylamide)-SiO2 nanocomposites interpenetrated by starch: Stimuli-responsive hydrogels with attractive tensile properties. *European Polymer Journal* 88 (2017) 349–372. DOI: https://doi.org/10.1016/j.eurpolymj.2017.01.038

[51] A. Strachota, I. Kroutilová, J. Kovářová, L. Matějka, Epoxy Networks Reinforced with Polyhedral Oligomeric Silsesquioxanes (POSS). Thermomechanical Properties. *Macromolecules* 37 (2004) 9457−9464. DOI: https://doi.org/10.1021/ma048448y

[52] L. Matějka, A. Strachota, J. Pleštil, P. Whelan, M. Steinhart, M. Šlouf, Epoxy Networks Reinforced with Polyhedral Oligomeric Silsesquioxanes (POSS). Structure and Morphology. *Macromolecules* 37 (2004) 9449−9456. DOI: https://doi.org/10.1021/ma0484577

[53] A. Strachota, P. Whelan, J. Kříž, J. Brus, M. Urbanová, M. Šlouf, L. Matějka, Formation of nanostructured epoxy networks containing polyhedral oligomeric silsesquioxane (POSS) blocks. *Polymer* 48 (2007) 3041−3058. DOI: https://doi.org/10.1016/j.polymer.2007.03.052

[54] J. Brus, M. Urbanová, A. Strachota, Epoxy networks reinforced with polyhedral oligomeric silsesquioxanes: structure and segmental dynamics as studied by solid-state NMR. *Macromolecules* 41 (2008) 372−386. DOI: https://doi.org/10.1021/ma702140g

[55] A. Strachota, F. Ribot, L. Matějka, P. Whelan, L. Starovoytova, J. Plestil, M. Steinhart, M. Slouf, J. Hromadkova, J. Kovarova, M. Spirkova, B. Strachota, Preparation of novel, nanocomposite stannoxane-based organic-inorganic epoxy polymers containing ionic bonds. *Macromolecules* 45 (2012) 221–237. DOI: https://doi.org/10.1021/ma201178j

[56] A. Strachota, K. Rodzen, F. Ribot, M. Perchacz, M. Trchová, M. Steinhart, L. Starovoytova, M. Slouf, B. Strachota, Tin-based "super-POSS" building blocks in epoxy nanocomposites with highly improved oxidation resistance. *Polymer* 55 (2014) 3498–3515. DOI: https://doi.org/10.1016/j.polymer.2014.06.002

[57] A. Strachota; K. Rodzeń; F. Ribot; M. Trchová; M. Steinhart; L. Starovoytova; E. Pavlova, Behavior of Tin-Based "Super-POSS" Incorporated in Different Bonding Situations in Hybrid Epoxy Resins. *Macromolecules* 47 (2014) 4266–4287. DOI: https://doi.org/10.1021/ma500507j

[58] K. Rodzeń, A. Strachota, F. Ribot, M. Šlouf, Effect of network mesh size on the thermo-mechanical properties of epoxy nanocomposites with the heavier homologue of POSS, the inorganic butylstannoxane cages. *European Polymer Journal* 57 (2014) 169–181. DOI: https://doi.org/10.1016/j.eurpolymj.2014.05.016

[59] A. Strachota, K. Rodzeń, V. Raus, F. Ribot, M. Janata, E. Pavlova, Incorporation and chemical effect of Sn-POSS cages in poly(ethyl methacrylate). *European Polymer Journal* 68 (2015) 366–378. DOI: https://doi.org/10.1016/j.eurpolymj.2015.04.024

[60] K. Rodzeń, A. Strachota, F. Ribot, L. Matějka, J. Kovářová, M. Trchová, M. Šlouf, Reactivity of the tin homolog of POSS, butylstannoxane dodecamer, in oxygen-induced crosslinking reactions with an organic polymer matrix: Study of long-time behavior. *Polymer Degradation and Stability* 118 (2015) 147–166. DOI: https://doi.org/10.1016/j.polymdegradstab.2015.04.020

[61] K. Rodzeń, A. Strachota, V. Raus, E. Pavlova, Polyhedral oligomeric butyl stannoxane cages (Sn-POSS) as oxidation activated linear repairing units or crosslinking nano-building blocks, depending on structure of the polymer matrix. *Polymer Degradation and Stability* 142 (2017) 1–20. DOI: https://doi.org/10.1016/j.polymdegradstab.2017.05.019

[62] B. Strachota, A. Strachota, S. Horodecka, M. Steinhart, J. Kovářová, E. Pavlova, F. Ribot, Polyurethane nanocomposites containing the chemically active inorganic Sn-POSS cages Reactive and Functional Polymers. *Reactive and Functional Polymers* 143 (2019) #104338; DOI: https://doi.org/10.1016/j.reactfunctpolym.2019.104338

[63] M. Slouf, S. Krejcikova, T. Vackova, J. Kratochvil, L. Novak, In situ observation of nucleated polymer crystallization in polyoxymethylene sandwich composites. *Frontiers in Materials* 2, article 23 (2015) 1–12. DOI: https://doi.org/10.3389/fmats.2015.00023.

[64] T. Vackova, J. Kratochvil, A. Ostafinska, S. Krejcikova, M. Nevoralova, M. Slouf, Impact of particle morphology on structure, crystallization kinetics, and properties of PCL composites with TiO2-based particles. *Polymer Bulletin* 74 (2017) 445–464. DOI: https://doi.org/10.1007/s00289-016-1723-2.

[65] P. A. Klonos, Crystallization, glass transition, and molecular dynamics in PDMS of low molecular weights: A calorimetric and dielectric study, Polymer 2018, 159, 169–180. DOI: https://doi.org/10.1016/j.polymer.2018.11.028

[66] A. M. Kansara, G. L. Jadav, S. G. Chaudhri, P. S. Singh, Preparation of Poly(dimethylsiloxane)-Polysulfone Composite Membrane by Sequential Absorption-Reaction-Evaporation Process and its Application in Treatment of Aqueous Solution Containing Volatile Organics. *Separation Science and Technology* 49 (2014) 2834–2846. DOI: https://doi.org/10.1080/01496395.2014.944619.

[67] H.H. Winter, F. Chambon, Analysis of linear viscoelasticity of a crosslinking polymer at the gel point. *Journal of Rheology* 30 (1986) 367–382. DOI: https://doi.org/10.1122/1.549853.

SUPPLEMENTARY INFORMATION

Meltable copolymeric elastomers based on polydimethylsiloxane with multiplets of pendant liquid-crystalline groups as physical crosslinker: A self-healing structural material with a potential for smart applications

Sabina Horodecka[1,2], Adam Strachota[1]*, Beata Mossety-Leszczak[3], Miroslav Šlouf[1], Alexander Zhigunov[1], Michaela Vyroubalová[1], Dana Kaňková[1], Miloš Netopilík[1]

[1] *Institute of Macromolecular Chemistry, Czech Academy of Sciences,*
Heyrovskeho nam. 2, CZ-162 06 Praha, Czech Republic

[2] *Faculty of Science, Charles University,*
Albertov 6, CZ-128 00 Praha 2, Czech Republic

[3] *Faculty of Chemistry, Rzeszow University of Technology,*
al. Powstancow Warszawy 6, PL-35-959 Rzeszow, Poland

1. Synthesis

SI-Scheme 1: *Most likely procedure of the synthesis of the employed polydimethylsiloxane precursor polymers, which leads to the occurrence of Si–H units in quartets.*
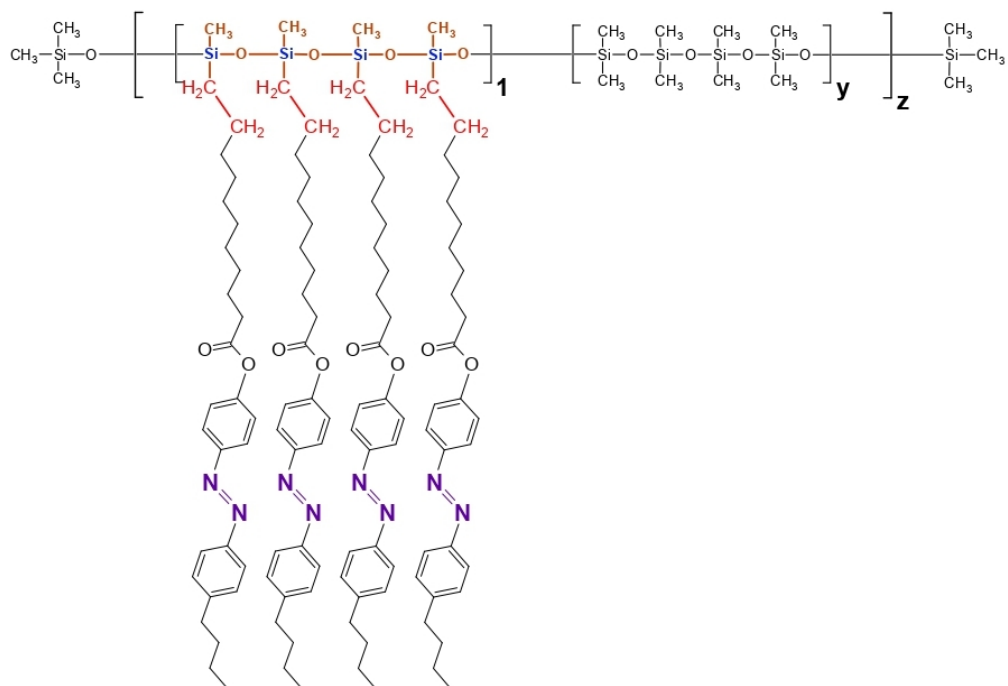
SI-Scheme 2: *General structure of the BAFKU-PDMS copolymers.*

1.1. FTIR and ^{1}H-NMR: Evaluation of conversion of the PDMS grafting with BAFKU

The **completeness of conversion** in the hydrosilylation reactions was **verified by** means of **FTIR (*SI-Fig. 1a*) and** ^{1}**H-NMR (*SI-Fig. 1b*)**. Quantitative conversion would lead to the disappearance of the very characteristic signals of the Si–H bond in both spectra and also of vinyl-signals in ^{1}H-NMR. In case of the HMS064 precursor, the FTIR method already is not sufficiently sensitive (see *SI-Fig. 2* and *3*), but an NMR spectrum with a sufficient number of scans still offers a sensitive analysis (see zoom in *SI-Fig. 1b* or the *SI-Fig. 6 bottom*). In the zoomed NMR spectrum in *SI-Fig. 1b* it can be seen, that the SiH peak, which initially had half the area of one the aromatic multiplets (of the copolymer), nearly disappeared, except for a small reside corresponding to 6.3% of un-reacted groups. Also, the signals of the vinyl groups of BAFKU practically disappeared: Their nearly invisible residue corresponds to ca. 3.3% of un-reacted vinyl groups. In case of the copolymer HMS301/BAFKU, such residues are no more visible by ^{1}H-NMR (see *SI-Fig. 6 top*). The ^{1}H-NMR spectroscopy was also used to **verify the expected ratio** of the **BAFKU** units (represented e.g. by the aromatic signals) **to** the **PDMS repeat units** (represented by the methyl(-Si) signals), which **corresponded very well** with the experimental ratios of the respective signal integrals in the products (see *SI-Fig. 6*).
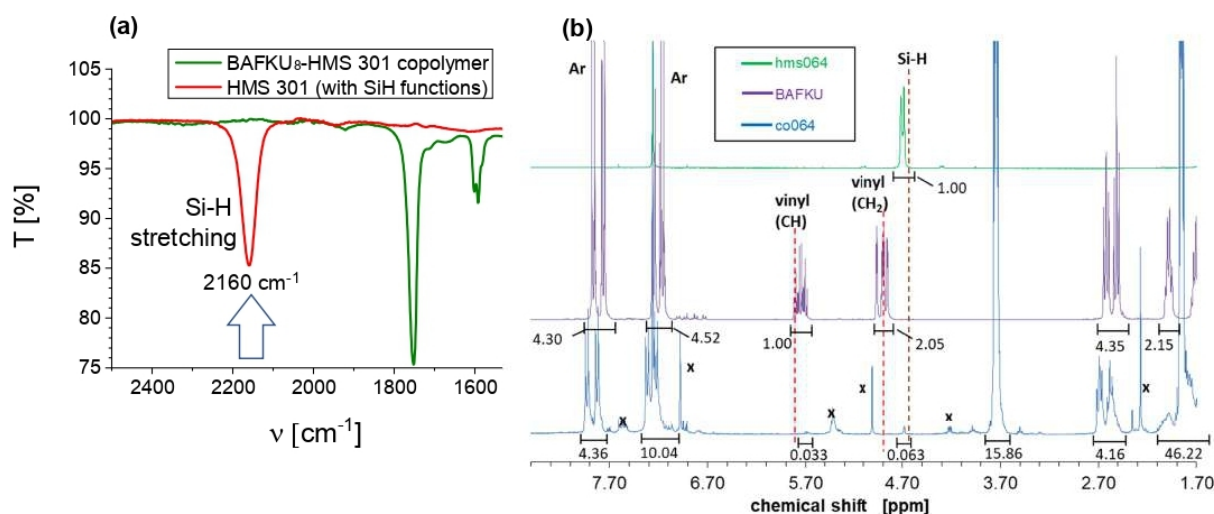
SI-Fig. 1: *Spectroscopic evaluation of the completion of the grafting reaction: (a): FT-IR spectra of pure HMS 301 and of BAFKU$_8$–HMS 301 with Si-H peak highlighted (the entire FTIR spectra are shown in **SI-Fig. 2** and their complete assignment is given in **SI-Table 1** and **2**); (b):* ^{1}*H-NMR of pure HMS 064, BAFKU and BAFKU$_{41}$–HMS 064 with value of integrals, which showing the surface of the peaks.*
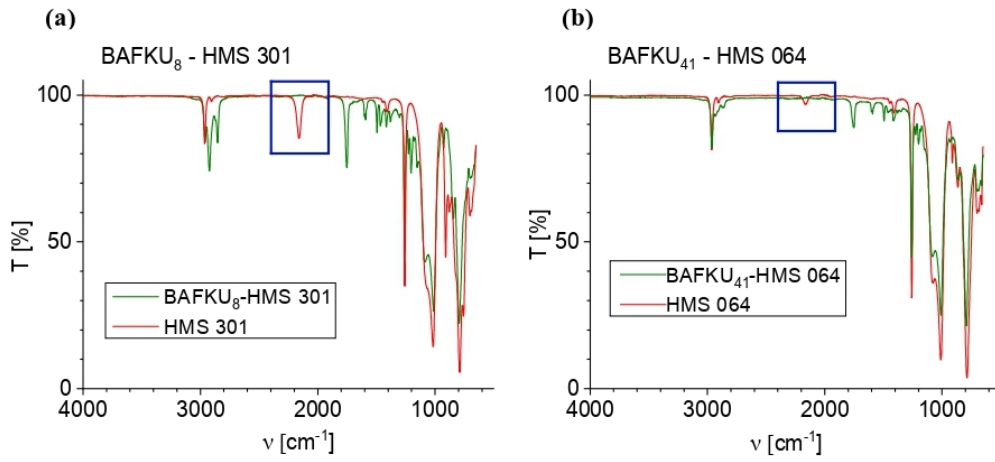
SI-Fig. 2: *FT-IR spectra of (a): pure HMS 301 and of BAFKU$_8$–HMS 301; (b): pure HMS 064 and of BAFKU$_{41}$–HMS 064; the characteristic peak of the Si-H bond stretching is highlighted.*
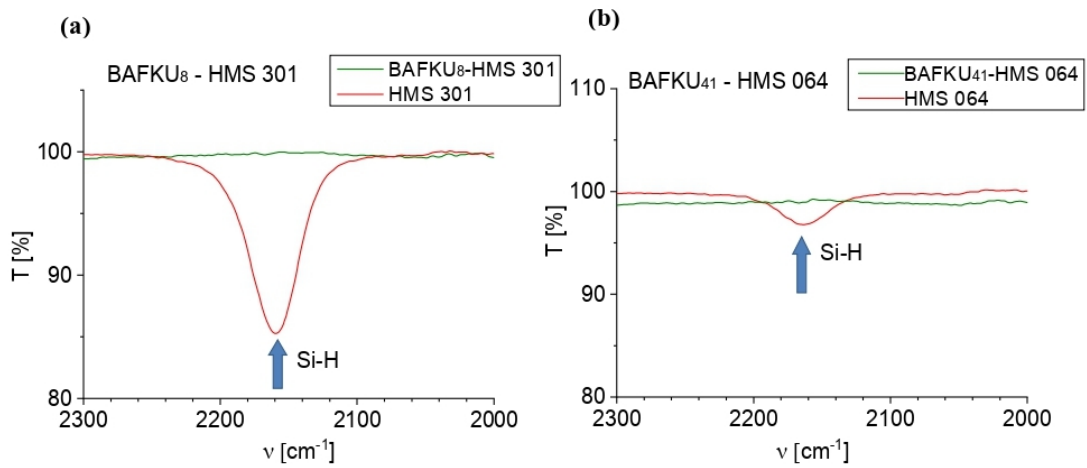
SI-Fig. 3: *Detail of the characteristic FT-IR peak of the Si-H bond stretching: (a): BAFKU$_8$–HMS 301 vs. HMS 301; (b): BAFKU$_{41}$–HMS 064 vs. HMS 064.*

SI-Table 1: *Assignment of FTIR peaks of HMS 301.*

HMS 301	
Characteristic Absorption(s) (cm^{-1})	**Group**
2960	Medium C-H
2158	Strong Si-H
1415	Medium C-H
1258	Strong Si-CH3
1016	Strong [(CH3)2SiO]x
911	Si-H
881	Si-H
789	Strong Si-CH3
704	Strong C-H

SI-Table 2: *FTIR spectral peaks of copolymer BAFKU$_8$ – HMS 301.*

BAFKU$_8$-HMS 301	
Characteristic Absorption(s) (cm^{-1})	**Functional Group**
2962	Medium C-H
2920	Medium C-H
2850	Medium C-H
1751	Strong C=O
1592	Strong C=C
1490	Medium C-H
1464	Medium C-H
1416	Medium C-H
1374	Medium C-H
1305	Strong C-O
1257	Strong Si-CH3
1204	Strong C-O
1151	Strong C-O/ Medium C-N
1087	Strong C-O
1013	Strong [(CH3)2SiO]x
922	Si-H
843	Medium C=C
795	Strong Si-CH3
689	Strong C-H

1.2. ^{1}H-NMR: Purity of components and products, as well as synthesis conversion

1.2.1. BAFKU mesogen: ^{1}H-NMR analysis
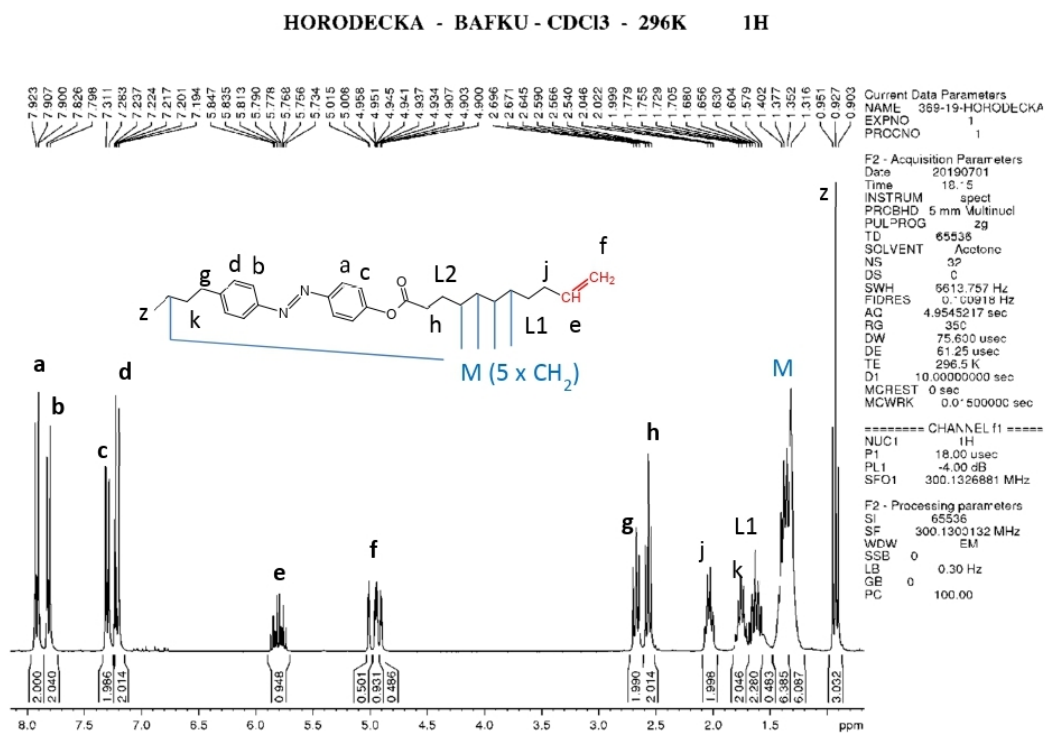
SI-Fig. 4: ^{1}H-NMR spectrum of the pure BAFKU mesogen with assigned peaks.

1.2.2. PDMS components: ¹H-NMR analysis

HORODECKA - HMS 301 - CDCl3 - 295K   1H

HORODECKA - HMS 064 - CDCl3 - 294K   1H
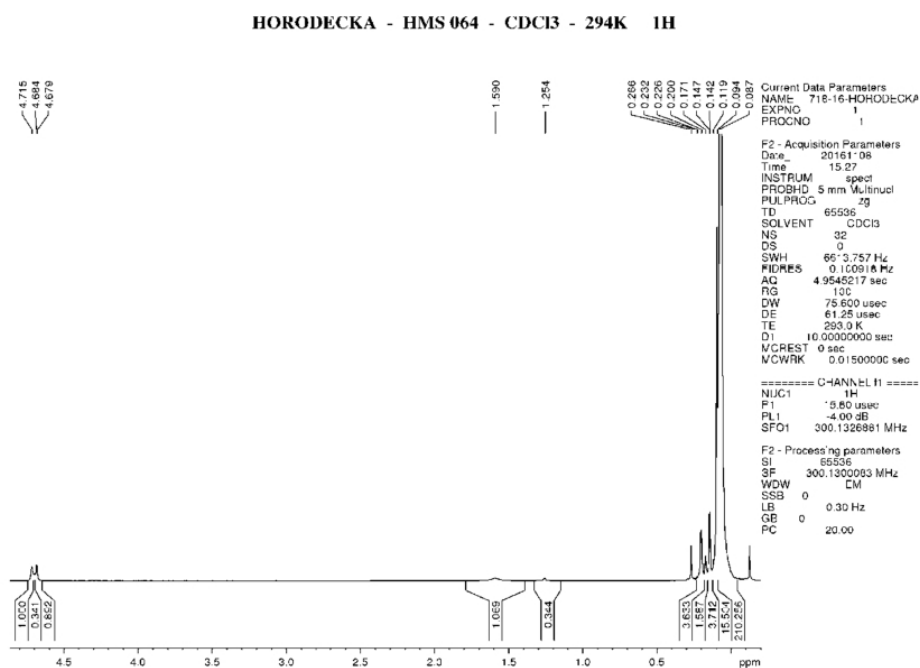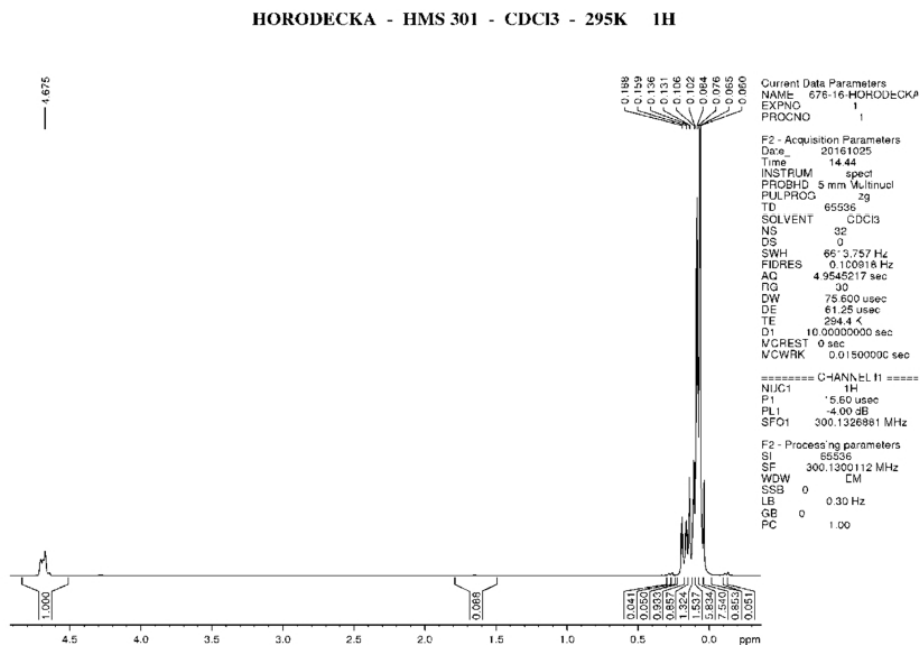
SI-Fig. 5: *¹H-NMR spectra of the PDMS precursors: (top): HMS 301; (bottom): HMS 064; the peak of the methyl groups is near 0.06 ppm, the Si-H peak near 4.68 ppm.*

Structure parameters of HMS (PDMS) polymers from ^{1}H-NMR analysis:
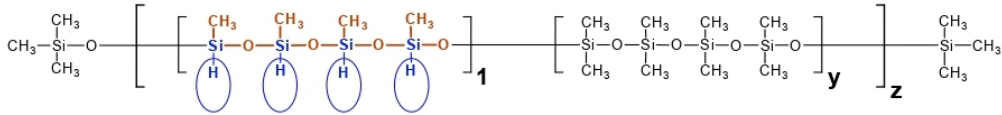
Aim:

calculation **y**, **z** : coefficients from above structure formula, and of the equivalent molecular weight per SiH function (*EqMW*), as needed to calculate accurate reactant amounts for synthesis.

Magnitudes for calculation:

y, **z** : coefficients from above structure formula

H ≡ molecular mass of the block $[\{(CH_3)(H)SiO\}_4]$ = 240.5094 g/mol

D ≡ molecular mass of the block $[\{(CH_3)_2SiO\}_4]$ = 296.6158 g/mol

E ≡ molecular mass of both end groups ≡ $(CH_3)_3Si\text{-}O\text{-}Si(CH_3)_3$ = 162.3775 g/mol

M = molecular mas of the whole HMS molecule (as shown in above structure formula): the value stated by the manufacturer was used

R = apparent ratio of the number of 'normal' PDMS repeat units to the number of methyl-hydrido-functional repeat units, which does not take into account the trimethylsilyl end groups (it is similar but not equal to **y**, it comes close to **y** at high **z** values); its calculation from the ^{1}H-NMR spectra in *SI-Fig. 5* is described below:

Obtaining ratio R from the ^{1}H-NMR spectra in SI-Fig. 5:

at first, the integrals are normalized so, that the value of the integral of the SiH peak is equal to 1.00 (as done in *SI-Fig. 5 top*)

next, the sum of all integrals of the CH₃(-Si) peak group, '*CH3_norm*' is calculated

as every SiH repeat unit also contains one methyl group (see structure), the corresponding intensity (threefold of SiH integral, normalized to 1.00) has to be subtracted from *CH3_norm* in order to obtain the integral of normal PDMS units (including the trimethylsilyl end groups, which cannot be resolved):

CH3_PDMS_norm = CH3_norm – 3.00

in order to use the integrals *CH3_PDMS_norm* and   *CH3_from_SiH_norm* for the calculation of the ratio of the repeat units, it has to be taken into account that the 'normal' units have the double number of methyl groups than the hydrido-functional ones

hence:

R = *CH3_PDMS_norm / CH3_from_SiH_norm*

R = {(*CH3_ norm* - 3) / 2} / (3 * *SiH_norm)*

R = {(*CH3_ norm* - 3) / 2} / 3

R = (*CH3_ norm* - 3) / 6

in this way, the apparent (inaccurate) ratio **R** of PDMS to SiH repeat units is obtained from the ^{1}H-NMR-spectra in *SI-Fig. 5* (this R does not take into account the end groups)

the experimentally determined **R** values for HMS-301 and HMS-064 are listed in *SI-Table 3.*

[1]*H-NMR signal integrals and the precise structure of the precursor polymers:*

If the further-above-depicted structure of the precursor (HMS) polymers is taken into account, the following relations concerning the numbers of protons (H), and hence also integral values can be stated:

SiH (in hydrido-quartets)	CH$_3$ (in hydrido-quartets)	(CH$_3$)$_2$ (in 'normal' quartets of PDMS units)	((CH$_3$)$_3$)$_2$ (in end groups)
z*1* 4*H1	z*1* 4*H3	z*y* 4*H6	2*3*H3
4z	4z*3	4z*y*6	18
SiH integral normalized to 1.0 => division of all values by 4z			
1	3	y*6	18/4z = **4.5/z**

The ^{1}H-NMR peaks of the above listed structural units occur in two groups which were used for determining the above-discussed apparent ratio R of the both types of repeat units; their integral ratios then are:

Peak group	SiH peak	all CH$_3$-Si peaks
Integral value	1	3 + y*6 + 4.5/z

if the experimentally determined ratio **R** is expressed using the structural coefficients **y** and **z**, we obtain:

R = {(6*y + 4.5/z)/2}/3 = (6*y + 4.5/z)/6

R = y + 0.75/z

a second equation is needed for determining **y** and **z**

the relation describing the known molecular mass of the polymer can serve this purpose:

M = E + (H*1 + D*y)*z

Determining **y** *and* **z** *:*

The set of equations

   1) $M = E + (H*1 + D*y)*z$

   2) $R = y + 0.75/z$

yields the <u>solution</u> for **y** and **z** :

$y = (R*M - R*E - 0.75*H) / (0.75*D + M - E)$

$z = 0.75/(R - y)$

using the structural coefficients **y** and **z** , other molecular parameters, like the average number of functional groups per molecule, the equivalent molecular weight per SiH functional group, and other, can be calculated and are listed in **SI-Table 3**.

Results:

SI-Table 3: *Molecular parameters of the HMS precursor polymers determined by* ^{1}*H-NMR.*

precursor polymer name	M_n (supplier) [g/mol]	R from NMR	$y*$	$z*$	number of all repeat units (= number of Si atoms)*	functionality (number of SiH groups)	EqMW [g/mol]
HMS-301	1 950	2.646	2.264	1.960	27.59	7.841	248.700
HMS-064	55 000	17.017	16.945	10.412	749.389	41.65	1320.558

*) the average length of elastic spacers between the functional ('grafting') SiH quartets is equal to **4y** according to the above structure, and is equal to **9.05** repeat units **for HMS-301** and to **67.8** repeat units **for HMS-064** (real spacer lengths in real molecule segments always must be divisible by 4, due to above structure).

1.2.3. HMS-BAFKU copolymers: ^{1}H-NMR analysis

HORODECKA - (BAFKU)8-HMS 301 - CDCl3 - 295K   1H

HORODECKA - (BAFKU)45-HMS 064 - CDCl3 - 296K   1H
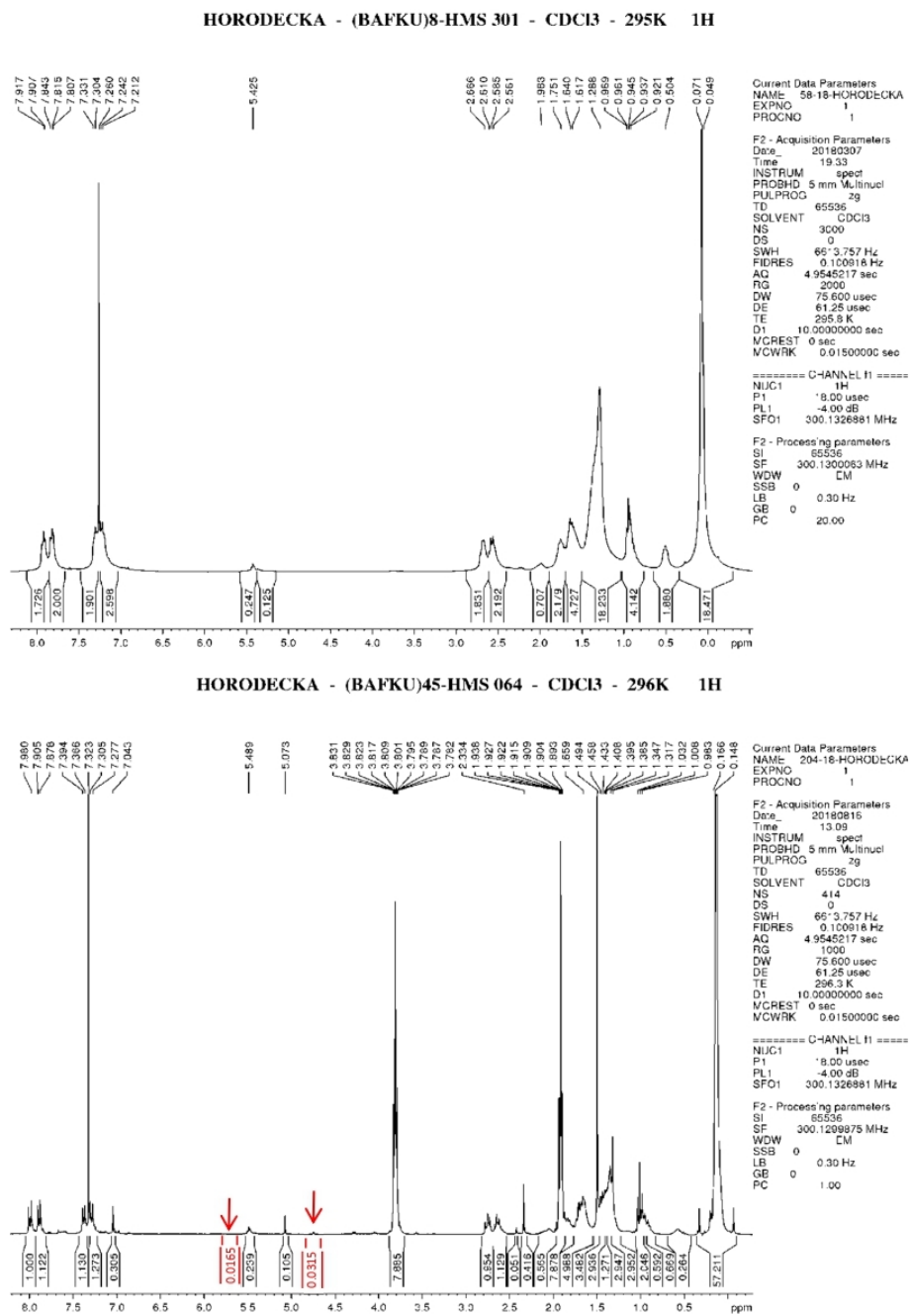
SI-Fig. 6: *^{1}H-NMR spectra of the copolymers (top): BAFKU$_8$–HMS 301; (bottom): BAFKU$_{41}$–HMS 064.*

1.3. GPC: Molecular mass analysis of the precursors and of the final copolymers

The **molecular masses** of the prepared grafted copolymers, and especially their distributions, were evaluated by means of size exclusion chromatography (**SEC, "GPC"**), using tetrahydrofuran as eluent (sample concentration: 5 mg/mL) and polystyrene standard calibration (valid for the range of 100–500 000 g/mol), with simultaneous UV/Vis-refraction-index- (at $\lambda = 254$ nm) and evaporative-light-scattering- (ELSD) detection. The results are shown in *SI-Fig. 7*: Copolymers are compared with BAFKU and precursor polysiloxanes, all compared samples are shown as traces in the ELSD detector, while for the copolymers, also the UV/Vis trace is shown.

If the NMR and GPC results are compared, it appears that the seemingly prominent amount of detected **non-bonded BAFKU** in the copolymeric products is strongly over-estimated in case of both GPC detection methods. Free BAFKU appears as narrow and intense peak with maximum between 500 and 700 Da in the traces of both copolymers in *SI-Fig. 7* (see also peak list in *SI-Table 4*). On the other hand, the above NMR results, which can be considered to be more accurate, indicate practically quantitative disappearance of non-bonded BAFKU. This contradiction can be explained by a relatively strong UV/Vis absorption peak of azobenzene (and hence of BAFKU) near 250 nm, and by the relative proximity of the ELSD wavelength (658 nm) to the long-wave absorption of azobenzene (a smaller peak between 400–500 nm).
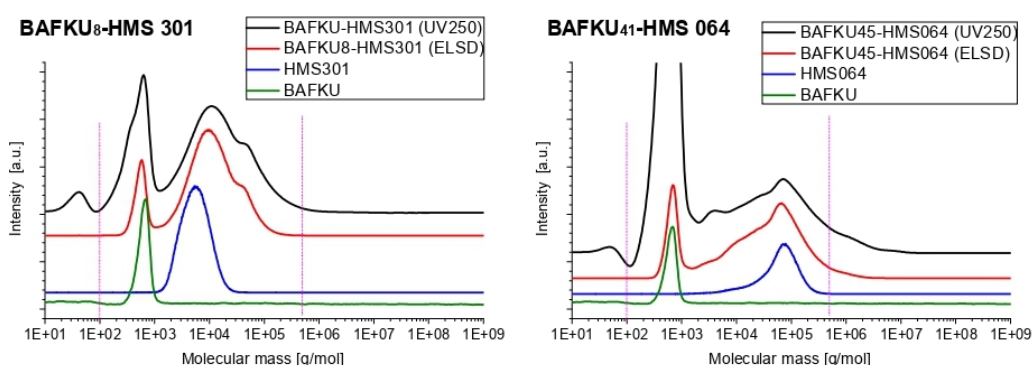
SI-Fig. 7: *GPC traces of the prepared copolymers, overlaid with the traces of their respective PDMS precursors and of BAFKU: (left): BAFKU₈–HMS 301; (right): BAFKU₄₁–HMS 064.*

The analysis of the GPC traces from *SI-Fig. 7* is summarized in *SI-Table 4*, including comparison with values stated by the producer, and the product molecular weights calculated from them. It can be noted, that due to 'non-typical' properties of the analysed materials (if compared to polystyrene standard), the experimental molecular masses display large deviations from the expected values.

The **rigid-rod-like BAFKU** displays a higher apparent molecular mass (see *SI-Table 4*), most likely due to lack of flexibility which leads to the preference of larger pores in the column.

The relatively small **PDMS precursor HMS 301** displays a two times higher apparent molecular mass, than the one stated by its producer (see *SI-Table 4*). On the other hand, the larger **HMS 064** molecule displays GPC characteristics closer to expectation (see *SI-Table 4*), but it also contains lower-molecular fractions, which manifest themselves as somewhat gradual decrease of the peak on the low-molecular side (see blue curve in *SI-Fig. 7b*).

In case of the **BAFKU$_8$–HMS301 copolymer**, in which the grafted BAFKU units are responsible for ca. 60% of the volume (see Discussion, Synthesis, in main paper document), a nearly twofold apparent molecular mass increase in comparison to HMS301 is observed by GPC (see *SI-Fig. 7 left* and *SI-Table 4*). Theoretically (see *SI-Table 4*), a 2.5-fold increase would be expected, which is a good agreement. A small high-molecular shoulder is additionally observed in BAFKU$_8$–HMS301, possibly due to small-extent SiH-crosslinking.

On the other hand, in case of **BAFKU$_{41}$–HMS064**, in which the mesogen constitutes only ca. 20 Vol.% (ca. 1.25-fold increase in M_n expected), the observed change in the GPC trace in comparison to the PDMS precursor is more complex (see *SI-Fig. 7 right* and *SI-Table 4*): The polydispersity highly increases (the product peak expands to both higher and lower masses), while the peak maximum stays practically unchanged (a slight shift to lower masses even can be concluded). Both the apparent decrease and increase of the molecular mass of BAFKU$_{41}$–HMS064 could be attributed to intra-molecular (apparent MW decrease, formation of denser coils) and inter-molecular (MW increase, formation of multi-molecular adducts) aggregations of BAFKU quartets grafted onto this large molecule (see aggregation in *Scheme 2* and full copolymer structure in *Scheme 3* in Discussion, Synthesis, in the main paper document). Also, the radical side-reactions of SiH, mentioned in Discussion/Synthesis (main paper), which led to micro-gelation of a part of the BAFKU$_{41}$–HMS064 reaction mixture, could be responsible for the formation of a part of the observed higher-molecular fraction (multiple product molecules coupled covalently, see also the above-mentioned shoulder in BAFKU$_8$–HMS301).

To sum up, it can be concluded, that the **GPC analysis** provides **valuable information** about the obtained copolymers, **but it is not well-suited to analyse** their molecular masses **with high precision**, due to the complex structure and properties of the copolymers (possible BAFKU aggregation).

SI-Table 4: *GPC: data obtained by the analysis of GPC traces of the prepared copolymers, as well as of their precursors.*

Sample	Peak maximum [g/mol]	M_n from automatic evaluation [g/mol]	PD (autom. eval.) [ ]	M_n [g/mol] from producer
BAFKU	687	687.33	1.07	420.59
HMS 301	5 600	4 040	1.39	1 950 ±50
BAFKU$_8$-HMS301	(580 = BAFKU) 11 000 (+ high-molecular shoulder at 42 000)	9 400 (+ high-molecular shoulder at 59 000)	1.35 (shoulder: 1.03)	5 315 ±50 calculated*
HMS 064	75 000	28 300 (would be ca. 57 000 without the low-molecular fraction)	2.43	55 000 ±5000
BAFKU$_{41}$-HMS064	(698 = BAFKU) 65 000 (extends from 9 000 to 230 000)	19 700	6.36	72 244 ±5000 calculated*

*) theoretical value calculated from the components' M_n values given by the producer, while assuming quantitative coupling of the components

1.3.1. GPC Source data
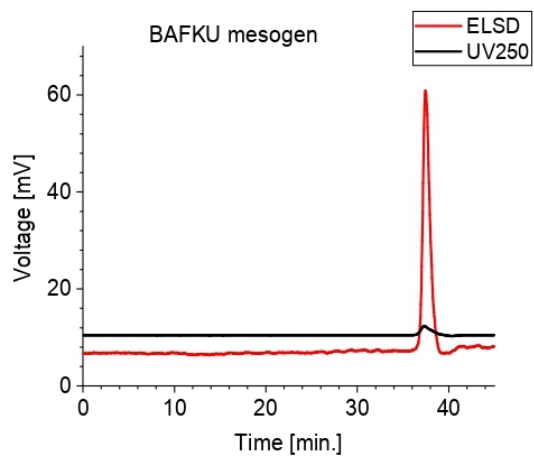
BAFKU

nr.	Max. RT	Start RT	End RT	flow rate correction	Mp	Mn	Mw	Mz	PD	I [mV]	I [%]
x	37.45	34.67	39.45	1	750	654	703	769	1.074924	54.41	100

SI-Fig. 8: *GPC trace of pure BAFKU.*

HMS301

nr.	Max. RT	Start RT	End RT	flow rate correction	Mp	Mn	Mw	Mz	PD	I [mV]	I [%]	Integral [mV.s]
x	34.16	29.28	40.13	1	4635	4036	5624	7823	1.393459	84.44	100	12109.73
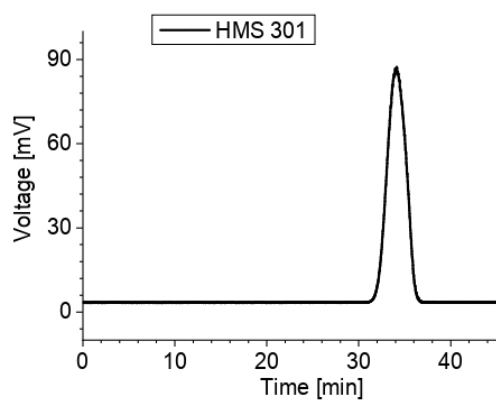
SI-Fig. 9: *GPC trace of pure HMS 301 polydimethylsiloxane precursor.*
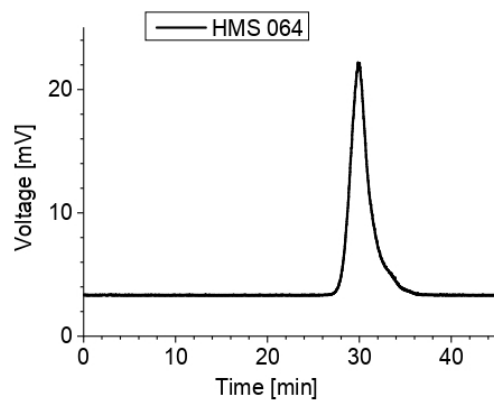
HMS064

nr.	Max. RT	Start RT	End RT	flow rate correction	Mp	Mn	Mw	Mz	PD	I [mV]	I [%]	Integral [mV.s]
x	29.85	25.43	39.07	1	71318	28257	68638	106693	2.429062	18.94	100	2816.86

SI-Fig. 10: *GPC trace of pure HMS 064 polydimethylsiloxane precursor.*
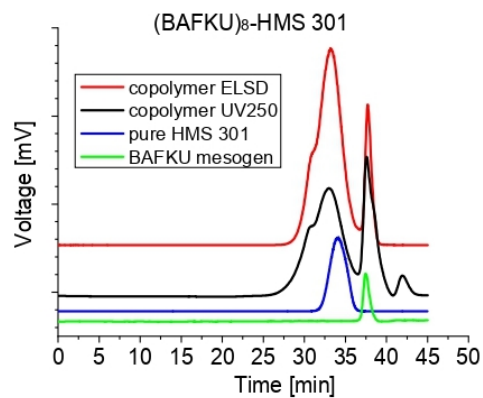
BAFKU$_8$-HMS301

nr.	Max. RT	Start RT	End RT	flow rate correction	Mp	Mn	Mw	Mz	PD	I [mV]	I [%]
1	31.31	29.8	31.33	1	41433	59198	61131	63204	1.032653	2.03	0.68
2	33.19	31.34	36.15	1	13002	9382	12657	16323	1.349073	147.8	49.38
x	37.72	36.64	39.19	1	796	715	751	786	1.05035	149.46	49.94

SI-Fig. 11: *GPC trace of the copolymer BAFKU$_8$–HMS 301 overlaid with traces of pure BAFKU and pure HMS 301.*
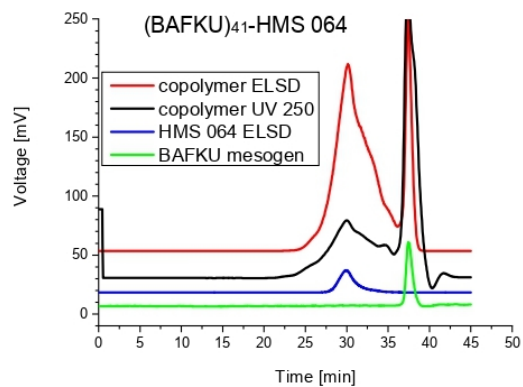
BAFKU₄₁-HMS064

nr.	Max. RT	Start RT	End RT	flow rate correction	Mp	Mn	Mw	Mz	PD	I [mV]	I [%]
1	30.1	23.44	36.27	1	70147	19671	125134	575984	6.361344	234.68	53.98
x	37.42	36.27	40.04	1	764	693	750	812	1.082251	200.04	46.02

SI-Fig. 12: *GPC trace of the copolymer BAFKU₄₁–HMS 064 overlaid with traces of pure BAFKU and pure HMS 064.*

2. Thermo-mechanical properties
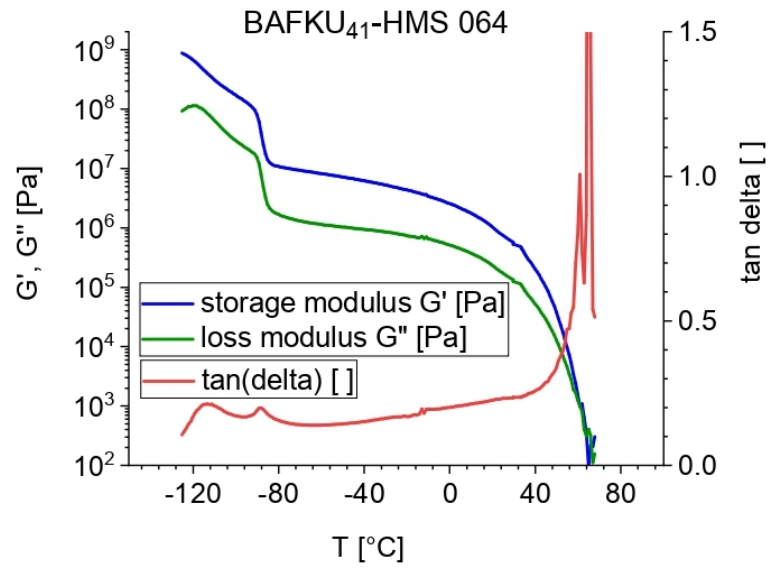
SI-Fig. 13: *full DMTA profile of the copolymer BAFKU₄₁–HMS 064 in cooling regime, showing the temperature-dependence of the storage modulus G', of the loss modulus G'' and of tan δ.*

3. Phase transitions and morphology

3.1. Thermal transitions observed by DSC

The DSC experiments also elucidate the behaviour of the elastic PDMS chains of BAFKU$_{41}$–HMS064 during its apparent vitrification / glass→rubber transition (seen as large DMTA step with hysteresis in Discussion, Synthesis, in the main paper document, ***Figure 1b***): At the employed DSC scanning rate of 10°C/min (see ***SI-Fig. 14b***), the solidification of PDMS during the cooling run resembles a glass transition, connected with an unusually large change in heat capacity. In the low-temperature range -140 to -80°C, which was characterized separately (see ***SI-Fig. 14a***), another glass transition is observed near -123°C, which can be assigned to the freezing of the wagging movement of pendant methyl groups. In case of the first and second low-temperature-range heating run from -140 to -80°C (***SI-Fig. 14a***), no distinct transitions are observed at all, while in the 'high temperature range' (from -80 to 100°C, see ***SI-Fig. 14b***), a distinct melting peak of PDMS is recognizable near -50°C, in the region where in DMTA (see ***Figure 1b*** in Discussion, Synthesis, in the main paper document) an apparent glass → rubber transition occurs. It can be noted that this PDMS melting peak is smaller in case of the second heating run. The first higher-temperature-range heating run (in ***SI-Fig. 14b***) was namely carried out after a thorough cooling at -80°C (well suitable for cold crystallization: cool enough, but above T_g). The second heating run in ***SI-Fig. 14b*** was started shortly after the sample reached -80°C in the previous run, hence there was not enough time for a thorough cold crystallization of PDMS and the PDMS melting peak in the second heating scan was smaller (lower crystallinity of PDMS).
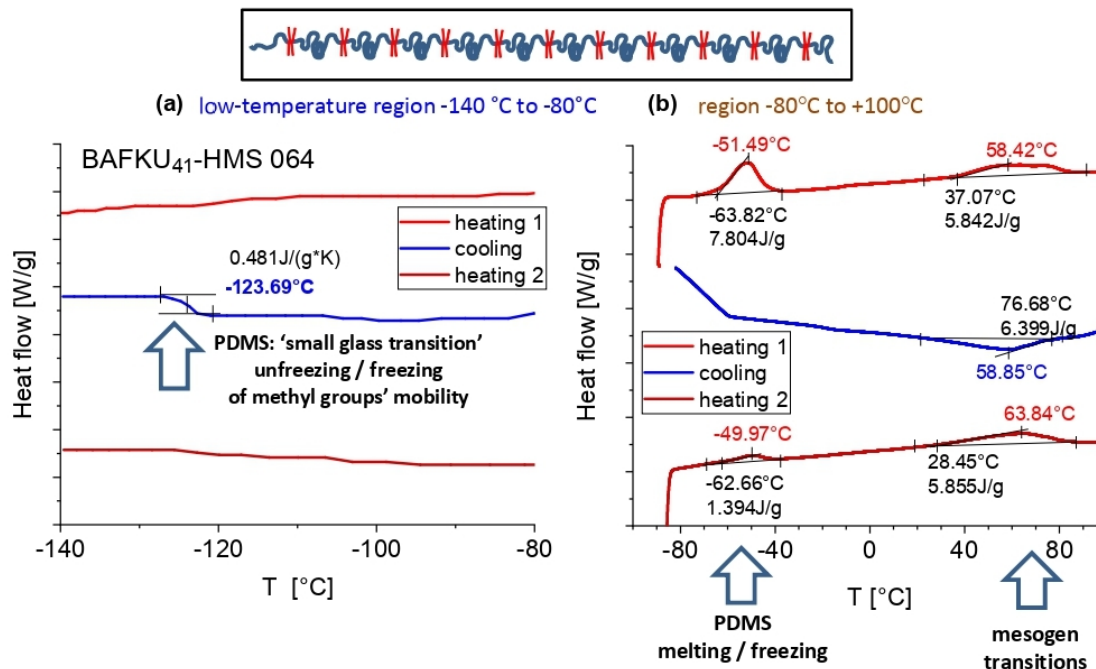
SI-Fig. 14: *DSC traces of the copolymer BAFKU$_{41}$–HMS064: (a): in the low-temperature region (-140°C to -80°C); (b): in the region from -80°C to +100°C.*

3.2. X-ray diffraction
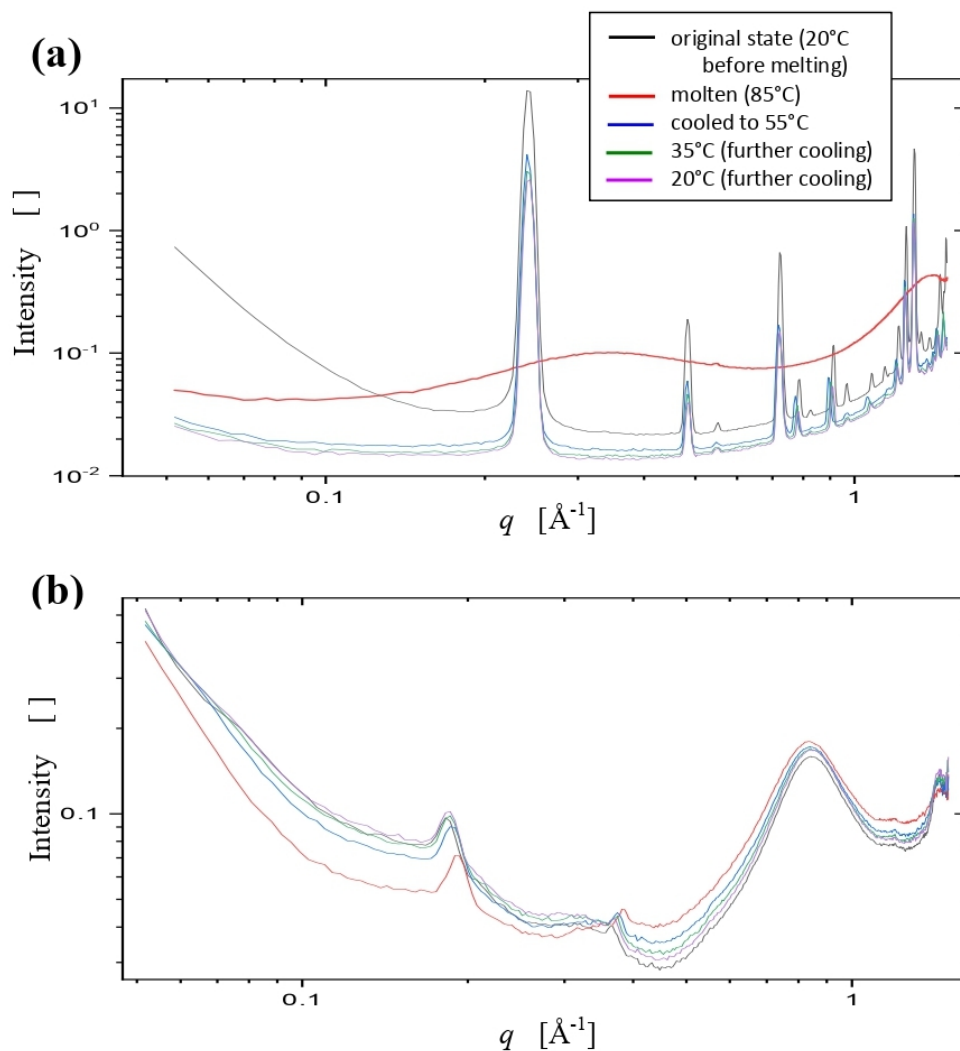
SI-Fig. 15: *X-ray scattering patterns in the combined SAXS and WAXS range, in the format Scattering intensity =f(q), with both axes in logarithmic format: (a) neat BAFKU; (b) BAFKU$_{41}$–HMS064 copolymer; the patterns were recorded at room temperature (20°C), then at 85°C (molten), and after subsequent cooling to 55°C, to 35°C and to 20°C (back at room temperature).*

SI-Table 5: *X-ray diffraction results: neat BAFKU: detailed list of interference maxima and the corresponding characteristic distances.*

BAFKU			
2Θ [°]	**q** [Å⁻¹]	**d** [nm]	comment
3.40	**0.242**	**2.60**	<u>very intense</u>, somewhat diminishes irreversibly
6.80	**0.484**	**1.30**	<u>medium/weak</u>, diminishes irreversibly
7.73	0.55	1.14	weak
10.18	**0.724**	**0.87**	<u>medium</u>, diminishes irreversibly
11.07	0.787	0.80	weak, reversibly shifts
11.62	0.826	0.76	weak
12.84	0.912	0.69	weak, reversibly shifts to 12.56° ≡ 0.922Å⁻¹ (0.70 nm)
13.60	0.966	0.65	weak, diminishes irreversibly
15.20	1.079	0.58	weak, shifts reversibly and diminishes irreversibly
16.11	1.143	0.55	weak, diminishes irreversibly and markedly
17.12	1.214	0.52	weak, shifts reversibly and diminishes irreversibly
17.70	**1.255**	**0.50**	<u>medium</u>, slightly shifts and somewhat diminishes
18.36	**1.301**	**0.48**	<u>intense</u>, somewhat diminishes
18.93	1.341	0.47	weak, markedly diminishes
19.61	1.389	0.45	weak, shifts slightly and somewhat diminishes
20.51	1.452	0.43	weak, slightly shifts to 20.37° ≡ 1.442Å⁻¹ (0.44 nm), markedly diminishes
21.08	1.492	0.42	weak, shifts to 20.72° ≡ 1.467Å⁻¹ (0.43 nm), markedly diminishes

SI-Table 6: *X-ray diffraction results: copolymer BAFKU$_{41}$–HMS064: detailed list of interference maxima and the corresponding characteristic distances.*

copolymer BAFKU$_{41}$–HMS064			
2Θ [°]	**q** [Å⁻¹]	**d** [nm]	comment
2.57	**0.183**	**3.43**	medium/weak, somewhat broad, fully reversibly shifts to 2.68° ≡ 0.191Å⁻¹ (3.29nm), perhaps related to BAFKU peak at 3.40° (0.24Å⁻¹ / 2.60 nm)
4.51	0.321	1.96	very weak, flat and broad, directly neighbours the peak at 5.14°
5.14	**0.366**	**1.72**	weak, partly reversibly shifts to 5.42° ≡ 0.386 Å⁻¹ (1.63 nm), returns only to 5.28° ≡ 0.376 Å⁻¹ (1.67 nm), secondary reflection of 2.57°
11.86	**0.843**	**0.75**	intense and very broad, irreversibly slightly diminishes: it is an amorphous halo observed in neat PDMS (besides the main one above 20°)
16.92	1.200	0.52	very weak, perhaps related to the BAFKU peaks between 16.11 and 18.36° ≡ 1.14 – 1.30Å⁻¹ (≡ d = 0.55 – 0.48 nm)
20.34	**1.440**	**0.44**	medium, broadened, reversibly diminishes, perhaps related to the BAFKU peaks at 20.5 and 21.1° ≡ 1.45 and 1.49 Å⁻¹

BAFKU$_{41}$–HMS064 copolymer XRD peaks:

The broad flat peak which precedes the reflection at 0.366 Å^{-1} / 5.14° (see *SI-Fig. 15b*) could possibly be related to similar but disordered structures: an analogous feature adjacent to the primary reflection at 0.183 Å^{-1} / 2.57° also can be suspected, but is less visible (due to underlying SAXS pattern) in *SI-Fig. 15b*.

In *SI-Fig. 15b*, one or more very weak peaks near 1.200 Å^{-1} (16.92° / d = 0.52 nm) can be observed, which are likely related to the weak BAFKU reflections at 16.11 − 18.36° (see *SI-Table 5*).
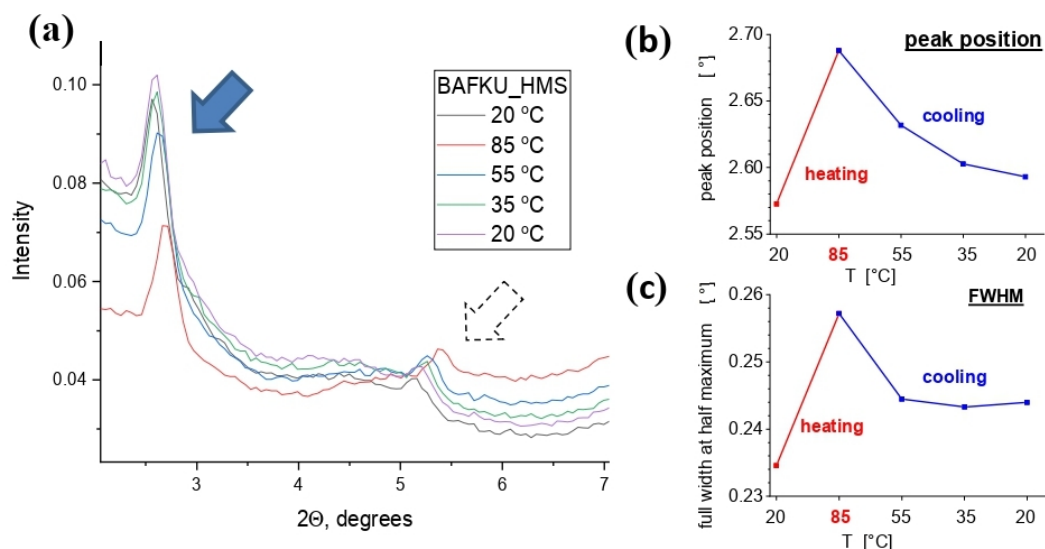
SI-Fig. 16: *(a) Temperature-dependent shift of the peak near 2.57° (highlighted with full arrow) in the copolymer BAFKU$_{41}$–HMS064; the second-order reflection related to this peak at 5.14° (highlighted with dotted arrow) also shows an analogous position shift; the different temperature trends of the underlying curve below both peaks generate different trends in apparent intensity of the reflections at 2.57° and 5.14°; (b) position of the '2.57° peak' in dependence of temperature; (c) T-dependent full-width at half maximum of this peak.*

SI-Table 7: *Shift of the peak near 0.17 Å^{-1} in the copolymer BAFKU$_{41}$–HMS064 and the corresponding characteristic distances.*

co 064 detail of 0.17 Å^{-1} **peak shift**			
T [°C]	**2Θ** [°]	**q** [Å^{-1}]	**d** [nm]
20 (initial)	2.57	0.183	3.435
85	2.69	0.191	3.28
55	2.63	0.187	3.36
35	2.60	0.185	3.395
20 (cooled down)	2.456	0.184	3.41

The initial distance of 3.43 nm (room temperature, before heating) shrinks to 3.28 nm (85°C). Cooling the sample back to 20°C does not fully revert this distance (**SI-Fig. 16**): It remains at 3.40 nm even after 2 hours at 20°C.

3.3. Polarized light microscopy
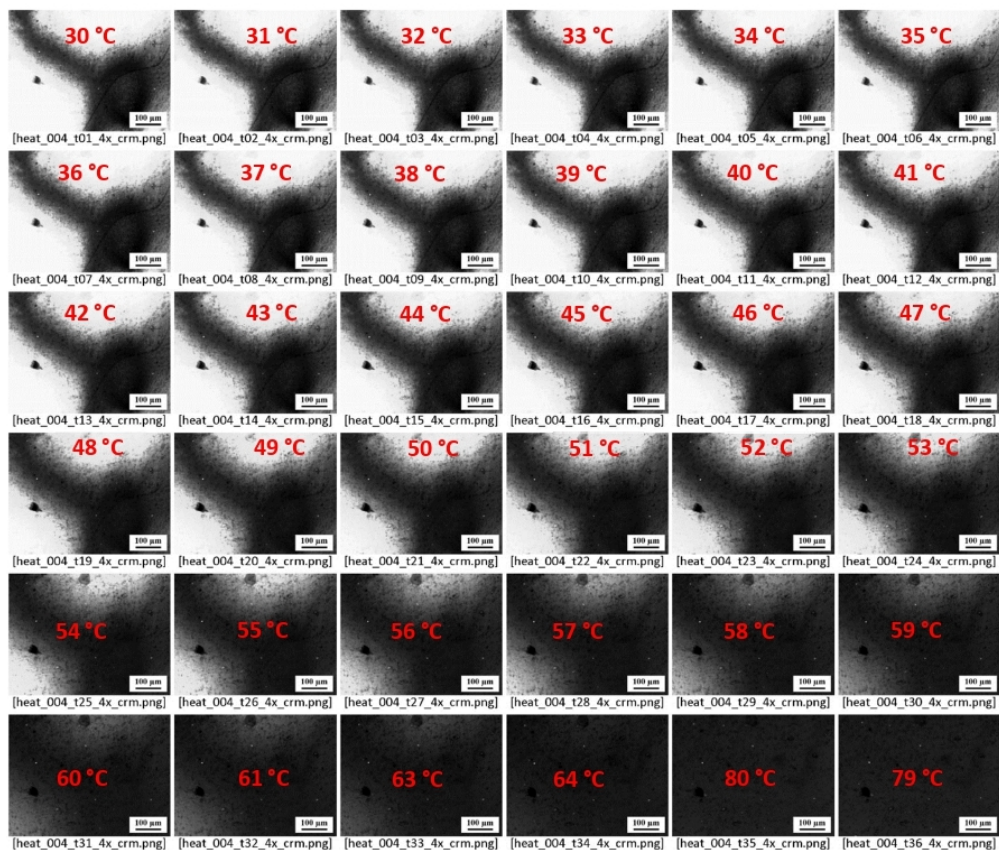
SI-Fig. 17: *Temperature-dependent changes in the images of a selected group of anisotropic domains in the copolymer BAFKU$_{41}$–HMS064, observed by PLM in the 'black and white mode' (all colours are reproduced as white light), during a heating scan (from 30 to 80°C) of a previously shear-oriented sample (oriented in melt): all images.*

4. Rheology investigations

4.1. Rate of physical crosslinking upon cooling
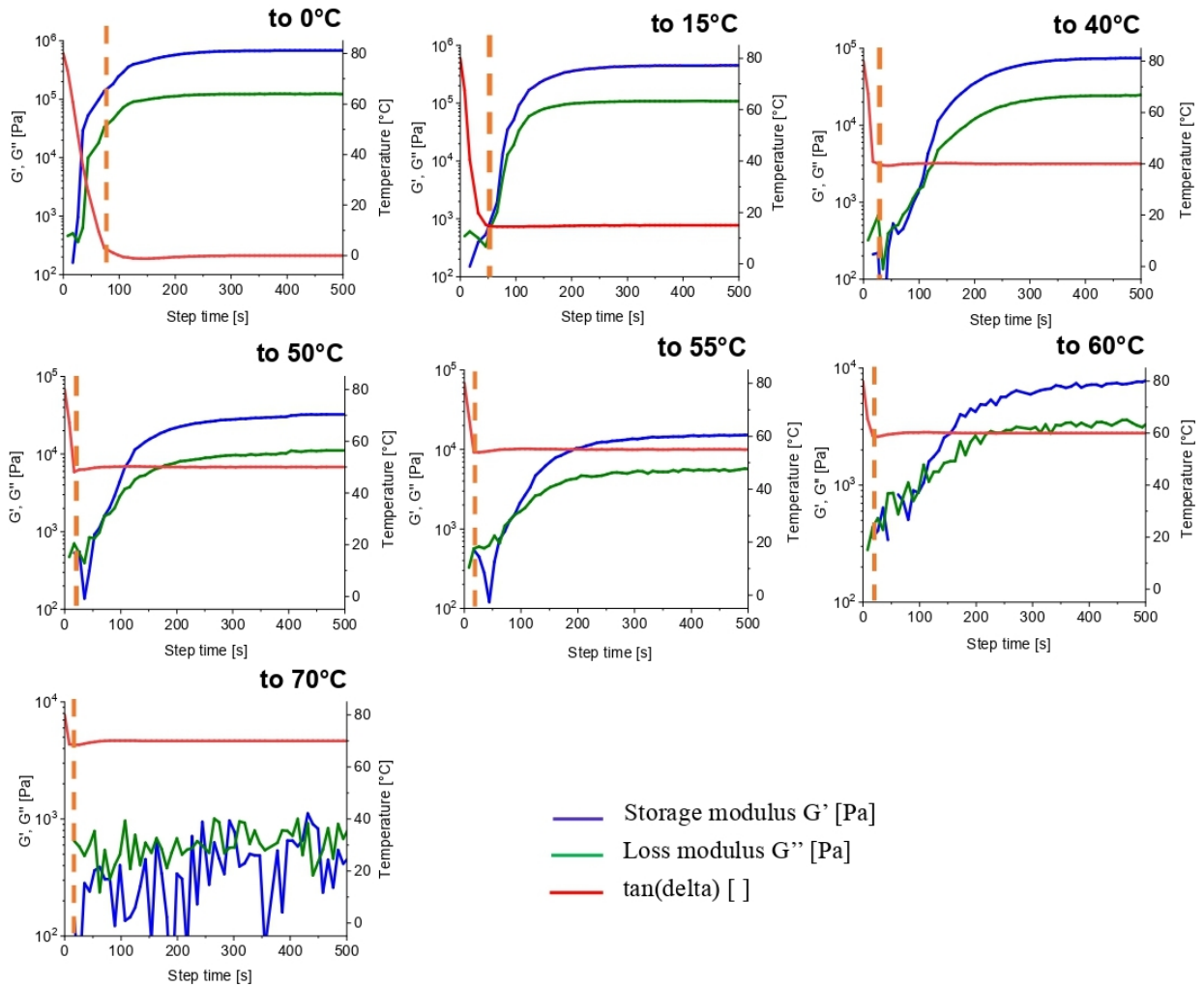
SI-Fig. 18: *Kinetics of the change in storage (G') and loss (G") modulus (kinetics of physical gelation) upon cooling molten BAFKU$_{41}$–HMS064 from 80°C to different temperatures ranging from 0 to 70°C; the course of the temperature of the plates (between which the sample was loaded) is also depicted; the dotted line depicts the approximate end of the sample cooling.*

4.2. Disconnection of the physical network by high mechanical strain
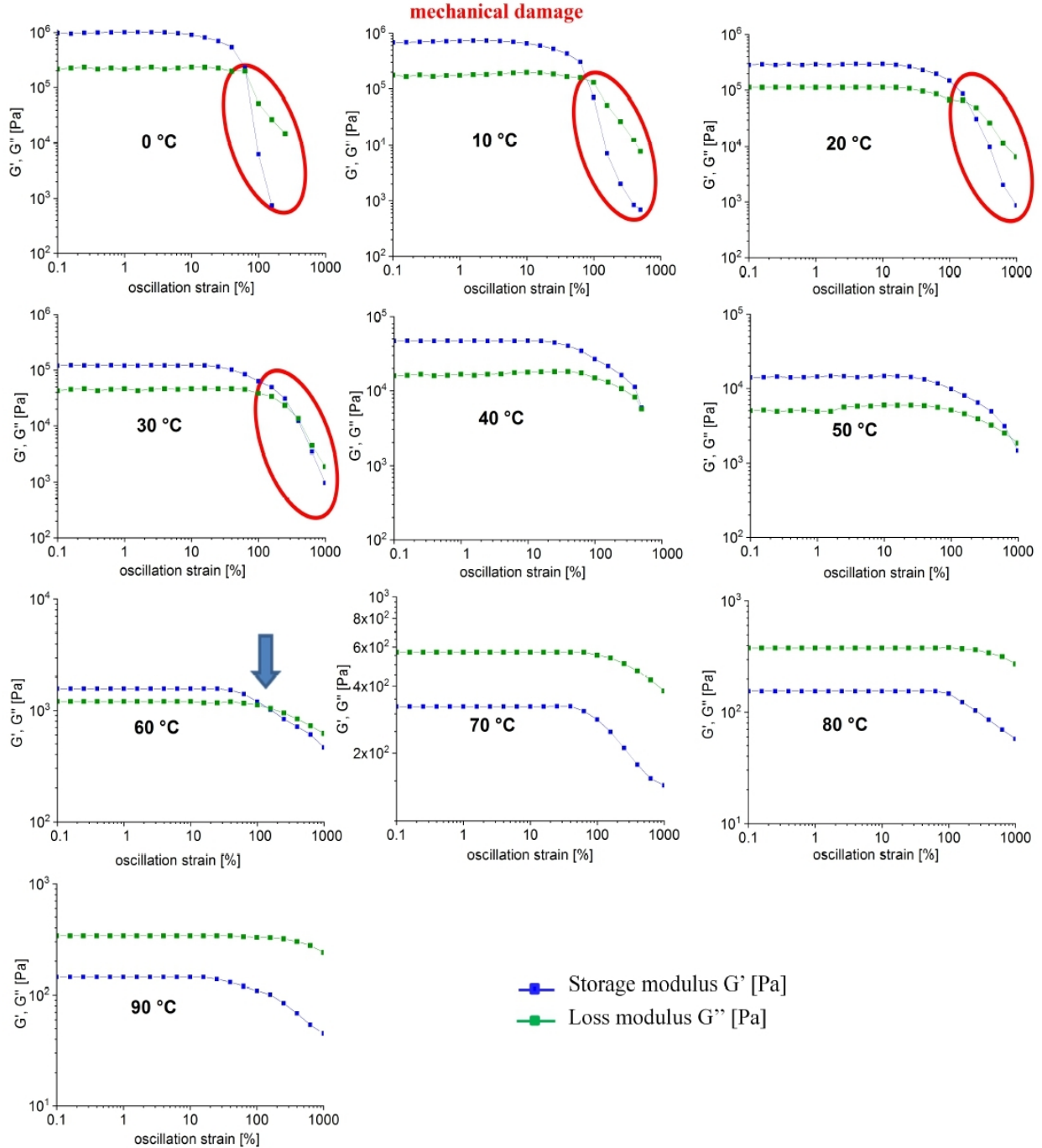
SI-Fig. 19: *Disconnection of the physical crosslinks in BAFKU₄₁–HMS064 by mechanical strain: strain-dependence of storage (G') and loss (G") modulus at different temperatures ranging from 0 to 90°C, respectively.*

4.3. High-frequency stiffening and self-healing effects
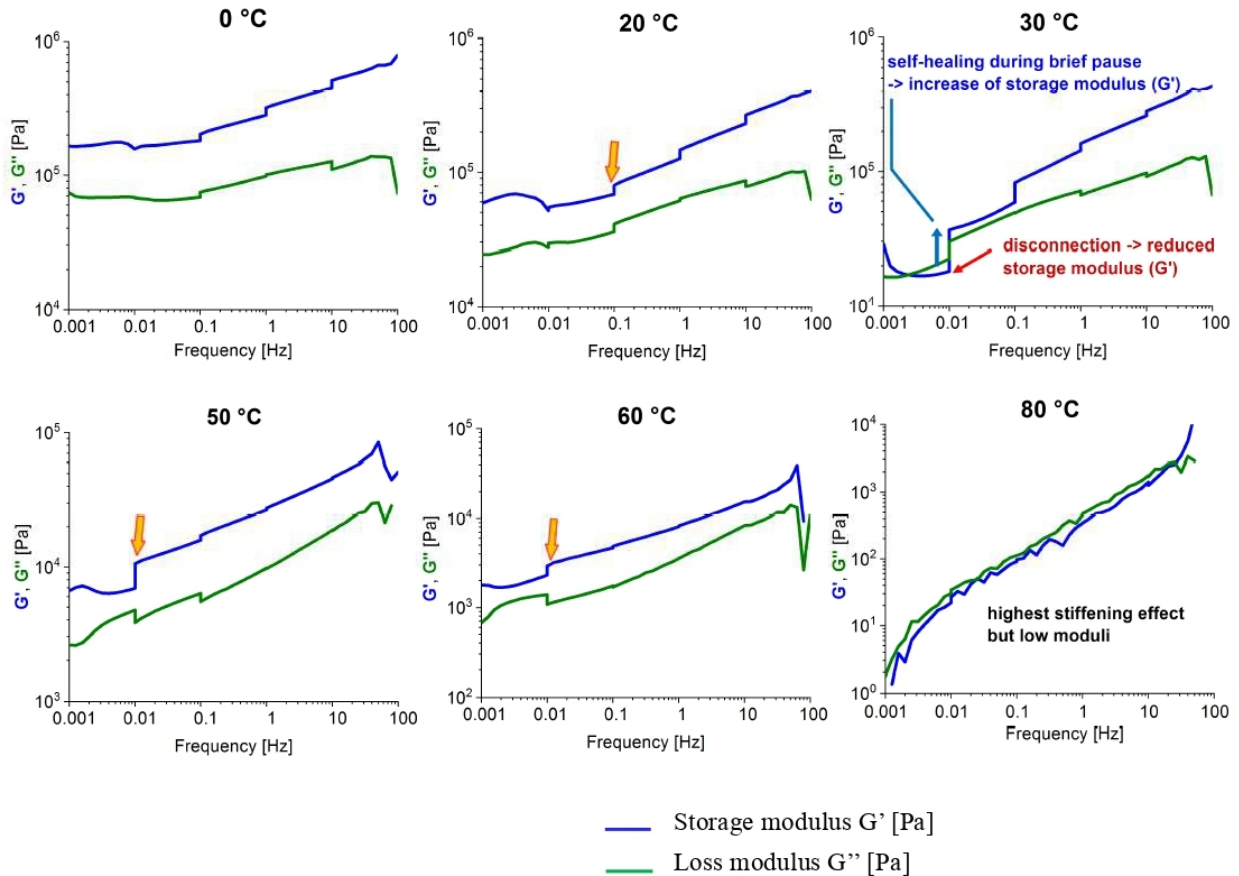
SI-Fig. 20: *Frequency-stiffening of BAFKU$_{41}$–HMS064 observed in frequency sweep tests (1 mHz to 100 Hz) conducted at different temperatures ranging from 0 to 80°C; the strain amplitude was different in each frequency decade, ranging from 50% at 1 mHz to 1% at 100 Hz; the effect of strain-induced damage to the network, as well as of its recovery between the frequency decades is clearly visible, especially in case of G' curves at lower temperatures.*

The frequency sweep tests in **SI-Fig. 20** (and in the main paper text) supply an additional interesting result, namely the indication of **self-healing ability** in the tested BAFKU$_{41}$–HMS064 elastomer, which manifests itself as steps in many of the experimental curves (see **SI-Fig. 20**). The origin of the observed steps is connected with the detailed experiment setup: Each frequency sweep was divided into decades of points for each frequency order, and different deformation amplitudes (higher at low frequency) were applied in each decade. For

technical reasons, the rheometer made brief (in the range of seconds) delays between the frequency decades, which in case of simultaneous strain damage and self-healing would lead to step-wise (vertical) increase in G'. The sequence of graphs in **SI-Fig. 20** illustrates, that the observed 'step-effect' is the strongest at 30°C. The effect decreases if the temperature increases: The dynamics of the reversible crosslinking becomes fast (and physical crosslinking becomes weaker) at these temperatures, so that an increasing part of the damage to the crosslinking density recovers before the delay between the decades. The step effect also becomes weaker if the temperature decreases below 30°C, as the crosslinking becomes stronger (thus limiting damage) and the self-healing slower. Generally, the 'step effect' in the frequency sweep tests of the BAFKU$_{41}$–HMS064 copolymer is most prominent in the temperature range of its thermotropic transitions observed by DSC. Additionally, the steps are the greatest at the lowest frequencies (combination of long deformation times and high strains). The step effect is completely absent in the molten state (80°C).

The curves of G" show similar but more complex trends: The temperature-dependence of the size of the steps is analogous like in case of G', but along the frequency scale, the steps in G" are initially upward ('anomalous'), then downward (expected 'normal' behaviour). With raising experiment temperature, the 'region of downward steps' in G" expands: at 50°C all steps in G" are already downward. Hence, low temperatures and low frequencies (at these frequencies the applied deformations were high) favour the anomalous upward steps in the G" curves.

While simple self-healing should lead to G" decrease (stronger elastomer character due to more crosslinks, shorter elastic chains and hence less friction), the mentioned upward steps in G" at lower temperatures and frequencies could be explained by resistance caused by re-assembled weak secondary aggregates of primary BAFKU crystallites, which have time to disconnect at lower frequencies (and high applied strains). Their gradual destruction by shear generates resistance, but also leads to a decrease in the number of these secondary aggregates and thus in turn to decreasing resistance (smaller growth, or even decrease in G"). During the experimental delay, these secondary aggregates are re-assembled, and hence can generate more resistance again (upward step in G").

At higher frequencies, the simple effect of additional crosslinking prevails (stronger elastomer character due to more crosslinks, shorter elastic chains and hence less friction) and also the applied deformations are smaller (eventually not enough to destroy the secondary aggregates), so that the steps in G" are downward, as it would be expected for 'normal' materials.

At higher temperatures, the formation of weaker secondary aggregates is less favoured, so that the 'simple behaviour of G" increasingly prevails (downward steps).

Appendix 2:

Article

Low-Temperature Meltable Elastomers Based on Linear Polydimethylsiloxane Chains Alpha, Omega-Terminated with Mesogenic Groups as Physical Crosslinkers: A Passive Smart Material with Potential as Viscoelastic Coupling. Part I: Synthesis and Phase Behavior

Sabina Horodecka [1,2]**, Adam Strachota** [1,]*****, Beata Mossety-Leszczak** [3]**, Beata Strachota** [1]**, Miroslav Šlouf** [1]**, Alexander Zhigunov** [1]**, Michaela Vyroubalová** [1]**, Dana Kaňková** [1]**, Miloš Netopilík** [1] **and Zuzana Walterová** [1]

[1]   Institute of Macromolecular Chemistry, Czech Academy of Sciences, Heyrovskeho nam. 2, CZ-162 06 Praha, Czech Republic; horodecka@imc.cas.cz (S.H.); beata@imc.cas.cz (B.S.); slouf@imc.cas.cz (M.Š.); zhigunov@imc.cas.cz (A.Z.); vyroubalova@imc.cas.cz (M.V.); kankova@imc.cas.cz (D.K.); netopilik@imc.cas.cz (M.N.); walterova@imc.cas.cz (Z.W.)
[2]   Faculty of Science, Charles University, Albertov 6, CZ-128 00 Praha 2, Czech Republic
[3]   Faculty of Chemistry, Rzeszow University of Technology, al. Powstancow Warszawy 6, PL-35-959 Rzeszow, Poland; mossety@prz.edu.pl
*   Correspondence: strachota@imc.cas.cz; Tel.: +420-296-809-451

Abstract: Physically crosslinked low-temperature elastomers were prepared based on linear polydimethylsiloxane (PDMS) elastic chains terminated on both ends with mesogenic building blocks (LC) of azobenzene type. They are generally (and also structurally) highly different from the well-studied LC polymer networks (light-sensitive actuators). The LC units also make up only a small volume fraction in our materials and they do not generate elastic energy upon irradiation, but they act as physical crosslinkers with thermotropic properties. Our elastomers lack permanent chemical crosslinks—their structure is fully linear. The aggregation of the relatively rare, small, and spatially separated terminal LC units nevertheless proved to be a considerably strong crosslinking mechanism. The most attractive product displays a rubber plateau extending over 100 °C, melts near 8 °C, and is soluble in organic solvents. The self-assembly (via LC aggregation) of the copolymer molecules leads to a distinctly lamellar structure indicated by X-ray diffraction (XRD). This structure persists also in melt (polarized light microscopy, XRD), where 1–2 thermotropic transitions occur. The interesting effects of the properties of this lamellar structure on viscoelastic and rheological properties in the rubbery and in the melt state are discussed in a follow-up paper ("Part II"). The copolymers might be of interest as passive smart materials, especially as temperature-controlled elastic/viscoelastic mechanical coupling. Our study focuses on the comparison of physical properties and structure–property relationships in three systems with elastic PDMS segments of different length (8.6, 16.3, and 64.4 repeat units).

Keywords: reversible networks; self-assembly; self-healing; liquid crystals; smart materials

---

1. Introduction

This work is dedicated to low-temperature reversible elastomers which melt somewhat below room temperature and which are based on linear polydimethylsiloxane (PDMS) of different chain

lengths, terminated with liquid crystalline (LC) units in the α- and ω- position. The LC end-groups act as physical crosslinkers in this special variety of polysiloxane/LC copolymers.

Generally, polysiloxane copolymers with mesogenic (LC) building blocks are compounds which can offer fascinating material properties, due to the combination of the highly flexible and hydrophobic polysiloxane with the phase behavior of the mesogenic (LC) units [1,2]. These materials have attracted deserved research interest since Finkelmann's pioneering works in the 1980s [3–7]. Subsequently, numerous studies were dedicated to liquid crystalline siloxane polymers (LCPs) with mesogens as side chains (comb-like LCPs; see e.g., [1,8], (Volume 3: pp. 121–302) and [9–11]), whereas main-chain siloxane LC copolymers, to which the studied materials also belong as a special case, were studied only in a few works in total [12–17].

All the abovementioned polysiloxane LCPs studied in the literature were very rich in the LC component, which made up a dominant volume fraction, and the behavior of the usually more or less fixed (via chemical crosslinking) mesogens was responsible for practically all the material properties. In contrast to that, in the presented work, the mesogen makes up a relatively small volume fraction of most of the copolymers, the elastic properties originate from the PDMS component, while the melting, the gelation, and the mechanical disconnection and reconnection of the physical crosslinks are controlled by the phase behavior of the mesogen.

Synthesis routes to polysiloxane LCPs most frequently employed the hydrosilylation reaction, as is the case in this work, namely by connecting vinyl-functional mesogens with hydrido-functional (Si–H) PDMS. All the abovementioned main-chain siloxane LCPs were prepared via this route, while in the case of the more frequently investigated comb-like polysiloxane LCPs, alkyne/SiH addition [11], thiol-ene addition [18], or the Huisgen "click reaction" [19] are employed as alternative synthesis routes.

From the application point of view, polysiloxane LCPs have been investigated as electro-optic [20], light-emitting [21], gas separation (membrane-) [22,23], and chromatography materials [24], as well as actuators (see e.g., [16,25–27]). In the latter application, which gained by far the most research attention, especially in recent years, they are often referred to as "liquid-crystalline elastomers" (LCEs). The relatively rarely studied main-chain polysiloxane LCPs, to which the materials studied in this work belong, were investigated mainly for their thermotropic phase behavior (polyester-*co*-PDMS systems) [12–15], for their thermomechanical properties [15], as thermosensitive actuators (mechanism via smectic ↔ isotropic transition of the polyester LC units) [16], or as photoresponsive optical material (azo units' cis/trans isomerization) [17]. In contrast to that, in the present work, the polysiloxane LCPs were studied as potential structural smart materials, namely as thermoresponsive viscoelastic coupling, with marked phase transitions also in the oily (melt) state.

The physical crosslinking in the copolymers which are studied in this work is based on the aggregation and microphase separation of the terminal mesogenic (LC) units, and thus, results in an organic–organic nanocomposite morphology. This morphology plays a key role in the copolymers' material properties, especially in the efficiency of the crosslinking and in the thermomechanical properties. In their previous work [28,29], the authors studied in detail the nano-aggregation behavior of rigid inorganic polyhedral oligomeric silsesquioxane (POSS) building blocks in epoxy–POSS hybrid copolymers. The nanodomains of POSS (physical crosslinker and simultaneously, a hard nanofiller) caused a very strong mechanical reinforcement, as well as thermal stabilization. The organic substituents which covered the POSS surface were found to control its aggregation; substituents with the strongest crystallization tendency were the most efficient in achieving physical crosslinking and mechanical reinforcement by POSS. Similar results concerning aggregation behavior were also observed for the heavier homologue of POSS, the stannoxane dodecamer cages ("Sn-POSS"), which additionally introduced the specific chemical reactivity of the filler phase, namely matrix repair reactions under oxidizing conditions [30,31].

The authors' experience with physical crosslinking via aggregation (nanocrystallization) of the abovementioned POSS nano-building blocks, as well as the previous study on liquid crystalline epoxy copolymer networks that were able to be orientated [32], inspired the present work. The authors also

recently studied [33] a PDMS–LC copolymer which is structurally highly different from the presently investigated materials. In the mentioned study, a linear PDMS chain was tethered with spatially separated quartets of pendant LC groups. The study in [33] was the authors' first foray into the broader topic of the present work. In this present work, however, the same LC groups are tested in a completely different copolymer architecture.

Related to the presented work also is the topic of physical (non-covalent) crosslinking of PDMS. Several interesting approaches were studied in the literature, namely crosslinking via strongly hydrogen-bridging groups attached to PDMS macromolecules (or oligomers), like urea [34], ureidopyrimidinone [35], benzene-1,3,5-tricarboxamide (BTA) derivatives [36], or cyclodextrin (in α,ω-positions) [37]. Other studied non-covalent crosslink-forming groups attached to PDMS included π-stacking moieties [38–40]. Combinations of Lewis acidic and Lewis basic functional groups, both attached to PDMS molecules (cyclic boronic esters and amines) [41] or combinations of mildly bonding ligand groups on PDMS and free metal cations [42] already could be considered as PDMS crosslinking via reversible covalent bonds, rather than physical crosslinking. Depending on the crosslink strength, the described products, which were often referred to as "thermoplastic elastomers", were processable by the combination of heat and solvent, by melting or dissolution alone, or even by cold pressing. In contrast to the above, the PDMS copolymers studied in the presented work are crosslinked by a rather mild variety of non-covalent interactions. The aggregation of the "active" structural units is driven by their crystallization tendency, with no hydrogen bridging, no strong π-stacking, and no strong electrostatic attraction.

The aim of the presented work was to prepare physically crosslinked meltable elastomers based on linear polydimethylsiloxane chains (PDMS macromonomer) α,ω-terminated with mesogenic (LC) building blocks. The nanophase separation and crystallization of the latter was favored by PDMS/mesogen incompatibility and was expected to efficiently crosslink the elastic PDMS chains. Thus, the LC building blocks were expected to play a somewhat similar role (non-covalent crosslinker) like the inorganic POSS units studied in the authors' early work. Moreover, due to their specific properties, the LC units could cause interesting thermotropic behavior of the physical crosslinks in the studied materials. This would be of interest for smart applications, such as viscoelastic coupling materials, behaving as oils with greatly varying temperature-controlled viscoelasticity near room temperature, and as rubbers at lower temperatures. The detailed aims of this work included the elucidation of the structure–property relationships in the PDMS–LC elastomers, especially the efficiency as a physical crosslinker of the relatively small mesogen unit, and the effect of the length of the elastic PDMS chains. While the presented work focuses on the synthesis and on the comprehensive characterization of the thermotropic phase behavior, including simple mechanical properties, a follow-up paper [43] ("Part II") is dedicated to the study of the complex viscoelastic and rheological properties of the copolymers in the molten as well as in the rubbery state.

2. Experimental Section

2.1. Materials

2.1.1. Commercial Chemicals

The hydride-α,ω-terminated polydimethylsiloxanes—DMS H03 (M_n = 623.9 g/mol), DMS H11 (M_n = 1196.5 g/mol), and DMS H21 (M_n = 4764 g/mol) were purchased from Gelest, Morrisville, PA, USA. Chloroform (solvent) was purchased from Sigma-Aldrich, St. Louis, MO, USA, while a 2% solution of Karstedt's catalyst was purchased from Merck (Darmstadt, Germany). All the commercial products were used as received. Prior to use, however, the equivalent molecular masses per SiH group of the DMS H03, DMS H11, and DMS H21 were more precisely determined by ^{1}H-NMR. The so-obtained equivalent molecular masses (per Si–H function: DMS H03—311.9325 g/mol; DMS H11—598.241 g/mol; DMS H21—2382.2 g/mol) were then used for calculations of the amounts of reactants in the syntheses.

2.1.2. Synthesis of the Liquid Crystalline Mesogen named "BAFKU"

The synthesis of the azo-type mesogen BAFKU (M_w = 420.587 g/mol) was described in detail in a previous work by some of the authors of this paper [44].

2.1.3. Preparation of the Main Chain Liquid Crystalline Copolymers Based on PDMS (DMS H03, DMS H11, or DMS H21) and LC Mesogen BAFKU

Appropriate quantities of the BAFKU mesogen and of PDMS (see Table 1) were placed into a small vessel equipped with a magnetic stirring bar. In total, 2 mL of chloroform was added, and after flushing the reactants with argon, they were dissolved by brief stirring at 60 °C. Subsequently, Karstedt's catalyst (8.7 mg of a 2 wt.% solution, 0.0228 mmol Pt) was added and the solution was stirred at 60 °C for 5 min. Thereafter, the reaction mixture was cooled down to room temperature and the solvent was removed under reduced pressure. The so-obtained copolymer was further dried under vacuum (10 mbar) for 30 min at 90 °C (molten state). The product was then cooled down to room temperature and stored. The trace amounts of the Karstedt catalyst (between 0.008 and 0.02 wt.%) were tolerated as non-problematic impurity in the case of standard syntheses (it was possible to remove them by adsorption on silica or on activated carbon at the cost of reduced yield).

Table 1. Amounts of the components used in the synthesis of the main chain liquid crystalline copolymers based on polydimethylsiloxane (PDMS) and liquid crystalline (LC) mesogen.

Sample Name	BAFKU Mesogen				Precursor DMS H03				Precursor DMS H11				Precursor DMS H21				Chloroform		Karstedt's Catalyst 2 wt.% Solution	
	[g]	[mmol] of C=C Groups	wt%	Vol%	[g]	[mmol] of SiH Groups	wt%	Vol%	[g]	[mmol] of SiH Groups	wt%	Vol%	[g]	[mmol] of SiH Groups	wt%	Vol%	[g]	[mL]	[g] as 2% Solution	[mmol]
H03–BAFKU₂	0.5	1.19	57.4	52.44	0.371	1.19	42.6	47.56									2.956	24.76	0.0087	0.0228
H11–BAFKU₂	0.5	1.19	41.43	37.29					0.711	1.19	58.57	62.71					2.956	24.76	0.0087	0.0228
H21–BAFKU₂	0.5	1.19	15.1	13.47									2.832	1.19	84.9	86.53	2.956	24.76	0.0087	0.0228

The volume fractions of the mesogen BAFKU were calculated using Equation (1) under consideration of the densities (ρ(BAFKU) = 1.05 g/cm^3, ρ(H03) = 0.90 g/cm^3, ρ(H11) = 0.93 g/cm^3, and ρ(H21) = 0.97 g/cm^3) and of the stoichiometric synthesis amounts (see above in Table 1) of the individual components.

$$\text{volume percent (Vol\%)} = \frac{\frac{m(\text{component})}{\rho(\text{component})}}{\Sigma\left(\frac{m(i)}{\rho(i)}\right)} \times 100\% \tag{1}$$

Yield:

H03–BAFKU$_2$: 0.8715 g (1.19 mmol), 100% of theory (one-pot synthesis).
H11–BAFKU$_2$: 1.2069 g (1.19 mmol), 100% of theory (one-pot synthesis).
H21–BAFKU$_2$: 3.311 g (1.19 mmol), 100% of theory (one-pot synthesis).

Characterization by ^{1}H-NMR (proton nuclear magnetic resonance), in CDCl$_3$, δ (ppm) (see also spectra in SI Figures S7 and S8 in the Supplementary Materials):
H03–BAFKU$_2$: 7.94 (4H, d, arom.), 7.84 (4H, d, arom.), 7.33 (4H, d, arom.), 7.26 (4H, d, arom.), 2.69 (4H, m, CH$_2$), 2.58 (4H, m, CH$_2$), 1.75 (4H, m, CH$_2$), 1.65 (4H, m, CH$_2$), 1.55 (s, H$_2$O: moisture in CDCl$_3$), 1.29 (32H, m, CH$_2$), 0.94 (6H, m, CH$_2$), 0.53 (4H, m, CH$_2$), 0.06 (52H, s, CH$_3$ on Si, plus two CH$_2$ groups on Si, the latter two originating from BAFKU).
H11–BAFKU$_2$: 7.92 (4H, d, arom.), 7.82 (4H, d, arom.), 7.30 (4H, d, arom.), 7.22 (4H, d, arom.), 2.69 (4H, m, CH$_2$), 2.58 (4H, m, CH$_2$), 1.77 (4H, m, CH$_2$), 1.63 (4H, m, CH$_2$), 1.55 (s, H$_2$O: moisture in CDCl$_3$), 1.29 (32H, m, CH$_2$), 0.91 (6H, m, CH$_3$), 0.53 (4H, m, CH$_2$), 0.07 (96H, s, CH$_3$ on Si, plus two CH$_2$ groups on Si, the latter two originating from BAFKU).

H21–BAFKU$_2$: 7.92 (4H, d, arom.), 7.84 (4H, d, arom.), 7.33 (4H, d, arom.), 7.24 (4H, d, arom.), 2.69 (4H, m, CH$_2$), 2.58 (4H, m, CH$_2$), 1.77 (4H, m, CH$_2$), 1.65 (4H, m, CH$_2$), 1.29 (32H, m, CH$_2$), 0.94 (6H, m, CH$_3$), 0.52 (4H, m, CH$_2$), 0.06 (392H, s, CH$_3$ on Si, plus two CH$_2$ groups on Si, the latter two originating from BAFKU).

For comparison (see also spectra in SI Figures S4–S6):

Neat BAFKU: 7.90 (2H, d, arom.), 7.82 (2H, d, arom.), 7.31 (2H, d, arom.), 7.22 (2H, d, arom.), 5.79 (1H, m, CH), 4.94 (2H, m, CH$_2$), 2.59 (2H, m, CH$_2$), 2.56 (2H, m, CH$_2$), 2.03 (2H, m, allyl-type CH$_2$), 1.65 (2H, m, CH$_2$), 1.60 (2H, m, CH$_2$), 1.31 (12H, m, CH$_2$), 0.92 (3H, m, CH$_3$).

Neat DMS H03: 4.70 (2H, m, SiH), 0.18 (12H, s, CH$_3$ on Si in terminal units), 0.06 (40H, s, CH$_3$ on Si in internal repeat units).

Neat DMS H11: 4.71 (2H, m, SiH), 0.17 (12H, s, CH$_3$), 0.08 (84H, s, CH$_3$).

Neat DMS H21: 4.69 (2H, m, SiH), 0.13 (12H, s, CH$_3$), 0.06 (380H, s, CH$_3$).

Check of quantitative conversion:

FTIR (Fourier-transform infrared spectroscopy): Complete disappearance of the peak of the Si–H bond stretching at about 2120 cm^{-1} (see SI Figures S1–S3).

^{1}H-NMR: Complete disappearance of the peaks near 4.7 ppm (Si–H) and of the multiplets near 5.79 and 4.94 ppm (vinyl groups of LC mesogen), see spectra in SI Figures S7 and S8.

2.2. Characterization of the PDMS–BAFKU$_2$ Copolymers

2.2.1. Chemical Microstructure

^{1}H-NMR (proton nuclear magnetic resonance): The chemical structure (including the molecular masses, via end-group determination) of the synthesized PDMS–BAFKU$_2$ copolymers was verified using ^{1}H-NMR spectroscopy. The same method was also used for verifying the purity of the mesogen "BAFKU" and for determining the equivalent molecular masses per SiH of the α,ω-hydrido-functional polydimethylsiloxanes DMS H03, DMS H11, and DMS H21. The spectra were recorded on an Avance DPX 300 spectrometer (from Bruker, Karlsruhe, Germany) at 300 MHz. CDCl$_3$-d$_1$ was used as solvent for all experiments. Tetramethylsilane (TMS; δ = 0 ppm) was employed as internal standard.

FTIR (Fourier-transform infrared spectroscopy): The completion of hydrosilylation reactions between SiH-functional polydimethyl-siloxanes and the monovinyl-functional mesogen was verified by means of FTIR spectroscopy. The spectra were recorded in the attenuated total reflection (ATR) mode using a Nicolet 8700 spectrometer (from Thermo Scientific, Madison, WI, USA). The ATR spectra were recorded using a Golden Gate™ heatable Diamond ATR Top-Plate (MKII single reflection ATR system, from Specac, Orprington, Greater London, UK).

Molecular masses via SEC (size exclusion chromatography; or gel permeation chromatography "GPC"): The molecular masses of the prepared copolymers and of their precursors were determined by SEC. For this purpose, we used a Deltachrom pump with computer-controlled piston movement (from Watrex Praha, s.r.o., Praha, Czech Republic), the autosampler MIDAS (from Spark, Emmen, Holland), two columns "PLgel 5 μm MIXED-B" (10 μm particles; from Polymer Laboratories, now Agilent Technologies, Santa Clara, CA, USA), which according to the manufacturer, separate in the molecular mass range of approximately $10^2 \leq M \leq 1 \times 10^6$. Evaporative light scattering detector (ELSD) PL ELS 1000 (from Polymer Laboratories, Church Stretton, Shropshire, UK, laser wavelength: 658 nm) and a UV–vis (refraction index) DeltaChrom UVD 200 detector (from Watrex Praha, s.r.o., Praha, Czech Republic) with a flow-cell volume of 8 μL, operating at wavelength $\lambda = 264$ nm, were the detectors in the order of flow. The data were collected into the Clarity software (from DataApex Ltd., Praha, Czech Republic), which communicated with the detectors using a U-PAD2 USB acquisition device (also from DataApex). The mobile phase was tetrahydrofuran (Thermo Fisher Scientific, Waltham, MA, USA) at 25 °C (controlled ambient temperature), used as received. The concentration of measured solutions was 5 mg/mL. Polystyrene standards obtained from Polymer Standards Services (Mainz, Germany) were used for calibration.

Molecular masses via MALDI-TOF (matrix-assisted laser desorption ionization/time of flight) mass spectroscopy:

The samples were prepared by the "dried droplet method": THF (tetrahydrofuran, ≥99.9%, Sigma-Aldrich, St. Louis, MO, USA) solutions of the analyzed polymer (10 mg mL^{-1}), of the matrix DCTB (trans-2-[3-(4-t-butyl-phenyl)-2-methyl-2-propenyli-dene]malo-nitrile, Sigma-Aldrich, 10 mg mL^{-1}), and of the cationization agent sodium trifluoroacetate (CF$_3$COONa; Sigma-Aldrich, 10 mg mL^{-1}) were mixed in the volume ratio 4:20:1. Then, 1 µL of the mixture (the "droplet") was deposited on the ground-steel target plate, and dried at ambient atmosphere.

The MALDI-TOF mass spectra were acquired with an UltrafleXtreme apparatus (Bruker Daltonics, Bremen, Germany) in the positive ion reflectron and linear mode. Each spectrum was the sum of 25,000 shots with a DPSS (diode-pumped solid-state) Nd: YAG laser (neodymium-doped yttrium-aluminum garnet laser; 355 nm, 2000 Hz). Delayed extraction and external calibration were used.

2.2.2. Thermo-Mechanical and Thermal Properties

DMTA (dynamic-mechanical thermal analysis): The advanced multi-functional rheometer ARES-G2 (from TA Instruments, New Castle, DE, USA—part of Waters, Milford, MA, USA) was used for characterizing the thermomechanical properties of the prepared copolymers.

Typical combined tests, which covered the glassy state, the glass transition, the rubbery, as well as the melting region, were carried out using small parallel plate geometry (exchangeable stainless-steel plates, diameter: 6.1 mm). An oscillatory shear deformation at the constant frequency of 1 Hz and at a small strain amplitude (0.001% to 4%, adjusted by auto-strain) was applied. In the first scan, which was a cooling one, the samples were cooled down from the molten state at the rate of 3 °C/min, down to the final low temperature (−135 °C in the standard case). Subsequently, in the second scan, the heating one, the samples were heated at the same rate up to the final high temperature (40 °C in the standard case). For both scans, the temperature dependences of the storage and of the loss shear modulus were recorded, as well as of the loss factor (G', G'', and tan(δ), respectively).

Differential scanning calorimetry (DSC): The nature of the transitions observed in the copolymers in the DMTA tests was further investigated by DSC. The experiments were performed on a DSC Q2000 instrument from TA Instruments (New Castle, DE, USA) under a nitrogen atmosphere. The temperature range was from −90 to 100 °C. The heating and cooling rate was always 10 °C/min. The samples were first cooled down to −90 °C, after which they were subjected to the first heating scan from −90 to 80 °C (with final temperature corresponding to the isotropic state of the polymer melt), followed by the first cooling scan (80 to −90 °C) and the second heating scan.

2.2.3. Long-Range-Structure and Crystallinity Characterization

SAXS and XRD (small-angle X-ray scattering and X-ray diffraction): X-ray scattering experiments were performed using a MolMet pinhole camera from Rigaku, Tokyo, Japan, modified by SAXSLAB/Xenocs (headquarters: Grenoble, France) which was attached to a microfocused X-ray beam generator MicroMax 003 from Rigaku, operating at 50 kV and 0.6 mA (30 W). The camera was equipped with a vacuum version of the Pilatus 300K detector (from DECTRIS Ltd., Baden-Daettwil, Aargau, Switzerland). Variable detector positioning that covers the q range of 0.004–3.6 Å^{-1} was chosen. The scattering vector, q, is defined as: $q = (4\pi/\lambda)\sin\theta$, where $\lambda = 1.54$ Å is the wavelength of the installed source and 2θ is the scattering angle. The calibration of primary beam position and sample-to-detector distances was performed using Ag behenate and the Si powder sample. Homemade software based on the PyFAI Python library [45] was used for data reduction.

2.2.4. Polarized Light Microscopy (PLM) Observation of Phase Transitions

Polarized light microscopy (PLM) [46,47]: In order to visualize the phase transitions in the studied copolymers, polarized light microscopy was employed. PLM micrographs were recorded with a Nikon

Eclipse 80i (from Nikon, Shinagawa, Tokyo, Japan) microscope equipped with a ProgRes CT3 digital camera (Jenoptik, Jena, Germany) and THMS 600 heating stage (from Linkam Scientific Instruments Ltd. Tadworth, Surrey, UK).

Thin specimens for PLM (thickness < 10 μm) were prepared by compression molding on a heating bar (temperature of the bar 120 °C, compression between two glasses, load 5 kg for 10 min). The best PLM micrographs were obtained for the thinnest polymer films after slight shear deformation, which was induced by manual shift of the two glasses used for compression molding.

All PLM experiments started at room temperature. The samples were then gradually heated with the rate of 1 °C/min up to a final temperature, where the melt was fully isotropic. After a short pause at the maximum temperature (5 min), the sample was cooled down to room temperature using the same rate.

The intensity of illumination was kept constant and PLM micrographs were recorded during the whole process. The intensity of polarized light was evaluated from the image analysis of the individual micrographs as the mean intensity of all pixels within a given micrograph (using the software NIS Elements 4.0 from Laboratory Imaging s.r.o., Praha, Czech Republic; morphological descriptor MeanIntensity). As the final output, the normalized MeanIntensity as a function of temperature was plotted. It has been demonstrated in previous studies by some of the authors of this paper [46,47] that the polarized light intensity recorded in this way is proportional to the amount of crystalline/anisotropic structures in the investigated specimen.

3. Results and Discussion

3.1. Synthesis

Several copolymers consisting of polydimethylsiloxane (PDMS) of different chain length, α,ω-terminated with mesogenic units of azobenzene-type ("BAFKU"), were synthesized and studied as potential passive smart materials. The assembly of these medium/short copolymer molecules to reversible (meltable) elastomeric networks is shown in Scheme 1. The structure of the constituent components of the prepared low-temperature reversible rubbers is shown in Scheme 2; they were chosen in order to combine properties of PDMS, such as polymer backbone flexibility and a low glass transition temperature (T_g), with the crystallization tendency of the liquid crystalline BAFKU units, which had to act as thermotropic physical crosslinks, via BAFKU–BAFKU aggregation, as shown in Scheme 1. α,ω-SiH-terminated PDMS of three different lengths was employed: a 8.6-mer (on average, "H03"), a 16.3-mer ("H11"), and a 64.4-mer ("H21"). A potentially important feature of the prepared copolymers is the azo unit in their mesogenic building blocks. This unit, which normally is *trans*-configured, can be reversibly switched between *cis*- and *trans*- configurations by UV irradiation. In this way, the thermotropic properties of the physical crosslinks potentially could also be photo-switched between those of isomeric states. Photosensitivity was not studied in this already extensive work, however.

free (macro)molecules　　　　**rubber**
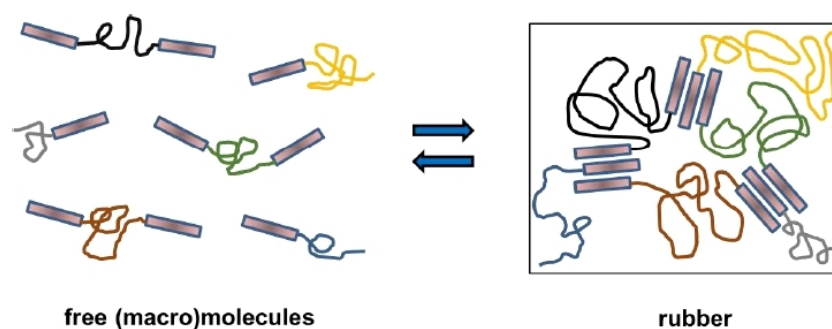
Scheme 1. Symbolic representation of the linear PDMS–BAFKU$_2$ copolymers and of their physical crosslinking via aggregation of the BAFKU units.

A key feature was the desired lack of miscibility (in the absence of solvent) of both components of the studied copolymers, which was achieved due to the specific properties of PDMS. This immiscibility favors nanophase separation in the copolymers via the formation of BAFKU aggregates, and hence, an easy formation of the physical network shown in Scheme 1. Additionally, the mesogen BAFKU introduces further interesting properties like the thermotropic behavior of the crosslinks.
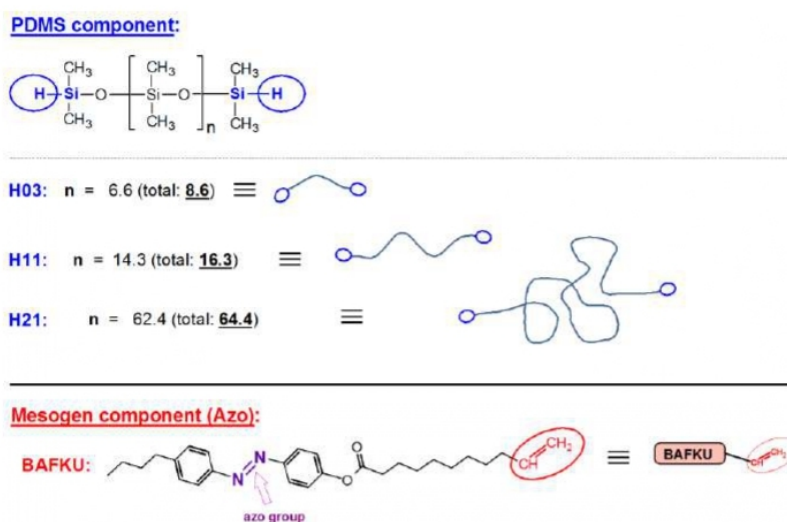
Scheme 2. Components used to synthesize the studied copolymers: (**top**): general structure of the PDMS precursors with Si–H functions in α and ω-position, as well as the representation of typical molecules of the "hydrido-polysiloxanes" DMS H03, DMS H11, and DMS H21; (**bottom**): the mono-vinyl-functional mesogen BAFKU.

SiH–PDMS and BAFKU were coupled via the hydrosilylation reaction (Scheme 3), which was considered to be practically a "click reaction". All the syntheses were carried out in chloroform at 60 °C and catalyzed by Karstedt's catalyst (also shown in Scheme 3). Prior to the syntheses, highly precise equivalent molecular masses per SiH functional group were determined for all the PDMS precursors by means of proton nuclear magnetic resonance (^{1}H-NMR) analysis (see SI Table S1 in the Supplementary Materials), as the copolymers' components had to be coupled in precisely stoichiometric ratios.
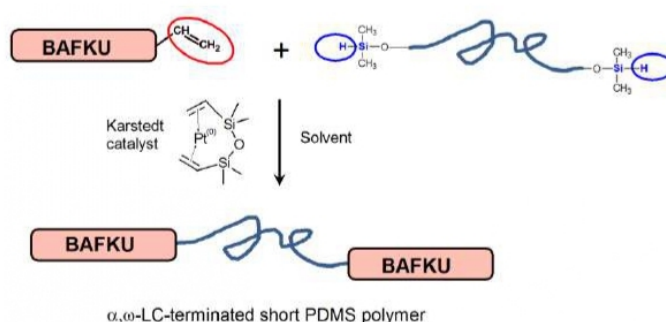
Scheme 3. Synthesis of PDMS–BAFKU$_2$ copolymers via hydrosilylation catalyzed by Karstedt's catalyst.

The structure of the obtained products with approximately realistic proportional sizes of the elastic chains and mesogens is shown in Scheme 4 further below. The latter scheme also shows diagrams with calculated volume fractions of PDMS and BAFKU in each copolymer. The volume fractions of BAFKU (see also Table 1) were calculated under consideration of the densities and of the stoichiometric

synthesis amounts (see Table 1) of the individual components (details of the calculation are given in the Supplementary Materials).
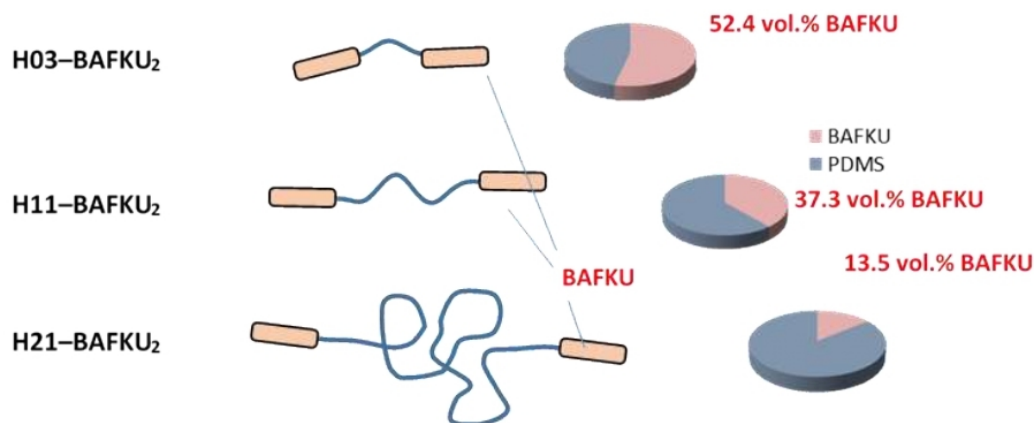
Scheme 4. (**Left**): Representation of the prepared PDMS–BAFKU$_2$ copolymers: H03–BAFKU$_2$, H11–BAFKU$_2$, and H21–BAFKU$_2$, highlighting elastic chain length between the BAFKU mesogens attached at both ends; (**Right**): diagrams of volume fractions of the BAFKU mesogen units in each copolymer.

General properties of the copolymers: All the obtained products were oily liquids at standard room temperature (25 °C), with melting points at 22 °C (H03–BAFKU$_2$), 8 °C (H11–BAFKU$_2$) and −15 °C (H21–BAFKU$_2$). The respective freezing points are: 5, 0 and −20 °C. The copolymers can be dissolved in some common organic solvents like chloroform, tetrahydrofuran or toluene. In contrast to the liquid but colorless (and very low-temperature freezing) PDMS precursors, the copolymers display a dark orange color, like the molten neat BAFKU mesogen.

The efficiency of the hydrosilylation reaction was of great importance for accurate characterization of the copolymers' material properties. A quantitative (100%) conversion was proven in all three reactant pairs by means of Fourier-transform infrared (FTIR) and ^{1}H-NMR spectroscopy, namely as the disappearance of the characteristic signals of the Si–H groups, and in the case of ^{1}H-NMR, also as the disappearance of distinct vinyl signals (see an example of H11–BAFKU2 in the Supplementary Materials in SI Figure S1a,b, respectively; all spectra are shown in SI Figures S1–S8.

The molecular masses of the prepared copolymers were evaluated by ^{1}H-NMR spectroscopy (end-group analysis: ratio of terminal groups to PDMS repeat units), as well as by size exclusion chromatography (SEC, "GPC") and by MALDI-TOF (matrix-assisted laser desorption ionization/time of flight mass spectroscopy; the results are shown in the Supplementary Materials). The latter two methods were useful for characterizing molecular mass distributions. The masses of the employed PDMS precursors and of the mesogen BAFKU also were evaluated. The results obtained by the different methods are all compared in SI Table S2 in the Supplementary Materials, where a detailed discussion is also included, together with all spectra. Generally, it was observed that the SEC analysis provided relatively accurate molecular mass values for all the PDMS–BAFKU$_2$ copolymers, but less accurate ones for the PDMS precursors, especially for the low-molecular-weight H03, but also for H11. The SEC analysis also indicated the presence of some non-bonded BAFKU mesogen, ca. 5% of the total intensity of all peaks if the sensitive but relatively unbiased evaporative light scattering (ELSD) detector was used. This seems to be overestimated if compared to ^{1}H-NMR data, where no characteristic peaks of the unreacted components were observed, neither vinyl (BAFKU excess) nor SiH (PDMS excess). Especially, in the case of the low-molecular-weight copolymer H03–BAFKU$_2$, such residues in amounts as high as 5% would be well visible (estimated possible residue in the latter case would be below 1%). The overestimation of the BAFKU residue can be explained by the high/very high sensitivity of both the

employed detectors to BAFKU, due to the employed wavelengths (see details in the discussion in the SI File). MALDI-TOF yielded very accurate values for the copolymers H03–BAFKU$_2$ and H11–BAFKU$_2$, but the vaporization of H21–BAFKU$_2$ was no longer successful, similarly like in the case of neat H21, due to the too high molecular mass. The H03 precursor underwent radical coupling (oligomerization, SiH reactivity) during the laser pulses of the MALDI-TOF experiment, while H11 was characterized relatively accurately (SiH groups already diluted, M_n not too high).

To sum up, ^{1}H-NMR spectroscopy was found to be the most sensitive method to verify the completeness of conversion during the synthesis (which was confirmed), and it also provided accurate values of the number average molecular masses of the PDMS precursors, as well as of the studied copolymers. The careful evaluation of SEC data also indicates only minimal amounts of unreacted components (BAFKU).

3.2. Thermo-Mechanical Properties

The reversible physical crosslinking in the prepared copolymers, as well as their rubbery properties, were investigated by dynamic-mechanical thermal analysis (DMTA) using parallel-plate tools with small plates (diameter 6.1 mm). This geometry made possible reasonably accurate characterization in the glassy and rubbery state, as well as in the early stages of melting.

Figure 1 illustrates the temperature dependence of the storage modulus in a heating and in a cooling run for all three studied copolymers. It can be observed that the copolymers with the longer PDMS chains, H11–BAFKU$_2$ and H21–BAFKU$_2$, behave like typical reversible elastomeric networks; they display a "rubbery plateau" with a storage modulus above (or well above) 1 MPa in relatively extended low-temperature regions. The short copolymer H03–BAFKU$_2$, on the other hand, is a typical vitrimer; it undergoes a transition from the glassy (or possibly crystalline) state directly into a melt. The chain length of the PDMS segments has a marked effect on the rubbery behavior of the other two copolymers; the one with the mid-sized PDMS chains, namely H11–BAFKU$_2$, displays the wider rubbery plateau (extent: 95 °C in heating scan, and 75 °C in cooling scan) and a higher melting point (ca. 8 °C; freezing point: 0 to −5 °C). Not surprisingly, due to the shorter elastic chains, the rubbery modulus of H11–BAFKU$_2$ is also higher than in the case of the longer H21–BAFKU$_2$; the width of the rubber plateau in H21–BAFKU$_2$ is 20 °C while heating, and 55 °C while cooling, and the melting point is ca. −15 °C, while the freezing point is −20 °C.

The trend can be explained as follows. In the case of the very short H03 PDMS chain, the volume fraction of BAFKU mesogen makes up 52.4% (see Scheme 4) and it already dominates the thermomechanical properties of the material, which is either a crystalline molecular solid or a melt, depending on the temperature. In H11–BAFKU$_2$ (37.3 vol% BAFKU), the elastic chains are sufficiently long for generating rubbery behavior, while the large volume fraction of BAFKU ensures highly efficient crosslinking via nano-aggregation of these terminal building blocks into domains which act as multiple junctions in the rubber (see further above, Scheme 1). Finally, in H21–BAFKU$_2$ (13.5 vol% BAFKU), the relatively small mesogenic units are already considerably diluted in the mass of the PDMS chains, so that their aggregation is less efficient, resulting in a narrower rubbery plateau and a lower melting point.

H11–BAFKU$_2$, the best low-temperature elastomer among the studied copolymers, displays a fairly high rubbery modulus in its extended rubber plateau, namely 30 MPa in the heating run and 60 MPa in the cooling run (see Figure 1b). It undergoes a glass transition near −110 °C. The melting region of the rubbery phase near 8 °C (freezing point: 0 °C; melting region—heating scan: 0 to 11 °C; cooling scan: −20 to 10 °C) is relatively steep, but still gradual, in contrast to molecular solids, which would melt abruptly. Some thermotropic transitions of the BAFKU aggregates can be suspected to occur in the melting region (progressive loosening or dissociation of the aggregates), in view of the step-like course of the modulus in this region. Additionally, gelation-type thermotropic transitions in the liquid region were confirmed by highly sensitive multi-frequency rheological tests (carried out using large parallel plates), which are discussed in a follow-on work [43]. The moderate increase in the

modulus of H11–BAFKU$_2$ with rising temperature practically in the whole rubbery region, which is typical of ideal elastomers, indicates an efficient physical crosslinking.
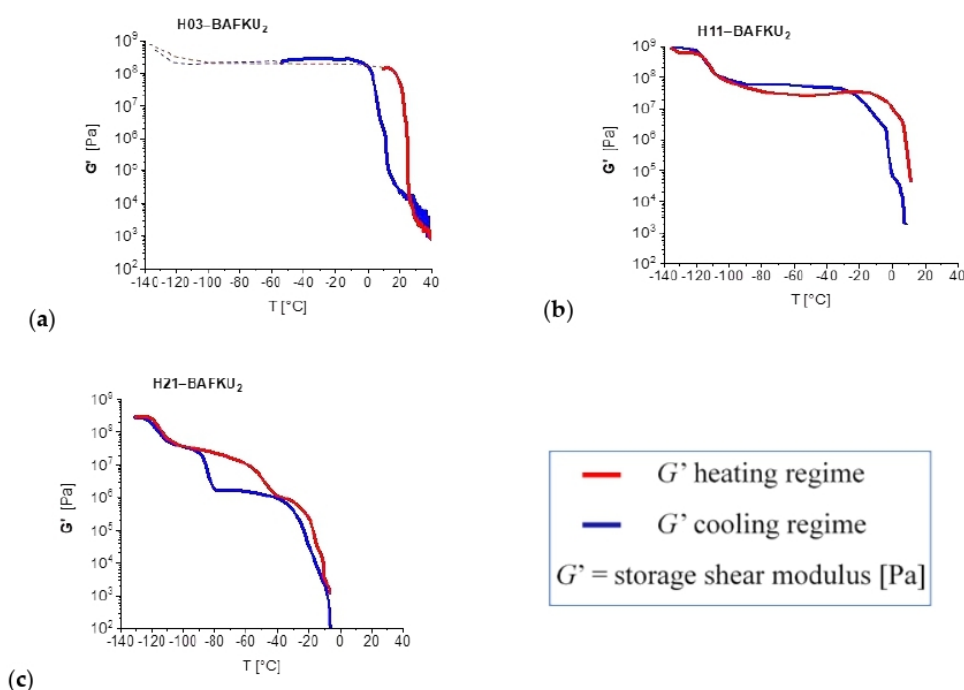
Figure 1. Dynamic-mechanical thermal analysis (DMTA) profiles (temperature-dependent storage modulus G' only) of the copolymers (**a**) H03–BAFKU$_2$, (**b**) H11–BAFKU$_2$, and (**c**) H21–BAFKU$_2$, recorded as heating and cooling scans.

H21–BAFKU$_2$, which is also a low-temperature elastomer (see Figure 1c), displays a much more complex behavior than H11–BAFKU$_2$. In the heating scan, it displays only a very small rubbery region, or rather, a sloped step, but in the cooling scan, a much wider thermodynamically metastable rubbery plateau is observed. In both cases, the rubbery modulus is around 1 MPa. The vast difference in the width of the rubbery plateau during cooling and heating is caused by the behavior of the long linear PDMS chains in H21–BAFKU$_2$. The latter display glass transition (−85 °C during cooling scan)/hidden cold crystallization (gradually occurring below −85 °C but above −110 °C)/melting (at −50 °C: during heating after cold crystallization). Such a behavior in pure PDMS is known from the literature, e.g., from [48]. Near −110 °C, there is a small step in the G' = f(T) curve of H21–BAFKU$_2$, which is assigned to freezing/unfreezing of segmental movements of the pendant methyl groups in PDMS chains, and which could be referred to as a minor glass transition. Below −110 °C, the H21–BAFKU$_2$ copolymer is fully frozen and ideally glassy. It can be noted that in the case of the H11–BAFKU$_2$ discussed above (see Figure 1b), which has shorter PDMS chains than H21–BAFKU$_2$, only a single glass transition of the material occurs, namely at the temperature of the freezing of methyl groups movement in PDMS (−110 °C), while the vitrification/cold crystallization/melting hysteresis loop of PDMS is absent: the H11 chains are too short for such a behavior. The G' = f(T) curve of H21–BAFKU$_2$ is always decreasing with rising temperature in the rubbery plateau, which indicates that the physical crosslinking is not very efficient, and that some nanoaggregates of BAFKU end-groups dissociate even at temperatures relatively distant from the melting region. The onset of the melting (near −20 °C) is also distinctly more gradual ("melting point" itself is at ca. −15 °C) in H21–BAFKU$_2$ than in H11–BAFKU$_2$. (Freezing point of H21–BAFKU$_2$: −20 °C melting region: −25 to 0 °C in heating and cooling scans).

Although the rubbery plateau is small in H21–BAFKU$_2$, the specific hysteresis behavior of this material could make it an interesting viscoelastic low-temperature rubber/oil.

H03–BAFKU$_2$, the copolymer with the shortest elastic polysiloxane segments, displays very simple and rather unattractive thermomechanical characteristics (see Figure 1a). It behaves like a brittle "vitrimer", which near 22 °C transforms directly from glass into melt (softening onset already at 14 °C), with no glass-to-rubber transition (freezing point of H03–BAFKU$_2$: 5 °C melting region: heating scan: 15 to 25 °C; cooling scan: 0 to 25 °C). The melting transition is very steep in the heating run, but in the case of the cooling run, the freezing region is somewhat structured, thus indicating possible thermotropic transitions in the physical crosslinks in this temperature region. Rheological tests, which are discussed in a follow-on work [43], indeed confirmed this suspicion. The difference between the melting and the freezing temperature is also fairly high in H03–BAFKU$_2$ (the difference is smaller in H11–BAFKU$_2$ and nearly negligible in H21–BAFKU$_2$). Due to its brittleness in the glassy state, it was impossible to study its thermomechanical properties below −40 °C, but in analogy to the other studied PDMS copolymers, a small step in the $G' = f(T)$ curve (dotted line in Figure 1a) would be expected in the range from −100 to −90 °C, caused by the freezing/unfreezing of the wagging movement of pendant methyl groups on PDMS segments. The H03–BAFKU$_2$ copolymer might be of interest as a model compound or as a "plasticized BAFKU dimer".

3.3. Phase Transitions in the Copolymers

3.3.1. DSC: Specific Heat of Phase Transitions in the Copolymers

The thermally induced transitions, which were observed by DMTA in the prepared copolymers, were further investigated by means of differential scanning calorimetry (DSC), in order to find out the nature and especially the involved values of specific heat of these transitions. The results are summarized in Figures 2 and 3. The DSC trace of the neat mesogen BAFKU is also shown in Figure 2a for comparison.
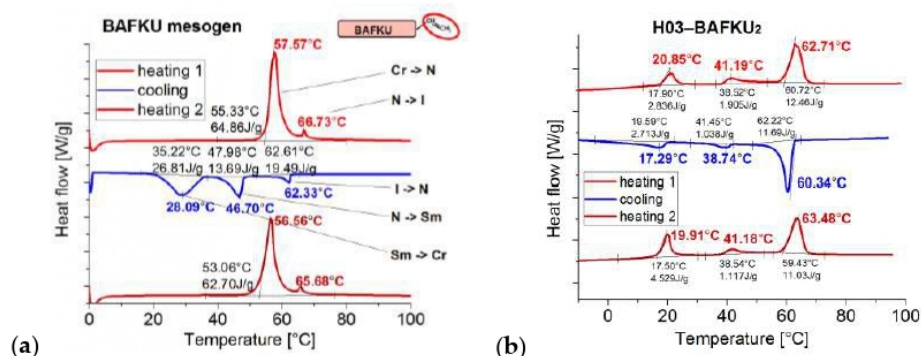
Figure 2. Differential scanning calorimetry (DSC) traces (**a**) of the neat BAFKU mesogen and (**b**) of the copolymer H03–BAFKU$_2$.
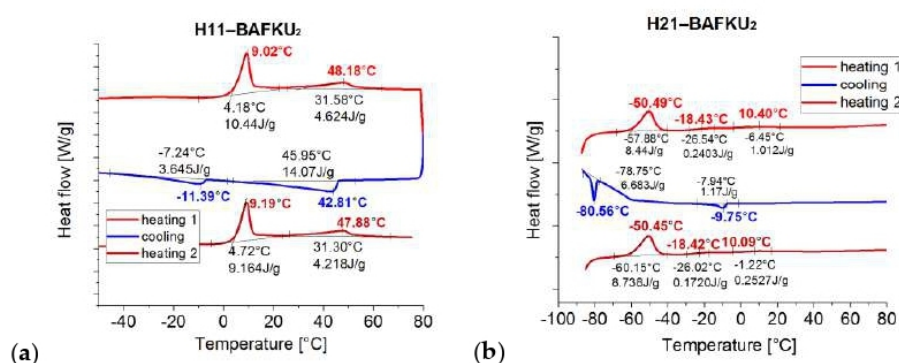
Figure 3. DSC traces of the copolymers (**a**) H11–BAFKU₂ and (**b**) H21–BAFKU₂.

The following trends can be observed. The specific heat values of the observed LC transitions distinctly decrease with increasing PDMS chain length, especially if going from H11 to H21.

Neat BAFKU in the heating DSC scan undergoes only the shorter phase sequence crystalline (Cr) →smectic C (SmC)→isotropic (I) [44], while in the cooling run, it undergoes the "full" phase sequence I→nematic (N)→smectic (Sm)→Cr transitions. The free mesogen is hence characterized by several monotropic transitions.

H03–BAFKU₂ (see Figure 2b), the copolymer with the shortest PDMS chains, displays highly similar transition temperatures in its DSC trace like neat BAFKU in its cooling scan (compare Figure 2a,b), but all the transitions of H03–BAFKU₂ are shifted to slightly lower temperatures. There are also some additional notable differences like different peak intensities, but also in the strictly enantiotropic nature of all transitions in H03–BAFKU₂, with nearly identical specific heat values of the reverse processes. Notable in this context is also the near absence of undercooling effects in the copolymer. The N→I transition is always the most intense one in the copolymer, while in neat BAFKU, I→N is low-intensity and monotropic. The transitions in H03–BAFKU₂ were assigned by correlating the DSC results with polarized light microscopy analysis discussed further below: highest temperature—N/I; medium temperature—Sm/N; lowest temperature—Cr/Sm. The slight down-shift of the transition temperatures in the copolymer (if compared to neat BAFKU) can be attributed to the moderately increased mobility of the mesogen units, which are attached to short, monodisperse (PDI = 1.11, see SI Table S2 in the Supplementary Materials), and highly flexible PDMS chains. These specific short spacers also apparently similarly strongly stabilize the smectic as well as the nematic phase in the copolymer, which is still dominated by BAFKU (52 vol%, see Table 1), thus leading to the absence of undercooling.

It can be further noted that H03–BAFKU₂ melts at ca. 22 °C (see DMTA in Figure 1a), near its first thermotropic transition (19.9 °C, Cr→Sm), while the remaining transitions occur in the liquid phase (up to 63 °C). This means that residual ordered liquid crystalline aggregates must persist as branching points in the copolymer melt from 22 to 63 °C (N→I) and thus, can have interesting effects on its viscoelastic behavior.

H11–BAFKU₂ (see Figure 3a) displays a smaller number of transitions than H03–BAFKU₂, two instead of three, and also, the characteristic temperatures are lower in H11–BAFKU₂. The "width" of the temperature range of the combined LC transitions in H11–BAFKU₂ is practically the same as in H03–BAFKU₂, however, suggesting that similar interactions play a role in both copolymers. The down-shift of the transitions in H11–BAFKU₂ indicates a higher mobility of BAFKU due to the attached relatively long and segmentally very mobile of PDMS chains. In addition, the "dilution" of the aggregates in the now dominant PDMS phase (63 vol%, see Table 1) may play a role. The DSC peaks of H11–BAFKU₂ were assigned in view of the polarization microscopy textures discussed further below as Cr/N (lower temperature) and N/I (flat peak extended over a wider region). In the case of the Cr/N peak, if the heating and cooling scans are compared, the change of the intensity (much less intense if cooling) and of the characteristic temperature (down-shift by 20 °C if cooling), indicates a

difficult crystallization. This effect was also observed by PLM (as discussed further below), and it correlates with the down-shifted solidification of molten H11–BAFKU$_2$ to rubber, which was observed by DMTA (see Figure 1b). On the other hand, the N/I transition in the melt displays only a small undercooling effect. This latter transition also shows the highest specific heat among the peaks in the cooling run, thus indicating that the formation of the nematic phase is fairly strongly favored by the H11 chains. The absence of a smectic phase in H11–BAFKU$_2$ indicates that the medium–long H11 chains, albeit monodisperse, do not stabilize the highly ordered Sm phase in contrast to short H03 chains.

H21–BAFKU$_2$ (see Figure 3b) displays practically no visible LC transitions in heating scans, and one weak but distinct transition in the cooling scan at −9.8 °C (quasi a monotropic one), which is positioned in the region of the onset of the solidification of the melt to rubber (see further above, DMTA) and was assigned to the N→Cr transition in the BAFKU nanoaggregates of H21–BAFKU$_2$. The polarization microscopy (PLM) investigations, and also the X-ray-diffraction (XRD) patterns, which are both discussed further below, support the existence of BAFKU nanodomains (lamellae) in H21–BAFKU$_2$, also in an extended temperature region of the liquid state. If an analogy would be drawn to the shorter H11–BAFKU$_2$, the longer copolymer H21–BAFKU$_2$ also could contain its mesogen nanoaggregates in the nematic ordering state. The anisotropic domains in PLM (see further below) are very small, however, and the textures are not very characteristic, so the assignment of the nematic phase in H21–BAFKU$_2$ is only tentative. The suggested analogy between H21–BAFKU$_2$ and H11–BAFKU$_2$ is further supported by the analogous rheological behavior of both copolymers, which was studied in a separate work [43]. The low transition temperature, as well as the quasi-monotropic character (and small specific heat) of the single thermotropic transition observed in H21–BAFKU$_2$ suggest the formation only of weaker and smaller BAFKU aggregates in this longest copolymer, in contrast to the shorter ones. It can be clearly concluded that in H21–BAFKU$_2$, the effect of BAFKU on the thermal properties is diminutive. In spite of this, the physical crosslinking as observed by DMTA still is considerably strong in this copolymer, albeit it is the weakest in the compared series.

In contrast to the other copolymers, the DSC traces of H21–BAFKU$_2$ additionally display distinct thermal transitions of the long PDMS chains of H21 (vitrification/cold crystallization/melting), which in fact dominate the whole DSC trace. The region of these transitions is marked by a frame in Figure 3b. In the heating scans, a broad melting peak is observed with a maximum at −50.5 °C, while in the cooling scan, a sloped course of the DSC trace, which corresponds to a glass transition, is observed between −60 and −85 °C, which also contains a cold crystallization peak (−80.6 °C). The vitrification/cold crystallization/melting of PDMS was discussed in detail in the literature, e.g., in [48].

3.3.2. X-ray Diffraction (XRD) Analysis of the Phase Transitions

The phase transition behavior of the studied copolymers was deeper elucidated by means of recording temperature-dependent X-ray scattering (small-angle X-ray scattering SAXS and wide-angle X-ray scattering WAXS) of the products and by comparing them with the patterns of the pure mesogen BAFKU. The results of the X-ray experiments are summarized in Figure 4. The observed XRD peaks are commented on in Tables 2 and 3. Generally, all three copolymers were found to possess a distinctly lamellar structure, with BAFKU nanoaggregates as the lamellae.

In the case of the neat BAFKU (Figure 4a), the following assignment to the dimensions of the mesogen molecule can be done. The peak at 3.40° (scattering vector $q = 0.242$ Å^{-1}, corresponding to the distance $d = 2.60$ nm) can be well correlated with the length of this rod-like building block, while the very weak peak at 6.80° (0.484 Å^{-1}) appears to be a second-order reflection of the same distance. The peak at 10.18° (0.72 Å^{-1}/0.87 nm—it is more intense than the one at 6.80°, and hence, it cannot be the 3rd order of the peak at 3.40°) can be assigned to the width of the whole mesogen (similarly like in [44]). Finally, both the peaks in the range of 18–20° (1.4 Å^{-1}/0.45 nm) can be assigned to standard Van der Waals distances between organic molecules, e.g., in different directions in the crystal. The peaks of

the neat mesogen are all sharp, thus indicating a highly ordered state at all the tested temperatures, except in the isotropic melt at 85 °C (see Figure 4a).
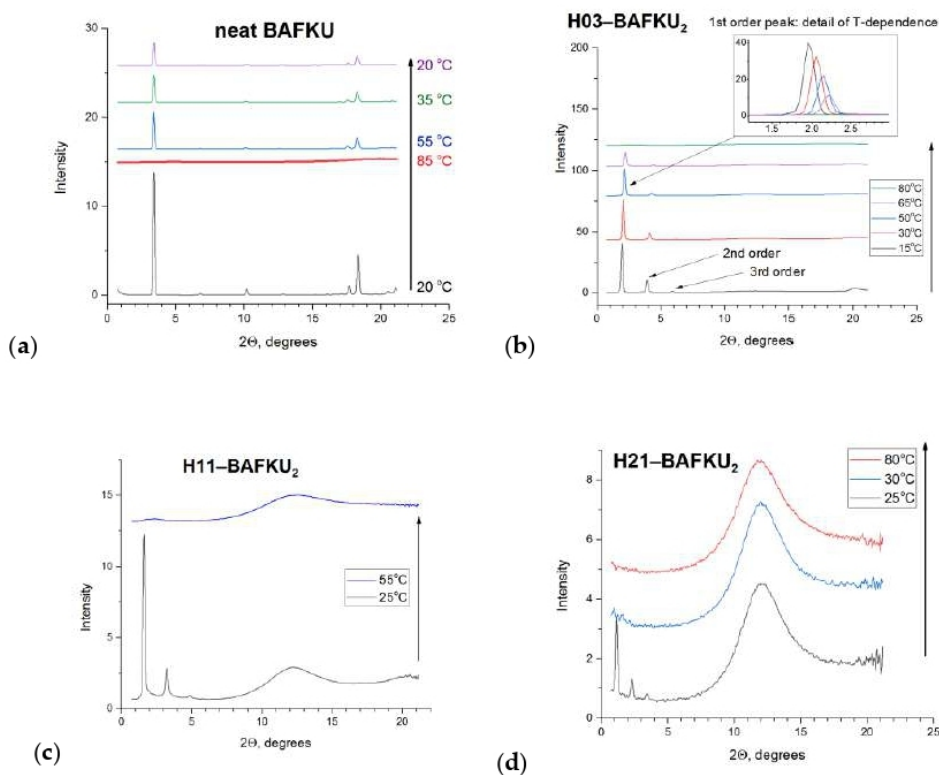
Figure 4. Temperature-dependent XRD patterns of: (**a**) neat BAFKU, (**b**) H03–BAFKU$_2$, (**c**) H11–BAFKU$_2$, and (**d**) H21–BAFKU$_2$; in the case of neat BAFKU (**a**), the sample was first characterized at 20 °C, then heated up to 85 °C, and subsequently, step-wise cooled down back to 20 °C. This was done because the full series of phase transitions in BAFKU occurs only in the cooling scan; in the case of all the copolymer samples (**b**–**d**), they were step-wise heated from low temperature to high temperature during the XRD analyses.

Table 2. X-ray diffraction results. BAFKU: interference maxima and the corresponding characteristic distances.

BAFKU			
2θ [°]	q [Å^{-1}]	d [nm]	comment
3.40	0.242	2.60	BAFKU length
6.80	0.484	1.30	-"- (second order of 3.40°)
10.18	0.724	0.87	BAFKU width
17.70	1.255	0.50	standard Van der Waals distance in crystal
18.36	1.301	0.48	standard Van der Waals distance in crystal

Table 3. X-ray diffraction results. PDMS–BAFKU$_2$ copolymers: Interference maxima and the corresponding characteristic distances.

H03			H11			H21			
2θ [°]	q [Å^{-1}]	d [nm]	2θ [°]	q [Å^{-1}]	d [nm]	2θ [°]	q [Å^{-1}]	d [nm]	comment
1.95	0.139	4.53	1.644	0.117	5.37	1.13	0.0804	7.81	main reflection
3.90	0.277	2.26	3.28	0.233	2.69	2.26	0.161	3.90	2nd order
5.85	0.416	1.509	4.93	0.351	1.79	3.39	0.241	2.60	3rd order
8–16	0.57–1.13	1.1–0.55	8–16 (12.24)	0.57–1.13 (0.896)	1.1–0.55 (0.723)	8–16 (12.24)	0.57–1.13 (0.896)	1.1–0.55 (0.723)	PDMS
20.1	1.42	0.44	20.6	1.46	0.43	–	–	–	org.–org. (+PDMS)

In the case of the PDMS–BAFKU$_2$ copolymers (Figure 4b–d), the BAFKU units also generate sharp X-ray diffractions, but their diffraction pattern is much simpler. Only one characteristic distance is observed, which generates a main peak, as well as second- and third-order reflections of this distance. This characteristic distance in the BAFKU domains of the copolymers becomes distinctly wider with the increasing length of the polysiloxane spring. The presence of such distinct 2nd and 3rd order reflections, as well as the relatively sharp peaks, are indicative of a well-developed lamellar structure (see Schemes 5 and 6 and structure discussion further below). The increasing characteristic distance corresponding to these reflections can be well correlated with the increasing spatial demand of the increasingly long and increasingly coiled PDMS chains (see Scheme 5), which separate the lamellae. Additionally, two very broad peaks (near 12° and near 21°) appear in the diffractograms of the copolymers, corresponding to amorphous halo structure, which is characteristic of PDMS. Especially, the first PDMS peak dramatically grows with increasing chain length of the PDMS component, and hence, with the PDMS fraction in the copolymer, while the second is only partly visible.
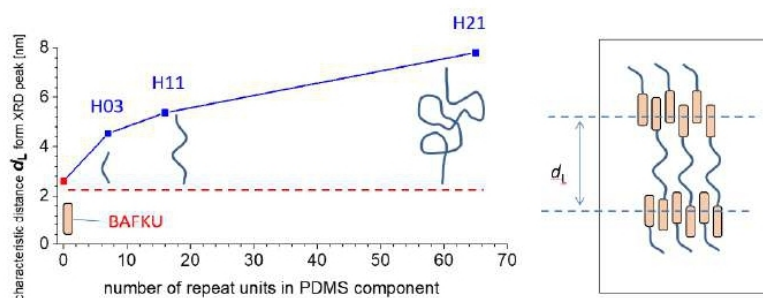
Scheme 5. Lamellar structure of the copolymers and the effect of the chain length of the PDMS component on the characteristic distance observed by X-ray diffraction. (**Left**): plot of the observed (XRD) characteristic distance with in-laid approximate relative sizes of the segments of the studied copolymers; the coiling of PDMS chains plays an important role; (**Right**): idealized representation of the lamellar nanoaggregates of the BAFKU end-groups present in the copolymers below the isotropization temperature.

reversible joining and splitting of lamellar nano-domains of BAFKU
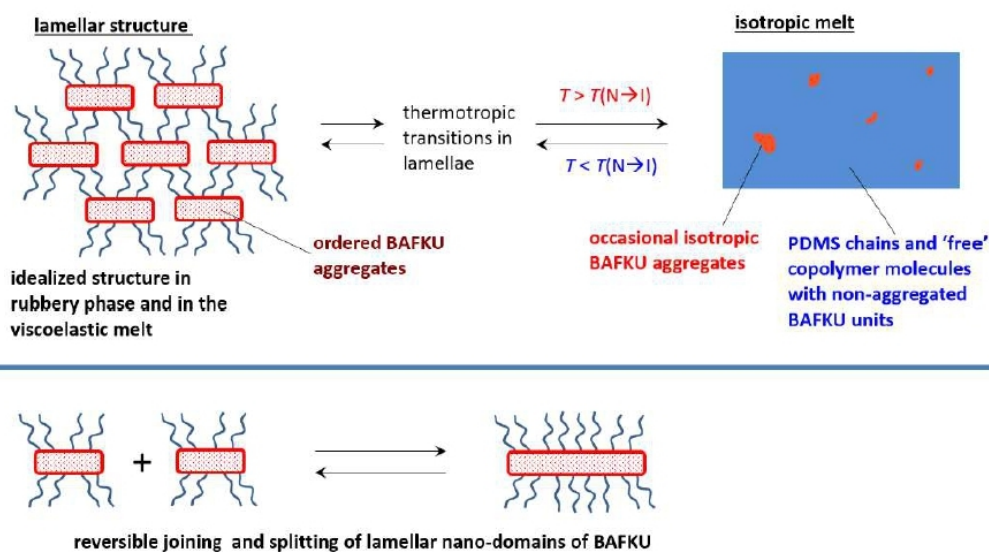
Scheme 6. Postulated lamellar structure in the studied copolymers, composed of lamellar nanoaggregates of BAFKU and of elastic PDMS chains, its isotropization (according to Scheme 7 **bottom**), as well as the reversible growth and fragmentation of the lamellar BAFKU nanoaggregates.

crystalline aggregates, well-ordered, rigid (**Cr**)

smectic aggregates, dynamic (**Sm**)

nematic aggregates, dynamic (**Sm**)

isotropic state (I): possible disordered small dynamic aggregates, which dissociate and recombine
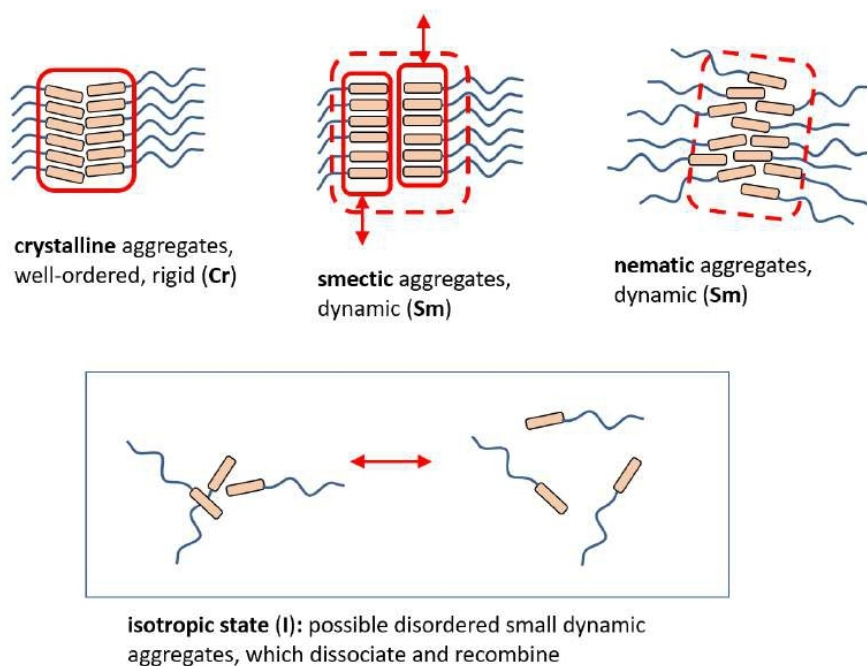
Scheme 7. Postulated idealized structure in the crystalline (Cr), smectic (Sm), and nematic nanoaggregates of BAFKU end-groups in the studied copolymers, as well as the arrangement in the copolymers' molecules in the isotropic melt.

The diffractograms of the sample H03–BAFKU$_2$ (Figure 4b) were measured at temperatures between and beyond the ones of the characteristic DSC transitions (discussed further above), namely at 15, 30, 50, 65, and 80 °C. We can see a systematic shift of the main reflection peak of the BAFKU domains with increasing temperature. Originally, the peak is positioned at $2\theta = 1.96°$, which corresponds to d = 4.50 nm (2nd order reflection at 3.94°; 3rd order at 5.87°). Sample heating leads to a higher

angle 2θ, which means a shorter characteristic distance. A shorter distance between the lamellar BAFKU aggregates at higher temperatures could be explained by a more coiled average conformation of the PDMS chains, which is a known entropy effect in elastomers. The change of 2θ with *T* is almost linear, starting with 4.498 nm at 15 °C, via 4.288 nm at 30 °C, 4.114 nm at 50 °C, and, finally, 3.959 nm at 65 °C. Like the main reflection, the higher order interference maxima all show a proportional *T*-induced shift. Analogous behavior is observed for the reflections in all the copolymers (compare Figure 4b–d). The intensity of the peaks originating from BAFKU units gradually decreases with the temperature, indicating partial melting (dissociation of larger aggregates). No peaks are observed at 80 °C, which is in agreement with the isotropization of H03–BAFKU$_2$ observed by DSC already at 63 °C (see further above).

The sample H11–BAFKU$_2$ (Figure 4c) exhibits an analogous behavior like H03–BAFKU$_2$, but the fundamental peak of its single reflection is found at 2θ = 1.62° (2nd order at 3.25°; 3rd at 4.88°), which corresponds to 5.435 nm. The distance is 21% larger than the characteristic one in H03–BAFKU$_2$. Similarly, like in the latter sample, no XRD reflections of BAFKU are observed in the isotropic melt state of H11–BAFKU$_2$.

The similarly behaving H21–BAFKU$_2$ (Figure 4d) exhibits the largest characteristic distance in the BAFKU domains. At 25 °C, already in the liquid range (nematic), the sharp reflection is positioned at 2θ = 1.15° (2nd order at 2.31°; 3rd at 3.43°), which corresponds to d = 7.69 nm. This reflection is no longer observed at 30 °C, where the melt already is fully isotropic. No changes in amorphous halo were observed at higher temperature (between 25 and 80 °C). While the sensitivity of DSC was too low to detect phase transitions in H21–BAFKU$_2$ in the heating regime, the X-ray results together with the light microscopy data presented further below indicate a phase transition (isotropization) near 30 °C, which to some extent, is also confirmed by rheology tests, which are discussed in a follow-on work [43].

3.3.3. PLM Observation of Anisotropy and of Phase Transitions

The phase transition behavior as well as ordering effects in the domains of the mesogenic units of the prepared copolymers were additionally evaluated by means of polarized light microscopy (PLM). The PLM analysis was of special interest, because the XRD patterns discussed above were dominated by the reflections caused by lamellae of BAFKU and on PDMS interchain distances, but these patterns did not provide any information about the arrangement in the lamellae. The PLM results are summarized in Figures 5–8. It should be noted that the extended sub-millimeter-sized highly anisotropic regions observed in the copolymer samples at appropriate temperatures cannot be lamellae of aggregated and well-separated BAFKU units, in view of their volume fractions in the copolymers (see Table 1 and Scheme 4), and also in view of their bonding situation (see Scheme 1), which does not allow for the growth of very large 3D domains made from phase-separated pure BAFKU. The observed anisotropic areas hence can be assigned to regions in which the lamellar BAFKU nanodomains have some prevalent orientation, while being separated by PDMS, so that both the ordering inside of the nanodomains (lamellae), as well as their "global arrangement" (some analogy to lyotropic systems), contribute to the dichroism of the respective observed specimen.

As the reference compound, the neat mesogen BAFKU was also characterized. It can be seen in Figure 5 (representative high-resolution images of the characteristic textures are shown in SI Figures S20 and S21 in the Supplementary Materials) that its changes of PLM texture during the heating run fairly closely follow the temperature course of the phase transitions observed by DSC (see Figure 2a); one abrupt change is observed at 58 °C (DSC peak maximum: 57 °C: Cr→SmC, as assigned in [44]), while the second occurs between 63 and 64 °C (DSC: 67 °C: SmC→I). A fan-shape texture is observed for the crystalline phase. The transition at 58 °C is followed by a temporary darkening (isotropization), which precedes the formation of new, differently ordered extended textures. The second transition (SmC→I) occurs at a somewhat lower temperature in PLM than in DSC, which might be the result of a higher rate in the DSC scan (10 vs. 1 °C/min) and/or of the dissolution of the larger oriented domains of BAFKU molecules. This would lead to "earlier" apparent disappearance of anisotropy in PLM. In the

cooling run studied by PLM (Figure 5), a distinct apparent undercooling is observed in comparison to the DSC scan in Figure 2a for the I→N transition, which starts at 43 °C in PLM (DSC: 62 °C), but this is possibly a consequence of the fact that only larger oriented domains or regions become visible (similarly like in the case of heating). This undercooling is also observed if the mean polarized light intensity from the whole image area is evaluated (see SI Figure S16 in the Supplementary Materials). The formation of small anisotropic domains directly invisible by the microscope would manifest itself as an increase in background light intensity, but due to an efficient undercooling, no such "hidden" intensity increase is observed (in contrast to some other samples). The next PLM-observed transition, N→Sm (fan-shape structure appears, similar to the original crystal), starting at 40 °C (well visible at 39 °C, finished at 38 °C) is less low-temperature shifted (47 °C in DSC). Both low-temperature shifts in the cooling PLM run might be a result of the narrow (<10 µm) distance of the microscopy glass platelets, which might cause a more difficult crystallization than in the thicker DSC samples. Because the texture observed after the N→Sm transition of BAFKU is already practically identical with the one observed for the crystalline phase (see heating scan in Figure 5), the Sm→Cr transition of neat BAFKU (DSC: 28 °C) cannot be recognized by PLM.
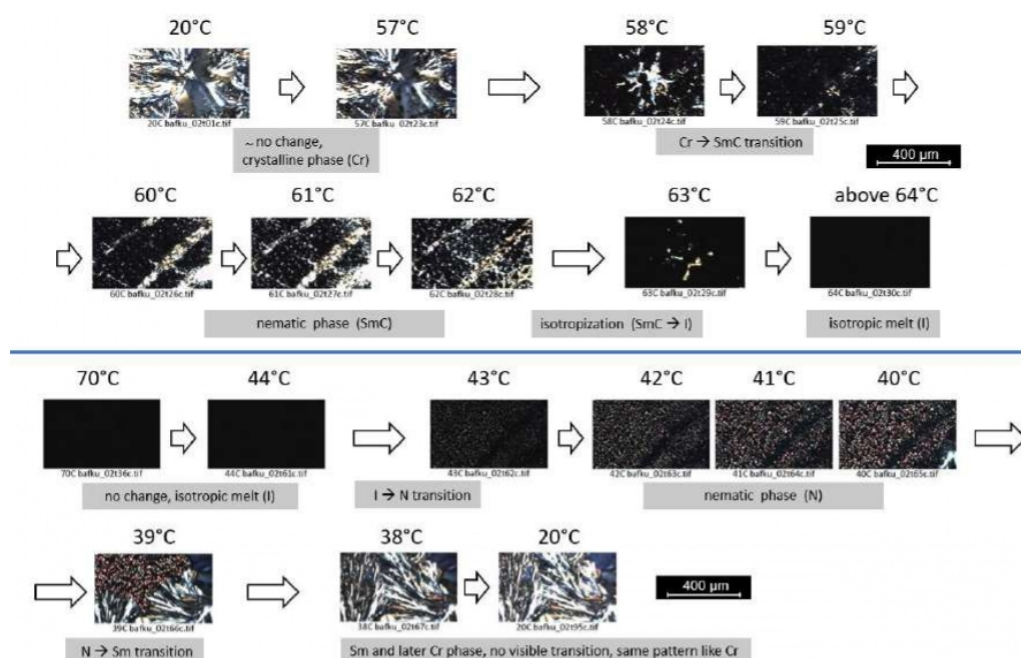
Figure 5. Textures observed in neat BAFKU mesogen. **Top**: heating run; **bottom**: cooling run; large representative images of each characteristic texture are shown in the Supplementary Materials, SI Figures S20 and S21.

The H03–BAFKU$_2$ copolymer in a certain sense displays similar trends in the temperature-dependent PLM textures (Figure 6; representative high-resolution images of the characteristic textures are shown in SI Figures S22–S24 in the Supplementary Materials) like neat BAFKU, but the textures are of somewhat different appearance and their interconversions are rather gradual than abrupt, in contrast to PLM of BAFKU, or to the DSC traces of this same copolymer, H03–BAFKU$_2$, where the peaks are fairly sharp and where only negligible undercooling is observed. Between 10 and 20 °C in the heating run, an apparent increase in long-range ordering of H03–BAFKU$_2$ can be observed, which manifests itself by increasing texture intensity, without any change of pattern. Above 20 °C (Cr→Sm transition in DSC), the intensity does not change any more, but while the global pattern does not change markedly (nor do the colors), the fine pattern of the texture changes from

fibrillar to particulate. Above 40 °C, the domains of the fine pattern at first visibly increase in size and change their color (DSC: 41 °C: Sm→N). As the temperature further rises, the fraction of anisotropic areas decreases, while larger apparently isotropic domains start to grow (considerable isotropization at 56 °C and nearly complete one at 58 °C). In DSC (Figure 2b), the isotropization (N→I) peak is observed near 63 °C. The "earlier" occurrence of the isotropization in the PLM scan can be attributed to the dissolution of the larger regions with oriented nano-lamellae of BAFKU units in the nematic state, in some analogy to neat BAFKU.
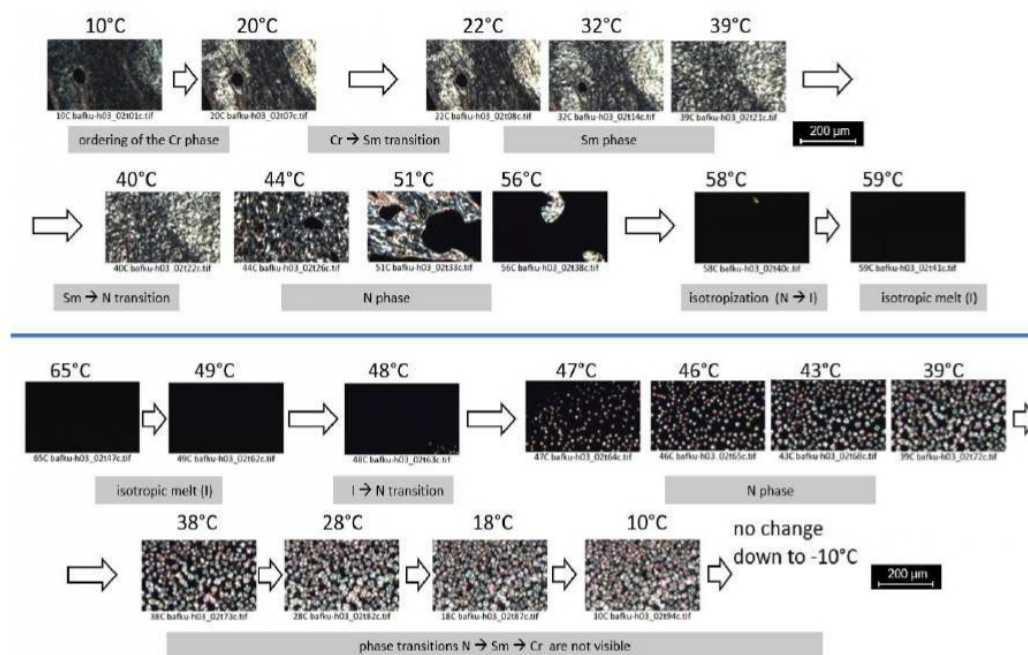
Figure 6. Textures observed in BAFKU–H03. **Top**: heating run; **bottom**: cooling run; large representative images of each characteristic texture are shown in the Supplementary Materials, SI Figures S22–S24.

In the cooling PLM experiment, the H03–BAFKU$_2$ copolymer displays even greater undercooling effects than neat BAFKU; the onset of visible nematic ordering (nematic dots) is observed near 48/47 °C (DSC peak: 60 °C). At lower temperatures, these "dots" grow and finally cover the whole observed area, but no change of pattern is observed at any temperature (in DSC, peaks are observed at 39 and 17 °C), as if the sample froze to a nematic glass. This behavior may be attributed to the thin sample layer (similarly like in neat BAFKU). Efficient undercooling is also confirmed, if the mean polarized light intensity from the whole image area is evaluated (see SI—Figure S17 in the Supplementary Materials). No "hidden" intensity increase is observed prior to the appearance of the visible patterns at 48/47 °C. The sample undergoes slow "ageing" at room temperature, however. After 3 days, the dot texture, which was obtained at the end of the cooling run, changes to the texture observed for the smectic phase in the heating run (very similar to the crystalline one). Theoretically, this slow ageing could be explained in two ways—either the transition N→Sm is very slow and gradual or the observed texture is strongly influenced by the arrangement of slowly growing lamellae to large "global" patterns. The second explanation is supported (and the first disproven) by the fact, that the DSC trace of H03–BAFKU$_2$ displays nearly identical transition temperatures and peak intensities (and shapes) in both heating and cooling runs. The role of the lamellae (texture generation similar to lyotropic systems) also would explain why the textures of H03–BAFKU$_2$ change so gradually also in the heating scan, where no "delaying effects" would be expected (as the DSC transitions are very sharp).

The H11–BAFKU$_2$ copolymer, which is richer in PDMS, displays similar but simpler trends (see PLM textures in Figure 7; representative high-resolution images of the characteristic textures are shown in SI Figures S25–S27 in the Supplementary Materials) like H03–BAFKU$_2$. In the heating run, the difference is small between the texture of the sample with crystalline domains of BAFKU (according to DSC in Figure 3a, below 10 °C) and between the subsequently occurring liquid crystalline state at higher temperature, assigned as nematic. The transition at 10 °C mainly manifests itself as a subsequent very gradual intensity decrease in the rotated light. Above 35 °C, a progressing apparent isotropization (decay of larger regions with oriented lamellae) is observed, and the visible anisotropic domains nearly disappear at 45 °C (last smallest remnants until 49 °C). In DSC, the maximum of the corresponding N→I peak is observed at 48 °C. As the copolymer H11–BAFKU$_2$ displays only one liquid crystalline phase in melt, no distinct changes in texture type are observed above 10 °C.
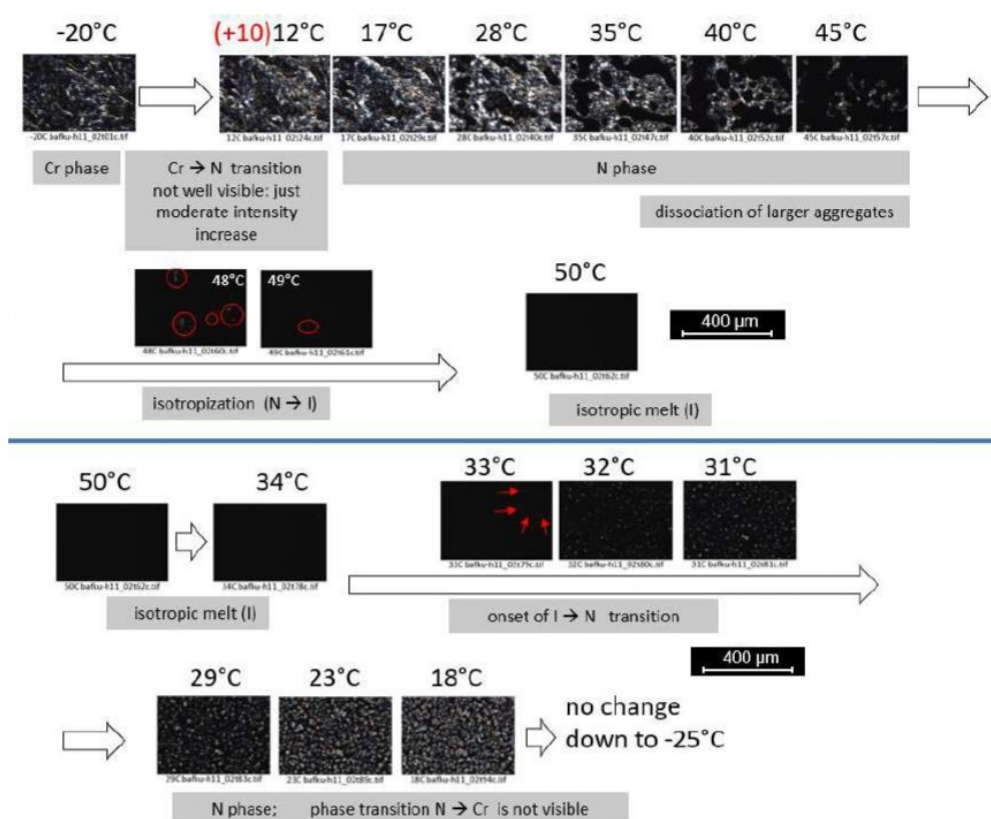
Figure 7. Textures observed in BAFKU–H11. **Top**: heating run; **bottom**: cooling run; large representative images of each characteristic texture are shown in the Supplementary Materials, SI Figures S25–S27.

In the cooling run, the H11–BAFKU$_2$ copolymer behaves very similarly like H03–BAFKU$_2$. It seems to undercool and to apparently freeze to a nematic glass. The process weakly sets on at 33 °C (DSC: I→N transition: 43 °C) and becomes well-visible at 29 °C. The nematic dot domains grow less dramatically than in H03–BAFKU$_2$. No change in texture is observed upon further cooling. If the mean polarized light intensity from the whole image area is evaluated (see SI Figure S18a), then an increase in intensity is observed, which already starts during the cooling run just below 38 °C, only 5 °C below the DSC transition where small BAFKU nano-lamellae are expected to start to assemble. Hence, the apparent undercooling does not mean a complete absence of BAFKU aggregation in this whole temperature region. The easier ordering of the mesogenic units of H11–BAFKU$_2$ in the cooling scan, if compared to H03–BAFKU$_2$, could be attributed to a higher mobility of the BAFKU units attached to

the longer flexible chains. In the case of the heating run of H11–BAFKU$_2$ (see SI Figure S18a), the light intensity curve closely follows the trends noted by "simple" PLM observation, as would be expected.

The H21–BAFKU$_2$ copolymer, which is the richest in PDMS, displays much simpler PLM textures (see Figure 8; representative high-resolution images of the characteristic textures are shown in SI Figures S28–S30 in the Supplementary Materials) than H03–BAFKU$_2$ and H11–BAFKU$_2$.
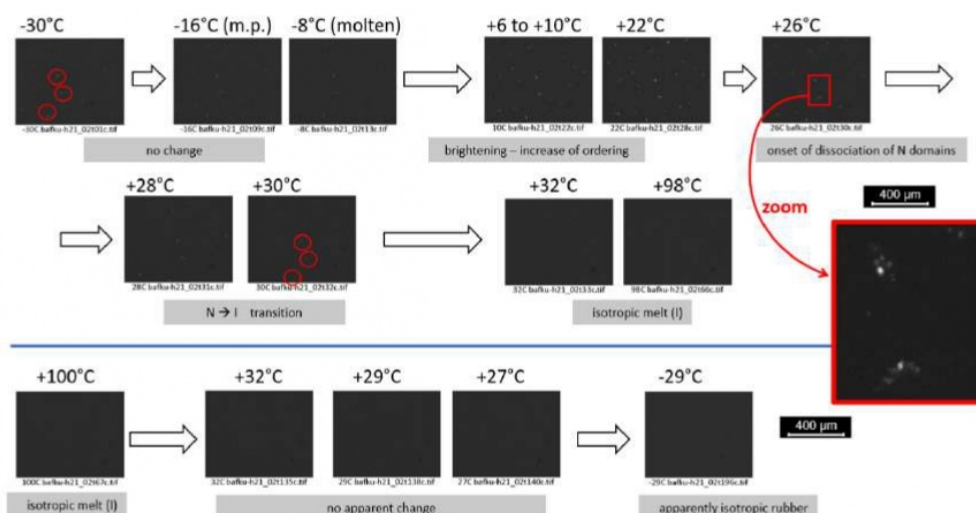
Figure 8. Textures observed in BAFKU–H21, top: heating run; **bottom**: cooling run; large representative images of each characteristic texture are shown in the Supplementary Materials, SI Figures S28–S30.

In the heating run, only small dots are observed in H21–BAFKU$_2$ for the rubbery state (with solid BAFKU aggregates), as well as in melt until 30 °C. The texture is somewhat similar like the nematic dots observed in H11–BAFKU$_2$ during its cooling near 31 °C, but the dots are smaller and less characteristic in the case of H21–BAFKU$_2$. The melting of rubbery H21–BAFKU$_2$ near −15 °C does not cause any marked change in the texture. The critical temperature is near 30 °C, where XRD experiments observe the disappearance of the ordering of the LC units in H21–BAFKU$_2$, and where rheology experiments, which are discussed in a follow-on work [43], suggest a drop in elasticity. While approaching this temperature in the heating scan (PLM), the small dots intensely brighten. The brightening occurs between 6 and 10 °C, the high intensity persists until 22 °C, thereafter it fades until 28 °C, and completely disappears above 30 °C (efficient dynamic disconnection of nanoaggregates of LC units). The ordering which causes the mentioned brightening of the texture can be attributed to an increased mobility of the BAFKU units.

Similarly, like in the case of the other copolymers, the cooling scan of H21–BAFKU$_2$ yields different results (apparent "undercooling"), then would be expected in view of DSC results (H21–BAFKU$_2$ has a distinct peak at −9.8 °C), or of the known solidification point (melt→rubber, observed by DMTA, −15 to −20 °C for H21–BAFKU$_2$). No change in texture appears during the whole cooling scan of H21–BAFKU$_2$, the texture remains isotropic, down to −29 °C. Similarly, like in the case of the other copolymers, this "undercooling" might be the result of the slow formation of extended ordered regions of the lamellar structure observed in XRD, if the sample is present as a very thin layer (PLM). Small randomly oriented lamellar regions do not generate sufficient optical anisotropy to be simply visible by PLM. If, however, the mean polarized light intensity from the whole image area is evaluated (see SI Figure S19b), then, like in the case of H11–BAFKU$_2$, an increase in intensity is observed in the "undercooled isotropic region". It starts during the cooling run just below 30 °C, where in view of the X-ray (further above) and rheology results, which are discussed in a follow-on work [43], small BAFKU

nano-lamellae are expected to start to assemble. In the case of the heating run, (see SI Figure S19a), the light intensity curve follows the trends noted by the "simple" PLM observation.

3.3.4. Structure of the BAFKU Aggregates

In view of the combined characteristics of the copolymers obtained by DSC, XRD, and by polarization microscopy (PLM), as well as by thermomechanical analysis (DMTA), important conclusions can be drawn about the aggregating behavior in BAFKU end-groups. First, the single characteristic reflection (XRD) of BAFKU structures, accompanied by well-visible 2nd and 3rd order peaks, indicates a distinct lamellar structure in all the copolymers. Secondly, the different characteristic distances corresponding to the mentioned reflection in the different copolymers well correlate (see Scheme 5 further above) with the approximate "effective length" of the coiled PDMS chains in each of them, and thus, with the distance between the BAFKU lamellae (rather than with their thickness).

Depending on the temperature, the BAFKU aggregates change their internal arrangement, as indicated by DSC and PLM, but below the isotropization temperature, they always must be lamellar in shape, and the lamellae must be at regular distances (like in the example in Scheme 6 further above), in order to generate the mentioned relatively sharp XRD reflection combined with the higher order peaks. Larger areas with regularly and hence, anisotropically arranged BAFKU aggregates (lamellae) can generate textures visible by PLM, in contrast to small regions of regularity. The latter nevertheless can produce significant background intensity in PLM, which is not easily seen by the naked eye, but which still was possible to evaluate, as mentioned further above (see PLM analysis of H21–BAFKU$_2$).

Thermally induced fragmentation and recombination of BAFKU aggregates is also shown in Scheme 6, as well as the isotropization (maximum fragmentation and loss of ordering in the residual small dynamic aggregates or associates of BAFKU end-groups). Analogous aggregate reorganizations are also expected to occur in the case of strain damage and self-healing.

The postulated thermotropic phase transitions in the BAFKU lamellae are illustrated in Scheme 7. In the rubbery state, the nanoaggregates (lamellae) are in the crystalline state and are rigid. In the BAFKU-rich H03–BAFKU$_2$ copolymer, a smectic structure (as observed by PLM and DSC) is stable in the melt region in a favorable temperature range; the layers in the aggregates can move (see Scheme 7). Additionally, besides the mentioned shear deformation, the smectic aggregates are "dynamic", and can undergo fragmentation and recombination (see Scheme 6). Such effects make possible the flow of the molten smectic copolymer, but the necessary reorganization of the aggregates during the flow consumes a considerable amount of energy, as is illustrated by rheology experiments discussed in a follow-up paper [43], including thixotropy effects (see e.g., the high storage and loss moduli of the melt of H11–BAFKU$_2$ at 25 °C, after abrupt melt cooling, in the Supplementary Materials of [43]). The smectic state is not observed in the copolymers with the longer PDMS chains, H11–BAFKU$_2$ and H21–BAFKU$_2$, where, as demonstrated by DSC, the "nematic aggregate phase" is directly formed from the rigid aggregates during the melting of the rubbery copolymer.

The nematic-ordered aggregates are of "dynamic" nature, similarly like the smectic-ordered ones. In the molten H03–BAFKU$_2$ copolymer, the thermotropic transition Sm→N occurs in the interior of the aggregates at a characteristic temperature, as observed by DSC (41.2 °C). In the "longer copolymers", no difference in texture is observed between the "crystalline" and the "molten nematic" state of the mesogen aggregates, in both the heating and the cooling run, in strong contrast to neat BAFKU or H03–BAFKU$_2$ (Cr→Sm: no change, but Sm→N: vast change). This implies that the "crystalline state" in the longer copolymers could in fact be a less ordered "frozen nematic" state. The somewhat different PLM textures observed during the heating and cooling runs of these longer copolymers could be the result of prolonged "aging" at room temperature in the nematic molten state, which always occurred (sample storage) prior to the initial heating run. The reversible reorganizations of the aggregates discussed above would namely allow for the growth of larger domains with anisotropic ordering

during long storage, in contrast to the cooling PLM run (starting from isotropic melt, running at 1 °C/min), during which the samples dwelt only for a relatively short time in the nematic molten state.

As mentioned in the section dedicated to the synthesis of the copolymers, the azo units incorporated in the BAFKU building blocks of the copolymers offer the potential of reversibly photo-switching the mesogenic units between the *cis*- and *trans*- state. In this way, the stability, the transition temperatures, as well as the tendency of the lamellae discussed above to grow or to split would be greatly altered, resulting in switching of elastic/viscoelastic properties.

4. Conclusions

Physically crosslinked thermo-reversible low-temperature rubbers with interesting viscoelastic properties in the melt state (very large step-wise changes of elasticity and viscosity) were successfully prepared; they are based on linear polydimethyl-siloxane (PDMS) capped in α,ω-positions with liquid crystalline (LC) building blocks called "BAFKU". The LC building blocks make reversible UV light-induced switching of material properties possible.

Copolymers based on three different commercial α,ω-Si–H-functional PDMS molecules, namely DMS H03 (8.6-mer), DMS H11 (16.3-mer), and DMS H21 (64.4-mer), were obtained via hydrosilylation reactions of these PDMS precursors with the mono-vinyl-functional mesogen BAFKU.

Thermomechanical analysis (DMTA) proved that the PDMS–BAFKU$_2$ copolymers, based on namely the H11–BAFKU$_2$ and H21–BAFKU$_2$, behave like typical reversible elastomer networks. The physical crosslinking via nano-aggregation of BAFKU units was found to be reversible by heat, as well as by organic solvents.

On the other hand, the copolymer based on the short polydimethylsiloxane DMS H03 is a brittle (vitrimeric) material, with no transition glass→rubber. Upon heating (DMTA), it transforms directly from glass to melt. This is due to the high-volume fraction (52 vol%) of rigid BAFKU.

DSC study of the phase behavior indicates similar sharp transitions in neat BAFKU and in LC-rich H03–BAFKU$_2$ (three transitions at similar T values); H11–BAFKU$_2$ shows different, less intense, simpler, but still multiple (two) and sharp, low-T-shifted transitions; H21–BAFKU$_2$ displays no well-visible LC transitions upon heating, but one LC transition during the cooling scan; other methods (XRD, PLM) indicate, however, that H21–BAFKU$_2$ displays two LC transitions, similarly like H11–BAFKU$_2$; the increasing chain length of PDMS leads to higher mobility of BAFKU, thus down-shifting its LC transitions in the copolymers and reducing the number of stable LC phases to one, namely the nematicum.

XRD analyses indicate a distinct lamellar structure in all three PDMS–BAFKU copolymers; the lamellar structure (as branched macromolecule associates) was found to persist also in the molten state, until the isotropization transition temperature observed by DSC.

PLM investigations support the existence of smectic and nematic phases in the molten state of H03–BAFKU$_2$, and of nematic phases in the melt of H11–BAFKU$_2$ and H21–BAFKU$_2$, as well as the transition temperatures observed by DSC and XRD; in the case of the copolymers with longer PDMS chains (H11, H21), the solid nanoaggregates of BAFKU end-groups seem to be of the frozen nematic type, rather than of a distinct crystalline one.

The studied low-temperature elastomers might be of interest as passive smart materials for advanced applications such as viscoelastic coupling (melting/gelation to rubber), but also as damping materials (energy absorption via physical crosslink disconnection).

A follow-up paper is dedicated to the effects of the structure of the studied copolymers on their viscoelastic and rheological properties in the rubbery state, as well as in melt.

H21–BAFKU2. SI Figure S9: GPC traces of the prepared copolymers, overlaid. SI Figure S10: GPC trace of pure BAFKU. SI Figure S11: GPC trace of pure precursors H03, H11, H21. SI Figure S12: GPC trace of the copolymer H03–BAFKU2, H11–BAFKU2, H21–BAFKU. SI Figure S13: MALDI-TOF spectra: H03 and H03–BAFKU2. SI Figure S14: MALDI-TOF spectra: H11 and H11–BAFKU2. SI Figure S15: MALDI-TOF spectra: H21 and H21–BAFKU2. SI Figure S16: neat BAFKU: Temperature-dependent PLM intensity. SI Figure S17: H03–BAFKU2: Temperature-depend ent PLM intensity. SI Figure S18: H11: Temperature-dependent PLM intensity. SI Figure S19: H21–BAFKU2: Temperature-dependent PLM intensity. SI Figure S20: High-resolution textures of neat BAFKU: top: at 21 °C, bottom: at 61 °C, both in heating run. SI Figure S21: High-resolution textures of neat BAFKU: top: at 62 °C (heating run), bottom: at 39 °C (cooling run). SI Figure S22: High-resolution textures of H03–BAFKU2: top: at 10 °C, bottom: at 20 °C, both in heating run. SI Figure S23: High-resolution textures of H03–BAFKU2: top: at 46 °C, bottom: at 51 °C, both in heating run. SI Figure S24: High-resolution textures of H03–BAFKU2: top: at 45 °C, bottom: at 20 °C, both in cooling run. SI Figure S25: High-res H11–BAFKU2: top: at 10 °C, bottom: at 21 °C, both in heating run. SI Figure S26: High-resolution textures of H11–BAFKU2: top: high detail at 29 °C, bottom: at 22 °C, both cooling run. SI Figure S27: High-resolution textures of H11–BAFKU2: very high detail at 29 °C. SI Figure S28: High-resolution textures of H21–BAFKU2: top: at 10 °C, bottom: at 21 °C, both in heating run. SI Figure S29: High-resolution textures of H21–BAFKU2: top: at 10 °C, bottom: at 21 °C, both in heating run. SI Figure S30: High-resolution textures of H21–BAFKU2: texture at −29 °C, end of cooling run. SI Table S1: Molecular parameters of the DMS precursor polymers determined by 1H-NMR. SI Table S2. Characterization of molecular mass.

References

1. Dubois, J.C.; LeBarny, P.; Mauzac, M.; Noel, C.; Demus, D.; Goodby, J.W.; Gray, G.W.; Spiess, H.W.; Vill, V. *Handbook of Liquid Crystals*; Wiley-VCH: Weinheim, Germany, 1998; Print ISBN 9783527292707; Online ISBN 9783527620760. [CrossRef]

2. Hsu, C.S. The application of side-chain liquid-crystalline polymers. *Prog. Polym. Sci.* **1997**, *22*, 829–871. [CrossRef]

3. Finkelmann, H.; Rehage, G. Investigations on liquid crystalline polysiloxanes, 1. Synthesis and characterization of linear polymers. *Macromol. Rapid Commun.* **1980**, *1*, 31–34. [CrossRef]

4. Finkelmann, H.; Rehage, G. Investigations on liquid crystalline polysiloxanes, 2. Optical properties of cholesteric phases and influence of the flexible spacer on the mobility of the mesogenic groups. *Macromol. Rapid Commun.* **1980**, *1*, 733–740. [CrossRef]

5. Finkelmann, H.; Kock, H.J.; Rehage, G. Investigations on liquid crystalline polysiloxanes 3. Liquid crystalline elastomers—A new type of liquid crystalline material. *Macromol. Rapid Commun.* **1981**, *2*, 317–322. [CrossRef]

6. Finkelmann, H.; Rehage, G. Investigations on liquid crystalline polysiloxanes, 4. Cholesteric homopolymers—synthesis and optical characterization. *Macromol. Rapid Commun.* **1982**, *3*, 859–864. [CrossRef]

7. Finkelmann, H.; Kock, H.J.; Gleim, W.; Rehage, G. Investigations on liquid crystalline polysiloxanes 5. Orientation of LC-elastomers by mechanical forces. *Macromol. Rapid Commun.* **1984**, *5*, 287–293. [CrossRef]

8. Küpfer, J.; Finkelmann, H. Nematic liquid single crystal elastomers. *Macromol. Rapid Commun.* **1991**, *12*, 717–726. [CrossRef]

9. Wang, M.; Guo, L.X.; Lin, B.P.; Zhang, X.Q.; Sun, Y.; Yang, H. Photo-responsive polysiloxane-based azobenzene liquid crystalline polymers prepared by thiol-ene click chemistry. *Liq. Cryst.* **2016**, *43*, 1626–1635. [CrossRef]

10. Wang, G.F.; Xiong, Y.; Tang, H.D. Synthesis and characterization of a graft side-chain liquid crystalline polysiloxane. *J. Organomet. Chem.* **2015**, *77*, 50–54. [CrossRef]

11. Zhao, W.; Lin, B.P.; Zhang, X.Q.; Sun, Y.; Yang, H. Polysiloxane Side-chain Liquid Crystalline Polymers Prerpared by Alkyne Hydrosilylation. *Chin. J. Polym. Sci.* **2015**, *33*, 1431–1441. [CrossRef]

12. Aguilera, C.; Bartulin, J.; Hisgen, B.; Ringsdorf, H. Liquid crystalline main chain polymers with highly flexible siloxane spacers. *Macromol. Chem. Phys.* **1983**, *184*, 253–262. [CrossRef]

13. Braun, F.; Willner, L.; Hess, M.; Kosfeld, R. Synthesis and thermal properties of liquid-crystalline polyesters with mesogenic units and siloxane spacers in the main chain. *Die Makromol. Chem.* **1990**, *191*, 1775–1785. [CrossRef]

14. Donnio, B.; Wermter, H.; Finkelmann, H.A. Simple and Versatile Synthetic Route for the Preparation of Main-Chain, Liquid-Crystalline Elastomers. *Macromolecules* **2000**, *33*, 7724–7729. [CrossRef]

15. Patil, H.P.; Liao, J.; Hedden, R.C. Smectic Ordering in Main-Chain Siloxane Polymers and Elastomers Containing p-Phenylene Terephthalate Mesogens. *Macromolecules* **2007**, *40*, 6206–6216. [CrossRef]

16. Burke, K.A.; Rousseau, I.A.; Mather, P.T. Reversible actuation in main-chain liquid crystalline elastomers with varying crosslink densities. *Polymer* **2014**, *55*, 5897–5907. [CrossRef]

17. Samui, A.B.; Pandey, S.; Mishra, S.P. Main chain photoresponsive liquid crystalline polymer synthesized through hydrosilylation. *RSC Adv.* **2015**, *5*, 68351–68355. [CrossRef]

18. Saed, M.O.; Volpe, R.H.; Traugutt, N.A.; Visvanathan, R.; Clark, N.A.; Yakacki, C.M. High strain actuation liquid crystal elastomers via modulation of mesophase structure. *Soft Matter* **2017**, *13*, 7537–7547. [CrossRef] [PubMed]

19. Pandey, S.; Kolli, B.; Mishra, S.P.; Samui, A.B. Siloxane polymers containing azo moieties synthesized by click chemistry for photo responsive and liquid crystalline applications. *J. Polym. Sci. Part A Polym. Chem.* **2012**, *50*, 1205–1215. [CrossRef]

20. Shenouda, I.G.; Chien, L.C. New ferroelectric liquid-crystalline polysiloxanes containing cyanohydrin chiral mesogens: L-norleucine series. *Macromolecules* **1993**, *26*, 5020–5023. [CrossRef]

21. Zhou, Q.L.; Zhang, J.T.; Ren, Z.J.; Yan, S.K.; Xie, P.; Zhang, R.B. A Stable and High-Efficiency Blue-Light Emitting Terphenyl-Bridged Ladder Polysiloxane. *Macromol. Rapid Commun.* **2008**, *29*, 1259–1263. [CrossRef]

22. Kawakami, H.; Mori, Y.; Abe, H.; Nagaoka, S. Gas transport properties of liquid crystalline polysiloxane with laterally attached side chain. *J. Membr. Sci.* **1997**, *133*, 245–253. [CrossRef]

23. Rao, H.X.; Zhang, Z.Y. Preparation, Characterization, and Permeation Property of a Liquid Crystal/PDMS Membrane Material. *J. Appl. Polym. Sci.* **2012**, *123*, 191–199. [CrossRef]

24. Ganicz, T.; Stanczyk, W.A.; Chmielecka, J.; Kowalski, J. Liquid crystalline polycarbosilanes and poly(di-n-butylsiloxane) as stationary phases in gas chromatography. *Polym. Int.* **2009**, *58*, 248–254. [CrossRef]

25. Warner, M.; Terentjev, E. *Liquid Crystal Elastomers*; Oxford University Press: Oxford, UK, 2003; ISBN 9780198527671.

26. Ikeda, T.; Mamiya, J.; Yu, Y. Photomechanics of Liquid-Crystalline Elastomers and Other Polymers. *Angew. Chem. Int. Ed.* **2007**, *46*, 506–528. [CrossRef]

27. Ohm, C.; Brehmer, M.; Zentel, R. Liquid Crystalline Elastomers as Actuators and Sensors. *Adv. Mater.* **2010**, *22*, 3366–3387. [CrossRef]

28. Strachota, A.; Kroutilová, I.; Kovářová, J.; Matějka, L. Epoxy Networks Reinforced with Polyhedral Oligomeric Silsesquioxanes (POSS). Thermomechanical Properties. *Macromolecules* **2004**, *37*, 9457–9464. [CrossRef]

29. Strachota, A.; Whelan, P.; Kříž, J.; Brus, J.; Urbanová, M.; Šlouf, M.; Matějka, L. Formation of nanostructured epoxy networks containing polyhedral oligomeric silsesquioxane (POSS) blocks. *Polymer* **2007**, *48*, 3041–3058. [CrossRef]

30. Strachota, A.; Rodzeń, K.; Ribot, F.; Trchová, M.; Steinhart, M.; Starovoytova, L.; Pavlova, E. Behavior of Tin-Based "Super-POSS" Incorporated in Different Bonding Situations in Hybrid Epoxy Resins. *Macromolecules* **2014**, *47*, 4266–4287. [CrossRef]

31. Rodzeń, K.; Strachota, A.; Ribot, F.; Matějka, L.; Kovářová, J.; Trchová, M.; Šlouf, M. Reactivity of the tin homolog of POSS, butylstannoxane dodecamer, in oxygen-induced crosslinking reactions with an organic polymer matrix: Study of long-time behaviour. *Polym. Degrad. Stab.* **2015**, *118*, 147–166. [CrossRef]

32. Mossety-Leszczak, B.; Strachota, B.; Strachota, A.; Steinhart, M.; Šlouf, M. The orientation-enhancing effect of diphenyl aluminium phosphate nanorods in a liquid-crystalline epoxy matrix ordered by magnetic field. *Eur. Polym. J.* **2015**, *72*, 238–255. [CrossRef]

33. Horodecka, S.; Strachota, A.; Mossety-Leszczak, B.; Šlouf, M.; Zhigunov, A.; Vyroubalová, M.; Kaňková, D.; Netopilík, M. Meltable copolymeric elastomers based on polydimethylsiloxane with multiplets of pendant liquid-crystalline groups as physical crosslinker: A self-healing structural material with a potential for smart applications. *Eur. Polym. J.* **2020**, *137*. [CrossRef]

34. Colombani, O.; Barioz, C.; Bouteiller, L.; Chaneac, C.; Fomperie, L.; Lortie, F.; Montes, H. Attempt toward 1D Cross-Linked Thermoplastic Elastomers: Structure and Mechanical Properties of a New System. *Macromolecules* **2005**, *38*, 1752–1759. [CrossRef]

35. Botterhuis, N.E.; van Beek, D.J.M.; van Gemert, G.M.L.; Bosman, A.W.; Sijbesma, R.P. Self-Assembly and Morphology of Polydimethylsiloxane Supramolecular Thermoplastic Elastomers. *J. Polym. Sci. Part A Polym. Chem.* **2008**, *46*, 3877–3885. [CrossRef]

36. Ślęczkowski, M.L.; Meijer, E.W.; Palmans, A.R.A. Cooperative Folding of Linear Poly(dimethyl siloxane)s via Supramolecular Interactions. *Macromol. Rapid Commun.* **2017**, *38*, 1–5. [CrossRef] [PubMed]

37. Rambarran, T.; Bertrand, A.; Gonzaga, F.; Boisson, F.; Bernard, J.; Fleury, E.; Ganachaud, F.; Brook, M.A. Sweet supramolecular elastomers from a,x-(b-cyclodextrin terminated) PDMS. *Chem. Commun.* **2016**, *52*, 6681–6684. [CrossRef] [PubMed]

38. Fawcett, A.S.; Brook, M.A. Thermoplastic Silicone Elastomers through Self-Association of Pendant Coumarin Groups. *Macromolecules* **2014**, *47*, 1656–1663. [CrossRef]

39. Lamers, B.A.G.; Graf, R.; de Waal, B.F.M.; Vantomme, G.; Palmans, A.R.A.; Meijer, E.W. Polymorphism in the Assembly of Phase-Segregated Block Molecules: Pathway Control to 1D and 2D Nanostructures. *J. Am. Chem. Soc.* **2019**, *141*, 15456–15463. [CrossRef]

40. Lamers, B.A.G.; Ślęczkowski, M.L.; Wouters, F.; Engels, T.A.P.; Meijer, E.W.; Palmans, A.R.A. Tuning polymer properties of non-covalent crosslinked PDMS by varying supramolecular interaction strength. *Polym. Chem.* **2020**, *11*, 2847–2854. [CrossRef]

41. Dodge, L.; Chen, Y.; Brook, M.A. Silicone Boronates Reversibly Crosslink Using Lewis Acid–Lewis Base Amine Complexes. *Chem. A Eur. J.* **2014**, *20*, 9349–9356. [CrossRef]

42. Li, C.H.; Wang, C.; Keplinger, C.; Zuo, J.L.; Jin, L.; Sun, Y.; Zheng, P.; Cao, Y.; Lissel, F.; Linder, C.; et al. A highly stretchable autonomous self-healing elastomer. *Nat. Chem.* **2016**, *8*, 618–624. [CrossRef]

43. Horodecka, S.; Strachota, A.; Mossety-Leszczak, B.; Strachota, B.; Šlouf, M. Low-temperature-meltable elastomers based on linear polydimethylsiloxane chains alpha,omega-terminated with mesogenic groups as physical crosslinker: A passive smart material with potential as viscoelastic coupling. Part II: Viscoelastic and rheological properties. *Polymers* **2020**. Submitted.

44. Miniewicz, A.; Girones, J.; Karpinski, P.; Mossety-Leszczak, B.; Galina, H.; Dutkiewicz, M. Photochromic and nonlinear optical properties of azo-functionalized POSS nanoparticles dispersed in nematic liquid crystals. *J. Mater. Chem. C* **2014**, *2*, 432–440. [CrossRef]

45. Kieffer, J.; Karkoulis, D. PyFAI, a versatile library for azimuthal regrouping. *J. Phys. Conf. Ser.* **2013**, *425*, 1–6. [CrossRef]

46. Slouf, M.; Krejcikova, S.; Vackova, T.; Kratochvil, J.; Novak, L. In situ observation of nucleated polymer crystallization in polyoxymethylene sandwich composites. *Front. Mater.* **2015**, *2*, 1–12. [CrossRef]

47. Vackova, T.; Kratochvil, J.; Ostafinska, A.; Krejcikova, S.; Nevoralova, M.; Slouf, M. Impact of particle morphology on structure, crystallization kinetics, and properties of PCL composites with TiO2-based particles. *Polym. Bull.* **2017**, *74*, 445–464. [CrossRef]

48. Klonos, P.A. Crystallization, glass transition, and molecular dynamics in PDMS of low molecular weights: A calorimetric and dielectric study. *Polymer* **2018**, *159*, 169–180. [CrossRef]

Publisher's Note: MDPI stays neutral with regard to jurisdictional claims in published maps and institutional affiliations.

SUPPLEMENTARY INFORMATION

Low-temperature-meltable elastomers based on linear polydimethylsiloxane chains alpha,omega-terminated with mesogenic groups as physical crosslinker: A passive smart material with potential as viscoelastic coupling. Part I: Synthesis and phase behaviour

Sabina Horodecka[1,2], Adam Strachota[1]*, Beata Mossety-Leszczak[3], Beata Strachota, Miroslav Šlouf[1], Alexander Zhigunov[1], Michaela Vyroubalová[1], Dana Kaňková[1], Miloš Netopilík[1], Zuzana Walterová[1]

[1]) *Institute of Macromolecular Chemistry, Czech Academy of Sciences, Heyrovskeho nam. 2, CZ-162 06 Praha, Czech Republic*

[2]) *Faculty of Science, Charles University, Albertov 6, CZ-128 00 Praha 2, Czech Republic*

[3]) *Faculty of Chemistry, Rzeszow University of Technology, al. Powstancow Warszawy 6, PL-35-959 Rzeszow, Poland*
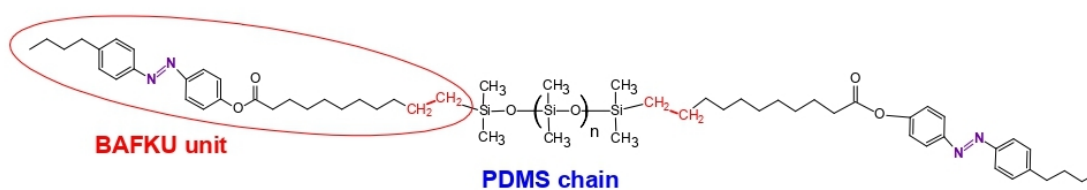
1. Synthesis and chemical microstructure

1.1. Evaluation of conversion of the PDMS during hydrosilylation reaction by means of FTIR
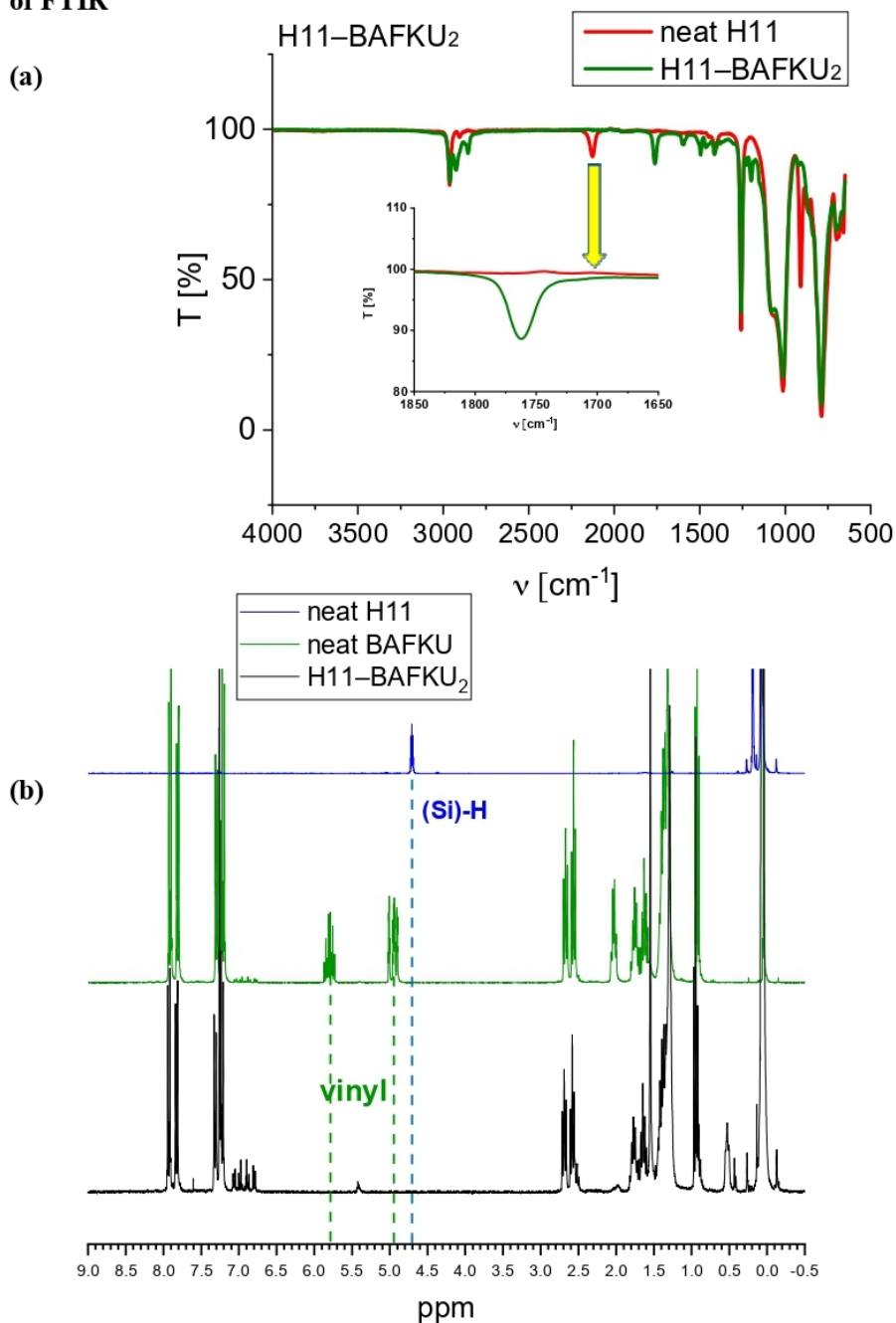
SI-Fig. 1: *Spectroscopic evaluation of the completion of the hydrosilylation reaction: (a): FTIR spectra of pure H11 and of H11–BAFKU$_2$ highlighting the disappearance of the Si-H as zoomed inlay; (b): ^{1}H-NMR of pure H11, BAFKU and H11–BAFKU$_2$ - details in **SI-Fig. 7**.*
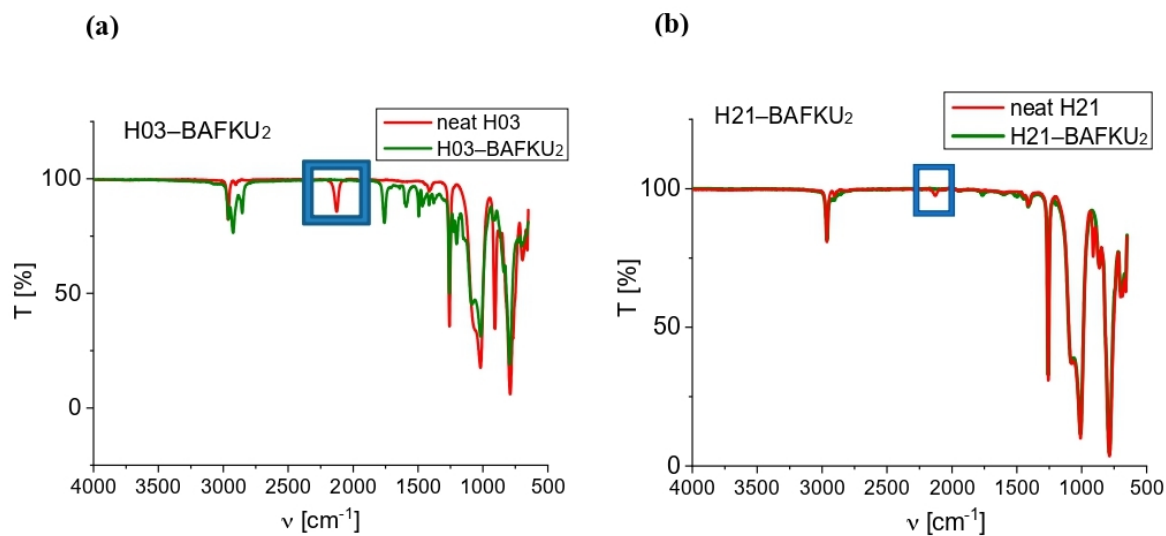
SI-Fig. 2: *FT-IR spectra of (a): pure H03 and of H03–BAFKU$_2$; (b): pure H21 and of H21-BAFKU$_2$; the characteristic peak of the Si-H bond stretching is highlighted.*
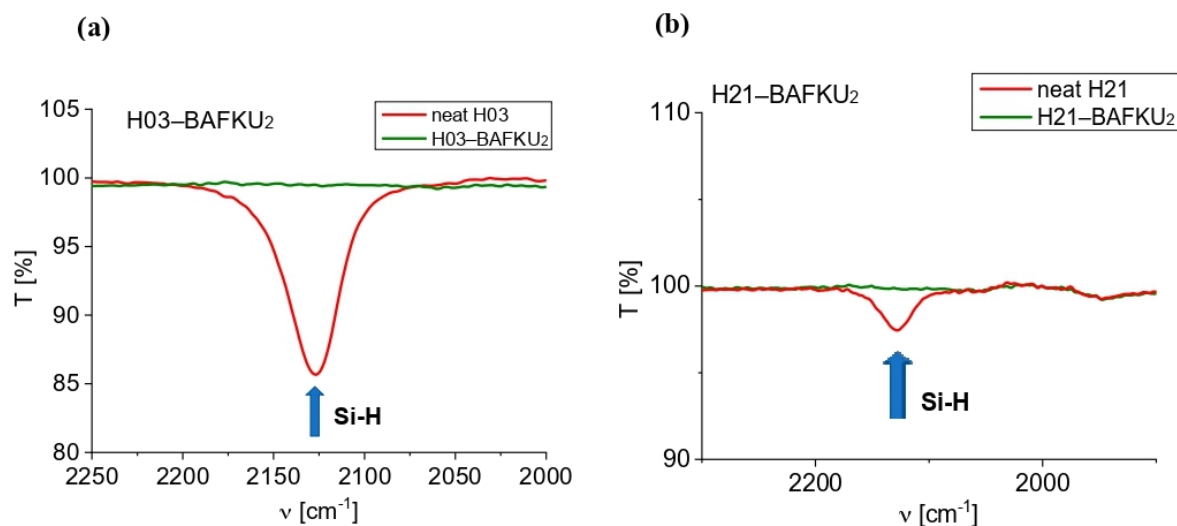
SI-Fig. 3: *Detail of the characteristic FT-IR peak of the Si-H bond stretching: (a): H03-BAFKU$_2$ vs. H03; (b): H21–BAFKU$_2$ vs. H21.*

1.2. ¹H-NMR: Purity of components and products, as well as synthesis conversion
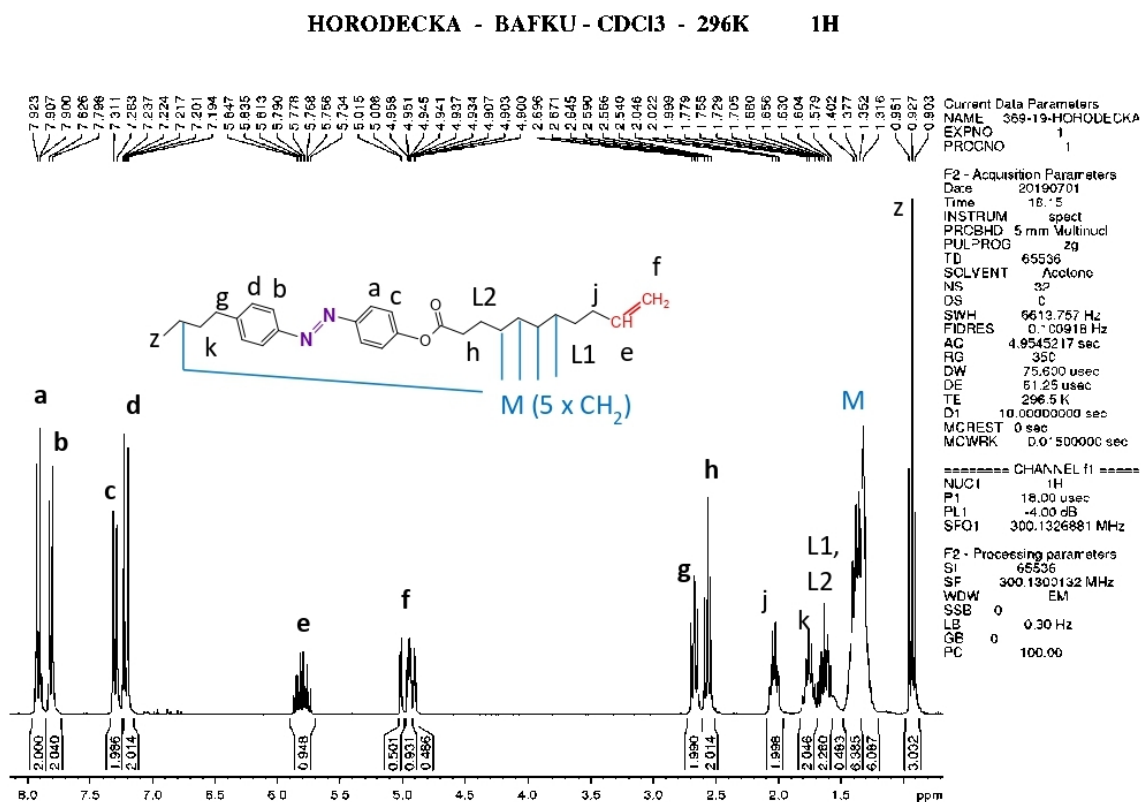
SI-Fig. 4: ¹H-NMR spectrum of the pure BAFKU mesogen with assigned peaks.

¹H-NMR: analysis of the PDMS components
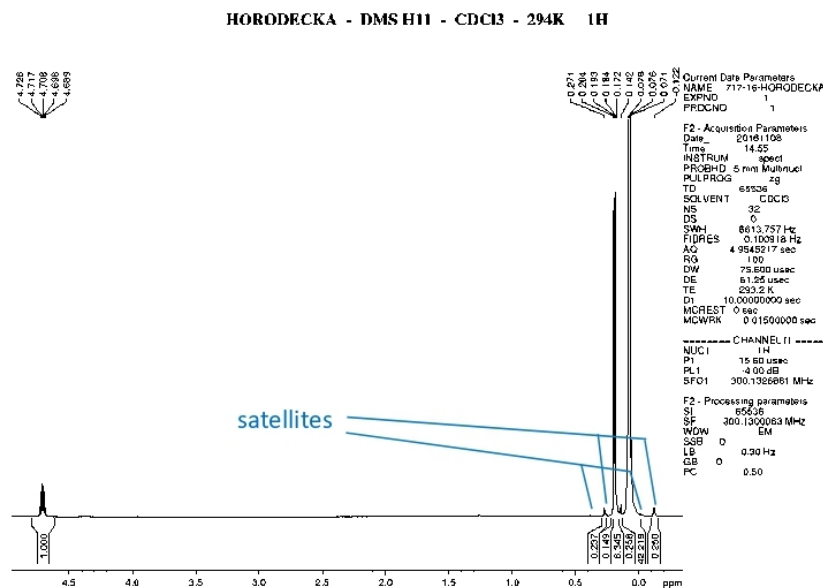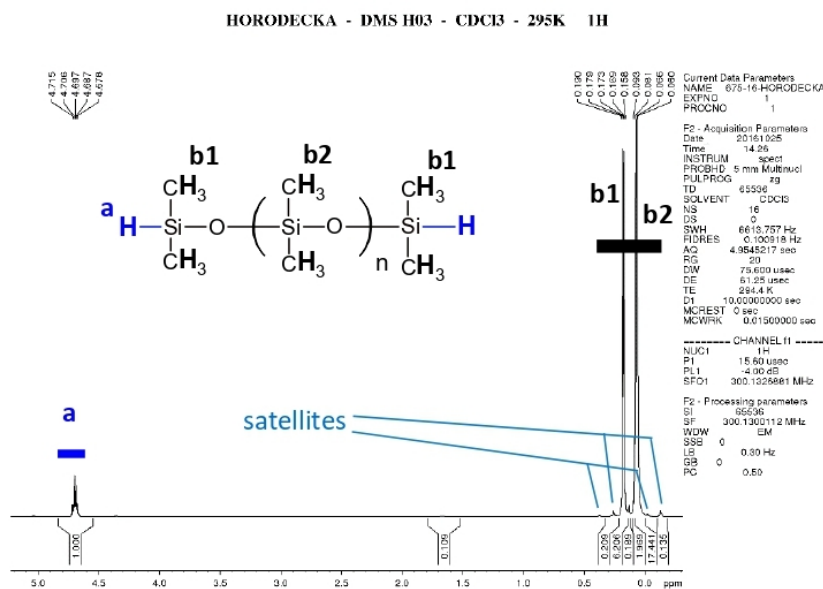
SI-Fig. 5: *¹H-NMR spectra of the PDMS precursors: (top): H03; (bottom): H11; the peak of the methyl groups is near 0.1 ppm, the Si-H peak near 4.70 ppm.*
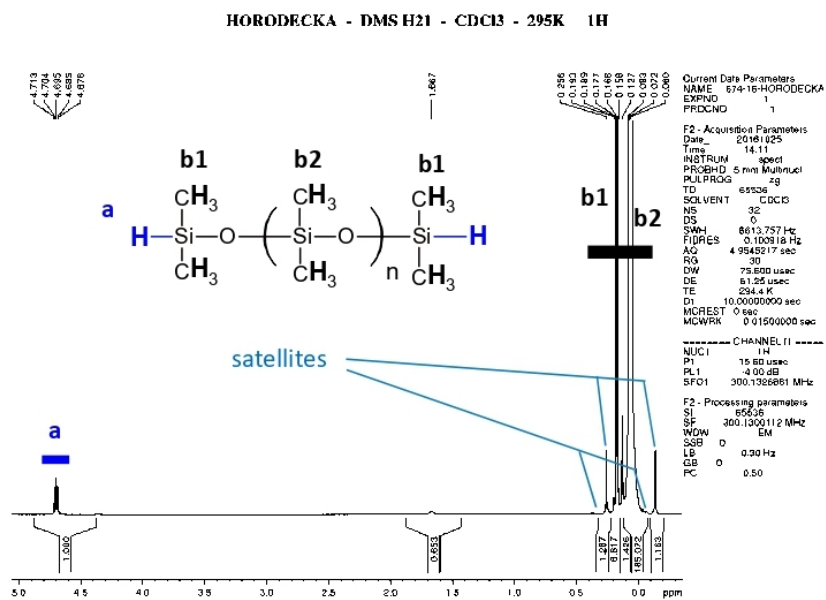
SI-Fig. 6: ^{1}H-NMR spectrum of the PDMS precursor H21; the peak of the methyl groups is near 0.1 ppm, the Si-H peak near 4.70 ppm.

1.2.1.   Structure parameters of "DMS" (PDMS) polymers from ^{1}H-NMR analysis
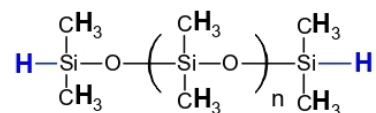
Aim:

calculation of   **n (number of internal repeat units)**, coefficient from above structure formula, of the molecular mass of the whole molecule, as well as of the equivalent molecular mass per SiH function (**EqMW**); the latter is needed to calculate accurate reactant amounts for syntheses.

Ratios of signal integrals from the 1H-NMR spectra (**SI-Fig. 5 and 6**) in relation to the above structure formula:

H in **SiH** end groups	**H** in **CH$_3$** groups in all siloxane repeat units
2	(2*3)*n
if the SiH integral is normalized to 1.0, the following integral ratios are obtained:	
1	3*n

Magnitudes for calculation:

n: coefficient from above structure formula (number of internal repeat units)

m = n + 2 : number of all siloxane repeat units

RU = molecular mass of an internal repeat unit (of the block [(CH$_3$)$_2$SiO])
  = 74.154 g/mol

E = molecular mass of both end groups taken together, hence of (CH$_3$)$_2$(H)Si-O-Si(H)(CH$_3$)$_2$
  = 134.325 g/mol

M = molecular mass of the whole "DMS" molecule (as shown in the above structure formula)

*Obtaining **n** from the ^{1}H-NMR spectra in **SI-Fig. 5 and 6**:*

-at first, the integrals in the spectra are normalized so, that the value of the integral of the SiH peak is equal to 1.00 (as done in **SI-Fig. 5 and 6**); it is then assigned 1 = '*SiH_norm*'; each molecule contains two hydrogens from SiH groups;

-next, the sum of all integrals of the peaks of $(CH_3)_2Si<$ groups, '*CH3*' is calculated; each siloxane repeat unit in the DMS molecule contains 6 hydrogens from two methyl groups; as result of the above normalization of the SiH signal, an integral value of 3 corresponds to one siloxane repeat unit; the normalized value '*CH3_norm*' is calculated by dividing '*CH3*' by three;

-finally, the coefficients **m** (number of all Si-containing units) and **n** (number of internal siloxane units) are calculated, using '*CH3_norm*' and '*SiH_norm*':

m = *CH3_norm* / *SiH_norm* =   *CH3_norm* / 1 =   *CH3_norm* =   '*CH3*' / 3

hence   **m = '*CH3*' / 3**

and   **n = m − 2**

M = E + n*RU   (with molecular masses of the constants E, RU taken from above)

EqMW = M/2

**Results**:

**SI-Table 1:** Molecular parameters of the PDMS precursor polymers as determined by ^{1}H-NMR, compared with the data given by the manufacturer (last two columns, italics).

name of siloxane precursor	'*CH₃*' from NMR	*m* (number of all repeat units) from NMR	*n* (number of internal repeat units) from NMR	M_n (= 'M') from NMR [g/mol]	EqMW = M_n/2 [g/mol]	M_n (supplier) [g/mol]	*m* (supplier, calculated)
H03	25.805	8.602	6.602	623.865	311.9325	_450±50_	_6.257_
H11	48.971	16.324	14.324	1196.482	598.241	_1 050±50_	_14.348_
H21	193.315	64.438	62.438	4764.377	2382.189	_4 500±500_	_60.873_

1.2.2. Copolymers PDMS–BAFKU$_2$: ^{1}H-NMR analysis

The ^{1}H-NMR spectra of the copolymers are shown in *SI-Fig. 7–8*. In *SI-Fig. 7*, the assignment of the peaks is shown on the example of H03–BAFKU$_2$. It can be seen that the characteristic peaks of the BAFKU units are preserved, except for the vinyl groups (atoms "e", "f"), which disappeared completely (the signals of "e", "f" are newly found among the alkyl groups). From the PDMS precursors, the SiH peaks also quantitatively disappeared, while the signals of the methyl groups persist. The disappearance of the vinyl- and SiH-signals was mentioned above as a proof of quantitative conversion of accurately stoichiometric amounts of the copolymer components. The integral of the peak of the methyl groups of PDMS (near 0.06 ppm) is 'reinforced' by the intensity of former terminal methylene units of the vinyl groups of BAFKU.

If an isolated signal of BAFKU is taken as 'end group signal', e.g. the one of the aromatic H atoms "a" at 7.93 ppm, then it can be compared with the intensity of the methyl signals of the PDMS repeat units. If the signal "a" is calibrated to 2.00, then the integrals of the PDMS methyl groups should be approximately the same like in case of the PDMS precursors (there are 4 hydrogens "a" per copolymer molecule, while there were only 2 SiH hydrogens, hence the value of the calibration). In order to obtain the intensity of the 'original' methyl groups of the PDMS precursor, the value of the integral of the methyl groups of PDMS has to be corrected by subtracting 2.00: under the given calibration, this corresponds to 4 H atoms of the terminal CH$_2$ units from BAFKU which now are bonded to Si atoms ("f" in *SI-Fig. 7 top*). The corrected integral then should be identical with 'CH3' from *SI-Table 1*, while the number of repeat units m = 'CH3'/3 should be identical. The results can be seen below:

copolymer name	*'CH$_3$'* from NMR	*corrected 'CH$_3$'*	*m* (number of all repeat units) **according to NMR**	expected *m* according to precursor	*deviation* (expressed as excess of PDMS) [%]
H03–BAFKU$_2$	27.443	25.443	8.481	8.602	-1.4
H11–BAFKU$_2$	57.342	55.342	18.447	16.324	+13.0
H21–BAFKU$_2$	243.869	241.869	81.290	64.438	+26.1

It can be observed, that the end-group analysis (numbers of the repeat units of PDMS, **m**) yields nearly identical results in case of the shortest PDMS chain (H03), while in case of the longer chains, an increasing excess of PDMS seemingly is observed. This result rather can be attributed to the very different relaxation dynamics of the highly mobile PDMS chains and of the rigid BAFKU units, which gain influence with increasing chain length. The seeming excess of PDMS (up to 26%) namely is not accompanied by the appearance of a residual SiH peak, which should be expected in such a case. In view of the missing signals of the functional groups of the reactants, and of the probable highly different relaxation behaviour of the molecular segments, the most accurate ^{1}H-NMR-derived molecular masses of the copolymers appear to be sums of NMR-determined M_n of PDMS precursors (from *SI-Table 1*) plus two masses of the BAFKU units. This calculation was used in the respective column in *SI-Table 2* as M_n from ^{1}H-NMR.
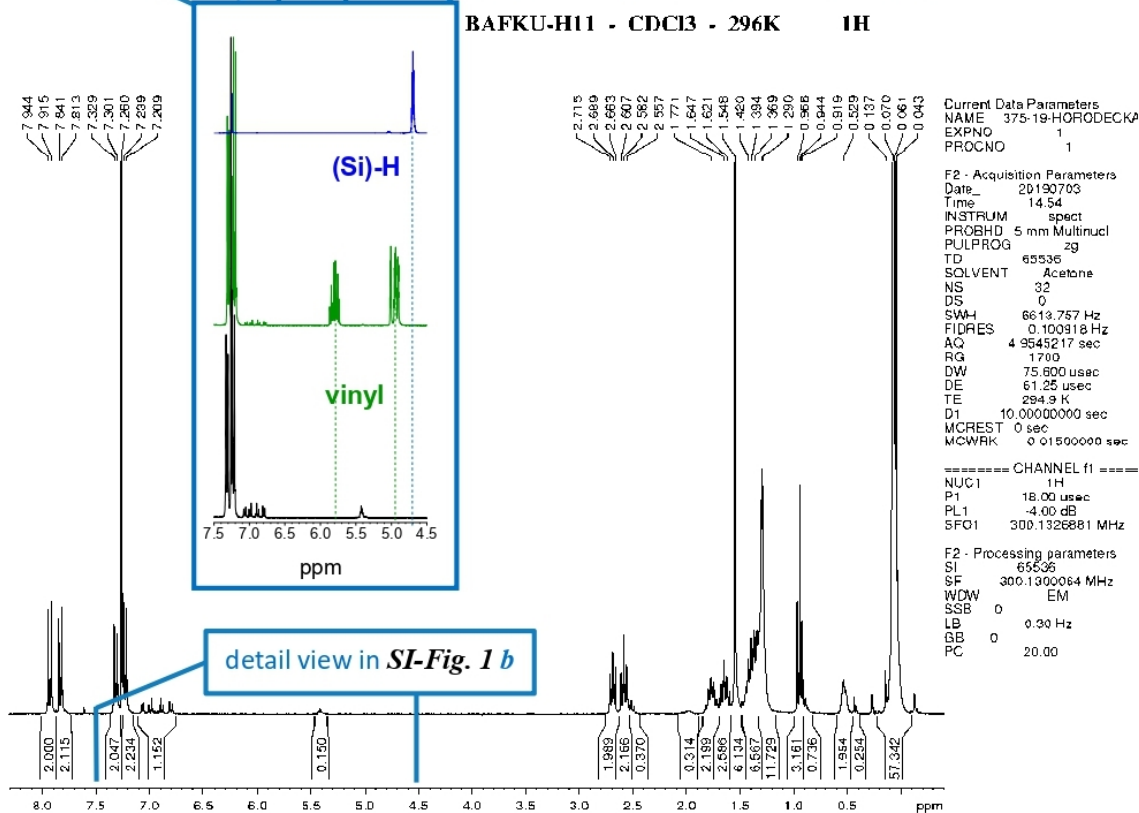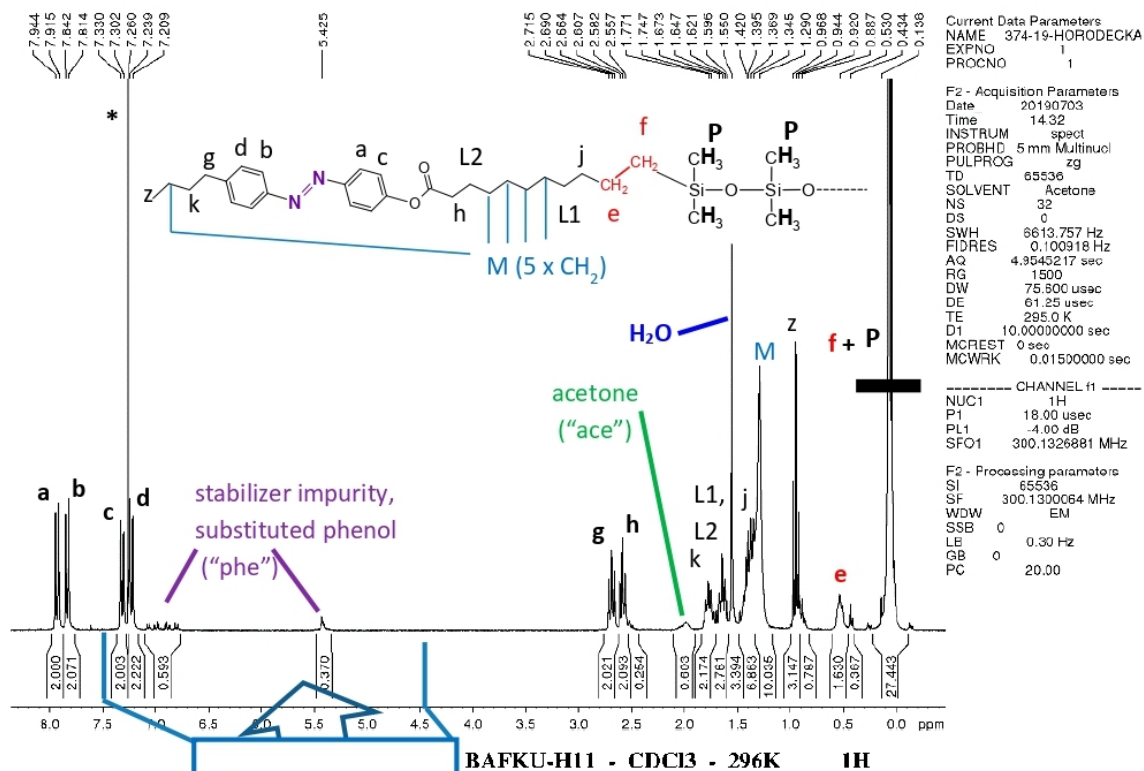
SI-Fig. 7: ^{1}H-NMR spectra of the copolymers (top): H03–BAFKU$_2$; (bottom): H11–BAFKU$_2$.
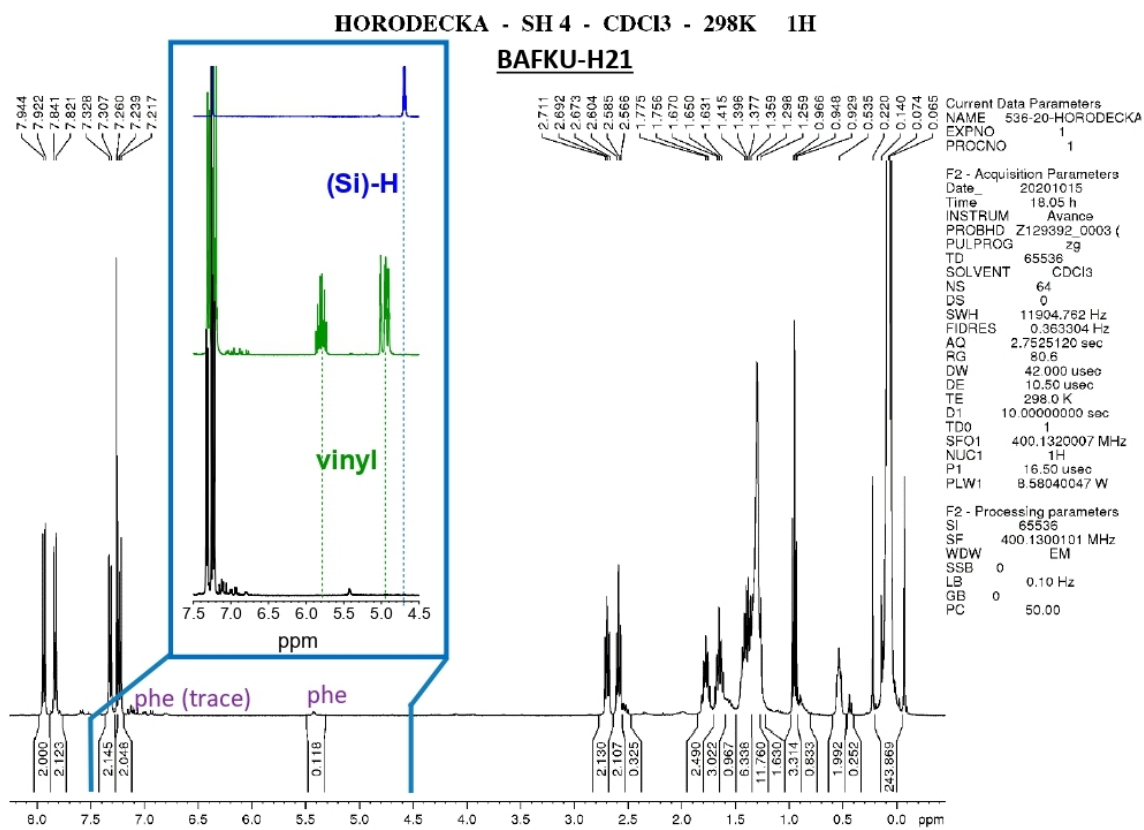
SI-Fig. 8: *¹H-NMR spectrum of the copolymer H21–BAFKU₂.*

1.3.   Molecular mass analysis of the copolymers, as well as of the precursors

The molecular masses of the prepared copolymers were verified using several methods, namely SEC (GPC), MALDI-TOF and ^{1}H-NMR (equipment and setup: see Experimental Part of the main Manuscript). If the results (*SI-Table 2*) obtained by NMR, GPC and MALDI-TOF are compared, some differences can be clearly seen:

The ^{1}H-NMR spectroscopy (see spectra of copolymers: *SI-Fig. 7* and *8*, reactants: *SI-Fig. 4–6*) proved itself as the most accurate, albeit indirect method for numeric average molecular mass determination, as will be explained below: The characteristic groups of 'hydrido-PDMS' precursor polymers generate well-separated and sufficiently distinct signals in all the studied cases, namely the signals of SiH end-groups near 4.70 ppm and the signals of the PDMS methyl groups at 0.18–0.06 ppm, which make possible a fairly exact determination of the ratio of the two terminal repeat units to the remaining ones (see assignment of peaks in *SI-Fig. 5*). In this way, the average length of the PDMS precursor is determined (see *SI-Table 1*). In this way, the exact molecular masses of the precursors were determined prior to the syntheses, as described above, in order to use precisely stoichiometric reactant ratios. In case of the copolymers, the nearly quantitative conversion of the constituent components BAFKU and PDMS prepolymers was subsequently confirmed by the disappearance of the vinyl and SiH signals, which otherwise persist in case of non-stoichiometric or un-reacted mixtures. If the end-group analysis was carried out after the hydrosilylation coupling – which was carried out at precise stoichiometry and with no residues of reactive groups were observed after the synthesis – then the end group analysis (aromatic protons of mesogen vs. protons of PDMS methyl groups, as described above) yielded satisfactory results in case of the shortest PDMS chain (H03): identical PDMS chain length of precursor and final copolymer was then obtained from the evaluation of integrals. In case of the longer precursors, differences in relaxation behaviour led to over-estimated PDMS content in the copolymer spectra (but no residual SiH signals), as was discussed above (in the same samples, GPC indicated contrarily a small excess of BAFKU). Hence, the most precise determination of molecular weight (M_n) of the prepared copolymers by ^{1}H-NMR was achieved, if two masses of BAFKU were added to one mass of the PDMS precursor determined by ^{1}H-NMR prior to the synthesis, under the condition of confirmed absence of un-reacted functional groups via post-synthesis ^{1}H-NMR.

The SEC (GPC) results are illustrated by *SI-Fig. 9* (see also *SI-Table 2*; source data are shown in *SI-Fig. 10–12*): The GPC traces of copolymers are compared with BAFKU and with the PDMS precursors, and all are shown as traces in the ELSD (evaporative-light-scattering) detector, while for the copolymers, also the UV/Vis trace (refraction index (at $\lambda = 264$ nm) detector) also is shown. GPC yields fairly realistic results (if compared to the indirect NMR method which was considered most accurate) for products with molecular weights in

the range of 4 to 6 kDa. For molecular masses of 2 kDa and smaller, the accuracy of GPC was already poor (over-estimated by +50%). The addition of the BAFKU end groups to the mass of the whole molecule is best visible by GPC in case of the mid-sized H11–BAFKU$_2$. The difference between the NMR and GPC results seems to partly originate in the different molecular masses of repeat units of polystyrene (calibration standard), and of PDMS and BAFKU. Moreover, the coiling/uncoiling tendency of the product molecules is affected by the aggregation tendency of BAFKU, which also could cause the formation of associates of several molecules under favourable conditions. Similar effects in GPC were also observed by the authors on distantly related PDMS copolymers with BAFKU in a previous work [1].

The GPC traces in *SI-Fig. 9* suggest the presence of some amount of non-bonded BAFKU in the final product, ca 5% of the integral area – if the more accurate ELSD detector is used. In case of the more biased refraction-index-detector (UV light, 264 nm), the residual BAFKU peak amounts to up to 25% of integral area. Comparison with NMR (*SI-Fig. 1b*, invisible vinyl groups of free BAFKU, nor Si-H from PDMS), however, indicates that the amount of free BAFKU is greatly over-estimated by the UV detector, and possibly somewhat over-estimated by the ELSD detector. At least in case of the short copolymer H03–BAFKU$_2$, a 5 wt.% excess of BAFKU should be well visible as vinyl signals, and also as discrepance in the ratio aromatic / PDMS signals. The strong bias of the UV detector (264 nm) can be explained by a relatively strong UV/Vis absorption of azobenzene and hence of BAFKU near 250 nm, while the relative proximity of the ELSD laser wavelength (658 nm) to the long-wave absorption peaks of azobenzene between 400–500 nm also could generate some over-estimation.

The MALDI-TOF results are listed in *SI-Table 2* while the mass spectra are shown in *SI-Fig. 13–15*. In case of MALDI-TOF, good results are obtained for small or mid-sized and reasonably stable molecules like neat BAFKU, or the copolymers H03–BAFKU$_2$ and H11–BAFKU$_2$. In case of the larger macromolecules like H21–BAFKU$_2$ and neat H21, their fragmentation or vaporization of low-molecular fractions dominates and the MALDI-TOF results highly under-estimate the molecular mass. In case of the small H03 (neat) molecule, a doubled molecular mass is observed, most likely due to condensation of SiH end-groups during vaporisation. This latter effect is suppressed in H11 and H21, due to the 'dilution' of the end groups.
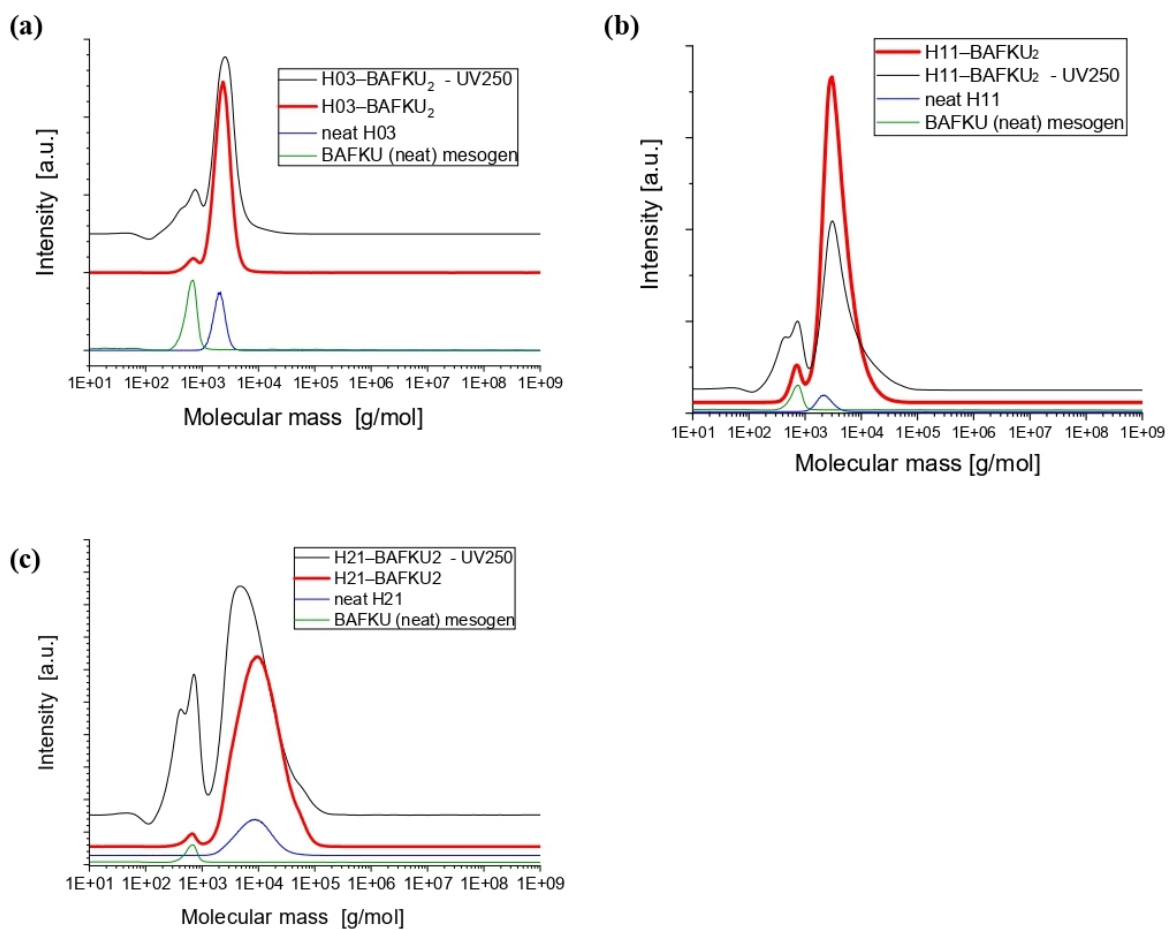
SI-Fig. 9: *GPC traces of the prepared copolymers, overlaid with the traces of their respective PDMS precursors and of the BAFKU mesogen: (a): H03–BAFKU$_2$; (b): H11–BAFKU$_2$; (c): H21–BAFKU$_2$; all samples were analysed using the ELSD detector, while the copolymers were additionally analysed also using the UV-refraction index (at $\lambda = 264$ nm) detector, as noted in the legend.*

SI-Table 2. *Characterization of molecular mass of the prepared copolymers, as obtained by GPC, ^{1}H-NMR and MALDI-TOF; data obtained for the precursors are also listed for comparison.*

Sample	GPC: Peak maximum [g/mol]	GPC: M_n from automatic evaluation [g/mol]	GPC: PD (autom.) [ ]	M_n from producer [g/mol]	M_n by ^{1}H-NMR [g/mol]	M_n by MALDI-TOF [g/mol]
BAFKU	732	654	1.07	420.587	n.a.	421
H03	1 759	1 595	1.11	450±50	624	1250 (!)
H03–BAFKU$_2$	2 371	1 693	1.11	1 391	1 465	1 442
H11	2 157	2 105	1.12	1 050±50	1 196	1 368
H11–BAFKU$_2$	3 008	3 161	1.40	1 891	2 037	1 886
H21	7 367	5 710	1.63	4 500±500	4 764	1 590 (!)
H21–BAFKU$_2$	9 605	7 819	1.93	5 341	5 605	2 331 (!)

1.3.1. GPC source data
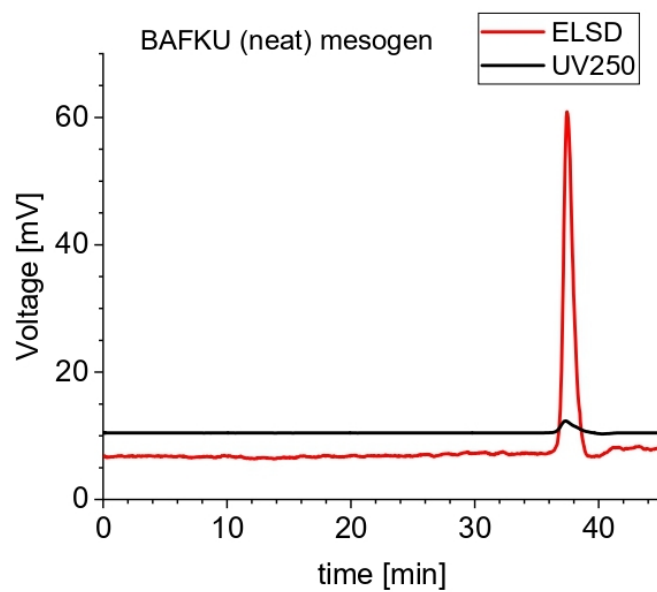
BAFKU

nr.	Max. RT	Start RT	End RT	flow rate correction	Mp	Mn	Mw	Mz	PD	I [mV]	I [%]
x	37.45	34.67	39.45	1	750	654	703	769	1.074924	54.41	100

SI-Fig. 10: *GPC trace of pure BAFKU, the trace of the UV-vis detector is given in mV and not magnified.*
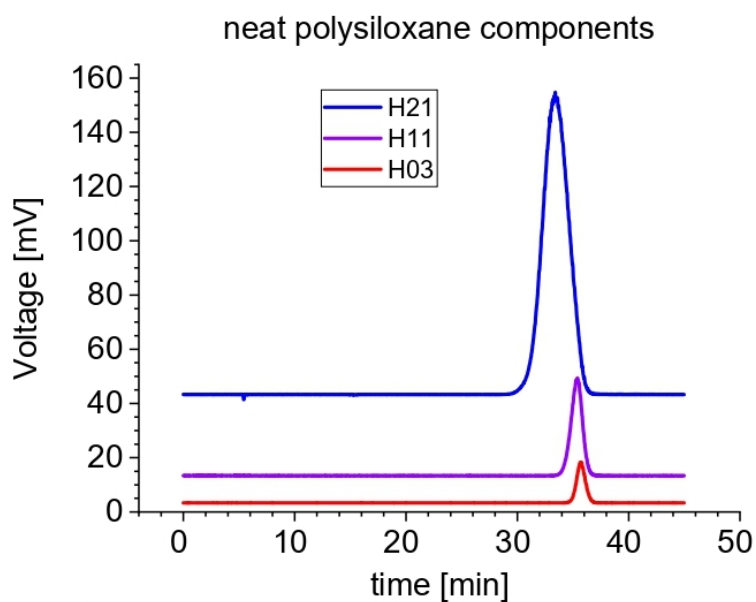
DMSH03

nr.	Max. RT	Start RT	End RT	flow rate correction	Mp	Mn	Mw	Mz	PD	I [mV]	I [%]
x	35.65	32.27	40.87	1	1801	1595	1771	1951	1.1102	15.10	100

DMSH11

nr.	Max. RT	Start RT	End RT	flow rate correction	Mp	Mn	Mw	Mz	PD	I [mV]	I [%]
x	35.42	32.38	38.58	1	2091	2105	2356	2661	1.1193	36.29	100

DMSH21

nr.	Max. RT	Start RT	End RT	flow rate correction	Mp	Mn	Mw	Mz	PD	I [mV]	I [%]
x	33.41	27.92	40.04	1	7471	5710	9322	15792	1.6327	111.81	100

SI-Fig. 11: *GPC traces of pure polydimethylsiloxane precursors H03, H11 and H21, as detected by ELSD.*
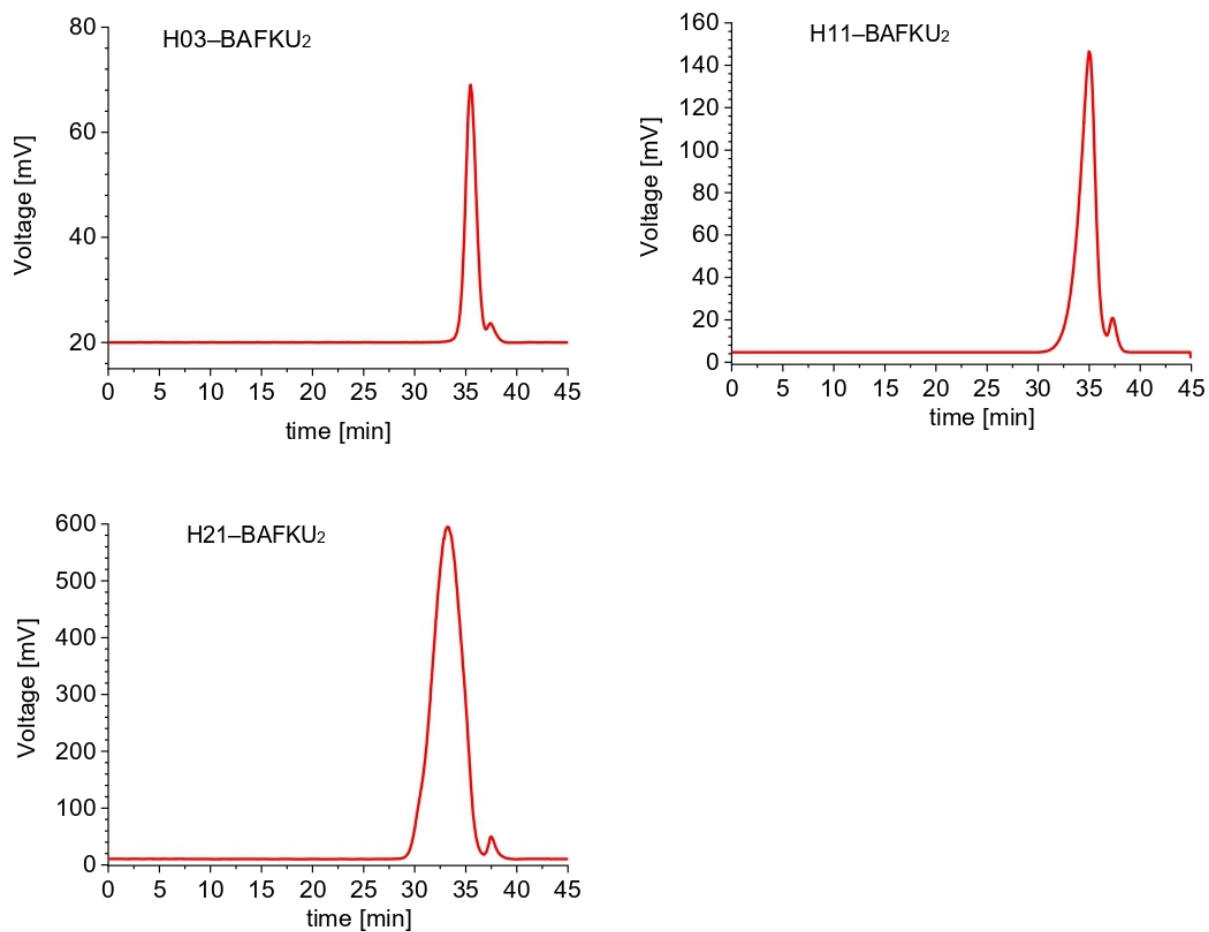
SI-Fig. 12: *GPC traces of the copolymers H03–BAFKU₂, H11–BAFKU₂ and H21–BAFKU₂, as detected by the more accurate ELSD detector; small peaks of un-reacted neat BAFKU are visible to the left from the main peak: in view of the ¹H-NMR results, the BAFKU peaks appear to be somewhat over-estimated also by the ELSD detection.*

Data from *SI-Fig. 12*:

H03–BAFKU₂

nr.	Max. RT	Start RT	End RT	flow rate correction	Mp	Mn	Mw	Mz	PD	I [mV]	I [%]
1	35.49	33.61	36.87	1	1825	1693	1882	2097	1.1121	735.04	93.19
x	37.45	36.87	39.34	1	525	475	510	542	1.0741	53.72	5.66

H11–BAFKU₂

nr.	Max. RT	Start RT	End RT	flow rate correction	Mp	Mn	Mw	Mz	PD	I [mV]	I [%]
1	35.25	31.02	36.85	1	2698	3046	3905	5492	1.2822	515.28	94.75
x	37.50	36.95	38.62	1	663	603	623	642	1.0327	28.54	5.25

H21–BAFKU₂

nr.	Max. RT	Start RT	End RT	flow rate correction	Mp	Mn	Mw	Mz	PD	I [mV]	I [%]
1	33.27	28.45	36.63	1	9941	7819	15076	29164	1.9283	585.65	93.65
x	37.50	36.63	39.85	1	729	636	697	754	1.0967	39.69	6.35

1.3.2.   MALDI-TOF spectra
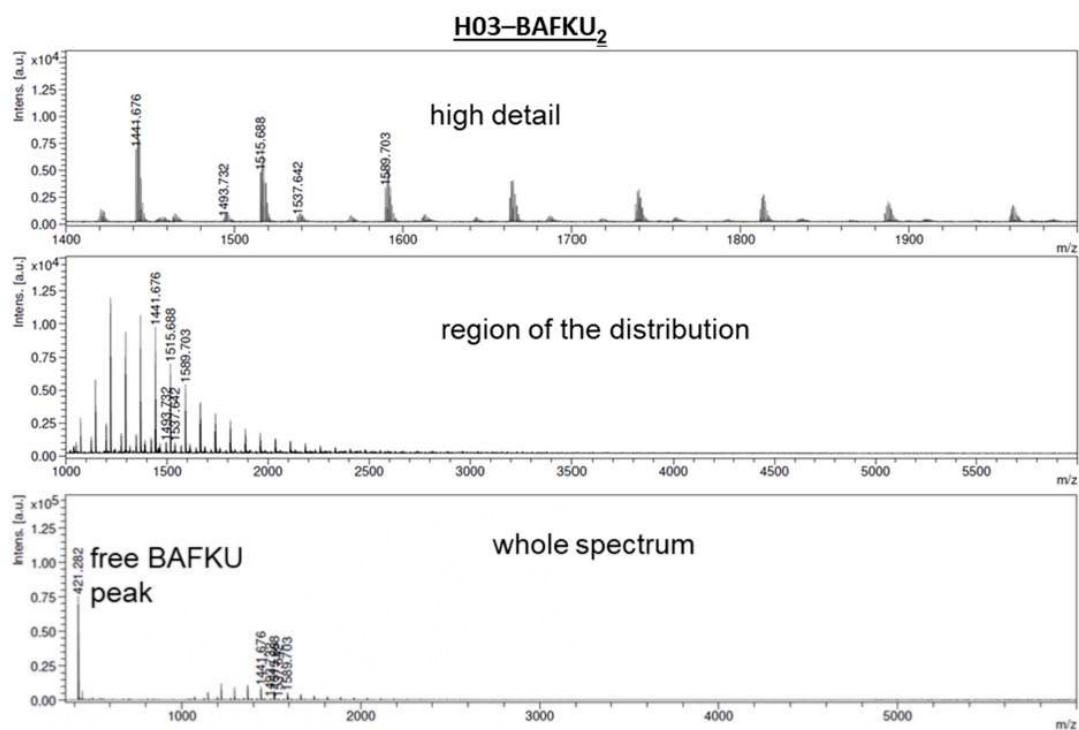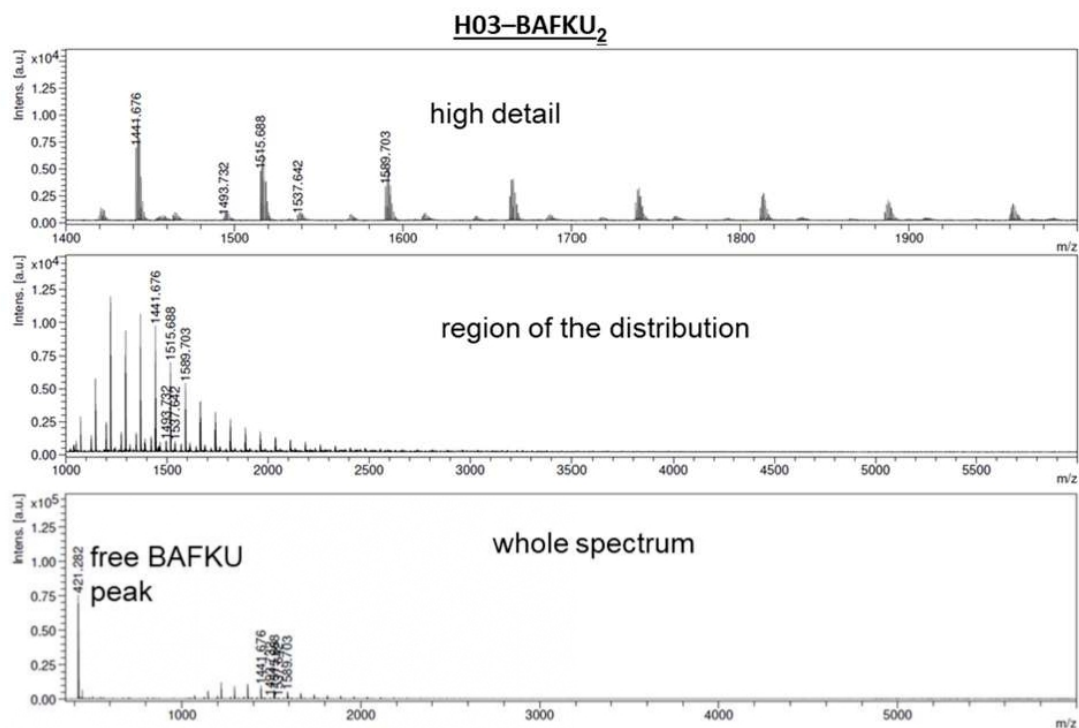
SI-Fig. 13: *MALDI-TOF spectra: H03–BAFKU2 (top) vs. neat H03 (bottom).*
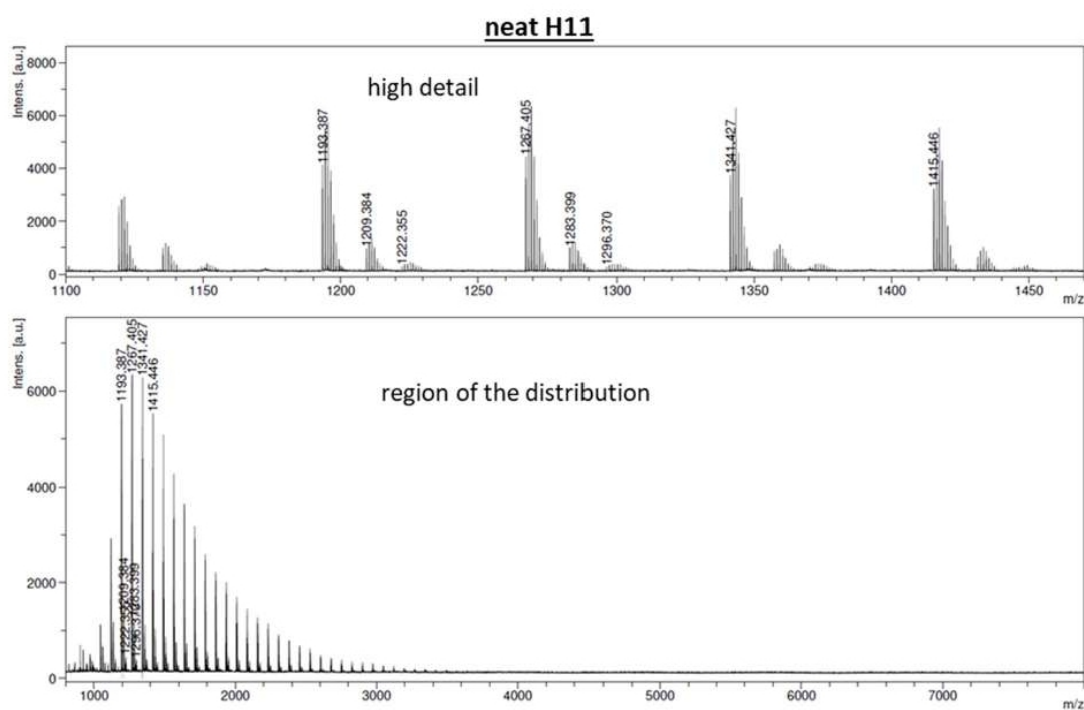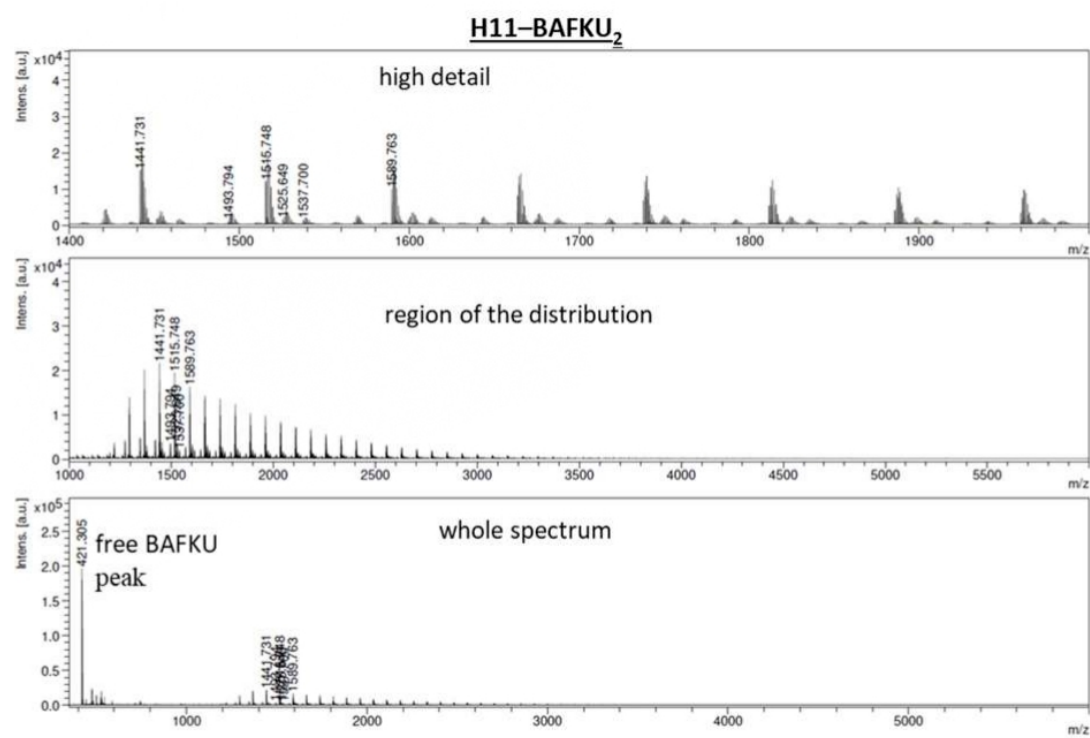
SI-Fig. 14: *MALDI-TOF spectra: H11–BAFKU₂ (top) vs. neat H11 (bottom).*
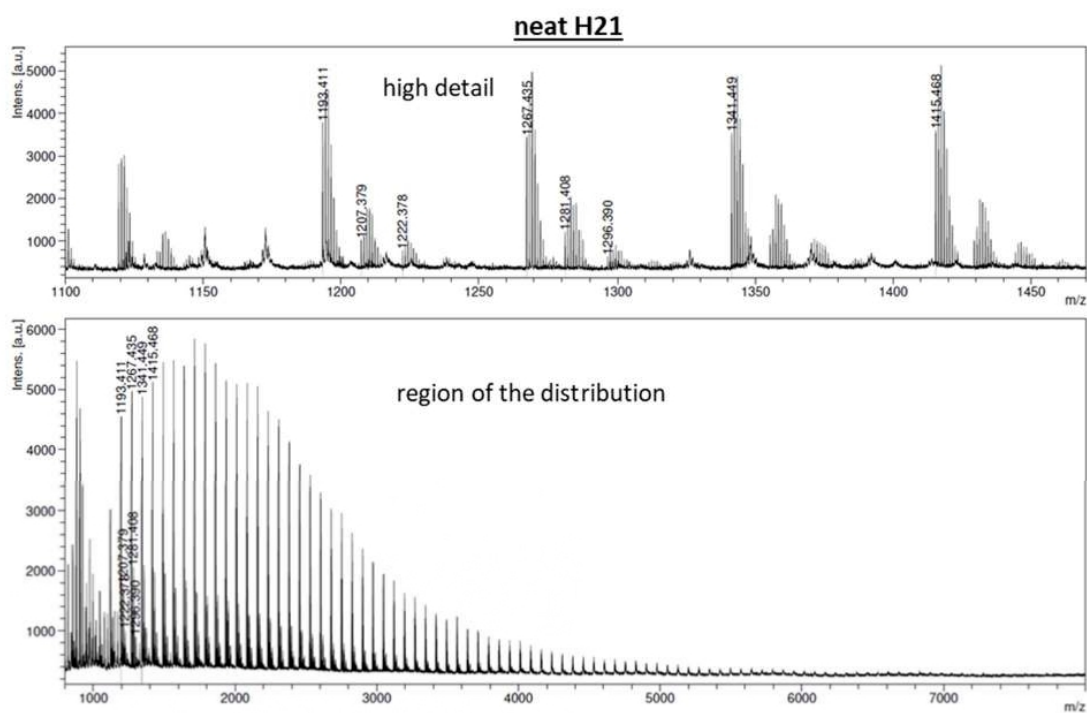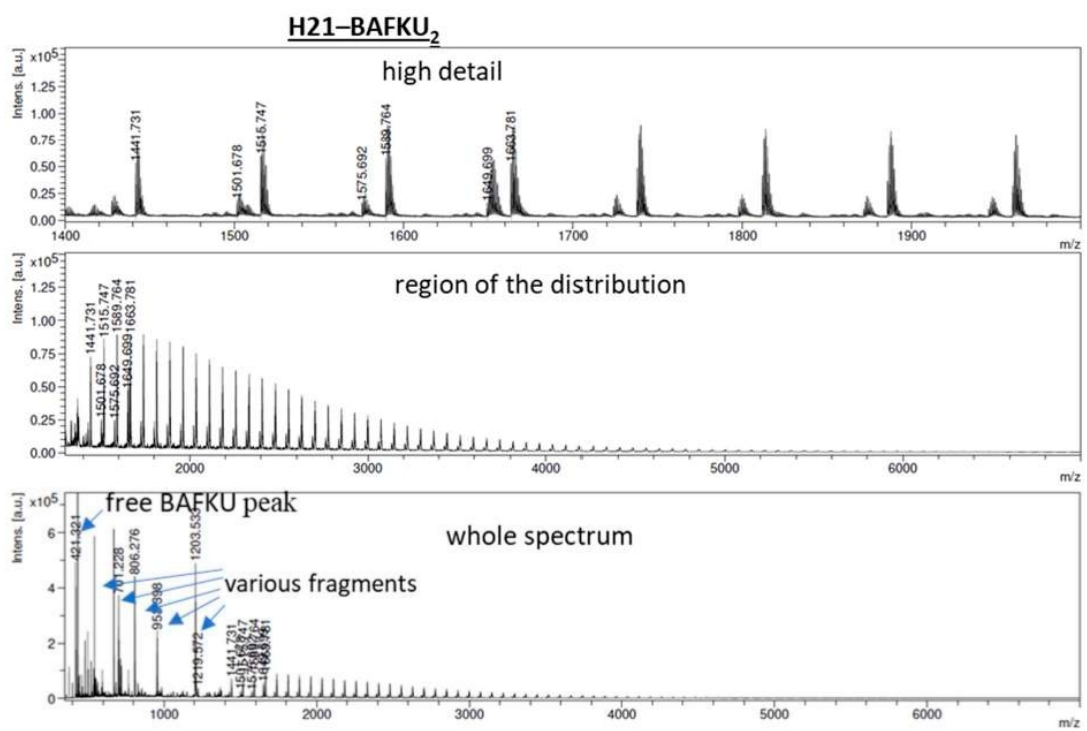
SI-Fig. 15: *MALDI-TOF spectra: H21−BAFKU₂ (top) vs. neat H21 (bottom).*

1.4. Polarized light microscopy (PLM)

PLM intensity: neat BAFKU2

(a)   **(b)**
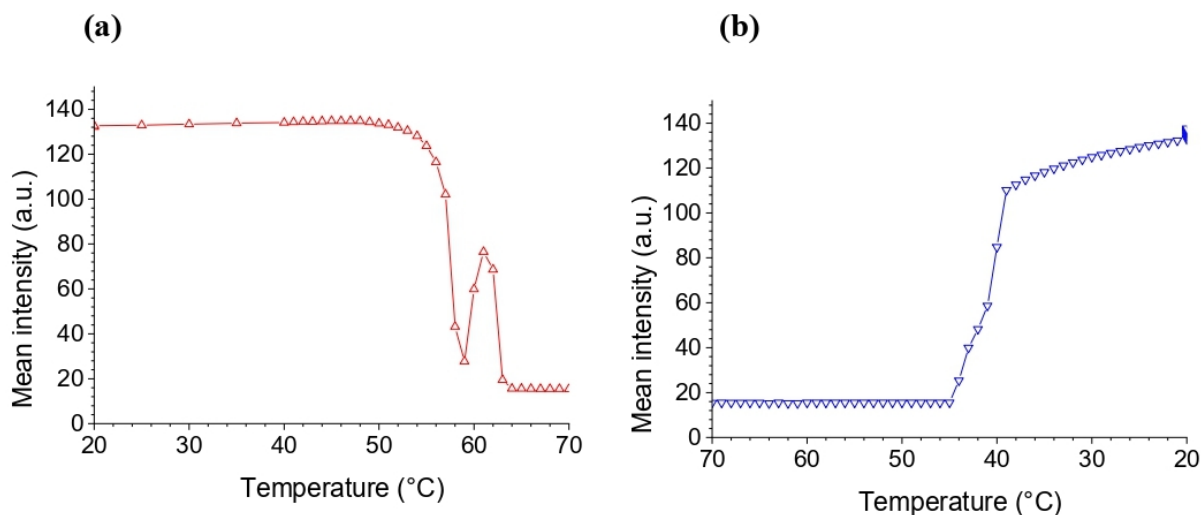
SI-Fig. 16: *Temperature-dependence of the average polarized light intensity ('black and white mode') calculated from the whole image frames taken during the PLM investigation of* **neat BAFKU***:   (a) heating run from 20 to 70°C;   (b) cooling run from 70 to 20°C.*

PLM intensity: H03-BAFKU2
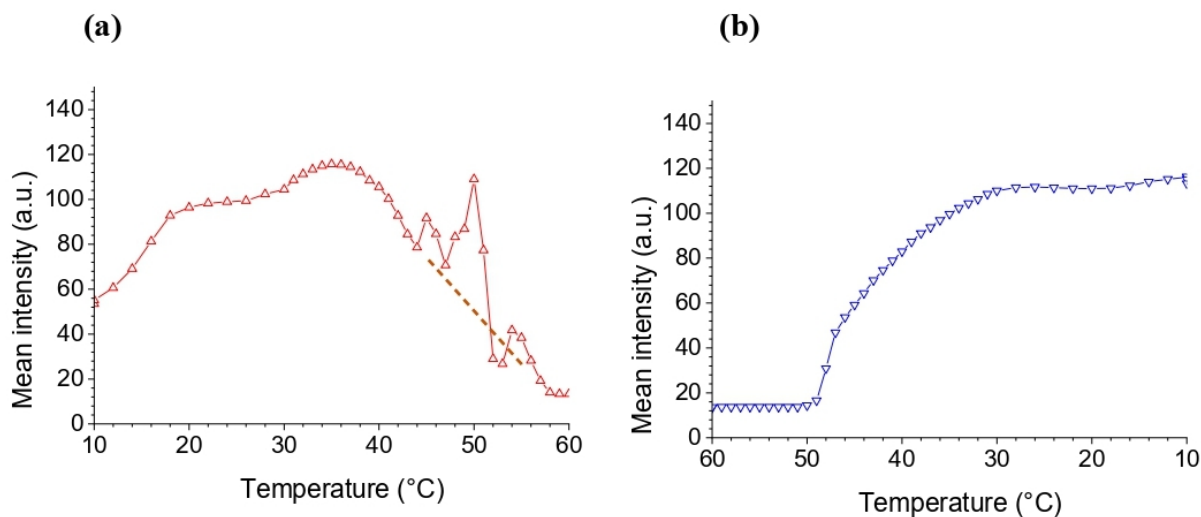
(a)   **(b)**

SI-Fig. 17: *Temperature-dependence of the average polarized light intensity ('black and white mode') calculated from the whole image frames taken during the PLM investigation of* **H03-BAFKU₂** *:   (a) heating run from 10 to 60°C;   (b) cooling run from 60 to 10°C.*

PLM intensity: H11-BAFKU2

(a)

(b)
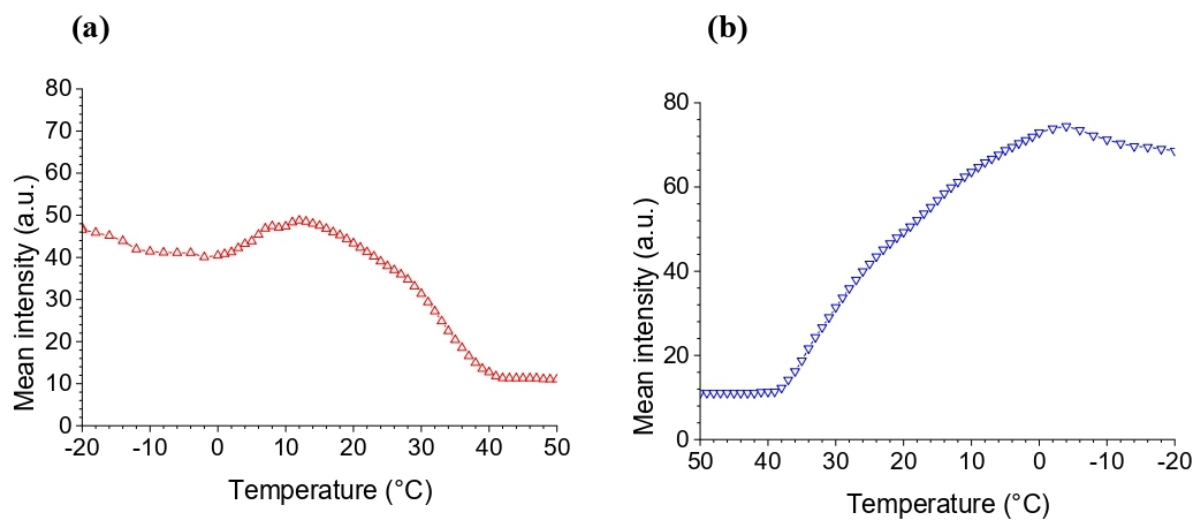
SI-Fig. 18: *Temperature-dependence of the average polarized light intensity ('black and white mode') calculated from the whole image frames taken during the PLM investigation of* **H11-BAFKU₂ :** *(a) heating run from -20 to 50°C; (b) cooling run from 50 to -20°C.*

PLM intensity: H21-BAFKU2

(a)

(b)

(c)

(d)
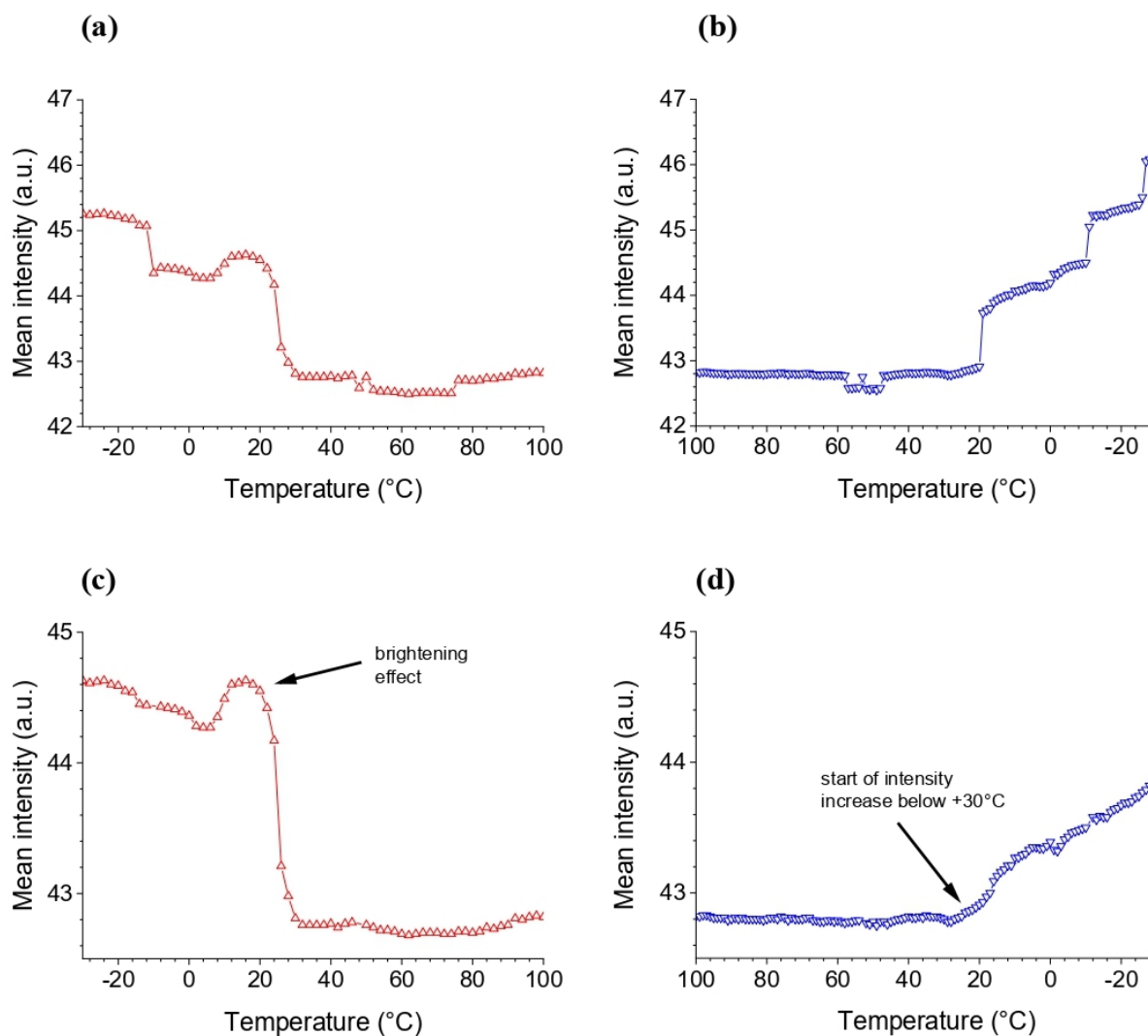
SI-Fig. 19: Temperature-dependence of the average polarized light intensity ('black and white mode') calculated from the whole image frames taken during the PLM investigation of H21–BAFKU₂ : (a, c) heating run from -30 to 100°C; (b, d) cooling run from 100 to -30°C; (a, b) original data; (c, d) data with corrected effect of change of focusing.

1.4.1.   Details of PLM textures of <u>neat BAFKU</u>
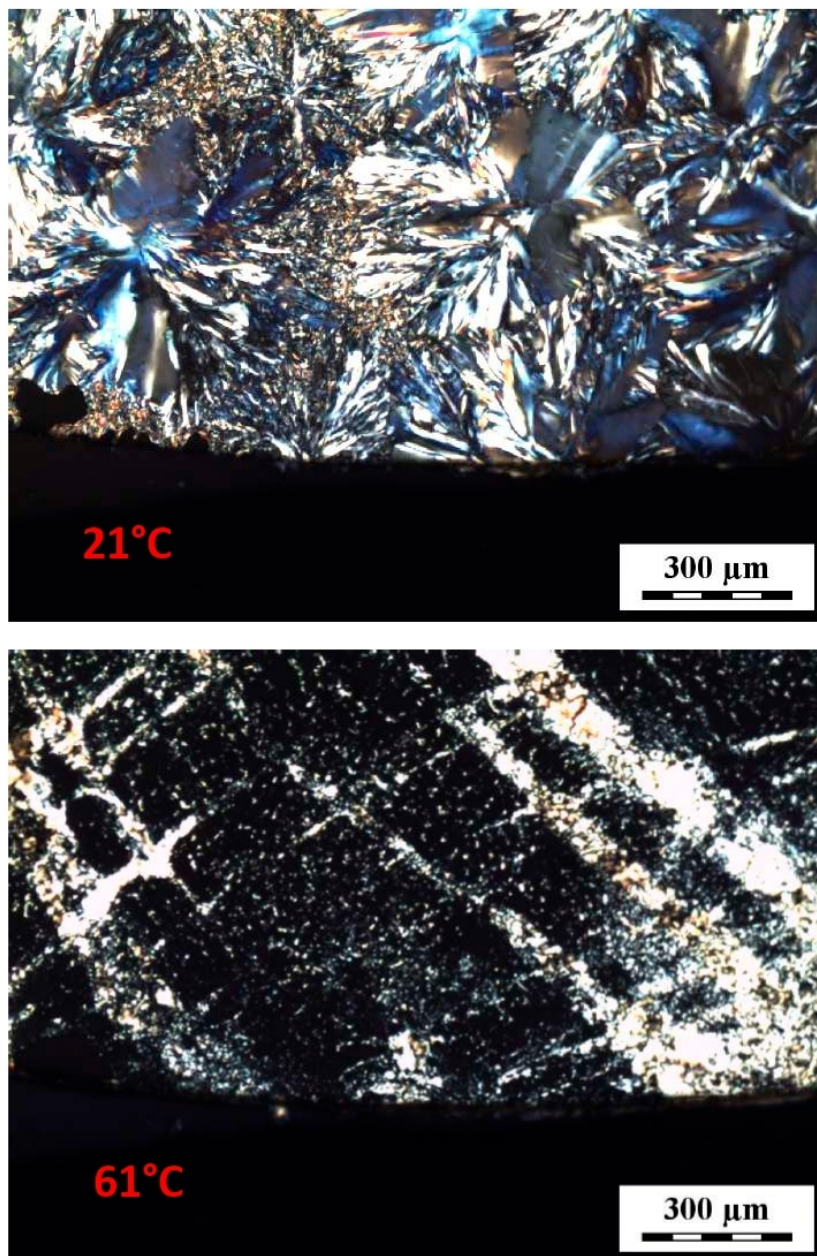
SI-Fig. 20: *High-resolution images of textures of neat BAFKU: top: 21°C, bottom: 61°C, both in heating run.*

Neat BAFKU
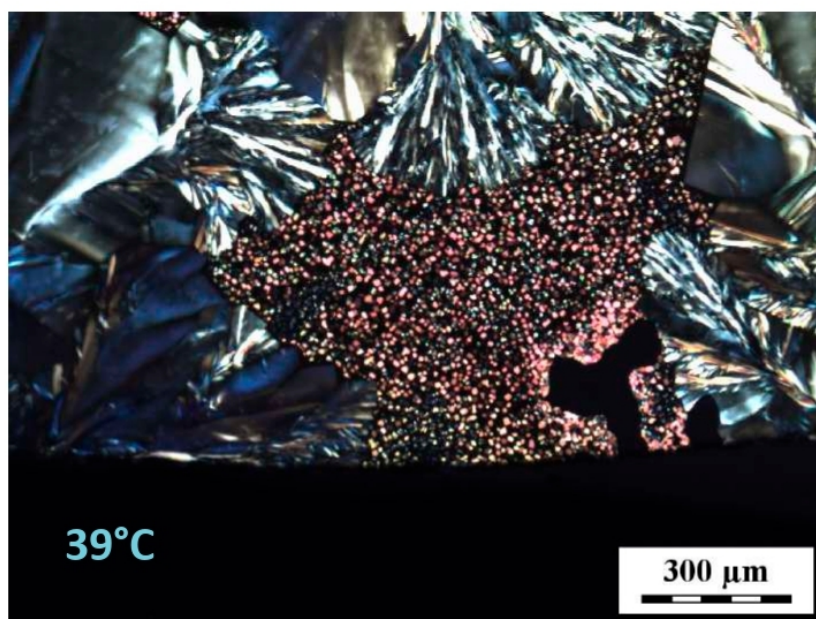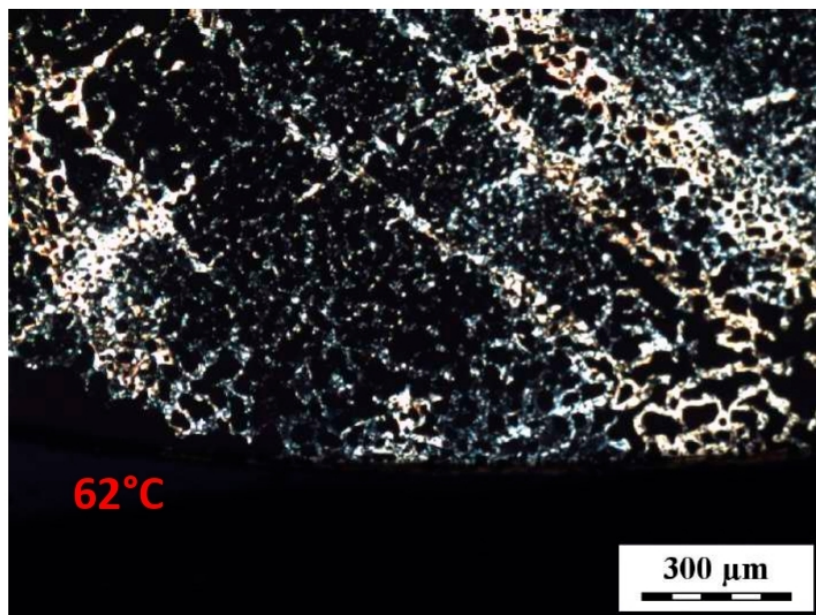
SI-Fig. 21: *High-resolution images of textures of neat BAFKU: top: 62°C (heating run), bottom: 39°C (cooling run).*

1.4.2. Details of PLM textures: <u>H03–BAFKU$_2$</u>
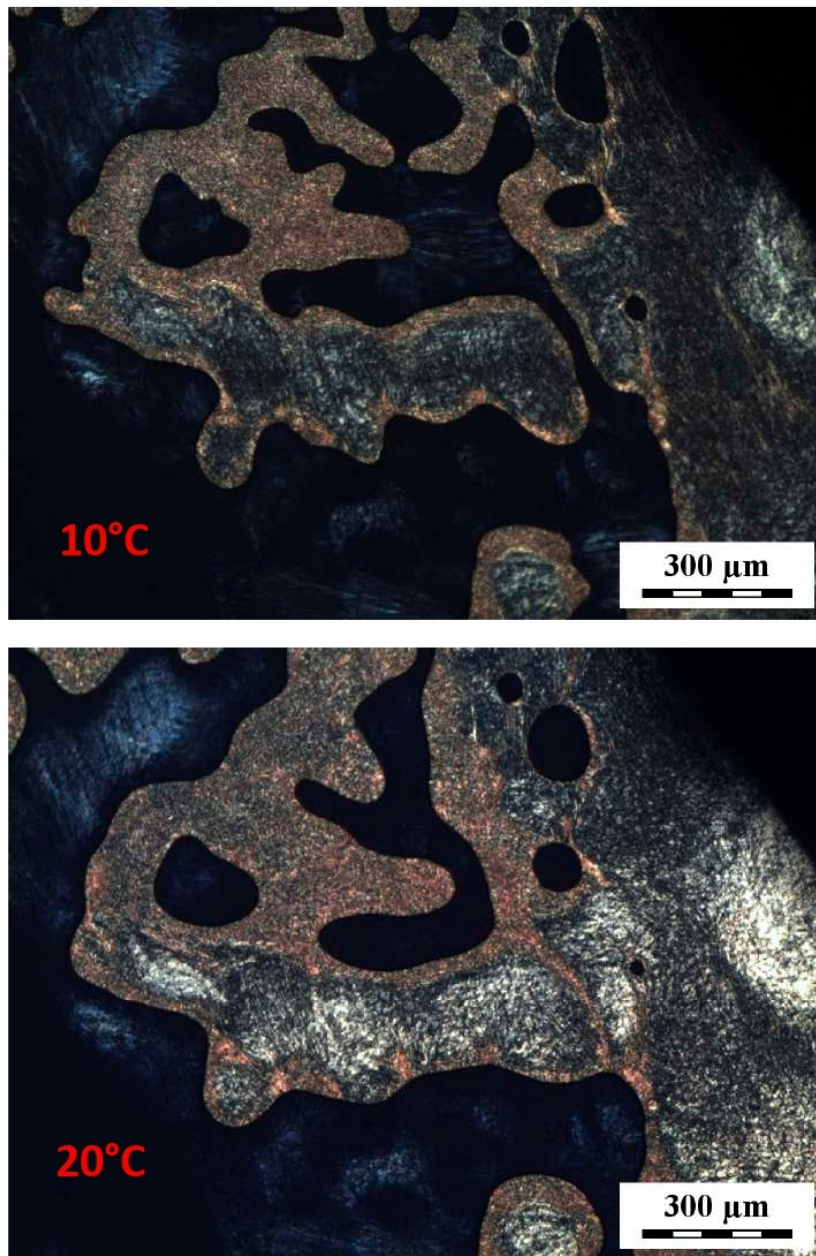
SI-Fig. 22: *High-resolution images of textures of H03–BAFKU$_2$: top: 10°C, bottom: 20°C, both in heating run.*
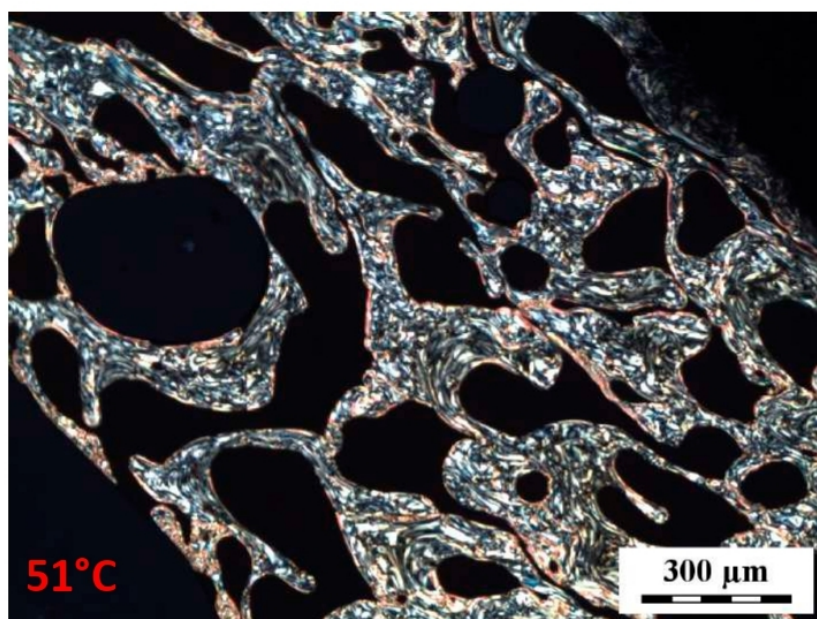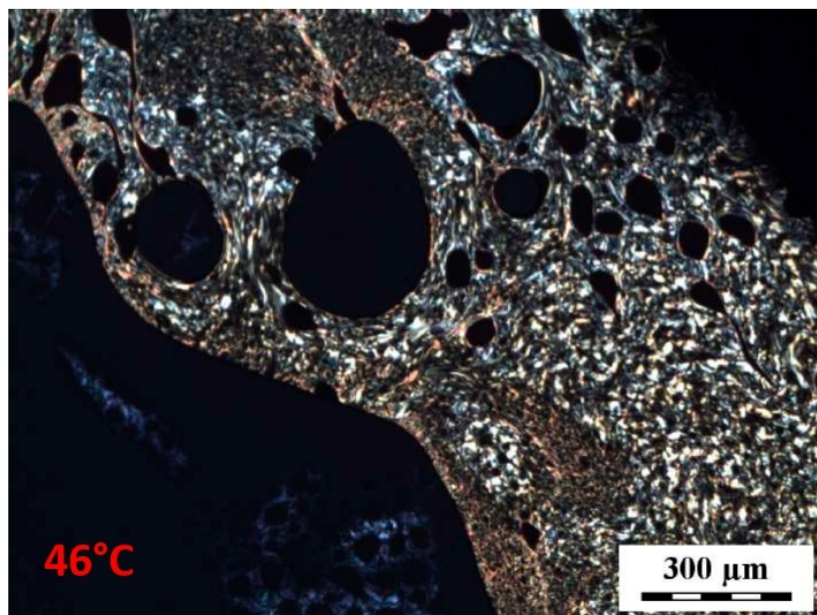
H03–BAFKU$_2$

SI-Fig. 23: *High-resolution images of textures of **H03–BAFKU$_2$**: top: 46°C, bottom: 51°C, both in heating run.*
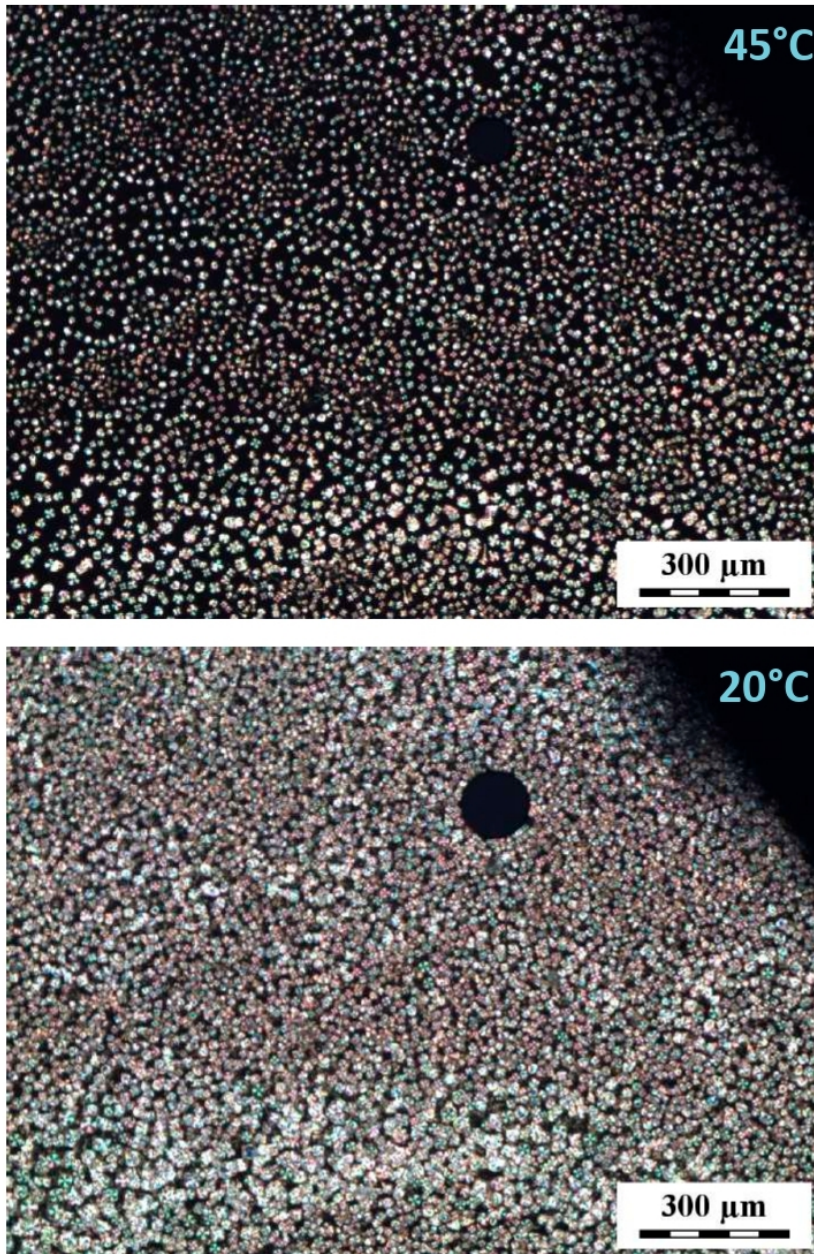
H03–BAFKU₂

SI-Fig. 24: *High-resolution images of textures of **H03–BAFKU₂**: top: 45°C, bottom: 20°C, both in cooling run.*

1.4.3. Details of PLM textures: <u>H11–BAFKU$_2$</u>

SI-Fig. 25: *High-resolution images of textures of H11–BAFKU$_2$: top: 10°C, bottom: 21°C, both in heating run.*

H11–BAFKU$_2$
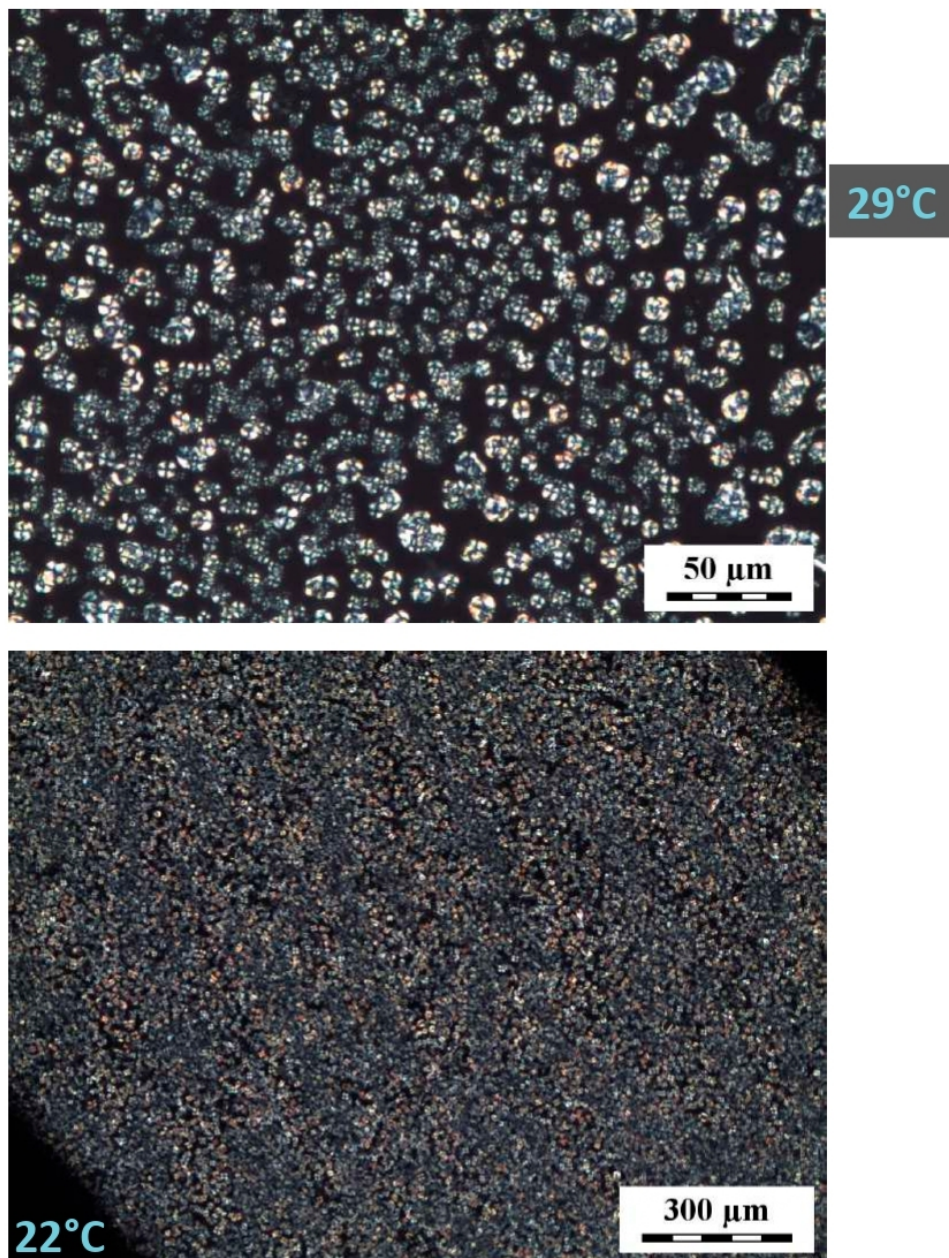
SI-Fig. 26: *High-resolution images of textures of **H11–BAFKU$_2$**: top: high detail at 29°C, bottom: 22°C, both in cooling run.*

H11–BAFKU$_2$
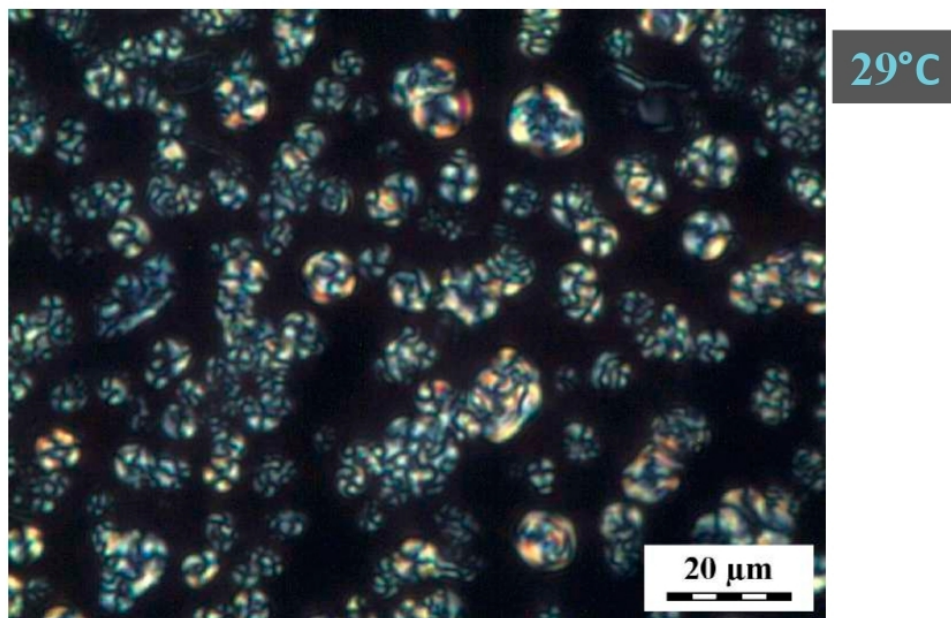
SI-Fig. 27: *High-resolution images of textures of **H11–BAFKU$_2$**: very high detail at 29°C.*

1.4.4. Details of PLM textures: <u>H21−BAFKU₂</u>
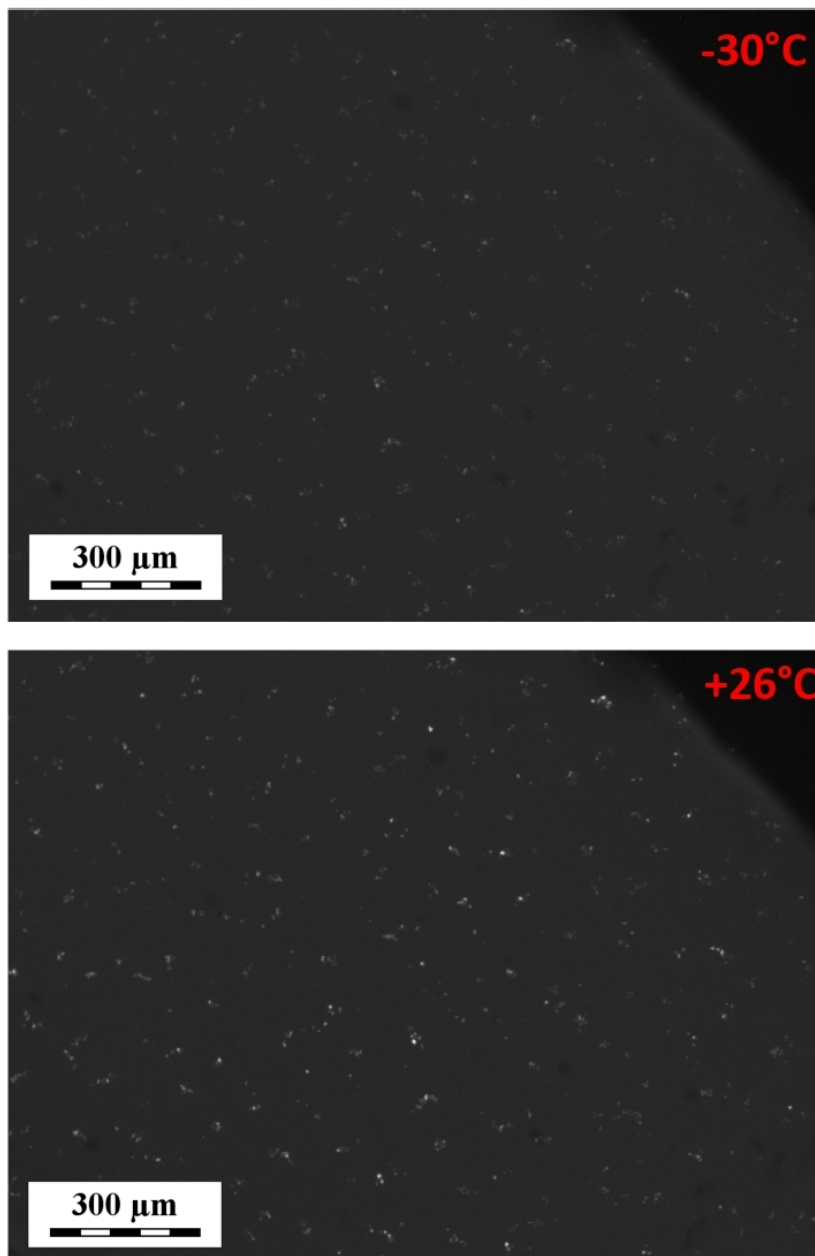
SI-Fig. 28: *High-resolution images of textures of **H21−BAFKU₂**: top: 10°C, bottom: 21°C, both in heating run.*
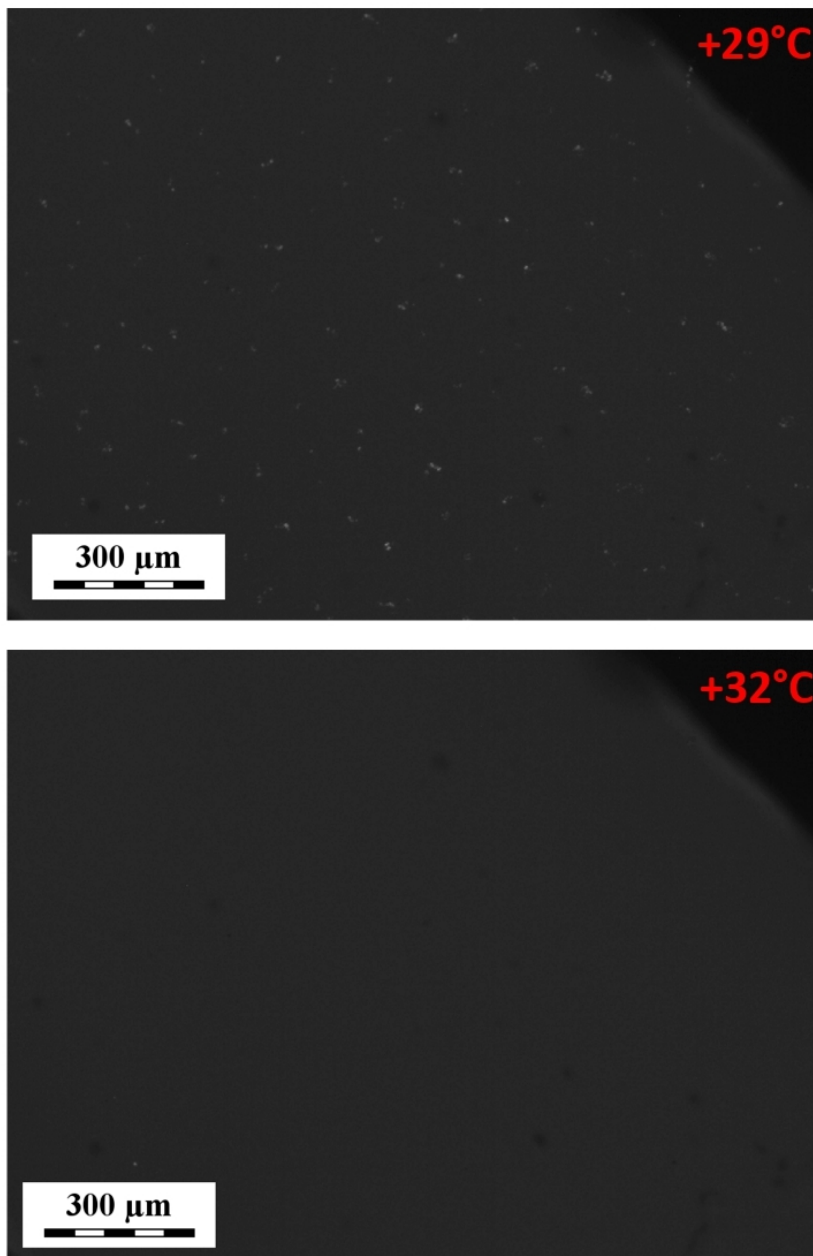
H21−BAFKU₂

SI-Fig. 29: *High-resolution images of textures of **H21−BAFKU₂**: top: 10°C, bottom: 21°C, both in heating run.*
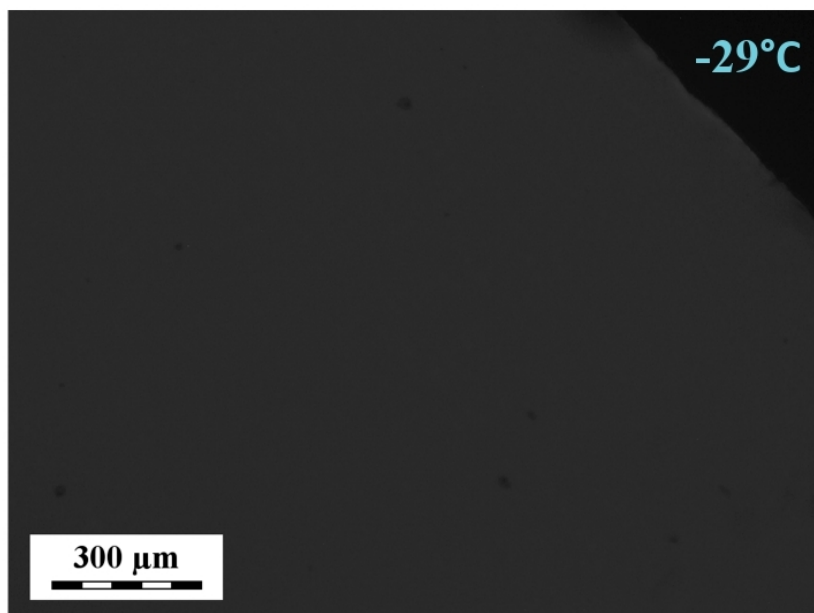
H21–BAFKU$_2$

SI-Fig. 30: *High-resolution images of textures of **H21–BAFKU$_2$**: -29°C, end of cooling run.*

References

[1] S. Horodecka, A. Strachota, B. Mossety-Leszczak, M. Šlouf, A. Zhigunov, M. Vyroubalová, D. Kaňková, M. Netopilík, Meltable copolymeric elastomers based on polydimethylsiloxane with multiplets of pendant liquid-crystalline groups as physical crosslinker: A self-healing structural material with a potential for smart applications. *European Polymer Journal* 137 (2020) #109962. DOI: https://doi.org/10.1016/j.eurpolymj.2020.109962

Appendix 3:

Article

Low-Temperature-Meltable Elastomers Based on Linear Polydimethylsiloxane Chains Alpha, Omega-Terminated with Mesogenic Groups as Physical Crosslinker: A Passive Smart Material with Potential as Viscoelastic Coupling. Part II—Viscoelastic and Rheological Properties

Sabina Horodecka [1,2], **Adam Strachota** [1,*], **Beata Mossety-Leszczak** [3], **Maciej Kisiel** [3], **Beata Strachota** [1] **and Miroslav Šlouf** [1]

[1] Institute of Macromolecular Chemistry, Czech Academy of Sciences, Heyrovskeho nam. 2, CZ-162 06 Praha, Czech Republic; horodecka@imc.cas.cz (S.H.); beata@imc.cas.cz (B.S.); slouf@imc.cas.cz (M.Š.)

[2] Faculty of Science, Charles University, Albertov 6, CZ-128 00 Praha, Czech Republic

[3] Faculty of Chemistry, Rzeszow University of Technology, al. Powstancow Warszawy 6, PL-35-959 Rzeszow, Poland; mossety@prz.edu.pl (B.M.-L.); m.kisiel@prz.edu.pl (M.K.)

[*] Correspondence: strachota@imc.cas.cz; Tel.: +420-296-809-451

Abstract: Rheological and viscoelastic properties of physically crosslinked low-temperature elastomers were studied. The supramolecularly assembling copolymers consist of linear polydimethylsiloxane (PDMS) elastic chains terminated on both ends with mesogenic building blocks (LC) of azobenzene type. They are generally and also structurally highly different from the well-studied LC polymer networks or LC elastomers: The LC units make up only a small volume fraction in our materials and act as fairly efficient physical crosslinkers with thermotropic properties. The aggregation (nano-phase separation) of the relatively rare, small and spatially separated terminal LC units generates temperature-switched viscoelasticity in the molten copolymers. Their rheological behavior was found to be controlled by an interplay of nano-phase separation of the LC units (growth and splitting of their aggregates) and of the thermotropic transitions in these aggregates (which change their stiffness). As a consequence, multiple gel points (up to three) are observed in temperature scans of the copolymers. The physical crosslinks also can be reversibly disconnected by large mechanical strain in the 'warm' rubbery state, as well as in melt (thixotropy). The kinetics of crosslink formation was found to be fast if induced by temperature and extremely fast in case of internal self-healing after strain damage. Thixotropic loop tests hence display only very small hysteresis in the LC-melt-state, although the melts show very distinct shear thinning. Our study evaluates structure-property relationships in three homologous systems with elastic PDMS segments of different length (8.6, 16.3 and 64.4 repeat units). The studied copolymers might be of interest as passive smart materials, especially as temperature-controlled elastic/viscoelastic mechanical coupling.

Keywords: reversible networks; self-assembly; self-healing; liquid crystals; smart materials; rheology

---

1. Introduction

This work is dedicated to 'smart' viscoelastic and rheological properties of low-temperature-reversible elastomers, which melt close below room temperature. The materials are based on linear

polydimethylsiloxane (PDMS) of different chain length, terminated with liquid-crystalline (LC) units in α- and ω-position. The LC end-groups act as physical crosslinkers in this special variety of PDMS /LC copolymers. To the authors best knowledge, no explicit studies were carried out about materials, which freeze to elastomers at low temperatures (while they are molten at the ambient one), at least not under such a title. On the other hand, numerous studies appeared about low-temperature elasticity, which are dedicated to the behavior of 'normal' and most often of commercially important elastomers at low temperatures, see for example, [1]. Fusible rubbers with low melting points offer interesting potential applications (e.g., in soft robotics) as temperature-sensitive smart coupling or energy absorbing materials, which display temperature-switchable viscoelasticity in the melt state, down to 'freezing' to a rubbery phase.

In a preceding work ("Part I", [2]), the synthesis, as well as the phase behavior of the presently studied α,ω-LC-terminated copolymers is subjected to a comprehensive study. In that mentioned publication, the Introduction deals in detail with the specific architecture of the copolymers and especially with the marked difference between them and the 'liquid-crystalline elastomers' much-studied in literature: the latter contain a much higher mesogen fraction and thus display wholly different properties.

The study of reversible non-covalent crosslinking via crystallization of small rigid structural units was inspired by the authors' previous work about epoxy-nanocomposites tethered with polyhedral oligomeric silsesquioxanes (POSS) [1–4] and about oriented epoxy-LC polymers [5]. In both these systems, however, due to the parallel presence of physical and of relatively dense covalent crosslinking, the possibilities of deeper study of viscoelasticity and rheology were very limited.

1.1. Physically Crosslinked Polydimethylsiloxane

Related to the presented study is the broader topic of physical (non-covalent) crosslinking of PDMS. Several interesting approaches were studied in literature, including the attachment of hydrogen-bridging groups [3,6–10] or of π-stacking units [11–14]. Other physically crosslinked PDMS derivatives include such with grafted side chains consisting of long hydrocarbons with polar end-fragments [15] or A-B-A triblock copolymers with PDMS as central block [16,17]. Combinations of Lewis-acidic and -basic functional substituents on PDMS [18] or of attached mildly bonding ligands and free metal cations [19] also were tested, as well as coordinative crosslinking by borate units [20,21] but such systems rather represent reversible covalent crosslinking. In contrast to the above mentioned so-called 'thermoplastic elastomers', the PDMS copolymers studied in the presented work are crosslinked by a rather mild variety of non-covalent interactions: The aggregation of the 'active' structural units is driven by their crystallization tendency, with no hydrogen bridging, no strong π-stacking and no strong electrostatic attraction. The authors of this work recently studied [22] a distantly related PDMS–LC copolymer, which, however, is structurally highly different from the presently investigated ones: it consisted of a linear PDMS chain tethered with spatially separated quartets of pendant LC groups. The highly different architecture led to a different thermo-mechanical behavior (compare References [22] and [2]), as well as rheological one (as will be shown in this work).

1.2. Rheology of Liquid Crystals and of Liquid-Crystalline Polymers (LCPs)

The presently studied copolymers display highly interesting viscoelastic properties due to the presence of significant amounts of liquid-crystalline building blocks in their structure. The rheology and viscoelasticity of rod-like molecular liquid crystals, as well as of liquid-crystalline polymers (LCPs), attracted a considerable research interest since early on, see reviews [4,5,7,23–27], in view of unusual and promising material properties of LCPs, especially of oriented ones and in view of their extraordinary flow behavior during processing. Lyotropic and thermotropic LCPs generally display similar rheology but the lyotropic ones were studied earlier and more frequently (see e.g., [8,28–30]) than thermotropic ones [25], due to the easier in-situ observation of the former by polarized light microscopy (PLM).

1.2.1. Models of Flow Behavior of LCPs

Based on their studies of LCP rheology with polarized light, Onogi, Asada and co-workers [31,32] proposed three regions of the dependence of viscosity on shear rate: a polydomain region with piled and randomly oriented and tumbling LC domains which occurs at low shear rates ("region I")—associated with thixotropic behavior; at higher shear rates, the "region II" occurs, characterized by dispersed domains in a nematic continuum and by a plateau of the viscosity dependence on shear rate; finally, at the highest shear rates ("region III"), the morphology transforms to nematic monodomain-type (flow alignment) and thixotropic behavior again is observed. Generally, in the aligned nematic state, the LCPs are observed to possess a distinctly lower viscosity than in the isotropic state [23].

The flow behavior of single LCP macromolecules (and also of LC molecules) was described by two models, which apply depending on material properties: The 'molecular (Doi-) model' [33,34] which assumes an uniform phase of the flowing fluid with some director wagging or tumbling in this phase. The viscoelasticity arises from the interplay of LC-distortional- (Frank-) elasticity and of hydrodynamic forces. On the other hand, the 'polydomain (Larson-Doi-) model' [35,36] is based on a polydomain morphology (similar to the polycrystalline one in solid materials), where not the director in the uniform fluid but the small domains undergo wagging and tumbling [37]. If the rheological behavior of lyotropic and thermotropic LCPs was compared [38,39], it was found, that the molecular (Doi) theory well fits diluted lyotropic LCPs, while concentrated lyotropic LCPs and thermotropic LCPs are better described by the polydomain model (Larson-Doi). The latter is favored by topological exclusion and insufficient flexibility of the macromolecules.

1.2.2. Effect of LCP Architecture

Several studies compared the rheology of the two main structural families of LCPs:

In case that thermotropic main-chain-LCPs (MC-LCPs) possess semi-flexible properties due to suitable spacers, flow aligning behavior was found to be greatly favored [27,40], even in a moderately crosslinked MC-LCP [41]. Because of this, MC-LCPs are also subjected to rather durable consequences of previous shear flow ('thermal and shear history'), which are difficult to reset, even by isotropic melting [27,42,43].

The side-chain-LCPs (SC-LCPs) were reported to possess a much more extended linear viscoelastic region than MC-LCPs [44] and even to lack the rheological 'region I' [42], as well as having a tendency to persistent domain tumbling during flow [27], instead of flow alignment. In contrast to MC-LCPs, shear history effects quickly disappear in SC-LCPs (rapid 'reset' of initial viscoelastic properties) [27]. SC-LCPs with the rod-like mesogens attached side-on (laterally) [45] are generally similar to 'normal' SC-LCPs with end-on-attached LC units but they can be oriented by creep, while subsequent isotropization easily occurs via oscillatory deformation. Their rheology is controlled mainly by their backbone.

Spacer moieties in MC-LCPs influence their tendency to flow alignment by their flexibility [27,40], as well as their viscosity (odd/even effect in shorter polymethylene spacers) [46]. In SC-LCPs, a longer spacer favors stronger LC-LC interaction and eventually the formation of a smectic phase [47,48], while shorter spacers favor nematic ordering. Smectic SC-LCPs display a specific shear behavior [49].

1.3. Rheology-Related Studies on α,ω-LC-Terminated Polymers

The α,ω-LC-terminated PDMS polymers studied in this work belong to a unique structural group, distinct from SC-LCPs and MC-LCPs. In case of a not too long central chain, such compounds were called 'LC-dimers' in older literature. Early examples of rheological investigations on such compounds (which however contained different central chains than PDMS) are the publications [50] and [51,52]. A relatively small degree of segmental phase separation (LC/central chain) was achieved in Reference [50] and in most products in Reference [51], which reduced the 'smart' properties of such 'LC-dimers'. In Reference [51], smectic ordering was achieved in one of the 'LC-dimers', via suitable choice of the central chain. In Reference [52], polytetrahydrofuran-28-mer α,ω-terminated with an aromatic

diester ("diES2-polyTHF"), was subjected to comprehensive rheological investigation. In contrast to molecular liquid crystals or to MC-LCPs, diES2-polyTHF displayed a higher viscosity in the nematic state than in the isotropic melt, obviously due to supramolecular assembly (nano-phase-separation of LC). Large strains were found to induce solid → liquid transition in diES2-polyTHF (in contrast to MC-LCPs). After shear treatment or large oscillatory deformation, the recovery of original material properties was very slow, which was attributed to a slow build-up of nano-phase-separated domains. Flexibility and nano-phase-separation tendency of the central chain were considered to be the key factors in the smart behavior of "diES2-polyTHF" in Reference [52]. In the present work, these both parameters of an α,ω-LC-terminated copolymer were much improved, which led to very interesting rheological behavior.

1.3.1. Rheological Properties of Physically Crosslinked PDMS

One of the first viscoelastic studies on PDMS-LC copolymers (of loosely crosslinked SC-LCP) was done by Finkelmann and co-workers [53]. Some persistent shear-induced anisotropy was observed, as well as 'liquid-crystalline elasticity' upon isotropic → nematic transition. More related to the studied copolymers are the PDMS polymers α,ω-terminated with various physically crosslinking groups, which were mentioned further above. As these products displayed intriguing properties in many aspects, their rheology or viscoelasticity was studied only to a moderate extent, in the further-above cited works [7,8,13,18]. Similar was also the situation with rheological characterization of the less structurally related PDMS physically crosslinked by pendant groups [12,14,54,55]. All the mentioned works contain rather simple rheological characterizations like the study of the melting process by recording temperature-dependent moduli [7] or viscosity [13]. More sophisticated investigations included stress relaxation tests which characterized the re-organization of the reversible physical crosslinks and its dynamics [14,54,55], as well as deformation recovery tests [54].

1.3.2. Aim of This Work

The aim of the presented work was a comprehensive study of the complex viscoelastic and rheological properties of the α,ω-LC-terminated PDMS copolymers recently prepared by the authors, in the molten, as well as in the rubbery state and also the evaluation of structure property relationships in this context. While the rheology and viscoelasticity of typical liquid crystalline polymers was studied to a considerable depth, the presently investigated materials are novel, due to their low volume fraction of LC units. Their rheology and viscoelasticity is expected to be highly different, dominated by the interplay of nano-phase-separation effects, of the elasticity of the PDMS chains and by the thermotropic behavior of the physical crosslinks, made up of LC aggregates. The studied low-temperature-melting elastomers are interesting because of potential applications as thermo-responsive viscoelastic coupling materials, behaving as oils with greatly varying temperature-controlled viscoelasticity near room temperature and as rubbers at lower temperatures. An attractive feature of the studied products are their azo LC groups, which offer development potential for photo-sensitivity.

2. Experimental Section

2.1. Materials

In this work, the rheological properties of three α,ω-mesogen-terminated copolymers were studied, which consisted of polydimethylsiloxane (PDMS) central chains and of diaromatic azo mesogen end groups (called "BAFKU" in continuation of nomenclature from previous work). The copolymers differed in the length of the central PDMS chain and were named "H03–BAFKU$_2$", "H11–BAFKU$_2$" and "H21–BAFKU$_2$" (where "Hxx" denoted the different central chains). The synthesis and basic characterization of these materials is described in a preceding work by the authors ("Part I" of the present one) [2]. As reference compounds for some of the tests, the neat PDMS spacer components were also

employed, namely "DMS H03" (M_n = 623.9 g/mol), "DMS H11" (M_n = 1196.5 g/mol) and "DMS H21" (M_n = 4764 g/mol), which were purchased as commercial products (Gelest, Inc., Morrisville, PA, USA).

2.2. Rheological Characterization of the PDMS–BAFKU$_2$ Copolymers

2.2.1. Equipment

The advanced multi-functional rheometer of the type ARES-G2, from TA Instruments, New Castle, DE, USA—part of Waters, Milford, MA, USA, was used for characterizing the rheological properties of the prepared copolymers. Different experimental procedures were carried out on this rheometer, in order to perform the below-described investigations.

2.2.2. Sample Geometry

The samples were measured between parallel plates, the diameter of which was: 35 mm for BAFKU2-H21, 25 mm for BAFKU2-H11 and most experiments with BAFKU2-H03 and 12.6 mm for the most viscous samples of BAFKU2-H03. Pure polysiloxane components H03, H11, H21 were measured as references using the 12.6 mm plates. The thickness of the tested samples was always between 0.2 and 0.25 mm.

2.2.3. Determination of Gel Points in Multi-Frequency Oscillatory Tests

The temperature-controlled gelation behavior of the studied copolymers was evaluated using the multi-frequency temperature sweep test (method name in ARES-G2 software: "Oscillation Multiwave"): the samples were loaded as melt between parallel plates, the geometry of which is specified above and were izotropized by a 5 min dwell at 80 °C. Subsequently, two tests were run, the first one in cooling regime and a second one in heating regime. The first test started at the 'loading temperature' of +80 °C, where all samples were isotropic and all history effects in them erased. The final temperature of the cooling run depended on the sample: 0 °C for H03–BAFKU$_2$, −15 °C for H11–BAFKU$_2$ and −40 °C for H21–BAFKU$_2$. The heating scan started at the final cooling temperature of each sample and ended at +70 °C. The rate of temperature change was 1 °C/min in both scans. The deformation regime in both scans consisted in simultaneously applied ('multi-frequency') deformations of following frequencies and amplitudes: 1 Hz/strain amplitude of 1%, 2 Hz/1%, 4 Hz/0.8%, 8 Hz/0.6%, 16 Hz/0.4%, 32 Hz/0.3% and 64 Hz/0.1%. The results were depicted as curves sets of temperature dependent storage shear modulus $G' = f(T)$, of the loss shear modulus $G'' = f(T)$ and of the loss factor $\tan(\delta) = f(T)$. The latter sets of curves were used to determine the gel points (as $\tan \delta$ crossover points) according to the theory of Chambon and Winter [56].

2.2.4. Rate of Thermally Induced Physical Gelation

In order to evaluate the rate with which the physical network is formed after abrupt cooling of molten copolymer to different temperatures, oscillatory time sweep tests (method name in ARES-G2 software: "Oscillation/Time") with a constant oscillatory frequency of 1 Hz and a constant strain amplitude of 1% have been performed. The samples were measured between parallel plates, the geometry of which is specified further above. The tested copolymer samples were rapidly cooled from +70 °C in the isotropic molten state to different final temperatures, which were positioned in the rubbery region, in the liquid-crystalline melt region and in the isotropic melt region. The "oscillatory time sweep test" recorded G', G'' and $\tan(\delta)$ as function of time, as well as the actual temperature, beginning with the start of the rapid melt cooling. In this way, eventual rapid crosslinking prior to temperature equilibration also could be observed, in addition to slower crosslinking which occurred after the temperature of the cooled melt stabilized.

2.2.5. Analysis of Mechanical Disconnection of Crosslinks: Strain Sweep Tests

The possibility to disconnect the reversible physical networks by mechanical strain was investigated using the oscillatory strain sweep test (method name in ARES-G2 software: "Oscillation Amplitude"). The samples were measured between parallel plates, the geometry of which is specified further above. At a constant deformation frequency of 1 Hz, the strain was gradually increased from 0.1% to 1000% and strain-dependent G', G'' as well as $\tan(\delta)$ were recorded. Such experiments were carried out at several constant temperatures positioned in characteristic regions of the studied samples.

2.2.6. Frequency Stiffening Tests

Eventual sample stiffening at high oscillatory deformation frequencies was studied by means of the frequency sweep test (method name in ARES-G2 software: "Oscillation Frequency"), where the oscillatory deformation frequency was gradually increased from 0.001 Hz to 100 Hz. The data were recorded in five logarithmic series of points—'decades', with a constant deformation amplitude in each decade, namely 50% (at 0.001 to 0.01 Hz), 20%, 10%, 5% and 1% (at 10 to 100 Hz). The samples were measured between parallel plates, the geometry of which is specified further above. Such frequency sweep tests were carried out at several constant temperatures positioned in characteristic regions of the studied samples.

2.2.7. Creep and Creep Recovery Tests

The creep and creep recovery tests were performed in order to further evaluate the strength of the physical crosslinks in the studied materials at different temperatures. In weaker-crosslinked samples, yield stress values could be obtained in these experiments. The samples were measured in the torsion regime between parallel plates, the geometry of which is specified further above. The method "Step (Transient) Creep" (method name in ARES-G2 software) was used for this purpose. The experiment consisted of several subsequent stages, each of which contained a loading step followed by an un-loading one (two subsequent "Step (Transient) Creep" modules). During the loading step, a constant stress was applied for a pre-defined time period and the deformation (strain) adjusted automatically in order to maintain the constant stress. In the subsequent un-loading step, the value of the applied constant stress was set to be zero. The measured time-dependent values of the automatically adjusted strain were the final results. The subsequent two-step stages differed in the strain values applied in their respective first step. The creep and creep recovery tests were performed at several characteristic temperatures for each studied copolymer. The standard sequence of applied stress loadings (in the first steps of each stage) was: 0.1, 1, 200, 500, 1000, 2000 and finally 10,000 Pa. In view of the properties of the studied samples, the duration of the loading and un-loading steps was set to 3 min, with 200 data points recorded during this time.

2.2.8. Stress Relaxation Tests

Stress relaxation tests (method name in ARES-G2 software: "Step (Transient) Stress Relaxation") were used as an additional method to further evaluate the strength of the physical crosslinks and the dynamics of their splitting and reconnection. The samples were measured in the torsion regime between parallel plates, the geometry of which is specified further above. During each test, a pre-defined constant deformation (strain) was applied and the time-dependence of the resulting stress was recorded by the force detector and later evaluated as the final experiment result. The experiment was stopped after the stress value apparently reached equilibration. For each copolymer sample, a series of tests was done at several characteristic temperatures. Each of the series consisted of tests with the applied deformation (strain) values of: 0.4%, 1%, 2%, 3%, 4%, 5%, 10% and 20%. The data sampling rate was 1 point/s.

2.2.9. Simple Oscillatory Tests of Thixotropy

The destruction of physical crosslinking by high deformations, as well as its recovery upon substantial reduction of such deformations was tested in simple oscillatory time sweep tests (method name in ARES-G2 software: "Oscillation/Time"). The experiments were carried out as multi step procedures. In each step, a constant oscillatory frequency (1 Hz) and at constant oscillatory deformation was applied and the time-dependent values of storage shear modulus and of loss shear modulus were recorded. The individual steps in the procedure differed by highly contrasting values of the deformation amplitudes, which ranged between 0.1 and 5030%. The duration of each step was between 50 and 150 s.

2.2.10. Thixotropic Loop Tests

Thixotropy loop tests were performed in order to evaluate changes in viscosity caused by continuous shear flow, as well as the degree of eventual recovery vs. 'shear damage' in short-time term. The samples were measured between parallel plates, the geometry of which is specified further above.

Two experimental setups were used: "Flow Ramp" and "Flow Sweep" (method names in ARES-G2 software):

In the "Flow Ramp" tests, in the first step, the materials were subjected to a continuously increasing shear rate (during continuous rotatory mode) while the stress generated by the shearing was recorded. The shear-rate-dependent viscosity values were calculated from form the stress values. In the second step, the shear rate was continuously reduced down to 0 s^{-1}. In a standard test, the range of applied shear rates was 0 to 100 s^{-1}, followed by 100 to 0 s^{-1}. The duration of each step was set to 10 min. In case of highly viscous or semi-solid samples, shorter "Thixotropy ramp" tests were performed, with shear rate ranges of 0 to 0.1 s^{-1}, 0 to 1 s^{-1} or 0 to 10 s^{-1}. The values of stress and of viscosity in dependence of shear rate were obtained in the result plot.

The "Flow Sweep" tests were used to perform a rapid scan of the shear rate region from 100 to 400 s^{-1}. The experiments were performed in two steps: In the first step, the shear rate was step-wise increased, with measured points at: 100, 200, 300 and 400 s^{-1} and with equilibration time of 2 min per each point (while the point's data were measured and averaged for an additional 30 s). In the second analogous step, the shear rate was step-wise decreased, to 300, 200 and 100 s^{-1}. The values of stress and of viscosity in dependence of shear rate were obtained in the result plot.

The thixotropy loop tests were carried out at several characteristic temperatures of each copolymer, in order to characterize their semi-liquid and liquid regions.

3. Results and Discussion

3.1. Description of the Studied Copolymers

Three copolymers (structure: Scheme 1) consisting of highly flexible polydimethylsiloxane (PDMS) chains, α,ω-terminated with mesogenic units of azobenzene type ("BAFKU"), were subjected to a comprehensive rheological characterization as potential passive smart materials. The copolymers differed in the length of the central PDMS chain, namely 8.6-mer ("H03"), 16.3-mer ("H11") and 64.4-mer ("H21"). Their synthesis and basic characterization was described in a previous work [2] by the authors. From the point of view of nomenclature, however, the most proper designation of the studied products would be "mesogen end-capped polymers".
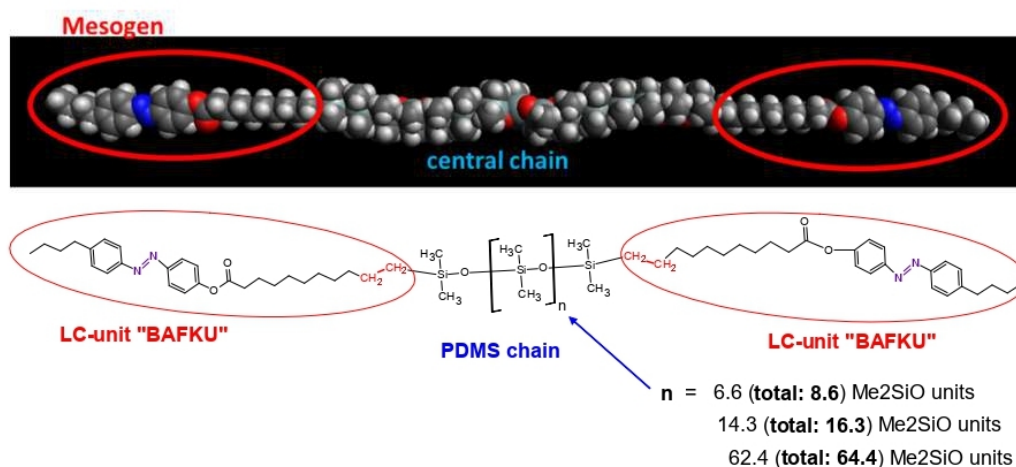
Scheme 1. Top: structure of the prepared copolymers with different length of the central PDMS segment: $n = 6.6$ (in H03–BAFKU$_2$), $n = 14.3$ (in H11–BAFKU$_2$) and $n = 62.4$ (in H21–BAFKU$_2$).

The combination of the highly flexible central chain with two rigid and PDMS-incompatible mesogenic BAFKU groups leads to nano-phase-separation and to physical crosslinking (see Scheme 2) via the aggregation of BAFKU end-groups (nano-crystallization). The latter effect was found to result in the formation of a distinct lamellar morphology in the copolymers [2], which also persists in the lower-temperature region of the copolymer melt, until the regular lamellae break-up above the isotropization temperature [2] (see Scheme 2). Thermotropic transitions of the liquid-crystalline (LC) end-groups assembled in the lamellae were expected to cause interesting viscoelastic and rheological behavior of the studied materials, that is, melting vs. solidification of the rubbery phase or temperature-induced changes in viscoelasticity of the melt.
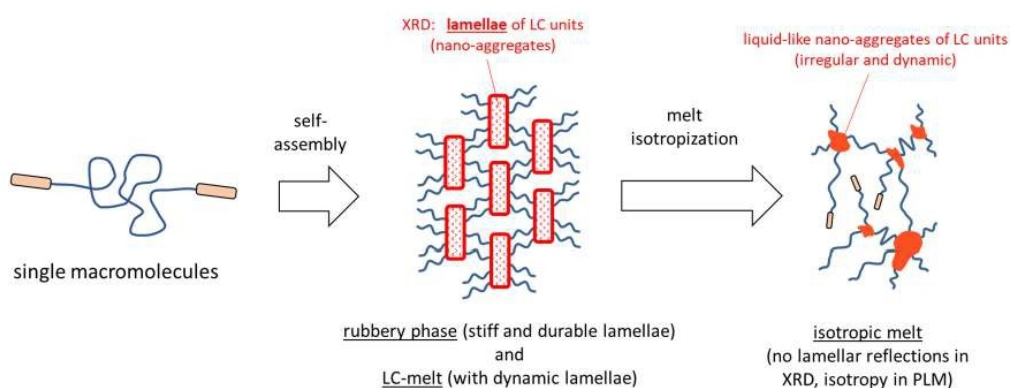
Scheme 2. Supramolecular assembly (nano-phase-separation) of PDMS–BAFKU$_2$ macromolecules to a physically crosslinked lamellar structure and the melting of this structure above the isotropization temperature.

In Schemes 3–5, the previously determined [2] thermal characteristics of the studied copolymers are summarized, which will be important for the evaluation of their rheology:
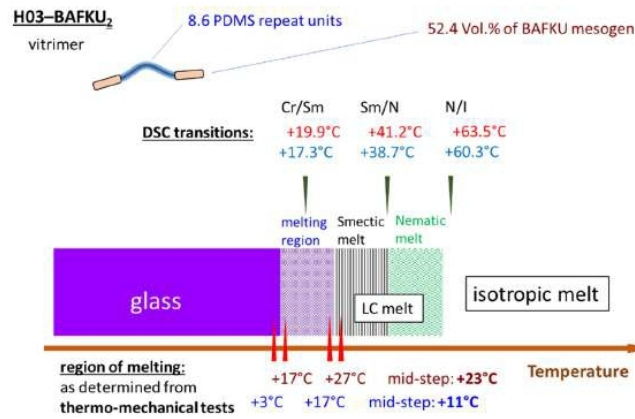
Scheme 3. H03–BAFKU$_2$: schematic overview of values (measured in [2]) of thermal and phase properties (DSC = differential scanning calorimetry). Characteristic temperatures observed in cooling scans are noted with blue font, in heating scans with red/brown.
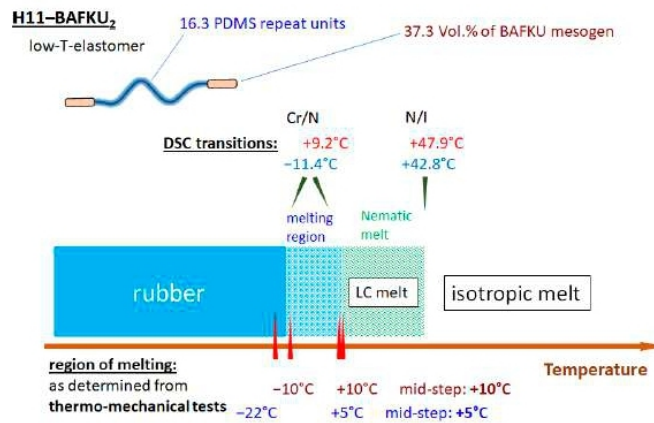
Scheme 4. H11–BAFKU$_2$: schematic overview of values (measured in [2]) of thermal and phase properties. Characteristic temperatures observed in cooling scans are noted with blue font, in heating scans with red/brown.
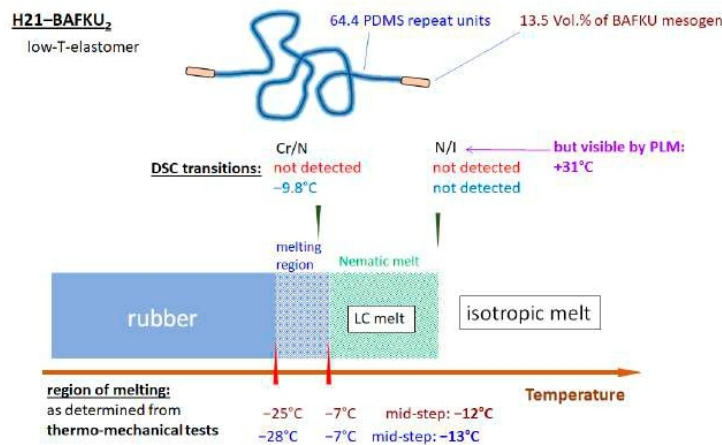
Scheme 5. H21–BAFKU$_2$: schematic overview of values (measured in [2]) of thermal and phase properties Characteristic temperatures observed in cooling scans are noted with blue font, in heating scans with red/brown.

The H03–BAFKU$_2$ copolymer displays the richest phase behavior [2] (Scheme 3): In the solid state it is glassy, then, upon heating, this vitrimeric material transforms directly from glass to melt. In the liquid state, first a smectic (Sm) phase forms, followed by a nematic (N) one and finally by the isotropic (I) melt phase, in the order of increasing temperature. The lamellar structure, as shown in Scheme 2, exists in the solid (glassy) state, where the ordering of the BAFKU units in the lamellae is crystalline (Cr), as well as in the Sm and N state of the melt. The Cr → Sm and Sm → N transitions occur inside of the lamellae, while the N → I transition is connected with lamellae breakup to irregular and dynamically splitting/recombining 'nano-droplets' (final superstructure in Scheme 2). The H03–BAFKU$_2$ copolymer also is characterized by the highest volume fraction of the LC units ("BAFKU"), namely 52%.

The H11–BAFKU$_2$ copolymer somewhat differs from H03–BAFKU$_2$ [2] (Scheme 4) but it also is characterized by the same lamellar structure (see Scheme 2). This copolymer is glassy at the lowest temperatures, thereafter it transforms into a rubbery phase, which subsequently melts to a nematic liquid (without undergoing a smectic state) and it finally transforms into an isotropic liquid, in the order of increasing temperature.

H21–BAFKU$_2$ (Scheme 5) generally was found [2] to be very similar to H11–BAFKU$_2$, except for the values of the characteristic temperatures. The DSC transitions were much less intense in the longest copolymer: they were partly below DSC detection threshold.

The longer copolymers are dark red viscoelastic liquids at standard room temperature (25 °C), with melting/freezing points at +10/+5 °C (H11–BAFKU$_2$) and −12/−13 °C (H21–BAFKU$_2$). The mesogen-rich H03–BAFKU$_2$ is turbid (smectic) sticky and highly viscoelastic paste of orange color at 25 °C (dark red in nematic and isotropic melt) and its melting/freezing points are at +23/+11 °C.

The viscoelastic and rheological properties of the studied non-covalently crosslinked copolymers in the rubbery and in the molten state were investigated by multiple methods, while focusing on four aspects: First, the gelation behavior was studied at the transition melt/solid, as well as during thermotropic transitions in the melt. Secondly, the kinetics of thermally induced gelation to solid (or to partly crosslinked viscoelastic liquid) was characterized. Thirdly, the mechanical reversibility of the non-covalent crosslinks also was evaluated. Finally, the shear thinning (thixotropic) behavior was investigated, which also is related to the mechanical disconnection of crosslinks.

3.2. Reversible Gelation Processes Induced by Temperature Change

The thermally-induced gelation of the studied copolymers was investigated in temperature areas stretching from temperatures somewhere below their respective solid/melt transition, up to the region of isotropic melt. Temperature scans over the whole interesting range were carried out, in multi-frequency oscillatory deformation mode. The experiments were performed both in the cooling- as well as in the heating regime, in order to compare the inverse processes of crosslink formation and dissociation. As will be demonstrated further below, both the effects of thermotropic transitions in LC-nano-aggregates, as well as the wider-scale effects of nano-phase-separation (LC-lamellae fragmentation vs. growth) appear to play an important role in the gelation behavior. Generally, multiple gel-points were observed in the copolymers, up to three in case of H03–BAFKU$_2$. As a point of gelation, the point (the temperature) of *tan δ* crossover was sought (point of frequency-independence of *tan δ*), in accordance with the theory of Chambon and Winter [56].

H03–BAFKU$_2$: The results of the 'multi-frequency gelation tests' obtained for the H03–BAFKU$_2$ copolymer are shown in Figure 1: In Figure 1a,b, the temperature-dependence of the storage shear modulus (*G′*: blue curves), of the loss shear modulus (*G″*: green curves), as well as of the complex viscosity (*Eta**: black curves) is shown. Curves of each temperature-dependent magnitude were recorded at different frequencies (1, 2, 4, 8 and 16 Hz) and the order of the curves for these frequencies is denoted in the graphs. Figure 1a summarizes the results from the cooling run and Figure 1b the heating run (both at 1 °C/min). These graphs illustrate the temperature- and the frequency-dependence of the basic viscoelastic properties. Figure 1c,d and display the temperature-dependence of the loss factor (*tan δ*) alone, which was equally measured at the same multiple frequencies. Figure 1c shows the cooling

run and Figure 1d the heating run. These latter graphs were used to find the temperature-induced gel points of the studied material.

(a)   **(b)**

(c)   **(d)**
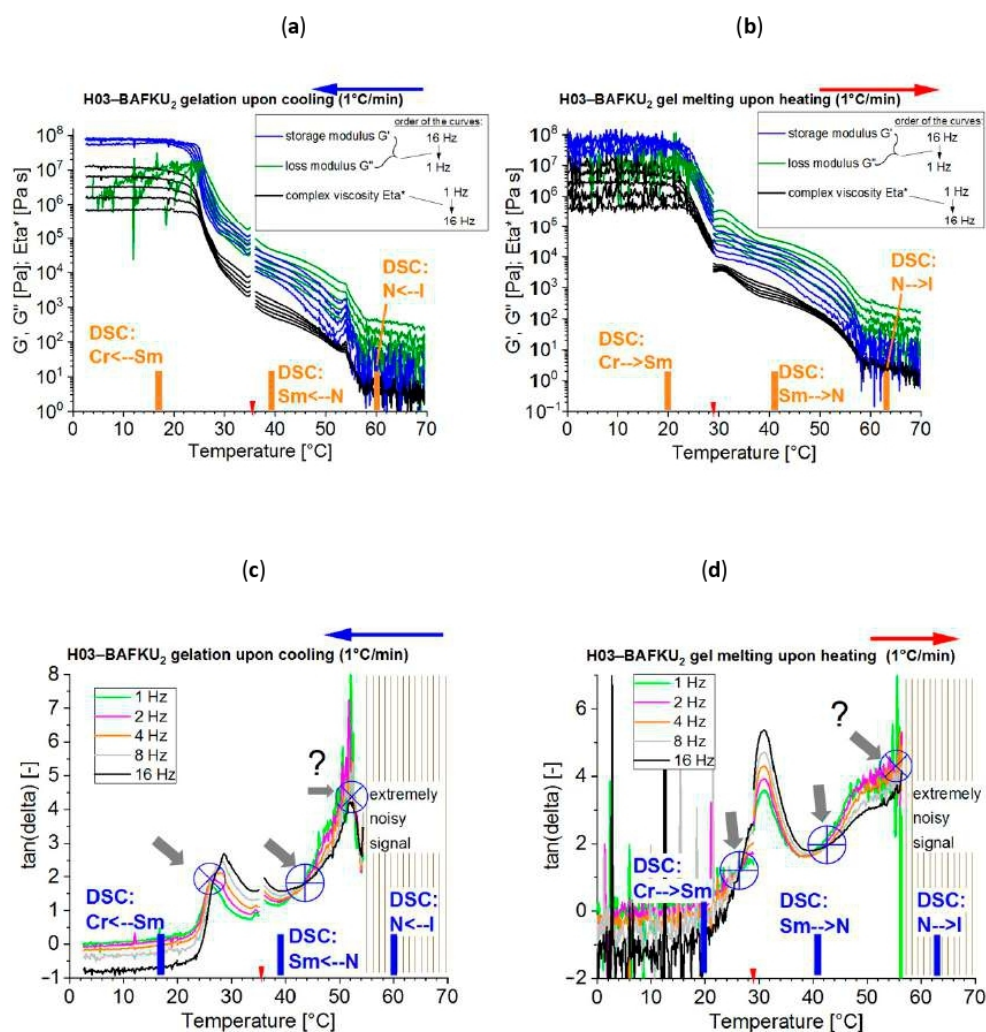
Figure 1. Multi-frequency temperature ramp tests carried out in the melting and rubbery temperature regions of H03–BAFKU$_2$: (**a**,**b**): temperature dependence of the storage shear moduli G' of the loss moduli G'' of the complex viscosities Eta* recorded at the simultaneously applied frequencies of 1, 2, 4, 8 and 16 Hz; (**a**): cooling scan; (**b**): heating scan; (**c**,**d**): detail of the sets of the tan δ curves with marked crossover (or near-crossover) points; (**c**): cooling scan, (**d**): heating scan; red markers indicate change in strain.

If the basic viscoelastic characteristics of H03–BAFKU$_2$ in the melting and in the low-temperature-melt region are evaluated (Figure 1a,b), it can be noted that this copolymer displays a 40 °C-wide region of thermally-induced transitions, where storage and loss moduli, as well as the viscosity change by many orders of magnitude, in several 'gradual steps'. At lower- (vitrimeric solid), as well as at higher temperatures (isotropic melt), the region of dramatic changes is bordered by 'plateau regions', where the mentioned magnitudes undergo little to moderate temperature-induced changes. The results recorded in the heating and in the cooling regime somewhat differ: A visible temperature shift is observed (delayed build-up of moduli and viscosity in the cooling run), which only partly correlates with the rather small shift (heating/cooling) in the temperatures of thermotropic

transitions of H03–BAFKU$_2$ which were determined by DSC in Reference [2] and which are included as markers in Figure 1. Also, the curves' shapes are somewhat different. Different dynamics of growth vs. fragmentation of nano-phase-separated lamellae might strongly contribute to the observed undercooling effect. It can be noted, that the complex viscosity is strongly frequency-dependent in the vitreous state and visibly frequency-dependent in the liquid-crystalline melt, while the frequency-dependence practically disappears in the isotropic melt.

The multi-frequency sets of *tan δ* = f(*T*) curves of H03–BAFKU$_2$ (see Figure 1c,d) indicate an interesting gelation behavior, with up to three gel points, both in the cooling and heating scan. Close to the solid/liquid transition, where a gelation would be expected, a narrowing (with *tan δ* curves nearly 'touching' in the cooling run) or a true crossover (in the heating run) of the curves indeed is observed. This gel point precedes a distinct *tan δ* maximum, which occurs at a somewhat higher temperature. The mentioned two features appear to be directly connected with the Cr/Sm transition in the lamellar aggregates of BAFKU end-groups: The gel-point marks the solid/liquid transition, while the maxima in *tan δ* can be assigned to energy absorption by friction of smectic layers in the lamellar aggregates (see Schemes 6 and 7).
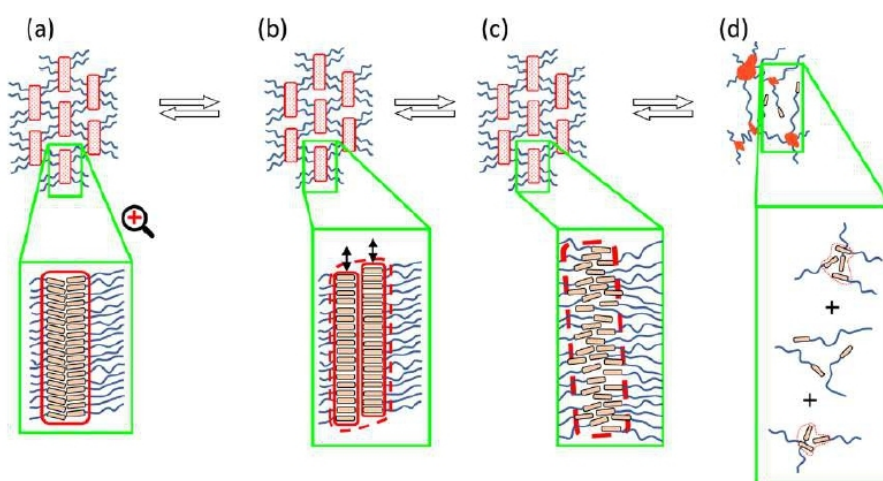
Scheme 6. Thermotropic transitions inside of the lamellar nano-aggregates of BAFKU: (**a**) crystalline lamellae in the rubbery state, (**b**) smectic lamellae in the liquid-crystalline (LC) melt, (**c**) nematic lamellae, (**d**) isotropic small droplet like aggregates in the isotropic melt.
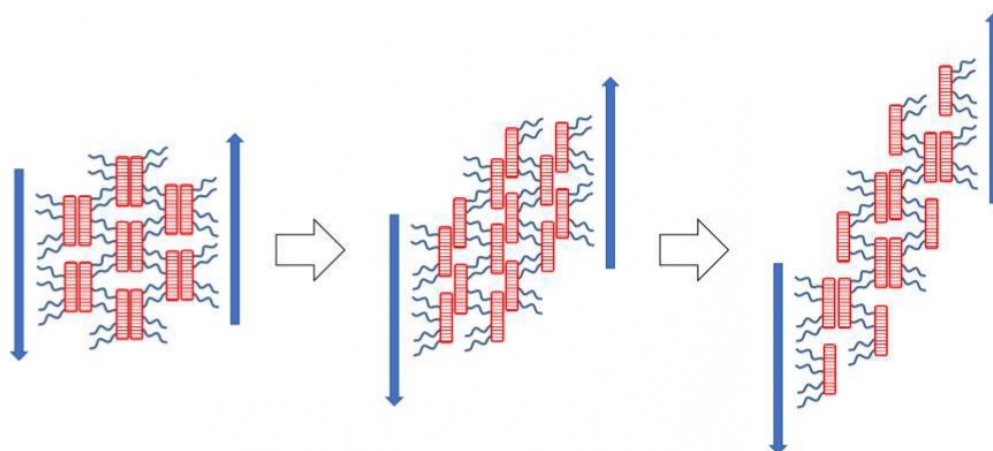
Scheme 7. Possible sliding of 2-dimensional layers in smectic lamellae of BAFKU and its role in flow of the liquid-crystalline melt.

At even higher temperatures, a distinct *tan δ* crossover is observed in both runs. This second gel point is can be correlated with the Sm/N transition (reported in Reference [2] and marked in Figure 2), which occurs at a temperature slightly below the second gel point. The physical reason for this gelation likely is (in the cooling run) the increased spatial crosslinking, via the transition from 1-dimensionally ordered nematic lamellae to 2-dimensionally ordered smectic lamellae (see Scheme 6) and possibly also the growth of more rugged lamellar superstructure upon this transition. (An opposite process occurs in the heating run).
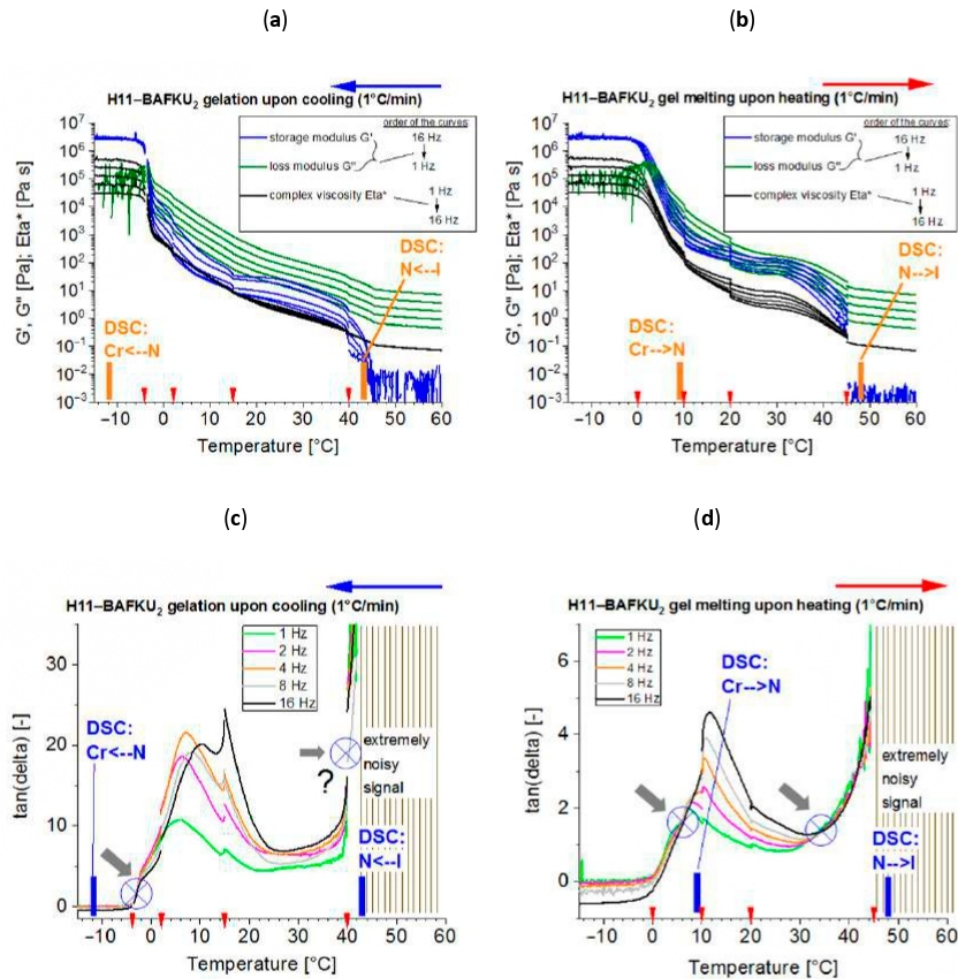
Figure 2. Multi-frequency temperature ramp tests carried out in the melting and rubbery temperature regions of H11–BAFKU$_2$: (**a,c**): temperature dependence of the storage shear moduli *G′* of the loss moduli *G″* and of the complex viscosities *Eta** recorded at the simultaneously applied frequencies of 1, 2, 4, 8 and 16 Hz; (**a**): cooling scan; (**b**): heating scan; (**c,d**): detail of the sets of the tan δ curves with marked crossover (or near-crossover) points; (**c**): cooling scan, (**d**): heating scan; red dotted lines indicate change in strain.

Finally, most likely a third gel point occurs at the temperature approaching the one of the N → I transition (reported in Reference [2] and marked in Figure 2), although the sensitivity of the experiments was not high enough to confirm definitely this third crossover. This gel point would correspond (upon cooling) to the formation of 1-dimensional crosslinking in isotropic droplet-like BAFKU nano-domains (see Scheme 6) and probably also to the growth of much more robust nematic-ordered

lamellar nano-aggregates, starting from droplet-like liquid ones. (An opposite process occurs in the heating run).

H11–BAFKU$_2$: The 'multi-frequency gelation results' obtained for the longer H11–BAFKU$_2$ copolymer are shown in Figure 2 (changes in basic viscoelastic properties in Figure 2a,b; analysis of gel points—*tan δ* crossovers in Figure 2c,d), recorded both as cooling run (Figure 2a,c) and as heating run (Figure 2b,d). The H11–BAFKU$_2$ copolymer displays similar trends like the shorter H03–BAFKU$_2$ but a notable difference is the absence of a smectic phase: Upon melting of the whole material, as well as of the BAFKU lamellae, the ordering in the latter transforms from crystalline to nematic (as reported in Reference [2]). A step is observed in the basic viscoelastic magnitudes at this temperature (Figure 2a,b), as well as a *tan δ* crossover (Figure 2c,d). This transition, similar to the corresponding DSC peak (reported in Reference [2] and marked in Figure 2) undergoes a strong undercooling in the cooling scan. The gelation to rubber/rubber melting (also Cr/N transition) is followed by a large maximum in *tan δ*, which can be assigned to energy absorption in the lamellar aggregates of BAFKU: In the heating scan, the mesogenic units become more mobile and additionally the lamellae more easily undergo splitting (see Scheme 8).
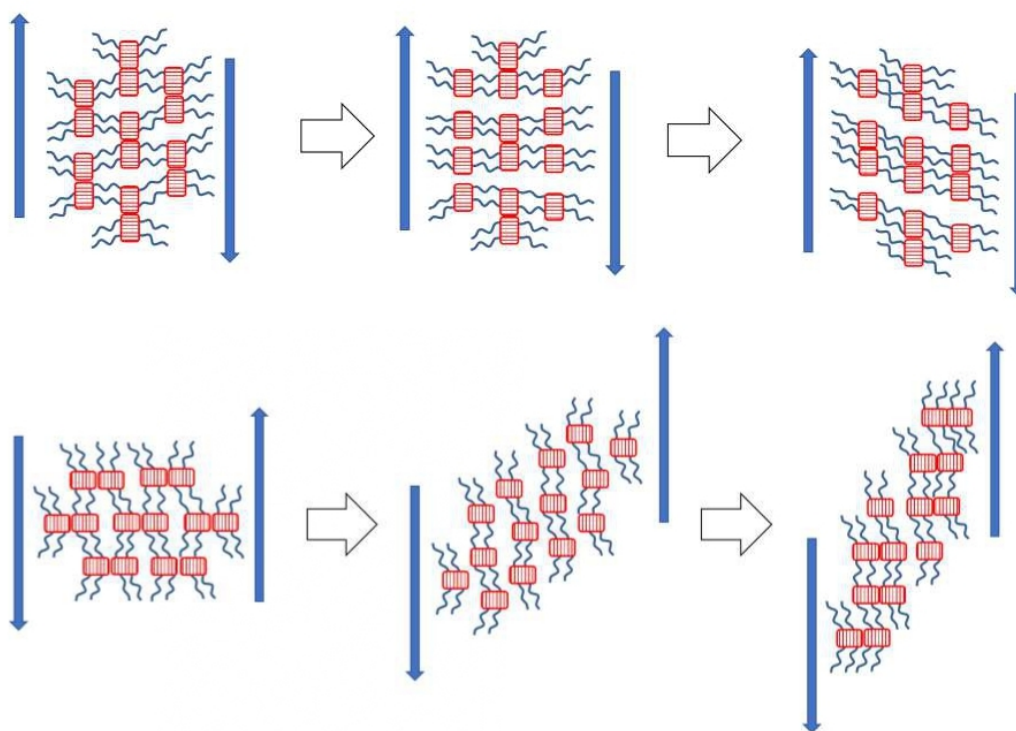
Scheme 8. Possible splitting of BAFKU lamellae in two different deformation modes and its role in flow of the liquid-crystalline melt.

A second gel point (*tan δ* crossover) as well as a distinct step in the storage modulus (and a flat step in viscosity and loss modulus) is observed near 45 °C, at a temperature close to the DSC peak of the N/I transition (reported in Reference [2] and marked in Figure 2). A similar N/I gel point was also observed in the copolymer H03–BAFKU$_2$. Similarly like in the latter case, there is only a small undercooling effect, if comparing the cooling and heating run of this transition. The *tan δ* crossover is well-visible in the cooling scan but its precise position might be influenced by thixotropy effects resulting from changed strain amplitudes (highlighted by red markers on the Temperature axis in Figure 2; the amplitude was changed in order to compensate for strongly decreasing sample resistance, in order to keep signal quality). Such thixotropy effects are distinctly visible on several occasions in

Figure 2. A distinct difference between the heating and cooling scans are the markedly lower values of *tan δ* in case of the cooling scan. This might be attributed to the mentioned thixotropy effects, which were different in case of cooling- and heating scan, because the cooling scans started with larger deformations.

H21–BAFKU$_2$: The longest copolymer generally displays nearly analogous features in the multi-frequency gelation tests, like the other 'long copolymer', the above-discussed H11–BAFKU$_2$, albeit with different characteristic temperatures. The results are shown in the Supplementary Information File, as Figure S1 (cooling run) and Figure S2 (heating run). H21–BAFKU$_2$ contains only 13.5 Vol.% of the mesogen units and hence the physical crosslinking via BAFKU aggregation in the nematic melt region (or more precisely region of where the BAFKU aggregates are nematic) is less efficient and the moduli *G'* and *G''* are markedly lower than in case of H11–BAFKU$_2$. The *tan δ* curves in the melt region are thus very noisy but nevertheless, a *tan δ* crossover in the region of the melting of the rubbery phase can be discerned, especially well in case of the heating run (Figure S2b). An adjacent region with *tan δ* maxima (similar like in H11–BAFKU$_2$) still can be recognized, albeit with some difficulty (heating run, Figure S2c). The suspected second *tan δ* crossover in the region of isotropization near 30 °C (invisible by DSC but clearly indicated by PLM in Reference [2]) cannot be discerned but the associated step in the *G'* = f(*T*) curves still can be seen, if the deformation amplitude is carefully selected (Figure S2a). Thixotropy effects are very strong in the melt of H21–BAFKU$_2$, which is attributed to a higher lability of the BAFKU aggregates, which are more dispersed in this copolymer. These effects can be seen especially well if comparing the sets of *tan δ* curves obtained for two different cooling runs carried out with strongly different deformation amplitudes, as shown in Figure S1c vs. Figure S1d.

3.3. Rate of Physical Gelation upon Quenching the Melt

An interesting aspect of the temperature-induced reversible crosslinking of via nano-aggregation of BAFKU units in the studied copolymers is the kinetics of this process. This could not be directly observed in the above-discussed experiments.

The kinetics was studied via 'quenching' polymer melt samples from the 'isotropic temperature' of 70 °C down to temperatures ranging between −50 and +60 °C. During the quenching and in the subsequent time period where the temperature was constant, the moduli of the tested samples were measured via an applied oscillatory deformation of constant frequency (1 Hz) and of a constant small strain (1%). Observation of the build-up and of the subsequent equilibration of the moduli gave a picture of the kinetics. The complete sets of results for all the three copolymers are shown in the Supplementary Information File, as Figures S3 and S4.

In general it was observed, that the temperature-induced gelation was relatively fast, with equilibration times ranging between 0.5 and 5 min. In case of slower gelations, especially of H21–BAFKU$_2$, it was possible to recognize that the gelation was a two-step process, starting with the rapid formation of small ordered aggregates of BAFKU end-groups from droplet-like isotropic liquid ones and followed by the slower growth of the aggregates to larger ones. Hence, the crosslinking process is not only connected with thermotropic (LC) transitions but also with the dynamics of nano-phase-separation. All the copolymers displayed similar trends.

H11–BAFKU$_2$: Selected results concerning the kinetics of the gelation of the isotropic melt of this copolymer upon quenching to different lower temperatures are shown in Figure 3. (All results are shown in Figure S3). The graphs in Figure 3 contain the time-dependent course of the storage and loss moduli (*G'* and *G''* respectively), as well as the course of the temperature of the sample. The equilibration time is short at the lowest quenching temperatures (40 s at −50 °C) but it gradually increases (see Figure S3). At +20 °C, it already is 240 s (6 min). The time value contains also the time needed for temperature equilibration, ca. 40 s in case of the +20 °C experiment in Figure 3. For final temperatures above +20°C, a distinct induction period appears, during which the moduli do not change and which makes most of the difference between the gelation times at the different final temperatures higher than +20 °C. This induction time is significantly longer than the time needed for

temperature equilibration (see Figure S3). The increasing induction time likely indicates the more difficult onset of LC lamellae growth (see Scheme 9) at higher final temperatures.
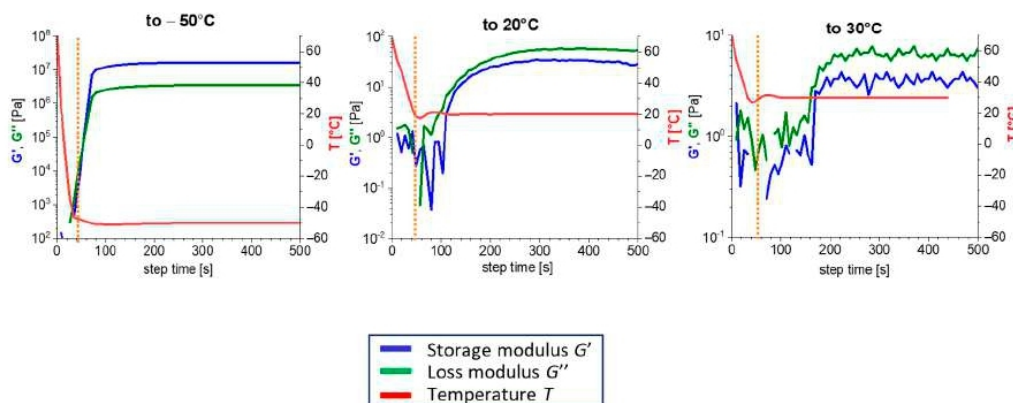
Figure 3. Exemplary kinetics of the change in storage (*G'*) and loss (*G''*) modulus (kinetics of physical gelation) upon quenching molten H11–BAFKU$_2$ from 70 °C down to −50 °C (left), to +20 °C (center) and to +30 °C (right); the entire set of results for the different final temperatures tested is shown in Figure S3; at final temperatures above +45 °C, practically no change in moduli is observed upon quenching.
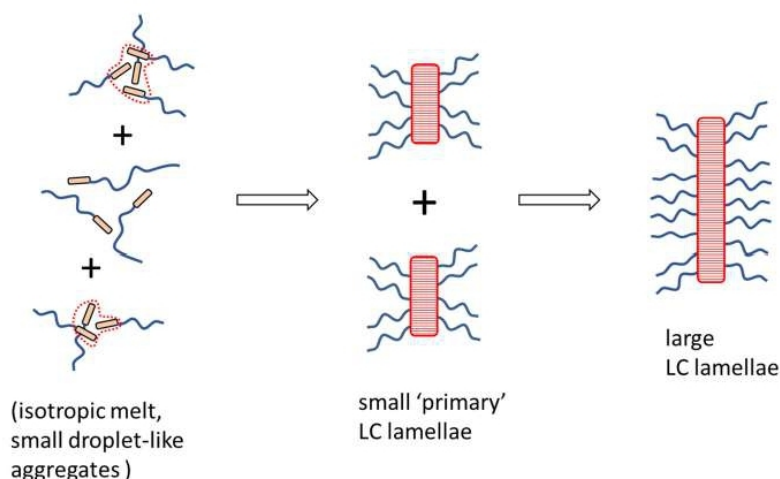
Scheme 9. Transition of isotropic melt to LC melt: ordering and growth of BAFKU nano-aggregates.

If the shape of the curves *G'* = f(*time*) and *G''* = f(*time*) is compared, similar courses are obtained if the 'hot melt' is frozen to a (rubbery) solid or only to a viscoelastic melt. In the latter case, the mentioned induction time prior to melt thickening appears as an additional feature. Also, the curves for *G'* have very similar courses and are always close to the ones of *G''* but in case of rubber as final state, *G'* has a higher value than *G''*, while the opposite case is found if cooling down to viscoelastic melt only.

The H21–BAFKU$_2$ copolymer displays fairly analogous gelation kinetics like H11–BAFKU$_2$ (see selected results in Figure 4 and all results in Figure S4) but the gelation process of H21–BAFKU$_2$ clearly displays a two-step character (see Figure 4, well visible above 4−0 °C). This can be assigned to a rapid formation of small 'primary' nano-aggregates of the BAFKU end-groups, which subsequently more slowly (second step in the curves) grow to larger, higher-functional-crosslinking ones (see Scheme 9). Induction periods prior to crosslinking are the longest in H21–BAFKU$_2$ among the tested copolymers, as well as the times of moduli equilibration. This appears to be connected with the very

long PDMS spacer segments and with the hence more difficult assembly of the domains which act as crosslinkers.
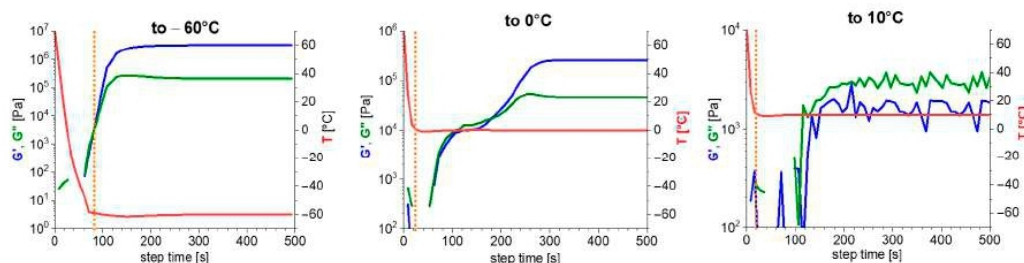
Figure 4. Exemplary kinetics of the change in storage (G') and loss (G'') modulus (kinetics of physical gelation) upon quenching molten H21–BAFKU$_2$ from 70 °C down to temperatures between −60 °C and +10 °C; the complete set of results for all the different final temperatures tested is shown in Figure S4; at final temperatures above +45 °C, practically no change in moduli is observed upon quenching the melt.

H03–BAFKU$_2$, a vitrimer, was tested only in its viscoelastic melt region. The gelation kinetics results are shown in Figure S5. It shows analogous trends to the ones observed for H11–BAFKU$_2$. A difference is, that in the smectic liquid region near the melting point (30 °C) of H03–BAFKU$_2$, the physical crosslinking achieves a much higher relative modulus increase (3 orders) than the nematic crosslinking in case of H11–BAFKU$_2$, although the absolute values of equilibrium moduli of both copolymers in the melting region are similar. At 30 °C, the sample H03–BAFKU$_2$ additionally displays visible thixotropy during the kinetics test: moduli somewhat decrease after initial build-up, as consequence of the oscillatory shear deformation of 1% amplitude. Another specific feature of H03–BAFKU$_2$ are the much shorter or even absent induction periods, if the isotropic melt is cooled down to temperatures higher than 30 °C. The longer times of equilibration are due exclusively to crosslinking. The absence of induction times in the 'viscoelastic gelation' of H03–BAFKU$_2$ can be attributed to the dominant (over 50%) volume fraction of the BAFKU mesogen, which facilitates the start of lamellae assembly.

3.4. Mechanical Disconnection of the Physical Network

After studying the thermal reversibility of the physical crosslinking via BAFKU units nano-crystallization, their resistance against mechanical disconnection was investigated. Several experimental methods were employed to this end: Short-time stability at small and high deformations was studied in strain sweep tests carried out at different characteristic temperatures. Additionally, creep tests and stress-relaxation tests were performed, in order to evaluate the crosslink stability on a moderately long time scale. The results indicated a high strength and durability of the non-covalent crosslinks in the rubbery state, if the temperature was sufficiently far below the melt solidification temperature. While approaching this temperature, the mechanical disconnection of the crosslinks became increasingly prominent.

3.4.1. Strain Sweep Tests

The strain sweep tests were carried out in oscillatory mode, at the frequency of 1 Hz. The applied deformation amplitudes were changed from 0.1% up to 1000%. Representative results, as obtained for H11–BAFKU$_2$ are shown in Figure 5.
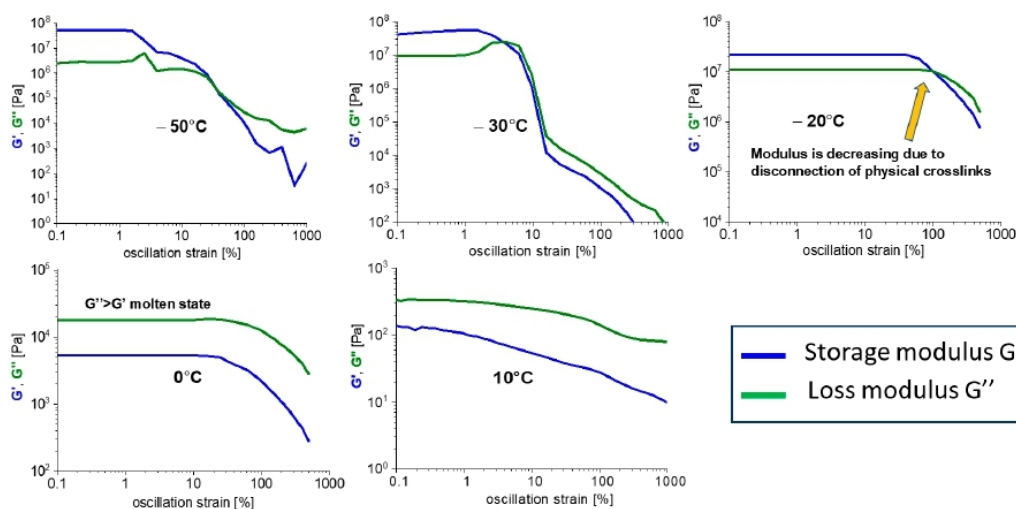
Figure 5. Disconnection of the physical crosslinks in H11–BAFKU$_2$ by mechanical strain: strain-dependence of storage (G') and loss (G'') modulus of H11–BAFKU$_2$ at temperatures from −50 to +10 °C—selected results; the full results collection is shown in Figure S6.

All the studied copolymers display similar trends, especially close are the two longer ones, the elastomers H11–BAFKU$_2$ and H21–BAFKU$_2$. The vitrimer H03–BAFKU$_2$ could be investigated only in the viscoelastic melt region, where it mostly shows analogous trends like the remaining copolymers. The collection of results for all the copolymers is shown in Figures S6–S8.

In case of H11–BAFKU$_2$, which is shown as an exemplary system in Figure 5 (all data are in Figure S6), it can be noted, that at very low temperatures far from the melting region (e.g., −50 °C in Figure 5) the physical network in the rubbery phase is rather robust: The sample undergoes macroscopic destruction at sufficiently high strains, which manifests itself as irregularities and sudden downward steps in the graphs. The mechanical destruction can also be observed visually. This damage occurs practically without dynamic disconnection of the physical crosslinks. At somewhat higher temperatures (−30 °C in Figure 5), a smoother destruction occurs, which besides macroscopic damage likely also includes some shear thinning in the material (crosslink disconnection). At even higher temperatures (−20 °C in Figure 5) no mechanical destruction is observed any more visually, the measured curves are smooth and the samples are able to endure even high deformations. The moduli smoothly decrease at sufficiently high deformations (100% and more at −20 °C in Figure 5), due to the disconnection of the physical crosslinks. At such a high deformation, the sample becomes liquid-like as G'' exceeds G' (G'' G' crossover). At even higher temperatures, for example, 0 and 10 °C in Figure 5, the strain dependence of the moduli shows similar trends like before but G'' always is higher than G', as the material already is a melt and also the 'shear degradation' of the moduli starts at lower strains. The curves also become flatter and the moduli smaller.

H21–BAFKU$_2$ (see Figure S7) differed from H11–BAFKU$_2$, only in the characteristic temperatures (really rigid crosslinks at −70 °C or lower),

The vitrimer H03–BAFKU$_2$ (see Figure 6 and all data in Figure S8) displays some interesting differences in the early post-melt state, which is a smectic phase: At 25 °C (see Figure 6), the melt is highly viscoelastic and the storage modulus G' even exceeds G'' at the lowest deformation amplitudes (below 1%). After a small plateau until the strain amplitude of ca. 1%, both moduli then display marked shear thinning, G', much more so than G''. This shear thinning behavior is similar to the one observed by Yang and Chang [49] for a well-characterized smectic polisiloxane-LC copolymer, albeit the latter had a different architecture than H03–BAFKU$_2$ (it was a side-chain LC-copolymer very rich

in LC). At higher temperatures, H03–BAFKU$_2$ displays similar trends in the viscoelastic melt like the other copolymers.
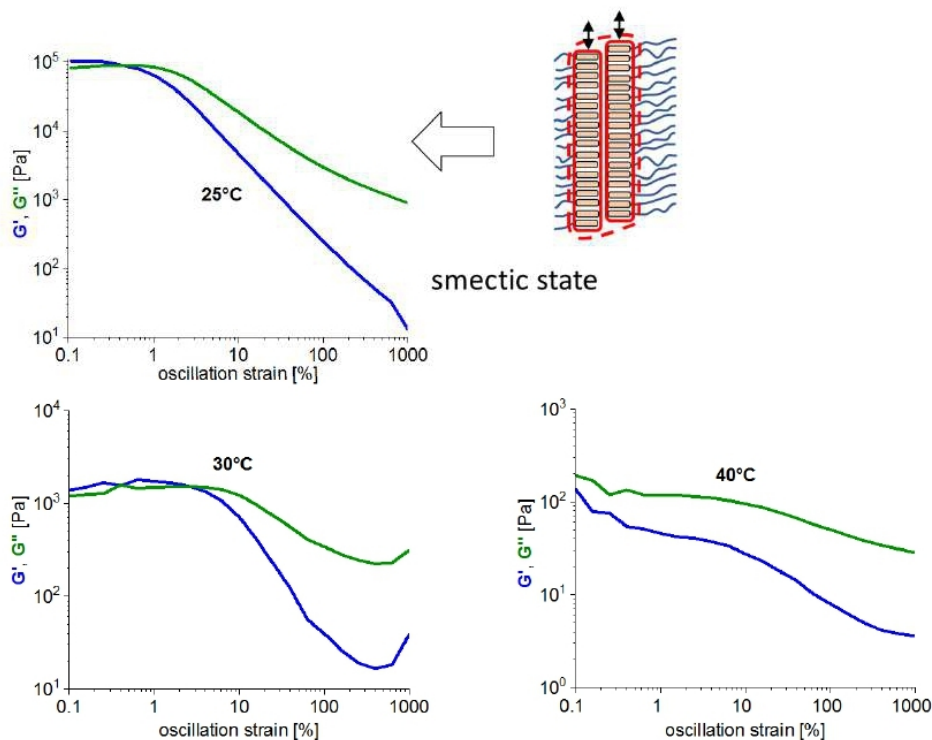
Figure 6. Disconnection of the physical crosslinks in H03–BAFKU$_2$ by mechanical strain: strain-dependence of storage (G') and loss (G'') modulus of H11–BAFKU$_2$ at temperatures from +25 to +40 °C—selected results; the full results collection is shown in Figure S8.

3.4.2. Creep Tests

The mechanical strength of the physical crosslinks also was studied in multi-step creep experiments, in which a constant stress was applied in each step and the resulting time-dependent strain was observed. After each loading step, a recovery step with stress automatically adjusted to zero was carried out. The copolymers displayed similar trends in their respective characteristic temperature regions. The crosslinks were found to be robust only in the low-temperature part of the rubbery region.

H11–BAFKU$_2$: Representative results for the copolymer H11–BAFKU$_2$ are shown in Figure 7, while the complete collections of results for all the three copolymers can be seen in Figures S9–S11. It can be seen, that in the low-temperature part of the rubbery region (−50 °C in Figure S9) nearly no creep (in view of the error margin) occurs on the time scale of 3 min at any applied stress (up to 10,000 Pa). In the warmer temperature region of the rubbery phase (−20 °C in Figure 7), distinct creep starts at 10,000 Pa and is no more fully recovered. At −5 °C, not far from the melting region, creep is observed already at the lowest loadings, although significant elastic recovery still occurs, especially at lower stress loadings. By applying 10,000 Pa at −5 °C, the sample is 'shear-liquefied' and an extreme deformation results: see inlay with different y-axis scale in the graph on the right side in Figure 7. This extreme deformation is plastic and does not significantly recover. At +5 °C and at higher temperatures, only plastic deformation without any recovery occurs and the strains resulting from the applied stresses become very large, as the sample becomes liquid, albeit a nematic viscoelastic one.
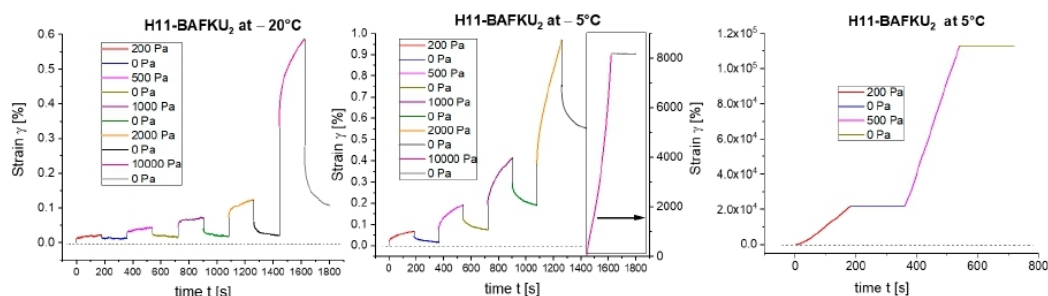
Figure 7. Multi-step creep tests of H11–BAFKU$_2$ at the temperatures of −20, −5 and +5 °C; stresses ranging between 200 and 10,000 Pa were applied, followed by recovery steps (at 0 Pa); more results at different temperatures are shown in Figure S9.

H21–BAFKU$_2$: The longest copolymer which displays the lowest melting point of the rubbery phase, H21–BAFKU$_2$, generally displays analogous trends like the shorter H11–BAFKU$_2$ (see results in Figure S10). In the rubbery region at low applied stresses, the creep tendency of H21–BAFKU$_2$ is smaller than in case of H11–BAFKU$_2$ but at the highest stresses, it is the longer copolymer which creeps more. This might be the combined effect of more numerous elastically active entanglements in H21–BAFKU$_2$ (due to longer chains) on one hand, as well as of smaller and hence less strong BAFKU aggregates (physical crosslinker). In this context, it is interesting that in the early post-melt nematic state, the sample still exhibits a considerable elastic recovery and starts to flow only if 2000 Pa or more are applied.

H03–BAFKU$_2$: The shortest copolymer, the vitrimer H03–BAFKU$_2$, could only be accurately rheologically investigated in the melt region. The results in Figure S11 clearly show, that from +15 °C upwards, the melting material already is fully plastic, with no significant elastic recovery.

3.4.3. Stress Relaxation

The mechanical stability of the physical crosslinks was further studied by means of stress relaxation tests, which practically evaluated 'internal creep phenomena': A sample, in which the crosslinks are dynamic, eventually would fully adjust to the new deformed shape via disconnection and more favorable recombination of crosslinks, behaving similarly like a viscoelastic liquid. All the copolymers displayed similar trends in their respective characteristic temperature regions, like in case of creep tests.

H21–BAFKU$_2$: Stress relaxation results for the longest copolymer, H21–BAFKU$_2$, are shown in Figure 8, while the results for the remaining two copolymers can be seen in Figures S12 and S13.

At low temperatures in the rubbery plateau (−50 °C in Figure 8), there is a small and fast initial relaxation, followed by practical time-independency of the measured stress (on the time scale of 10 min). The initial small relaxation might be due to the disconnection of easily reversible entanglements. At +15 °C, in the warmer temperature region of the rubbery phase, the initial fast relaxation becomes more intense, especially at higher applied strains but the measured stress seems to approach a non-zero final value (in the mid-term). At 0 °C, in the early nematic melt region, the stress relatively quickly relaxes ca. 85% of its value and subsequently stabilizes on a slowly decreasing course. The less than complete rapid stage of the relaxation seems to be connected with permanent entanglements, which are due to long H21 chains and to the stabilization of the entanglements by residual physical crosslinking (via BAFKU lamellae) in the nematic melt. At 20 °C, in the warmer region of the nematic melt, the stress relaxation is nearly immediate: the measured stress value after the applied deformation runs constantly at 0 Pa.
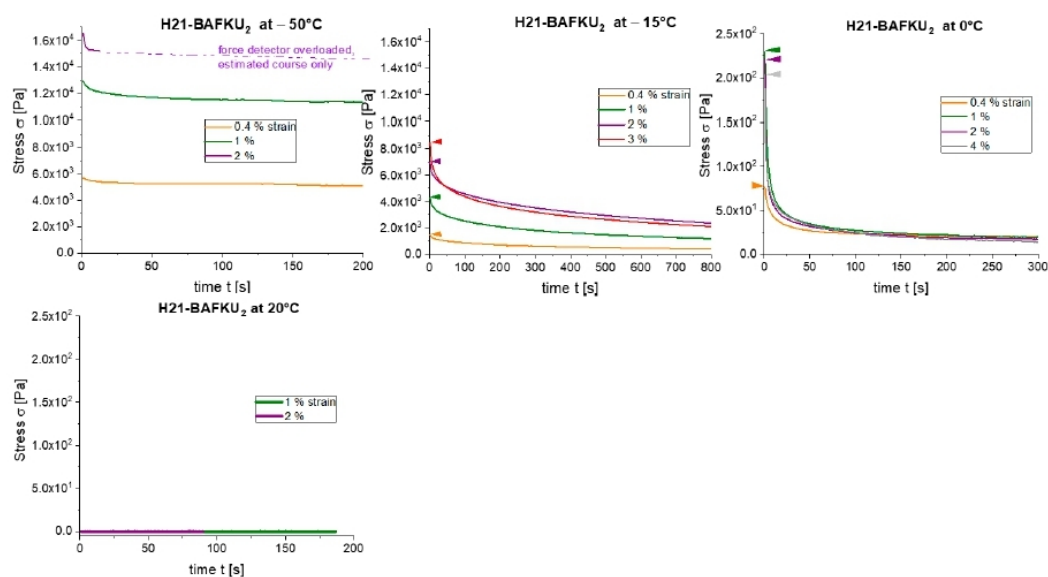
Figure 8. Stress relaxation tests of H21–BAFKU$_2$ at different temperatures; at each temperature, several constant strain values were applied.

H11–BAFKU$_2$: The shorter elastomer H11–BAFKU$_2$ displays very similar trends like H21–BAFKU$_2$ (see results in Figure S12) but the entanglements' effect is nearly absent, so that ca. 100% of the stress relaxes in the rapid relaxation stage already at the end of the temperature region of rubber melting (at +5 °C). A new interesting (albeit small) effect in this copolymer is, that at +5 °C and at high applied initial deformation, the stress relaxation in the viscous nematic melting material overshoots the value of zero stress and reaches small negative values. This likely is caused by shear-induced ordering of the nematic lamellae and of the whole lamellar structure, which is dynamic at this temperature. A similar effect of higher strength was observed for H03–BAFKU$_2$, which contains more of the mesogen, while the effect is absent in H21–BAFKU$_2$.

H03–BAFKU$_2$: The melt region of the vitrimer H03–BAFKU$_2$ (see Figure S13) displays similar characteristics like the H11–BAFKU$_2$ melt but the relaxation of the relatively low-molecular H03–BAFKU$_2$ is faster: At +15 °C (zone of glass melting), the fast stage of the relaxation already is nearly quantitative. The 'relaxation overshoot effect' is markedly more intense in H03–BAFKU$_2$ than in H11–BAFKU$_2$ and it occurs even in case of small initial deformations. It is the strongest in the early smectic melt region (at 25 °C).

3.5. High-Frequency Stiffening and Self-Healing Effects

Frequency sweep tests (1 mHz to 100 Hz) were performed with the prepared copolymers, in order to evaluate high-frequency stiffening and eventual frequency-induced transitions between liquid-like and rubber-like behavior at several characteristic temperatures. With the elastomers H11–BAFKU$_2$ and H21–BAFKU$_2$, the tests were conducted in the rubbery and in the liquid state (see Figure 9, as well as Figures S14 and S15), whereas with the vitrimer H03–BAFKU$_2$, this characterization was performed only in the melt range (Figure S16). The tests proved frequency stiffening in the copolymers, as well as self-healing effects at favorable temperatures, with crystalline as well as with smectic BAFKU lamellae.
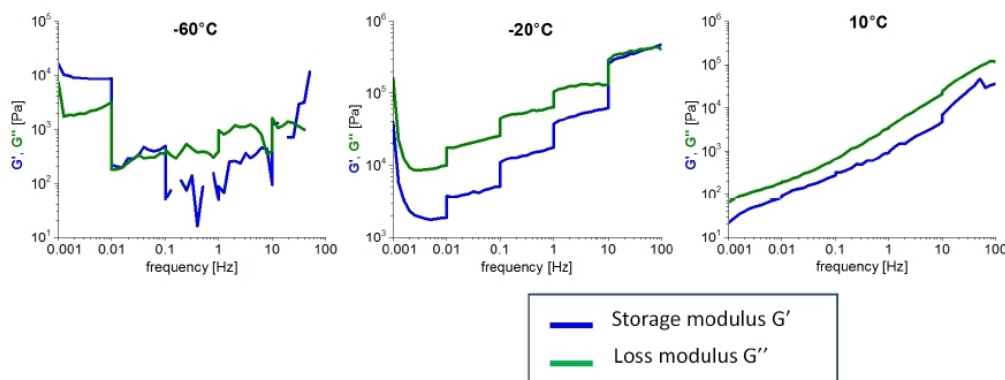
Figure 9. Frequency-stiffening of H11–BAFKU$_2$ observed in frequency sweep tests (1 mHz to 100 Hz) conducted at −60 to +10 °C—selected results; the full results collection is shown in Figure S14; the strain amplitude was different in each frequency decade, ranging from 50% at 1 mHz to 1% at 100 Hz; the effect of strain-induced damage to the network, as well as of its recovery between the frequency decades is clearly visible, especially in case of G′ curves at lower temperatures.

An important experimental detail was the division of the frequency sweeps into decades of points for each frequency order, where different deformation amplitudes (higher strains at low frequencies) were applied in order to achieve optimal signal quality. For technical reasons, the rheometer made brief (in the range of seconds) delays between the decades. These delays made possible to observe eventual internal self-healing after endured strain-damage, as steps in the measured curves.

H11–BAFKU$_2$: All the three copolymers display a very similar behavior in the frequency sweep tests. As an exemplary system, the results for the copolymer H11–BAFKU$_2$ are shown in Figure 9 (selected graphs only, all results are in Figure S14). The following trends can be observed: At low temperatures deep in the rubbery region (e.g., at −60 °C, see Figure 9), G′ always prevails over G″, even at the lowest frequency of 1 mHz and the samples hence are truly rubber-like. The physical crosslinks are robust in this temperature region, so that the test at −60 °C with high applied strains results in macroscopic mechanical damage (irregular curves, similarly like in the strain sweep test of the same copolymer at −50 °C shown in Figure 5; the damage worsens during the delays). At higher temperatures in the rubbery region (−20 °C), no macroscopic destruction is observed but only shear-thinning damage to the crosslink density. During the experimental delays, the internal damage is at least partly repaired by crosslink re-combination. The self-healing is very fast, as it generates marked effects during the brief (multi-second) delays. As the rubbery phase is fully molten (see example in Figure 9: 10 °C), the shear-thinning at low frequency (combined with large deformation amplitude), as well as the self-healing effects completely disappear and the measured curves become nearly linear in the nematic melt. Already below the melting region, G″ starts to dominate over G′ but G′ increases more steeply with frequency. In the nematic melt and at higher temperatures, G′ and G″ have a parallel course.

Except in the region of mechanical damage, all three copolymers display frequency-stiffening in the solid and in the molten state, like typical linear polymers.

H21–BAFKU$_2$: This sample displays generally nearly identical trends like H11–BAFKU$_2$, except for a lower melting temperature (see Figure S15).

H03–BAFKU$_2$: The shortest copolymer, H03–BAFKU$_2$ (Figure S16), which lacks a rubbery phase, also displays similar trends like H11–BAFKU$_2$ and H21–BAFKU$_2$, if the viscous melt ranges are compared. An interesting feature are the shear thinning and self-healing effects, which are observed in H03–BAFKU$_2$, although it is in the molten state: These effects are limited to the range of the smectic BAFKU aggregates, which split and self-heal similarly like the crystalline aggregates in the 'warmer rubbery phase' of the longer copolymers. In the nematic region of the melt, H03–BAFKU$_2$ behaves analogically to the longer copolymers.

3.6. Thixotropy

The physical nature itself of the crosslinking in the studied copolymers suggests that thixotropy (shear-thinning) effects could be prominent in the molten state and even at the fringe of the rubbery state, if the temperature is not very distant from the respective melting point. The final part of this study hence was dedicated to the evaluation of thixotropy. The effect was evaluated in oscillatory experiments, as well as in steady flow experiments (thixotropic loop). Very strong thixotropy could be documented and also a very fast recovery of the original viscoelastic properties. The latter was nearly instantaneous in case of samples which underwent oscillatory shear and somewhat slower in samples which have endured continuous shear flow.

As first experimental indication, several of the further-above-discussed characterization methods already indicated thixotropy, for example, the multi-frequency gelation tests (Figures 1 and 2, effect of switching the strain amplitude) or the kinetics of physical crosslinking upon melt quenching (Figure S3 at 10 °C: decrease of moduli after initial build-up). The mechanical crosslink disconnection observed in the strain sweep experiments (Figures 5 and 6) also can be considered a thixotropic effect. The strong effect of the applied different deformation amplitudes on the measured moduli is well visible in Figures S17–S20.

3.6.1. Oscillatory Tests of Thixotropy and of Recovery of Viscoelasticity

Direct tests of thixotropy and of the recovery of viscoelastic properties are shown in Figure 10, on the example of H11–BAFKU$_2$: The sample was subjected to an oscillatory shear deformation with the constant frequency of 1 Hz, while the deformation amplitude was multi-step-wise changed between the values of 0.1% and 5030%.
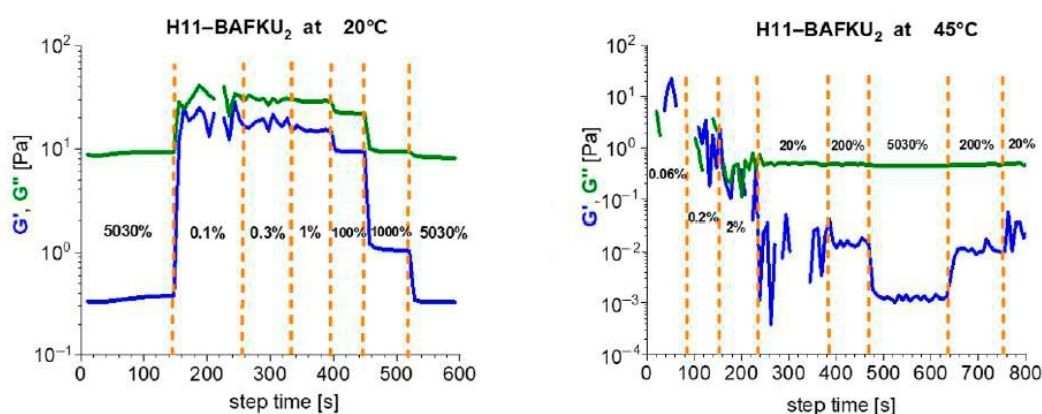
Figure 10. Exemplary thixotropy tests carried out on the copolymer H11–BAFKU$_2$ at 20 °C (**a**) and 45 °C (**b**); the tests were performed after a preparatory procedure, which consisted in heating up to the isotropic state (at 80 °C), followed by cooling down to the experiment temperature and waiting 5 min for equilibration (during which no deformation occurred); the thixotropy tests were conducted as rheological time sweeps conducted in several subsequent stages differing in the value of the applied constant deformation (strain) amplitude.

The tests were conducted at two temperatures: at +20 °C, not far above the melting point and at 45 °C, close to the point of isotropization of the nematic melt. It can be seen that at both temperatures, the storage (elasticity) modulus increases by more than two orders if going from the very high deformation amplitude of ca. 5000% to the small one of ca. 0.1%. The loss modulus displays a markedly lower sensitivity to deformation amplitude than the storage modulus.

Most importantly, it can be noted, that the thinning or the thickening of the copolymer melt occurs practically immediately upon the change of the deformation amplitude, also in case of smaller step-wise changes.

3.6.2. Thixotropic Loop Tests

The thixotropy of the studied copolymers was more profoundly investigated by standard thixotropic loop tests. In the first stage of these tests, the shear rate was continuously raised from 0 to $100\,s^{-1}$ and subsequently continuously reduced again to $0\,s^{-1}$. In a second stage, a fast scan was done of the higher shear rates, where several points were measured, namely at 100, 200, 300, 400, 300, 200 and $100\,s^{-1}$, in this order. In case of sufficiently slow re-generation of the elastic structures in the liquids, a distinct hysteresis would be expected between the 'shear-rate-up-curve' and the 'shear-rate-down-curve'. It was found that the copolymers display mutually similar trends in their respective characteristic temperature regions. The results indicate very fast recovery of flow-induced damage to crosslinking.

$H11–BAFKU_2$: The shorter elastomer $H11–BAFKU_2$ (see Figure 11) generates a considerable resistance, if measured in the boundary region between rubber and the liquid nematic phase at $+5\,°C$. Only a limited shear rate range could be investigated, up to $30\,s^{-1}$. A visible albeit not very large hysteresis of the curves of shear-rate-dependent stress and viscosity is observed at this experiment temperature, as well as oscillations in the 'down-curve' at lower shear rates. Both effects likely can be attributed to the behavior of the lamellar BAFKU nano-aggregates, which are on the boundary between the frozen crystalline state and the more dynamic nematic state. Their re-organization upon shearing is no more very fast, so that some shear damage persists on the time scale of the experiment. The oscillations can be possibly caused by the tumbling of fragments of the lamellar structure, in which the BAFKU lamellae are crystal-like and rigid. At $+20\,°C$, in the middle of the nematic temperature region, the hysteresis area between the thixotropic curves is very slim, both in the continuous loop up to $100\,s^{-1}$, as well as in the test of the high shear rates (up to $400\,s^{-1}$). At a first glance, the nearly negligible hysteresis might appear as a contrast to Figure 10 further above, where at the same temperature, oscillatory shear of high amplitude generates a thixotropic drop in modulus by nearly three orders. However, in Figure 10, the modulus (and hence the stress, as well as the complex viscosity) also is shown to recover immediately (in less than 1 s) if the oscillatory amplitude is reduced. This ultra-fast recovery in fact is in good agreement with the very slim hysteresis observed in the loop experiments in Figure 11. The still observed small hysteresis means that in continuous flow, some more intense damage to the elastic structure is done, which is not fully and immediately recovered during the continuous change of the shear rate. If the shear-rate-induced decrease in viscosity is evaluated, it can be noted that most of the shear thinning occurs between 0 and $20\,s^{-1}$ (largest part of it between 0 and $5\,s^{-1}$).

At $80\,°C$, in the isotropic melt region, the hysteresis in the thixotropic loop graph completely disappears, while an initial drop of viscosity upon the onset of shearing is observed, similarly like at the lower temperatures but it occurs in a narrower range of shear rates. After that, the characteristics are Newtonian. The initial high viscosity can be attributed to 'soft crosslinking' by droplet-like isotropic aggregates of BAFKU end-groups

$H21–BAFKU_2$: The longest copolymer $H21–BAFKU_2$ (see Figure S21) displays similar trends in thixotropy loops like $H11–BAFKU_2$. In spite of the lower melting point, its melt at $0\,°C$ generates a considerable resistance (and elasticity), as noticed already in case of creep experiments. Standard thixotropic loop tests were possible only with small maximum shear rates, where very high viscosity and a very marked hysteresis (Figure S21, top row) were observed. Due to the low content of the physically crosslinking BAFKU units, however, this copolymer can be more easily liquefied by intense shearing, than the shorter ones. After forcefully applying a $100–400–100\,s^{-1}$ loop, a dramatic shear thinning was achieved. A subsequent measurement of the continuous thixotropic loop ($0–100–0\,s^{-1}$) yields a wholly different thixotropic profile than in case of an intact sample (see Figure S21, last graph of top row), characterized by small viscosity (nearly two orders below original values) and a slim

hysteresis. The liquefication is possible because the recovery of elastic structures is slow at 0 °C in H21–BAFKU$_2$. At 20 °C, in the nematic region, the hysteresis of H21–BAFKU$_2$ is very slim but discernible in the continuous loop up to 100 s^{-1} and well visible albeit still moderate in the loop up to 400 s^{-1}. This stronger tendency to hysteresis might be due to the mentioned entanglements. At 80 °C, H21–BAFKU$_2$ displays no more hysteresis, in analogy to H11–BAFKU$_2$.
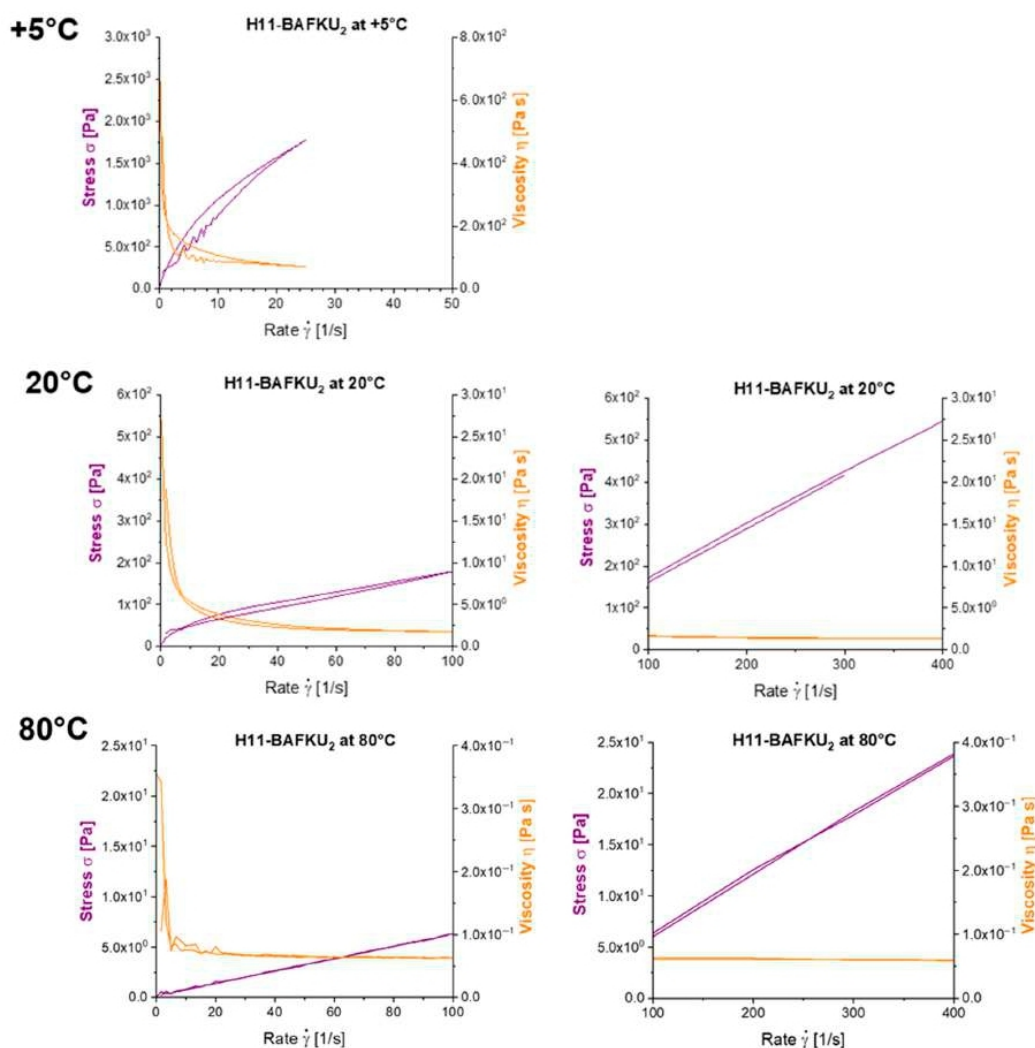
Figure 11. Thixotropic loop tests (dependence of shear stress and of viscosity on the shear rate) for the copolymer H11–BAFKU$_2$ at +5, 20 and 80 °C: at the left are continuous tests with shear rates rising up to 100 s^{-1}, at the right are step-wise tests with shear rates between 100 and 400 s^{-1}.

H03–BAFKU$_2$: The shortest copolymer, H03–BAFKU$_2$ (see results in Figure S22), displays the strongest hysteresis tendency in its thixotropic loop characteristics among the studied products. Only in the isotropic melt at 80 °C, (see Figure S22), the hysteresis is nearly absent. The nematic phase of H03–BAFKU$_2$ (50 °C, see Figure S22) displays the most distinct hysteresis among the nematic phases of the studied copolymers, as well as irregular oscillations of the curves. The hysteresis is even wider in the smectic phase (35 °C, see Figure S22), where also the strongest oscillations of the curves are observed, if shear rates higher then ca. 2 s^{-1} are applied. At 25 °C in the smectic phase, only limited shear rate scans were possible, which also display a significant hysteresis. Generally, it seems that

in H03–BAFKU$_2$, except at isotropic temperatures, the splitting of lamellae, as well as tumbling of fragments of lamellar structure (somewhat similar to domain tumbling in LC polymers discussed in Reference [37]) plays a strong role in the flow behavior and in thixotropic loop tests.

3.7. Comparison of Rheological Behavior of the Studied and of Classical LC Polymers

In view of all of the above-discussed results, it is interesting to compare the mechanisms of flow in the studied copolymers and in classical liquid-crystalline polymers (LCPs). The latter were discussed in the Introduction: The model of three regions of flow [31,32], as well as the Larson-Doi polydomain model [33,34] well describe the rheology of most LCPs, which are typically very rich in mesogen units. The flow mechanism corresponding to these models is summarized in Scheme 10: At the lowest shear rates, a tumbling of small oriented LC domains occurs (region I). At higher shear rates, these domains gradually diminish and an increasing number of macromolecules join the more or less flow-aligned 'nematic sea', while some domains still persist (region II). Finally, in region III, all material consists of the 'nematic sea'. Structural features of the respective LCPs influence the prominence and the properties of the rheological regions.
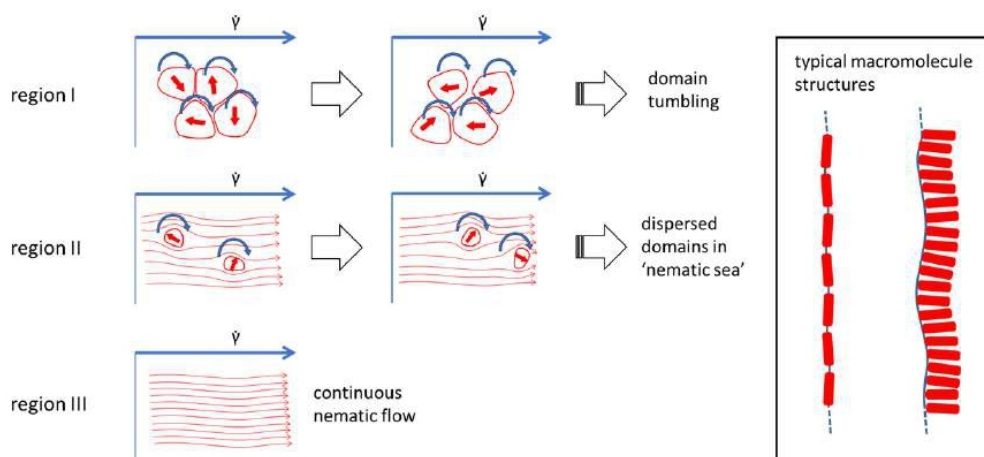
Scheme 10. Typical three-region flow behavior of liquid crystalline polymers [31–34].

In contrast to the typical LCPs, the presently studied copolymers are much less mesogen-rich, they contain 52, 37 and 16 Vol.% of mesogen, respectively. Additionally, they undergo strong nano-phase separation of the highly flexible central PDMS chains from the rigid mesogenic diaromatic azo end-groups. This phase separation, which persists also in the liquid phase, appears to play a key role in the mechanical as well as in the rheological properties of the studied copolymers. Scheme 11 illustrates the main factors, which appear to play a role in the flow behavior of the presently studied copolymers: (1) the splitting and recombination of the lamellae formed as result of the phase separation, which are liquid-crystalline in the molten polymers at not overly high temperatures; (2) the thermotropic phase transitions in these lamellae, which change their stiffness and the dynamics of their splitting and re-combination; both the effects (1) and (2) seem to be responsible for the multiple gel points observed in the copolymers; (3) finally, also the entanglements of the elastic PDMS chains were found to play a certain role.

If comparing the presently studied PDMS–BAFKU$_2$ compounds with a copolymer of similar basic architecture studied by Winter, Lin and co-workers [52], some similarities can be noted, like a higher viscosity of the nematic melt than of the isotropic, as well as the possibility of shear induced transition from solid to liquid state. Both effects in both systems are connected with the nano-phase-separation of the LC end-groups. The comparison further shows, that in the presently studied copolymers, the much-increased flexibility of the central chain, as well as a higher phase-separation tendency of the

constituent segments, tremendously increase the rate of recovery of strain- or even of flow-induced damage (e.g., the above-discussed immediate recovery during oscillatory tests).
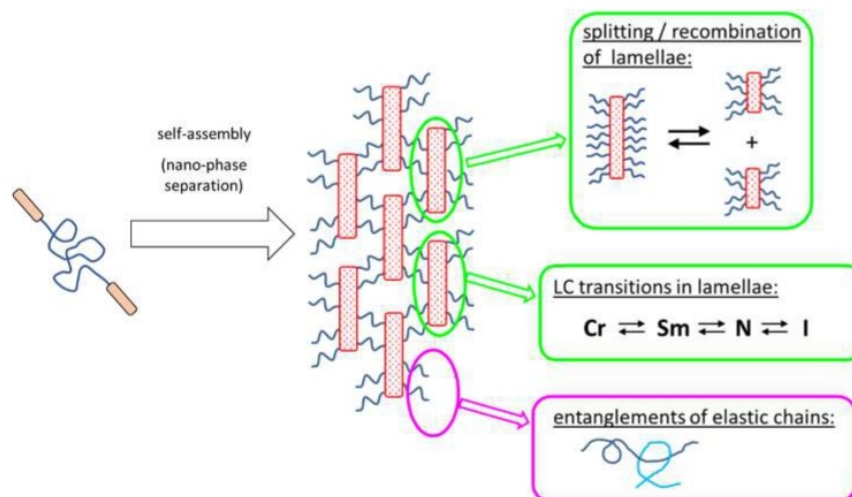
Scheme 11. Mechanisms of flow in the studied nano-phase-separated copolymers.

4. Conclusions

– Physically crosslinked thermo-reversible low-temperature-melting rubbers, based on linear polydimethylsiloxane (PDMS) capped in α,ω-positions with liquid-crystalline (LC) building blocks called "BAFKU", were studied concerning their viscoelastic and rheological properties in melt, as well as in the rubbery state.

– The properties of three copolymers were compared, which differed in the length of the central PDMS chain, namely DMS H03 (8.6 dimethyl siloxane repeat units), DMS H11 (16.3-mer) and DMS H21 (64.4-mer).

– Physical crosslinking via nano-aggregation of BAFKU units in all three tested copolymers was found to be fairly efficient and very large step-wise changes of elasticity and viscosity were observed, which correlated with the thermotropic properties of the crosslinks.

– The rheological behavior of the copolymers was found to be controlled by an interplay of nano-phase separation of the LC end-groups (growth and splitting of their aggregates) and of the thermotropic transitions in these aggregates (which change their stiffness). Entanglements of the elastic PDMS chains also were found to play a role.

– In contrast to LC-rich liquid crystalline (co)polymers (LCPs), the studied copolymers display viscosity increase if going form isotropic to nematic (or further to the smectic) state, because their viscoelasticity is controlled by the larger-scale morphology, which is responsible for the physical crosslinking. The latter in turn is controlled by nano-phase separation and by the strengthening or loosening of the aggregates of LC units via thermotropic transitions.

– The copolymers display up to three gel points, if a temperature scan (in both directions) is performed in the range from rubbery state to isotropic melt. The gel points correlate with the thermotropic transitions (I/N, N/Sm and Sm/Cr in the shortest copolymer and I/N, N/Cr in the longer ones) and with the associated changes in stiffness and dynamic size of LC nano-aggregates.

– The kinetics of (physical) gelation to network is fairly fast if induced by temperature (abrupt melt cooling): between 0.5 and 3 min (typically ca. 1 min). It slows down at higher final temperatures. This kinetics is controlled by temperature-dependent nano-phase-separation dynamics.

- The physical crosslinks can be reversibly disconnected by large mechanical strain in the rubbery state and in the melt (thixotropy in the latter case). The kinetics of subsequent re-generation was found to be extremely fast: ca. 1 s in oscillatory tests.

- Thixotropic loop tests, in which the samples were subjected to continuous flow, also indicate a very fast regeneration of destroyed physical crosslinks, so that only very small hysteresis is observed in these tests, in spite of very strong shear-thinning tendency in all the copolymers in wide temperature ranges. Nevertheless, in contrast to oscillation experiments, the crosslink regeneration in continuous flow is not immediate.

- The 'warmer' rubbery phase of the longer copolymers can be relatively easily transformed to liquid by strong shear.

- Frequency-stiffening was observed in the rubbery state, as well as in the melt. Such a behavior is characteristic of classical elastomers and linear polymers.

- The studied low-temperature elastomers might be of interest as passive smart materials for advanced applications such as viscoelastic coupling for example, in soft robotics (transitions melt/viscoelastic melt/rubber) but also as damping materials (energy absorption via physical crosslink disconnection). Additionally, the incorporated LC building blocks of azo type open the possibility of reversible UV-light-induced switching of material properties.

References

1. Jaunich, M.; Stark, W.; Wolff, D. Comparison of low temperature properties of different elastomer materials investigated by a new method for compression set measurement. *Polym. Test.* **2012**, *31*, 987–992. [CrossRef]

2. Horodecka, S.; Strachota, A.; Mossety-Leszczak, B.; Strachota, B.; Šlouf, M.; Zhigunov, A.; Vyroubalová, M.; Kaňková, D.; Netopilík, M.; Walterová, Z. Low-temperature-meltable elastomers based on linear polydimethylsiloxane chains alpha,omega-terminated with mesogenic groups as physical crosslinker: A passive smart material with potential as viscoelastic coupling. Part I: Synthesis and phase behaviour. *Polymers* **2020**, *12*, 2476. [CrossRef]

3. Strachota, A.; Kroutilová, I.; Kovářová, J.; Matějka, L. Epoxy Networks Reinforced with Polyhedral Oligomeric Silsesquioxanes (POSS). Thermomechanical Properties. *Macromolecules* **2004**, *37*, 9457–9464. [CrossRef]

4. Rodzeń, K.; Strachota, A.; Ribot, F.; Matějka, L.; Kovářová, J.; Trchová, M.; Šlouf, M. Reactivity of the tin homolog of POSS, butylstannoxane dodecamer, in oxygen-induced crosslinking reactions with an organic polymer matrix: Study of long-time behaviour. *Polym. Degrad. Stab.* **2015**, *118*, 147–166. [CrossRef]

5. Mossety-Leszczak, B.; Strachota, B.; Strachota, A.; Steinhart, M.; Šlouf, M. The orientation-enhancing effect of diphenyl aluminium phosphate nanorods in a liquid-crystalline epoxy matrix ordered by magnetic field. *Eur. Polym. J.* **2015**, *72*, 238–255. [CrossRef]

6. Strachota, A.; Whelan, P.; Kříž, J.; Brus, J.; Urbanová, M.; Šlouf, M.; Matějka, L. Formation of nanostructured epoxy networks containing polyhedral oligomeric silsesquioxane (POSS) blocks. *Polymer* **2007**, *48*, 3041–3058. [CrossRef]

7. Colombani, O.; Barioz, C.; Bouteiller, L.; Chaneac, C.; Fomperie, L.; Lortie, F.; Montes, H. Attempt toward 1D Cross-Linked Thermoplastic Elastomers: Structure and Mechanical Properties of a New System. *Macromolecules* **2005**, *38*, 1752–1759. [CrossRef]

8. Botterhuis, N.E.; van Beek, D.J.M.; van Gemert, G.M.L.; Bosman, A.W.; Sijbesma, R.P. Self-Assembly and Morphology of Polydimethylsiloxane Supramolecular Thermoplastic Elastomers. *J. Polym. Sci. Part A Polym. Chem.* **2008**, *46*, 3877–3885. [CrossRef]

9. Ślęczkowski, M.L.; Meijer, E.W.; Palmans, A.R.A. Cooperative Folding of Linear Poly(dimethyl siloxane)s via Supramolecular Interactions. *Macromol. Rapid Commun.* **2017**, *38*, 1700566. [CrossRef]

10. Rambarran, T.; Bertrand, A.; Gonzaga, F.; Boisson, F.; Bernard, J.; Fleury, E.; Ganachaud, F.; Brook, M.A. Sweet supramolecular elastomers from a,x-(b-cyclodextrin terminated) PDMS. *Chem. Commun.* **2016**, *52*, 6681–6684. [CrossRef]

11. Strachota, A.; Rodzeń, K.; Ribot, F.; Trchová, M.; Steinhart, M.; Starovoytova, L.; Pavlova, E. Behavior of Tin-Based "Super-POSS" Incorporated in Different Bonding Situations in Hybrid Epoxy Resins. *Macromolecules* **2014**, *47*, 4266–4287. [CrossRef]

12. Fawcett, A.S.; Brook, M.A. Thermoplastic Silicone Elastomers through Self-Association of Pendant Coumarin Groups. *Macromolecules* **2014**, *47*, 1656–1663. [CrossRef]

13. Lamers, B.A.G.; Graf, R.; de Waal, B.F.M.; Vantomme, G.; Palmans, A.R.A.; Meijer, E.W. Polymorphism in the Assembly of Phase-Segregated Block Molecules: Pathway Control to 1D and 2D Nanostructures. *J. Am. Chem. Soc.* **2019**, *141*, 15456–15463. [CrossRef] [PubMed]

14. Lamers, B.A.G.; Ślęczkowski, M.L.; Wouters, F.; Engels, T.A.P.; Meijer, E.W.; Palmans, A.R.A. Tuning polymer properties of non-covalent crosslinked PDMS by varying supramolecular interaction strength. *Polym. Chem.* **2020**, *11*, 2847–2854. [CrossRef]

15. Vasilev, V.G.; Pryakhina, T.A.; Shragin, D.I.; Kononevich, Y.N.; Papkov, V.S.; Muzafarov, A.M. Formation of a Physical Crosslinked Structure in Polydimethylsiloxanes Modified with Long-Chain Hydrocarbon Substituents with Polar Fragments. *Polym. Sci. Ser.* **2017**, *59*, 320–327. [CrossRef]

16. Dollase, T.; Spiess, H.W.; Gottlieb, M.; Yerushalmi-Rozen, R. Crystallization of PDMS: The effect of physical and chemical crosslinks. *Europhys. Lett.* **2002**, *60*, 390–396. [CrossRef]

17. Petr, M.; Katzman, B.; DiNatale, W.; Hammond, P.T. Synthesis of a New, Low-Tg Siloxane Thermoplastic Elastomer with a Functionalizable Backbone and Its Use as a Rapid, Room Temperature Photoactuator. *Macromolecules* **2013**, *46*, 2823–2832. [CrossRef]

18. Dodge, L.; Chen, Y.; Brook, M.A. Silicone Boronates Reversibly Crosslink Using Lewis Acid–Lewis Base Amine Complexes. *Chem. Eur. J.* **2014**, *20*, 9349–9356. [CrossRef] [PubMed]

19. Li, C.H.; Wang, C.; Keplinger, C.; Zuo, J.L.; Jin, L.; Sun, Y.; Zheng, P.; Cao, Y.; Lissel, F.; Linder, C.; et al. A highly stretchable autonomous self-healing elastomer. *Nat. Chem.* **2016**, *8*, 618–624. [CrossRef]

20. Li, X.; Zhang, D.; Xiang, K.; Huang, G. Synthesis of polyborosiloxane and its reversible physical crosslinks. *RSC Adv.* **2014**, *4*, 1–8. [CrossRef]

21. Seetapan, N.; Fuongfuchat, A.; Sirikittikul, D.; Limparyoon, N. Unimodal and bimodal networks of physically crosslinked polyborodimethylsiloxane: Viscoelastic and equibiaxial extension behaviors. *J. Polym. Res.* **2013**, *20*, 183. [CrossRef]

22. Horodecka, S.; Strachota, A.; Mossety-Leszczak, B.; Šlouf, M.; Zhigunov, A.; Vyroubalová, M.; Kaňková, D.; Netopilík, M. Meltable copolymeric elastomers based on polydimethylsiloxane with multiplets of pendant liquid-crystalline groups as physical crosslinker: A self-healing structural material with a potential for smart applications. *Eur. Polym. J.* **2020**, *137*. [CrossRef]

23. Wissbrun, K.F. Rheology of Rod-like Polymers in the Liquid Crystalline State. *J. Rheol.* **1981**, *25*, 619–662. [CrossRef]

24. Marrucci, G. Rheology of liquid crystalline polymers. *Pure Appl. Chem.* **1985**, *57*, 1545–1552. [CrossRef]

25. Guskey, S.M.; Winter, H.H. Transient shear behavior of a thermotropic liquid crystalline polymer in the nematic state. *J. Rheol.* **1991**, *35*, 1191–1207. [CrossRef]

26. Marrucci, G.; Greco, F. Flow Behavior of Liquid Crystalline Polymers. In *Advances in Chemical Physics*; Prigogine, I., Rice, S.A., Eds.; John Wiley & Sons, Inc.: New York, NY, USA, 1993; Volume 86, pp. 331–404. ISBN 9780471598459; 9780470141458. [CrossRef]

27. Jamieson, A.M.; Gu, D.; Chen, F.L.; Smith, S. Viscoelastic behavior of nematic monodomains containing liquid crystal polymers. *Prog. Polym. Sci.* **1996**, *21*, 981–1033. [CrossRef]

28. Kiss, G.; Porter, R.S. Rheology of concentrated solutions of poly(γ-benzyl-glutamate). *J. Polym. Sci. Polym. Symp.* **1978**, *65*, 193–211. [CrossRef]

29. Kiss, G.; Porter, R.S. Rheology of concentrated solutions of helical polypeptides. *J. Polym. Sci. Polym. Phys. Ed.* **1980**, *18*, 361–388. [CrossRef]

30. Moldenaers, P.; Mewis, J. On the nature of viscoelasticity in polymeric liquid crystals. *J. Rheol.* **1993**, *37*, 367–380. [CrossRef]

31. Asada, T.; Muramatsu, H.; Watanabe, R.; Onogi, S. Rheooptical Studies of Racemic Poly(γ-benzyl glutamate) Liquid Crystals. *Macromolecules* **1980**, *13*, 867–871. [CrossRef]

32. Onogi, S.; Asada, T. Rheology and Rheo-Optics of Polymer Liquid Crystals. In *Rheology*; Astarita, G., Marrucci, G., Nicolais, L., Eds.; Springer: Boston, MA, USA, 1980; Volume 1, pp. 127–147. ISBN 978-1-4684-3742-3; 978-1-4684-3740-9. [CrossRef]

33. Doi, M. Molecular dynamics and rheological properties of concentrated solutions of rodlike polymers in isotropic and liquid crystalline phases. *J. Polym. Sci. Polym. Physics Ed.* **1981**, *19*, 229–243. [CrossRef]

34. Doi, M.; Edwards, S.F. *The Theory of Polymer Dynamics*; Oxford University Press: Oxford, UK, 1986; ISBN 0198519761; 9780198519768.

35. Larson, R.G.; Doi, M. Mesoscopic domain theory for textured liquid crystalline polymers. *J. Rheol.* **1991**, *35*, 539–563. [CrossRef]

36. Larson, R.G. *The Structure and Rheology of Complex Fluids*; Oxford University Press: New York, NY, USA, 1999; ISBN 019512197X; 978-0195121971.

37. Burghardt, W.R. Molecular orientation and rheology in sheared lyotropic liquid crystalline polymers. *Macromol. Chem. Phys.* **1998**, *199*, 471–488. [CrossRef]

38. Baek, S.G.; Magda, J.J.; Larson, R.G. Rheological differences among liquid-crystalline polymers. I. The first and second normal stress differences of PBG solutions. *J. Rheol.* **1993**, *37*, 1201–1224. [CrossRef]

39. Baek, S.G.; Magda, J.J.; Larson, R.G.; Hudson, S.D. Rheological differences among liquid-crystalline polymers. II. Disappearance of negative N1 in densely packed lyotropes and thermotropes. *J. Rheol.* **1994**, *38*, 1473–1503. [CrossRef]

40. Ugaz, V.M.; Burghardt, W.R.; Zhou, W.; Kornfield, J.A. Transient molecular orientation and rheology in flow aligning thermotropic liquid crystalline polymers. *J. Rheol.* **2001**, *45*, 1029–1063. [CrossRef]

41. Azoug, A.; Vasconcellos, V.; Dooling, J.; Saed, M.; Yakacki, C.M.; Nguyen, T.D. Viscoelasticity of the polydomain-monodomain transition in main-chain liquid crystal elastomers. *Polymer* **2016**, *98*, 165–171. [CrossRef]

42. Lee, K.M.; Han, C.D. Rheology of Nematic Side-Chain Liquid-Crystalline Polymer: Comparison with Main-Chain Liquid-Crystalline Polymer. *Macromolecules* **2002**, *35*, 6263–6273. [CrossRef]

43. Kim, S.S.; Han, C.D. Effect of Thermal History on the Rheological Behavior of a Thermotropic Liquid-Crystalline Polymer. *Macromolecules* **1993**, *26*, 3176–3186. [CrossRef]

44. Colby, R.H.; Gillmor, J.R.; Galli, G.; Laus, M.; Ober, C.K.; Hall, E. Linear viscoelasticity of side chain liquid crystal polymer. *Liq. Cryst.* **1993**, *13*, 233–245. [CrossRef]

45. Berghausen, J.; Fuchs, J.; Richtering, W. Rheology and Shear Orientation of a Nematic Liquid Crystalline Side-Group Polymer with Laterally Attached Mesogenic Units. *Macromolecules* **1997**, *30*, 7574–7581. [CrossRef]

46. Chang, S.; Han, C.D. Effect of Flexible Spacers on the Rheological Behavior of Main-Chain Thermotropic Liquid-Crystalline Polymers Having Bulky Pendent Side Groups. *Macromolecules* **1997**, *30*, 2021–2034. [CrossRef]

47. Lee, K.M.; Han, C.D. Effect of Flexible Spacer Length on the Rheology of Side-Chain Liquid-Crystalline Polymers. *Macromolecules* **2003**, *36*, 8796–8810. [CrossRef]

48. Wewerka, A.; Viertler, K.; Vlassopoulos, D.; Stelzer, F. Structure and rheology of model side-chain liquid crystalline polymers with varying mesogen length. *Rheol. Acta* **2001**, *40*, 416–425. [CrossRef]

49. Yang, I.K.; Chang, S.H. The Smectic Rheology of a Polysiloxane Side Chain Liquid Crystalline Polymer. *J. Polym. Res.* **2002**, *9*, 163–168. [CrossRef]

50. Hoshio, H.; Jin, J.I.; Lenz, R.W. Liquid crystalline behavior of polymeric glycols terminated with aromatic diester and diacid mesogenic groups. *J. Appl. Polym. Sci.* **1984**, *29*, 547–554. [CrossRef]

51. Chien, J.C.W.; Zhou, R.; Lillya, C.P. Liquid-crystalline compounds and polymers from promesogens. *Macromolecules* **1987**, *20*, 2340–2344. [CrossRef]

52. Lin, Y.G.; Zhou, R.; Chien, J.C.W.; Winter, H.H. Rheology of a Twin Liquid Crystalline Polymer. *Macromolecules* **1988**, *21*, 2014–2018. [CrossRef]

53. Oppermann, W.; Braatz, K.; Finkelmann, H.; Gleim, W.; Kock, H.J.; Rehage, G. Viscoelastic properties of silicone polymers with liquid crystalline behaviour. *Rheol. Acta* **1982**, *21*, 423–426. [CrossRef]

54. Stukenbroeker, T.; Wang, W.; Winne, J.M.; Du Prez, F.E.; Nicolaÿ, R.; Leibler, L. Polydimethylsiloxane quenchable vitrimers. *Polym. Chem.* **2017**, *8*, 6590–6593. [CrossRef]

55. Meng, Y.; Xu, W.; Newman, M.R.; Benoit, D.S.W.; Anthamatten, M. Thermoreversible Siloxane Networks: Soft Biomaterials with Widely Tunable Viscoelasticity. *Adv. Funct. Mater.* **2019**, *29*, 1903721. [CrossRef]

56. Winter, H.H.; Chambon, F. Analysis of linear viscoelasticity of a crosslinking polymer at the gel point. *J. Rheol.* **1986**, *30*, 367–382. [CrossRef]

Publisher's Note: MDPI stays neutral with regard to jurisdictional claims in published maps and institutional affiliations.

Low-temperature-meltable elastomers based on linear polydimethylsiloxane chains alpha,omega-terminated with mesogenic groups as physical crosslinker: A passive smart material with potential as viscoelastic coupling. Part II: Viscoelastic and rheological properties

Sabina Horodecka[1,2], Adam Strachota[1]*, Beata Mossety-Leszczak[3], Maciej Kisiel[3], Beata Strachota[1], Miroslav Šlouf[1]

[1] *Institute of Macromolecular Chemistry, Czech Academy of Sciences,*
Heyrovskeho nam. 2, CZ-162 06 Praha, Czech Republic

[2] *Faculty of Science, Charles University,*
Albertov 6, CZ-128 00 Praha 2, Czech Republic

[3] *Faculty of Chemistry, Rzeszow University of Technology,*
al. Powstancow Warszawy 6, PL-35-959 Rzeszow, Poland

1. Gelation study via T-dependent multi-frequency rheology experiments

H21–BAFKU₂ *cooling scan*
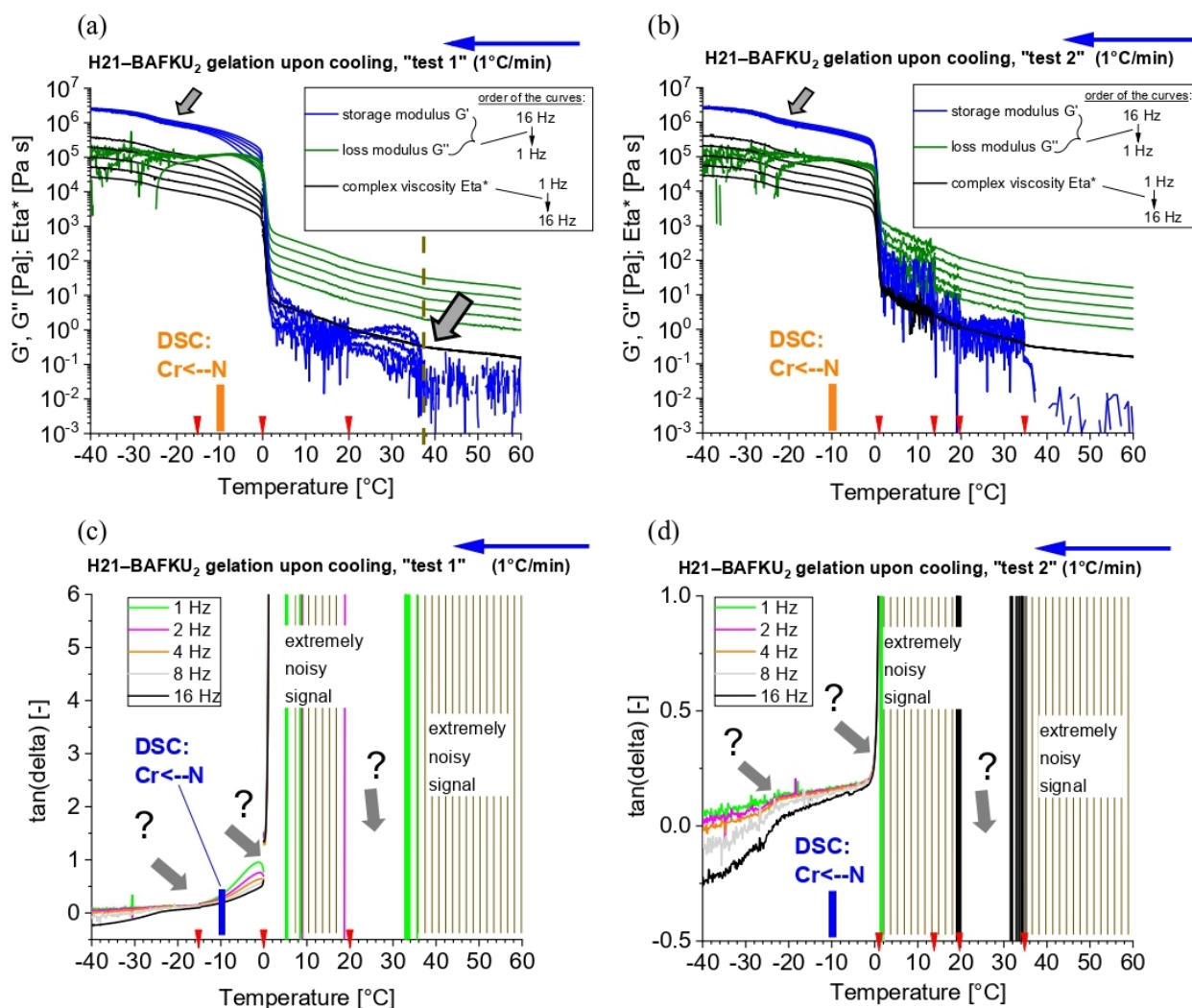
SI-Fig. 1: *Multi-frequency temperature ramp tests - **cooling scans** - carried out in the rubbery and melt temperature regions of H21–BAFKU₂ : (a), (b): temperature dependence of the storage shear moduli G', of the loss moduli G", of the complex viscosities Eta* recorded at the simultaneously applied frequencies of 1, 2, 4, 8 and 16 Hz; (c), (d): sets of the tan δ curves with marked crossover (or near-crossover) points; (a), (c): cooling scan conducted with **high deformation** amplitudes; (b), (d): cooling scan conducted with **low deformation** amplitudes; red dotted lines indicate change in strain.*

H21–BAFKU₂ *heating scan*
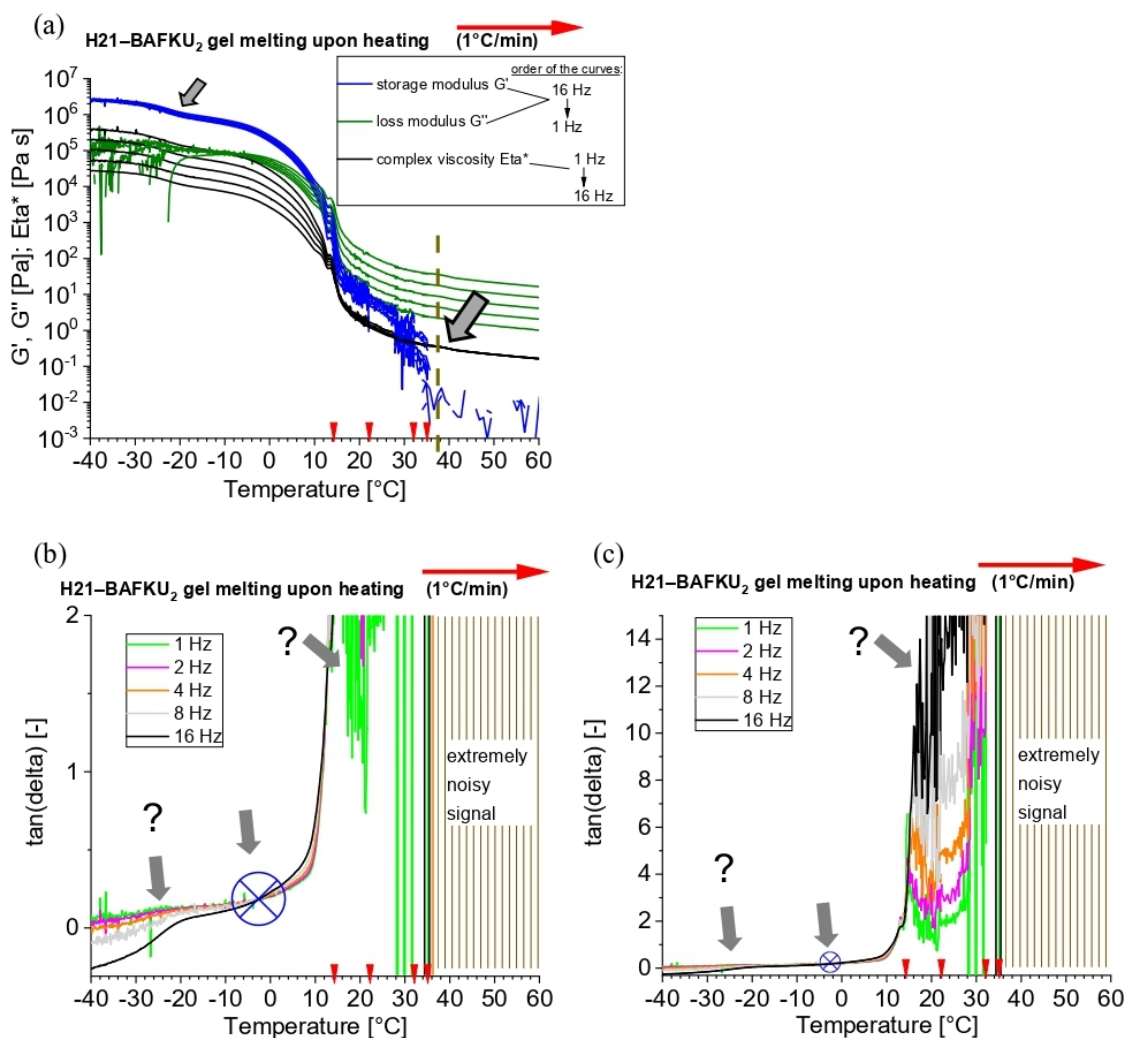
SI-Fig. 2: *Multi-frequency temperature ramp test - heating scan - carried out in the rubbery and melt temperature regions of H21–BAFKU₂ : (a): temperature dependence of the storage shear moduli G', of the loss moduli G", of the complex viscosities Eta* recorded at the simultaneously applied frequencies of 1, 2, 4, 8 and 16 Hz as heating scan; (b): sets of the tan δ curves with marked crossover (or near-crossover) points as heating scan; (c): a different zoom of the image (b) ; red dotted lines indicate change in strain.*

2. Kinetics of gelation upon abrupt cooling of melt

H11–BAFKU₂ : all graphs
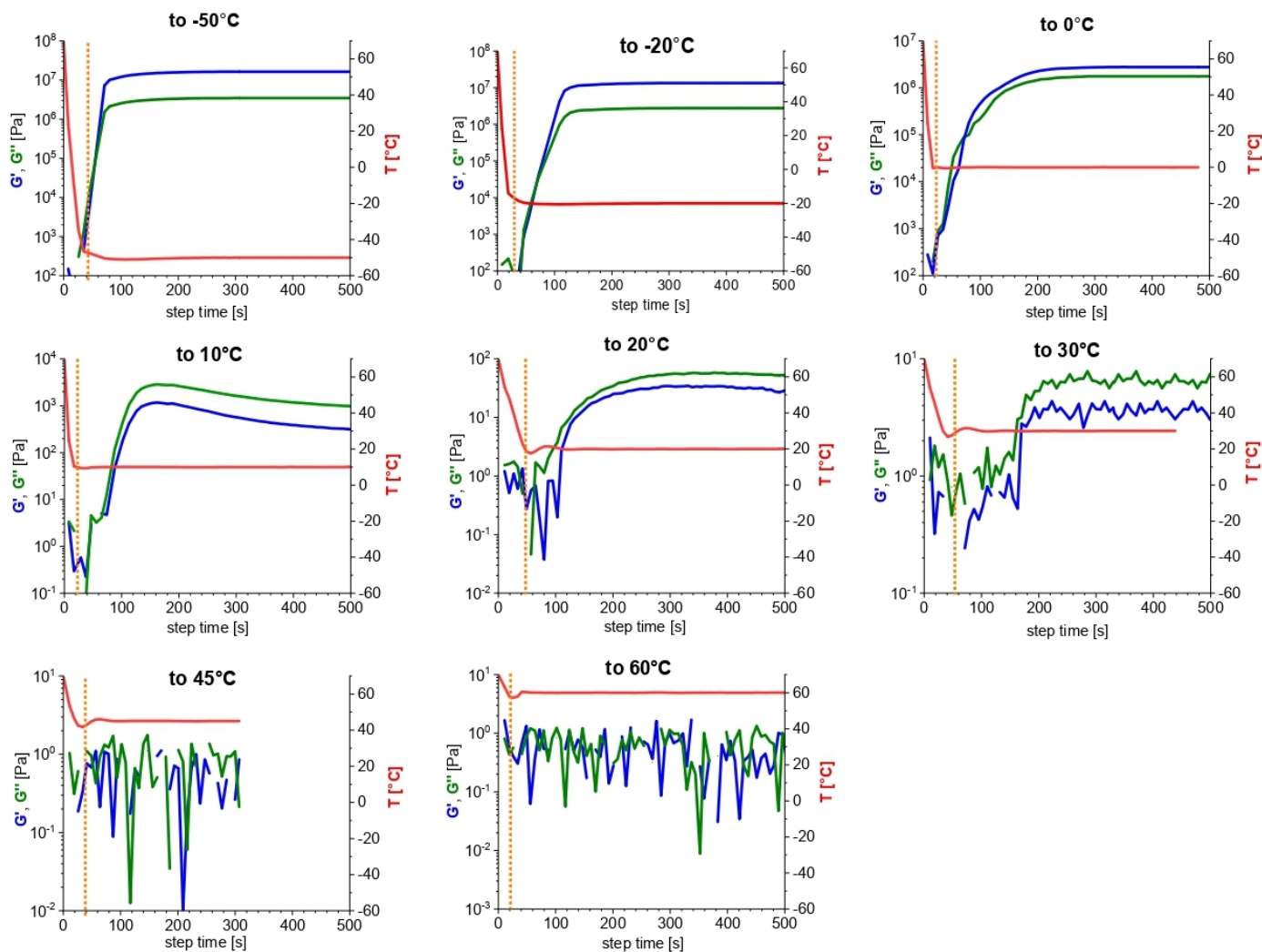
SI-Fig. 3: *Full data set: **Kinetics** of the change in storage (G') and loss (G") modulus (kinetics of physical gelation) upon **cooling molten H11–BAFKU₂** from 70°C down to different temperatures ranging between -50°C and +60°C; the course of the temperature of the plates between which the sample was loaded is also depicted.*
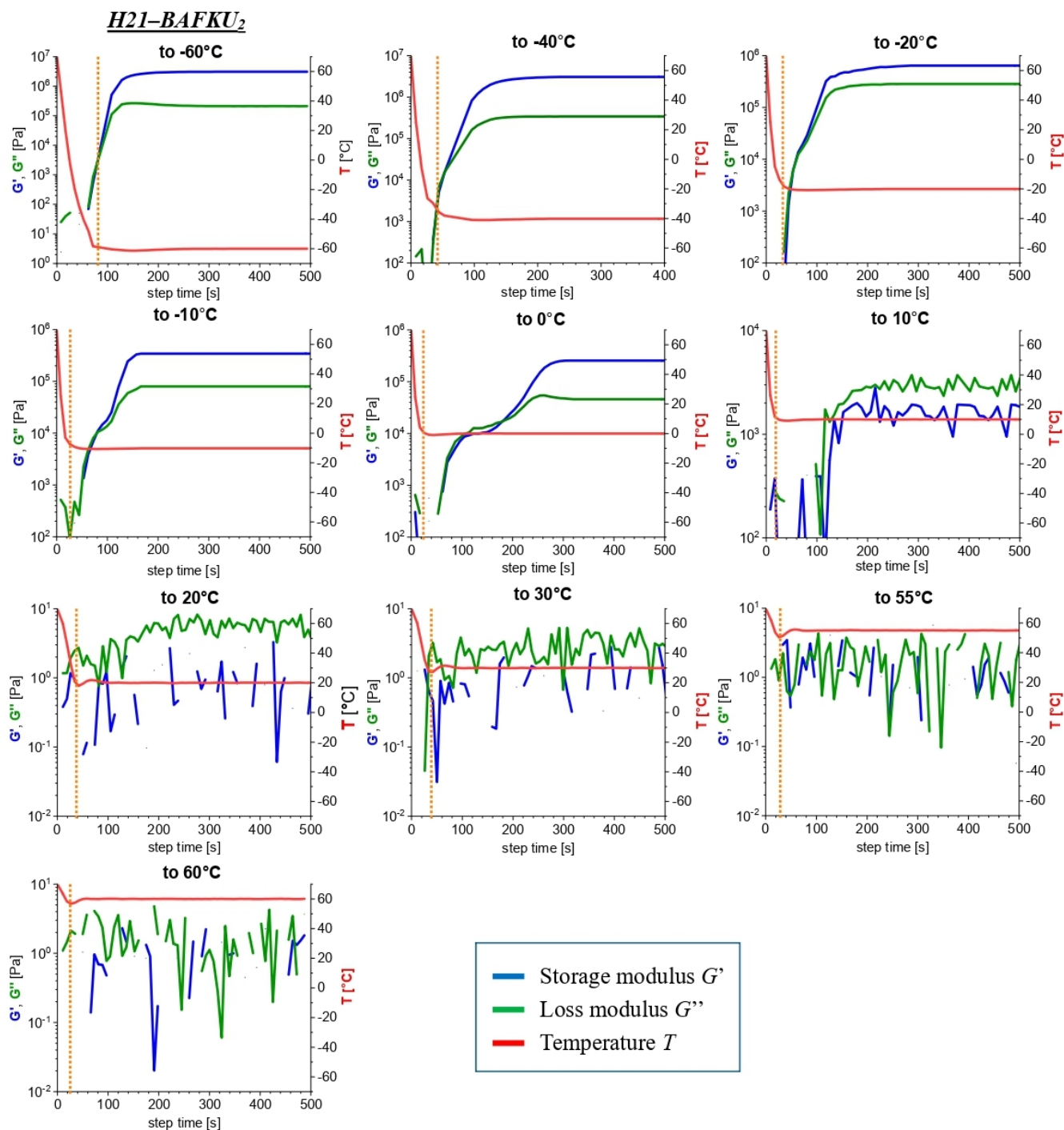
SI-Fig. 4: *Kinetics of the change in storage (G') and loss (G") modulus (kinetics of physical gelation) upon cooling molten H21–BAFKU₂ from 70°C to different temperatures ranging between -60°C and 60°C; the course of the temperature of the plates between which the sample was loaded is also depicted.*

H03–BAFKU₂
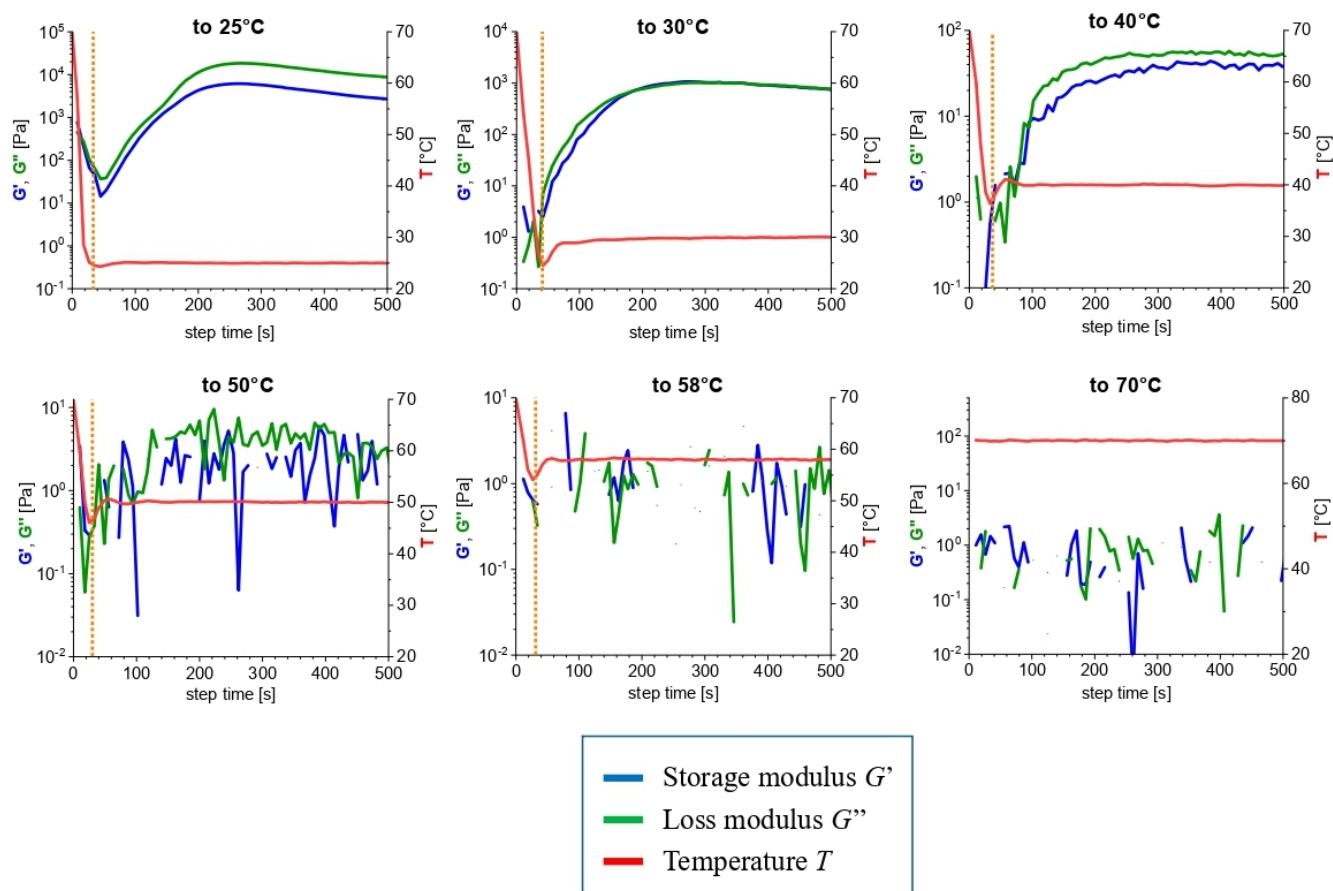
SI-Fig. 5: **Kinetics** _of the change in storage (G') and loss (G'') modulus (kinetics of physical gelation) upon_ **cooling molten H03–BAFKU₂** _from 70°C down to different temperatures ranging between +30°C and +70°C; the course of the temperature of the plates between which the sample was loaded is also depicted._

3. Disconnection of the physical network by high mechanical strain

H11–BAFKU$_2$
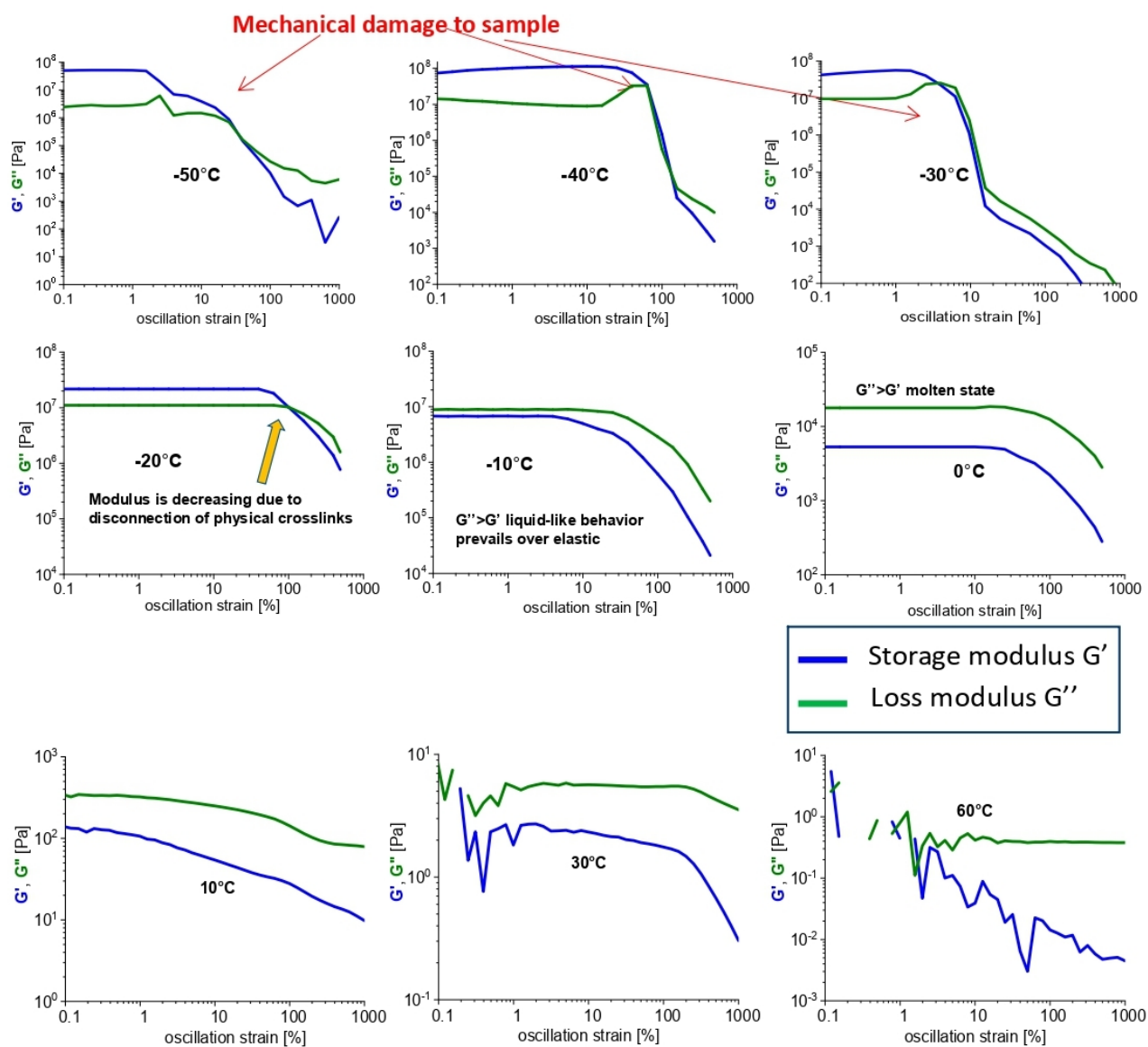
SI-Fig. 6: *All data: Disconnection of the physical crosslinks in H11–BAFKU$_2$ by mechanical strain: strain-dependence of storage (G') and loss (G") modulus of H21–BAFKU$_2$ at the temperatures from -50 to +60°C.*
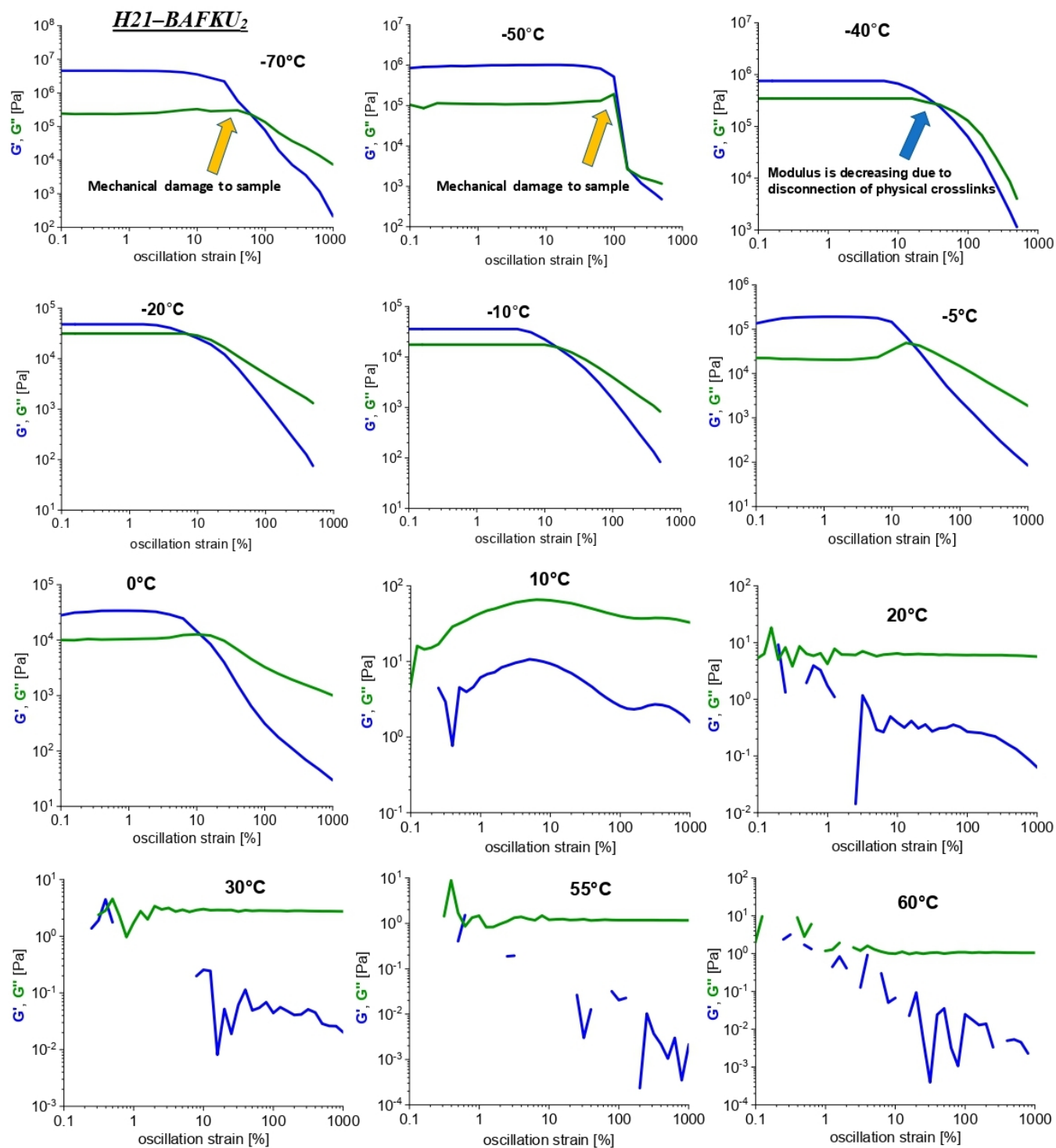
SI-Fig. 7: *Disconnection of the physical crosslinks in H21−BAFKU2 by mechanical strain: strain-dependence of storage (G') and loss (G'') modulus of H21−BAFKU2 at the temperatures from -70 to +60°C.*

Storage modulus G'

Loss modulus G''
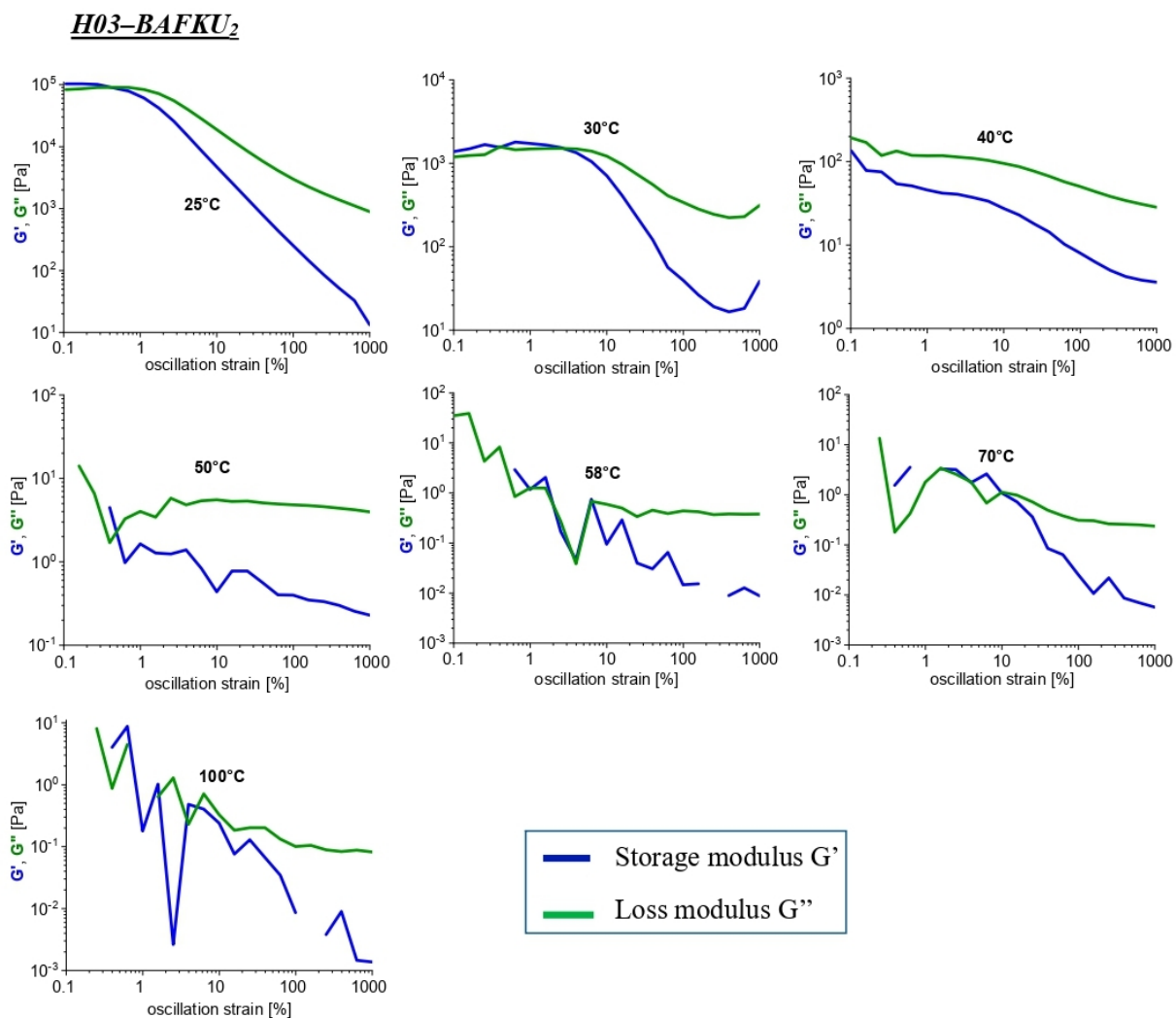
H03–BAFKU₂

SI-Fig. 8: _Disconnection of residual physical crosslinks in H03–BAFKU₂ melt by mechanical strain: strain-dependence of storage (G') and loss (G'') modulus of H03-BAFKU₂ at the temperatures from +25 to +100°C._

Creep tests

H11-BAFKU2 all data
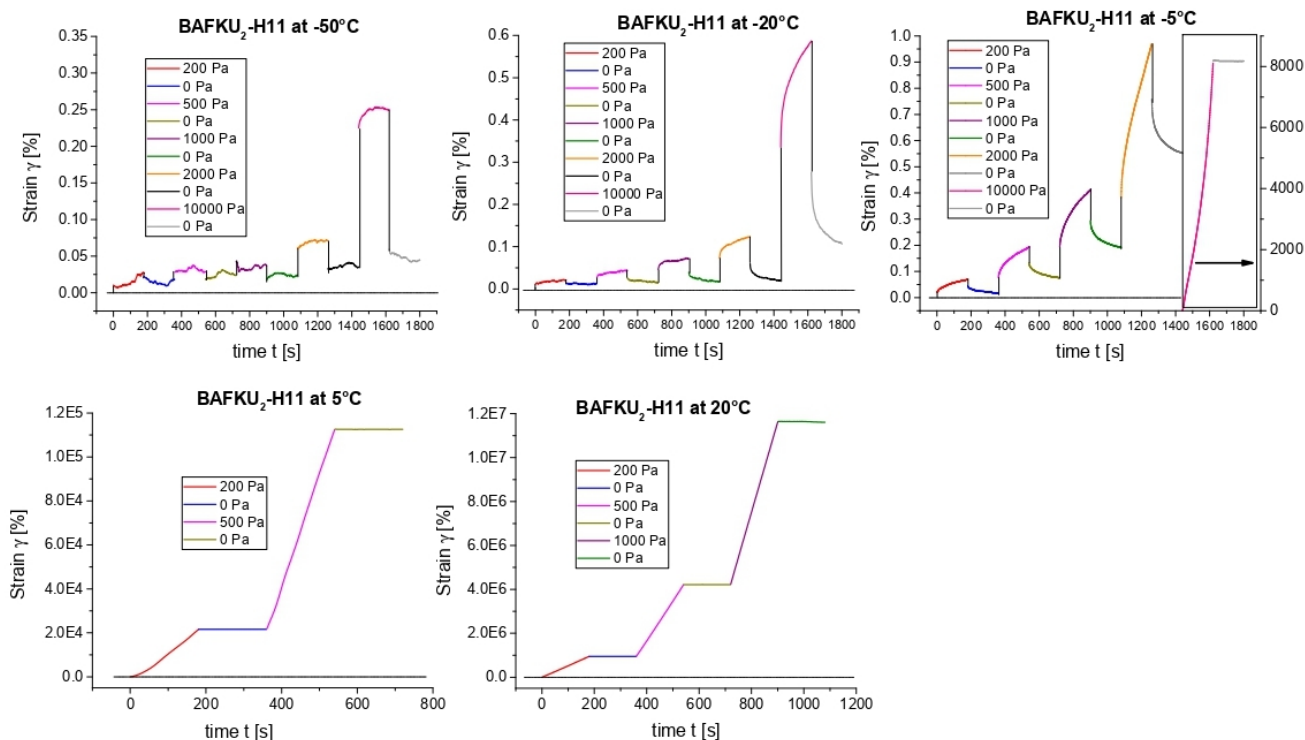
SI-Fig. 9: _Multi-step creep tests of H11–BAFKU2 all data: tests at temperatures between -50 and +20°C; stresses ranging between 200 and 10 000 Pa were applied, followed by recovery steps (at 0 Pa)._

H21-BAFKU2
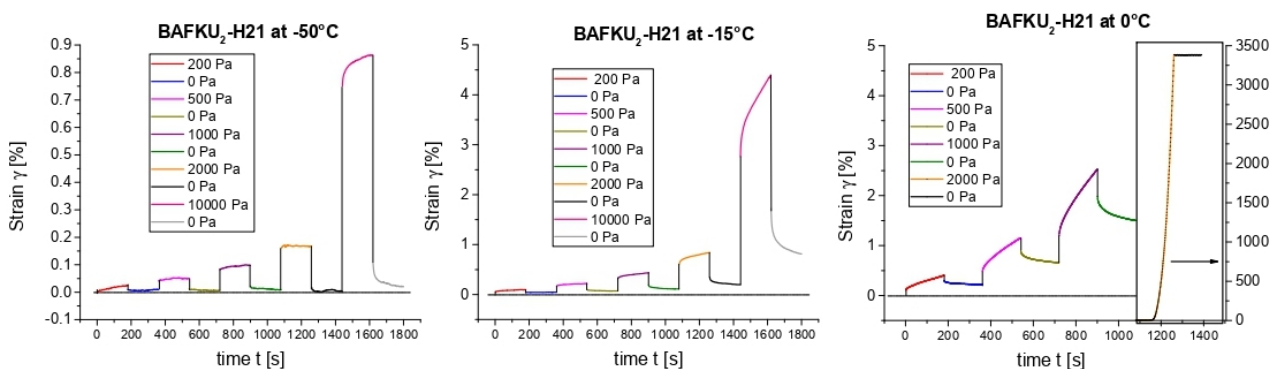
SI-Fig. 10: _Multi-step creep tests of H21–BAFKU2 at temperatures between -50 and 0°C; stresses ranging between 200 and 10 000 Pa were applied, followed by recovery steps (at 0 Pa)._

H03-BAFKU2
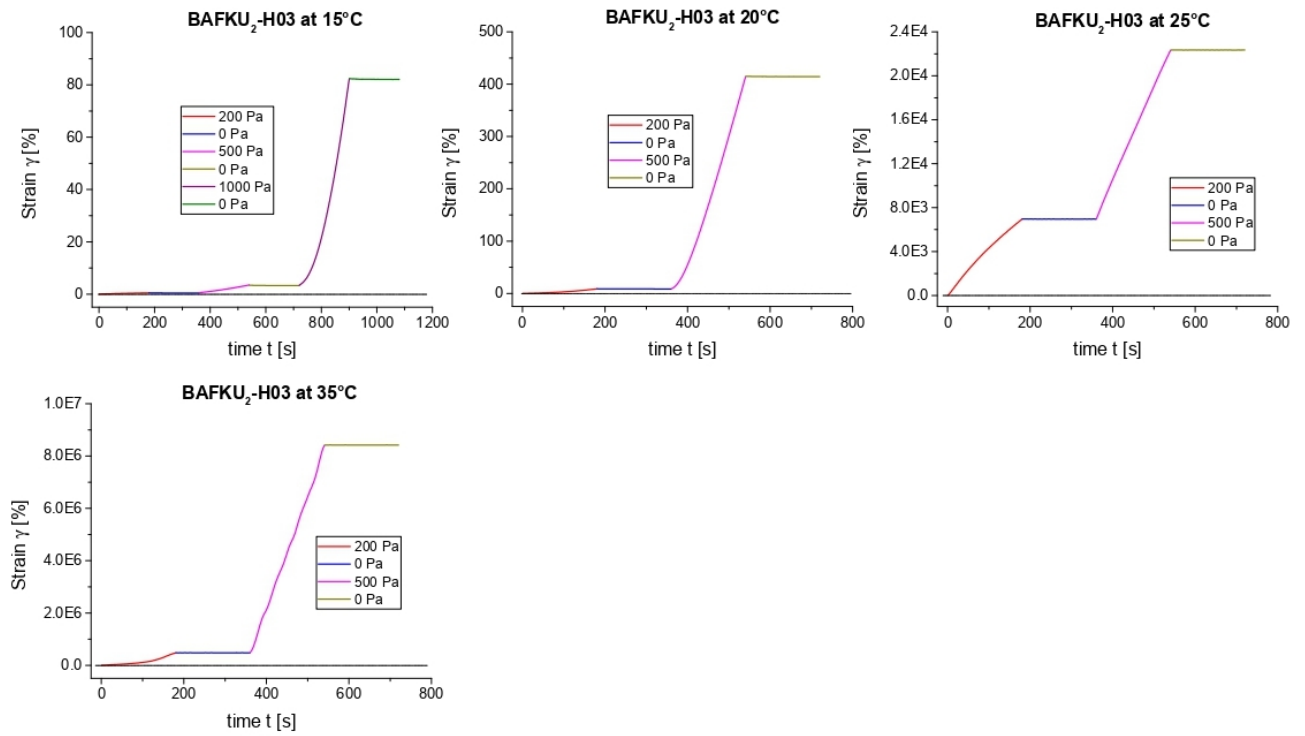
SI-Fig. 11: *Multi-step creep tests of H03–BAFKU₂ at temperatures between +15 and +35°C; stresses ranging between 200 and 1 000 Pa were applied, followed by recovery steps (at 0 Pa).*

Relaxation tests

H11-BAFKU2
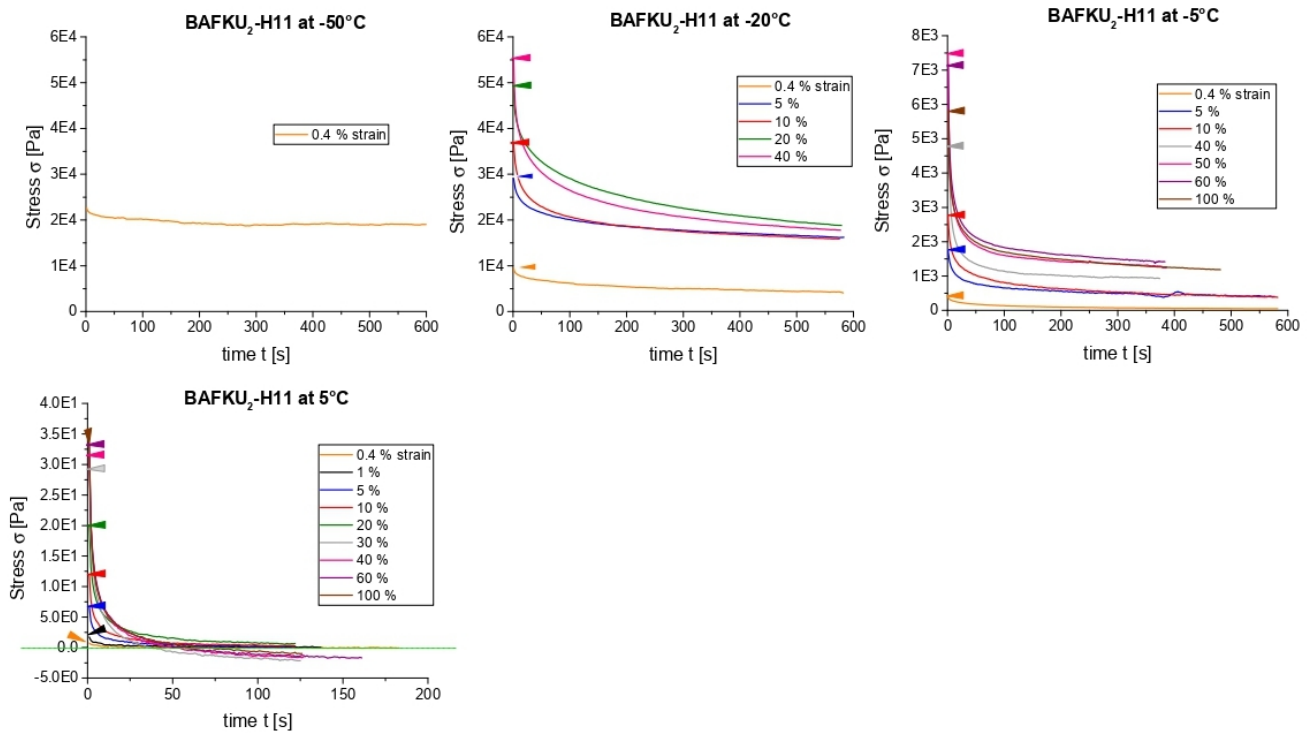
SI-Fig. 12: *Stress relaxation tests of H11−BAFKU$_2$ at temperatures between -50 and +5°C; at each temperature, several constant strain values were applied.*

Relaxation H03-BAFKU2
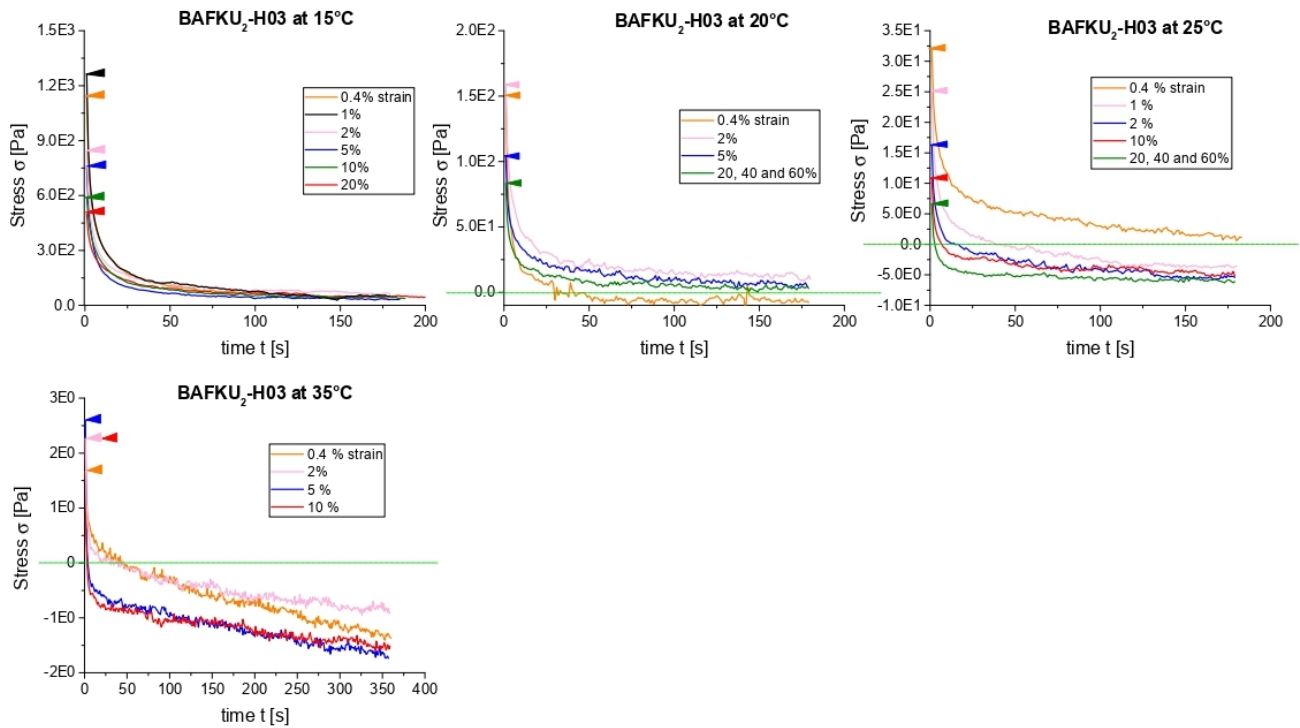
SI-Fig. 13: *Stress relaxation tests of H03−BAFKU$_2$ at temperatures between between +15 and +35°C; at each temperature, several constant strain values were applied.*

4. High-frequency stiffening and self-healing effects

H11–BAFKU$_2$
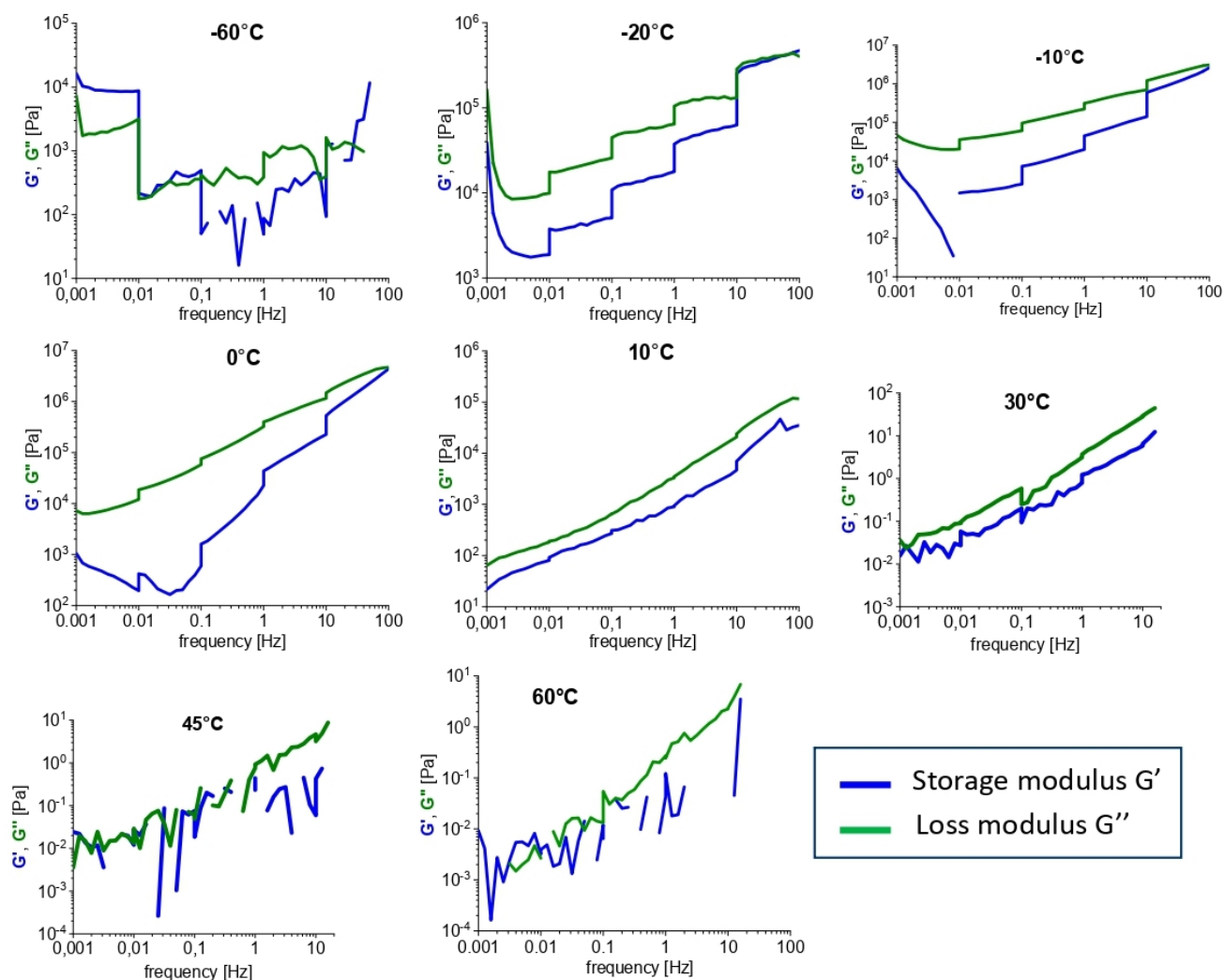
SI-Fig. 14: *All data: Frequency-stiffening of H11–BAFKU$_2$ observed in frequency sweep tests (1 mHz to 100 Hz) conducted at temperatures between -60 and +60°C; the strain amplitude was different in each frequency decade, ranging from 50% at 1 mHz to 1% at 100 Hz; the effect of strain-induced damage to the network, as well as of its recovery between the frequency decades is clearly visible, especially in case of G' curves at lower temperatures.*
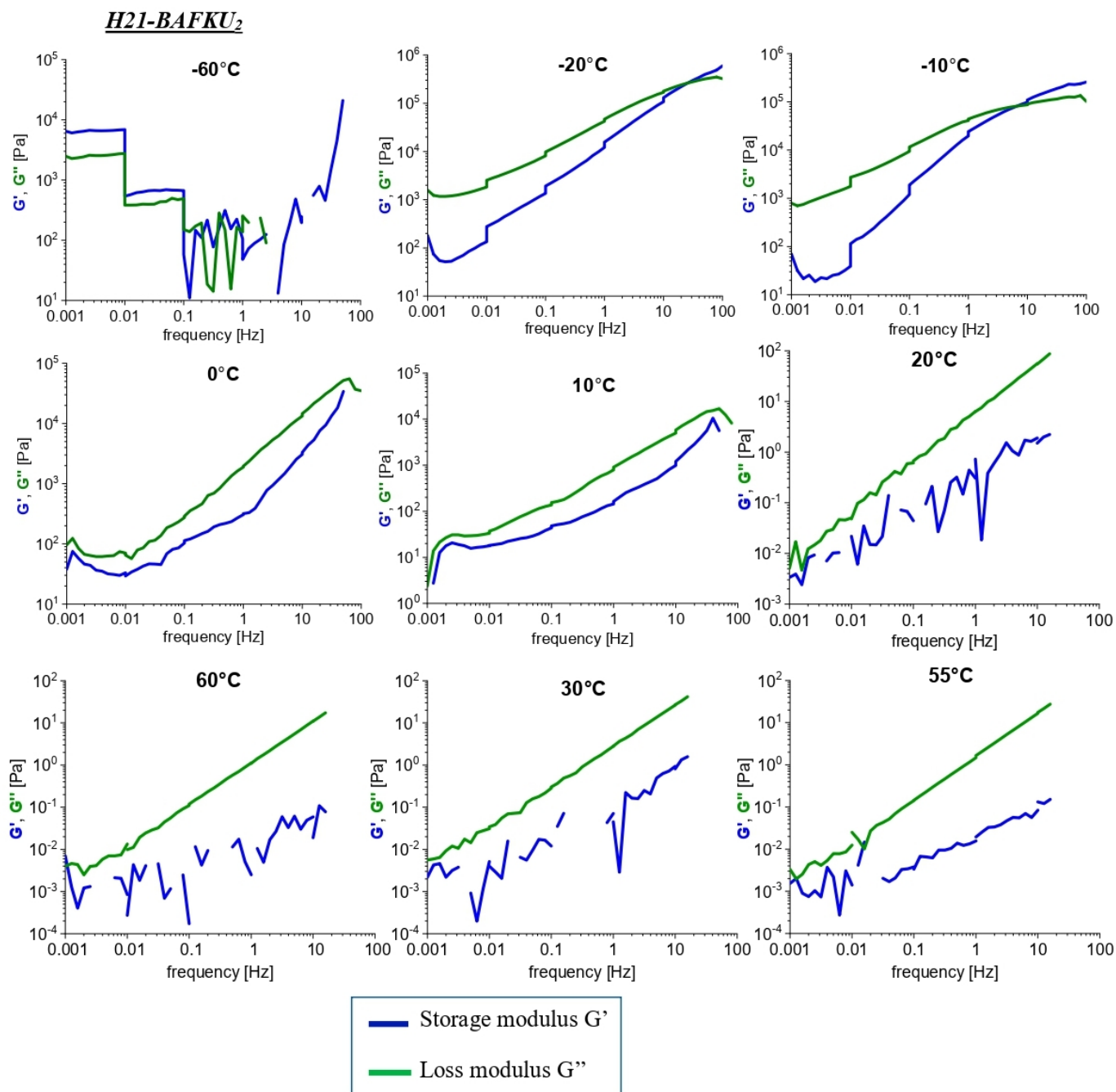
SI-Fig. 15: *Frequency-stiffening of H21−BAFKU₂ observed in frequency sweep tests (1 mHz to 100 Hz) conducted between -60 and +55°C; the strain amplitude was different in each frequency decade, ranging from 50% at 1 mHz to 1% at 100 Hz; the effect of strain-induced damage to the network, as well as of its recovery between the frequency decades is clearly visible, especially in case of G' curves at lower temperatures.*

H03-BAFKU₂
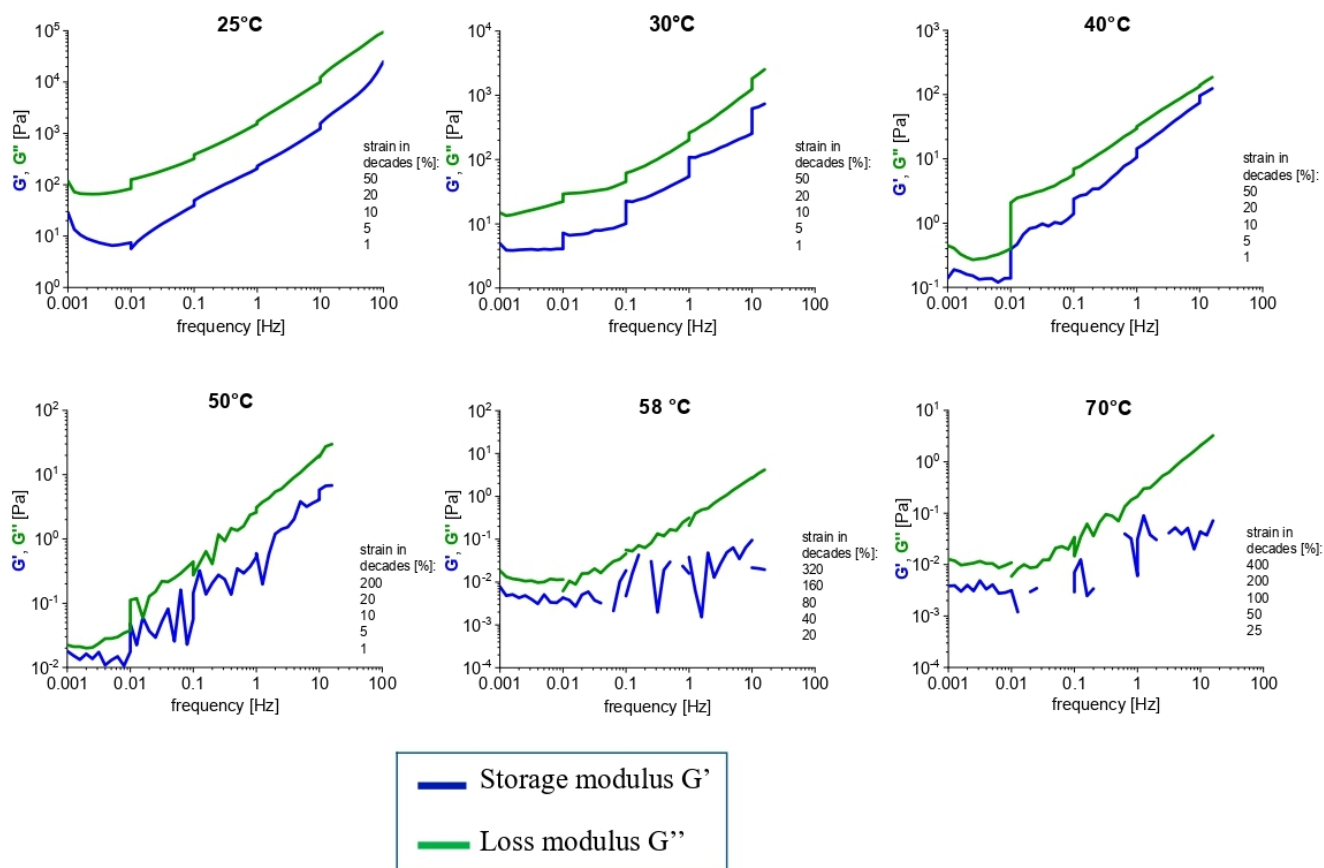
SI-Fig. 16: _Frequency-stiffening of H03–BAFKU₂ melt observed in frequency sweep tests (1 mHz to 100 Hz) conducted at temperatures between +25 and +70°C; the strain amplitude was different in each frequency decade, ranging from 50% at 1 mHz to 1% at 100 Hz; the effect of strain-induced damage to elastic structures in the melt, as well as their recovery between the frequency decades is clearly visible, especially at lower temperatures._

Explanation of the upward steps in G"

While simple self-healing should lead to decrease in $G"$ (stronger elastomer character due to more crosslinks, shorter elastic chains and hence less friction), the experimentally observed upward steps in $G"$ could be explained by resistance caused by re-assembled larger aggregates (lamellae) of BAFKU, which have time to disconnect at lower frequencies (and high applied strains). Their gradual destruction by shear generates resistance (high $G"$ value), but also leads to a decrease in the number of these secondary aggregates and thus in turn to less than maximum resistance (smaller growth, or in extreme cases even local decrease in $G"$). During the experimental delay, the smaller BAFKU aggregates ('fragments') re-assemble to larger ones again, and hence can generate considerably increased resistance after the delay (upward step in G").

5. Thixotropy effects

**H03-BAFKU₂ kinetics of gelation upon cooling**
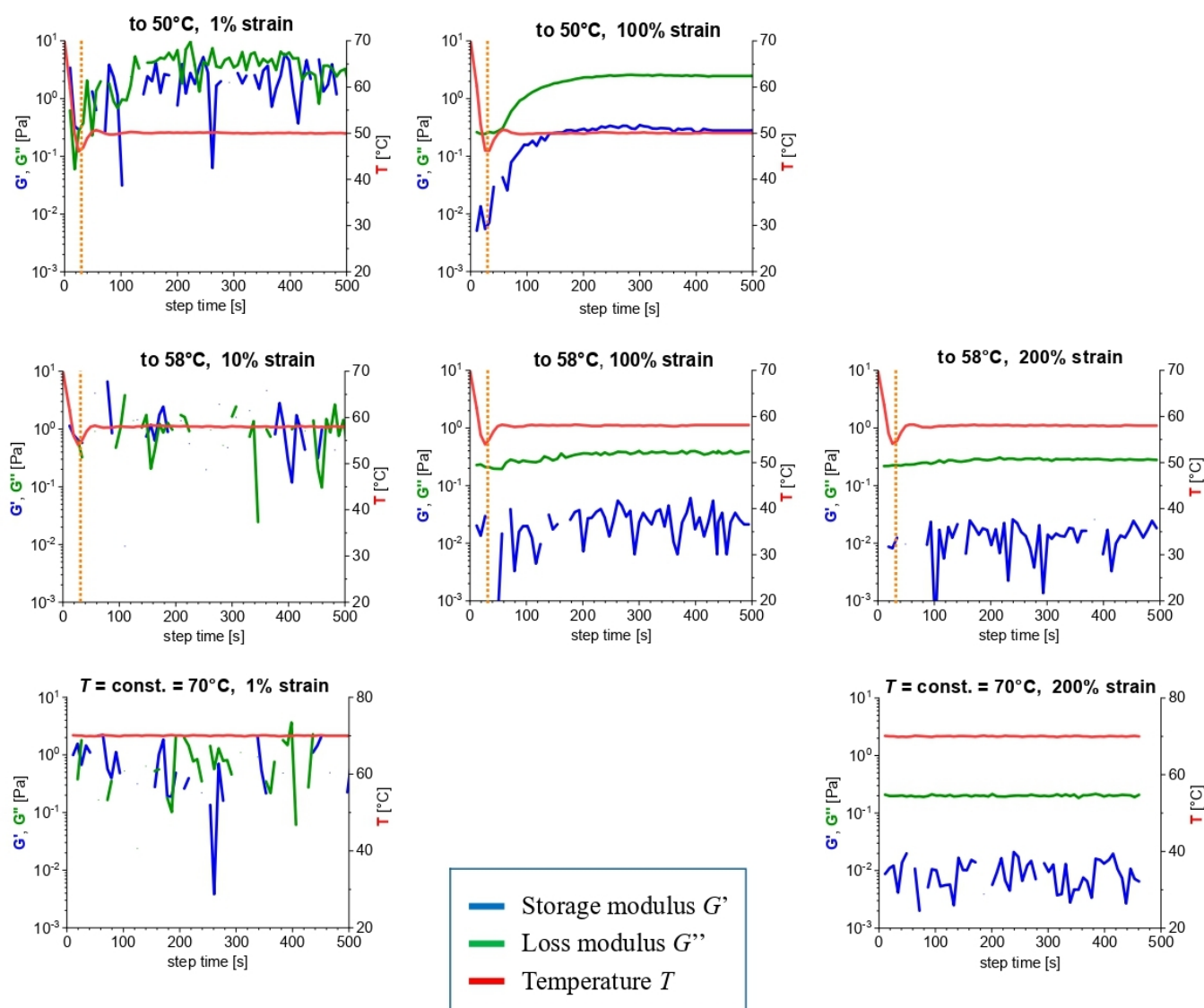
SI-Fig. 17: _Thixotropy effects visible as strong strain-dependence of the moduli values (G', G") in case of the kinetics of physical gelation of molten H03–BAFKU₂ upon abrupt cooling._

Very small strains also lead to change in measured moduli:
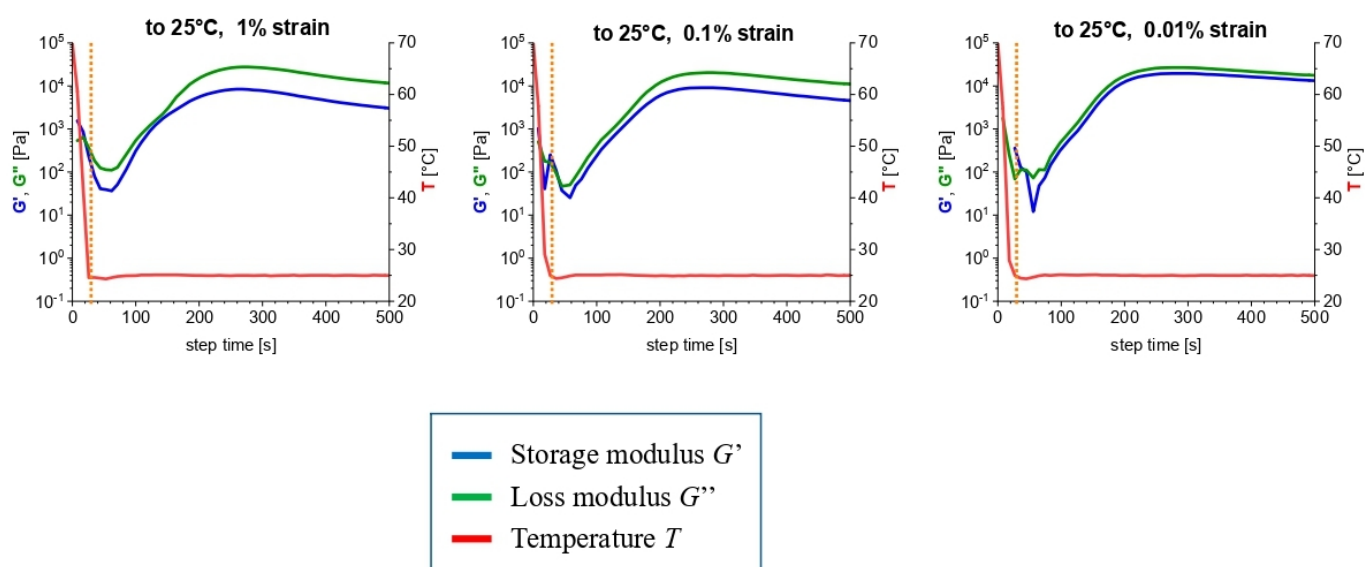
SI-Fig. 18: *Thixotropy effects as strain-dependence – study of very low strains – of the moduli values and curve course – especially G', less so G'', in case of the kinetics of physical gelation of molten H03–BAFKU₂ upon abrupt cooling.*

H11-BAFKU$_2$ kinetics of gelation upon cooling
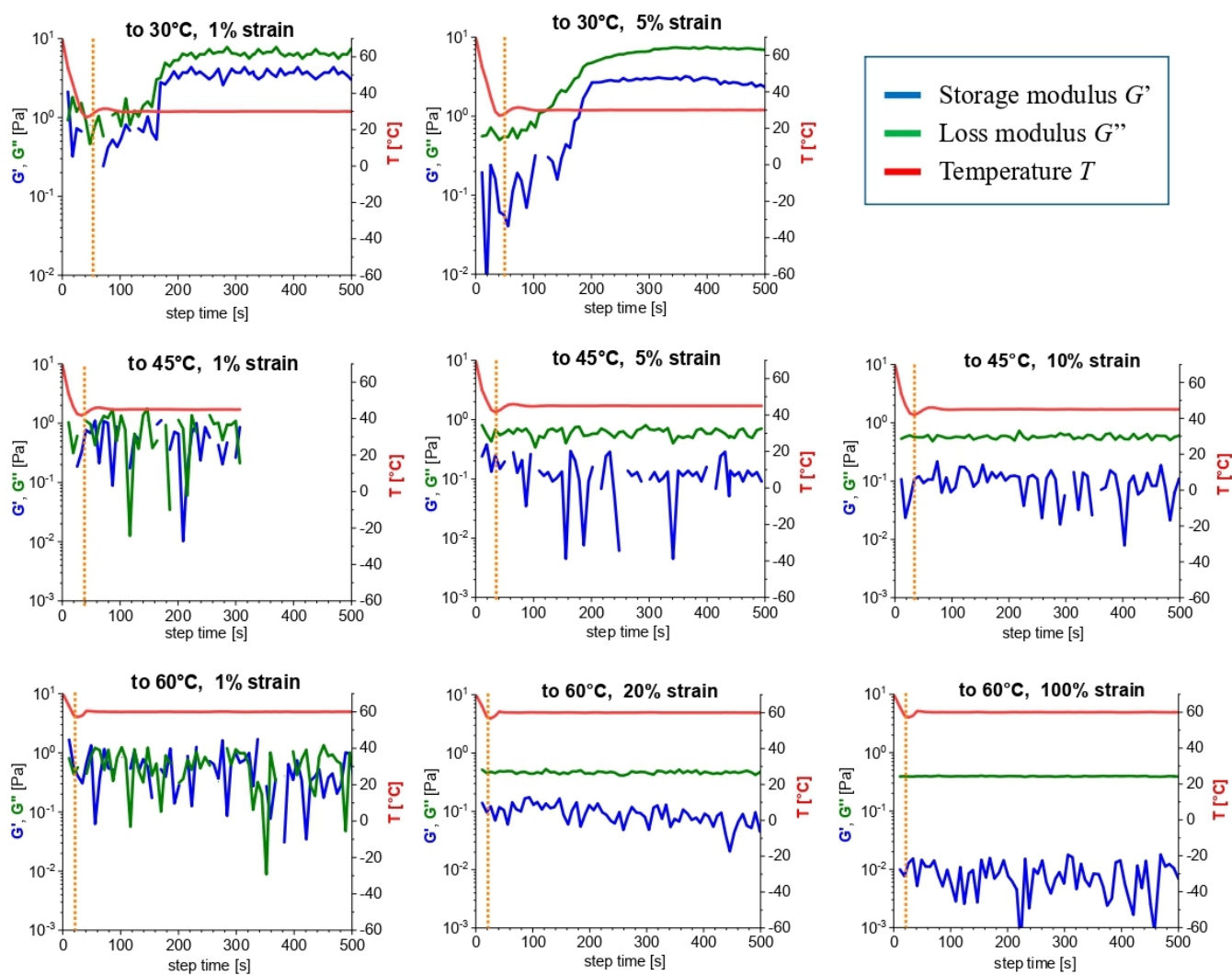
SI-Fig. 19: *Thixotropy effects visible as strong strain-dependence of the moduli values (G', G'') in case of the kinetics of physical gelation of molten H11–BAFKU$_2$ upon abrupt cooling.*
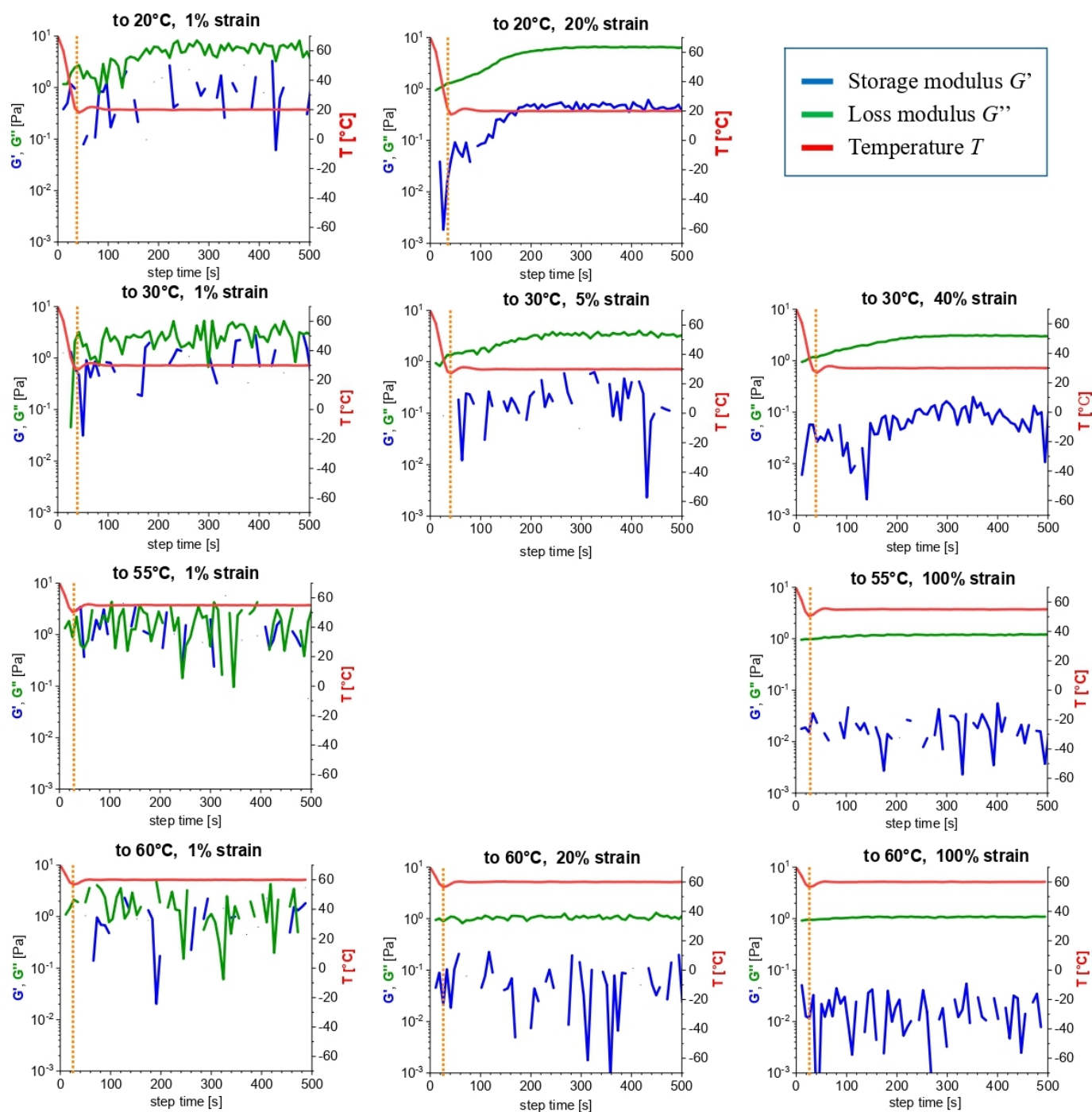
SI-Fig. 20: *Thixotropy effects visible as strong strain-dependence of the moduli values (G',
G") in case of the kinetics of physical gelation of molten H21–BAFKU₂ upon abrupt cooling.*

Thixotropic Loop tests

H21-BAFKU2

0°C
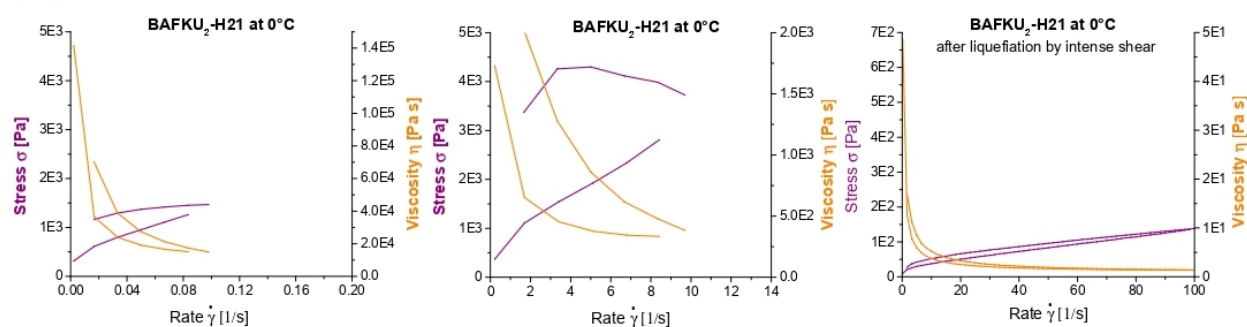
20°C
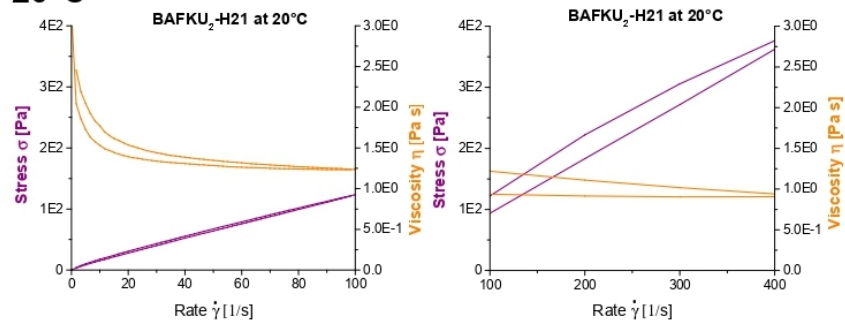
80°C
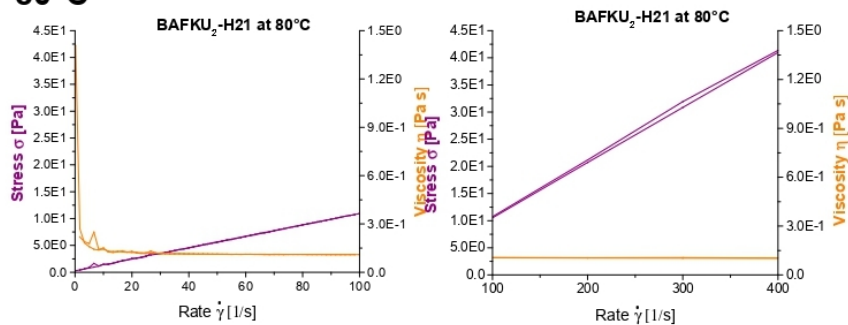
SI-Fig. 21: *Thixotropic loop tests (dependence of shear stress and of viscosity on the shear rate) for the copolymer H21–BAFKU$_2$ at 0, 20 and 80°C: at the left are continuous tests with shear rates rising up to 100 s^{-1}, at the right are step-wise tests with shear rates between 100 and 400 s^{-1}.*
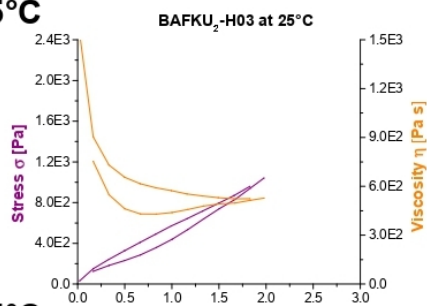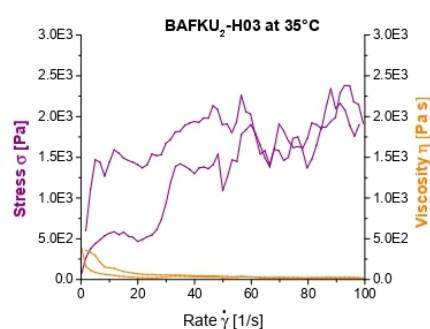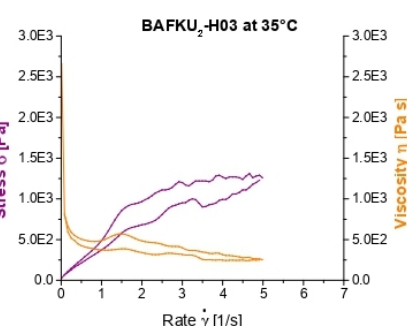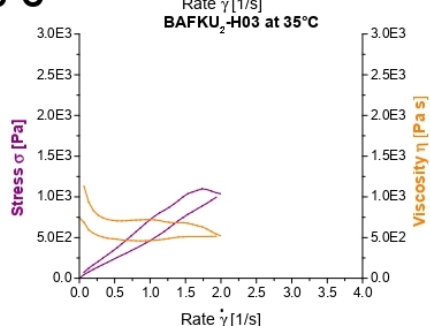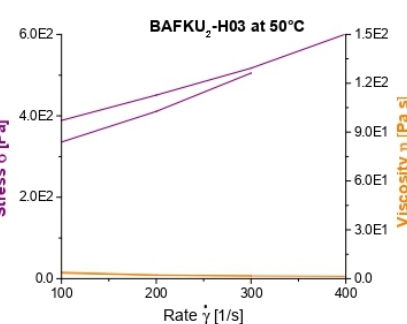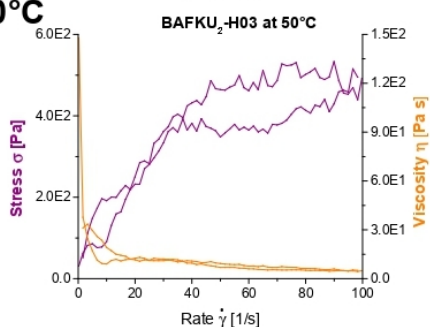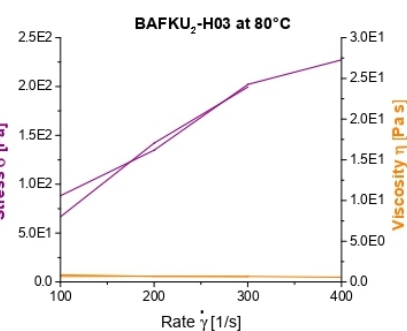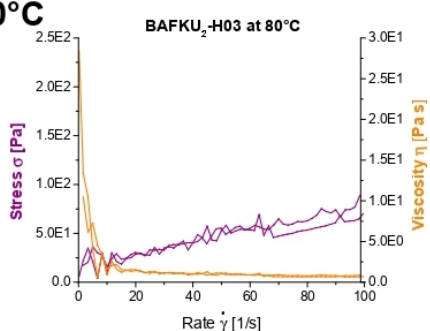
H03-BAFKU2

SI-Fig. 22: *Thixotropic loop tests (dependence of shear stress and of viscosity on the shear rate) for the copolymer H03–BAFKU2 at 25, 35, 50 and 80°C: at the left are continuous tests with shear rates rising up to 100 s⁻¹, at the right are step-wise tests with shear rates between 100 and 400 s⁻¹; at 35°C, only 100 s⁻¹ could be reached, but two low-shear-rates tests were performed.*

Appendix 4:

Thermo-reversible elastomers and smart oils based on linear infinite copolymers of azo-type mesogens and elastic polydimethylsiloxane blocks.

S. Horodecka, A. Strachota*, B. Mossety-Leszczak, M. Šlouf, A. Zhigunov, M. Vyroubalová, D. Kaňková, M. Netopilík, Z. Walterová.

Experimental

| Component		Sample name		
		A1-H03	A1-H11	A1-H21
A1	[g]	0.5	0.5	0.5
	[mmol] *	2.64	2.64	2.64
	wt%	37.72	24.14	7.41
	Vol% ‡	34.17	21.99	6.88
H03	[g]	0.8257	-	-
	[mmol] *	2.64	-	-
	wt%	62.28	-	-
	Vol% ‡	65.83	-	-
H11	[g]	-	1.5712	-
	[mmol] *	-	2.64	-
	wt%	-	75.9	-
	Vol% ‡	-	78.01	-
H21	[g]	-	-	6.249
	[mmol] *	-	-	2.64
	wt%	-	-	92.59
	Vol% ‡	-	-	93.12
Toluene	[g]	1.734	1.734	1.734
Karstedt's catalyst	[g]	0.0087	0.0087	0.0087
	[mmol]	0.02	0.02	0.02

Component		Sample name		
		A12- H03	A12-H11	A12- H21
A12	[g]	0.5	0.5	0.5
	[mmol] *	1.83	1.83	1.83
	wt%	46.66	31.5	10.18
	Vol% ‡	42.85	28.94	9.47
H03	[g]	0.5715	-	-
	[mmol] *	1.83	-	-
	wt%	53.54	-	-
	Vol% ‡	57.15	-	-
H11	[g]	-	1.0875	-
	[mmol] *	-	1.83	-
	wt%	-	68.5	-
	Vol% ‡	-	71.06	-
H21	[g]	-	-	4.413
	[mmol] *	-	-	1.83
	wt%	-	-	89.82
	Vol% ‡	-	-	90.53
Toluene	[g]	1.734	1.734	1.734
Karstedt's catalyst	[g]	0.0087	0.0087	0.0087
	[mmol]	0.02	0.02	0.02

Chemistry of Synthesis

α,ω-hydrido-functional PDMS precursors:

H03: n = 6.6 (total: **8.6**) ≡

H11: n = 14.3 (total: **16.3**) ≡

H21: n = 62.4 (total: **64.4**) ≡
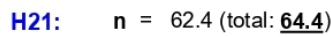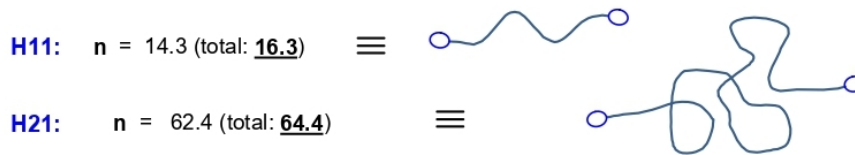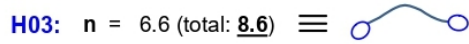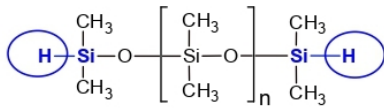
Divinyl-functional azo mesogens:

A1: ≡

A12:

azo group

 +

Karstedt's catalyst | solvent

≡
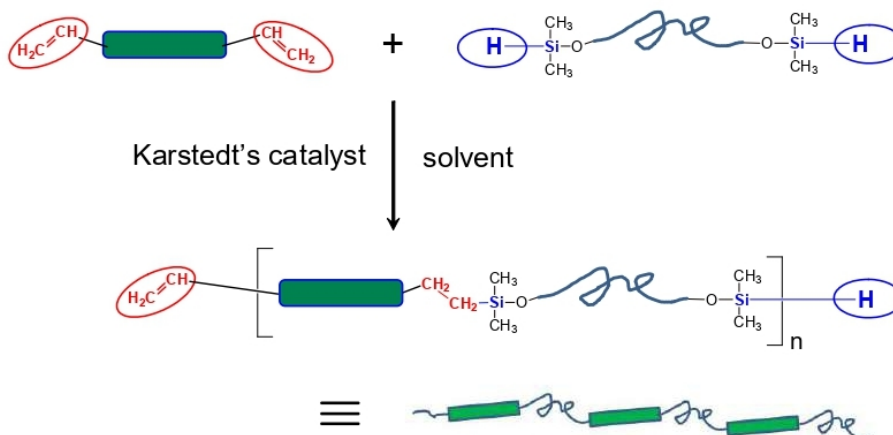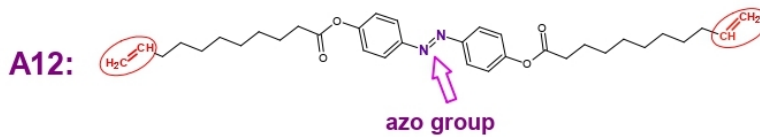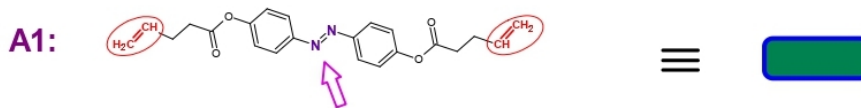
The products

Linear infinite PDMS-LC copolymers of azo type: (top): general chemical structure on the example of a copolymer containing the A1 mesogen ; (bottom): symbolic representation of the macromolecules of the studied copolymers with incorporated PDMS 'spring segments' H03, H11, and H21, as well as of the physical crosslinking in this type of copolymers; copolymers with the A12 mesogen have an analogous structure.

Volume fraction of liquid crystalline component in the prepared copolymers.

Name of the sample	Volume % of LC component *
linear infinite LC-PDMS copolymers with azo-type mesogens	
A1-*co*-H03	34.17
A1-*co*-H11	21.99
A1-*co*-H21	6.88
A12-*co*-H03	42.85
A12-*co*-H11	28.94
A12-*co*-H21	9.47
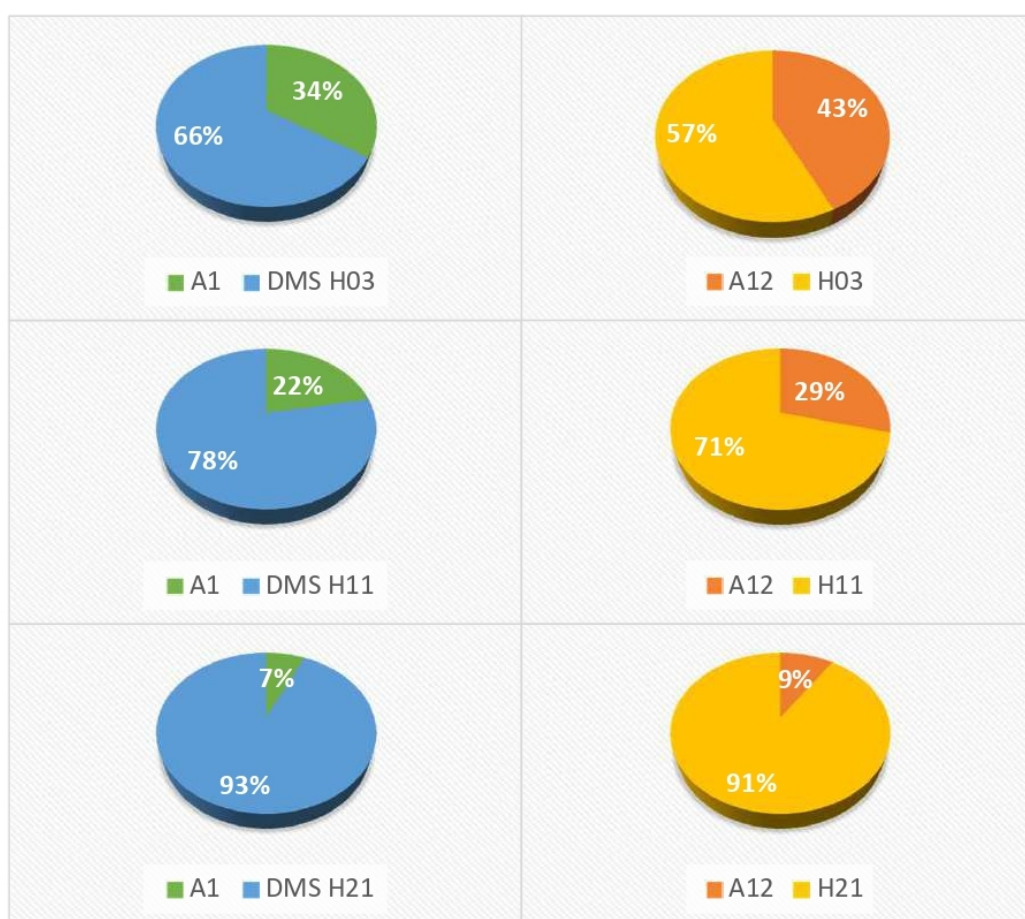
Diagrams of volume fractions of the A1 and A12 mesogens units in each copolymer.

DMTA: storage modulus (G') versus temperature in the cooling and heating run
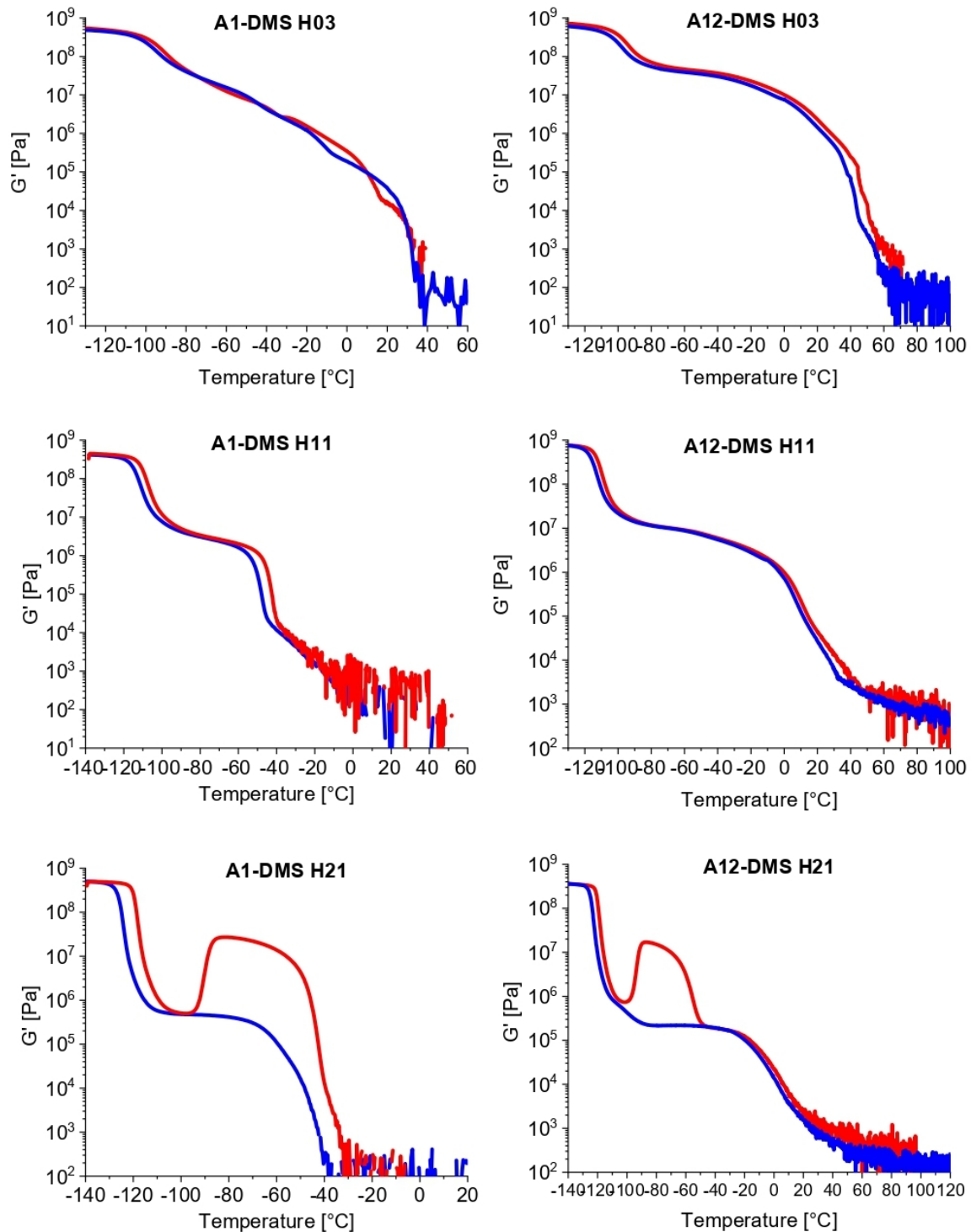
DMTA profiles (all data) of the copolymers (left column, top to bottom) H03-A1, H11-A1, H21-A1 and (right column, top to bottom) H03-A12, H11-A12, H21-A12 recorded as cooling (blue) and heating (red) scans.

DSC: specific heat of phase transitions in neat mesogens and in the copolymers
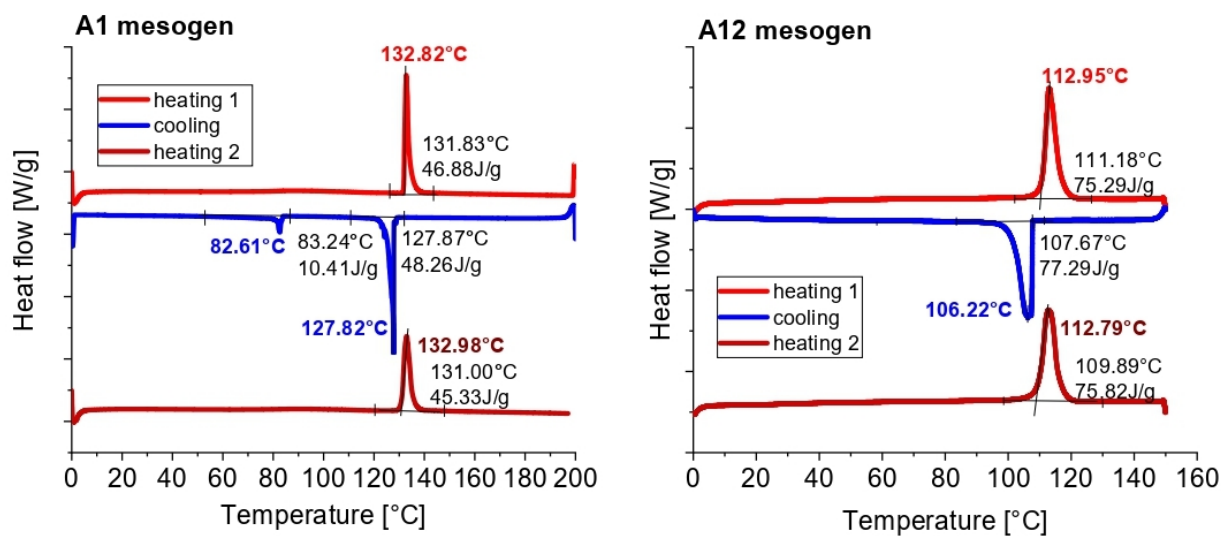
DSC traces (a) of the neat A1 mesogen and (b) A12 mesogen.
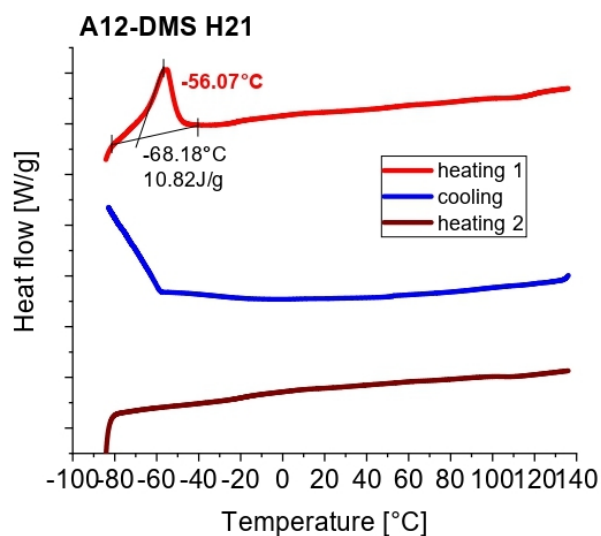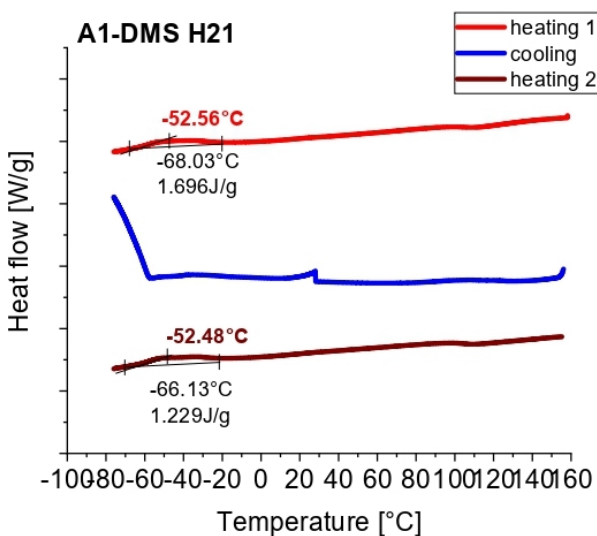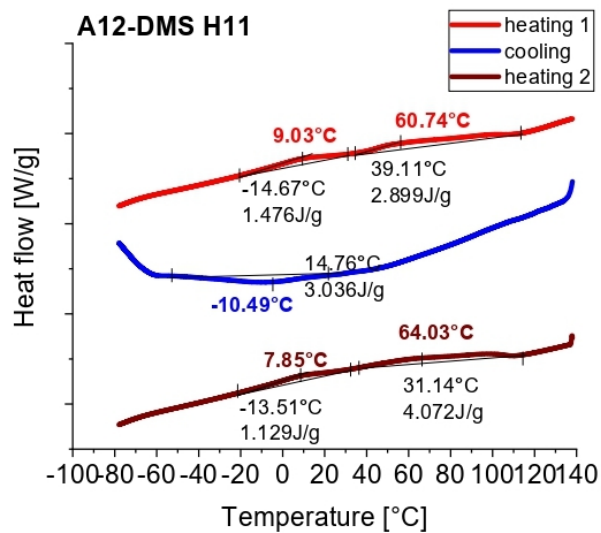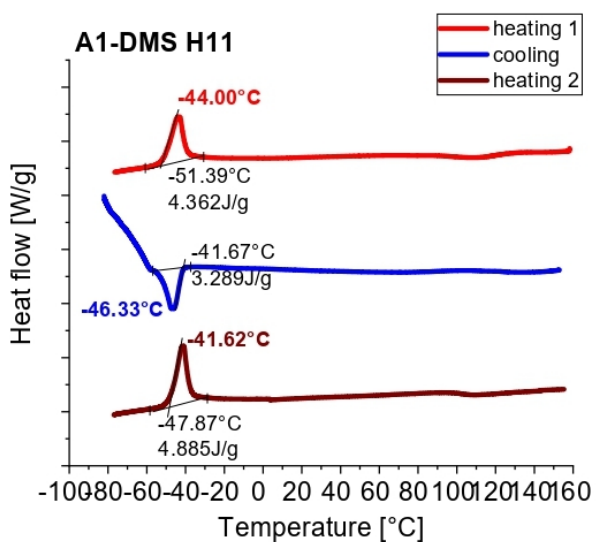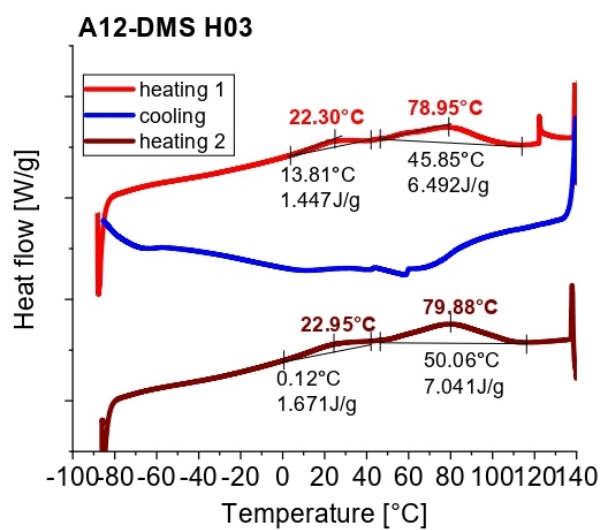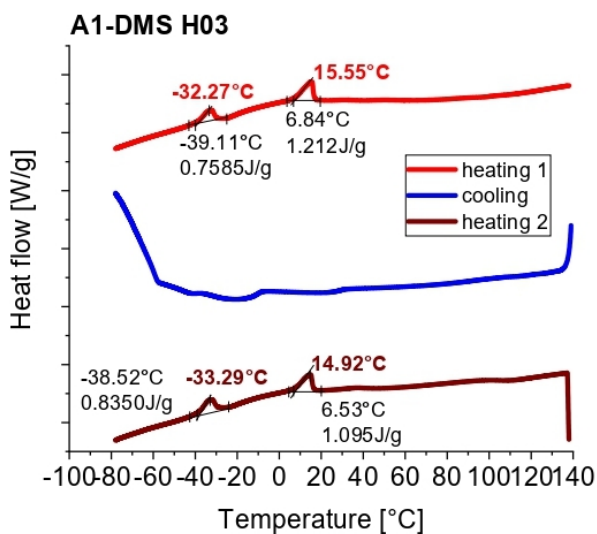
DSC traces (left column) of the copolymers with A1 mesogen and (right column) copolymers with A12 mesogen.

X-ray diffraction

not finished

PLM analysis

A1, neat

heating
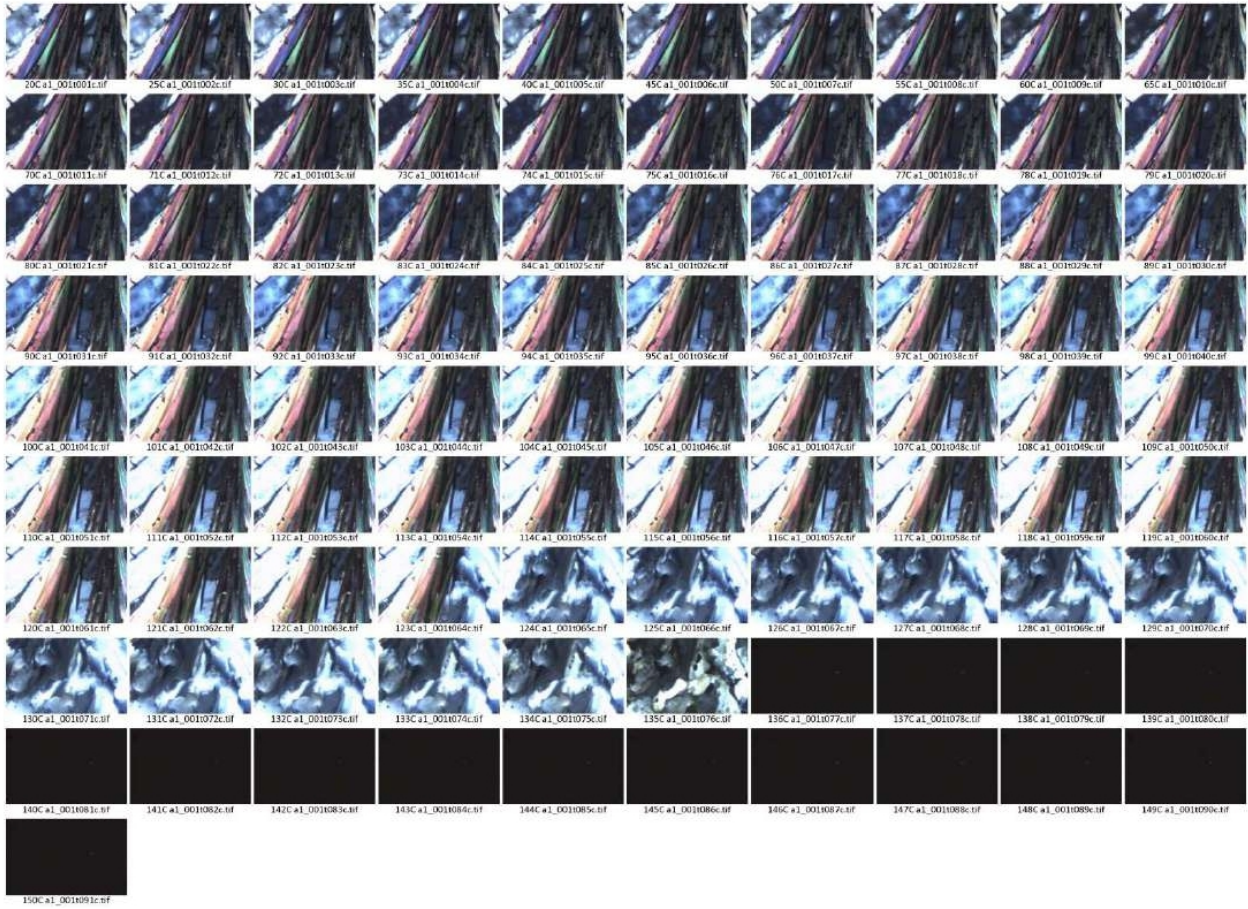
A1, neat

cooling
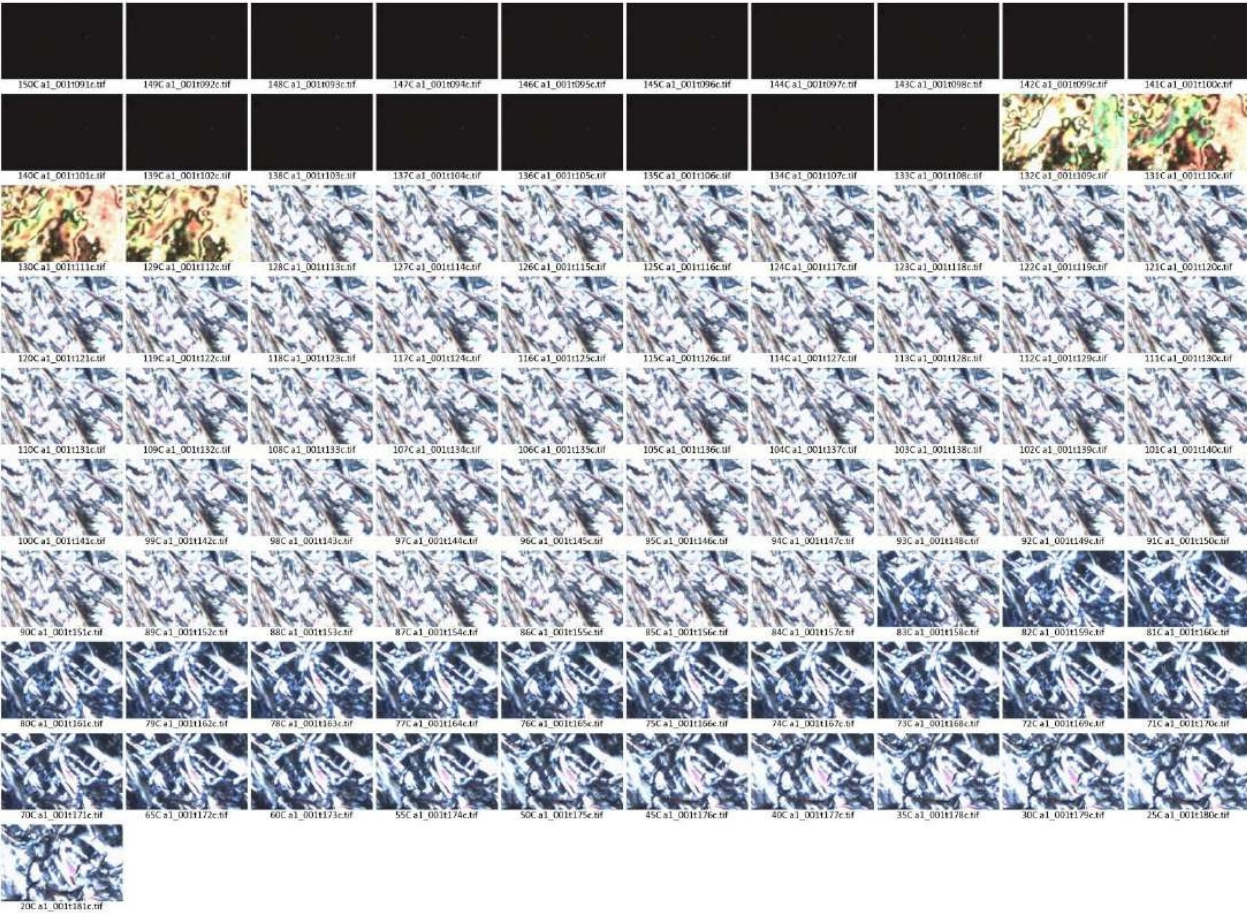
A1-*co*-H03

apparently isotropic

A1-*co*-H11

homogeneous submicron-anisotropy

A1-*co*-H21

not finished

A12, neat

A12-*co*-PDMS

not finished

Supporting information - Analyses

Evaluation of conversion of the PDMS during hydrosilylation reaction by means of FTIR
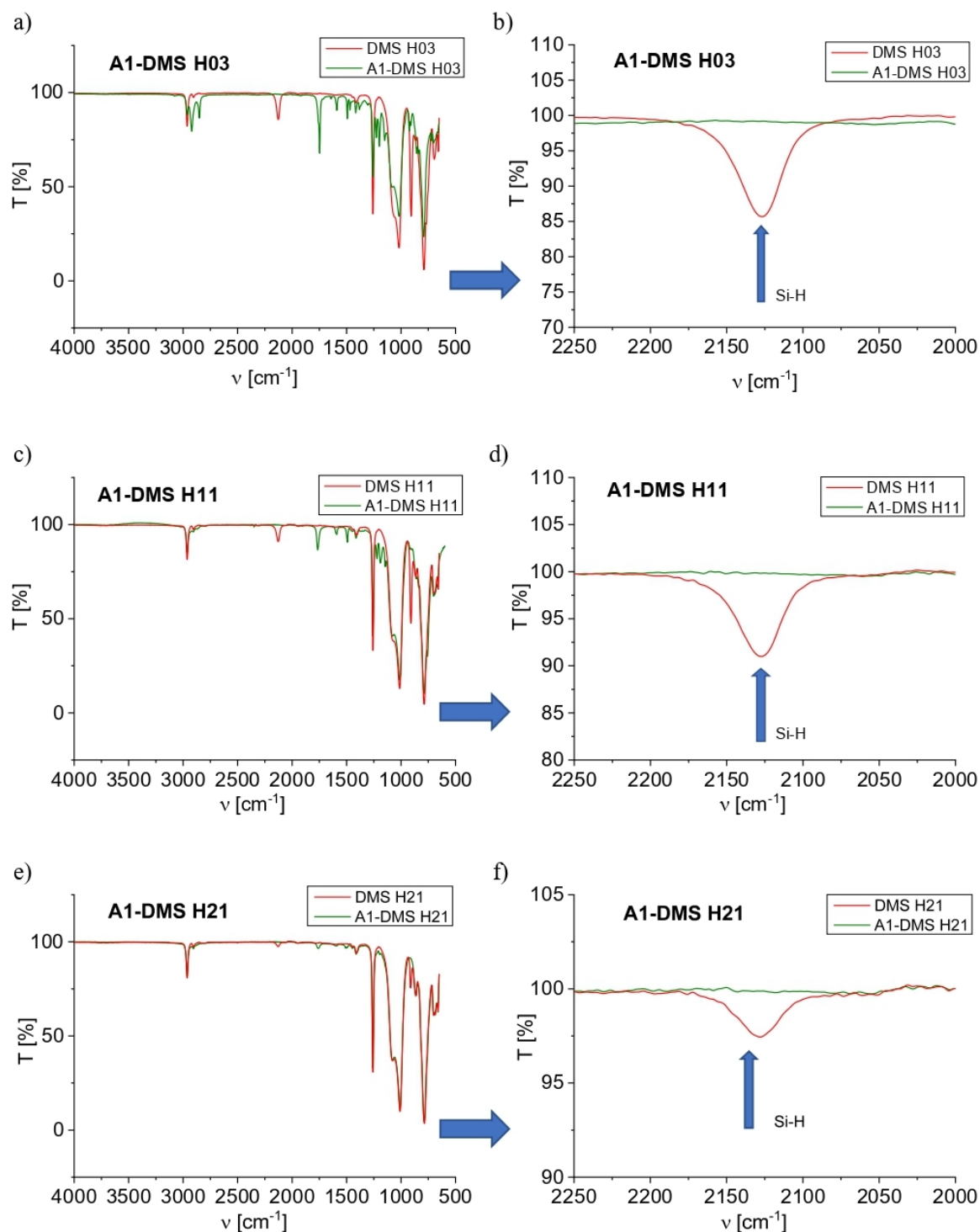
Spectroscopic evaluation of the completion of the hydrosilylation reaction: (a), (c), (e): FTIR spectra of pure PDMS and of LC-PDMS copolymers with A1 as mesogen; (b), (d), (f): highlighting the disappearance of the Si-H as zoomed inlay
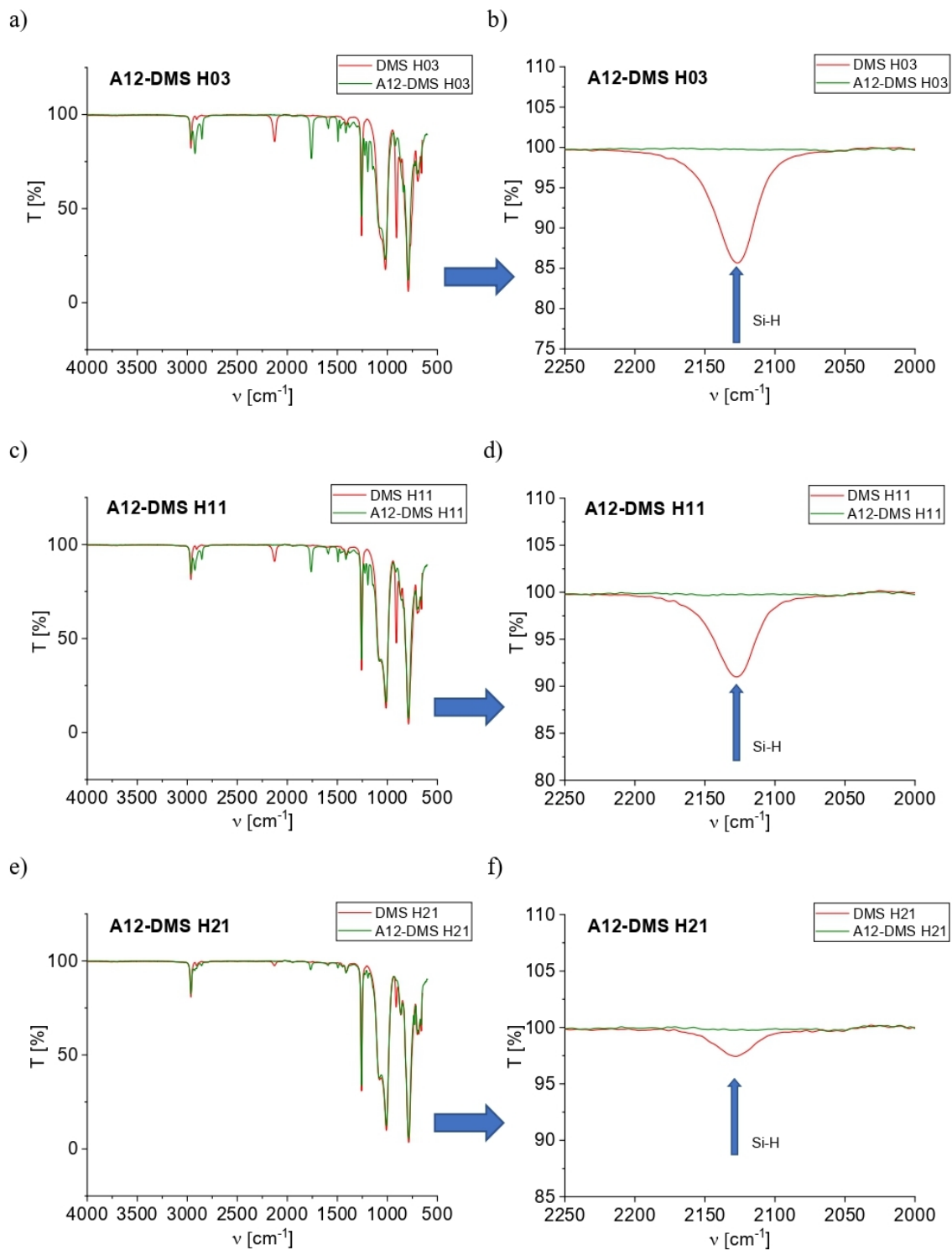
Spectroscopic evaluation of the completion of the hydrosilylation reaction: (a), (c), (e): FTIR spectra of pure PDMS and of LC-PDMS copolymers with A12 as mesogen; (b), (d), (f): highlighting the disappearance of the Si-H as zoomed inlay

^{1}H-NMR: Purity of components and products, as well as synthesis conversion

HORODECKA - A1 - CDCl3 - 299K   1H

HORODECKA - A12 - CDCl3 - 300K   1H
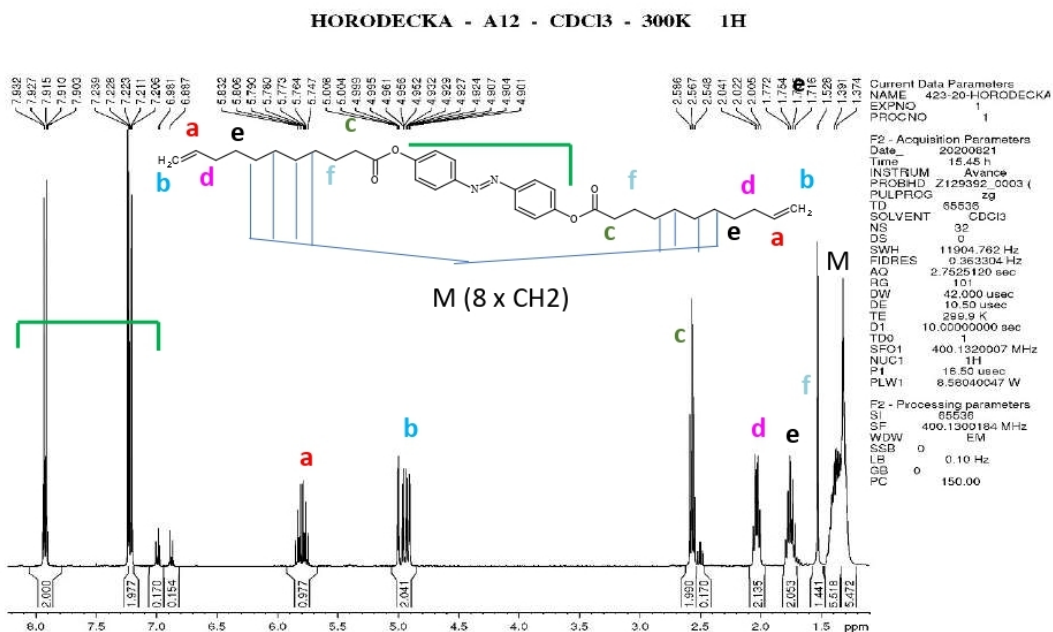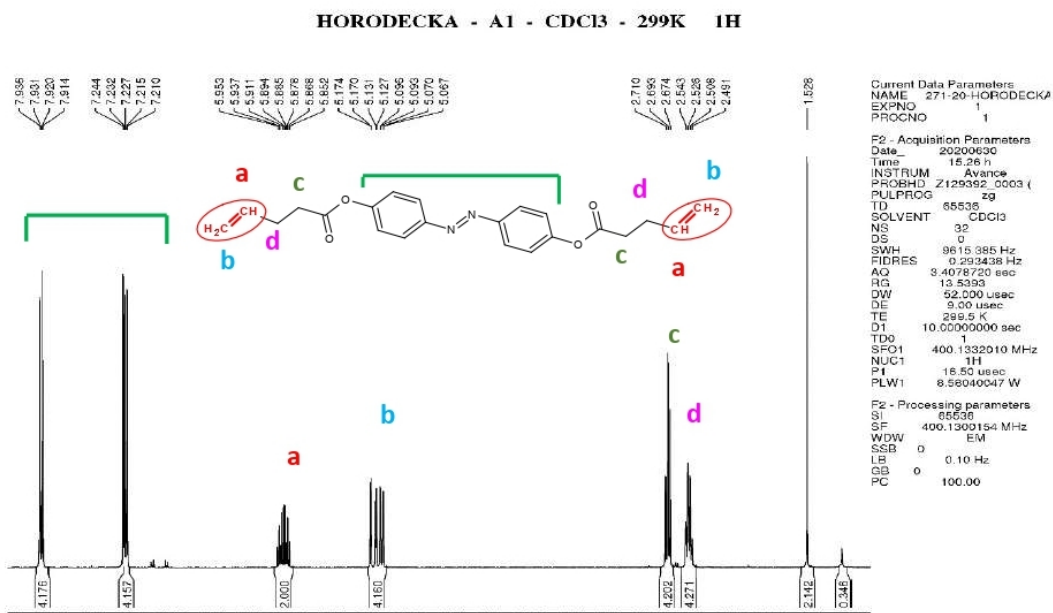
^{1}H-NMR spectrum of the pure A1 and A12 mesogens with assigned peaks.

Copolymers PDMS–LC (A1 and A12): ^{1}H-NMR analysis
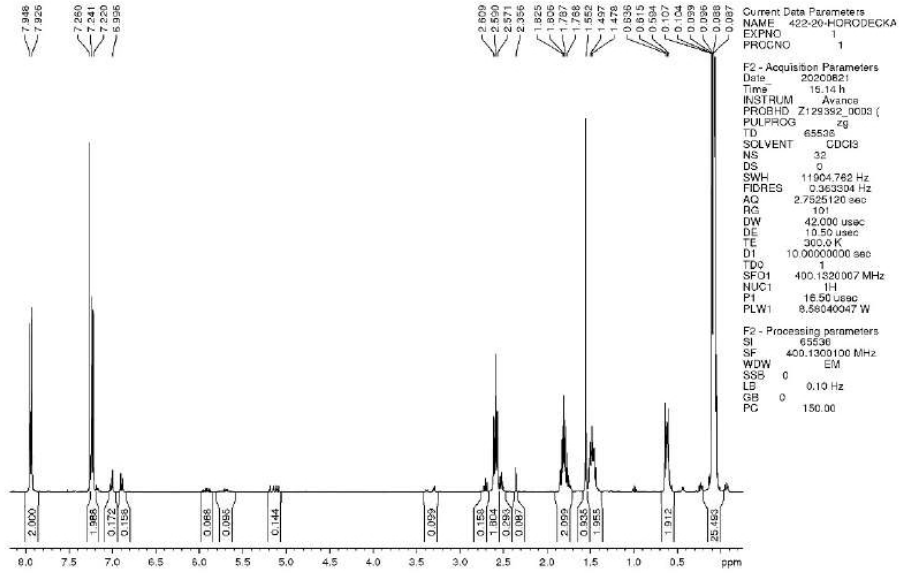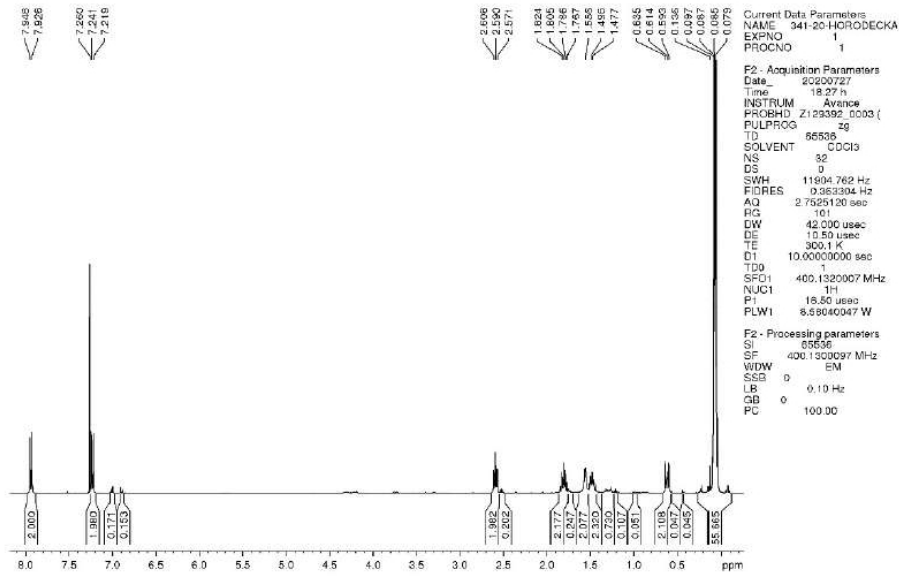
^{1}H-NMR spectra of the copolymers (top): H03–A1; (bottom): H11–A1.

HORODECKA - A1-H21 - CDCl3 - 300K   1H
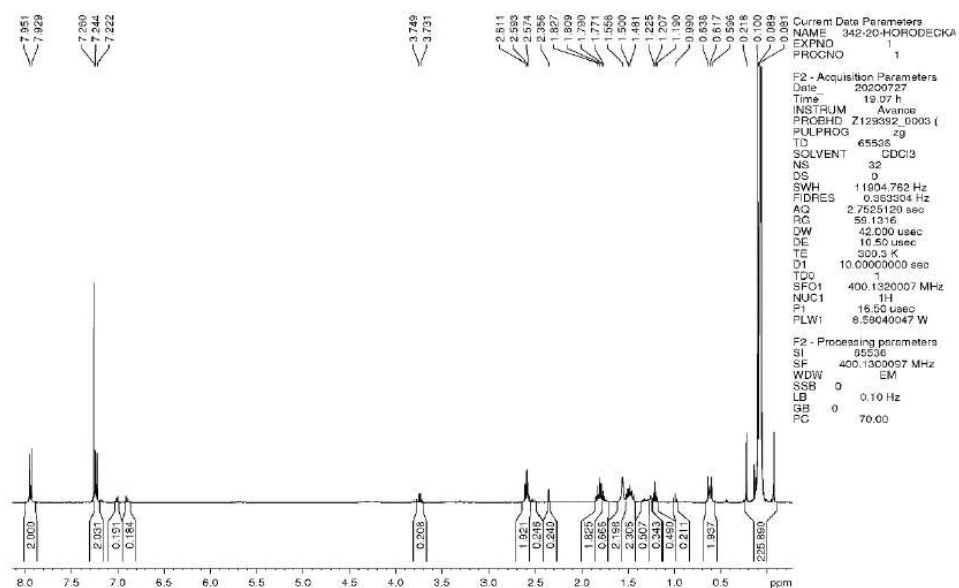
¹H-NMR spectra of the copolymer H21–A1.

HORODECKA - A12-H03 - CDCl3 - 300K   1H
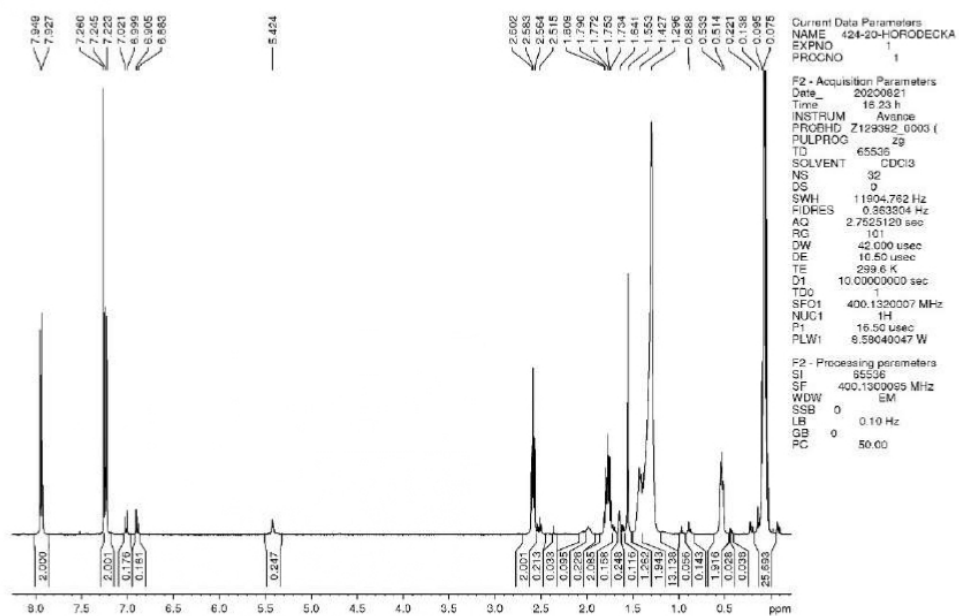
¹H-NMR spectra of the copolymer H03–A12.
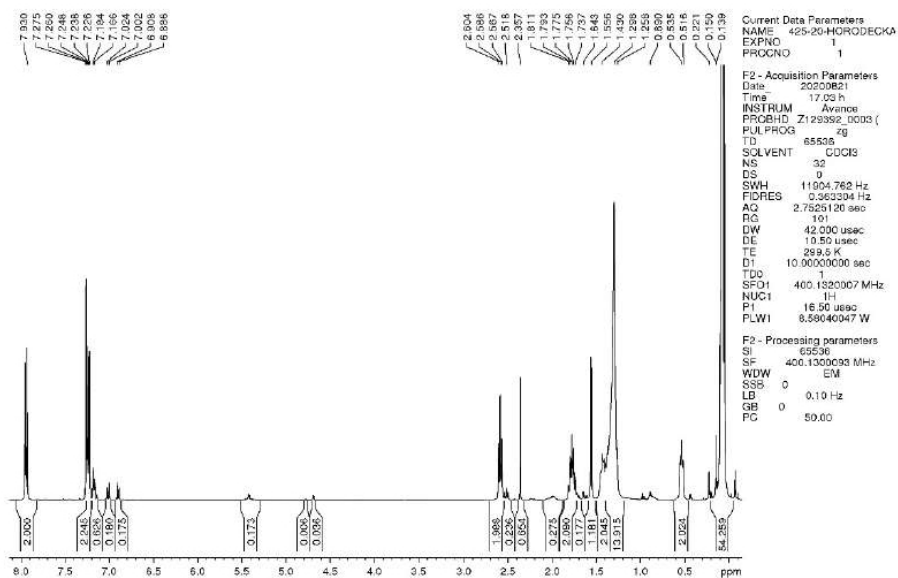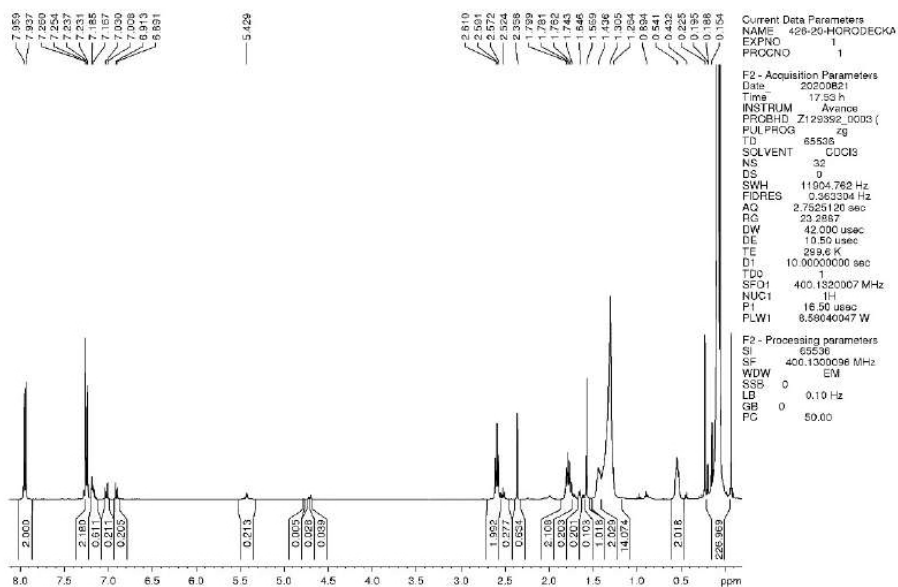
1H-NMR spectra of the copolymers (top): H11–A12; (bottom): H21–A12.

GPC traces of the neat mesogens and of the final copolymers, source data
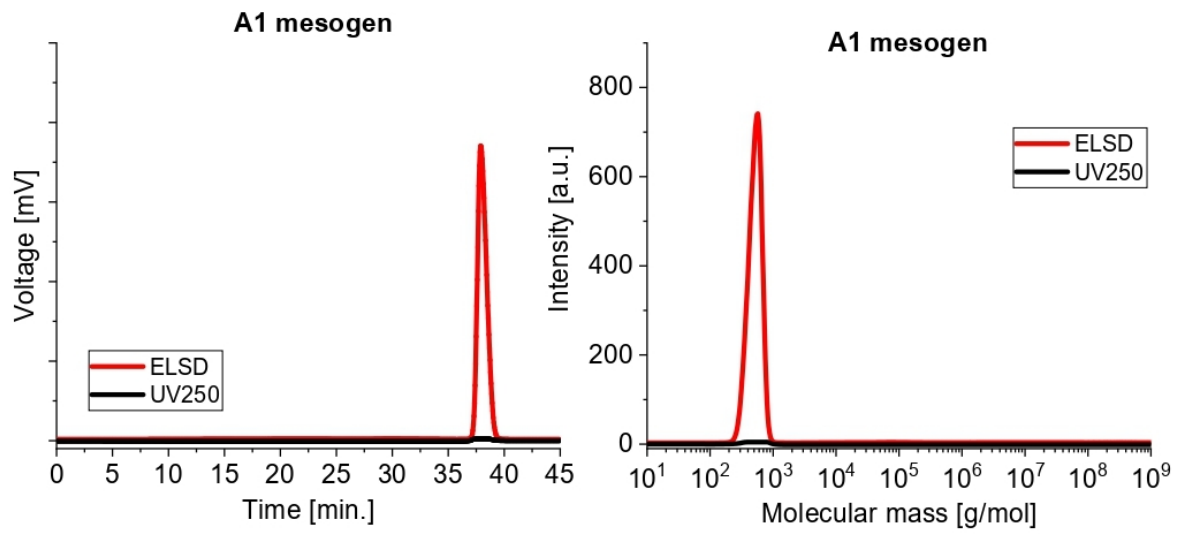
A1 mesogen										
nr.	Max. RT	Start RT	End RT	flow rate correction	Mp	Mn	Mw	Mz	PD	I [mV]	I [%]
1	37.96	36.32	40.98	1	547	489	518	545	1.0592	748.43	100

GPC trace of pure A1.
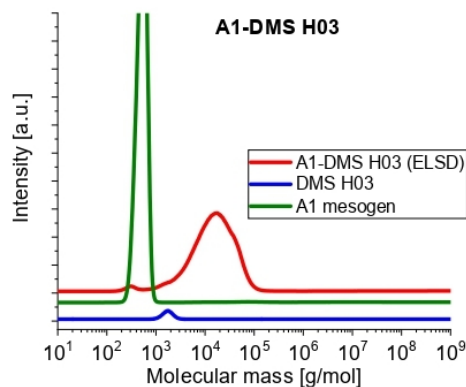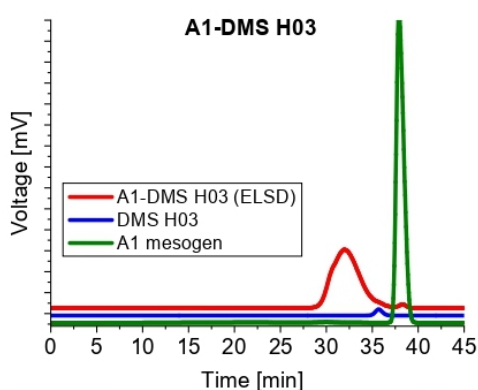
A1-DMS H03

nr.	Max. RT	Start RT	End RT	flow rate correction	Mp	Mn	Mw	Mz	PD	I [mV]	I [%]
1	31.93	27.69	37.40	1	17751	8472	20578	37661	2.4289	139.71	93.98
x	38.35	37.40	40.22	1	296	295	319	342	1.0788	8.96	6.02
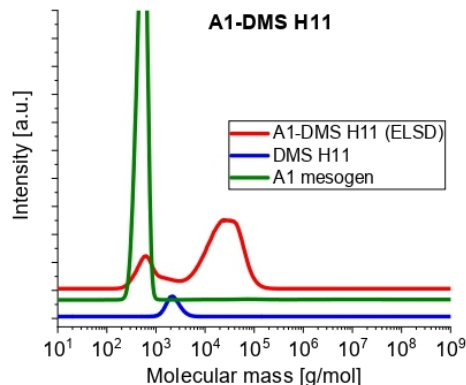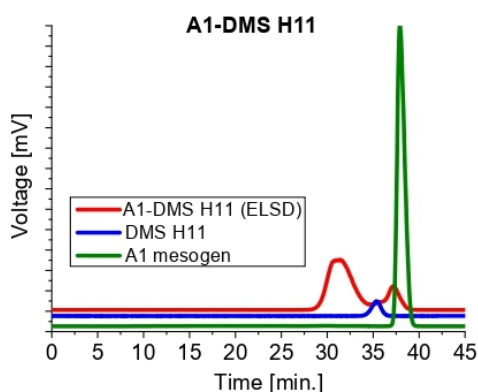
A1-DMS H11

nr.	Max. RT	Start RT	End RT	flow rate correction	Mp	Mn	Mw	Mz	PD	I [mV]	I [%]
1	31.45	28.08	34.66	1	24104	19558	31180	45898	1.5942	115.91	69.09
x	37.17	34.66	39.19	1	629	571	704	906	1.2326	51.85	30.91
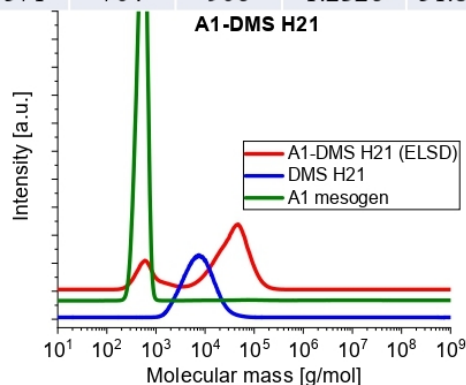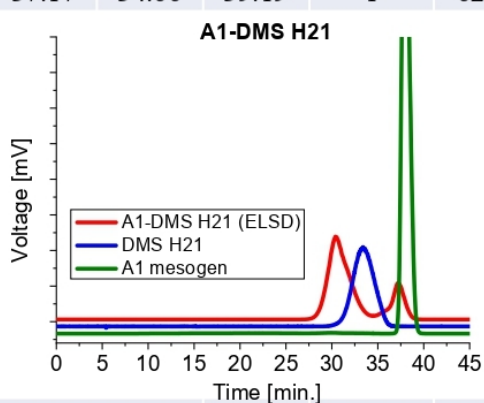
A1-DMS H21

nr.	Max. RT	Start RT	End RT	flow rate correction	Mp	Mn	Mw	Mz	PD	I [mV]	I [%]
1	30.45	26.81	34.58	1	45400	25046	44454	69265	1.7749	116.78	69.20
x	37.25	34.58	40.01	1	596	587	802	1179	1.3653	51.96	30.80

GPC trace of the copolymers H03–A1, H11-A1, H21-A1 overlaid with traces of pure A1 and pure PDMS.

A12-DMS H03
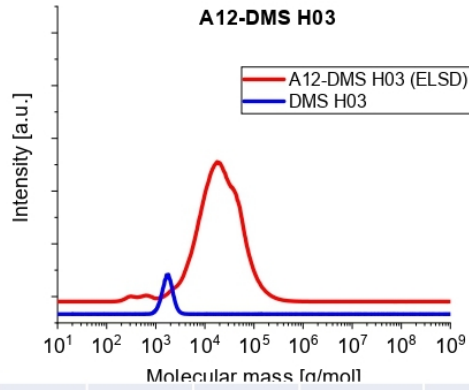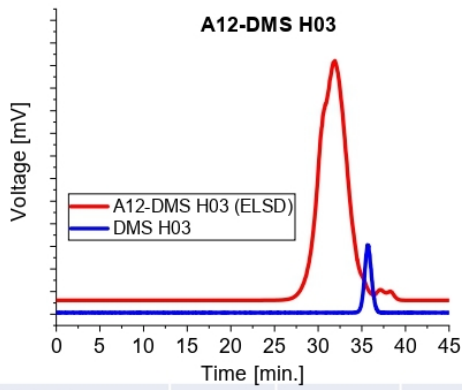
A12-DMS H03

A12-DMS H03										
nr.	Max. RT	Start RT	End RT	flow rate correction	Mp	Mn	Mw	Mz	PD	I [mV]	I [%]
1	31.92	25.75	36.28	1	17796	13266	30757	71044	2.3185	52.32	94.70
2	37.12	36.28	37.80	1	648	591	615	640	1.0408	1.43	2.58
X	38.31	37.80	39.48	1	304	292	304	315	1.0405	1.51	2.73

A12-DMS H11
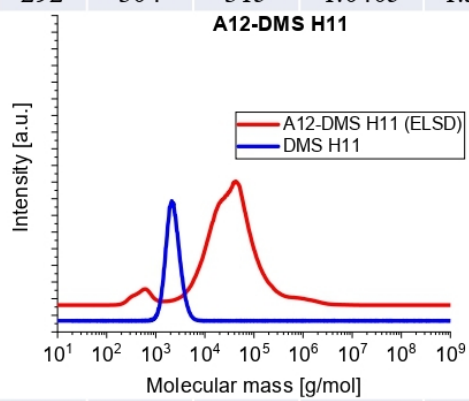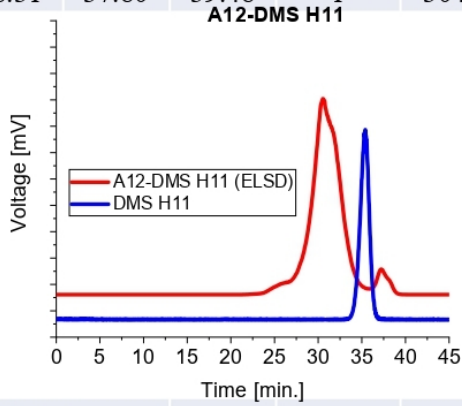
A12-DMS H11

A12-DMS H11										
nr.	Max. RT	Start RT	End RT	flow rate correction	Mp	Mn	Mw	Mz	PD	I [mV]	I [%]
1	30.63	21.80	35.66	1	40548	22459	83784	701502	3.7306	36.56	89.74
x	37.25	35.66	39.43	1	597	469	540	614	1.1518	4.18	10.26

A12-DMS H21
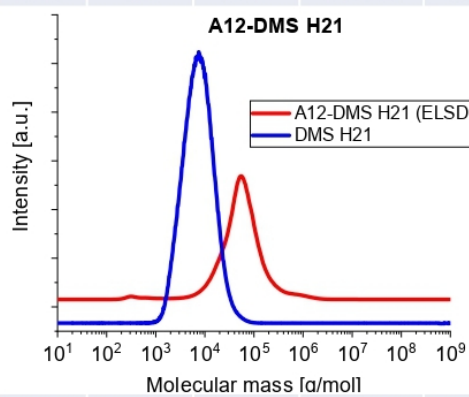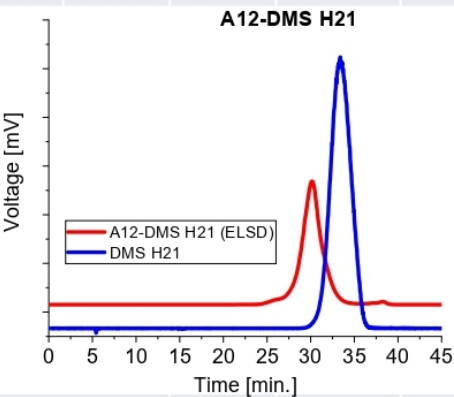
A12-DMS H21

A12-DMS H21										
nr.	Max. RT	Start RT	End RT	flow rate correction	Mp	Mn	Mw	Mz	PD	I [mV]	I [%]
1	30.13	23.59	35.68	1	55577	36408	93068	376301	2.5562	50.90	97.65
x	38.31	35.68	41.56	1	303	399	552	769	1.3840	1.23	2.35

GPC trace of the copolymers H03–A12, H11-A12, H21-A12 overlaid with traces of pure PDMS.

Appendix 5:

Rheological and viscoelastic properties of low-temperature-meltable elastomers and smart oils based on linear infinite copolymers of azo-type mesogens and elastic polydimethylsiloxane blocks.

S. Horodecka, A. Strachota*, B. Mossety-Leszczak.

Materials
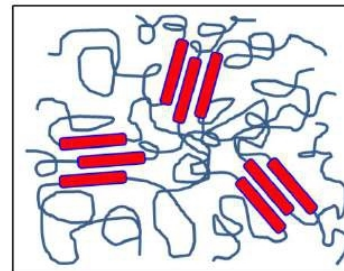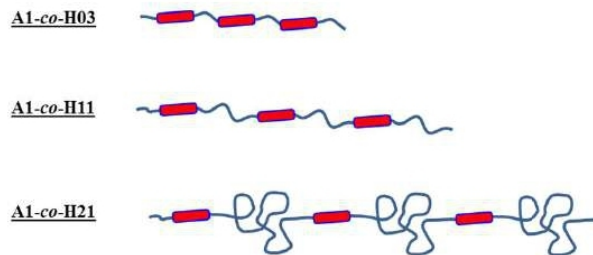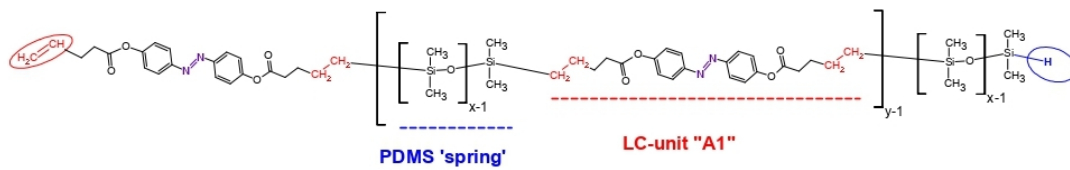
PDMS 'spring'

LC-unit "A1"

A1-*co*-H03

A1-*co*-H11

A1-*co*-H21

Linear infinite PDMS-LC copolymers of azo type: (top): general chemical structure on the example of a copolymer containing the A1 mesogen ; (bottom): symbolic representation of the macromolecules of the studied copolymers with incorporated PDMS 'spring segments' H03, H11, and H21, as well as of the physical crosslinking in this type of copolymers; copolymers with the A12 mesogen have an analogous structure.

Gelation study via T-dependent multi-frequency rheology experiments

A1-co-H03

(a)

(b)

(c)

(d)
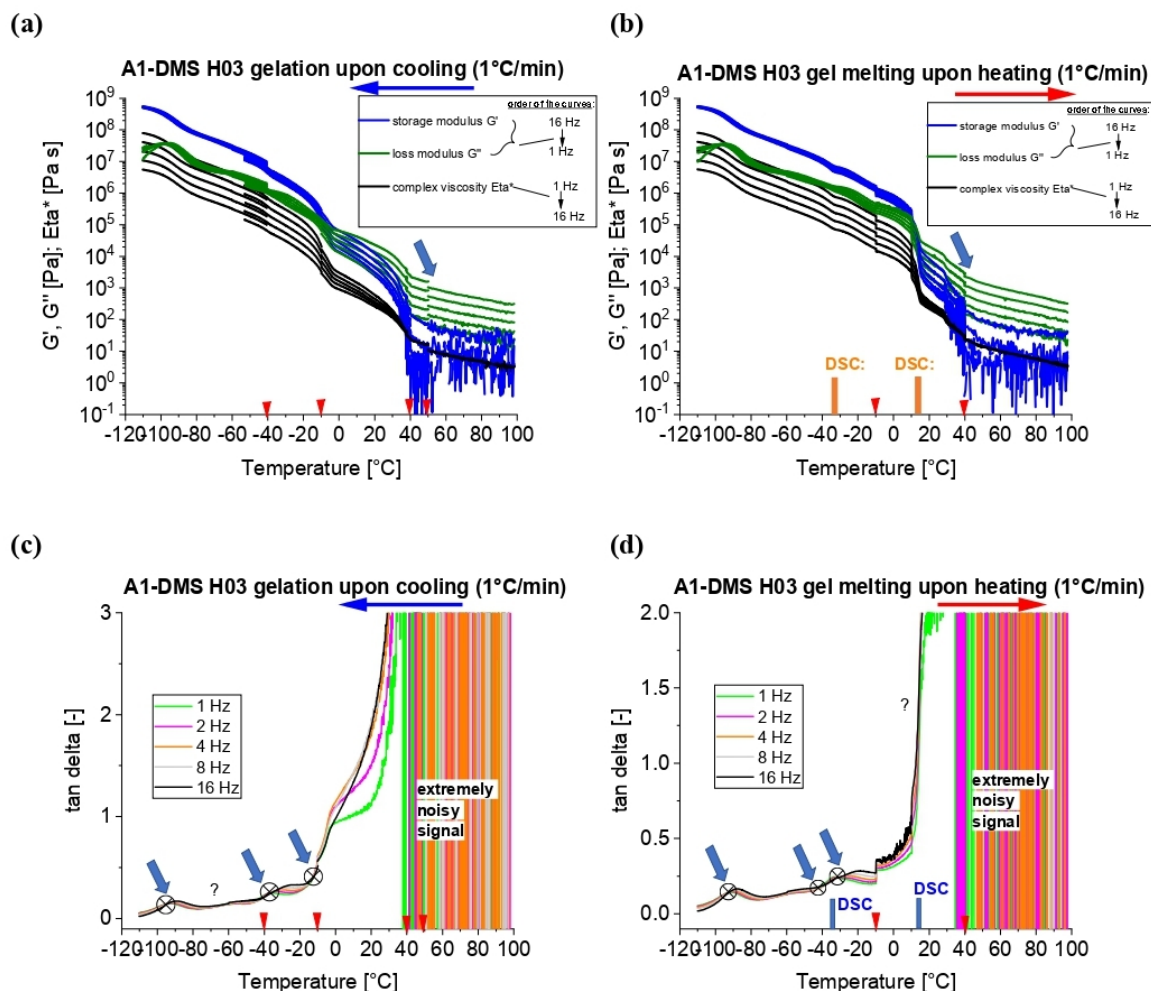
Multi-frequency temperature ramp tests carried out for vitrimeric copolymer H03–A1: (a), (b): temperature dependence of the storage shear moduli G', of the loss moduli G'', of the complex viscosities Eta* recorded at the simultaneously applied frequencies of 1, 2, 4, 8 and 16 Hz; (c), (d): sets of the tan δ curves with marked crossover (or near-crossover) points; red signs indicate change in strain.

A1-co-H11
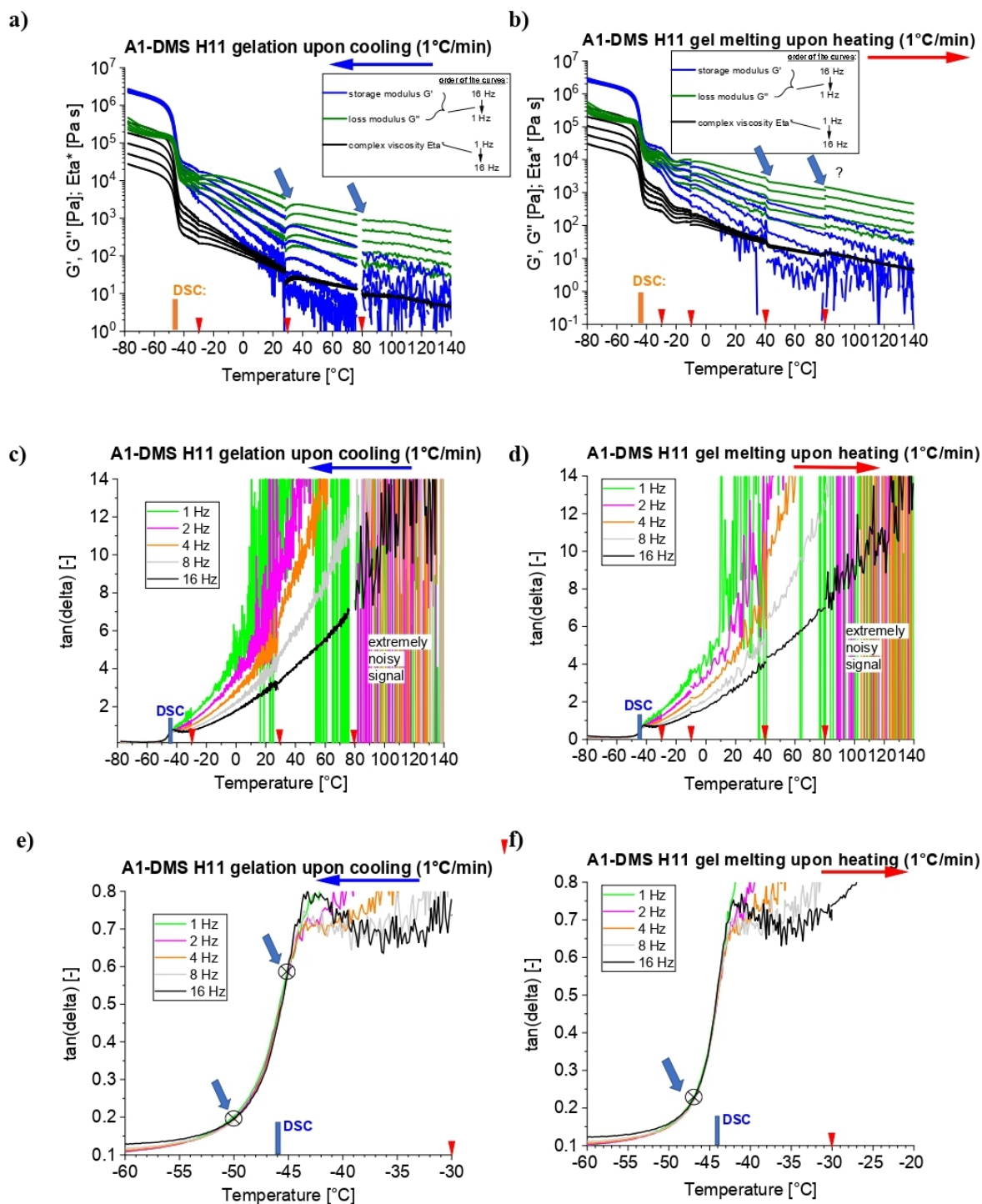
Multi-frequency temperature ramp tests carried out in melting and rubber state of the H11–A1: (a), (b): temperature dependence of the storage shear moduli G', of the loss moduli G'', of the complex viscosities Eta* recorded at the simultaneously applied frequencies of 1, 2, 4, 8 and 16 Hz; (c), (d): sets of the tan δ curves; (e), (f): details of the tan δ curves with marked crossover (or near-crossover) points; red signs indicate change in strain.

A1-co-H21

a)

A1-DMS H21 gelation upon cooling (1°C/min)

b)

A1-DMS H21 gel melting upon heating (1°C/min)

c)

A1-DMS H21 gelation upon cooling (1°C/min)

d)

A1-DMS H21 gel melting upon heating (1°C/min)

e)

A1-DMS H21 gelation upon cooling (1°C/min)

f)

A1-DMS H21 gel melting upon heating (1°C/min)
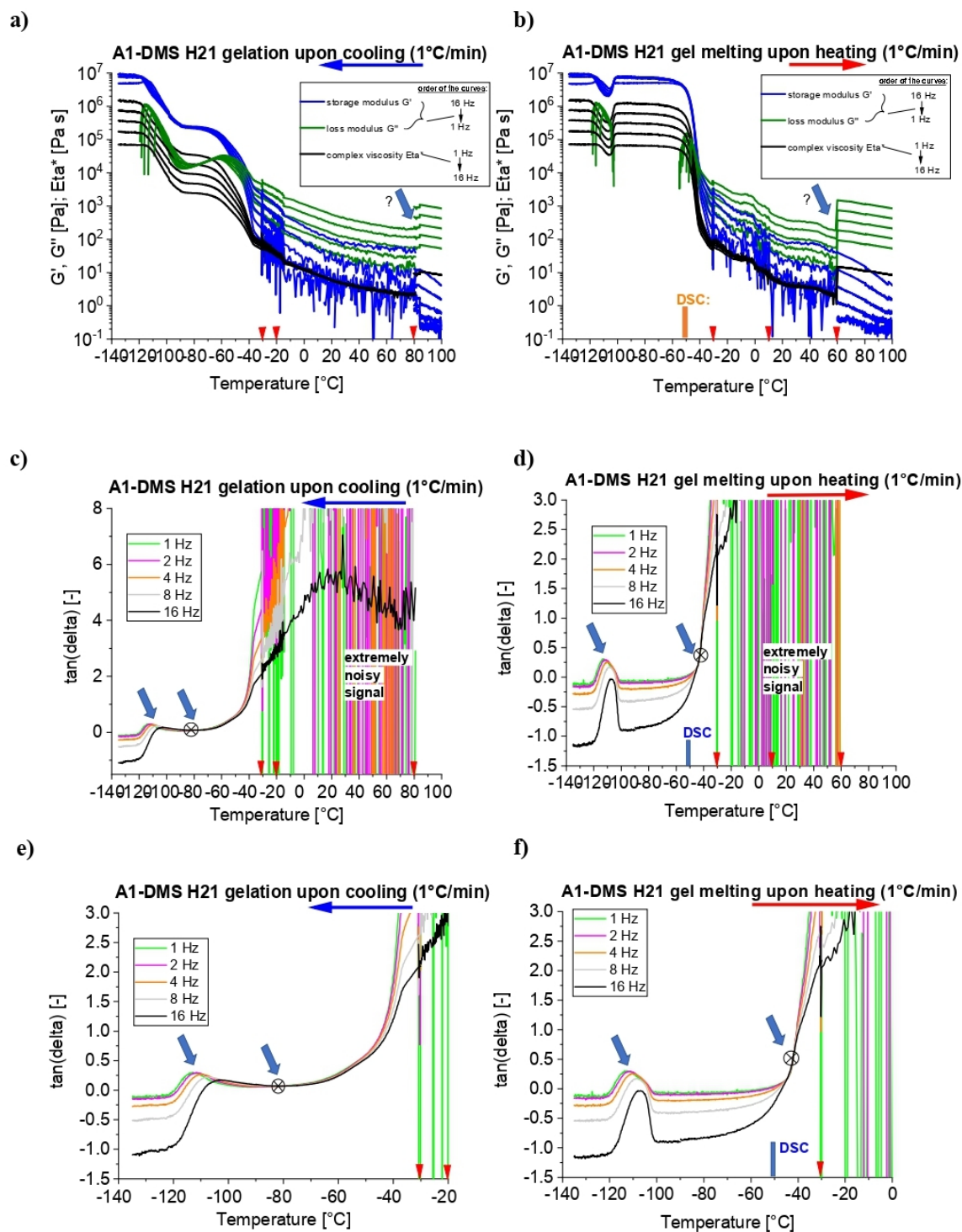
Multi-frequency temperature ramp tests carried out in melting, rubber and glassy state of the H21–A1: (a), (b): temperature dependence of the storage shear moduli G', of the loss moduli G'', of the complex viscosities Eta recorded at the simultaneously applied frequencies of 1, 2, 4, 8 and 16 Hz; (c), (d): sets of the tan δ curves; (e), (f): details of the tan δ curves with marked crossover (or near-crossover) points; red signs indicate change in strain.*

A12-co-H03

a)

A12-DMS H03 gelation upon cooling (1°C/min)

b)

A12-DMS H03 gel melting upon heating (1°C/min)

c)

A12-DMS H03 gelation upon cooling (1°C/min)

d)

A12-DMS H03 gel melting upon heating (1°C/min)
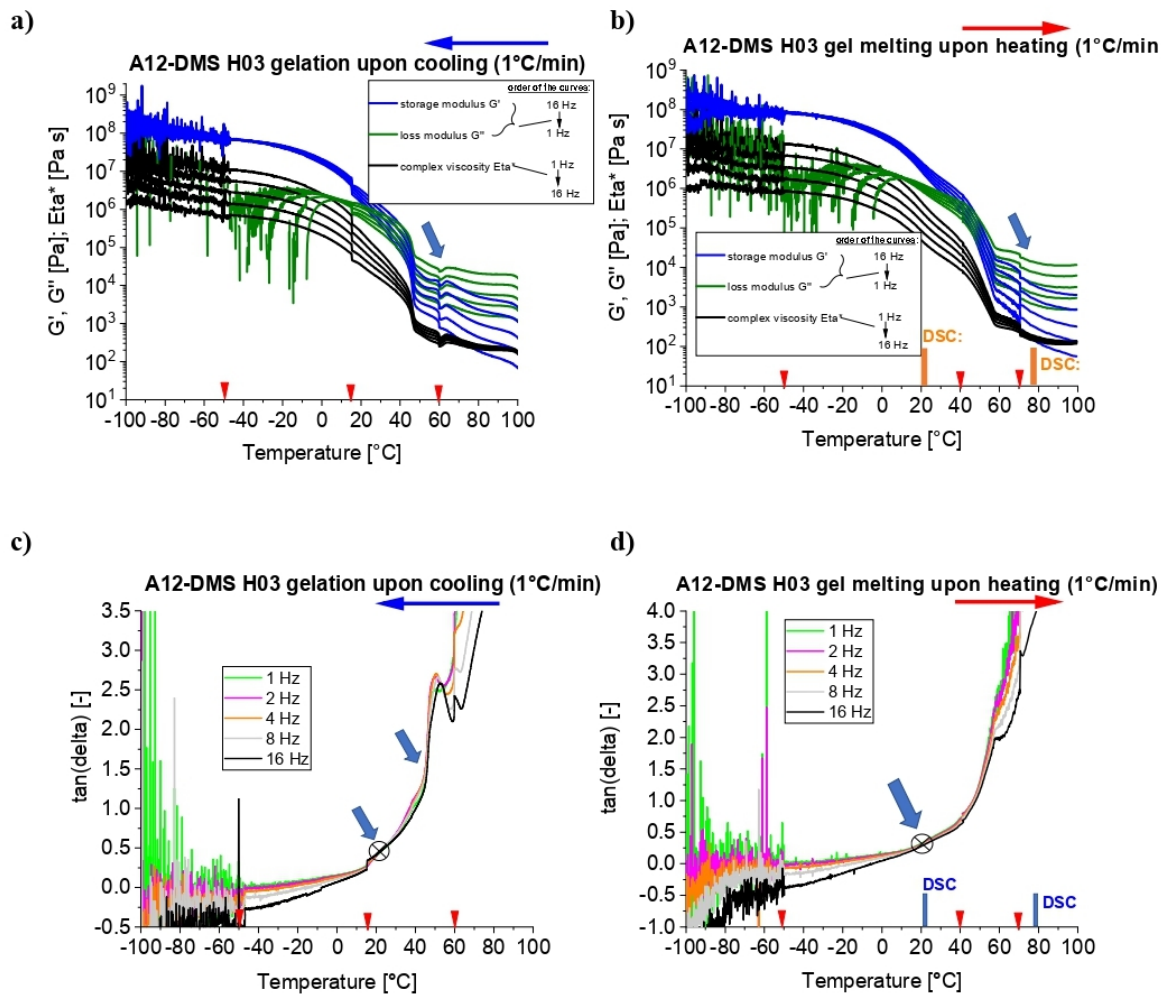
Multi-frequency temperature ramp tests carried out for vitrimeric copolymer H03–A12: (a), (b): temperature dependence of the storage shear moduli G', of the loss moduli G", of the complex viscosities Eta* recorded at the simultaneously applied frequencies of 1, 2, 4, 8 and 16 Hz; (c), (d): sets of the tan δ curves with marked crossover (or near-crossover) points; red signs indicate change in strain.

A12-co-H11
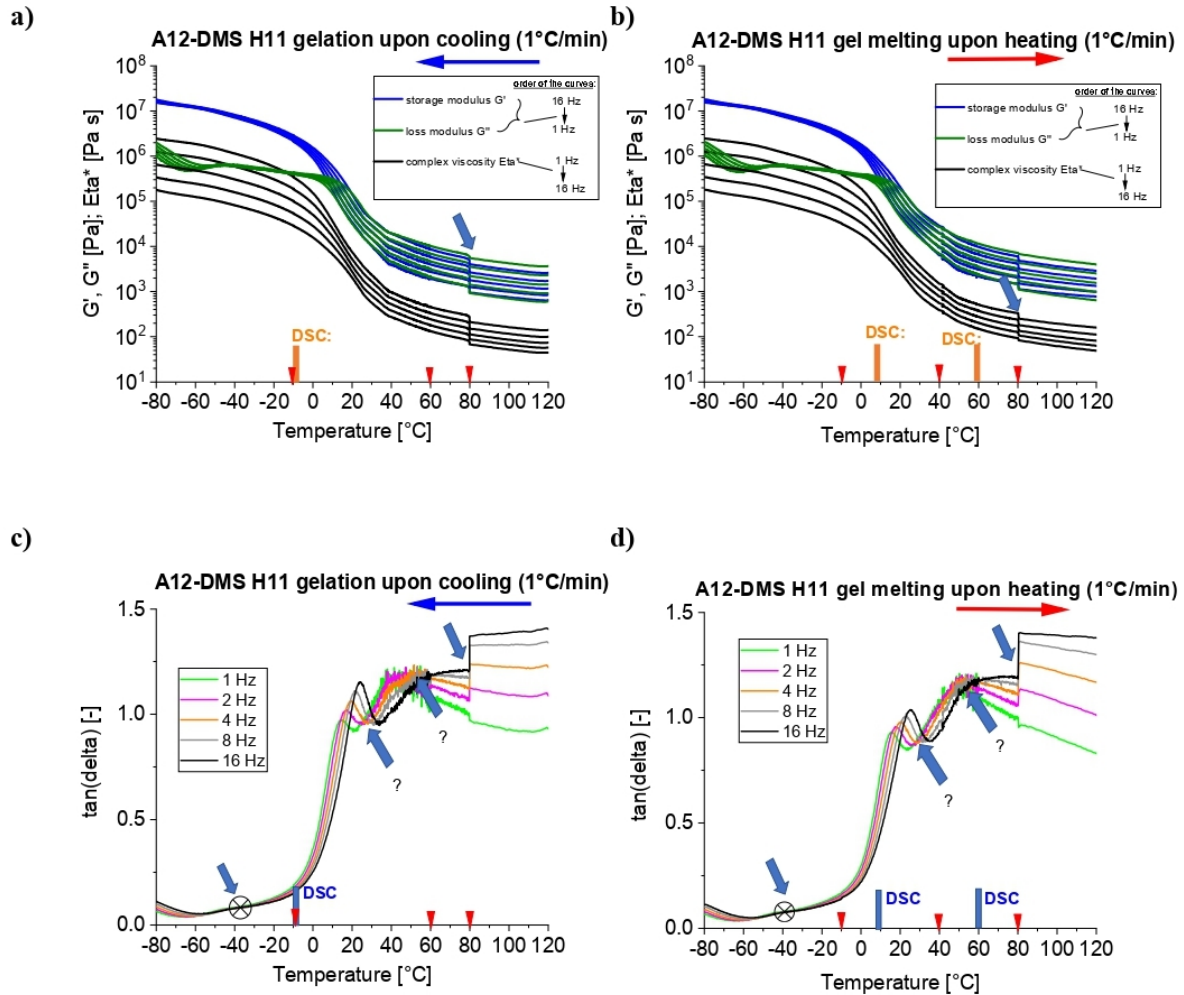
Multi-frequency temperature ramp tests carried out in melting and rubbery state of the H11–A12: (a), (b): temperature dependence of the storage shear moduli G', of the loss moduli G", of the complex viscosities Eta* recorded at the simultaneously applied frequencies of 1, 2, 4, 8 and 16 Hz; (c), (d): sets of the tan δ curves with marked crossover (or near-crossover) points; red signs indicate change in strain.

A12-co-H21

a)

A12-DMS H21 gelation upon cooling (1°C/min)

b)

A12-DMS H11 gel melting upon heating (1°C/min)

c)

A12-DMS H21 gelation upon cooling (1°C/min)

d)

A12-DMS H11 gel melting upon heating (1°C/min
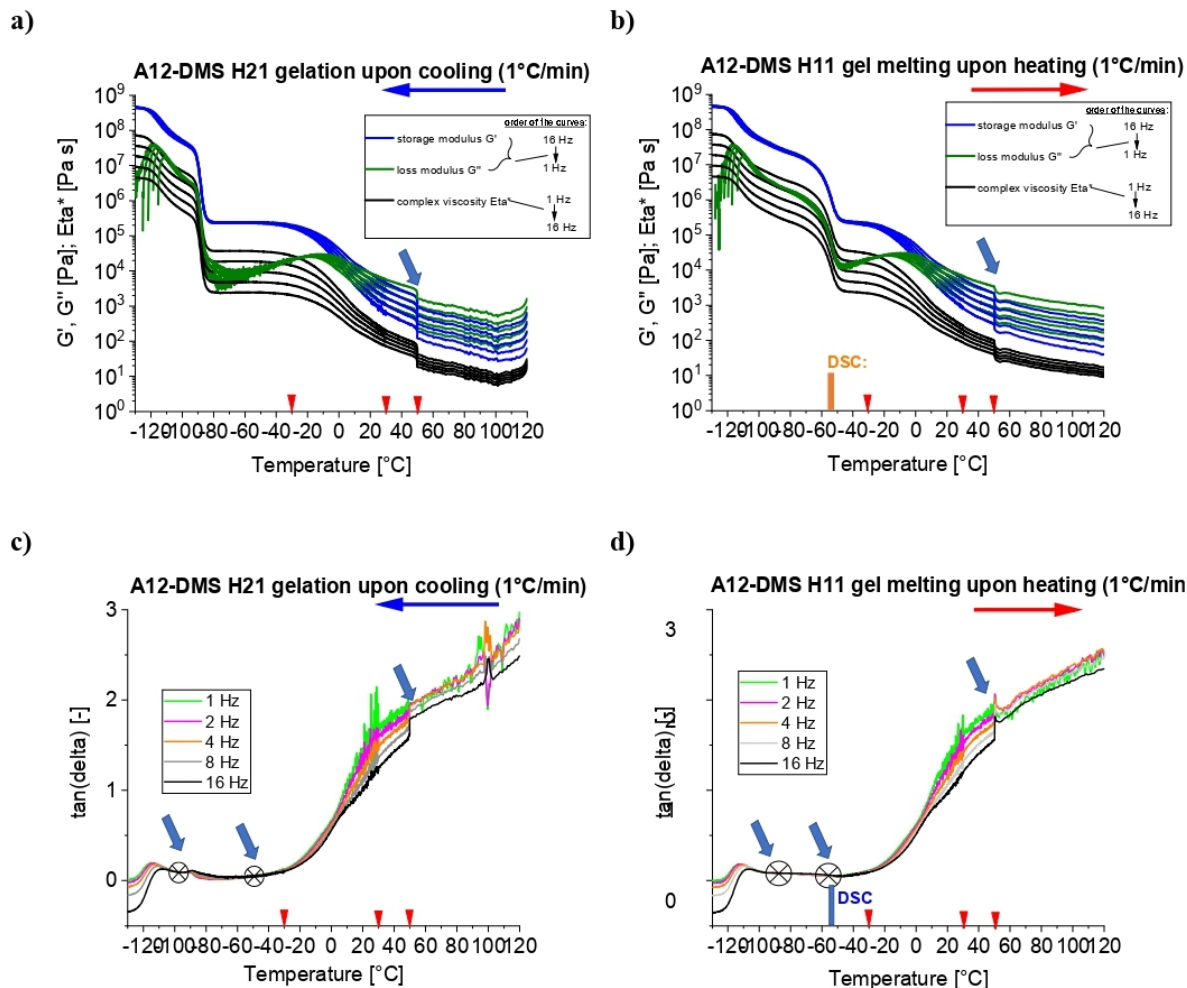
Multi-frequency temperature ramp tests carried out in melting, rubbery and glassy state of the H21–A12: (a), (b): temperature dependence of the storage shear moduli G', of the loss moduli G'', of the complex viscosities Eta* recorded at the simultaneously applied frequencies of 1, 2, 4, 8 and 16 Hz; (c), (d): sets of the tan δ curves with marked crossover (or near-crossover) points; red signs indicate change in strain.

Disconnection of the physical network by high mechanical strain

A1-co-H03
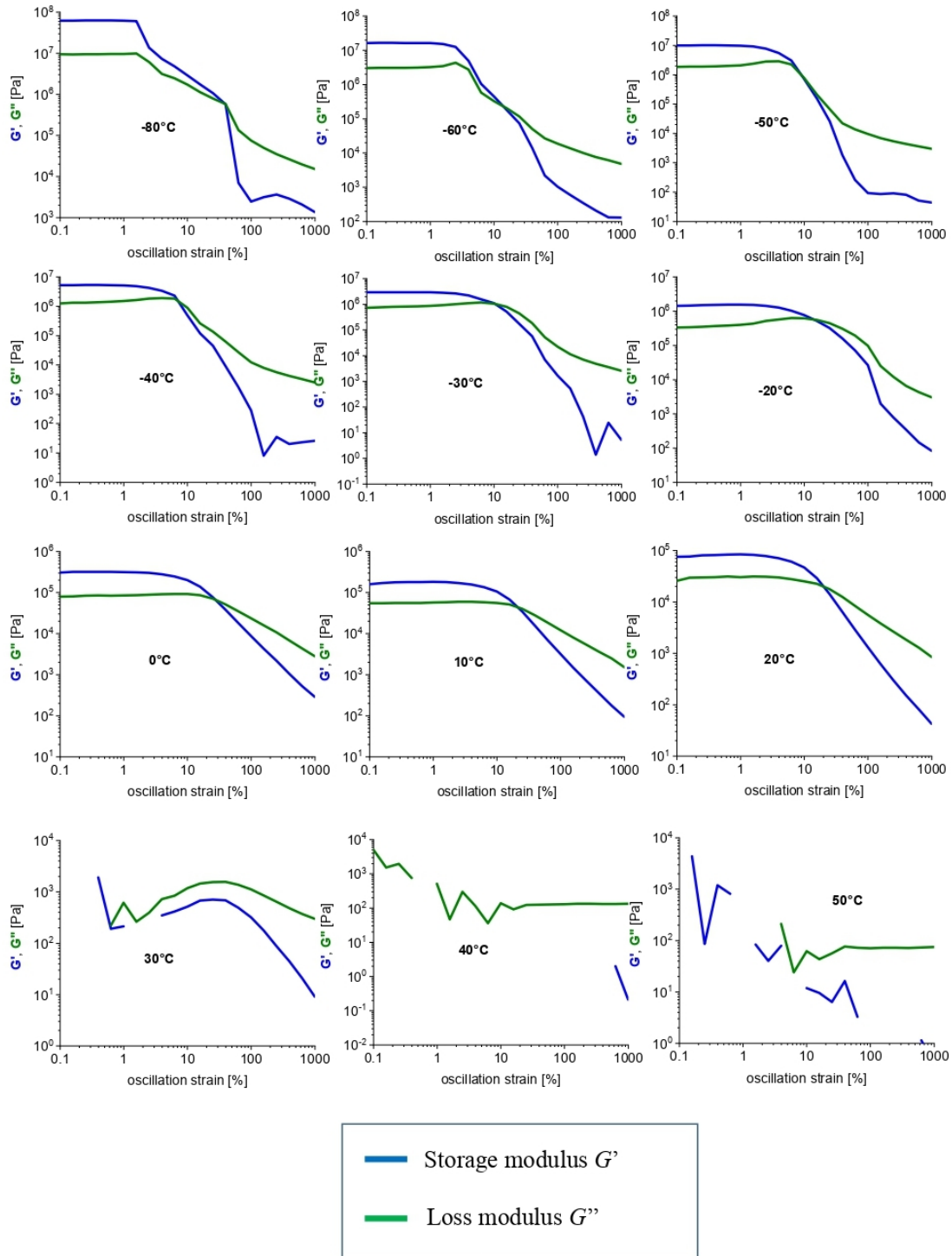
All data: Disconnection of the physical crosslinks in H03–A1 by mechanical strain: strain-dependence of storage (G') and loss (G") modulus of H03–A1 at the temperatures from -80 to +50°C.

A1-co-H11
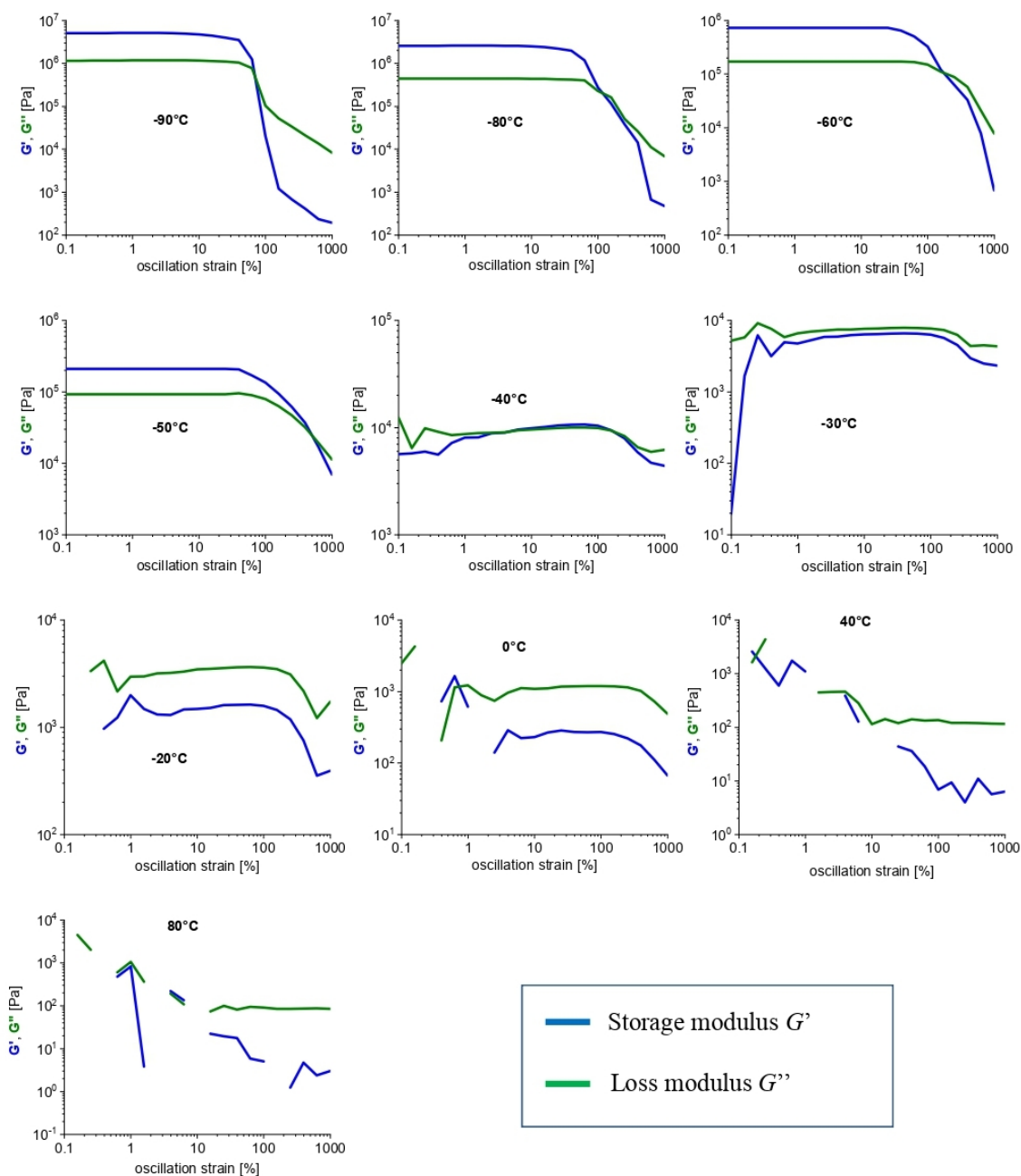
All data: Disconnection of the physical crosslinks in H11−A1 by mechanical strain: strain-dependence of storage (G') and loss (G") modulus of H11−A1 at the temperatures from -90 to +80°C.

A1-co-H21
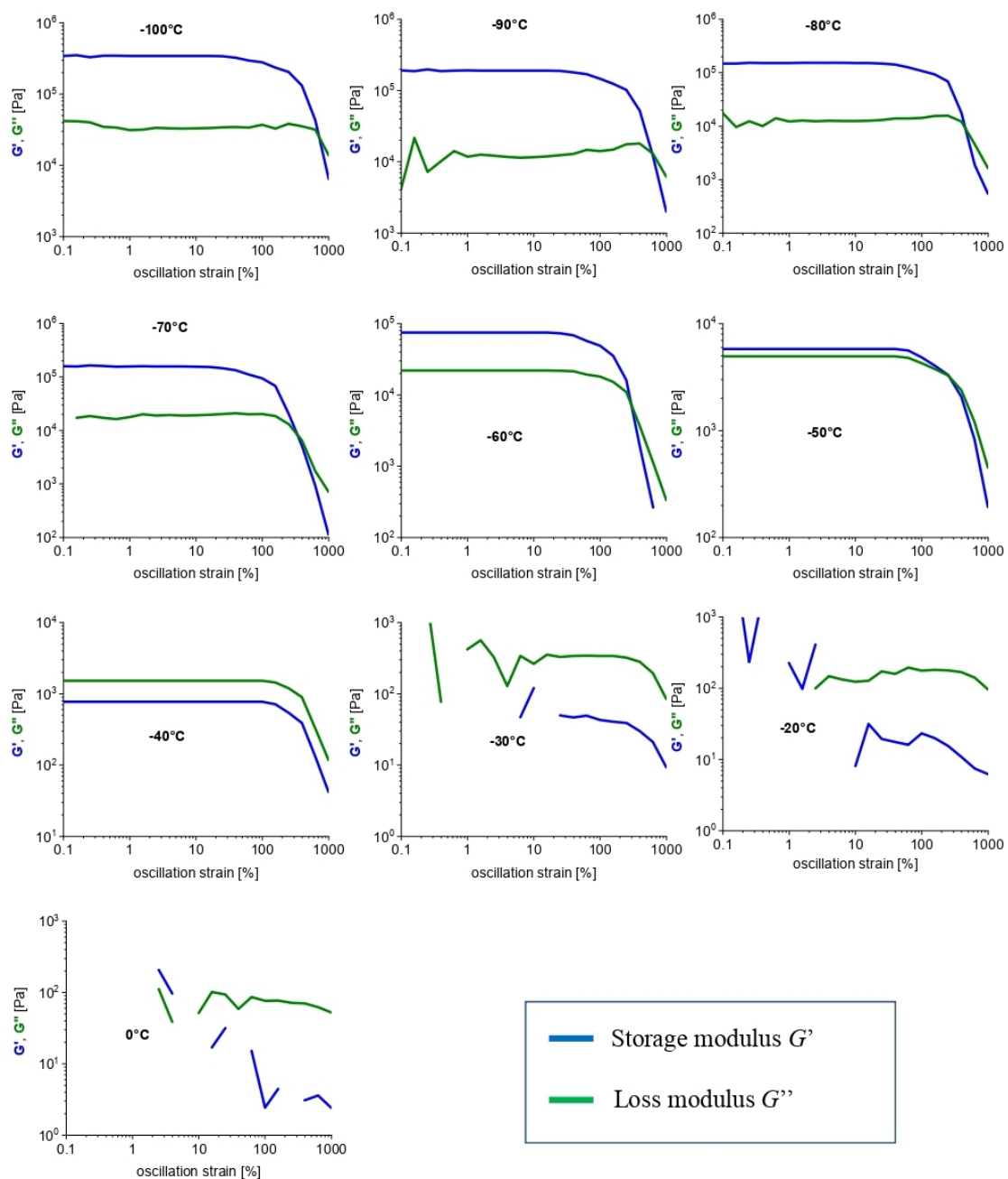
All data: Disconnection of the physical crosslinks in H21–A1 by mechanical strain: strain-dependence of storage (G') and loss (G'') modulus of H21–A1 at the temperatures from -100 to 0°C.

A12-co-H03
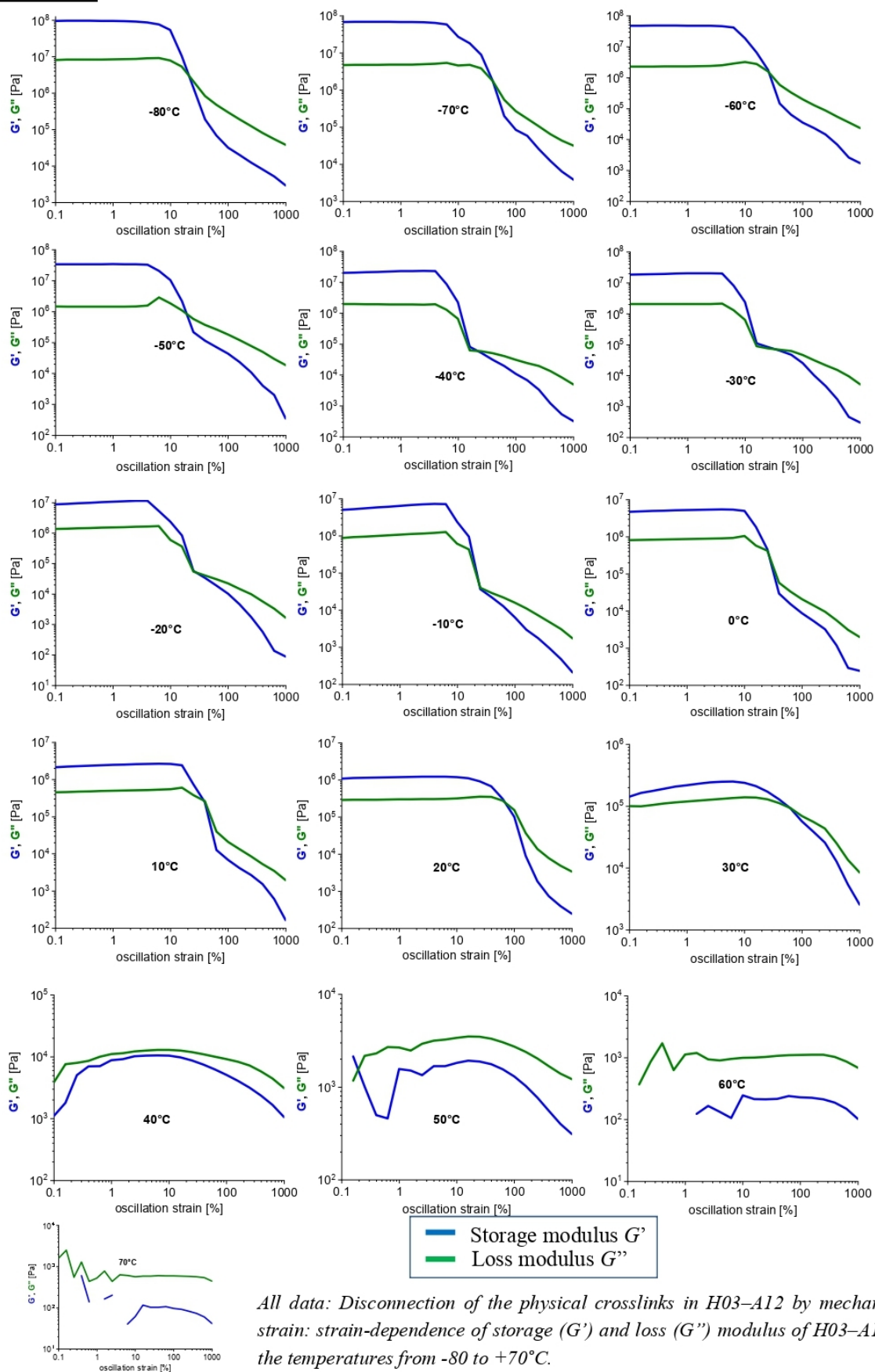
All data: Disconnection of the physical crosslinks in H03–A12 by mechanical strain: strain-dependence of storage (G') and loss (G") modulus of H03–A12 at the temperatures from -80 to +70°C.

A12-co-H11
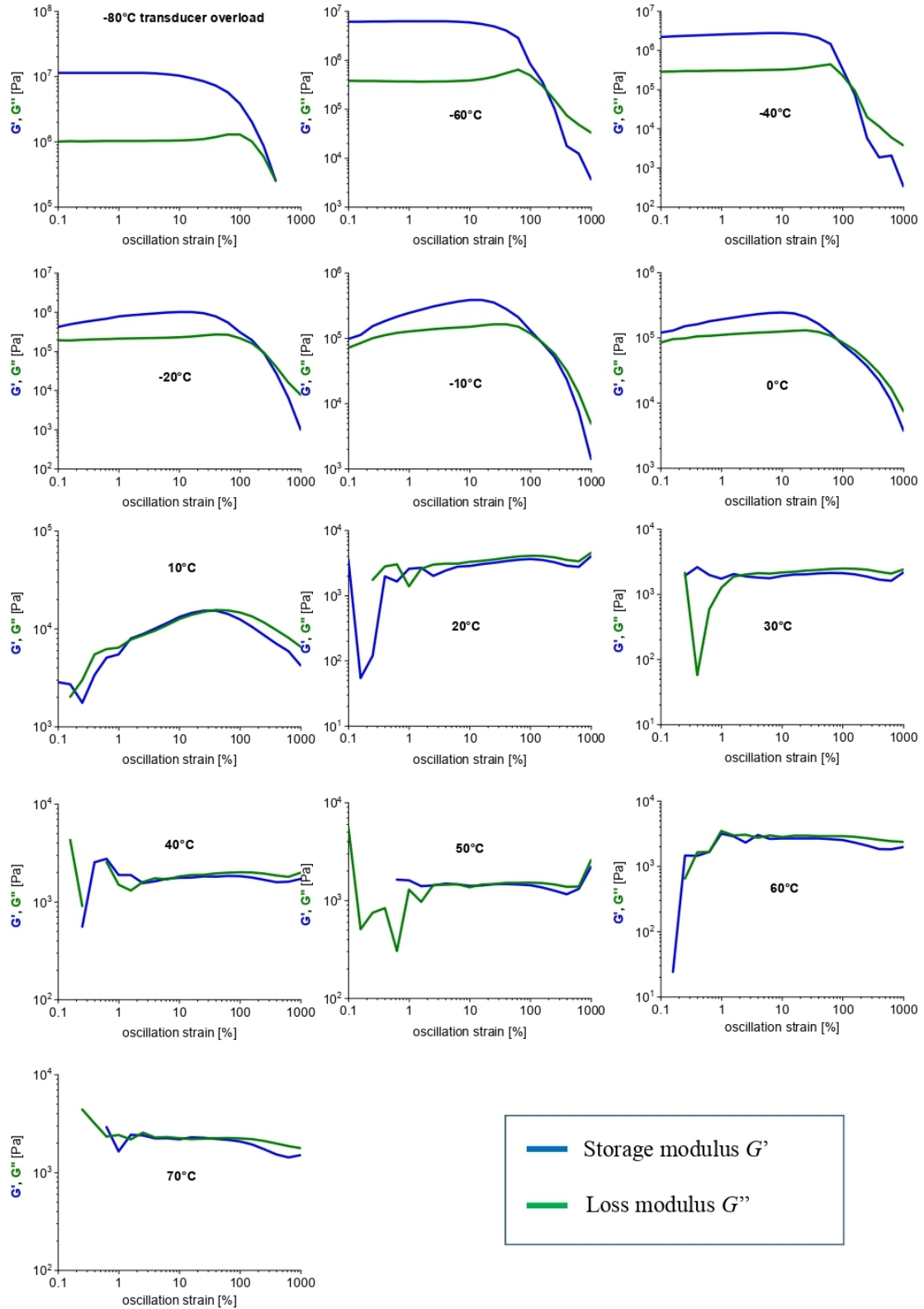
All data: Disconnection of the physical crosslinks in H11−A12 by mechanical strain: strain-dependence of storage (G') and loss (G") modulus of H11−A12 at the temperatures from -80 to +70°C.

A12-co-H21
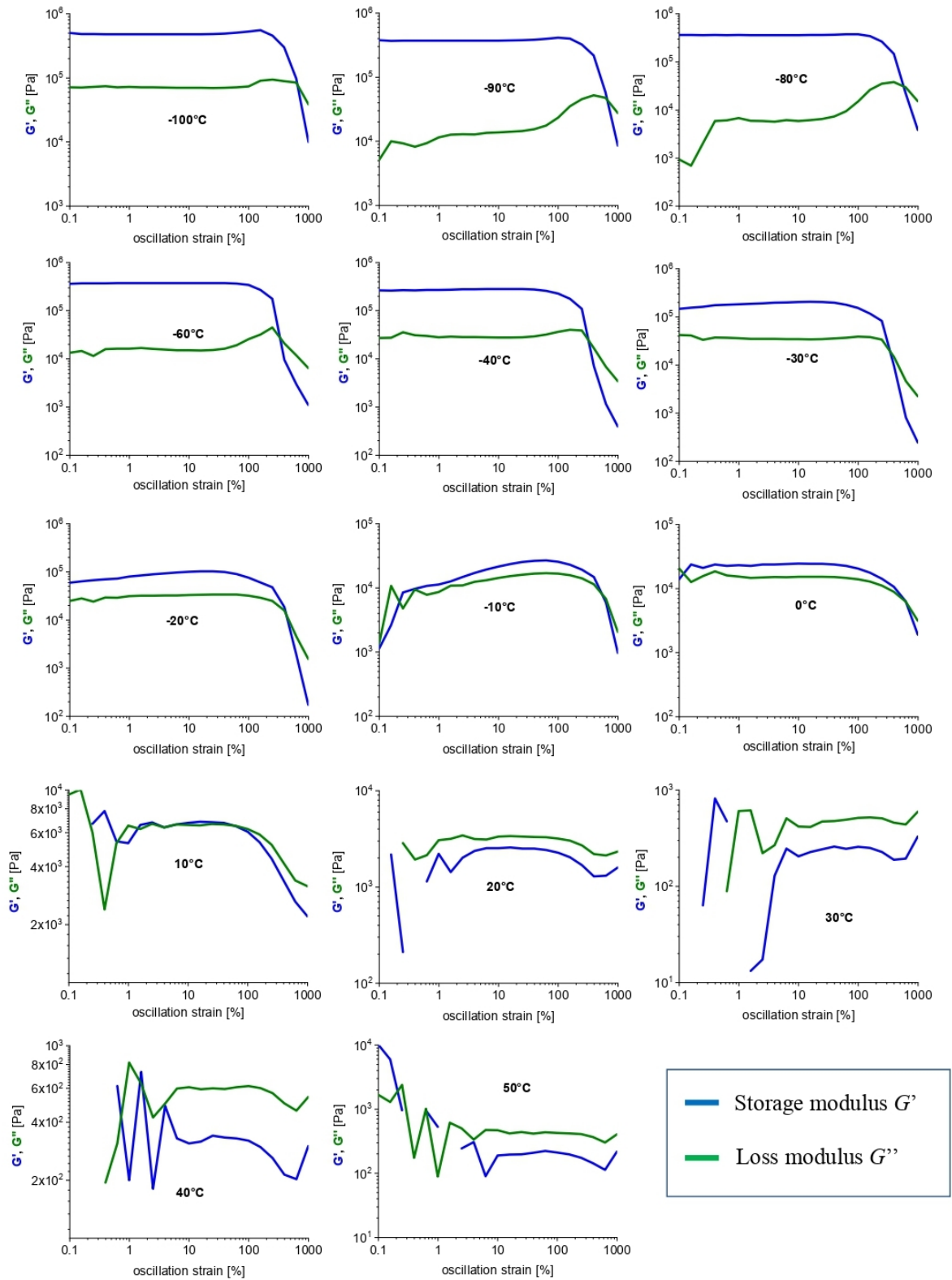
All data: Disconnection of the physical crosslinks in H21–A12 by mechanical strain: strain-dependence of storage (G') and loss (G'') modulus of H21–A12 at the temperatures from -100 to +50°C.

Kinetics of gelation upon abrupt cooling of melt

A1-co-H03
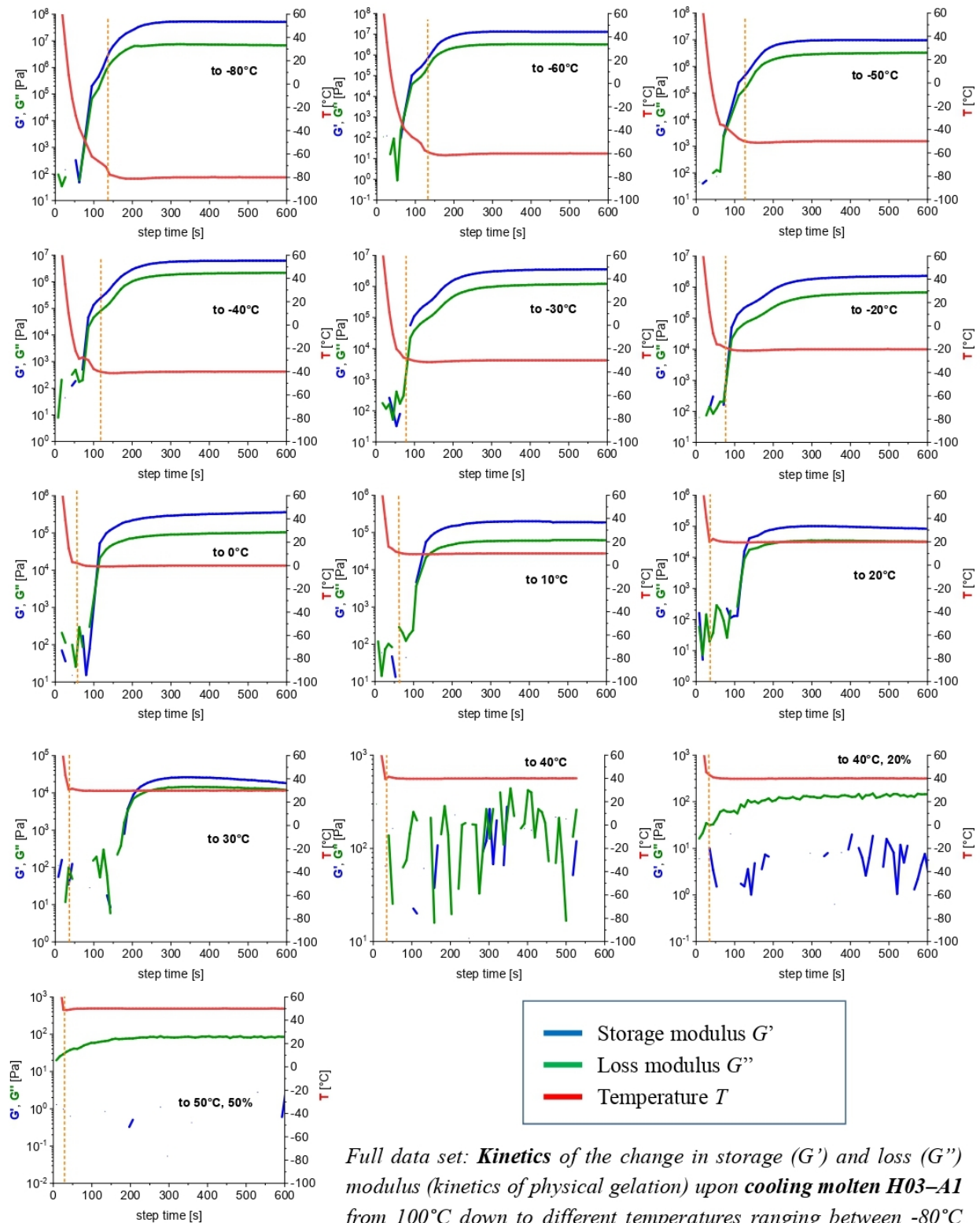
*Full data set: **Kinetics** of the change in storage (G') and loss (G") modulus (kinetics of physical gelation) upon **cooling molten H03–A1** from 100°C down to different temperatures ranging between -80°C and +50°C; the course of the temperature of the plates between which the sample was loaded is also depicted.*

A1-co-H11
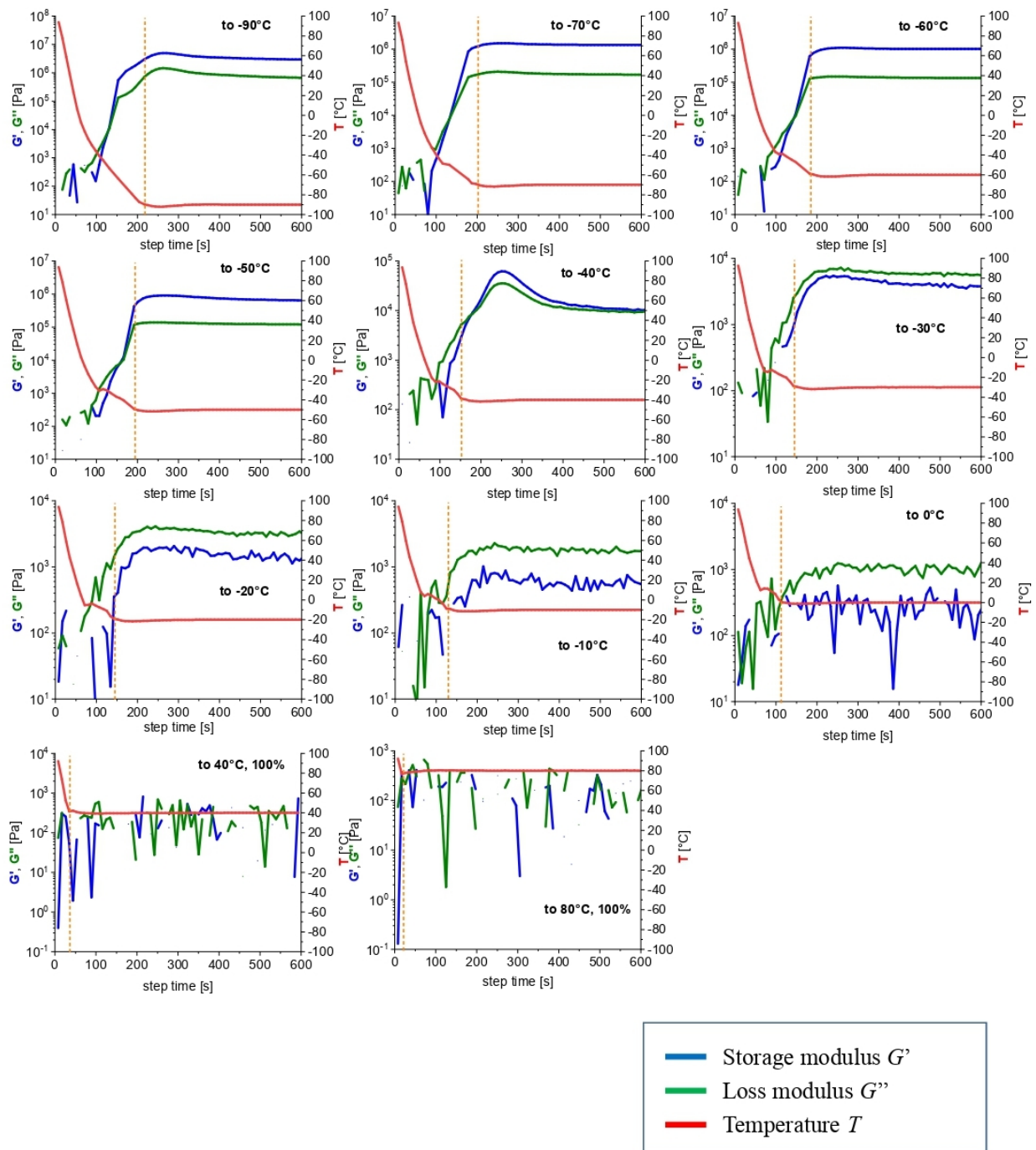
*Full data set: **Kinetics** of the change in storage (G') and loss (G") modulus (kinetics of physical gelation) upon **cooling molten H11–A1** from 100°C down to different temperatures ranging between -90°C and +80°C; the course of the temperature of the plates between which the sample was loaded is also depicted.*

A1-co-H21
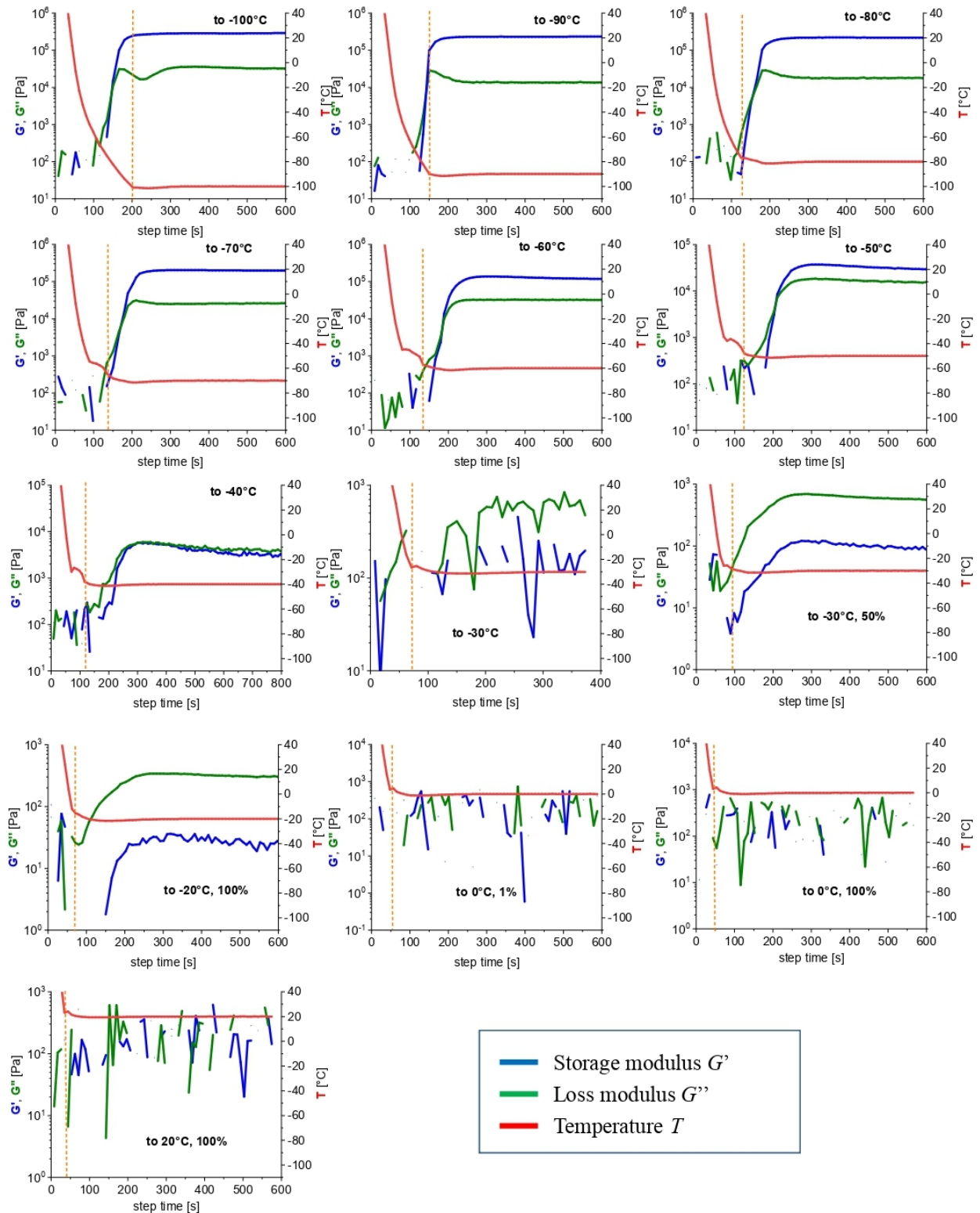
*Full data set: **Kinetics** of the change in storage (G') and loss (G'') modulus (kinetics of physical gelation) upon **cooling molten H21–A1** from 100°C down to different temperatures ranging between -100°C and +20°C; the course of the temperature of the plates between which the sample was loaded is also depicted.*

A12-co-H03
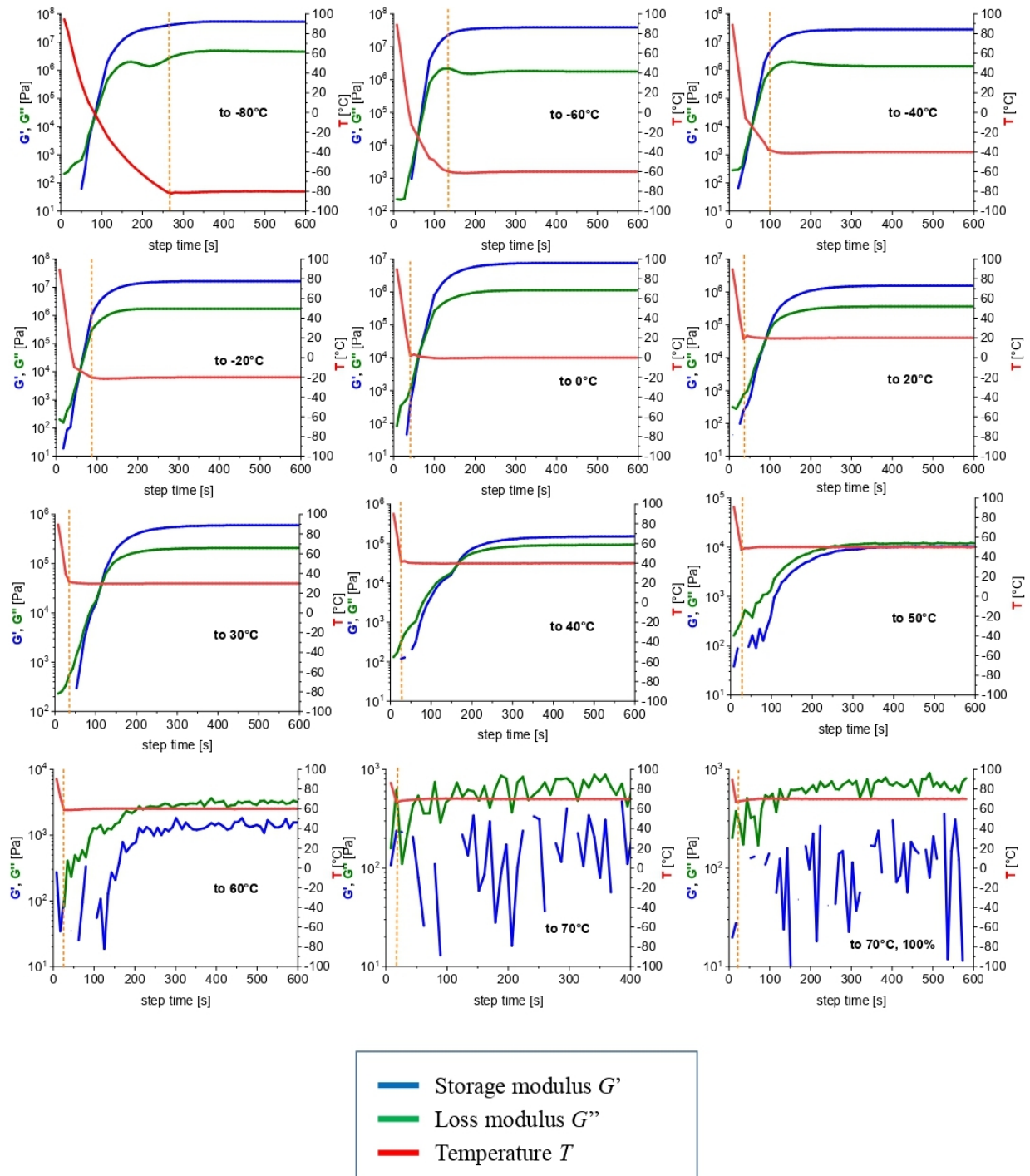
Full data set: **Kinetics** of the change in storage (G') and loss (G") modulus (kinetics of physical gelation) upon **cooling molten H03–A12** from 100°C down to different temperatures ranging between -80°C and +70°C; the course of the temperature of the plates between which the sample was loaded is also depicted.

A12-co-H11
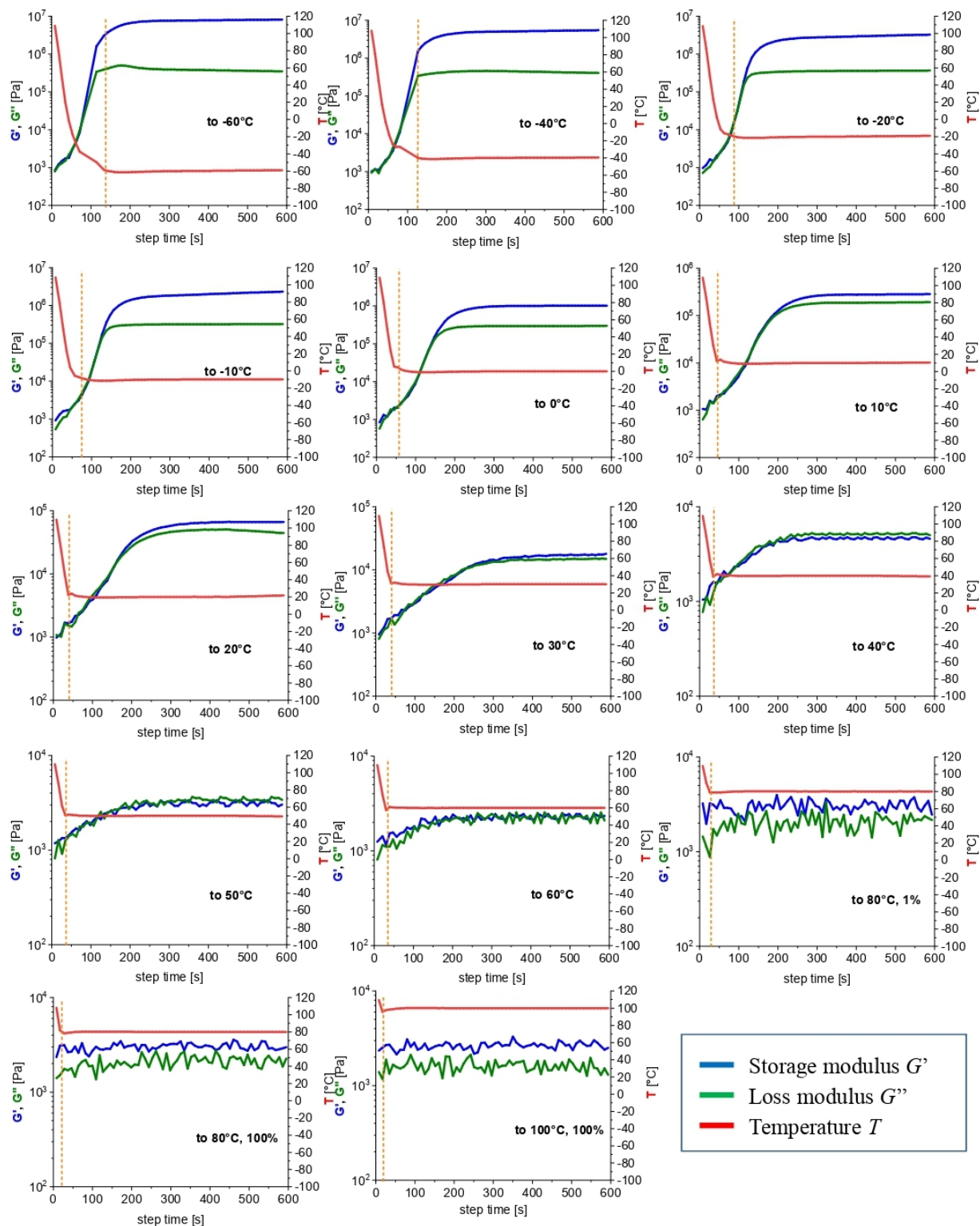
Full data set: **Kinetics** *of the change in storage (G') and loss (G") modulus (kinetics of physical gelation) upon* **cooling molten H11–A12** *from 120°C down to different temperatures ranging between -60°C and +100°C; the course of the temperature of the plates between which the sample was loaded is also depicted.*

A12-co-H21
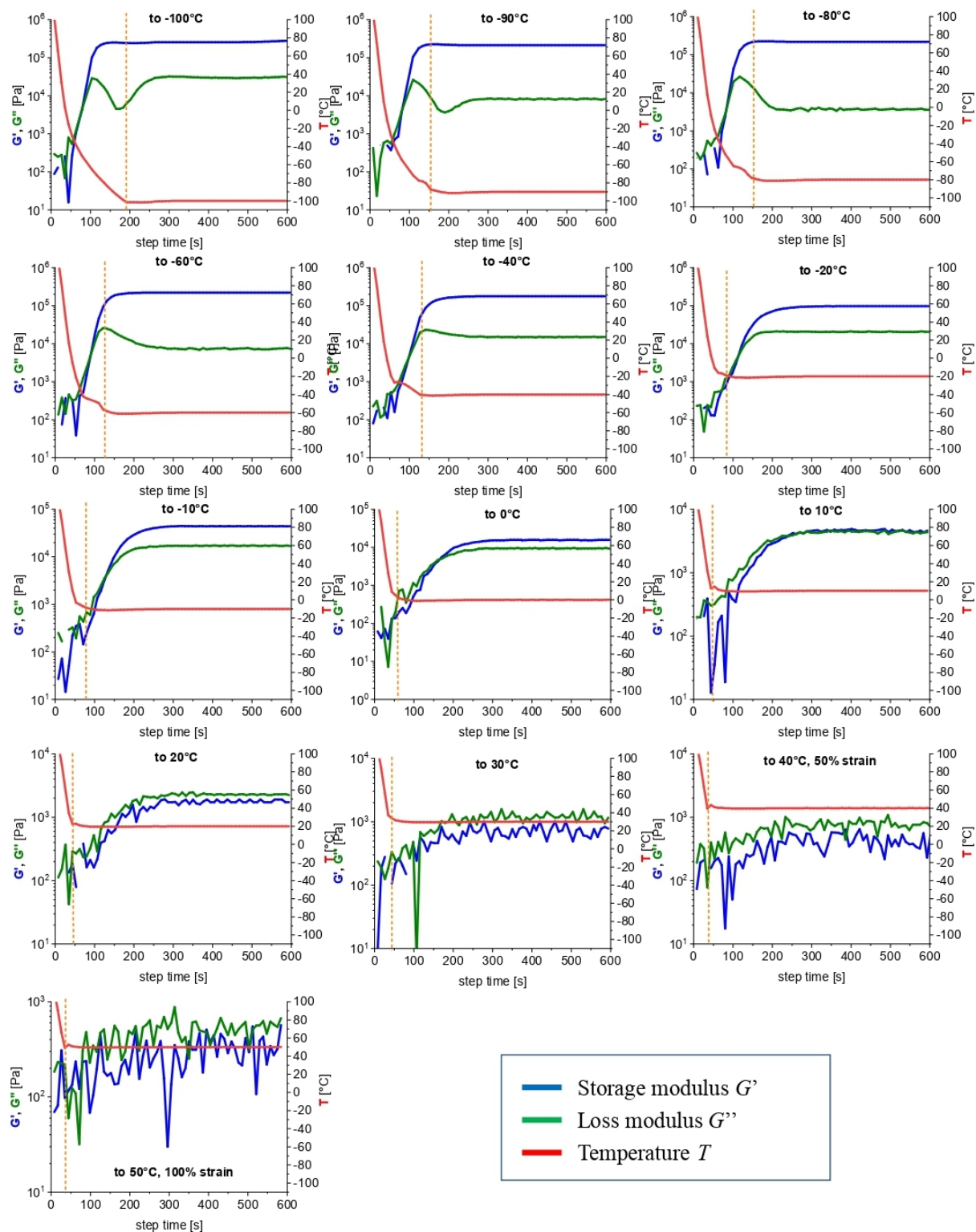
Full data set: **Kinetics** of the change in storage (G') and loss (G") modulus (kinetics of physical gelation) upon **cooling molten H21–A12** from 120°C down to different temperatures ranging between -100°C and +50°C; the course of the temperature of the plates between which the sample was loaded is also depicted.

High-frequency stiffening and self-healing effects

A1-co-H03
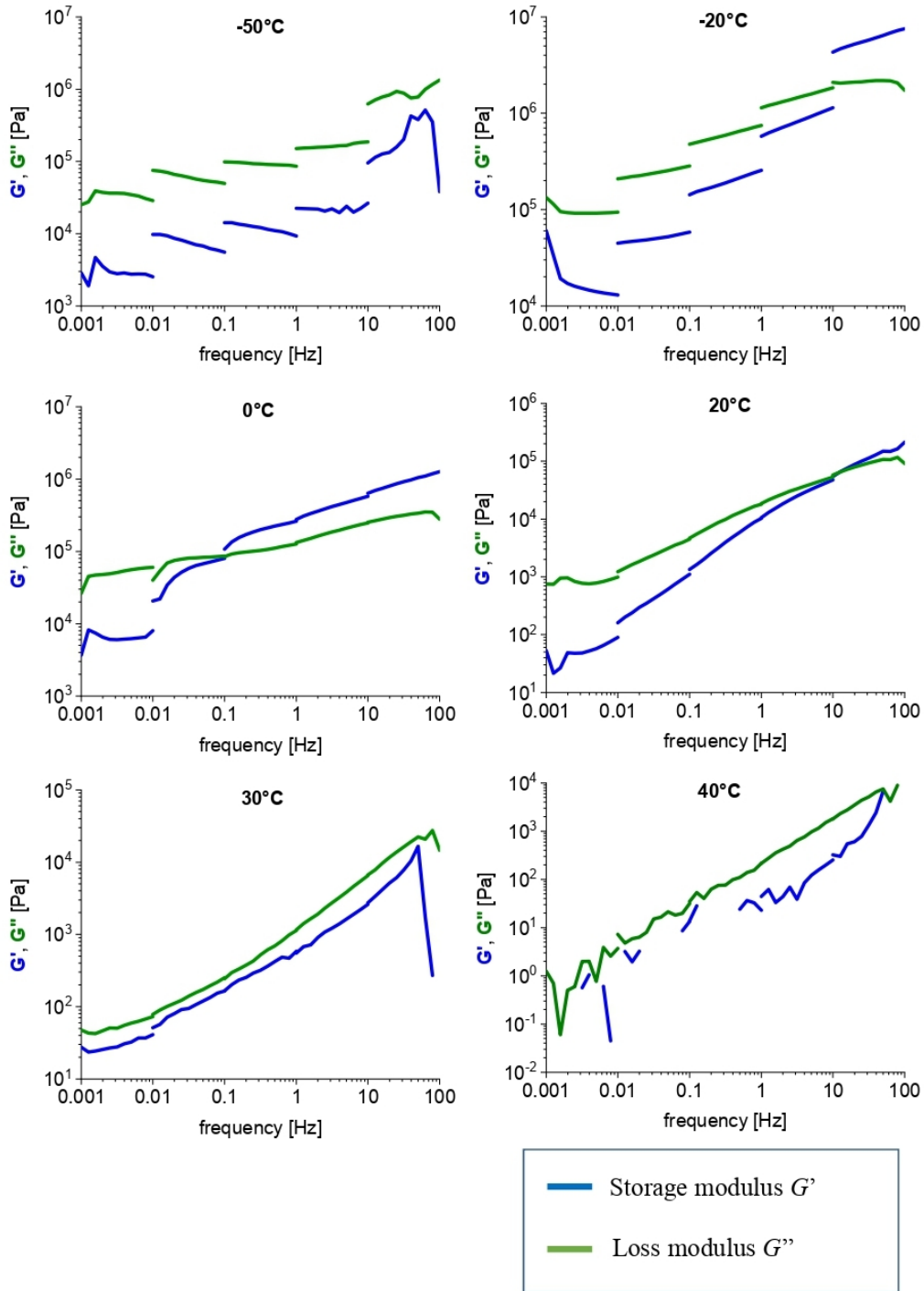
All data: Frequency-stiffening of H03–A1 observed in frequency sweep tests (1 mHz to 100 Hz) conducted at temperatures between -50 and +40°C; the strain amplitude was different in each frequency decade, ranging from 50% at 1 mHz to 1% at 100 Hz; the effect of strain-induced damage to the network, as well as of its recovery between the frequency decades is clearly visible, especially in case of G', G" curves at lower temperatures.

A1-co-H11
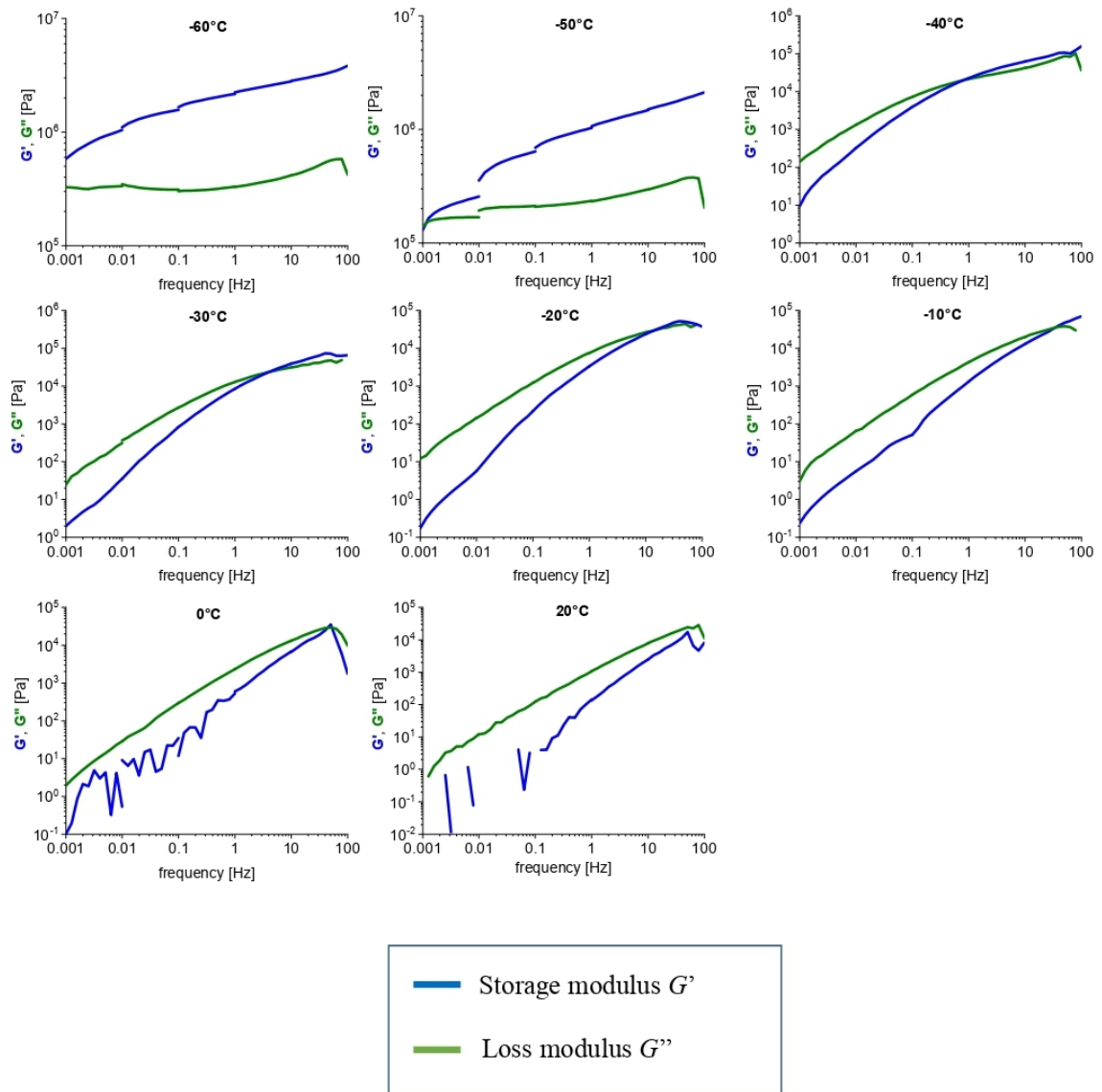
All data: Frequency-stiffening of H11–A1 observed in frequency sweep tests (1 mHz to 100 Hz) conducted at temperatures between -60 and +20°C; the strain amplitude was different in each frequency decade, ranging from 50% at 1 mHz to 1% at 100 Hz.

A1-co-H21
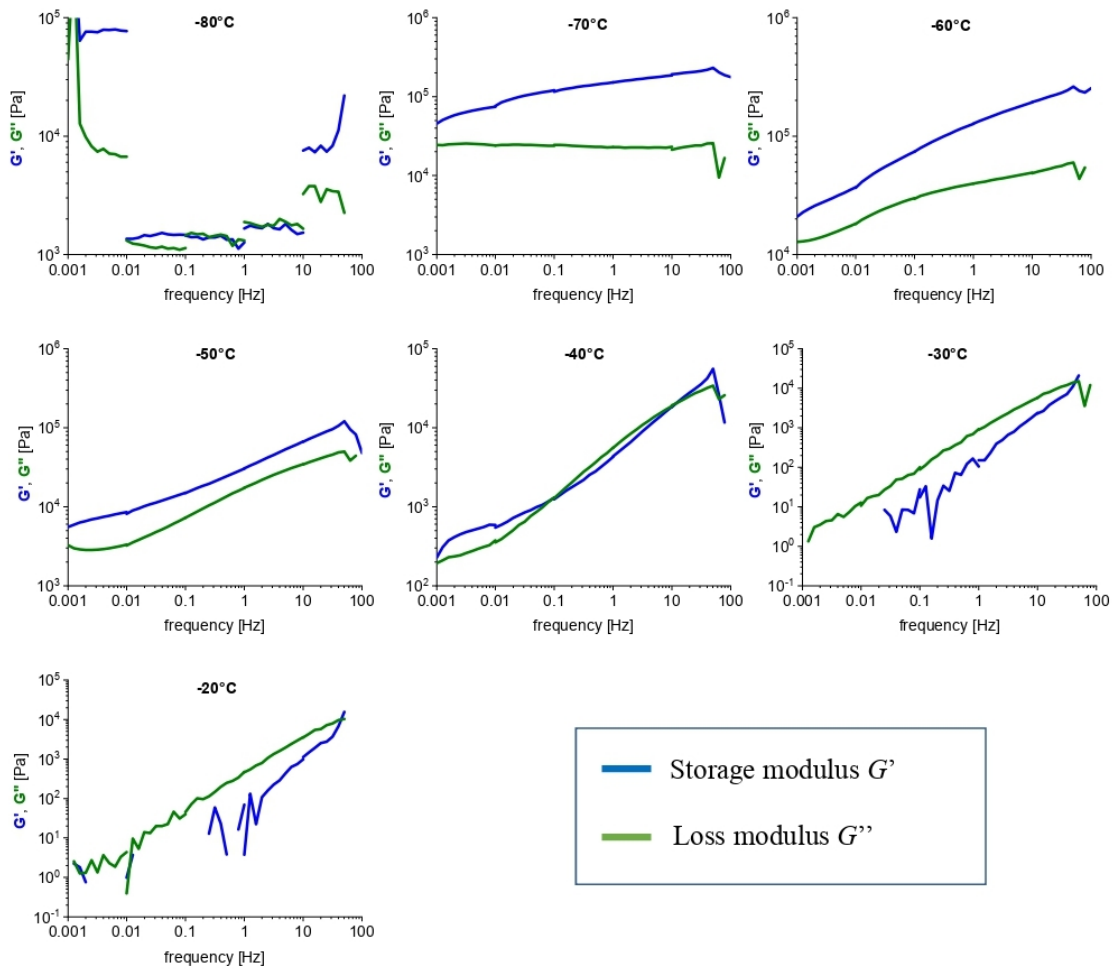
All data: Frequency-stiffening of H21–A1 observed in frequency sweep tests (1 mHz to 100 Hz) conducted at temperatures between -80 and -20°C; the strain amplitude was different in each frequency decade, ranging from 50% at 1 mHz to 1% at 100 Hz.

A12-co-H03
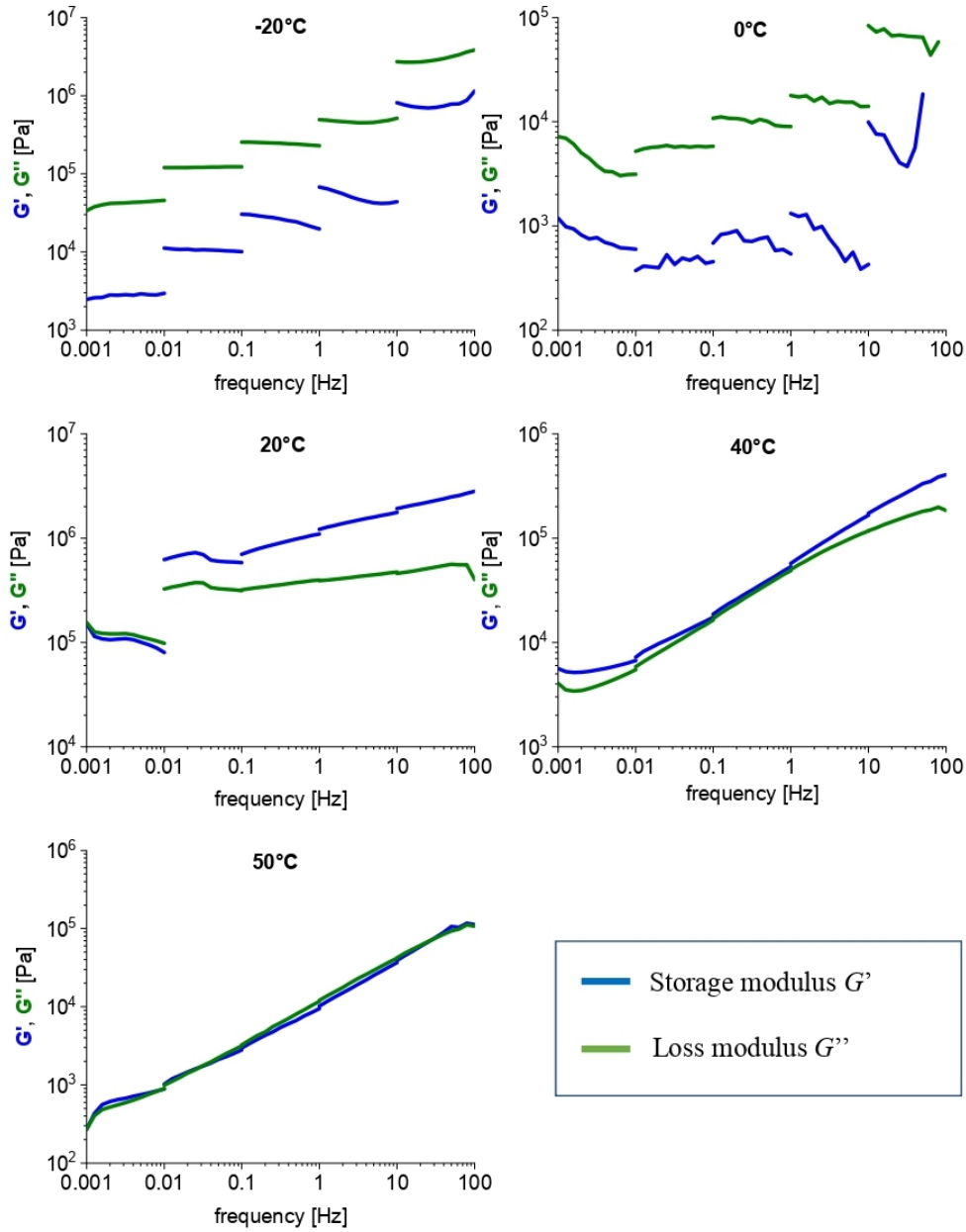
All data: Frequency-stiffening of H03–A12 observed in frequency sweep tests (1 mHz to 100 Hz) conducted at temperatures between -20 and +50°C; the strain amplitude was different in each frequency decade, ranging from 50% at 1 mHz to 1% at 100 Hz; the effect of strain-induced damage to the network, as well as of its recovery between the frequency decades is clearly visible, especially in case of G', G" curves at lower temperatures.

A12-co-H11
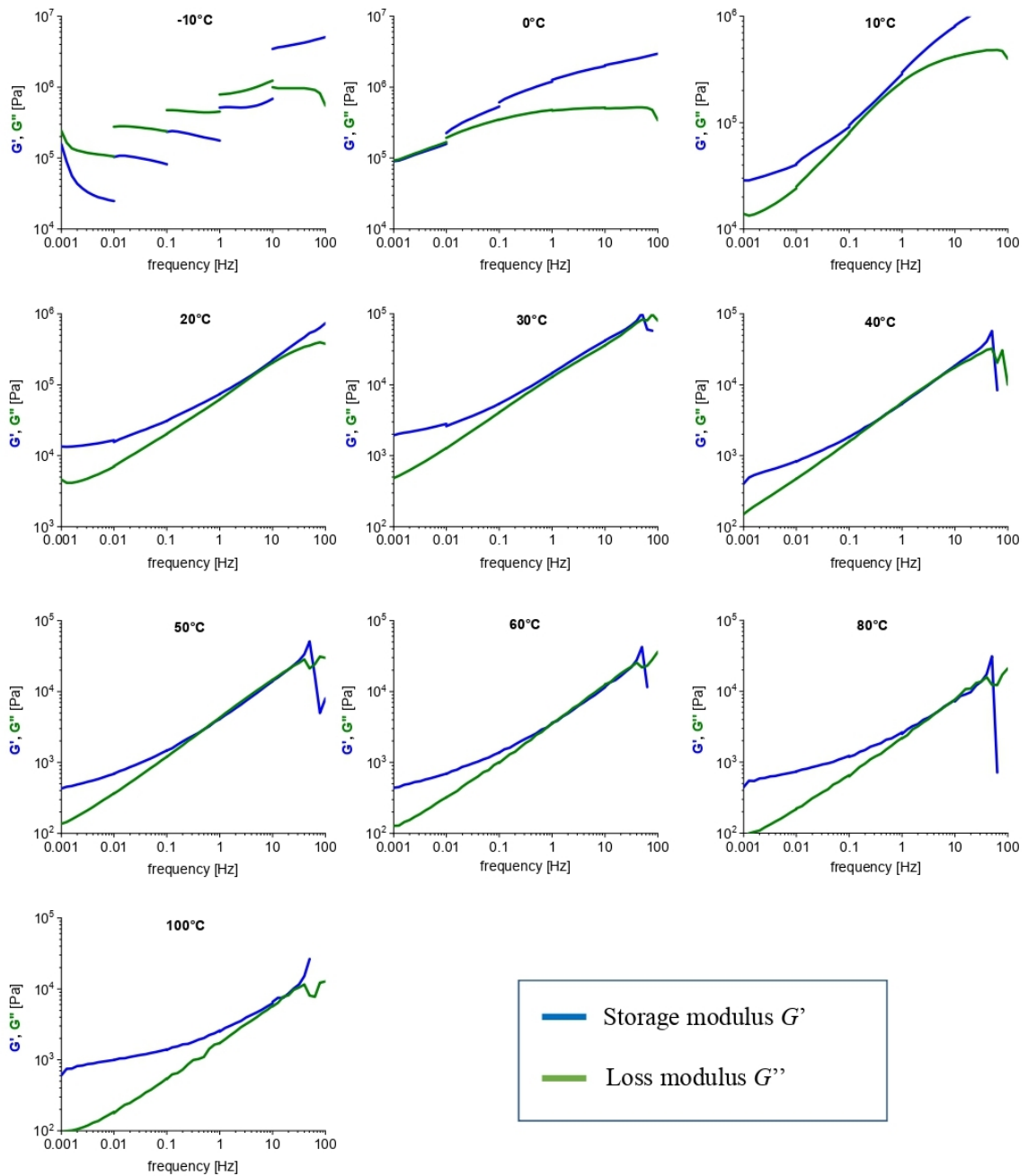
All data: Frequency-stiffening of H11–A12 observed in frequency sweep tests (1 mHz to 100 Hz) conducted at temperatures between -10 and +100°C; the strain amplitude was different in each frequency decade, ranging from 50% at 1 mHz to 1% at 100 Hz; the effect of strain-induced damage to the network, as well as of its recovery between the frequency decades is clearly visible, especially in case of G' curves at lower temperatures.

A12-co-H21
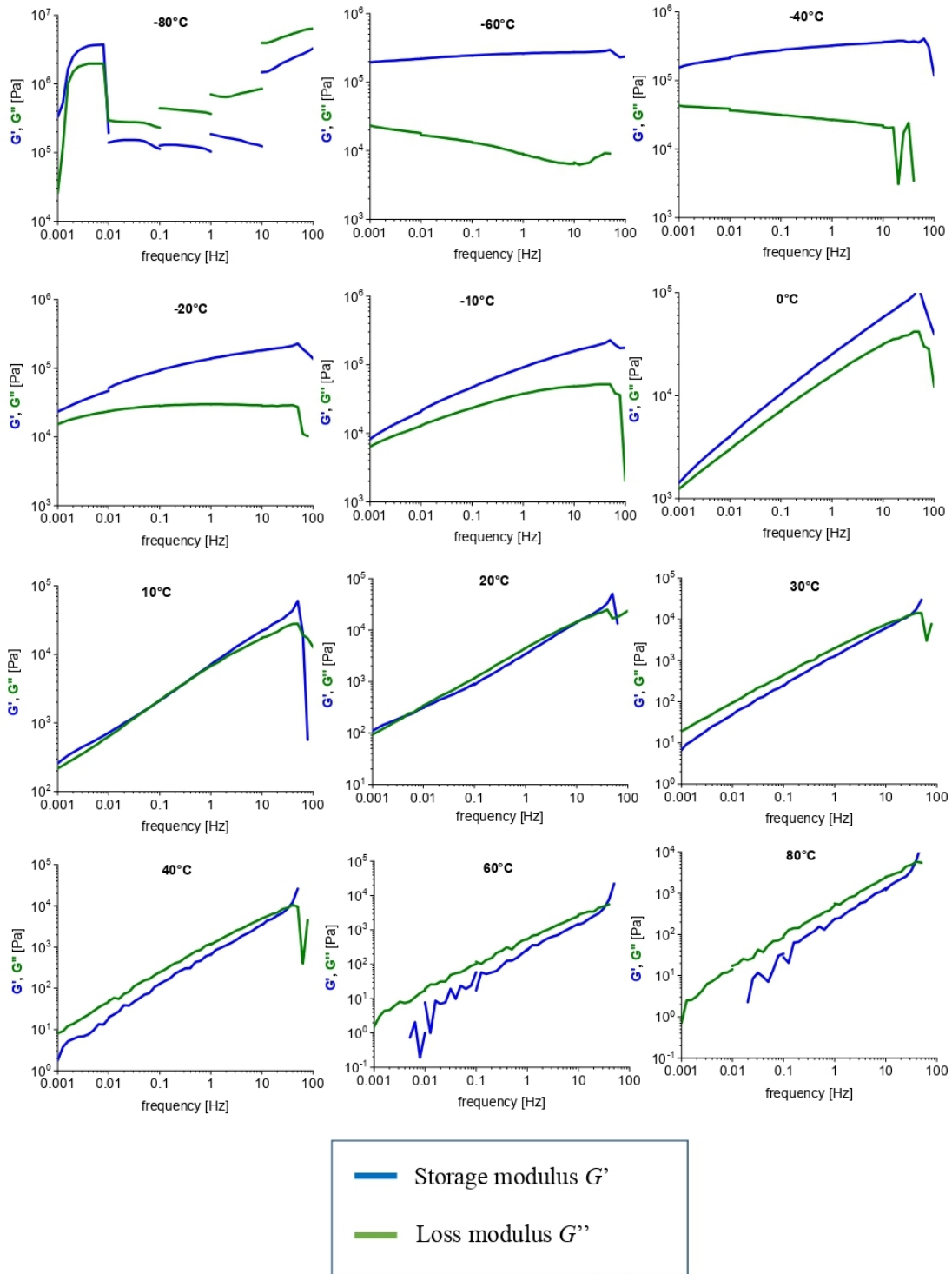
All data: Frequency-stiffening of H21–A12 observed in frequency sweep tests (1 mHz to 100 Hz) conducted at temperatures between -80 and +80°C; the strain amplitude was different in each frequency decade, ranging from 50% at 1 mHz to 1% at 100 Hz; the effect of strain-induced damage to the network, as well as of its recovery between the frequency decades is clearly visible, especially in case of G' curves at lower temperatures.

Appendix 6:

Thermo-reversible and soluble elastomers based on linear infinite copolymers of polyaromatic mesogens and elastic polydimethylsiloxane blocks.

S. Horodecka, A. Strachota*, B. Mossety-Leszczak, B. Strachota, M. Šlouf, A. Zhigunov, M. Vyroubalová, D. Kaňková, M. Netopilík, Z. Walterová.

Experimental

Amounts of the components used in the synthesis of 'infinite' alternating copolymers of PDMS and linearly bonded LC units of aromatic polyester type "M12".

Component		Sample name		
		M12-H03	M12-H11	M12-H21
M12	[g]	0.5	0.5	0.5
	[mmol] *	1.78	1.78	1.78
	wt%	47.38	32.12	10.63
	Vol% ‡	43.56	29.53	9.9
H03	[g]	0.5553	-	-
	[mmol] *	1.78	-	-
	wt%	52.62	-	-
	Vol% ‡	56.44	-	-
H11	[g]	-	1.057	-
	[mmol] *	-	1.78	-
	wt%	-	67.88	-
	Vol% ‡	-	70.47	-
H21	[g]	-	-	4.202
	[mmol] *	-	-	1.78
	wt%	-	-	89.37
	Vol% ‡	-	-	90.1
Toluene	[g]	2.956	2.956	2.956
Karstedt's catalyst	[g]	0.0087	0.0087	0.0087
	[mmol]	0.02	0.02	0.02

Experimental

Amounts of the components used in the synthesis of 'infinite' alternating copolymers of PDMS and linearly bonded LC units of aromatic polyester type "M22".

Component		Sample name		
		M22-H03	M22-H11	M22-H21
M22	[g]	0.5	0.5	0.5
	[mmol] *	1.46	1.46	1.46
	wt%	52.25	36.47	12.62
	Vol% ‡	48.36	33.71	11.76
H03	[g]	0.4576	-	-
	[mmol] *	1.46	-	-
	wt%	47.75	-	-
	Vol% ‡	51.64	-	-
H11	[g]	-	0.8708	-
	[mmol] *	-	1.46	-
	wt%	-	63.53	-
	Vol% ‡	-	66.29	-
H21	[g]	-	-	3.463
	[mmol] *	-	-	1.46
	wt%	-	-	87.38
	Vol% ‡	-	-	88.24
CHCl3	[g]	2.956	2.956	2.956
Karstedt's catalyst	[g]	0.0087	0.0087	0.0087
	[mmol]	0.02	0.02	0.02

Experimental

Amounts of the components used in the synthesis of 'infinite' alternating copolymers of PDMS and linearly bonded LC units of aromatic polyester type "M32".

Component		Sample name		
		M32-H03	M32-H11	M32-H21
M32	[g]	0.5	0.5	0.5
	[mmol] *	1.32	1.32	1.32
	wt%	54.88	38.96	13.83
	Vol%	51	36.12	12.91
H03	[g]	0.4117	-	-
	[mmol] *	1.32	-	-
	wt%	45.12	-	-
	Vol%	49	-	-
H11	[g]	-	0.7834	-
	[mmol] *	-	1.32	-
	wt%	-	61.04	-
	Vol%	-	63.88	-
H21	[g]	-	-	3.116
	[mmol] *	-	-	1.32
	wt%	-	-	86.17
	Vol%	-	-	87.09
CHCl₃	[g]	2.956	2.956	2.956
Karstedt's catalyst	[g]	0.0087	0.0087	0.0087
	[mmol]	0.02	0.02	0.02

Chemistry of Synthesis

α,ω-hydrido-functional PDMS precursors:

H03: n = 6.6 (total: **8.6**)

H11: n = 14.3 (total: **16.3**)

H21: n = 62.4 (total: **64.4**)
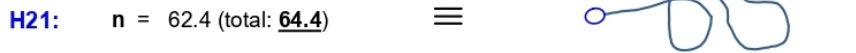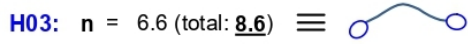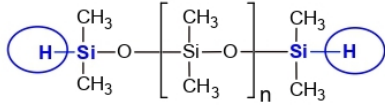
Divinyl-functional azo-free polyaromatic mesogens:

M12:

M22:

M32:

Karstedt's catalyst   solvent

Products

PDMS 'spring'

LC-unit "M12"
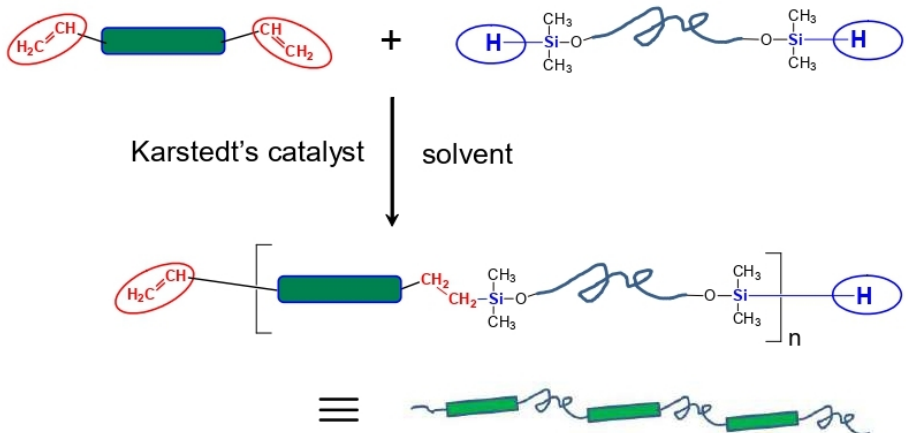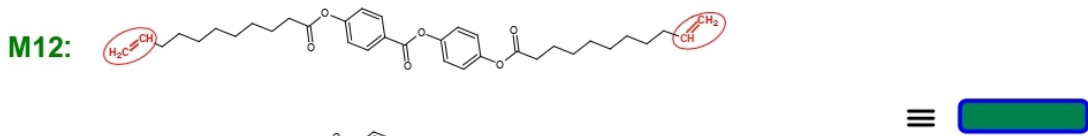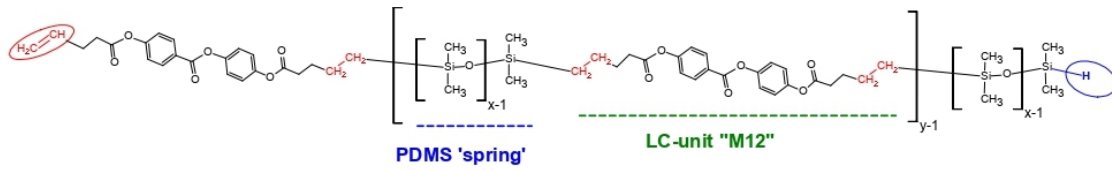
LC-*co*-H03

LC-*co*-H11

LC-*co*-H21

**LC =
M12, M22, M32**
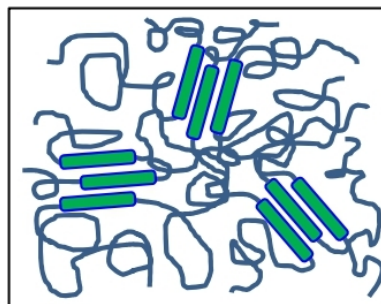
Name of the sample	Volume % of LC component *
azo-free linear infinite LC-PDMS copolymers	
M12-*co*-H03	43.56
M12-*co*-H11	29.53
M12-*co*-H21	9.90
M22-*co*-H03	48.36
M22-*co*-H11	33.71
M22-*co*-H21	11.76
M32-*co*-H03	51.00
M32-*co*-H11	36.12
M32-*co*-H21	12.91

Side reactions and stabilization
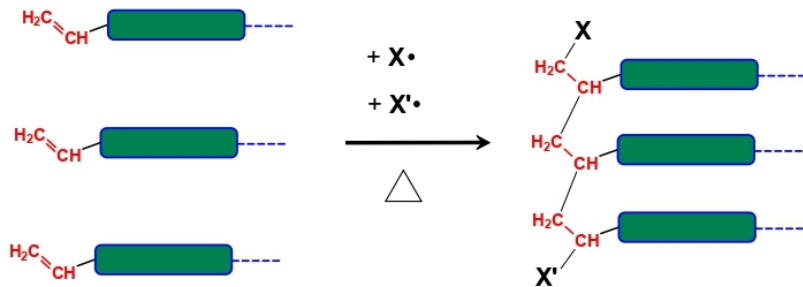
Polymerization of the vinyl groups before, during, and after the hydrosilylation coupling.
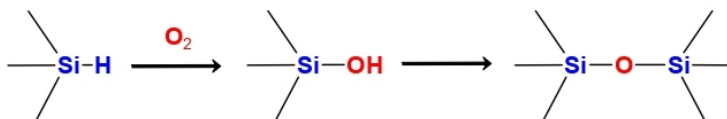
Oxidative coupling of unreacted SiH groups.
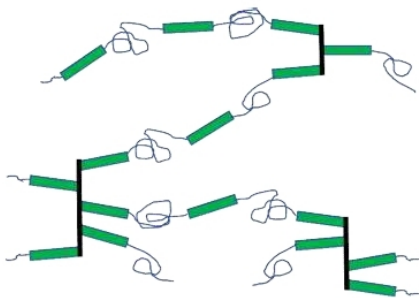
Crosslinked structure based on the one of the infinite linear LC-PDMS copolymer, in which some of the divinyl-functional-LC units are oligomerized, and hence polyfunctional instead of linearly bonding.

Side reactions and stabilization
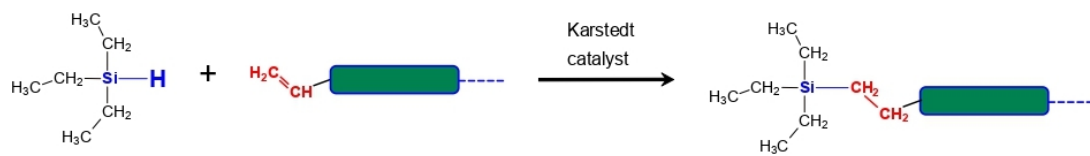
Protection of the terminal vinyl groups in the linear infinite LC-PDMS copolymers.

Thermo-mechanical properties:

storage modulus G' versus temperature for all of the copolymers with M12, M22 and M3 mesogens.
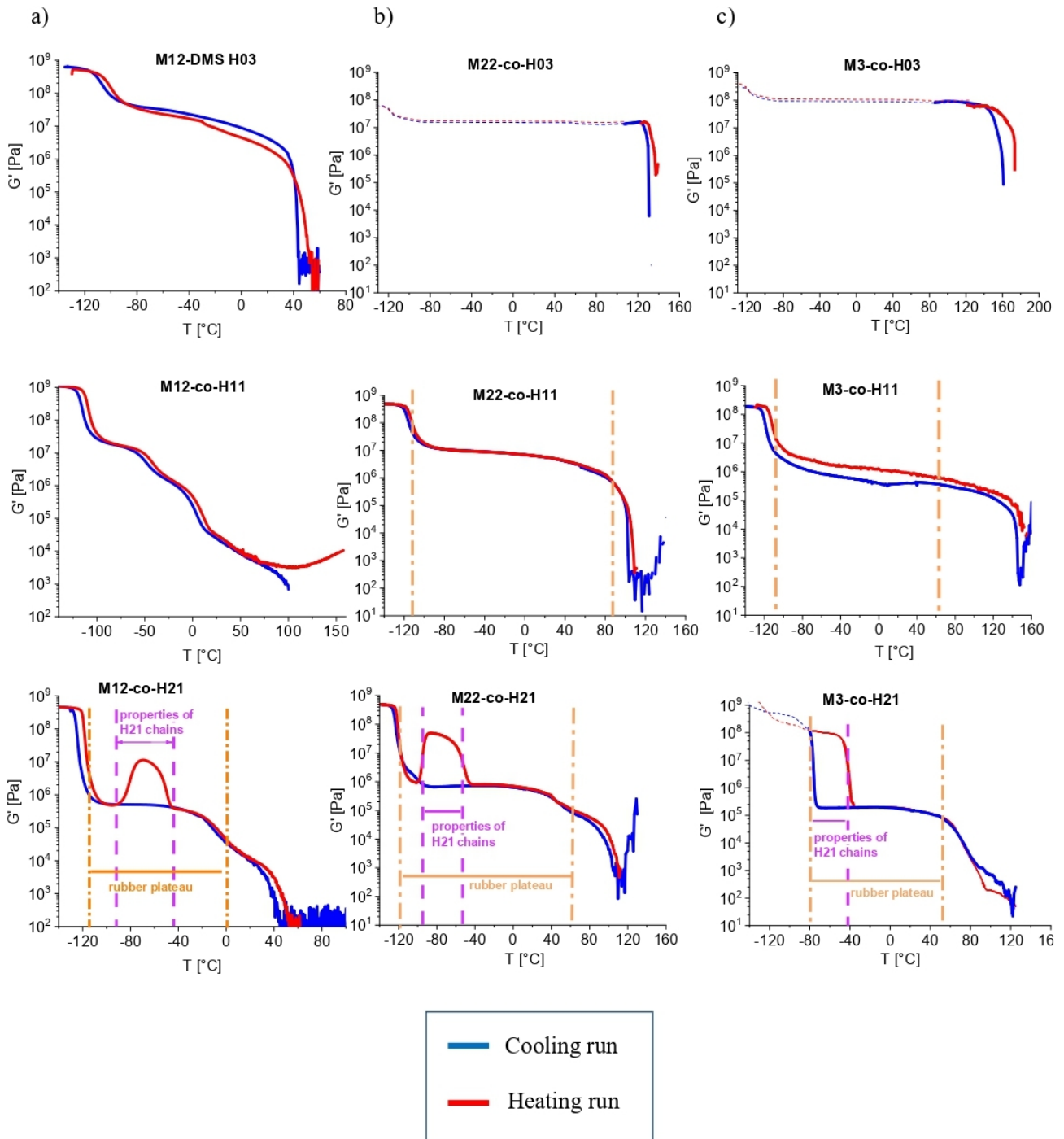
DMTA profiles (temperature-dependent storage modulus G' only) of the copolymers (a-column) M12-DMS H03, M12-DMS H11, M12-DMS H21, (b-column) M22-DMS H03, M22-DMS H11, M22-DMS H21, (c-column) M3-H03, M3-H11 and M3-H21 recorded in heating and cooling regime.

Thermo-mechanical properties: storage modulus G' versus temperature for all of the **pure PDMS**: H03, H11 and H21.
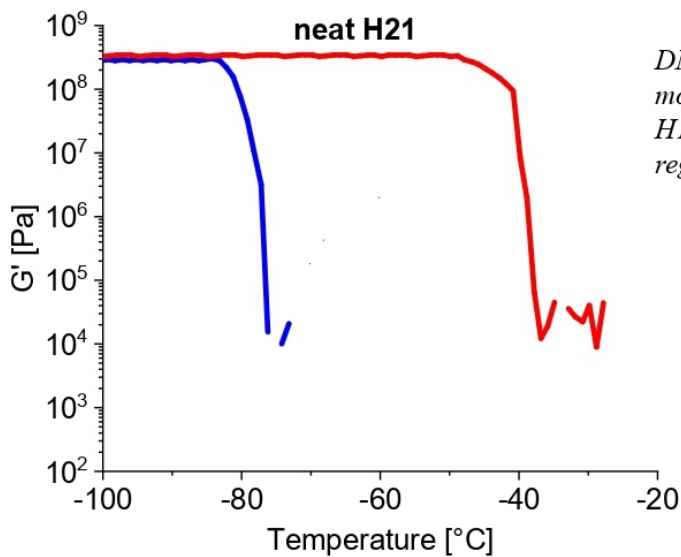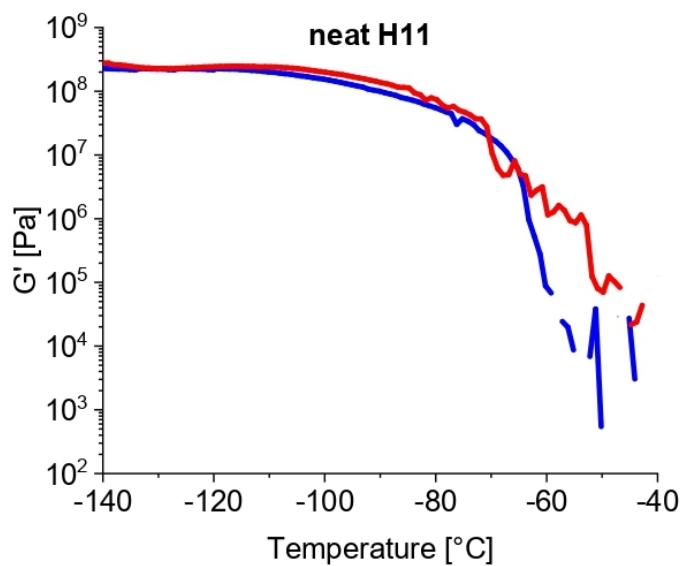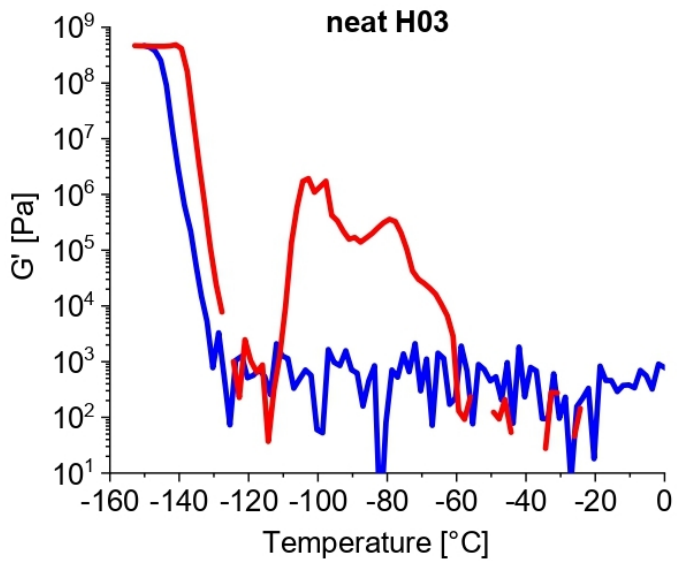
DMTA profiles (temperature-dependent storage modulus G' only) for all of the pure PDMS: H03, H11 and H21, recorded in heating and cooling regime.

Phase transitions in the neat mesogens and copolymers observed by DSC.
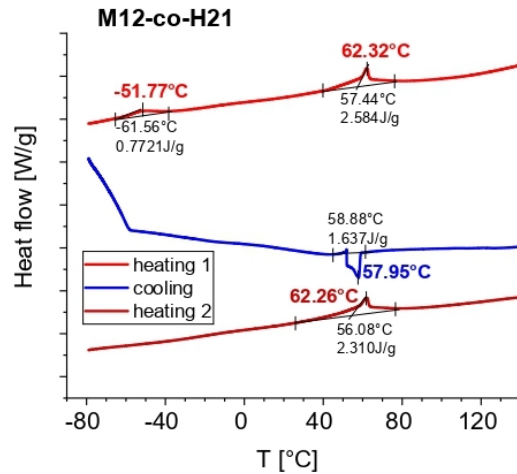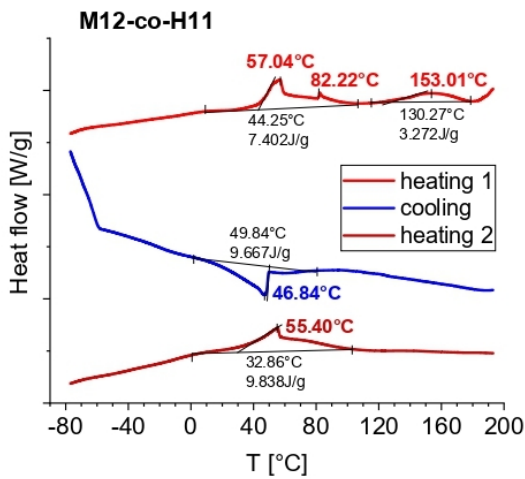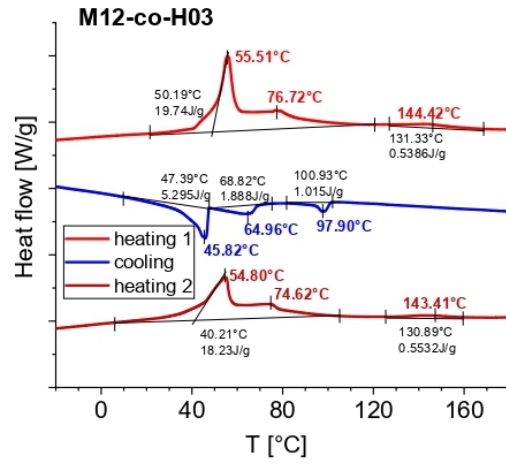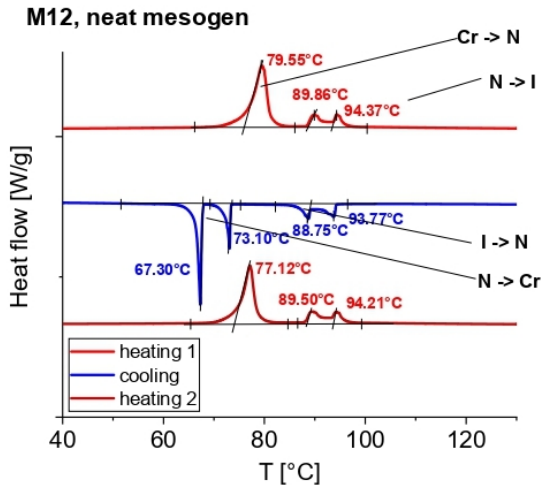
DSC traces of the LC mesogen- M12 and copolymers: M12-H03, M12-H11, M12-H21.
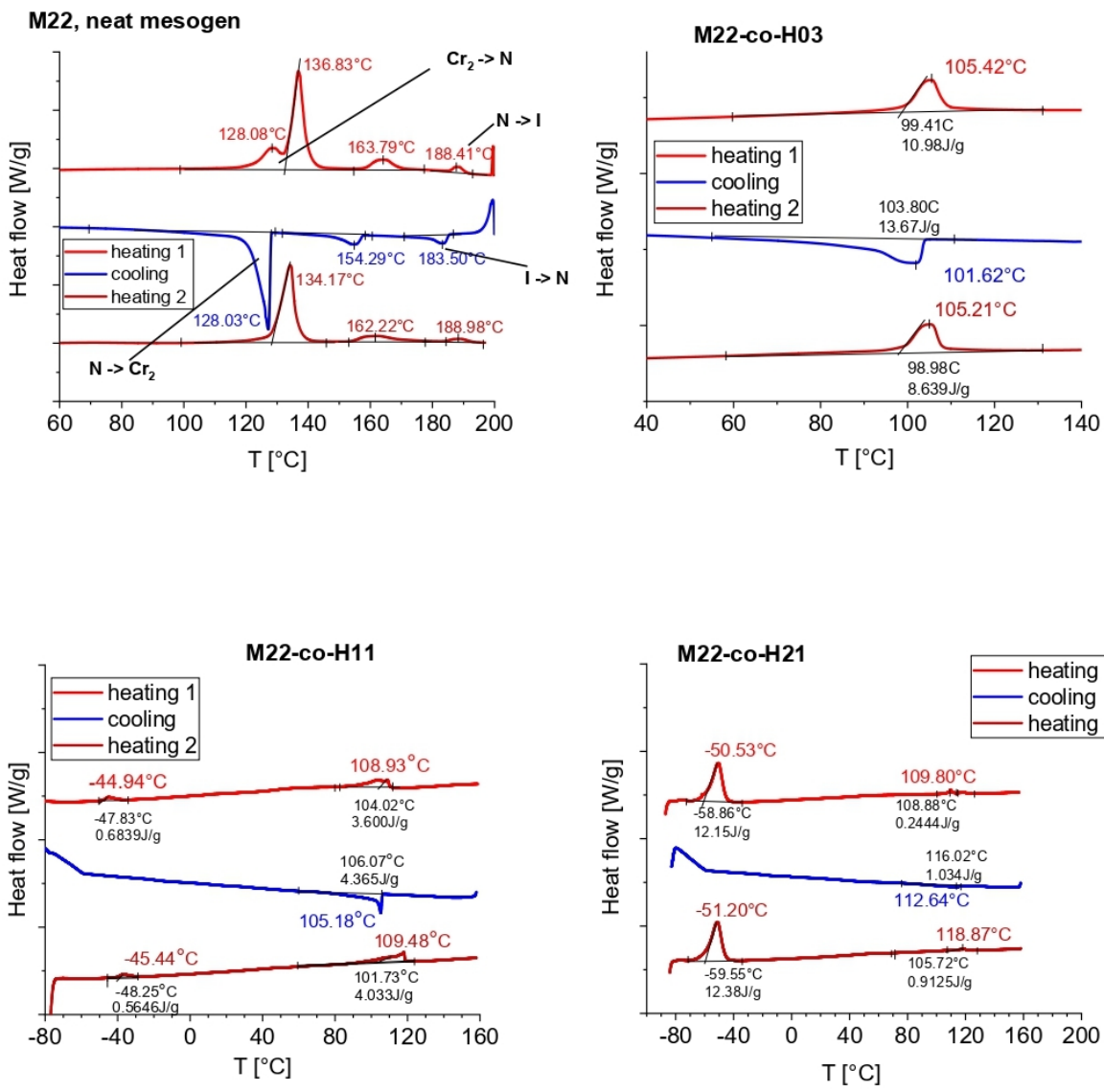
DSC traces of the LC mesogen- M22 and copolymers: M22-H03, M22-H11, M22-H21.
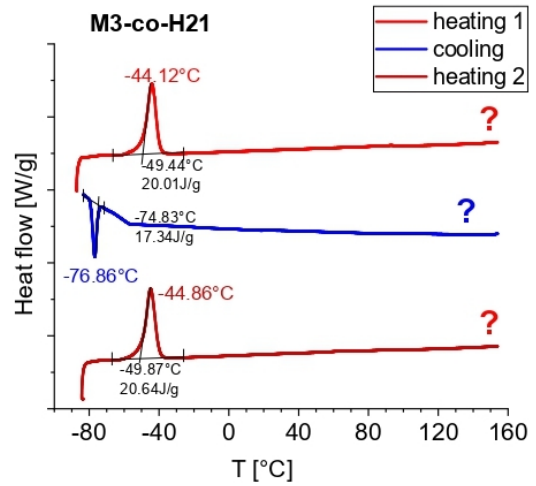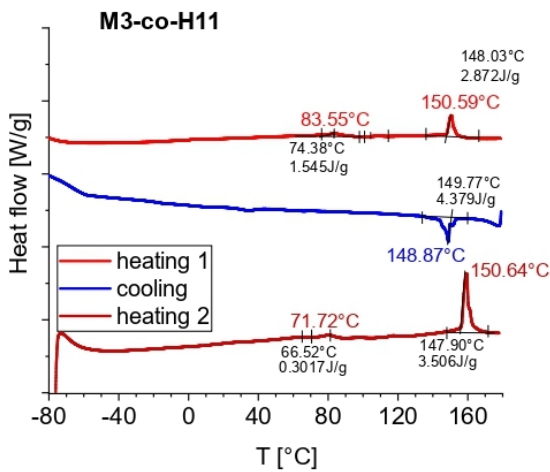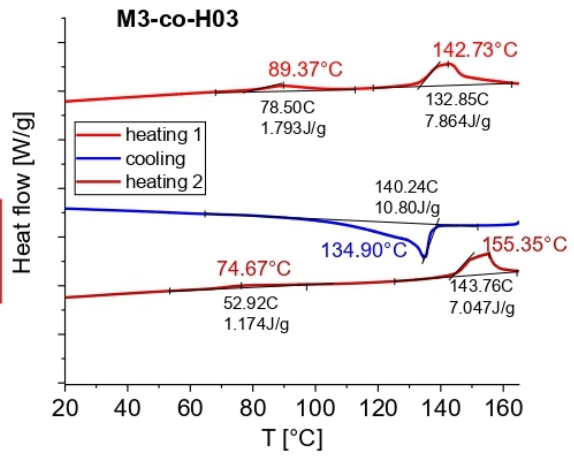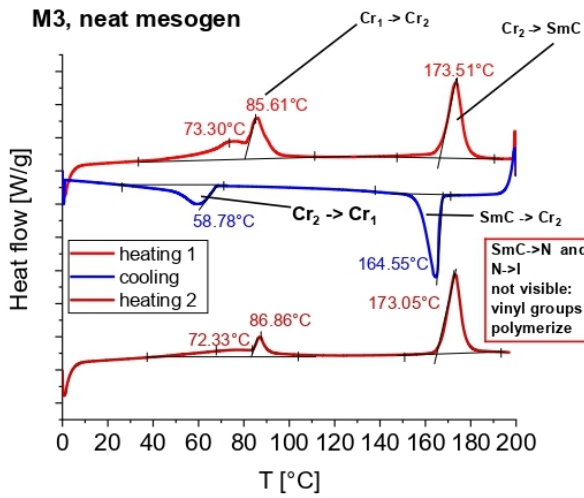
DSC traces of the LC mesogen- M3 and copolymers: M3-H03, M3-H11, M3-H21.

XRD investigations

(a) M12, neat

(b) M12-*co*-H11

(c) M12-*co*-H21

(a)

M22, neat

d, A
8.83   4.43

Intensity

— 23°C
— 95°C
— 85°C
— 23°C

5

0

10   20
2Θ, degrees

(b)

M22-*co*-H21

d, A
8.83   4.43

Intensity

— 23°C
— 95°C
— 60°C
— 55°C

SAXS

1.2
1.0
0.8
0.6
0.4
0.2
0.0

10   20
2Θ, degrees

(a)

M32, neat

at 25°C
at 95°C

2.044°

s.o. ?

20°

2Θ, degrees

(b)

M32-*co*-H11

d, A
44.12   22.06   14.71

SAXS

2°

23°C

2Θ, degrees

(c)

SAXS

2.044°

M32-*co*-H21

PDMS (halo)

PDMS
(2nd halo)

at 95°C
at 70°C
at 50°C
at 25°C

2.044°

2Θ, degrees
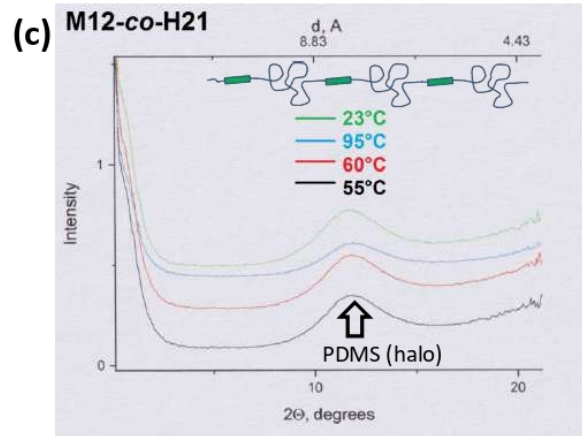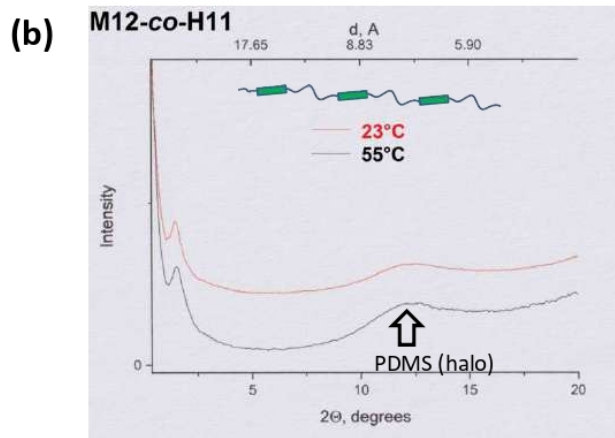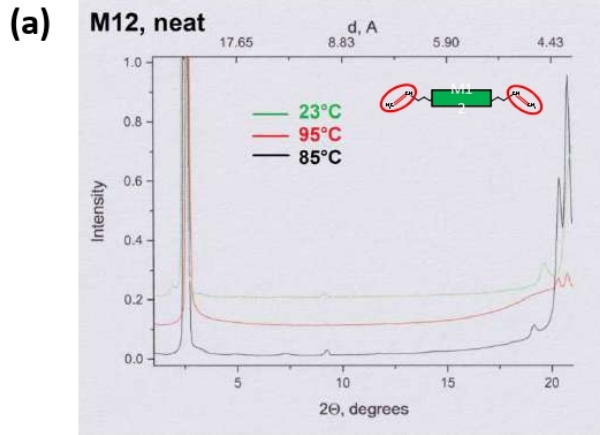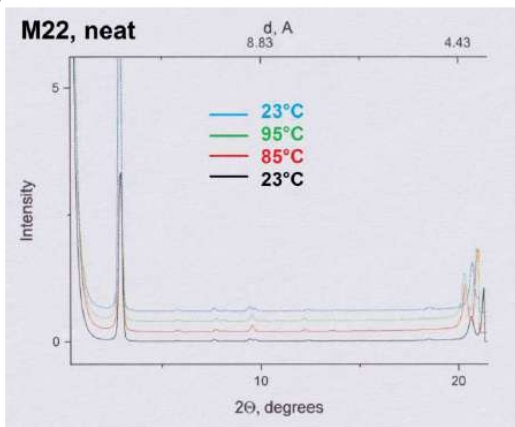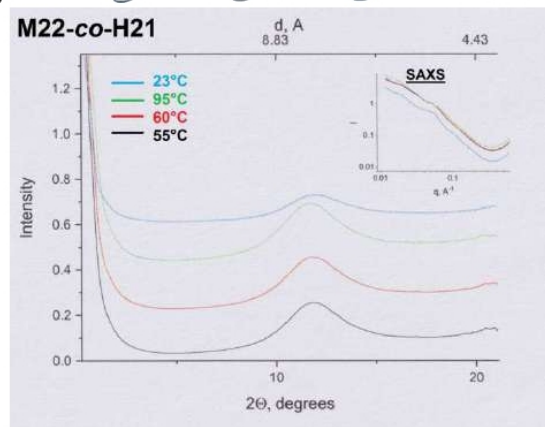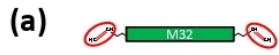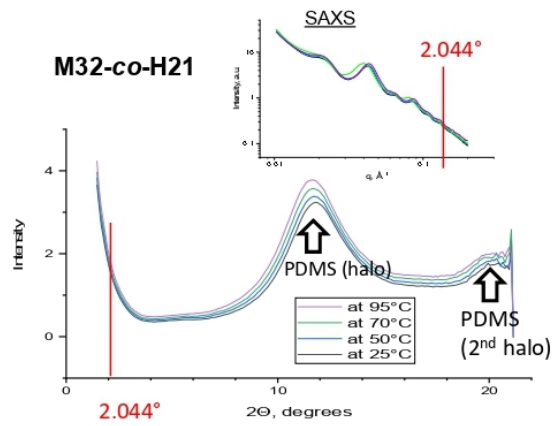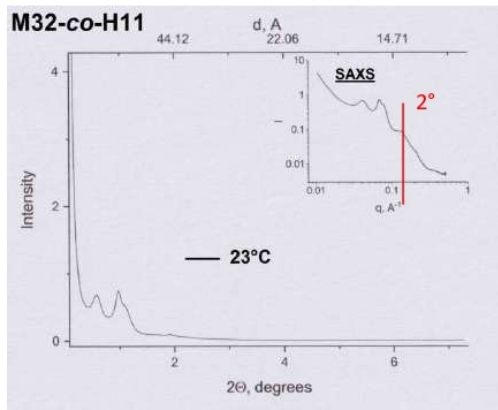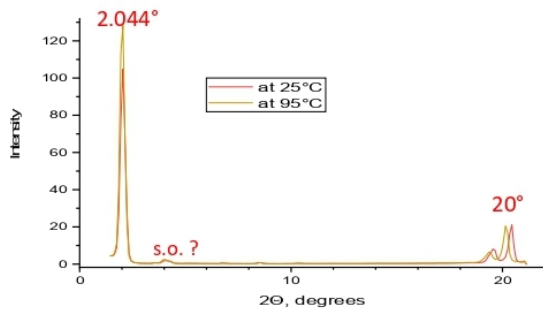
PLM observation of anisotropy and mesophases

M12 (neat) heating
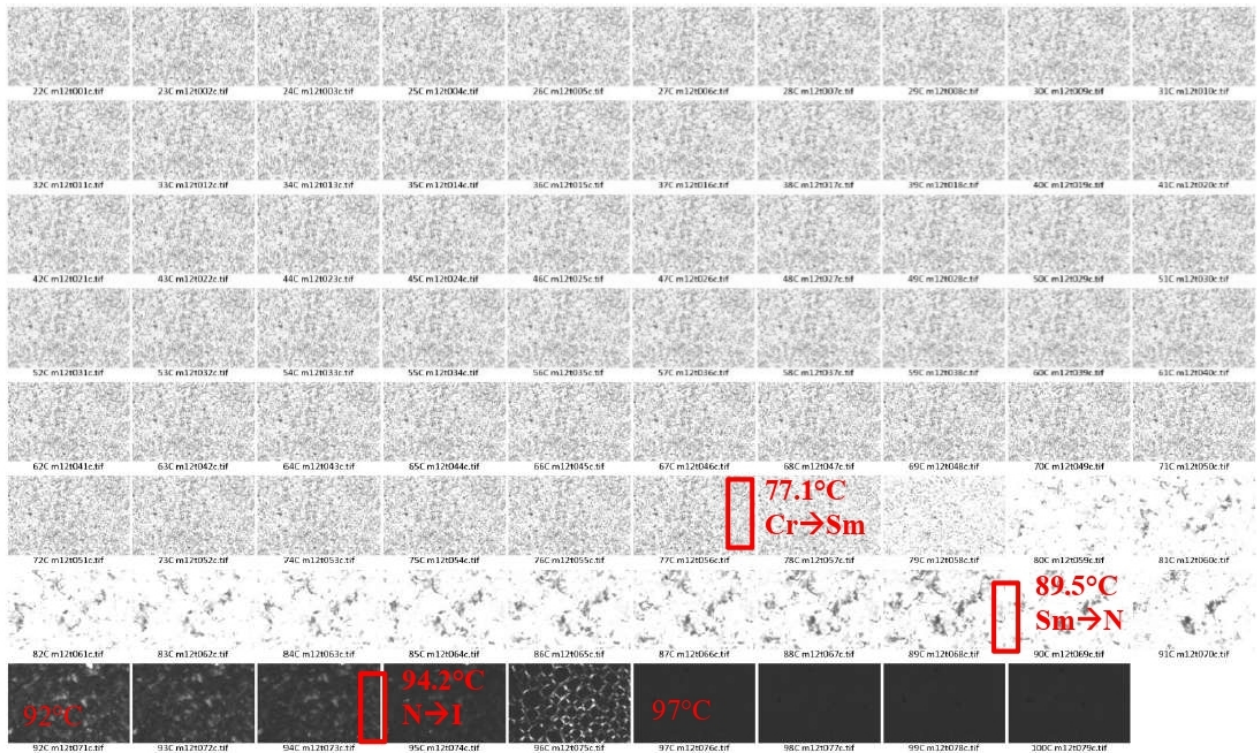
M12 (neat) cooling
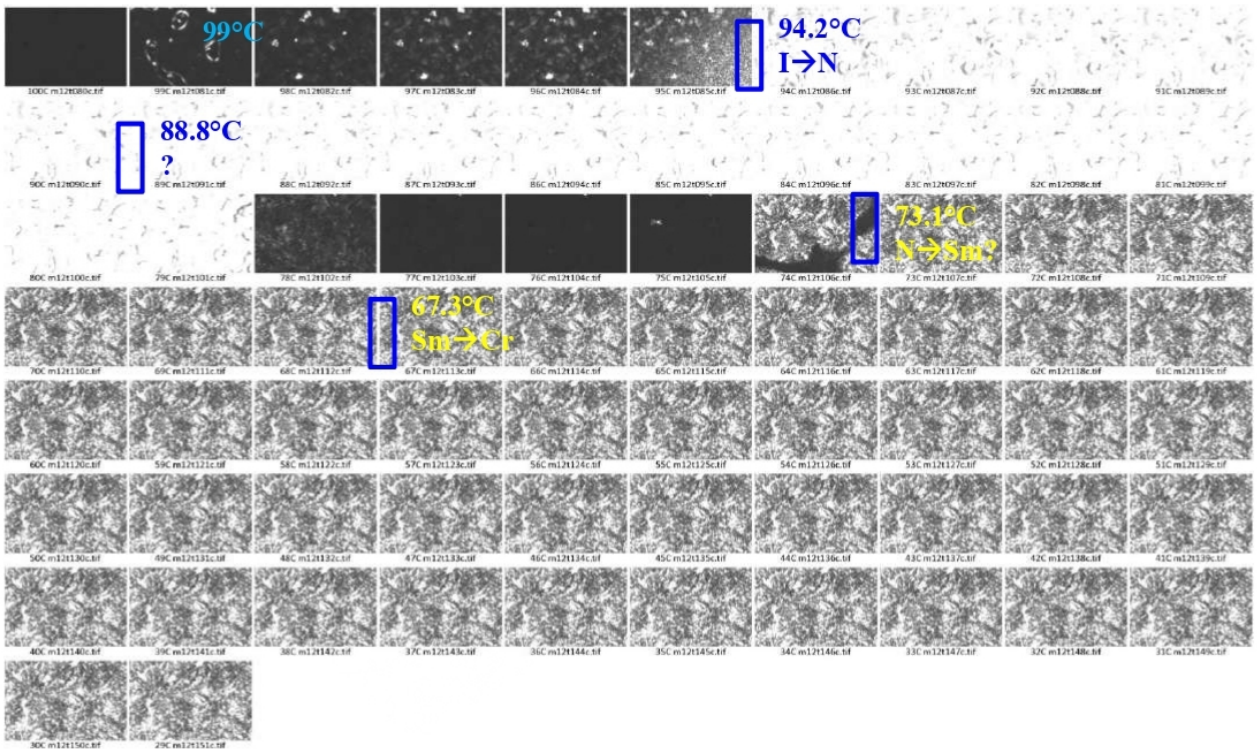
Textures observed in neat M12. Top: heating run; bottom: cooling run.

M12-H03 heating

40°C

(40 to) 55°C
Cr→N

75 (to 100°C)
N→I

82°C

M12-H03 cooling

98°C
I→N

73.1°C
N→Sm?

65°C
Sm→Cr

45.8°C ?
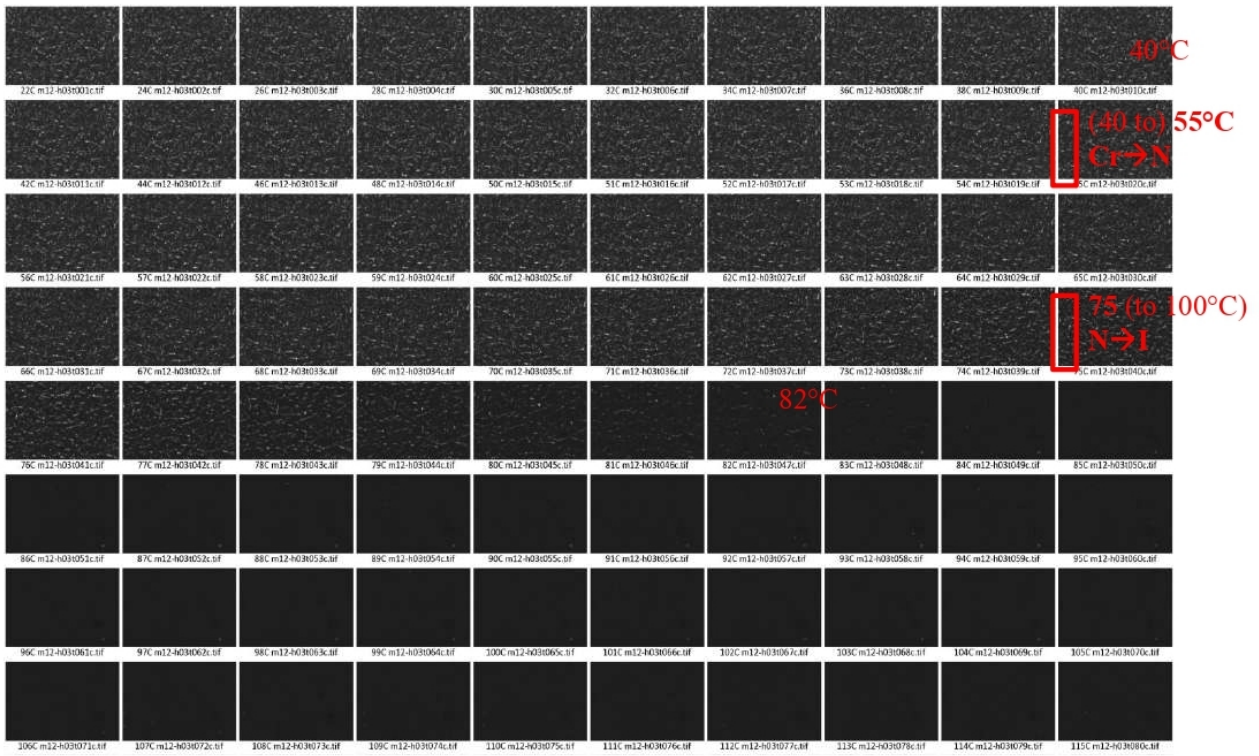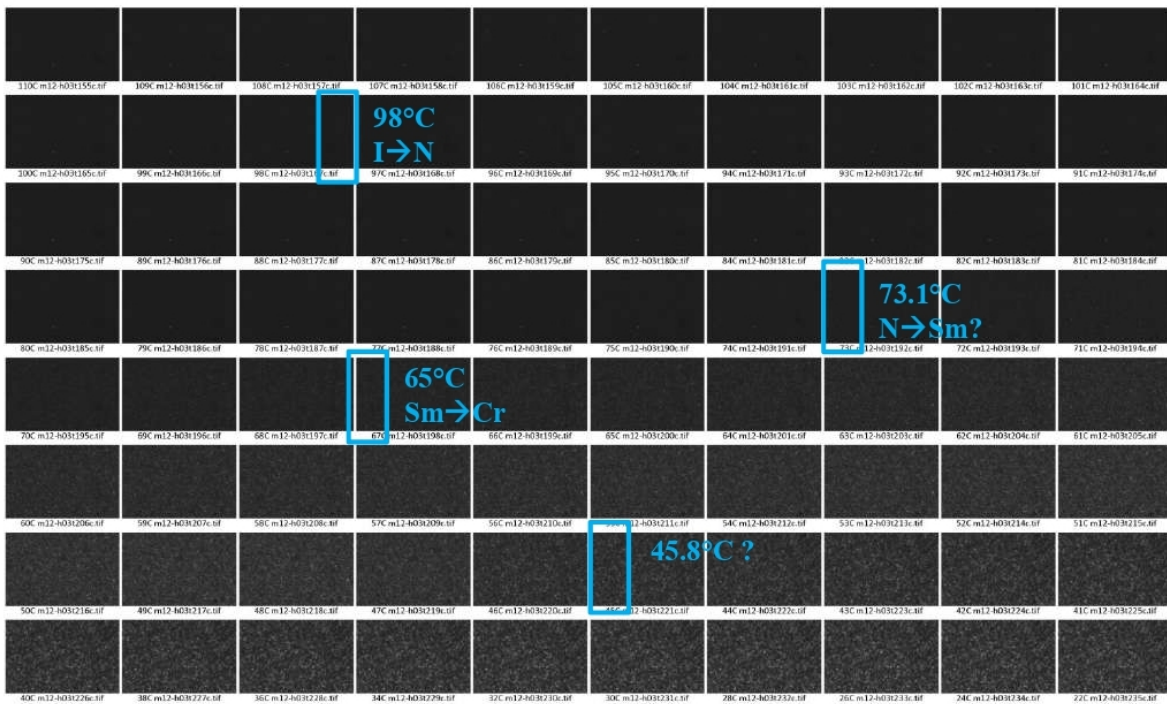
Textures observed in M12-H03. Top: heating run; bottom: cooling run.

M12-H11 heating

weak pattern

55°C
Cr→N

82°C
N→I

M12-H11 cooling

ca. 70°C
N→Sm?

67.3°C
Sm→Cr

37°C

weak pattern

Textures observed in M12-H11. Top: heating run; bottom: cooling run.

M12-H21 heating

M12-H21 cooling

Textures observed in M12-H21. Top: heating run; bottom: cooling run.

M22, neat

M22

heating

22-121°C:
no change

134.2°C
Cr→Sm

162.2°C
Sm→N

189°C
N→I

190°C

Textures observed in neat M22, heating run.

cooling

190°C 183.5°C I→N 154.3°C N→Sm 128°C Sm→Cr 121°C

Textures observed in neat M22, cooling run.
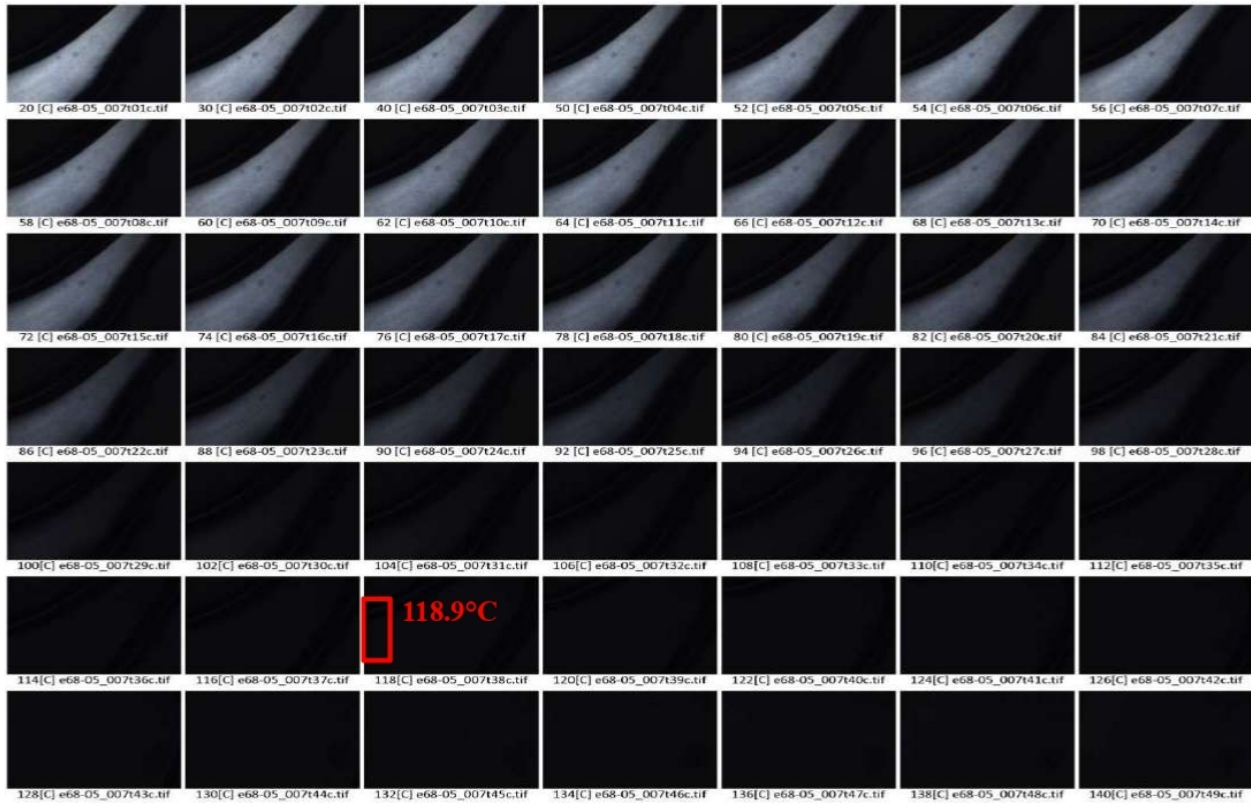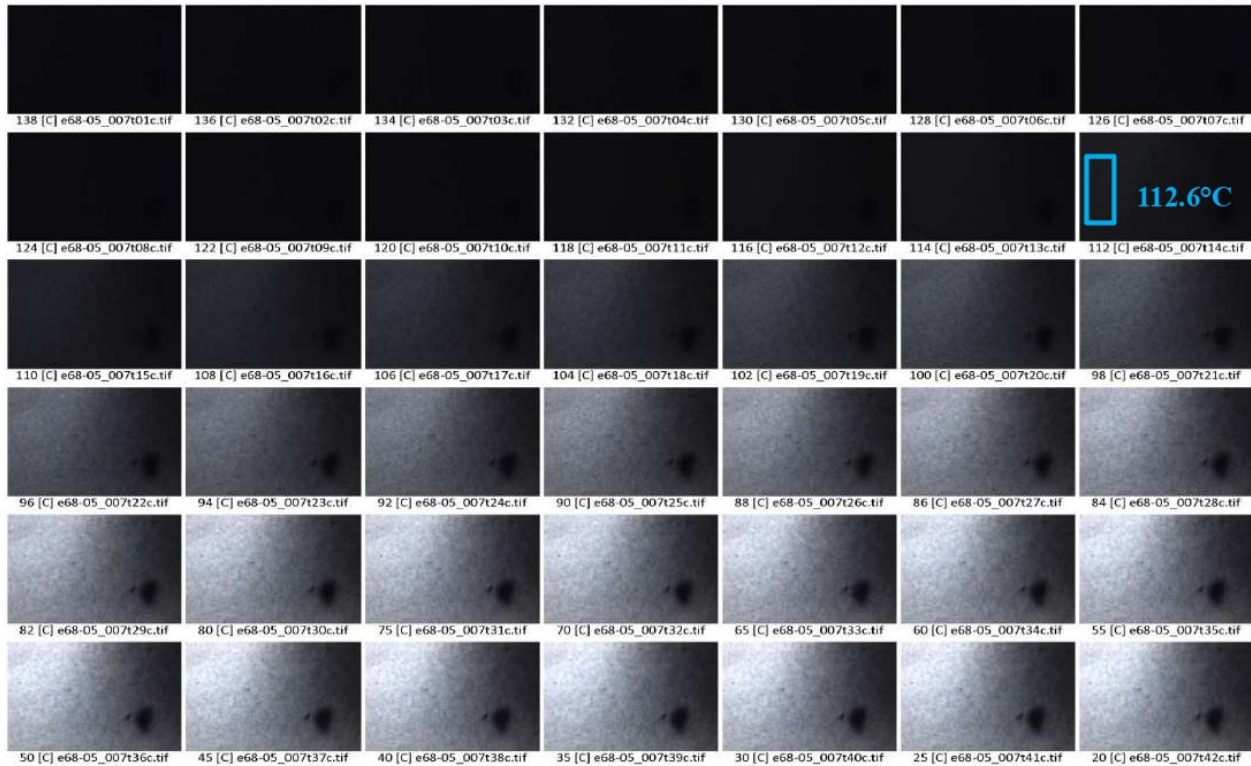
M22-*co*-H11

heating

cooling

Textures observed in M22-H11. Top: heating run; bottom: cooling run.

M22-H21 heating

20 [C] e68-05_007t01c.tif	30 [C] e68-05_007t02c.tif	40 [C] e68-05_007t03c.tif	50 [C] e68-05_007t04c.tif	52 [C] e68-05_007t05c.tif	54 [C] e68-05_007t06c.tif	56 [C] e68-05_007t07c.tif
58 [C] e68-05_007t08c.tif	60 [C] e68-05_007t09c.tif	62 [C] e68-05_007t10c.tif	64 [C] e68-05_007t11c.tif	66 [C] e68-05_007t12c.tif	68 [C] e68-05_007t13c.tif	70 [C] e68-05_007t14c.tif
72 [C] e68-05_007t15c.tif	74 [C] e68-05_007t16c.tif	76 [C] e68-05_007t17c.tif	78 [C] e68-05_007t18c.tif	80 [C] e68-05_007t19c.tif	82 [C] e68-05_007t20c.tif	84 [C] e68-05_007t21c.tif
86 [C] e68-05_007t22c.tif	88 [C] e68-05_007t23c.tif	90 [C] e68-05_007t24c.tif	92 [C] e68-05_007t25c.tif	94 [C] e68-05_007t26c.tif	96 [C] e68-05_007t27c.tif	98 [C] e68-05_007t28c.tif
100[C] e68-05_007t29c.tif	102 [C] e68-05_007t30c.tif	104[C] e68-05_007t31c.tif	106 [C] e68-05_007t32c.tif	108 [C] e68-05_007t33c.tif	110 [C] e68-05_007t34c.tif	112[C] e68-05_007t35c.tif
114[C] e68-05_007t36c.tif	116[C] e68-05_007t37c.tif	118[C] e68-05_007t38c.tif	120[C] e68-05_007t39c.tif	122[C] e68-05_007t40c.tif	124[C] e68-05_007t41c.tif	126[C] e68-05_007t42c.tif
128[C] e68-05_007t43c.tif	130[C] e68-05_007t44c.tif	132[C] e68-05_007t45c.tif	134[C] e68-05_007t46c.tif	136[C] e68-05_007t47c.tif	138[C] e68-05_007t48c.tif	140[C] e68-05_007t49c.tif

118.9°C

M22-H21 cooling

138 [C] e68-05_007t01c.tif	136 [C] e68-05_007t02c.tif	134 [C] e68-05_007t03c.tif	132 [C] e68-05_007t04c.tif	130 [C] e68-05_007t05c.tif	128 [C] e68-05_007t06c.tif	126 [C] e68-05_007t07c.tif
124 [C] e68-05_007t08c.tif	122 [C] e68-05_007t09c.tif	120 [C] e68-05_007t10c.tif	118 [C] e68-05_007t11c.tif	116 [C] e68-05_007t12c.tif	114 [C] e68-05_007t13c.tif	112 [C] e68-05_007t14c.tif
110 [C] e68-05_007t15c.tif	108 [C] e68-05_007t16c.tif	106 [C] e68-05_007t17c.tif	104 [C] e68-05_007t18c.tif	102 [C] e68-05_007t19c.tif	100 [C] e68-05_007t20c.tif	98 [C] e68-05_007t21c.tif
96 [C] e68-05_007t22c.tif	94 [C] e68-05_007t23c.tif	92 [C] e68-05_007t24c.tif	90 [C] e68-05_007t25c.tif	88 [C] e68-05_007t26c.tif	86 [C] e68-05_007t27c.tif	84 [C] e68-05_007t28c.tif
82 [C] e68-05_007t29c.tif	80 [C] e68-05_007t30c.tif	75 [C] e68-05_007t31c.tif	70 [C] e68-05_007t32c.tif	65 [C] e68-05_007t33c.tif	60 [C] e68-05_007t34c.tif	55 [C] e68-05_007t35c.tif
50 [C] e68-05_007t36c.tif	45 [C] e68-05_007t37c.tif	40 [C] e68-05_007t38c.tif	35 [C] e68-05_007t39c.tif	30 [C] e68-05_007t40c.tif	25 [C] e68-05_007t41c.tif	20 [C] e68-05_007t42c.tif

112.6°C
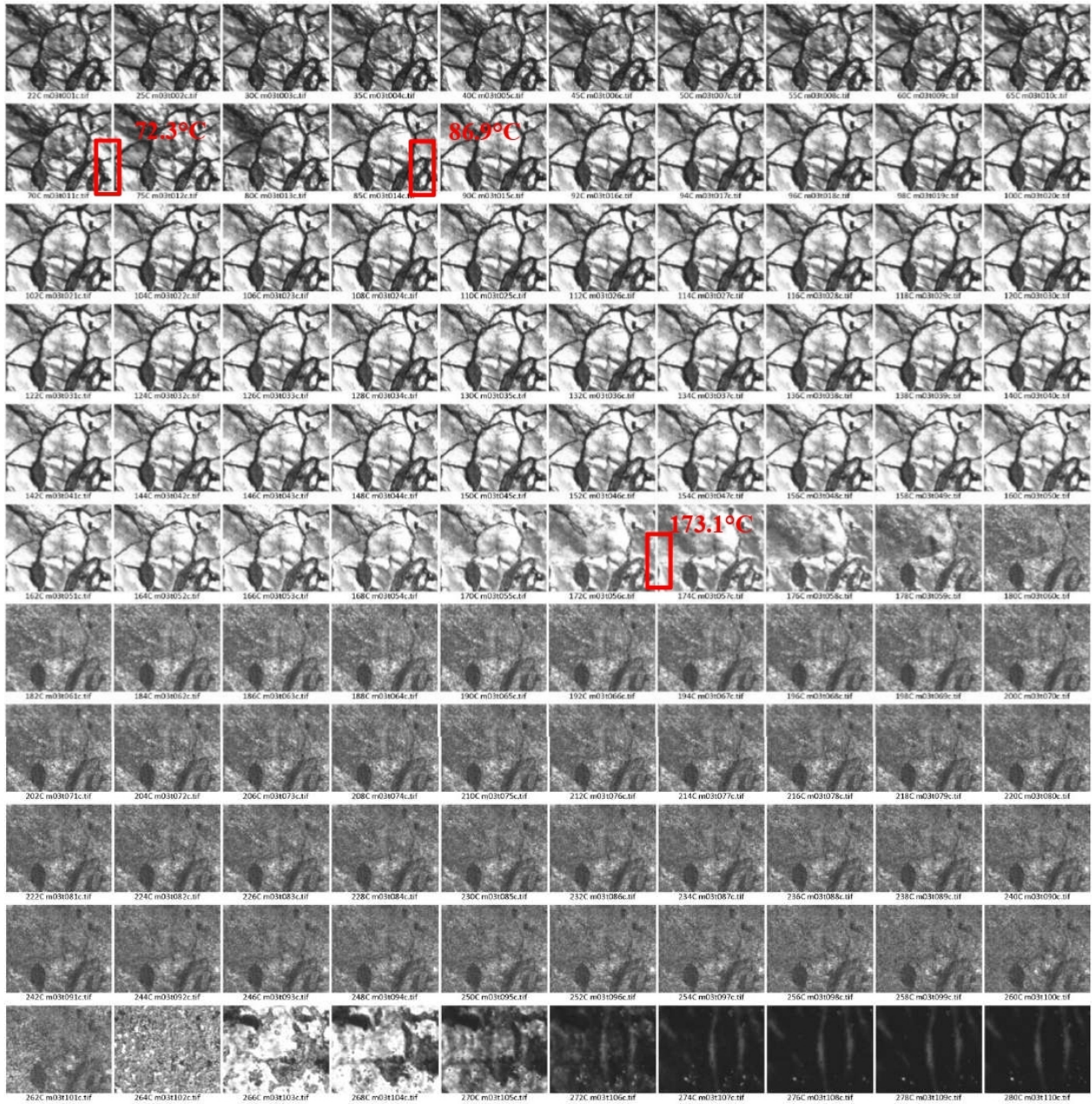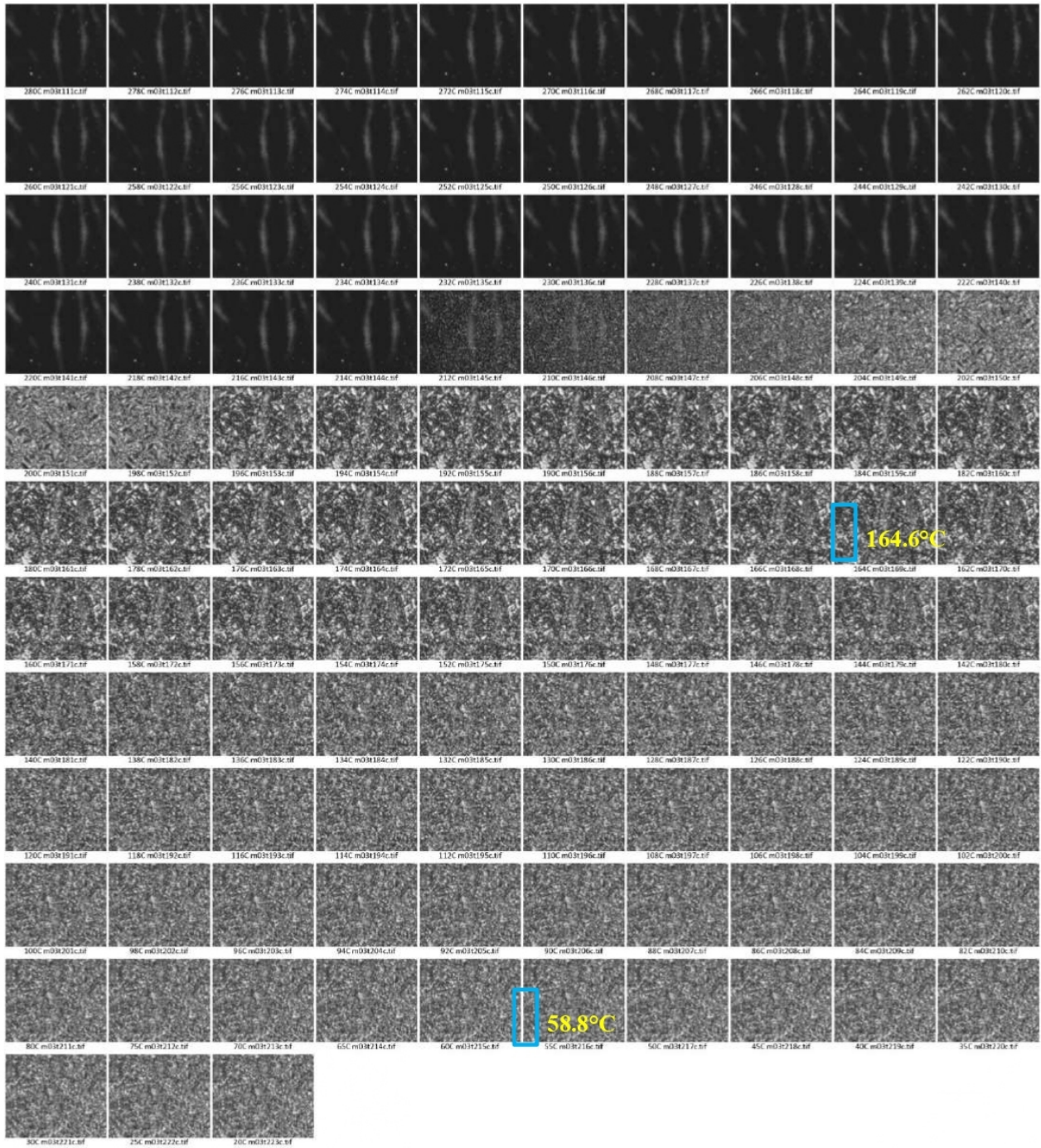
Textures observed in M22-H21. Top: heating run; bottom: cooling run.
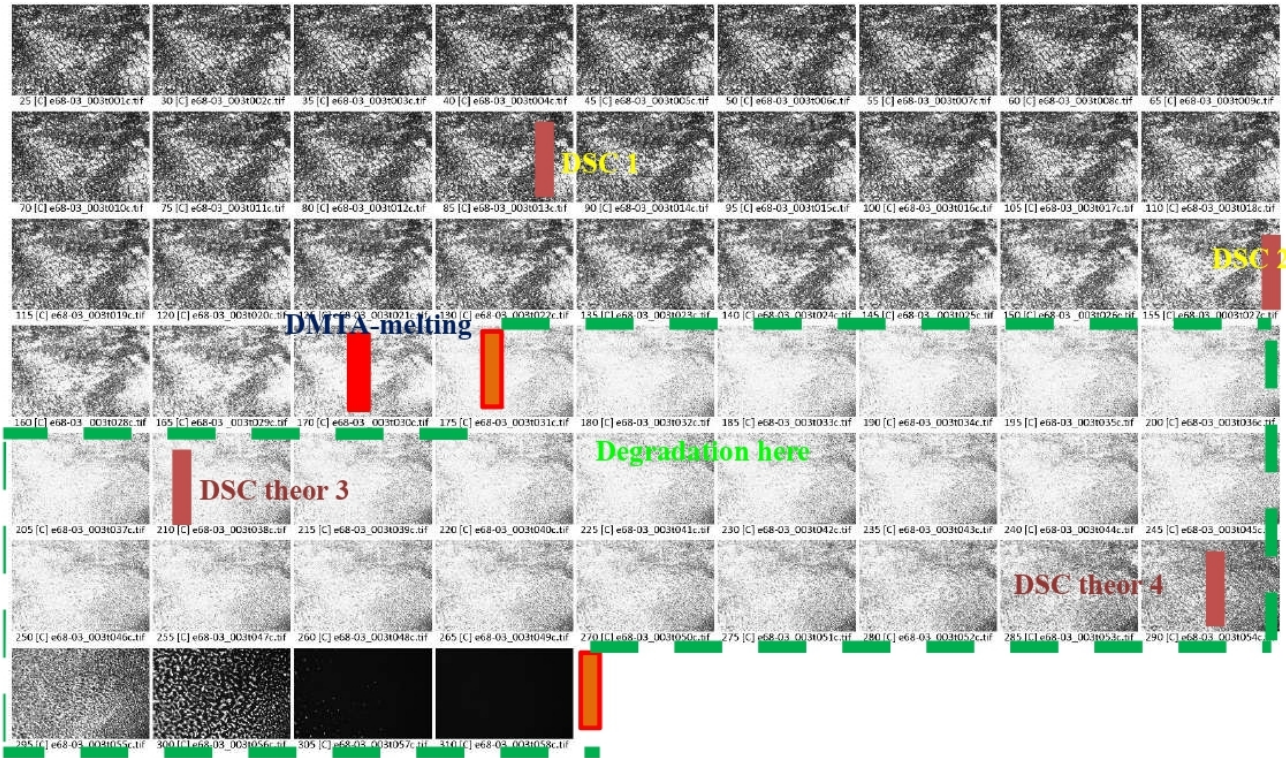
M3 (neat) heating

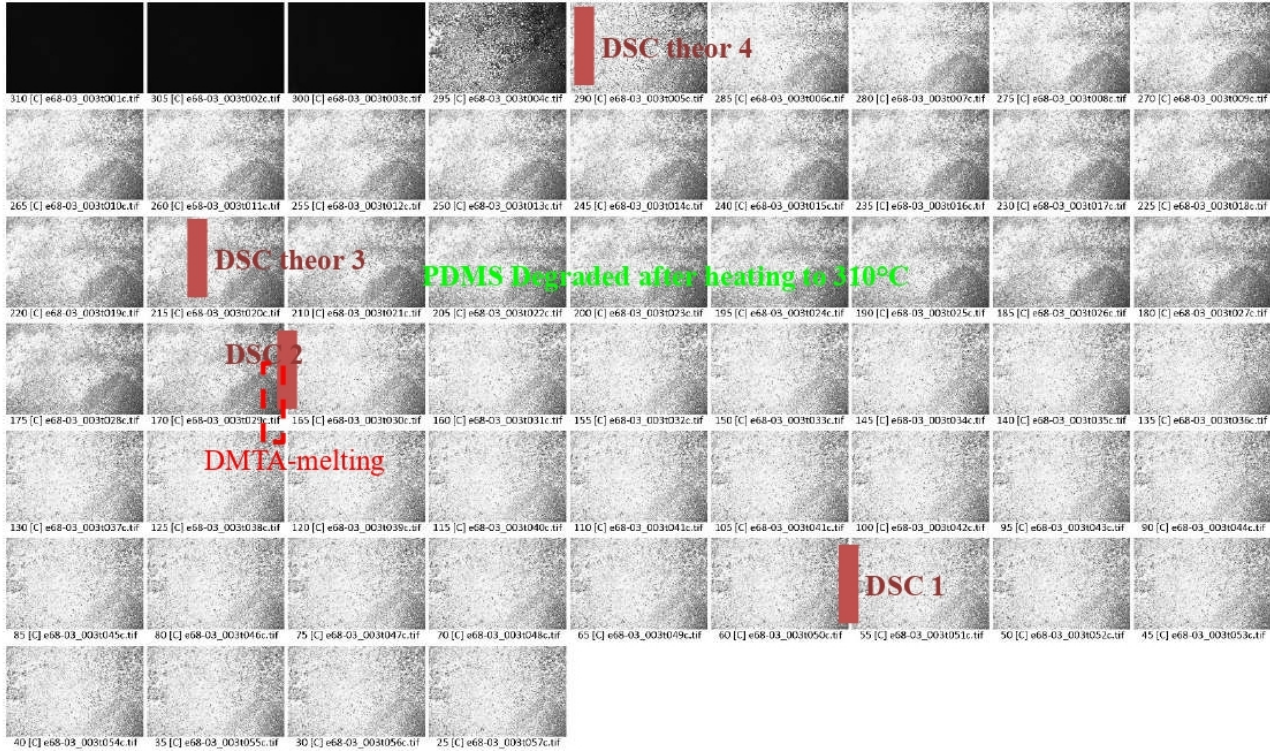*Textures observed in neat M3, heating run.*

M3 (neat) cooling

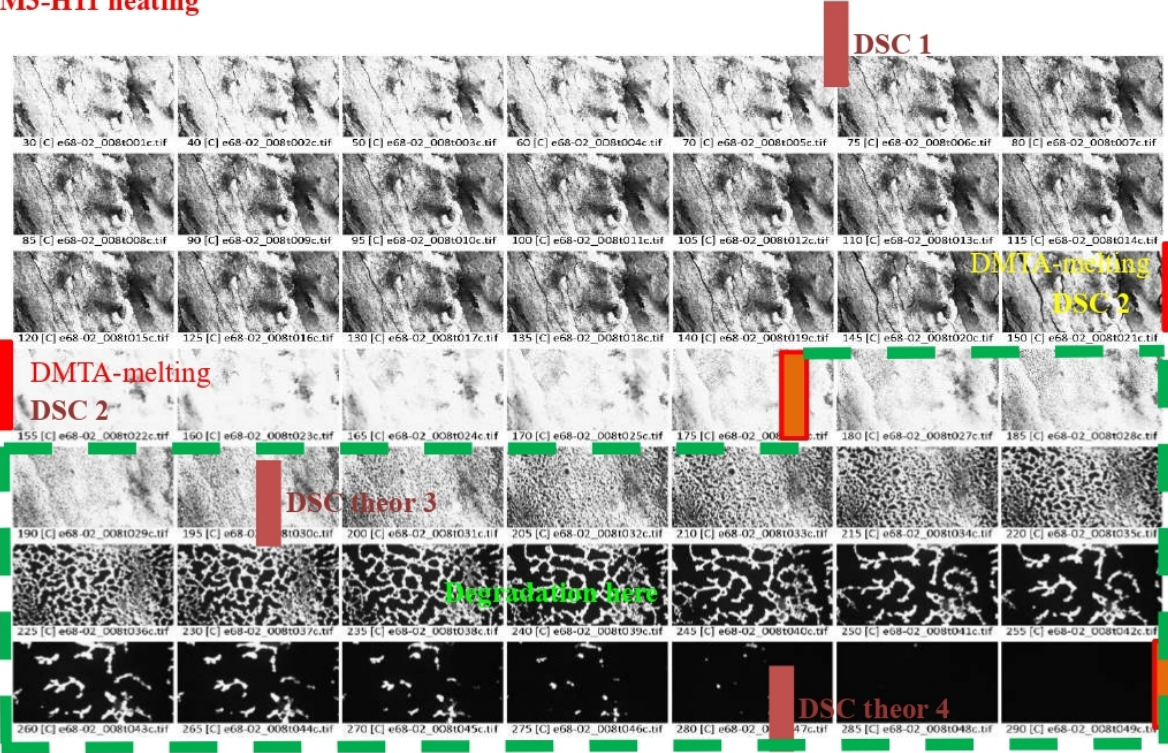*Textures observed in neat M3, cooling run.*

M3-H03 heating

M3-H03 cooling

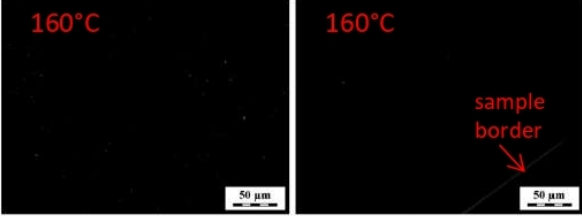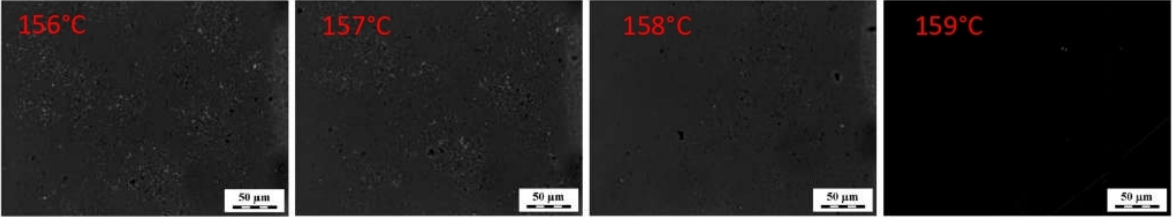*Textures observed in M3-H03. Top: heating run; bottom: cooling run.*

Textures observed in M3-H11, heating run.

M32-*co*-H21

heating

DSC 1 theor.
M32: Cr1→Cr2
87°C

DMTA-melting
80-90°C

20°C | 90°C | 100°C | 150°C

156°C | 157°C | 158°C | 159°C

160°C | 160°C

sample border
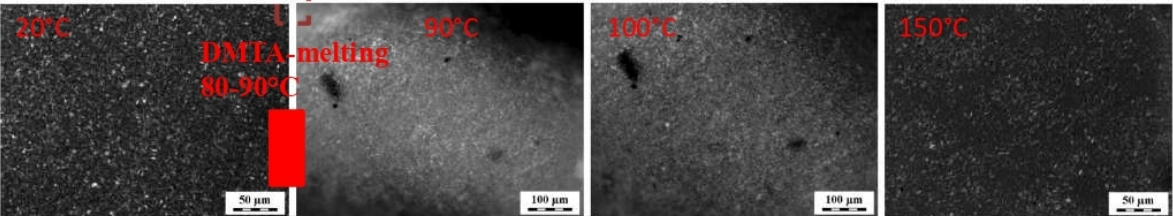
DSC 2 theor.
M32: Cr2→Sm
173°C

texture detail at 20°C

10 µm

20°C

cooling

150°C | 140°C | 130°C | 120°C
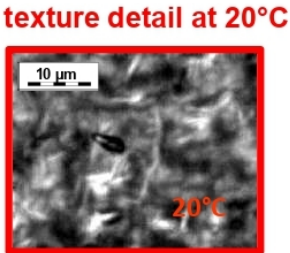
DSC 2 theor.
M32: Sm→Cr2
165°C

110°C | 100°C | 90°C | 70°C

DMTA-melting
80-90°C
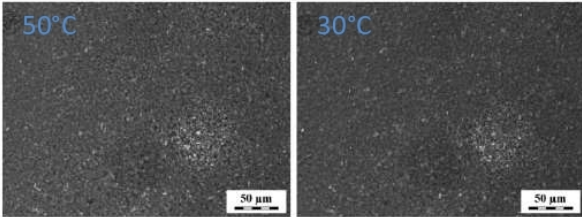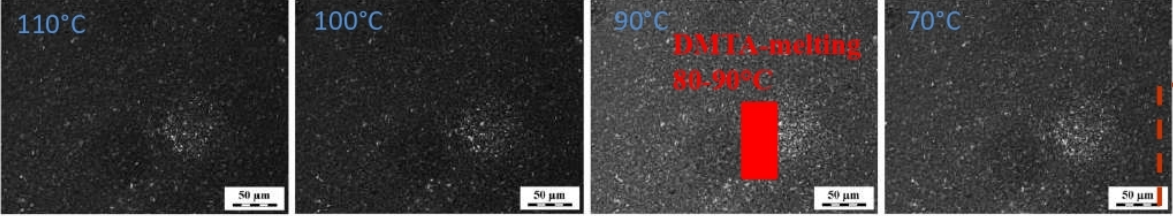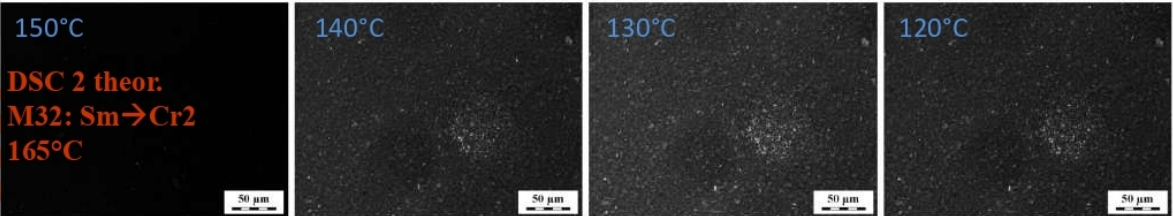
DSC 1 theor.
M32: Cr2→Cr1
87°C

50°C | 30°C

Textures observed in M3-H21. Top: heating run; bottom: cooling run.

Supporting information - Analyses

Evaluation of conversion of the PDMS during hydrosilylation reaction by means of FTIR.
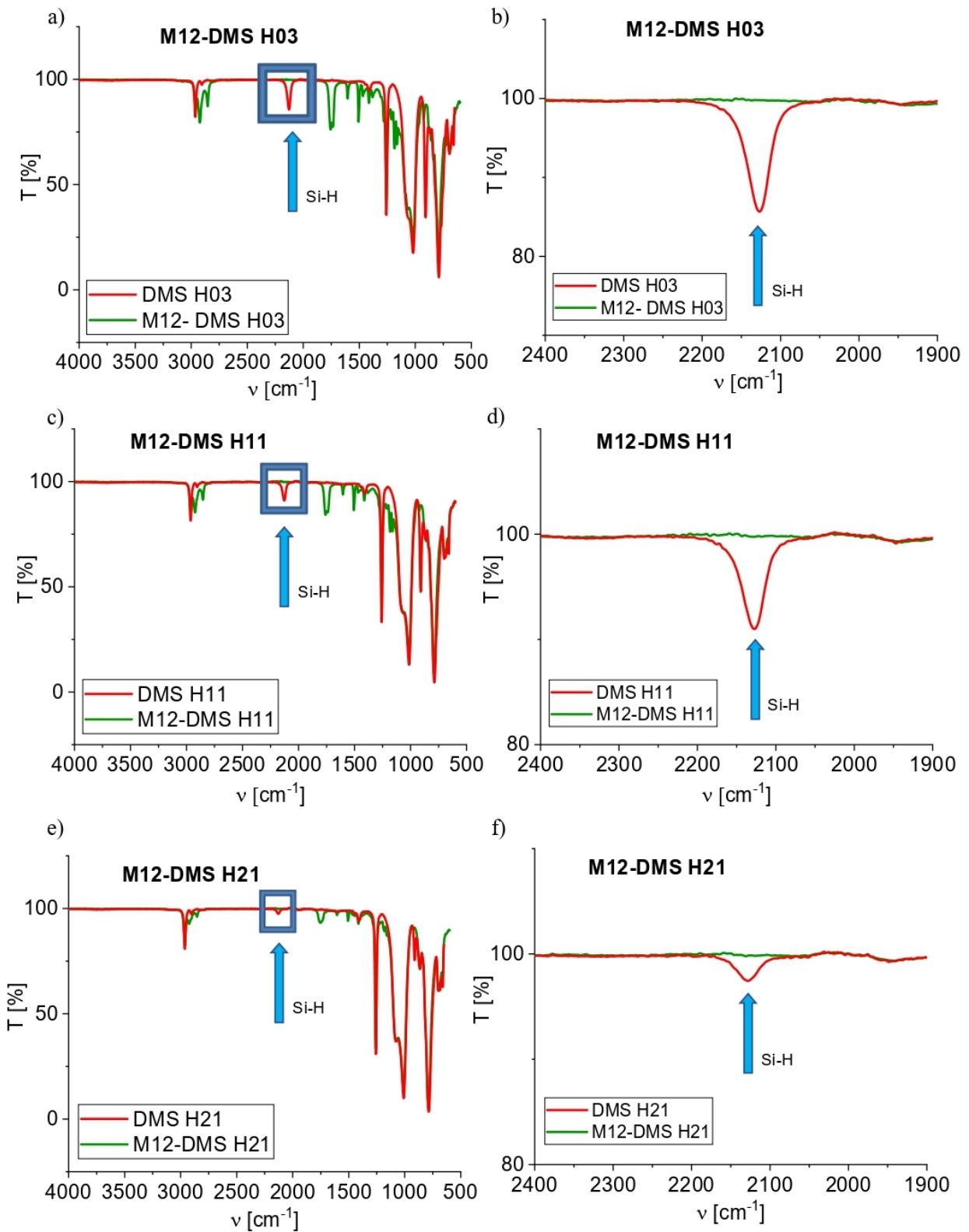
Spectroscopic evaluation of the completion of the hydrosilylation reaction: (a), (c), (e): FTIR spectra of pure PDMS and of LC-PDMS copolymers with M12 as mesogen; (b), (d), (f): highlighting the disappearance of the Si-H as zoomed inlay
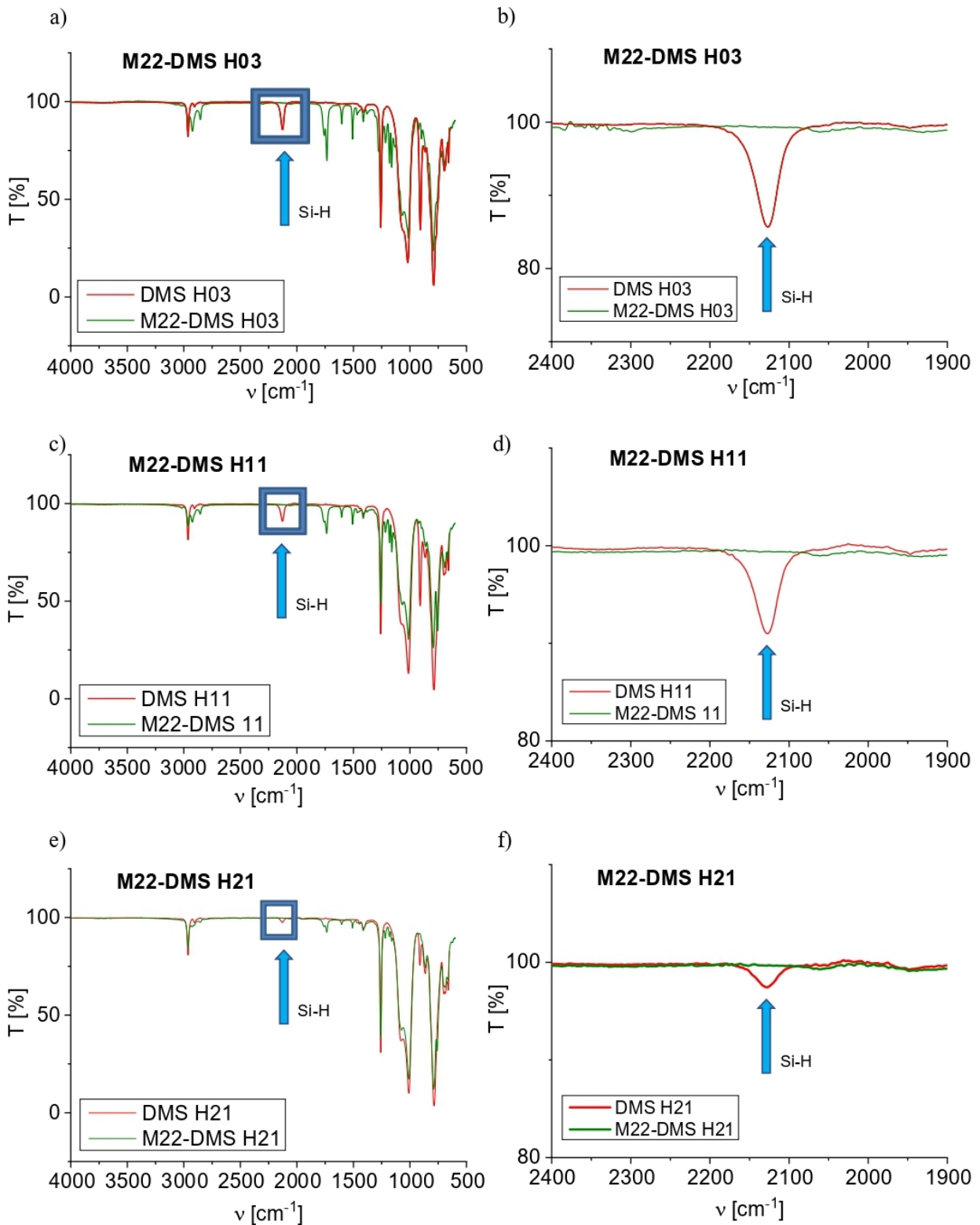
Spectroscopic evaluation of the completion of the hydrosilylation reaction: (a), (c), (e): FTIR spectra of pure PDMS and of LC-PDMS copolymers with M22 as mesogen; (b), (d), (f): highlighting the disappearance of the Si-H as zoomed inlay
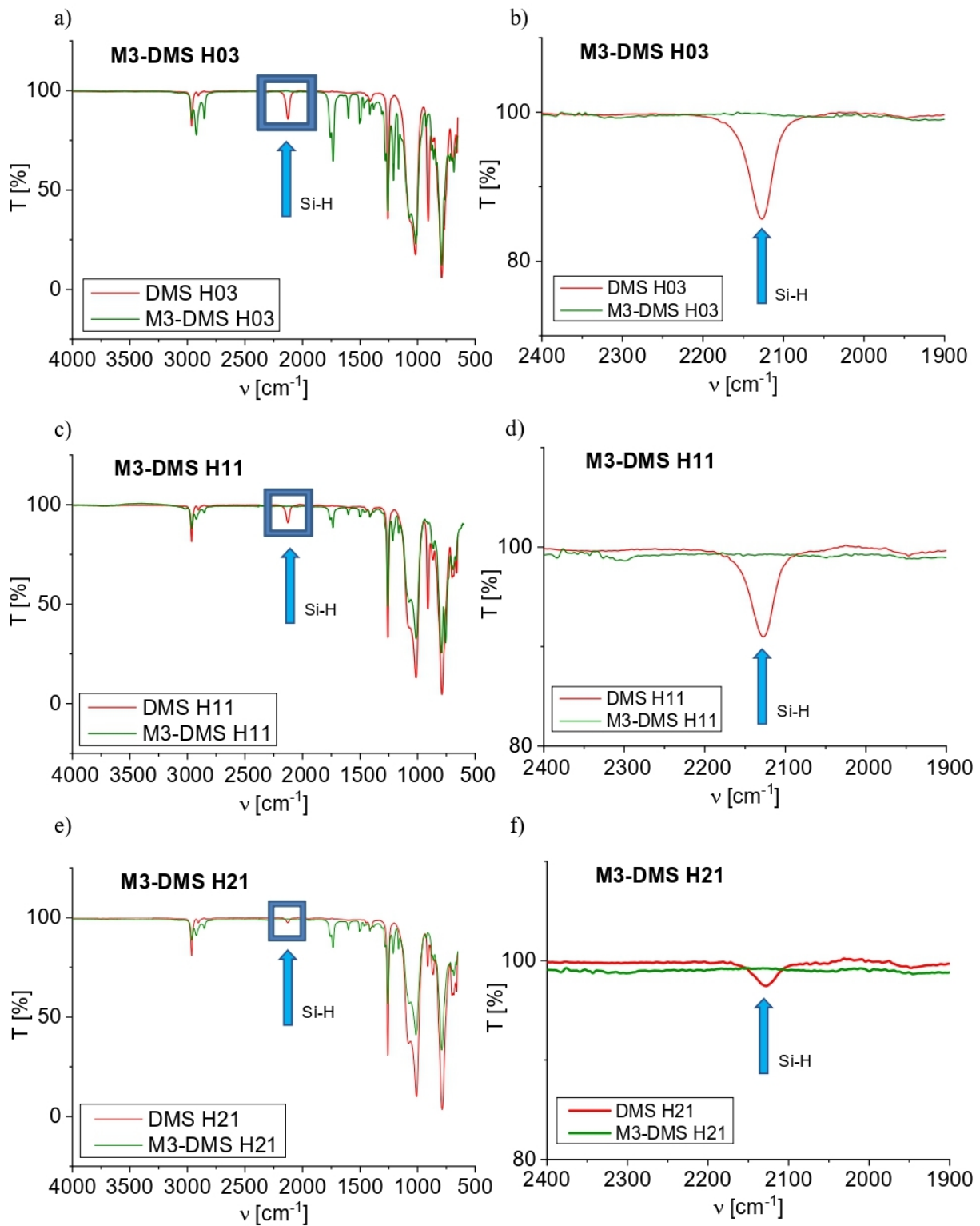
Spectroscopic evaluation of the completion of the hydrosilylation reaction: (a), (c), (e): FTIR spectra of pure PDMS and of LC-PDMS copolymers with M3 as mesogen; (b), (d), (f): highlighting the disappearance of the Si-H as zoomed inlay
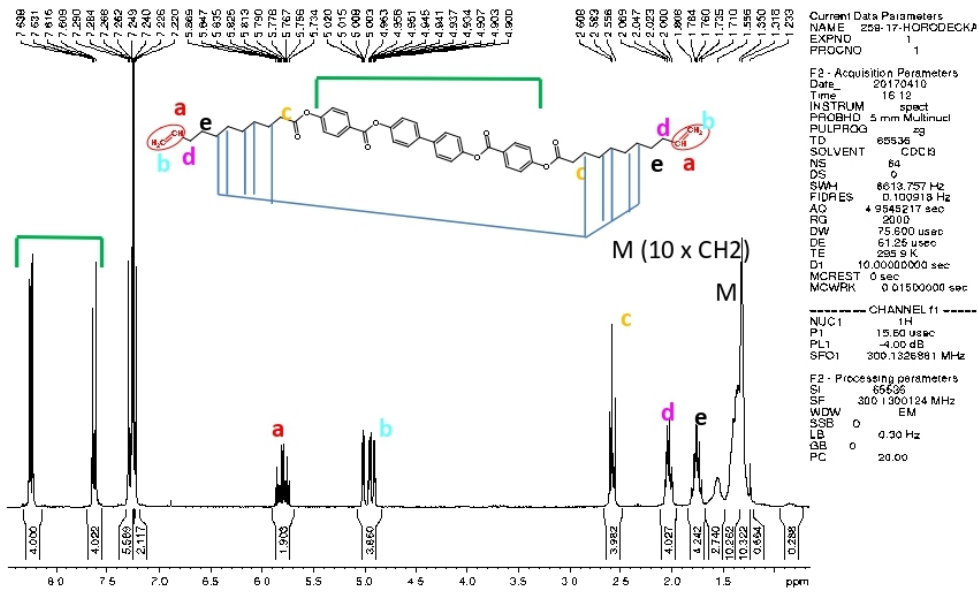
^{1}H-NMR: Purity of LC components and products.
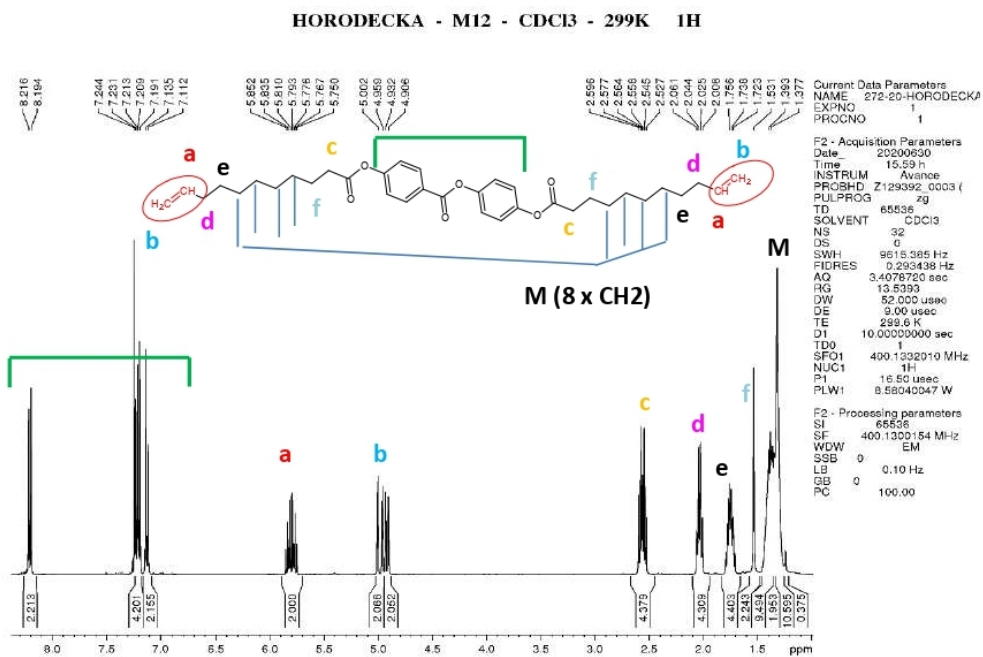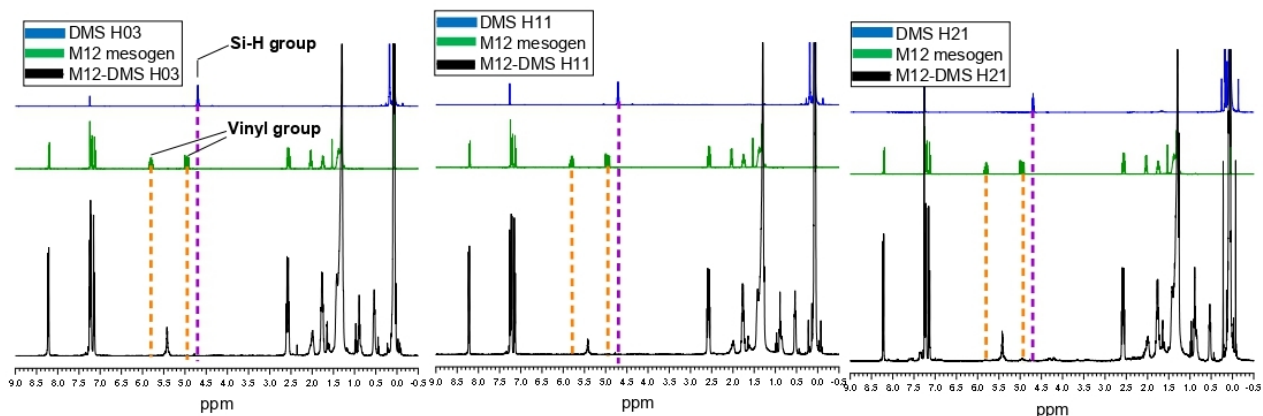

^{1}H-NMR spectrum of the pure M12 mesogen with assigned peaks.
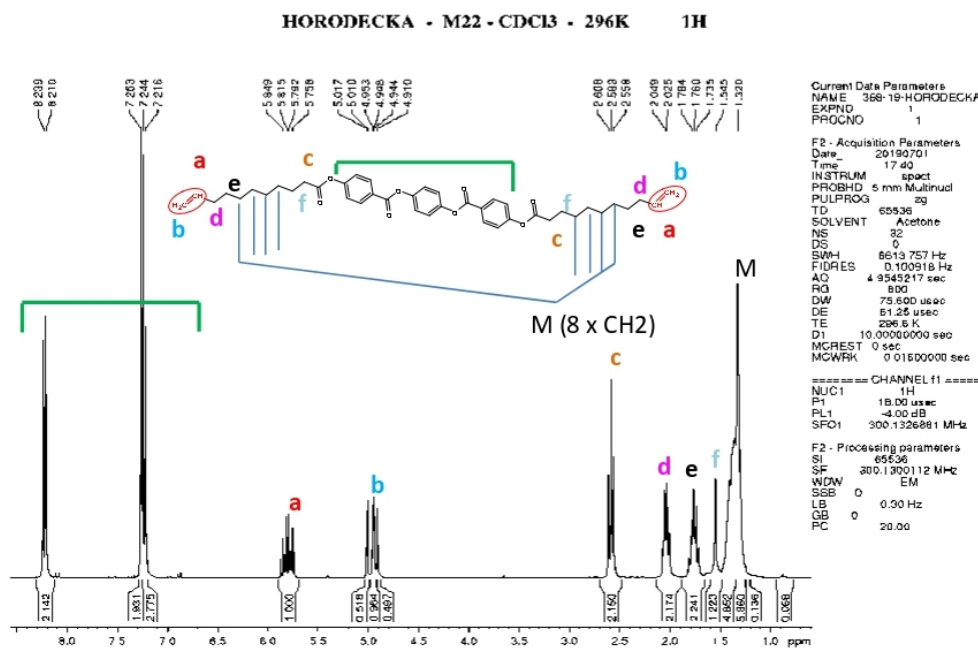
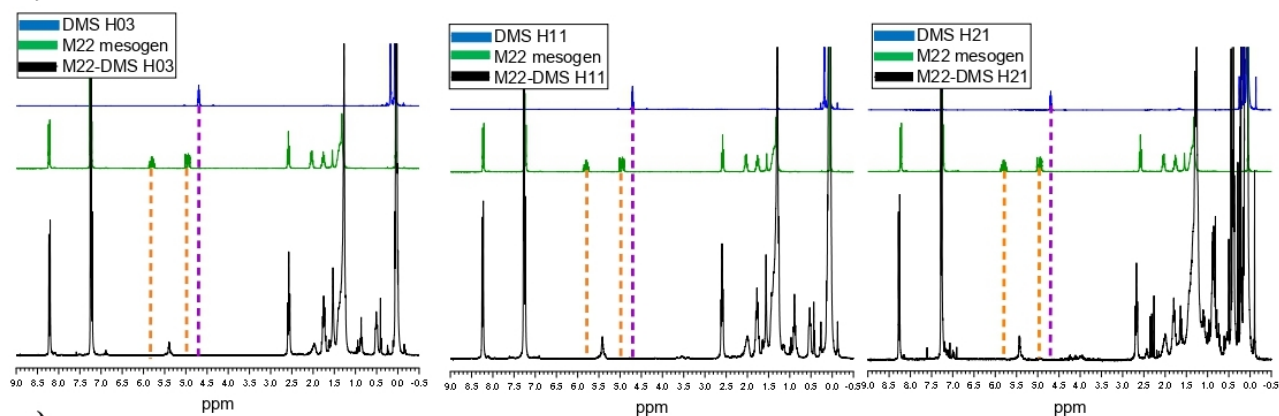*^{1}H-NMR spectrum of the pure M22 mesogen with assigned peaks.*
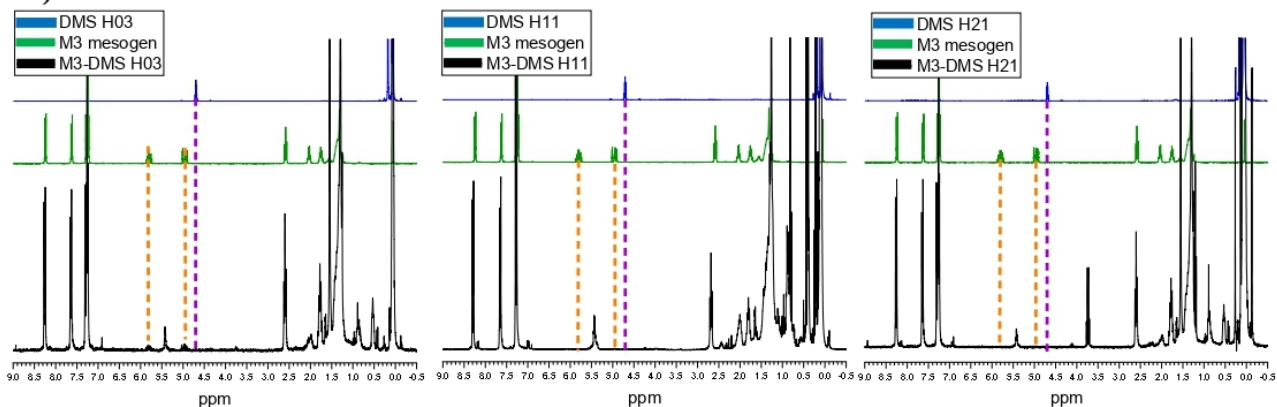
¹H-NMR spectrum of the pure M3 mesogen with assigned peaks.

a)

b)
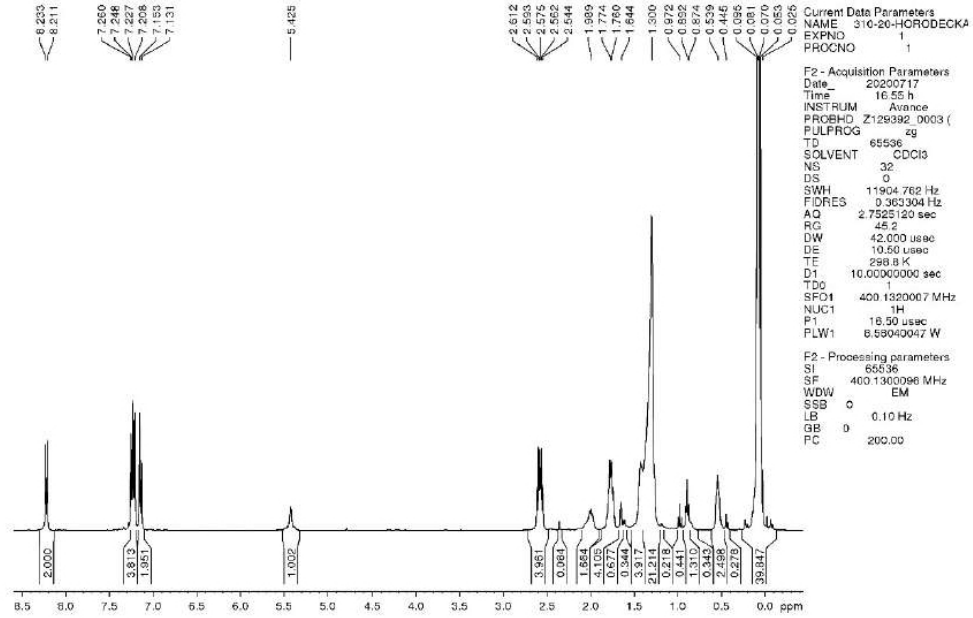
c)

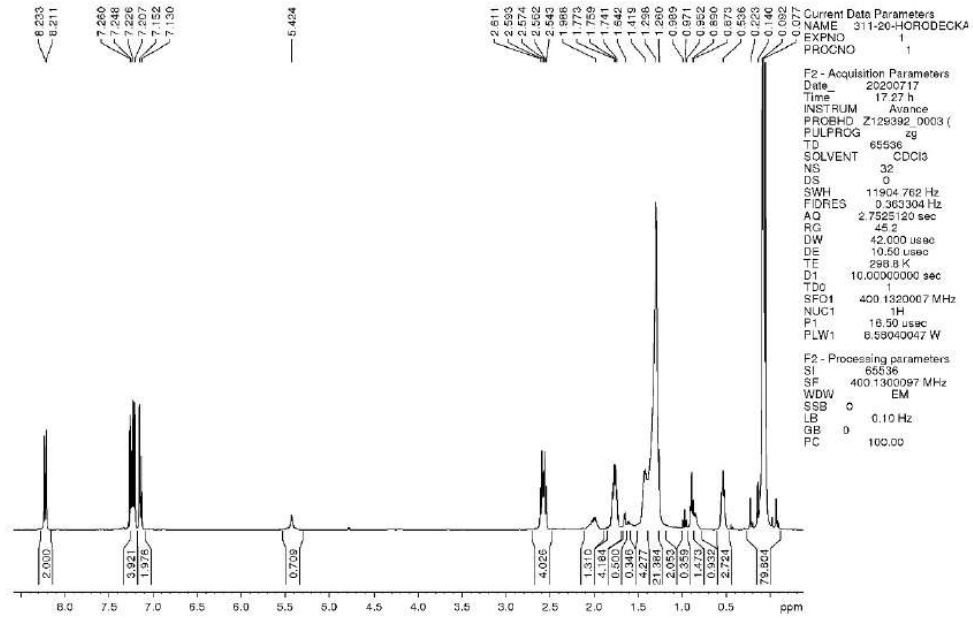*¹H-NMR spectrum of the neat LC mesogen, pure PDMS and copolymers with assigned dissapearance of Si-H and vinyl groups peaks; (a-row) M12-DMS H03, M12-DMS H11, M12-DMS H21, (b-row) M22-DMS H03, M22-DMS H11, M22-DMS H21, (c-row) M3-H03, M3-H11 and M3-H21.*

HORODECKA - M12-H03 - CDCl3 - 300K 1H

HORODECKA - M12-H11 - CDCl3 - 300K 1H

¹H-NMR spectra of the copolymers (top): M12-H03; (bottom): M12-H11.
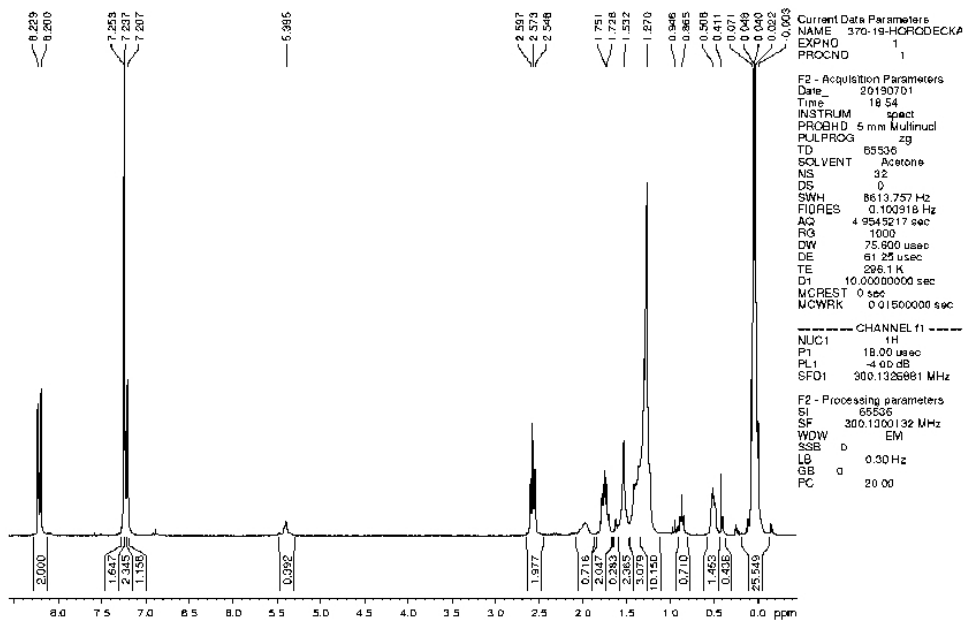
HORODECKA - M12-H21 - CDCl3 - 300K   1H
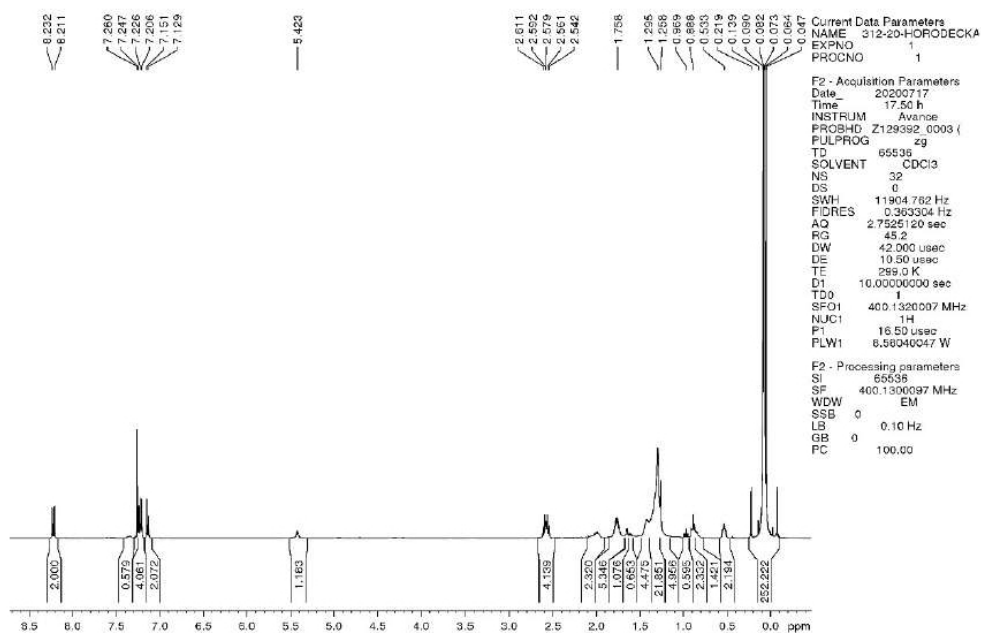
HORODECKA - M22-H03 - CDCl3 - 296K   1H

¹H-NMR spectra of the copolymers (top): M12-H21; (bottom): M22-H03.
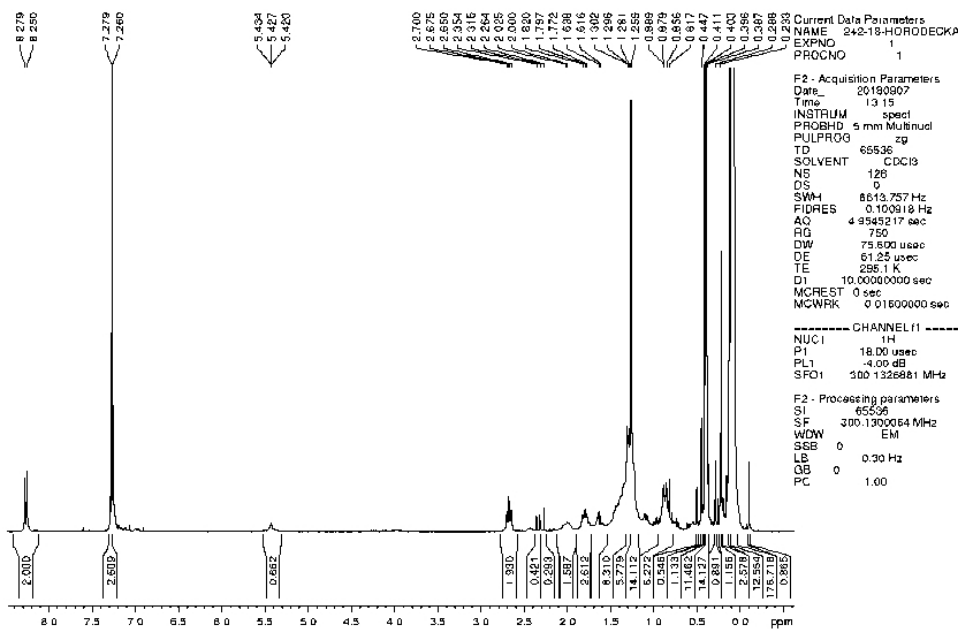
^{1}H-NMR spectra of the copolymers (top): M22-H11; (bottom): M22-H21.
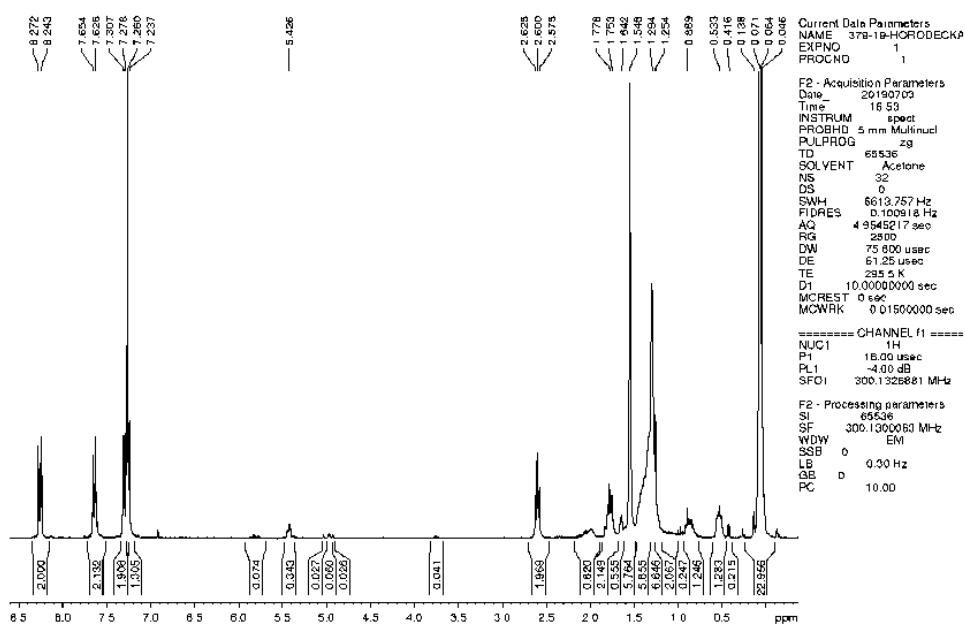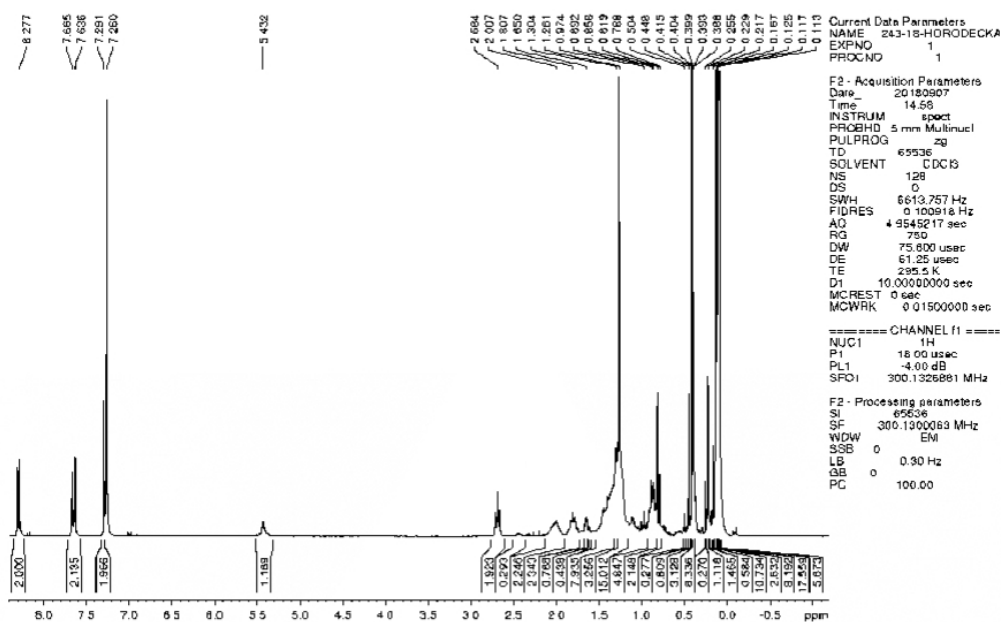
^{1}H-NMR spectra of the copolymers (top): M3-H03; (bottom): M3-H11.
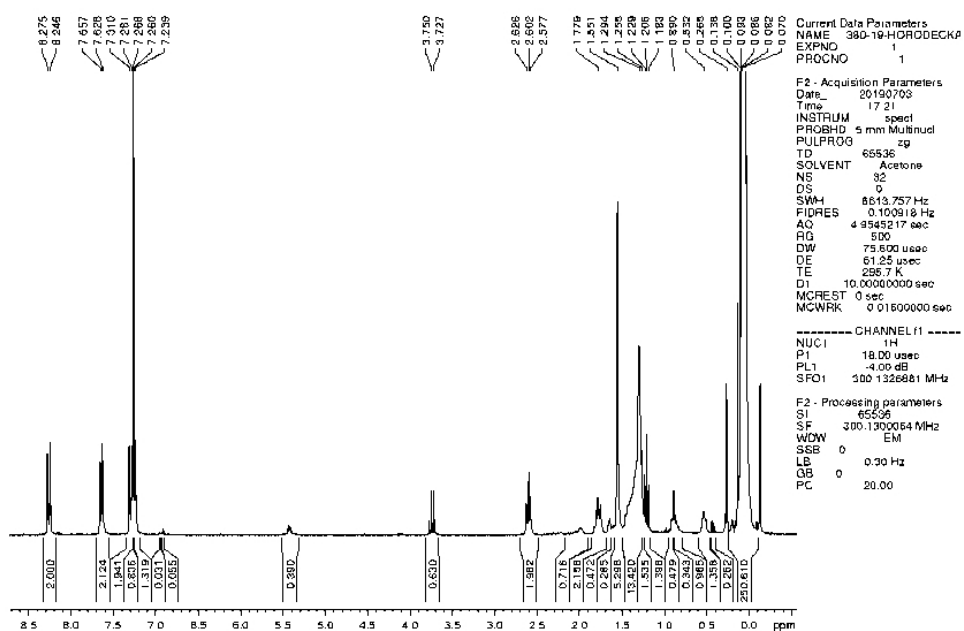
¹H-NMR spectra of the copolymer M3-H21.

Molecular mass analysis of the copolymers, as well as of the LC precursors.
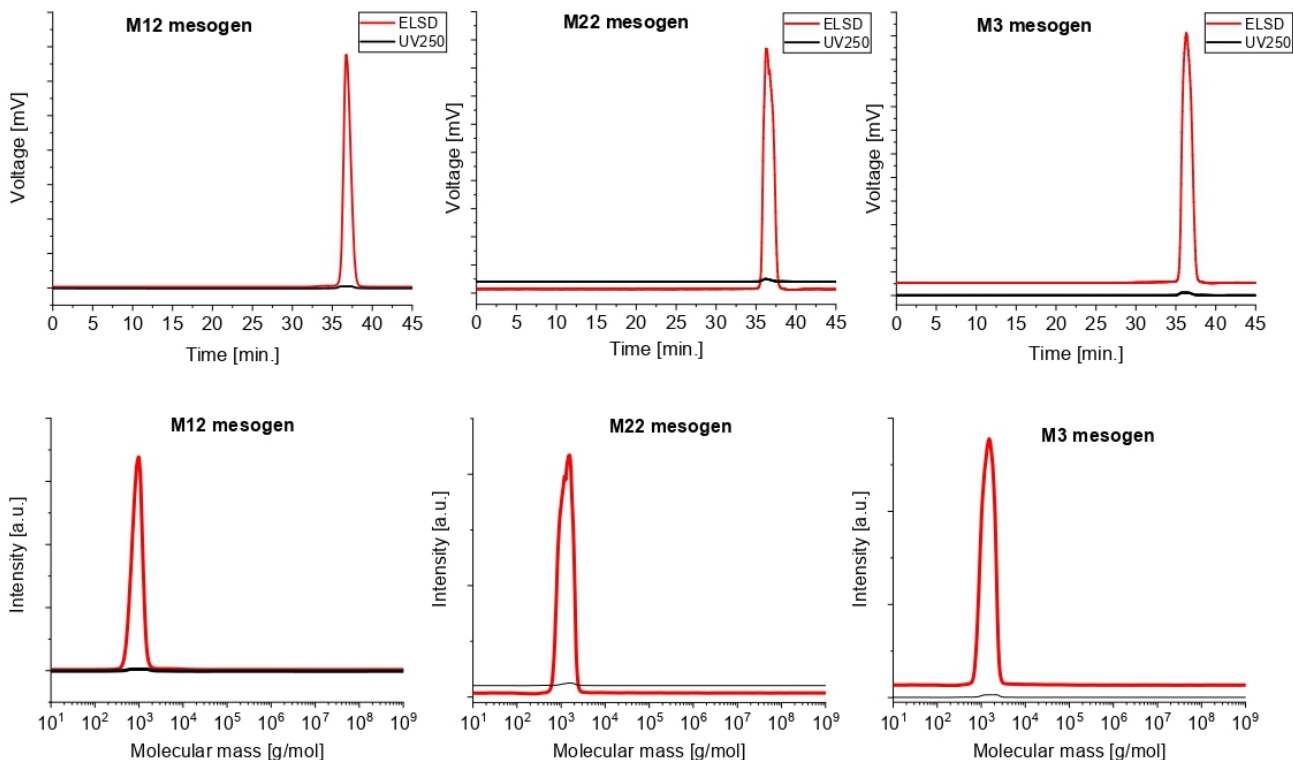
M12											
nr.	Max. RT	Start RT	End RT	flow rate correction	Mp	Mn	Mw	Mz	PD	I [mV]	I [%]
x	36.75	32.07	41.54	1	971	850	943	1230	1.1097	677.92	100

M22											
nr.	Max. RT	Start RT	End RT	flow rate correction	Mp	Mn	Mw	Mz	PD	I [mV]	I [%]
x	36.30	30.51	39.35	1	1287	1009	1151	1954	1.1407	430.47	100

M3											
nr.	Max. RT	Start RT	End RT	flow rate correction	Mp	Mn	Mw	Mz	PD	I [mV]	I [%]
x	36.34	34.51	39.32	1	1495	1323	1446	1568	1.0927	531.18	100

GPC trace of pure M12, M22 and M3.
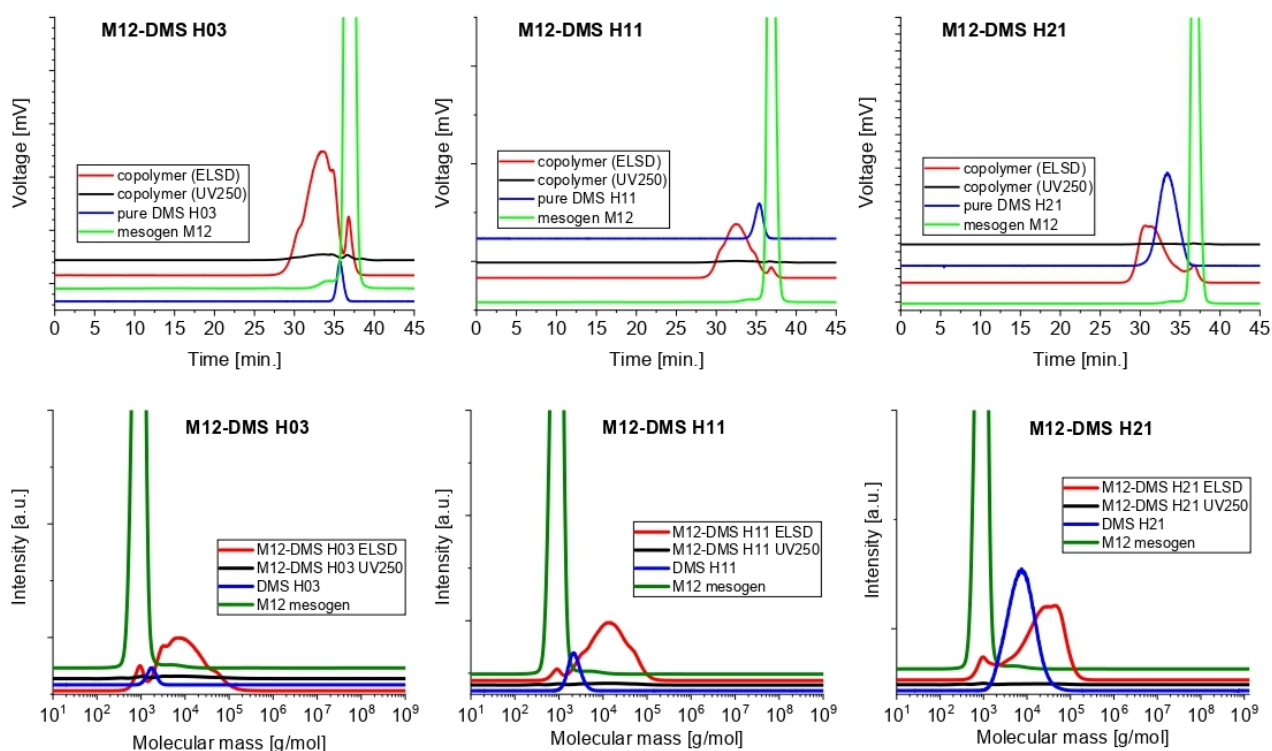
M12-DMS H03

nr.	Max. RT	Start RT	End RT	flow rate correction	Mp	Mn	Mw	Mz	PD	I [mV]	I [%]
1	33.47	28.01	36.12	1	7530	6299	16226	41758	2.5759	46.42	67.88
x	36.79	36.12	39.23	1	951	855	916	973	1.0720	21.96	32.12

M12-DMS H11

nr.	Max. RT	Start RT	End RT	flow rate correction	Mp	Mn	Mw	Mz	PD	I [mV]	I [%]
1	32.44	28.05	36.24	1	14345	8391	20149	40997	2.4012	55.01	83.47
x	36.88	36.24	39.65	1	897	822	878	928	1.0673	10.89	16.53

M12-DMS H21

nr.	Max. RT	Start RT	End RT	flow rate correction	Mp	Mn	Mw	Mz	PD	I [mV]	I [%]
1	30.70	27.97	35.52	1	42287	13541	32314	55708	2.3863	68.03	76.41
x	36.80	35.52	39.56	1	944	1008	1159	1310	1.1494	21.01	23.59

GPC trace of the copolymers: M12-H03, M12-H11 and M12-H21.
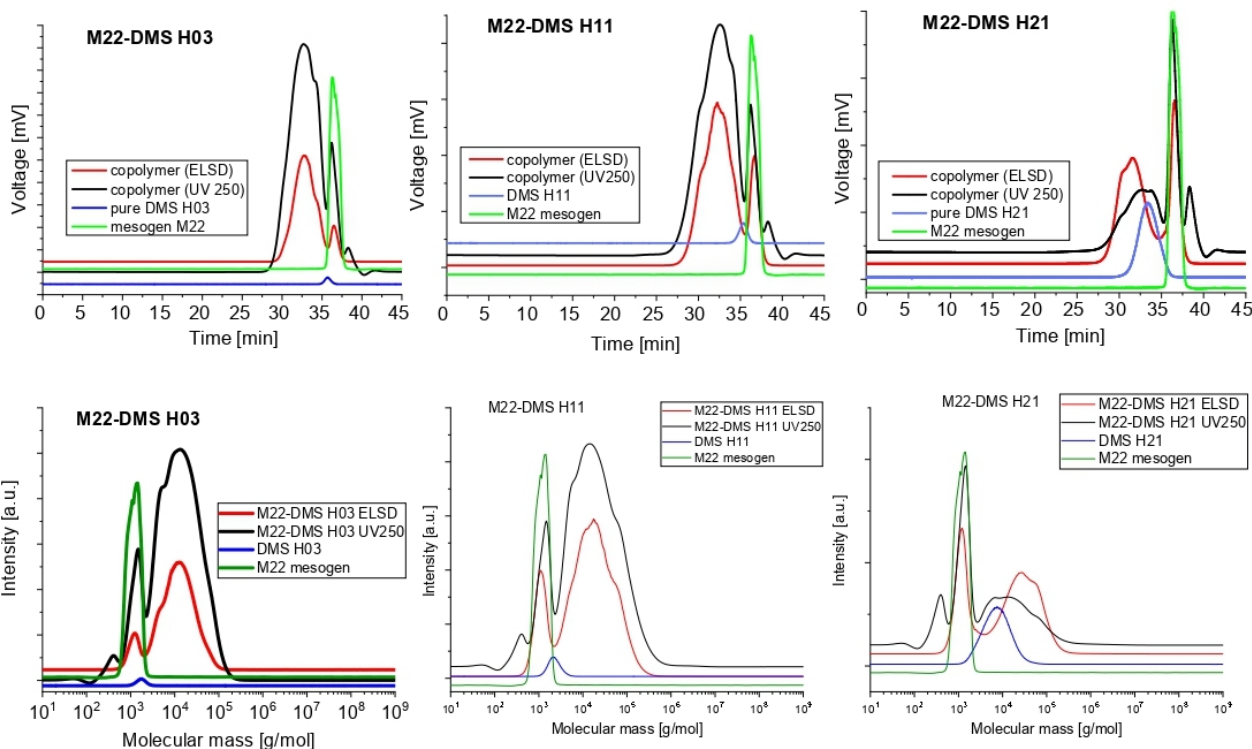
M22-DMS H03											
nr.	Max. RT	Start RT	End RT	flow rate correction	Mp	Mn	Mw	Mz	PD	I [mV]	I [%]
1	32.75	29.02	35.63	1	12868	9028	16436	28788	1.8206	238.44	74.74
x	36.56	35.63	38.88	1	1194	1130	1238	1343	1.0956	80.59	25.26
M22-DMS H11											
nr.	Max. RT	Start RT	End RT	flow rate correction	Mp	Mn	Mw	Mz	PD	I [mV]	I [%]
1	32.27	27.47	35.46	1	15917	10826	27170	62147	2.5098	289.92	59.68
x	36.74	35.46	39.49	1	978	961	1084	1215	1.1277	195.86	40.32
M22-DMS H21											
nr.	Max. RT	Start RT	End RT	flow rate correction	Mp	Mn	Mw	Mz	PD	I [mV]	I [%]
1	31.52	27.59	34.66	1	25441	21676	38268	62667	1.7654	136.86	37.66
x	36.58	34.66	38.38	1	1086	1003	1110	1242	1.1073	226.57	62.34

GPC trace of the copolymers: M22-H03, M22-H11 and M22-H21.
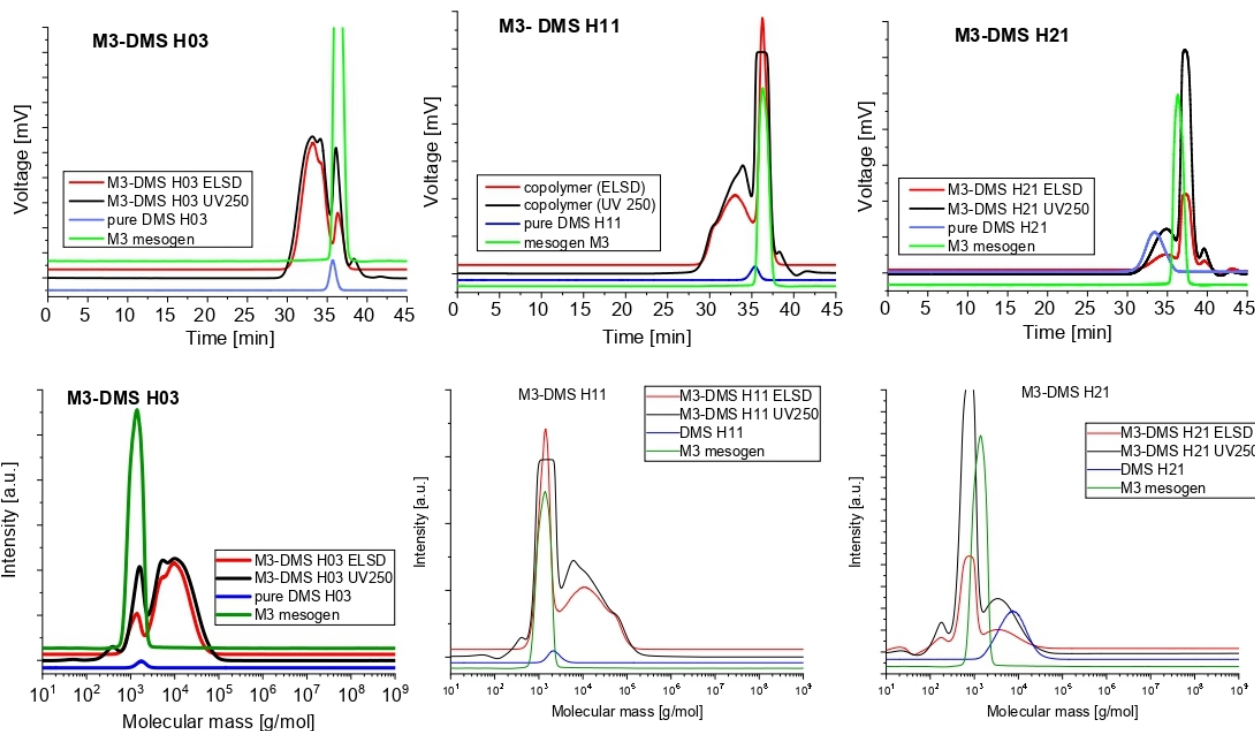
M3-DMS H03											
nr.	Max. RT	Start RT	End RT	flow rate correction	Mp	Mn	Mw	Mz	PD	I [mV]	I [%]
1	33.21	29.98	35.59	1	9611	8100	12151	17888	1.5001	177.99	74.15
x	36.34	35.59	37.75	1	1370	1159	1225	1289	1.0569	62.06	25.85

M3-DMS H11											
nr.	Max. RT	Start RT	End RT	flow rate correction	Mp	Mn	Mw	Mz	PD	I [mV]	I [%]
1	32.99	28.93	35.09	1	10167	11925	21945	37184	1.8402	111.39	15.79
x	36.28	35.09	38.05	1	1307	1127	1212	1296	1.0754	594.24	84.21

M3-DMS H21											
nr.	Max. RT	Start RT	End RT	flow rate correction	Mp	Mn	Mw	Mz	PD	I [mV]	I [%]
1	31.85	28.81	35.59	1	23845	14431	24809	37760	1.7191	465.13	74.12
x	36.32	35.59	39.14	1	1511	1297	1391	1477	1.0724	162.40	25.88

GPC trace of the copolymers: M3-H03, M3-H11 and M3-H21.

Characterization of molecular mass of the prepared copolymers, as obtained by GPC; data obtained for the precursors are also listed for comparison.

Sample	GPC: Peak maximum [g/mol]	GPC: Mn from automatic evaluation [g/mol]	GPC: PD (autom.) [-]	Mn from producer [g/mol]
M12	973	850	1.11	562.736
M22	1 506	1009	1.14	682.842
M3	1 370	1 323	1.09	758.938
DMS H03	1 759	1 595	1.11	450±50
DMS H11	2 157	2 105	1.12	1 050±50
DMS H21	7 367	5 710	1.63	4 500±500
M12-co-H03	7650	6299	2.58	x
M12-co-H11	14 066	8391	2.40	x
M12-co-H21	27 019 ?	13541	2.39	x
M22-co-H03	12 988	9028	1.82	x
M22-co-H11	14 600	10826	2.51	x
M22-co-H21	26 300	21676	1.77	x
M3-co-H03	5 220 ?	8100	1.50	x
M3-co-H11	10 750	11925	1.84	x
M3-co-H21	3 600 ?	14431	1.72	x

Number of macro-monomeric units.

Sample name	Number of monomeric units (consisting of LC unit and PDMS chain) according GPC
M12-co-H03	5.31
M12-co-H11	4.77
M12-co-H21	2.54
M22-co-H03	6.91
M22-co-H11	5.76
M22-co-H21	3.98
M3-co-H03	5.86
M3-co-H11	6.1
M3-co-H21	2.61